Pertanika Journal of

SCIENCE & TECHNOLOGY

JST

VOL. 31 (4) JUL. 2023

PERTANIKA JOURNALS

A scientific journal published by Universiti Putra Malaysia Press

Pertanika Journal of Science & Technology
Pertanika Journal of Science & Technology

PERTANIKA JOURNAL OF SCIENCE & TECHNOLOGY

About the Journal

Overview

Pertanika Journal of Science & Technology is an official journal of Universiti Putra Malaysia. It is an open-access online scientific journal. It publishes original scientific outputs. It neither accepts nor commissions third party content.

Recognised internationally as the leading peer-reviewed interdisciplinary journal devoted to the publication of original papers, it serves as a forum for practical approaches to improve quality on issues pertaining to science and engineering and its related fields.

Pertanika Journal of Science & Technology currently publishes 6 issues a year (*January, March, April*, *July, August,* and *October*). It is considered for publication of original articles as per its scope. The journal publishes in **English** and it is open for submission by authors from all over the world.

The journal is available world-wide.

Aims and scope

Pertanika Journal of Science & Technology aims to provide a forum for high quality research related to science and engineering research. Areas relevant to the scope of the journal include: bioinformatics, bioscience, biotechnology and bio-molecular sciences, chemistry, computer science, ecology, engineering, engineering design, environmental control and management, mathematics and statistics, medicine and health sciences, nanotechnology, physics, safety and emergency management, and related fields of study.

History

Pertanika Journal of Science & Technology was founded in 1993 and focuses on research in science and engineering and its related fields.

Vision

To publish a journal of international repute.

Mission

Our goal is to bring the highest quality research to the widest possible audience.

Quality

We aim for excellence, sustained by a responsible and professional approach to journal publishing. Submissions can expect to receive a decision within 90 days. The elapsed time from submission to publication for the articles averages 180 days. We are working towards decreasing the processing time with the help of our editors and the reviewers.

Abstracting and indexing of Pertanika

Pertanika Journal of Science & Technology is now over 27 years old; this accumulated knowledge and experience has resulted the journal being abstracted and indexed in SCOPUS (Elsevier), Clarivate Web of Science (ESCI), EBSCO, ASEAN CITATION INDEX, Microsoft Academic, Google Scholar, and MyCite.

Citing journal articles

The abbreviation for Pertanika Journal of Science & Technology is *Pertanika J. Sci. & Technol.*

Publication policy

Pertanika policy prohibits an author from submitting the same manuscript for concurrent consideration by two or more publications. It prohibits as well publication of any manuscript that has already been published either in whole or substantial part elsewhere. It also does not permit publication of manuscript that has been published in full in proceedings.

Code of Ethics

The *Pertanika* journals and Universiti Putra Malaysia take seriously the responsibility of all of its journal publications to reflect the highest in publication ethics. Thus, all journals and journal editors are expected to abide by the journal's codes of ethics. Refer to *Pertanika*'s **Code of Ethics** for full details, or visit the journal's web link at http://www.pertanika.upm.edu.my/code_of_ethics.php

Originality

The author must ensure that when a manuscript is submitted to *Pertanika*, the manuscript must be an original work. The author should check the manuscript for any possible plagiarism using any program such as Turn-It-In or any other software before submitting the manuscripts to the *Pertanika* Editorial Office, Journal Division.

All submitted manuscripts must be in the journal's acceptable similarity index range:

≤ 20% – PASS; > 20% – REJECT.

International Standard Serial Number (ISSN)

An ISSN is an 8-digit code used to identify periodicals such as journals of all kinds and on all media–print and electronic.

Pertanika Journal of Science & Technology: e-ISSN 2231-8526 (Online).

Lag time

A decision on acceptance or rejection of a manuscript is reached in 90 days (average). The elapsed time from submission to publication for the articles averages 180 days.

Authorship

Authors are not permitted to add or remove any names from the authorship provided at the time of initial submission without the consent of the journal's Chief Executive Editor.

Manuscript preparation

For manuscript preparation, authors may refer to Pertanika's **INSTRUCTION TO AUTHORS**, available on the official website of *Pertanika*.

Editorial process

Authors who complete any submission are notified with an acknowledgement containing a manuscript ID on receipt of a manuscript, and upon the editorial decision regarding publication.

Pertanika follows a **double-blind peer-review** process. Manuscripts deemed suitable for publication are sent to reviewers. Authors are encouraged to suggest names of at least 3 potential reviewers at the time of submission of their manuscripts to *Pertanika*, but the editors will make the final selection and are not, however, bound by these suggestions.

Notification of the editorial decision is usually provided within 90 days from the receipt of manuscript. Publication of solicited manuscripts is not guaranteed. In most cases, manuscripts are accepted conditionally, pending an author's revision of the material.

The journal's peer review

In the peer-review process, 2 to 3 referees independently evaluate the scientific quality of the submitted manuscripts. At least 2 referee reports are required to help make a decision.

Peer reviewers are experts chosen by journal editors to provide written assessment of the **strengths** and **weaknesses** of written research, with the aim of improving the reporting of research and identifying the most appropriate and highest quality material for the journal.

Operating and review process

What happens to a manuscript once it is submitted to *Pertanika*? Typically, there are 7 steps to the editorial review process:

1. The journal's Chief Executive Editor and the Editor-in-Chief examine the paper to determine whether it is relevance to journal needs in terms of novelty, impact, design, procedure, language as well as presentation and allow it to proceed to the reviewing process. If not appropriate, the manuscript is rejected outright and the author is informed.

2. The Chief Executive Editor sends the article-identifying information having been removed, to 2 to 3 reviewers. They are specialists in the subject matter of the article. The Chief Executive Editor requests that they complete the review within 3 weeks.

   Comments to authors are about the appropriateness and adequacy of the theoretical or conceptual framework, literature review, method, results and discussion, and conclusions. Reviewers often include suggestions for strengthening of the manuscript. Comments to the editor are in the nature of the significance of the work and its potential contribution to the research field.

Pertanika Journal of Science & Technology
Pertanika Journal of Science & Technology

3. The Editor-in-Chief examines the review reports and decides whether to accept or reject the manuscript, invite the authors to revise and resubmit the manuscript, or seek additional review reports. In rare instances, the manuscript is accepted with almost no revision. Almost without exception, reviewers' comments (to the authors) are forwarded to the authors. If a revision is indicated, the editor provides guidelines for attending to the reviewers' suggestions and perhaps additional advice about revising the manuscript.

4. The authors decide whether and how to address the reviewers' comments and criticisms and the editor's concerns. The authors return a revised version of the paper to the Chief Executive Editor along with specific information describing how they have addressed' the concerns of the reviewers and the editor, usually in a tabular form. The authors may also submit a rebuttal if there is a need especially when the authors disagree with certain comments provided by reviewers.

5. The Chief Executive Editor sends the revised manuscript out for re-review. Typically, at least 1 of the original reviewers will be asked to examine the article.

6. When the reviewers have completed their work, the Editor-in-Chief examines their comments and decides whether the manuscript is ready to be published, needs another round of revisions, or should be rejected. If the decision is to accept, the Chief Executive Editor is notified.

7. The Chief Executive Editor reserves the final right to accept or reject any material for publication, if the processing of a particular manuscript is deemed not to be in compliance with the S.O.P. of *Pertanika*. An acceptance letter is sent to all the authors.

   The editorial office ensures that the manuscript adheres to the correct style (in-text citations, the reference list, and tables are typical areas of concern, clarity, and grammar). The authors are asked to respond to any minor queries by the editorial office. Following these corrections, page proofs are mailed to the corresponding authors for their final approval. At this point, **only essential changes are accepted**. Finally, the manuscript appears in the pages of the journal and is posted on-line.

Pertanika Journal of

SCIENCE & TECHNOLOGY

Vol. 31 (4) Jul. 2023

A scientific journal published by Universiti Putra Malaysia Press

PJST

Pertanika Journal of Science & Technology

AN INTERNATIONAL PEER-REVIEWED JOURNAL

EDITORIAL OFFICE

JOURNAL DIVISION
Putra Science Park
1st Floor, IDEA Tower II
UPM-MTDC Technology Centre
Universiti Putra Malaysia
43400 Serdang, Selangor Malaysia.

General Enquiry
Tel. No: +603 9769 1622 | 1616
E-mail:
executive_editor.pertanika@upm.edu.my
URL: www.journals-jd.upm.edu.my

PUBLISHER

UPM Press
Universiti Putra Malaysia
43400 UPM, Serdang, Selangor, Malaysia.
Tel: +603 9769 8851
E-mail: penerbit@putra.upm.edu.my
URL: http://penerbit.upm.edu.my

ABSTRACTING AND INDEXING OF PERTANIKA JOURNALS

The journal is indexed in SCOPUS (Elsevier), Clarivate-Emerging Sources Citation Index (ESCI), BIOSIS, National Agricultural Science (NAL), Google Scholar, MyCite, ISC. In addition, Pertanika JSSH is recipient of "CREAM" Award conferred by Ministry of Higher Education (MoHE), Malaysia.

Pertanika Journal of Science & Technology
Vol. 31 (4) Jul. 2023

Contents

Foreword

Welcome to the fourth issue of 2023 for the Pertanika Journal of Science and Technology (PJST)!

PJST is an open-access journal for studies in Science and Technology published by Universiti Putra Malaysia Press. It is independently owned and managed by the university for the benefit of the world-wide science community.

This issue contains 30 articles; one short communication, two review articles and the rest are regular articles. The authors of these articles come from different countries namely Bangladesh, Belgium, England, India, Indonesia, Iraq, Japan, Malaysia, Mexico, Mozambique, Nigeria, Russia, Saudi Arabia and Thailand.

A review article titled "Knowledge mapping trends of Internet of Things (IoT) in plant disease and insect pest study: A visual analysis" was written by Muhammad Akmal Mohd Zawawi and colleagues from Malaysia and Indonesia. The primary aim of their review is to identify the current trends and explore hot topics of IoT in plant disease and insect pest research for future research direction via VOSviewer and R programming. A few highlights can be drawn from this study. First, global IoT application publication trends in plant disease and insect pest studies have grown for 12 years. This subject area is still an emerging topic with an annual scientific production growth rate of 48.74%. Second, the most productive country, such as India and China, produced 52% of the scientific document in the studied field. Collaboration among different countries in publishing research articles increases the published materials' visibility and quality. Third, integration between cross-multidisciplinary knowledge domains such as machine learning, deep learning, image processing, and artificial intelligence for crop monitoring and decision support systems can produce excellent crop yield and reduce dependency on human resources. Detailed information on this study can be found on page 1621.

Norliza Dzakaria and co-researchers from Malaysia evaluated the Effect of Transition Metals Addition on the Nickel Oxide (NiO) Catalyst toward Reduction Behaviour in the Carbon Monoxide Atmosphere. This research revealed that the reduction reaction obeyed the consecutive mechanism, and NiO was completely reduced to Nickel (Ni). The 3% cerium-doped nickel oxide (Ce/NiO) possessed a higher surface. Furthermore, adding Ce to NiO enhanced a lower reduction temperature than adding cobalt, molybdenum, tungsten, and zirconium. Adding Ce to the NiO shifted the temperature-programmed reduction peaks to the lower temperature. It can be concluded that the reduction temperature of NiO decreases by the Ce with 3% Ce loading, which is sufficient to reduce NiO to Ni at 370°C. Further details of the article are available on page 1717.

Another article that we wish to highlight is “The correlation of stromelysin-1 and tissue inhibitor of metalloproteinase-1 with lipid profile and atherogenic indices in end-stage renal disease patients: A neural network study” by Habiba Khdair Abdalsada et al. from Iraq. They assessed stromelysin-1, TIMP1, and lipid profile parameters in the serum of 60 ESRD patients and 30 healthy controls. A neural network study was conducted to determine the best factors for predicting ESRD patients more susceptible to developing CVD using the cut-off value of the atherogenic index of plasma (AIP) >0.24. There is a state of dyslipidemia with high atherogenic indices and increased stromelysin-1 and TIMP1 in ESRD patients. The increase in stromelysin-1 and its inhibitor are correlated with some atherogenic indices and lipids. The neural network results indicated good predictability of the top four parameters (stromelysin-1, followed by eGFR, TIMP1, and the TIMP-1/stromelysin-1 ratio) in discriminating between ESRD patients with high risk for CVD from the lower-risk patients. Detailed information on this study is presented on page 2067.

We anticipate that you will find the evidence presented in this issue to be intriguing, thought-provoking and useful in reaching new milestones in your own research. Please recommend the journal to your colleagues and students to make this endeavour meaningful.

All the papers published in this edition underwent Pertanika’s stringent peer-review process involving a minimum of two reviewers comprising internal as well as external referees. This was to ensure that the quality of the papers justified the high ranking of the journal, which is renowned as a heavily-cited journal not only by authors and researchers in Malaysia but by those in other countries around the world as well.

We would also like to express our gratitude to all the contributors, namely the authors, reviewers, Editor-in-Chief and Editorial Board Members of PJST, who have made this issue possible.

PJST is currently accepting manuscripts for upcoming issues based on original qualitative or quantitative research that opens new areas of inquiry and investigation.

Chief Executive Editor
executive_editor.pertanika@upm.edu.my

Pertanika J. Sci. & Technol. 31 (4): 1605 - 1619 (2023)

PERTANIKA JOURNALS

SCIENCE & TECHNOLOGY

Journal homepage: http://www.pertanika.upm.edu.my/

Optimization of Sugarcane Bagasse Conversion Technologies Using Process Network Synthesis Coupled with Machine Learning

Constantine Emparie Tujah[1], Rabiatul Adawiyah Ali[1] and Nik Nor Liyana Nik Ibrahim[1,2]*

[1]Department of Chemical and Environmental Engineering, Faculty of Engineering, Universiti Putra Malaysia, 43400 UPM, Serdang, Selangor, Malaysia
[2]Sustainable Process Engineering Research Centre (SPERC), Faculty of Engineering, Universiti Putra Malaysia, 43400 UPM, Serdang, Selangor, Malaysia

ABSTRACT

Sugarcane bagasse is a commonly generated item from the food industry in the world—the amount of sugarcane bagasse production is increasing yearly. In 2017, the reported sugarcane production in Malaysia was 30,000 kg, which resulted in 9,800 kg of sugarcane bagasse. Sugarcane bagasse produces steam as waste management in Malaysia or simply in landfills. This study aims to optimize sugarcane bagasse conversion technologies using process network synthesis. A superstructure of sugarcane bagasse was created via P-Graph, with multiple pathways or processes being considered. Data needed for the sustainability assessment of each pathway was acquired from various journal sources, including conversion fraction, operating and capital cost, greenhouse gas emission, and the selling price of products were implemented into the superstructure. Then, the data from the feasible structure generated would be analyzed using machine learning via Waikato Environment for Knowledge Analysis software. The data sets were analyzed using this software using the selected algorithm as P-graph developed 17 feasible solution structures. All 17 generated solution structures were analyzed using six different classifier algorithms. The multilayer perceptron algorithm had the best and the least error in classifying the data. Hence, the multilayer perceptron algorithm proved that the correlation between products produced from sugarcane bagasse and the profitability of the process was significant. Therefore, the model can be a basis for determining the best process for sugarcane bagasse conversion technologies.

Keywords: Biomass conversion technologies, machine learning, process network synthesis, sugarcane bagasse

ARTICLE INFO

Article history:
Received: 09 September 2021
Accepted: 24 February 2022
Published: 24 May 2023

DOI: https://doi.org/10.47836/pjst.31.4.01

E-mail addresses:
constantineemparie@gmail.com (Constantine Emparie Tujah)
adwyhali@gmail.com (Rabiatul Adawiyah Ali)
niknorliyana@upm.edu.my (Nik Nor Liyana Nik Ibrahim)
* Corresponding author

ISSN: 0128-7680
e-ISSN: 2231-8526

INTRODUCTION

Saccharum officinarum L., or sugarcane, is a perennial grass that becomes the main source producing sugar for beverages and food. In this industry, the major by-product of sugarcane is bagasse (Sindhu et al., 2016). Bagasse is produced from the extraction or milling process, generating roughly 32 dry weights % from a ton of sugarcane (Ameram et al., 2019). Conversion technologies are the main pillar in accomplishing a zero-waste goal (Lee et al., 2020). Besides reducing greenhouse gas emissions, they also create a beneficial product. Conversion technologies can be categorized into four main conversion types, which will be the focal point here. Firstly, a thermal treatment with air without energy valorization converts waste into gaseous liquid and solid (Puna & Teresa, 2010). The most common thermal conversion technology currently used is burning sugarcane bagasse as fuel for the boiler. Besides, biochemical conversion comprises using yeast and/or specialized bacteria to produce useful energy by converting biomass or waste (Baker, 2018). The conversion of sugarcane bagasse via anaerobic digestion is considered an encouraging plan since the by-product of the process, digestate could be used as fertilizer, and the product from the fermentation, biogas, could be sold as a bio-methane gas by the sugarcane plants (Janke et al., 2015). In this biomass conversion technology, chemicals transform waste into valuable products (Baker, 2018). The process involves but is not limited to pyrolysis, depolymerization, hydrolysis, or gasification. The final type of conversion technology is physical or mechanical conversion. The complex lignocellulosic properties of sugarcane bagasse made them suitable for carbon sources for fungal cultures (Sidana & Farooq, 2014).

Many existing conversion technologies for sugarcane bagasse have advantages and disadvantages. Many research papers on viable sugarcane bagasse conversion technologies have been published. However, at the moment, there is a minimal study on the performance of conversion technologies for sugarcane bagasse to be placed in Malaysia. The sugarcane bagasse conversion technologies are not developing as projected, even though having several critical information regarding the sugarcane bagasse (Monteiro et al., 2016). Besides, the high initial capital investment and long payback period carry a significant financial risk, which caused investors to be skeptical about venturing into sugarcane bagasse management (Bufoni et al., 2016). Thus, optimizing sugarcane bagasse conversion technologies is vital by utilizing process network synthesis to compute the most optimal pathway.

Process network synthesis involves an algorithm to be followed in other problem-solving operations (Friedler et al., 1992). In solving the process network synthesis efficiently and rigorously, the P-graph framework provides a mathematical approach for solving process synthesis problems and analyzing the resultant flowsheets with the aid of the built-in optimizer (Bertok & Heckl, 2016). The P-graph includes selecting and sizing processing chemical plant predefined parameters such as raw material, operating unit, and conversion rate (Cabezas et al., 2015). The P-graph method offers advantages such as adding a graphical

interface, efficient algorithms, and optimal results (Varbanov et al., 2017). Machine learning is an application of artificial intelligence that uses intelligent software to enable machines to conduct their employment competently (Witten et al., 2017). Data mining is widely used in machine learning to discover knowledge (Negnevitsky, 2011). Data mining is a computer science subdomain that can execute an implicit extraction from databases. A set of algorithms have been designed to discover a pattern of knowledge (Kulkarni & Kulkarni, 2016). However, the classification process, which includes rules to separate raw data into a predefined class, has become a significant issue (Naik & Samant, 2016).

This study applied the P-graph model to optimize sugarcane bagasse conversion technologies in Malaysia. As a result, the optimal technology to manage sugarcane bagasse was selected. Waikato Environment for Knowledge Analysis (WEKA) offers a platform of an established learning algorithm that can be easily applied to the dataset. P-graph and WEKA applications for sugarcane bagasse conversion technologies are still limited. Most P-graph cases involved crops such as rice husks and palm oil biomass (Sangalang et al., 2021; Tin et al., 2017). The integration of P-graph and WEKA was introduced for the municipal solid waste management case study (Ali et al., 2021). Therefore, this study aimed to provide an integrated framework to increase the decision-making tool's efficiency for sugarcane bagasse conversion technologies. Hence in this paper, the focus was shifted to several of the latest available conversion technologies. These were analyzed using a process network synthesis and machine learning framework in determining the most feasible optimum and systematic pathways.

MATERIALS AND METHODS

General Framework

Figure 1 shows the steps for generating a feasible process flow diagram for sugarcane bagasse conversion technologies. This raw material will be converted into the intermediate and final product via network synthesis through four conversion types: biological, chemical, mechanical, and thermal. These conversion technologies were selected based on technologies commonly found to convert biomass. Working with process network synthesis requires data collection for conversion technologies' efficiency and capital and operating expenditure. Common conversion technologies help to design a complete process flow for the superstructure. The sugarcane bagasse undergoes anaerobic digestion to produce biogas and bioethanol for the biological pathway. Also, the mechanical or physical conversion would grind the raw material into smaller sizes to produce brick supplement, fungal culture, and multi-armor composite.

On the other hand, thermal conversion has an intermediate product, high-pressure steam, for electricity generation and other uses at the plant. The intermediate product of this process is ash from the burned sugarcane bagasse. This intermediate product will be

further mechanically processed to produce supplementary cement. This research study uses a P-graph model to analyze sugarcane bagasse conversion technologies' economic performance and environmental impact. It evaluated the selected and optimized pathway of sugarcane bagasse conversion technologies.

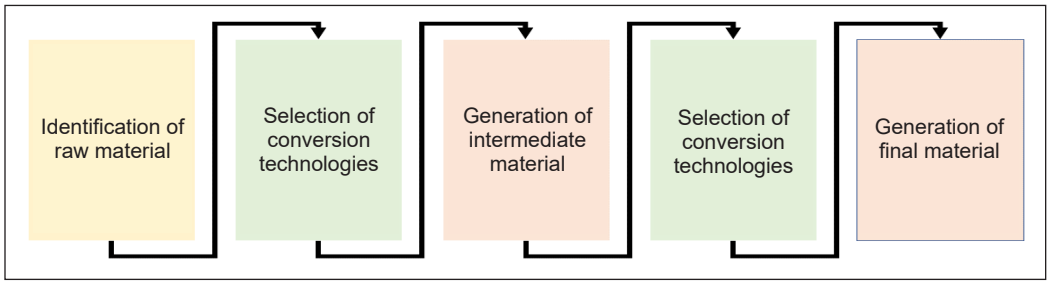

Figure 1. Process flow diagram for generation of sugarcane bagasse conversion technologies

Methodology for Process Network Synthesis

Identification of Materials and Streams. In this study, there is only one process feedstock. There are ten types of output or products along with their intermediate product. Table 1 shows the list of raw materials, intermediate products, and outputs of the process.

Table 1
List of material considered in this study

No	Symbols	P-Graph Classification	Description
1	SCB	Raw Material	Sugarcane Bagasse
2	COM_GAS	Intermediate Product	Combustible gas from the burning of sugarcane bagasse in an incinerator
3	Biochar	Output	Biochar
4	SCBA	Intermediate Product	Sugarcane bagasse ash, a by-product from the incineration of raw material
5	ETOH	Output	Bio-ethanol from fermentation
6	Electricity	Output	Electricity generated
7	Heat	Output	Heat generated
8	Methane	Intermediate product	Methane from an anaerobic digester
9	Digestate	Intermediate product	A by-product from the fermentation process
10	Grinded_SCB	Output	Ground sugarcane bagasse by using a grinder
11	Liquid_Fertilizer	Output	Fertilizer in a liquid state that is produced from digestate after treatment
12	Solid_Fertilizer	Output	Fertilizer in solid-state that is produced from digestate after treatment
13	GHG_Emission	Output	Greenhouse gases emission from conversion technologies

Note. Two inputs need to be inserted into the p-graph model: price and flow rate of the material and product.

Identification of Operating Units. For this case study, 11 operating units are included in the flowsheet-generation problem, as shown in Table 2, to be solved algorithmically with P-graphs.

Table 2
List of operating units considered in this study

No	Symbols	Description
1	COMBUSTION	Incinerator for sugarcane bagasse
2	BOILER	Boiler for the generation of heat and electricity.
3	AD	Anaerobic digester.
4	GAS_TURBINE	Turbine for the generation of heat and electricity.
5	F_D_ACID	Fermentation with dilute acid pre-treatment.
6	F_D_ALKALINE	Fermentation with dilute alkaline pre-treatment.
7	F_HW	Fermentation with hot water pre-treatment.
8	F_SE	Fermentation with steam explosion pre-treatment.
9	AD	Anaerobic digestion.
10	GASIFICATION	The gasifying process generates heat and electricity
11	GRINDER	Grinding machine that makes the sugarcane bagasse into smaller sizes.
12	Pre-treatment	Treatment for digestate to produce fertilizers.
13	Landfilling	Landfilling for waste

Note. Two inputs need to be inserted into the p-graph model: price and conversion to the material's product.

Maximal Superstructure and Solution Structure Generation. The maximal structure generation (MSG) and solution structure (SSG) algorithms execute the P-graph task. As aforementioned, MSG creates a union of all feasible solution structures, whereas SSG identifies the maximum combinatorically feasible solution structures while eliminating the unfeasible solutions from the results. Besides, SSG also allows the determination of an optimal structure for each feasible network. The generation of MSG and SSG ensures the network's consistency. Major processes and operating units are labeled in the superstructure. Overall performance data, such as conversion yield, are incorporated into the process and cluster operations.

Optimization of Superstructure. The SSG algorithm's generated result is selected using an accelerated branch-and-bound (ABB) algorithm to design an optimum process network where information such as flow rates and costs are added. As a result, the optimum feasible solution which provides the best and near-optimum is selected. The feasible solutions are further evaluated based on their environmental impact and economic performance. In this research, 2 cases are being considered: the design for maximum economic performance and minimal environmental impact.

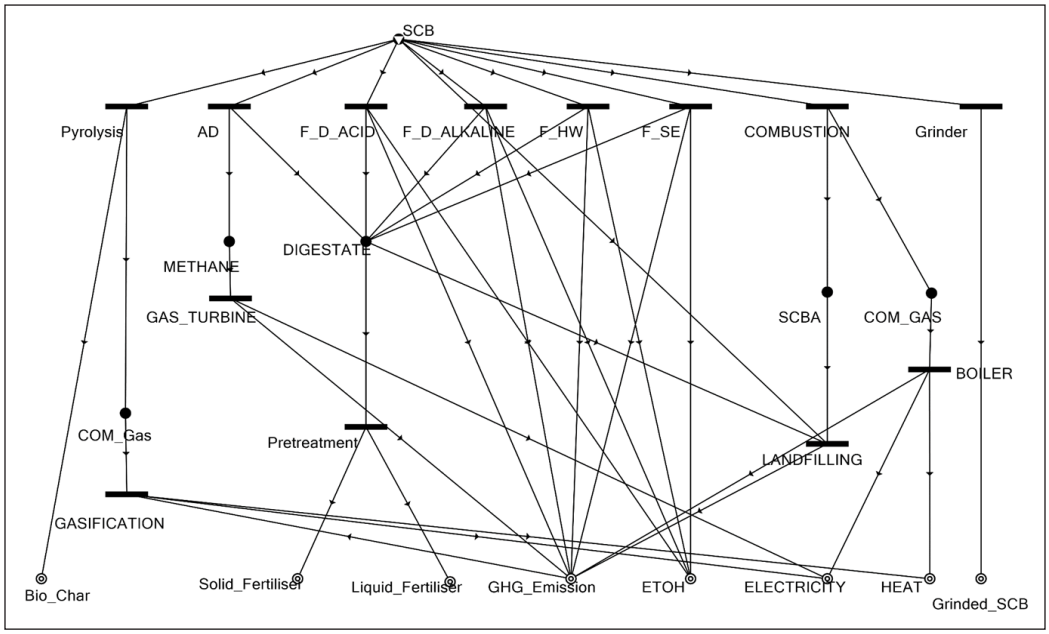

Figure 2. Superstructure for sugarcane bagasse conversion technologies

Integration of Machine Learning

The integration of Machine Learning to process network synthesis was done using WEKA. WEKA is a machine learning software that identifies hidden information from a raw dataset. This research analyzed the raw dataset using a set of algorithms. Six algorithms were selected to conduct the classification process in this research. The algorithms used are Logistics, Simple Logistics, Multilayer Perceptron, Stochastic Gradient Descent, IBk, and Kstar.

Simple Logistics is a simplified algorithm to encapsulate linear logistic regression. In WEKA, the Logistic algorithm was built based on multinomial logistic regression with a ridge estimator to build a class. The model for this algorithm fits the model's simple and stable process, which resulted in a low variance with a potentially high bias (Landwehr et al., 2003).

Implementing Stochastic Gradient Descent in WEKA is used to learn several linear models, such as binary class logistic regression and squared loss. In addition, the Multilayer Perceptron algorithm is assumed as a provider for nonlinear modeling between an input vector and a corresponding output vector. Besides being capable of modeling higher-order statistics, the algorithm can become an efficient prediction filter for nonlinear series because of their nonlinear nature (Gupta & Sinha, 2000).

In WEKA, the nearest neighbor algorithm was implemented in the form IBk algorithm, which selects the appropriate K value based on cross-validation. The next algorithm is an

instance-based classifier, a classification of test instances based on the class of the training instances that are similar to it. However, the difference between this algorithm and the other instance-based learner is that it uses an entropy-based distance function (Cleary & Trigg, 1995). The WEKA implementation for this is K* algorithm.

The acquired data from feasible solution structures were assembled in how the data can be mined using a group of algorithms in Explorer WEKA. All these algorithms are available in the WEKA feature, which is Explorer. Thus, the detailed result of the feasible solution structure was analyzed using WEKA. The 2 raw datasets involved in machine learning are product flow rate and its profitability and type of product and its profitability.

Each algorithm trained the dataset by allocating 70% of the data set to be analyzed and subsequently trained. Meanwhile, 30% of the data was used as a validation set. The performance of each algorithm is compared. The performance of each model was observed based on the model kappa statistics value, mean absolute error, root mean squared error, percentage relative absolute error, and percentage root relative squared error.

The algorithm that managed to identify hidden information with a significant performance that resulted in the least error would be chosen to be used as the algorithm the basis for decision tools.

RESULTS AND DISCUSSION

Simulation and Selection of the Best Solution Structures

Seventeen feasible solution structures have been produced by utilizing P-Graph Studio—all 17 feasible structures as attached in the supplementary data section. The structures were computed by Accelerated Branch and Bound (ABB) algorithm. The algorithm produced the most optimized solution structures of a Process Network Synthesis with a high-efficiency determination by reducing solution space. It eradicated any amalgamation of infeasible and superfluous solutions. Every solution structure produced is a subset of the maximal solution structure, signifying a probable network confirmation for the process network synthesis problem. ABB algorithm could also identify the best resolution with a specified set of conditions. All 17 produced feasible solution structures have been chosen to be acknowledged and scrutinized. The best solution structures were chosen from out of 17, which involved some operating units. The best solution structures will be further discussed.

Eight main operating units were included in the process network synthesis as conversion technologies to convert the sugarcane bagasse into products (Figure 2). The eight operating units involved three conversion technologies: biological, thermal, and mechanical. Also, five intermediate operating units converted either the intermediary product into the final product or by-products from the main operating units.

One of the biological conversion technologies was fermentation with four different pre-treatment types: dilute acid pre-treatment, dilute alkaline pre-treatment, hot water

pre-treatment, and steam explosion pre-treatment. The main product of these conversion technologies was bio-ethanol. Another biological conversion technology was an anaerobic digester that yielded methane as its main product. Both rendered the same by-product, specifically digestate, produced during the distillation process of ethanol.

Meanwhile, for thermal conversion and mechanical conversion, each had one primary operating and process, which were pyrolysis and incinerator that produced bio-char and combustible gas, respectively as their main products, and grinder, which simply grinds sugarcane bagasse into smaller sizes as a raw material in the manufacturing of fungal substrate, composite of multi-layered armor, and brick production.

As for the intermediate operating units, combustible gas from pyrolysis and incinerator went through the gasification process and boiler to produce heat for steam production, electricity, and greenhouse gases. The combustible gas production by incinerator generated a sugarcane bagasse ash, which can be sold to manufacturers of brick or cement as supplementary material. Methane, the main product of an anaerobic digester, could generate electricity via a gas turbine. The digestate from biological conversion technologies was in a significant amount. Practically, this by-product would undergo treatment to be transformed into fertilizers.

These conversion technologies and their product were compared to the performance of landfilling as the most common method for waste management in Malaysia. Based on the superstructure diagram in Figure 2, P-graph represents the sugarcane bagasse process network. Each conversion structure was specifically designated with its required information, such as the conversion rate of raw material to its respective product, capital, operating cost of conversion technologies, and the selling price of the product.

Only one raw material was analyzed in this research, namely sugarcane bagasse. The amount of raw material used was acquired from Malaysia's maximum value of sugarcane bagasse. All structures involved different conversion technologies and different types of products with varying volumes. Thus, the total net profit and the emission of greenhouse gases differed with various conversion technologies. All generated feasible solution structures did not

Table 3
Summary of greenhouse gases emission and net profit

Solution structures	Net profit/ year (MYR)	Greenhouse gases emission/year (m^3)
Solution 1	8,894.01	2,006.40
Solution 2	8,652.88	3,244.80
Solution 3	7,982.90	1,958.40
Solution 4	6,426.90	-
Solution 5	6,099.25	2,880.00
Solution 6	3,619.00	-
Solution 7	-15,760.10	-
Solution 8	-19,561.98	2,006.40
Solution 9	-20,129.64	1,958.40
Solution 10	-21,282.58	3,244.80
Solution 11	-22,404.30	2,880.00
Solution 12	-30,315.96	-
Solution 13	-31,607.28	2,666.40
Solution 14	-48,295.92	-
Solution 15	-61,014.36	2,666.40
Solution 16	-82,740.48	-
Solution 17	-319,971.55	288.00

include landfilling as part of the solutions. The result from P-Graph was assorted according to the best structures that granted the highest net profit with 8,000 working hours per year for inclusive plant operation in 10 years. Table 3 summarizes greenhouse gas emissions and net profit for each feasible solution structure.

Out of the 17 feasible solution structures, only 6 were profitable, as in Table 3, with the highest profit being 8,894.01 MYR per year. The greenhouse gas emission simulated using the P-Graph Studio for each solution structure was exhibited in Table 4 with the operating unit that influenced the emission rate as in Table 3. The result showed that 6 of 17 feasible solution structures produced no greenhouse gases. The highest generation of the gases involved all fermentation with varying pre-treatment processes. Apart from that, boiler and gas turbines also produce greenhouse gases.

Table 4
Summary of involved operating unit that affected the GHG emission

Types of operating units	Availability in feasible structure
Boiler	Structure 17
Fermentation with dilute acid pre-treatment	Structure 2 Structure 10
Fermentation with dilute alkaline pre-treatment.	Structure 3 Structure 9
Fermentation with hot water pre-treatment	Structure 1 Structure 8
Fermentation with steam explosion pre-treatment.	Structure 5 Structure 11
Gas Turbine	Structure 13 Structure 15

Maximum Economic Performance Model

Six feasible solution structures were profitable out of 17. These 6 solution structures only produced a single final product for each pathway, as in Table 5. From 6, only 4 profitable solution structures produced bioethanol. The 4 profitable solution structures were feasible 1,2,3 and 5. Even though the amount of digestate produced for each fermentation process is significant, the by-product did not undergo further processes to be converted into a value-added product, namely fertilizer. It was because of the high cost of operating units of digestate treatment. The P-Graph Studio did, however, simulate a process pathway that included additional processing of digestate. The generated pathways were represented in the feasible solution structures 9, 10, 11, and 12. All of them had an enormous operating cost which caused the cost of the product to fail to generate any profit. Meanwhile, feasible solution structures 4 and 6 yielded biochar and ground sugarcane bagasse.

A comparison study was conducted for the 6 profitable structures to maximize the use of sugarcane bagasse to generate a significant turnover. The imminent values that were highlighted were net profit margin and payback period. The net profit margin was calculated by dividing net profit by revenue. At the same time, the payback period was vital to know the duration to regain the investment. This information is shown in Table 6.

Based on the tabulated data in Table 6, solution structure 6 is the most attractive economic model. However, since solution structure 6 product was ground sugarcane

bagasse, the market for this product is small compared to bioethanol and biochar. Hence, solution structure 1 was chosen as the best model for maximum economic performance, producing bioethanol.

Table 5
Summary of product produced for each solution structure

Types of products	Availability in feasible structure
Biochar	Structure 4
	Structure 7
	Structure 14
	Structure 16
Electricity	Structure 7
	Structure 13
	Structure 14
	Structure 15
	Structure 16
	Structure 17
Bioethanol	Structure 1
	Structure 2
	Structure 3
	Structure 5
	Structure 7
	Structure 8
	Structure 9
	Structure 10
	Structure 11
Grinded Sugarcane Bagasse	Structure 6
Heat	Structure 7
	Structure 14
	Structure 16
	Structure 17
Liquid Fertilizer	Structure 8
	Structure 9
	Structure 10
	Structure 11
	Structure 12
	Structure 15
	Structure 16
Solid Fertilizer	Structure 8
	Structure 9
	Structure 10
	Structure 11
	Structure 12
	Structure 15
	Structure 16
Sugarcane Bagasse Ash	Structure 17
Methane	Structure 12

Table 6
Net profit margin and payback period for profitable pathway

Solution Structures	Net Profit Margin	Payback Period (year)
Solution 1	75%	2.49
Solution 2	73%	2.66
Solution 3	73%	2.73
Solution 4	74%	2.56
Solution 5	70%	3.04
Solution 6	75%	2.46

Minimum Environmental Impact Model

As aforementioned, out of 17 feasible solution structures, 6 solution structures produced no greenhouse gases. The greenhouse gas emission rate is summarized in Table 3. Notably, carbon dioxide gas was not considered a greenhouse house gas but a carbon neutral (Kiatkittipong et al., 2009). The emission of greenhouse gases originated from fuel consumption for each conversion technology. Also, in the case of landfilling, the escaped primary anaerobic compounds such as methane and ammonia gas contributed to the increase of greenhouse gases.

Thus, the feasible structure with the minimal environmental impact on the environment was solution structure 4. Besides the fact that this solution structure has zero greenhouse gases, it can also generate maximum economic performance. The operating unit that was involved in this solution structure was pyrolysis. Pyrolysis produced two products, an intermediary

product, and a final product. The final product was biochar, whereas the intermediary product was combustible gas. According to solution structure 4, the combustible gas was not being used by the gasification process due to the high investment cost of the gasifier.

On the other hand, solution structure 6 also proposed an acceptable, feasible pathway when considering both economic performance and environmental impact, albeit performing worse in the economy than solution structure 4. In this pathway, the sugarcane bagasse was simply ground into smaller sizes for the use of other manufacturers. The solution structure also only used a single operating unit. The operating unit, an industrial-sized grinder, only uses 13.37 kWh of electricity.

If economic performance were not considered, solution structures 7, 12, 14, and 16 would be viable options.

Integration of Machine Learning Via WEKA

P-Graph Studio generated 17 feasible solution structures on how to manage sugarcane bagasse. This set of data was further analyzed by data mining software called WEKA. The acquired data from feasible solution structures were assembled to determine how the data could be mined using a group of algorithms, as listed in Figure 3.

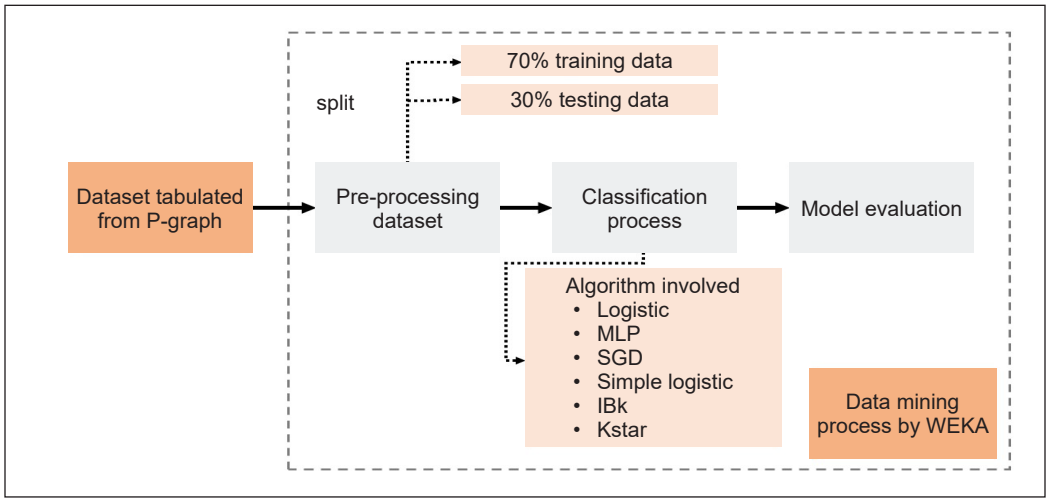

Figure 3. Flow diagram for the data classification process

Each algorithm trained the dataset by allocating 70% of the data set to be analyzed and subsequently trained. Meanwhile, 30% of the data was used as a validation set.

Correlation Between Product Flowrate and Profit

The correlation between product flow rate and profit from the generated data via P-Graph Studio was investigated using a group of algorithms mentioned earlier. In this case, the

product flow rate was kept in numerical form, maintaining its original value from the raw data. However, the profit for each solution structure was converted into nominal form, where a profitable solution structure will be classed as "YES," and an un-profitable solution structure, "NO." The performance for each algorithm was tabulated in Table 7.

Table 7
Performance for each algorithm for correlation of product flowrate and profit

Algorithm	Correctly Classified, %	Kappa Statistics	Mean absolute error	Root mean squared error	Relative absolute error, %	Root relative squared error, %
Logistic	66.67	0.40	0.33	0.58	55.17	85.89
Multilayer Perceptron	66.67	0.40	0.34	0.56	56.37	82.84
SGD	66.67	0.40	0.33	0.58	55.17	85.89
Simple Logistic	66.67	0.40	0.43	0.57	71.51	84.71
IBk	83.33	0.67	0.21	0.39	34.48	57.57
Kstar	83.33	0.67	0.25	0.46	41.38	67.90

By referring to tabulated results, algorithm IBk and KStar performed better than the others, correctly classifying 83.33% of the data. Whereas the other four algorithms only correctly classified 66.67% of the data. This result was reflected in the Kappa Statistics with 0.67 for IBk and Kstar. This analysis indicated a substantial correlation between product flow rate and profit.

Correlation Between Product and Profit

A similar procedure to the previous analysis, this data mining was performed to investigate the relationship between the final product and net profit generated for each feasible solution structure. Both data sets were input in the form of nominal. The result of each algorithm's performance was tabulated in Table 8.

Table 8
Performance for each algorithm for correlation of product and profit

Algorithm	Correctly Classified, %	Kappa Statistics	Mean absolute error	Root mean squared error	Relative absolute error, %	Root relative squared error, %
Logistic	66.67	0.40	0.33	0.58	55.17	85.89
Multilayer Perceptron	100.00	1.00	0.07	0.09	11.29	14.12
SGD	83.33	0.67	0.17	0.41	27.59	60.74
Simple Logistic	100.00	1.00	0.21	0.24	34.96	35.87
IBk	100.00	1.00	0.14	0.20	22.85	29.68
Kstar	100.00	1.00	0.14	0.23	23.67	34.70

Based on the result, four algorithms performed efficiently, correctly classifying the data with 100% accuracy. The algorithms were Multilayer Perceptron, Simple Logistic, IBk, and Kstar. The Multilayer Perceptron algorithm performed with the least error of the four algorithms. The result proved a significant relationship between the type of product produced and profitability.

In summary, 17 feasible structures were generated from the superstructure of sugarcane bagasse conversion technologies. Each feasible structure suggests a different pathway for sugarcane bagasse conversion technologies with different net profit and emission generation values. Two models were evaluated from feasible generated structures: maximal economic performance and minimal environmental impact. 6 feasible solution structures were profitable out of 17, while 6 solution structures produced no greenhouse gases. Besides, instead of manually selecting the best model for maximal economic performance and minimal environmental impact, WEKA helps analyze each dataset from the p-graph. For the algorithm model with the correlation between product flow rate and profit, the result was reflected in the Kappa Statistics with 0.67 for IBk and Kstar. At the same time, the Multilayer Perceptron algorithm performed with the 1 value of Kappa Statistic and the least error for the type of product produced and its profitability.

CONCLUSION

This study simulated the feasibility of sugarcane bagasse conversion technologies via process network synthesis. The model can be a basis for determining the best process for sugarcane bagasse conversion technologies. Besides, the relationship between parameters in this case study can be evaluated with machine learning. Machine learning proves that the types of products produced in sugarcane bagasse influenced the profitability of the process flow.

The information to set up the P-Graph was gathered from various resources. Therefore, this study is done with the limitation of information availability. The information needed for the costing aspect and conversion yield varied with different resources. Thus, a real case study in Malaysia should be conducted to acquire a more accurate simulation. Also, integrating Excel into WEKA would be useful and supplementary to an already robust data mining machine. This addition would simplify the analysis of each algorithm used in data mining via WEKA, as Excel is one of the most conventional and user-friendly software.

ACKNOWLEDGEMENT

The authors would like to thank those who have contributed and supported them throughout their journey of completing the study.

REFERENCES

Ali, R. A., Ibrahim, N. N. N., Ghani, W. A. W. A. K., Lam, H. L., & Sani, N. S. (2021). Utilization of process network synthesis and machine learning as decision-making tools for municipal solid waste management. *International Journal of Environmental Science and Technology, 19*, 1985-1996. https://doi.org/10.1007/s13762-021-03250-0

Ameram, N., Muhammad, S., Yusof, N. A. N., Ishak, S., Ali, A., Shoparwe, N. F., & Ter, T. P. (2019). Chemical composition in sugarcane bagasse: Delignification with sodium hydroxide. *Malaysian Journal of Fundamental and Applied Sciences*, *15*(2), 232-236. https://doi.org/10.11113/mjfas.v15n2.1118

Baker, J. (2018). *Biomass Conversion Technologies*. BBJ Group. https://www.bbjgroup.com/blog/biomass-conversion-technologies

Bertok, B., & Heckl, I. (2016). Process synthesis by the p-graph framework involving sustainability. In G. Ruiz-Mercado & H. Cabezas (Eds.), *Sustainability in the Design, Synthesis and Analysis of Chemical Engineering Processes* (pp. 203-225). Elsevier. https://doi.org/10.1016/b978-0-12-802032-6.00009-8

Bufoni, A. L., Oliveira, L. B., & Rosa, L. P. (2016). The declared barriers of the large developing countries waste management projects: The star model. *Waste Management*, *52*, 326-338. https://doi.org/10.1016/j.wasman.2016.03.023

Cabezas, H., Heckl, I., Bertok, B., & Friedler, F. (2015). Use the P-graph framework to design supply chains for sustainability. *Chemical Engineering Progress, 111*(1), 41-47.

Cleary, J. G., & Trigg, L. E. (1995). K*: An instance-based learner using an entropic distance measure. *Machine Learning Proceedings 1995*, 108-114. https://doi.org/10.1016/b978-1-55860-377-6.50022-0

Friedler, F., Tarjan, K., Huang, Y. W., & Fan, L. T. (1992). Combinatorial algorithms for process synthesis. *Computers & Chemical Engineering*, *16*, S313-S320. https://doi.org/10.1016/s0098-1354(09)80037-9

Gupta, P., & Sinha, N. (2000). Neural networks for identification of nonlinear systems: An overview. In N. K. Sinha & M. M. Gupta (Eds.), *Soft Computing and Intelligent Systems* (pp. 337-356). Elsevier. https://doi.org/10.1016/b978-012646490-0/50017-2

Janke, L., Leite, A., Nikolausz, M., Schmidt, T., Liebetrau, J., Nelles, M., & Stinner, W. (2015). Biogas production from sugarcane waste: Assessment on kinetic challenges for process designing. *International Journal of Molecular Sciences*, *16*(9), 20685-20703. https://doi.org/10.3390/ijms160920685

Kiatkittipong, W., Wongsuchoto, P., & Pavasant, P. (2009). Life cycle assessment of bagasse waste management options. *Waste Management, 29*(5), 1628-1633. https://doi.org/10.1016/j.wasman.2008.12.006

Kulkarni, E. G., & Kulkarni, R. B. (2016). WEKA powerful tool in data mining. *International Journal of Computer Applications, 975*, 10-15.

Landwehr, N., Hall, M., & Frank, E. (2003). Logistic model trees. *Machine Learning: ECML 2003*, 241-252. https://doi.org/10.1007/978-3-540-39857-8_23

Lee, R. P., Meyer, B., Huang, Q., & Voss, R. (2020). Sustainable waste management for zero waste cities in China: potential, challenges and opportunities. *Clean Energy, 4*(3), 169-201. https://doi.org/10.1093/ce/zkaa013

Monteiro, S. N., Candido, V. S., Braga, F. O., Bolzan, L. T., Weber, R. P., & Drelich, J. W. (2016). Sugarcane bagasse waste in composites for multilayered armor. *European Polymer Journal, 78*, 173-185. https://doi.org/10.1016/j.eurpolymj.2016.03.031

Naik, A., & Samant, L. (2016). Correlation review of classification algorithm using data mining Tool: WEKA, Rapidminer, TANAGRA, Orange and KNIME. *Procedia Computer Science*, *85*, 662-668. https://doi.org/10.1016/j.procs.2016.05.251

Negnevitsky, M. (2011). *Artificial Intelligence: A Guide to Intelligent System* (3rd ed.). Pearson Education.

Puna, J., & Teresa, M. (2010). Thermal conversion technologies for solid wastes: A new way to produce sustainable energy. In E. S. Kumar (Ed.), *Waste Management* (pp. 129-154). InTech. https://doi.org/10.5772/8461

Sangalang, K. P. H., Belmonte, B. A., Ventura, J. R., Andiappan, V., & Benjamin, M. F. D. (2021). P-graph method for optimal synthesis of Philippine agricultural waste-based integrated biorefinery. *Chemical Engineering Transactions, 83*, 103-108. ttps://doi.org/10.3303/CET2183018

Sidana, A., & Farooq, U. (2014). Sugarcane bagasse: A potential medium for fungal cultures. *Chinese Journal of Biology*, *2014*, 1-5. https://doi.org/10.1155/2014/840505

Sindhu, R., Gnansounou, E., Binod, P., & Pandey, A. (2016). Bioconversion of sugarcane crop residue for value added products - An overview. *Renewable Energy*, *98*, 203-215. https://doi.org/10.1016/j.renene.2016.02.057

Tin, Y. T., Kean, T. T., Hui, C. K., Ponniah, G. D., & Loong, L. H. (2017). Debottlenecking of the Integrated Biomass Network with Sustainability Index in Malaysia. *The Journal of The Institution of Engineers, Malaysia, 78*(1), 22-26. https://doi.org/10.54552/v78i1.15

Varbanov, P. S., Friedler, F., & Klemeš, J. J. (2017). Process network design and optimisation using process graph: The success, the challenges and potential roadmap. *Chemical Engineering Transaction, 61*, 1549-1554. https://doi.org/10.3303/CET1761256

Witten, I. H., Frank, E., Hall, M. A., & Pal, C. J. (2017). *Data Mining: Practical Machine Learning Tools and Techniques* (4th ed.). Morgan Kaufmann.

Pertanika J. Sci. & Technol. 31 (4): 1621 - 1643 (2023)

PERTANIKA JOURNALS

SCIENCE & TECHNOLOGY

Journal homepage: http://www.pertanika.upm.edu.my/

Review Article

Knowledge Mapping Trends of Internet of Things (IoT) in Plant Disease and Insect Pest Study: A Visual Analysis

Muhammad Akmal Mohd Zawawi[1], Mohd Fauzie Jusoh[1,2], Marinah Muhammad[3]*, Laila Naher[1,4], Nurul Syaza Abdul Latif[5], Muhammad Firdaus Abdul Muttalib[2], Mohd Nazren Radzuan[6] and Andri Prima Nugroho[7]

[1]*Department of Agricultural Science, Faculty of Agro Based Industry, Universiti Malaysia Kelantan, 17600 UMK, Jeli, Kelantan, Malaysia*
[2]*Department of Agrotechnology, Faculty of Mechanical Engineering & Technology, Kampus Alam UniMAP Pauh Putra, 02600 Arau, Perlis, Malaysia*
[3]*Faculty of Earth Science, Universiti Malaysia Kelantan,17600 UMK, Jeli, Kelantan, Malaysia*
[4]*Institute of Food Security and Sustainable Agriculture, Universiti Malaysia Kelantan, 17600, Jeli, Kelantan, Malaysia*
[5]*School of Mathematical Sciences, College of Computing, Informatics and Media, Universiti Teknologi MARA, 40450, Shah Alam, Selangor, Malaysia*
[6]*Department of Biological and Agricultural Engineering, Faculty of Engineering, Universiti Putra Malaysia, 43400 Serdang, Selangor, Malaysia*
[7]*Department of Agricultural and Biosystems Engineering, Faculty of Agricultural Technology, Universitas Gadjah Mada, Bulaksumur, Yogyakarta, 55281, Indonesia*

ABSTRACT

The study and literature on the Internet of Things (IoT) and its applications in agriculture for smart farming are increasing worldwide. However, the knowledge mapping trends related to IoT applications in plant disease, pest management, and control are still unclear and rarely reported. The primary aim of the present study is to identify the current trends and explore hot topics of IoT in plant disease and insect pest research for future research direction. Peer review articles published from Web of Science (WoS) Core Collection (2010-2021) were identified using keywords, and extracted database was analysed scientifically via Microsoft Excel 2019, VOSviewer and R programming software. A total of 231 documents with 5321 cited references authored by 878

ARTICLE INFO

Article history:
Received: 24 April 2022
Accepted: 07 September 2022
Published: 24 May 2023

DOI: https://doi.org/10.47836/pjst.31.4.02

E-mail addresses:
f20d0241f@siswa.umk.edu.my (Muhammad Akmal Mohd Zawawi)
fauziejusoh@studentmail.unimap.edu.my (Mohd Fauzie Jusoh)
marinah@umk.edu.my (Marinah Muhammad)
lailanaher@umk.edu.my (Laila Naher)
syazalatif@uitm.edu.my (Nurul Syaza Abdul Latif)
firdausmuttalib@unimap.edu.my (Muhammad Firdaus Abdul Muttalib)
mohdnazren@upm.edu.my (Mohd Nazren Radzuan)
andrew@ugm.ac.id (Andri Prima Nugroho)
* Corresponding author

ISSN: 0128-7680
e-ISSN: 2231-8526

scholars showed that the knowledge on the studied area has been growing positively and rapidly for the past ten years. India and China are the most productive countries, comprising more than half (52%) of the total access database on the subject area in WoS. IoT application has been integrated with other knowledge domains, such as machine learning, deep learning, image processing, and artificial intelligence, to produce excellent crop and pest disease monitoring research. This study contributes to the current knowledge of the research topic and suggests possible hot topics for future direction.

Keywords: Disease detection, Internet of Things, pest, visualisation analysis, web of science

INTRODUCTION

The prominence of plant diseases and pests has negatively affected crop productivity and quality. Even though the global percentage of yield loss due to plant diseases and pests varies, Oerke (2006) concludes that plant diseases and pests, including weeds, contributed about 20% to 50% of crop loss. Worries have been highlighted that agricultural production would be unable to serve the increasing global population, where United Nations projected the world population could reach up to 10 billion by 2050 (Alexandratos & Bruinsma, 2012). High population density would pressure the food production industry to fulfil the future food demand.

Previously, most growers implemented traditional approaches to detecting plant diseases and pests. Despite the required experts, manual identification is also a long-timing procedure that leads to late detection (Araújo et al., 2021; Singh & Misra, 2017; Fox & Narra, 2006). Consequently, the plant disease triangle concept demonstrated the interaction factors that develop plant disease occurrence: favourable environments, pathogens, and plant hosts (Back et al., 2002). Farmers are not guaranteed to monitor the weather and environmental attributes in field conditions to reduce plant disease outbreaks. Thus, the traditional approach to plant disease detection is no longer viable for monitoring and detecting plant diseases due to the changes in weather and environmental conditions (Ampatzidis et al., 2017), as well as soil characteristics (Van den Berg et al., 2012). For example, Olivares et al. (2021) have documented a review regarding the relationships between climates and the occurrence of Fusarium wilt disease in bananas. Due to the unpredictable weather conditions, plant disease monitoring and early diagnosis are essential to control the disease spread and help with the proper execution of contingency plans (Magdama et al., 2019).

The Internet of Things (IoT) is an excellent movement towards intelligent farming. The IoT technology is anticipated to be a new revolution toward precision agriculture where farmers can monitor their farms and crops' status through smart devices anywhere and anytime. The affordable sensors are embedded with other useful devices and internet connections, allowing remote capture of the desired data for further analysis and

decision-making (Khanna & Kaur, 2019). IoT technology opens opportunities to turn the management and control activities from manual to intelligent mode (Hu et al., 2020). Today, the potential for IoT as a mediated technology in plant disease and pest study is becoming popular these recent years, as indicated by the increasing number of published scientific research papers. Both local and international scholars are actively exploring IoT adoption as an early warning and prediction system for the presence of plant diseases and pests (Hadi et al., 2021; Mishra et al., 2021; Khan et al., 2020; Nawaz et al., 2020; Wang et al., 2015). The IoT technology could provide real-time data for environmental parameters contributing to plant health, such as humidity, light intensity, and carbon dioxide content from a cultivated area (Karnati et al., 2021). Most IoT plant disease and pest studies are applied to leaf diseases (Babu & Babu, 2020; Shafi et al., 2020), where the pathogen initially penetrated above ground. However, sensor-based technology, including IoT, has the potential to be applied for early soilborne disease detection (Wei et al., 2021).

Bibliometric analysis is a statistical tool for mapping the state of scientific knowledge using bibliographical data from various published scientific materials to find crucial information that influences scientific community publication (de Oliveira et al., 2019). The bibliometric analysis gives insight to scholars or practitioners to explore more in the subject area. In terms of scientific value, visual analysis is one of the review papers to analyse the trends and discover the emerging science in that field (Ding & Yang, 2020). There are a few scholars who explored bibliometric analysis practice to understand the topic of machine learning (Zhang, Liu et al., 2021), artificial intelligence (Vazquez et al., 2021) and IoT in irrigation (Jusoh et al., 2021) from an agriculture perspective. However, there is little information on bibliometric analysis explicitly addressing the topic of IoT in plant disease and insect pest research.

The main objective of this study is to identify the current trends and explore hot topics on IoT in plant disease and insect pest research. The research questions guiding this study are (1) What are the existing knowledge mapping trends in the subject area? (2) Who are the leading countries of the research topic? (3) What are the hot topics related to the subject area? As a result of the importance and relevance of IoT applications in crop disease and pest research in the future, the present study explores the research trend in the subject field. The outcome of this study is beneficial to scholars and inexperienced researchers. It provides an overview of the growing global knowledge on the application of IoT in plant disease and insect pest scientific research.

MATERIALS AND METHODS

This study was conducted based on the bibliometric analysis procedure (Donthu et al., 2021) and the Preferred Reporting Items for Systematic Reviews and Meta-Analysis (PRISMA) guideline (Page et al., 2021).

Searching Strategy and Data Extraction

The systematic searching strategy was applied to peer-reviewed documents recorded by the Web of Science, WoS database (Clarivate Analytics-Thomson ISI) on 23 November 2021. The database was accessed through MyAthens Gateway provided by the Office of Library and Knowledge Management, Universiti Malaysia Kelantan (UMK). The WoS was selected as the search database engine since it recorded high-quality articles and interdisciplinary coverage (Mongeon & Paul-Hus, 2016). The query string used in this study was (“internet of thing*” OR iot) AND (“plant disease*” OR “crop disease*” OR “leaf disease*” OR “crop health*” OR “plant health*” OR “leaf health*” OR “pest*” OR “insect*”). The keywords selected are based on the synonyms of the terms and decisions based on the preliminary screening of the keywords recorded by the WoS database (carried out on 25 October 2021). The database engine searched the query string using the topic field code function. It identified the keywords in the title, abstract, author, and keywords generated by the WoS database. In this searching strategy, phrase searching (“….”), Boolean operator (AND, OR) and truncation (*) were applied in the query string to obtain the relevant documents as guided by Mohamed Shaffril et al. (2021). The PRISMA flow diagram of the present study is shown in Figure 1.

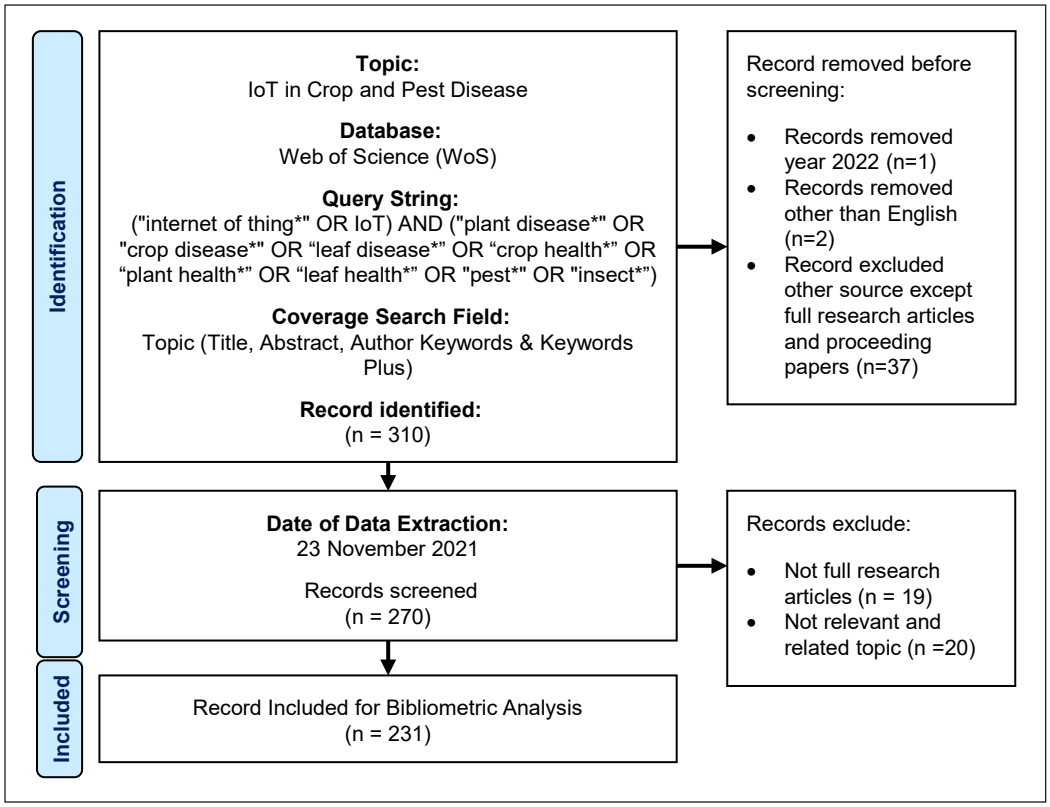

Figure 1. PRISMA flow diagram of the present study

In this screening phase, three authors evaluated the information in the title and abstract for 270 records. They agreed to exclude the documents which are not related. However, if the abstract is unclear to the authors, full-length articles were read before final decision-making. Although the review papers were excluded under refine section at the first filtering stage, some of the review or conceptual articles were not defined as review papers, and some were categorised as full papers by publishers. Therefore, manual screening is done since this study attempts to access and concentrate on the full research paper related to the studied topic and select the most relevant documents. Finally, the record with cited reference information was exported into the tab-delimited format and Bibtex file for further analysis.

Data Analysis and Visualisation

Two essential tools were used to analyse the data: R programming and VOSviewer software. A Biblioshiny apps web interface for the bibliometrix package in R programming version 4.1.2 (released on 01 November 2021) was used to evaluate the citation metric and visualise selected bibliometric data to answer the research questions. Bibliometrix is one of the comprehensive tools for bibliometric analysis and is widely used to conduct science mapping (Aria & Cuccurullo, 2017). Meanwhile, VOSviewer software version 1.6.17, released on 22 July 2021, was used for data visualisation to produce the co-occurrence maps network. VOSviewer is a free software tool for visualisation functionality for creating maps based on network data invented by Nees Jan van Eck and Ludo Waltman from Universiteit Leiden, The Netherlands (Van Eck & Waltman, 2021). As Börner et al. (2005) recommended, the visual analysis should incorporate several critical components, including the communities and networks of the scholars, the pattern of field study, and the dissemination of study topics. The graphs shown in this study were created by Microsoft Excel 2019. Research questions were developed at the initial stage of this study, as

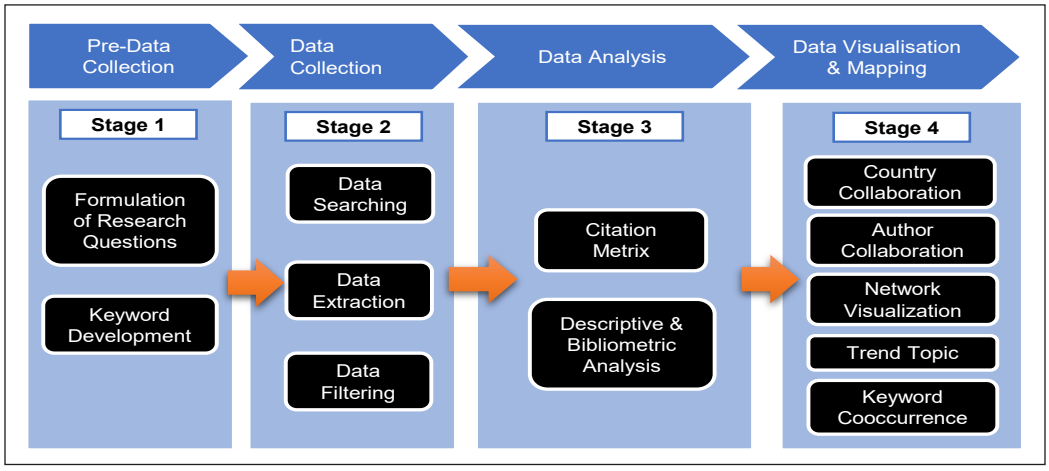

Figure 2. Main stages of workflow in methodology

suggested by Linnenluecke et al. (2020), to guide the research flow and analysis selection. The main stages of the workflow of this study are presented in Figure 2.

RESULTS AND DISCUSSION

Publication Trends and Knowledge Growth

Table 1 summarises the primary citation metrics of the bibliographic information of the research topic. This study includes 231 articles published between 2010 and 2021, which involved 5321 numbers of references. The peer-reviewed documents analysed were full research articles published in journals (45.02%) and conference proceedings (54.98%). Most research papers were multi-authored (99.09%) compared to single-authored documents (0.91%), which involved 878 scholars. On average, the value of documents per author, authors per document, and co-authors per document were 0.26, 3.8 and 4.17. Figure 3 shows the growth of publication trend from 2010 until 2021, where the number of publications follows the second order of a polynomial equation ($y = 0.6316x^2 - 2.767x + 3.0227$) with an R-squared value of 0.9649. The high R-squared value (0.9 or above) indicated a perfect data fitting to the regression model (Ostertagová, 2012). The first document (Wang & Chai, 2011) published, taken into account in this study, was in 2010, and the latest record (Seo & Umeda, 2021) was published in 2021. An analysis from biblioshiny in R programming revealed that the annual scientific production growth rate on the subject is 48.74%.

Table 1
Main information on citation metrics

No	Characteristics	Results (Percentage, %)
1	General	
	Timespan	2010–2021 (12 Years)
	No. of Documents	231
	Average years from publication	2.13
	Average citations per document	5.472
	Average citations per year per doc	1.59
	No. of References	5321
2	Document Type	
	No. of Journal Articles	104 (45.02)
	No. of Proceeding Articles	127 (54.98)
3	Authorship	
	No. of Authors Involved	878 (100.00)
	Authors of single-authored documents	8 (0.91)
	Authors of multi-authored documents	870 (99.09)
	Documents per Author	0.26
	Authors per Document	3.8
	Co-Authors per Documents	4.17

The knowledge growth in the field is increasing slowly from 2010 until 2015. A small number of research publications were published during this period, which may result in a low number of citations. It is one of the factors leading to the slow growth of knowledge. Then, the trend started to rise rapidly from 2015 onwards and became a hot topic in academic research. More researchers from various fields actively participated in IoT applications in plant disease and insect pests studies because the total publication and citation number have increased over the years by publishing research work in journals and presenting at conferences.

Figure 4 depicts citation information of the publications for 12 years from 2010–2021. Interestingly, the mean total citation per article (36) and mean total citation per year (4.5)

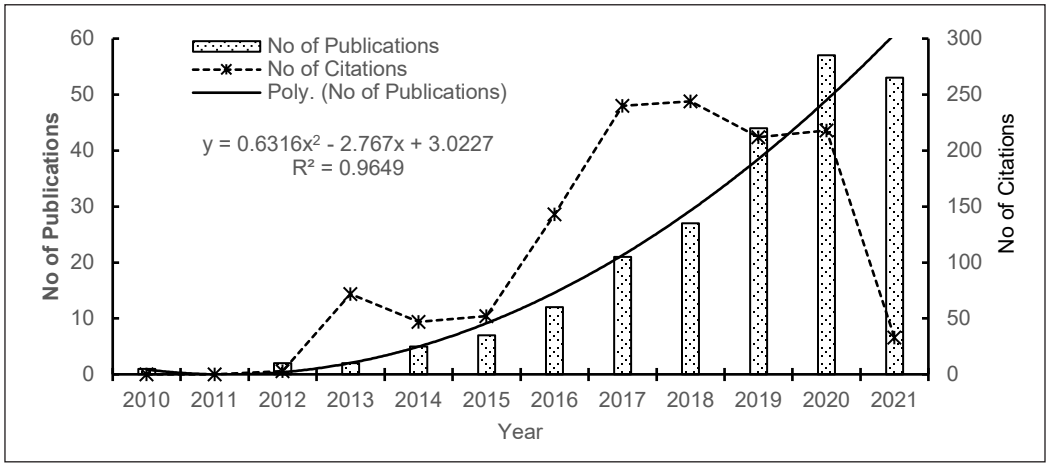

Figure 3. The growth of publication trends from the year 2010–2021

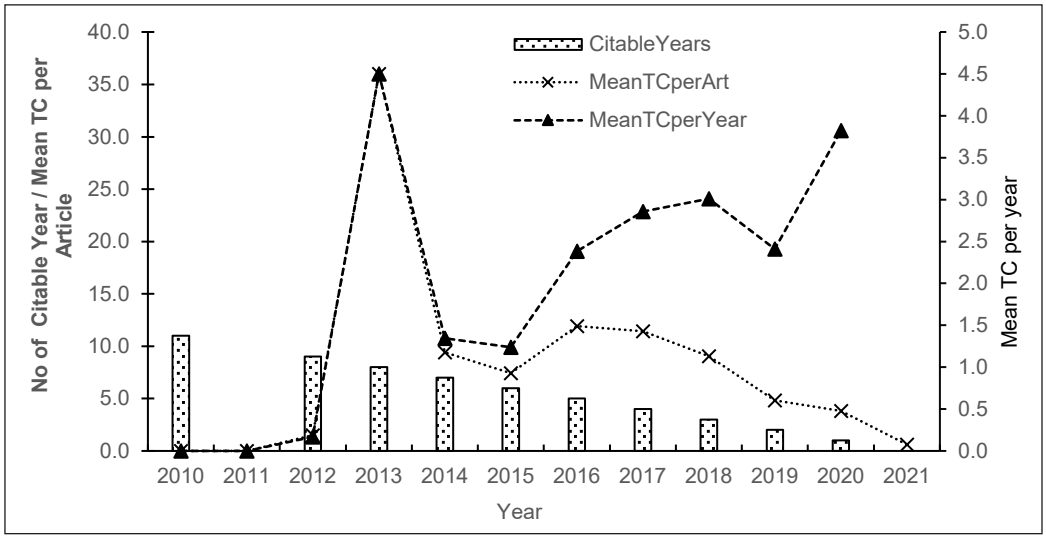

Figure 4. Citation information of the publication for 12 years (TC is total citation)

jumped to the highest level in 2013 compared to the previous year. Although the number of publications on related topics is only two documents (Harun et al., 2013 & Lee et al., 2013), the published articles have received quite a high number of total citations (72) respective to available publications on the stated year. In 2014 and 2015, the mean total citation per article and mean total citation per year had declined dramatically since the total citation on the search topic reduced to between 47 and 52 for the last 6 to 7 years backwards. However, the mean total citation per year generally shows increasing trends starting from 2015. Even if the mean total citation per year reflects a declining trend, the total citations per article are anticipated to increase over time.

Table 2 ranks the top 20 most productive scientific publications, with authors collaborating by country on IoT applications in plant disease and pest insects in WoS. India is the most productive country that publishes articles in the subject area, followed by China, Greece, Korea, Italy, Japan, Pakistan, USA, France, and Malaysia. Most of the top ten countries recorded more than five documents on the search topic.

Table 2
Scientific publication with authors collaboration by country

Rank	Country	No of Articles	Frequency	SCP	MCP	MCP Ratio
1	India	74	0.3204	67	7	0.0946
2	China	47	0.2035	36	11	0.2340
3	Greece	7	0.0303	7	0	0.0000
4	Korea	7	0.0303	7	0	0.0000
5	Italy	6	0.0260	5	1	0.1667
6	Japan	6	0.0260	5	1	0.1667
7	Pakistan	6	0.0260	5	1	0.1667
8	USA	6	0.0260	2	4	0.6667
9	France	5	0.0217	3	2	0.4000
10	Malaysia	5	0.0217	5	0	0.0000
11	Portugal	5	0.0217	5	0	0.0000
12	Bangladesh	4	0.0173	3	1	0.2500
13	Romania	4	0.0173	4	0	0.0000
14	Saudi Arabia	4	0.0173	1	3	0.7500
15	Australia	3	0.0130	1	2	0.6667
16	Egypt	3	0.0130	3	0	0.0000
17	Germany	3	0.0130	2	1	0.3333
18	Spain	3	0.0130	3	0	0.0000
19	Belgium	2	0.0087	2	0	0.0000
20	Brazil	2	0.0087	0	2	1.0000

Notes. SCP = single country publications; MCP = multiple country publications; Frequency = the ratio of no of articles published to the number of retrieved articles; MCP ratio = MCP divided by the total of published articles per country

India produced the highest number of documents with the highest single-country publications. In contrast, China had the most elevated collaboration among the authors with multiple country publications. India produced the highest number of documents with the highest single-country publications. In contrast, China had the most elevated collaboration among the authors with multiple country publications. Concerning food security, India and China are moving to the modernisation agriculture phase. The agriculture economy of India comprises almost 50% of the country's gross domestic product (GDP) and feeds up to 1.3 billion human population (Jarial, 2022). Despite challenging technological development for a country like India (Jaishetty & Patil, 2016), this study's findings revealed that Indian researchers actively explore the implementation of IoT technology in their agriculture industry to reshape the future of farming and meet the growing population, as well as increasing agriculture productivity. While in China, it is expanding the development of IoT in China and defining itself as a new economic growth engine with at least 9 billion interconnected electronics in China, with 24 billion devices anticipated by 2020 (Chen et al., 2014). Malaysia was in the top twenty, with five articles produced in single-country publications. The research on IoT and plant disease and insect pest study in Malaysia is currently being investigated by Malaysian scholars parallel to the active research institutions in developed countries (USA, Italy, Japan, Canada, Germany) and developing countries such as India, China and Brazil (Xie & Duan, 2020). However, the ranking might differ from time to time since the publication number and related information in the year 2021 are not complete since the WoS database is updated daily.

The interaction and relationship between country, abstract and keywords based on the WoS database were visualised by the Sankey diagram in Figure 5. Each attribute component has a different colour and rectangular height, indicating the intensity or value

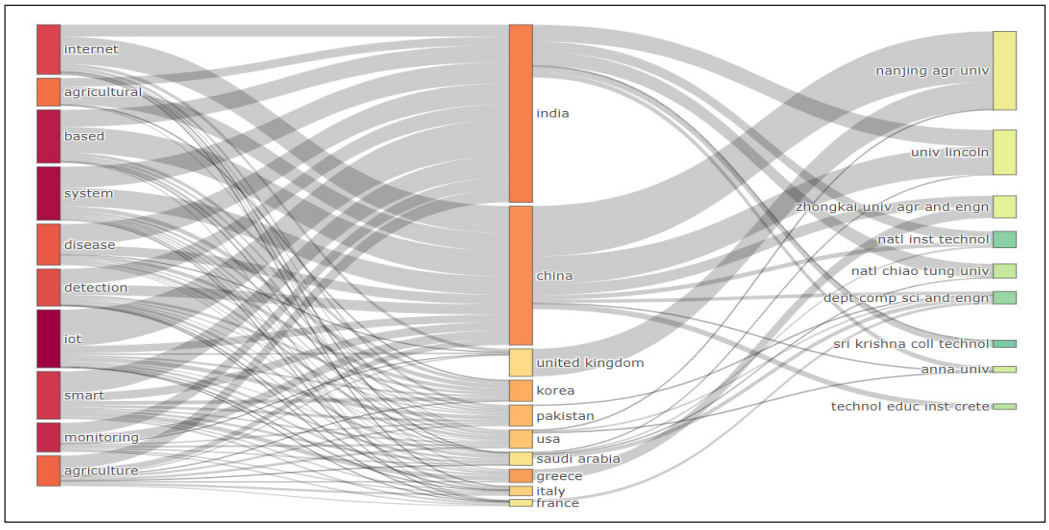

Figure 5. Sankey diagram of publication title (left), country (middle) and affiliation (right) for the research topic

of the summation of relations between attributes or elements. The shorter the rectangular of the attribute of elements represents low relations between each other and vice versa. The analysis revealed that the Asia region presented by India and China had more research institutions affiliated with IoT and plant disease and insect pest study publications compared to other countries. Among active research institutions on the list are Nanjing Agriculture University (China), Zhongkai University of Agriculture and Engineering (China), Sri Krishna College of Technology (India) and Anna University (India). Based on the published document title, the terms IoT, disease, detection, smart, monitoring, and internet were essential to generate the article's title.

Keyword Co-Occurrence Analysis

Figure 6 illustrates the visualisation of co-occurrence based on keywords. The keywords were presented in four selected slices: Internet of Things (IoT), precision agriculture, disease detection, and sensor. Co-occurrence analysis identifies hot topics and possible knowledge domains based on keywords extracted from the WoS database. IoT is one of the tools in smart agriculture that connect the sensors and environmental parameters through the internet and wireless sensor network (WSN). Various sensors are available and embedded into precision farming systems to capture environmental data (temperature, relative humidity, solar radiation, light intensity), media conditions (moisture content, pH, electrical conductivity), irrigation system indicators (water level, water flow rate, water quality parameters), soil fertility (nitrogen, potassium, phosphorus) and even image capture for crop monitoring status. The sensors are connected to a microcontroller like Raspberry Pi or Arduino through communication devices like Wi-Fi and Zigbee. The information collected from the agricultural field will be stored in the cloud for further analysis, data training and development of a decision support system. IoT technology and sensors act as a game-changer in gathering real-time soil and surrounding information for monitoring, controlling, prediction, and analysis (Rawi et al., 2020; Omar et al., 2020; Kim et al., 2018; Jawad et al., 2017). Farmers can use gathered data to use their land strategically, optimise agriculture activities, and use agrochemicals in controlled volume based on the collected data (Ratnaparkhi et al., 2020).

It can also be understood that IoT is not stand-alone technology used in smart farming and precision agriculture. Still, it has been integrated with various knowledge domains such as machine learning, deep learning, artificial intelligence and neural network at the decision-making stage. As reviewed by Hassan et al. (2021), multiple promising technologies such as the Internet of Things (IoT), aerial imagination, WSN, multispectral, hyperspectral, deep learning, artificial intelligence (Al), and RGB camera could be widely implemented as early plant disease and pest detection in agriculture activities. Consequently, the search for precision agriculture using IoT-based technology together with other technology such as

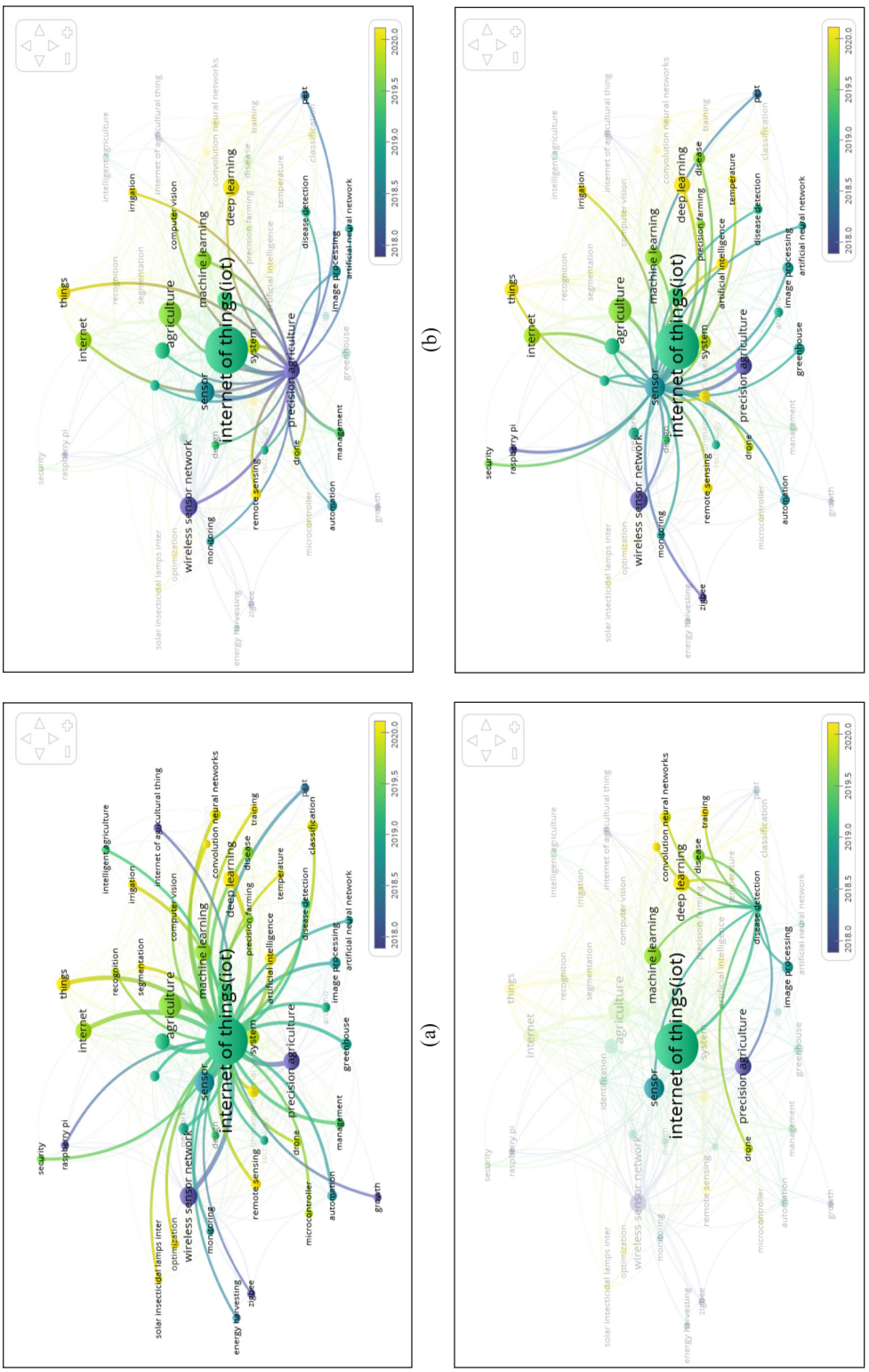

Figure 6. Overlay visualisation of co-occurrence based on keywords for (a) Internet of Things, (b) Precision agriculture, (c) Disease detection, and (d) Sensor

mobile applications (Chavan et al., 2020), WSN (Uddin et al., 2018), deep learning (Nasir et al., 2021; Saleem et al., 2021; Sethy et al., 2021; Zhang, Rao et al., 2021; Ale et al., 2019; Gupta et al., 2019; He et al., 2019), machine learning (Kundu et al., 2021; Chavan et al., 2020; Pawara et al., 2018; Patil & Thorat, 2016), aerial and remote sensing (Rochester et al., 2019) have become a key public strategy area of the study. In addition to IoT and other technological approaches, modelling techniques could be used to automate the identification and forecasting of plant diseases. Verma et al. (2018) have previously summarised the current techniques related to the statistical approaches based on IoT sensors and image processing for identifying and diagnosing tomato plant diseases. In the selected study, for example, Patil and Thorat (2016) developed an IoT monitoring system for grape diseases in its early stages by utilising a statistical model (Hidden Markov Model) to analyse IoT data. In addition, Materne and Inoue (2018) have estimated disease forecasting based on IoT data using a logistic regression algorithm.

Thus, the researchers have incorporated multiple IoT system architectures into their proposed IoT systems. Despite various sensors and microcontrollers in the market, different communication protocols also have been implemented in various IoT system architectures over the years. For instance, long-range (LoRa) communication has become integral to IoT and WSN. Ghazali et al. (2021) state that LoRa is one of the low-power wide area networks (LPWANs). In addition, the authors mentioned that LoRaWAN and LoRa are frequently confused and interchangeably used; LoRaWAN is the standard protocol for wide area network (WAN) communications, and LoRa is a WAN technology. In this present study, Varandas et al. (2020) and Kim et al. (2018) have integrated the LoRa communication network and WSN into their proposed IoT system due to its long-range transmission and low power consumption. The authors highlighted LoRa communication deployments because they could be considered a hot topic in relation to emerging IoT and WSN applications.

These technologies, including IoT, were chosen not just to increase efficiency in farming practices, but this alternative has the potential to act as a mediated technology in farming practices to recognise the plant disease and pests, which is promising in terms of gathering, investigating, transmitting, and dealing with all the sensed data to transform the data into actionable information (Nawaz et al., 2020). Despite existing agriculture practices, worldwide population growth, climate changes, and rapid urbanisation have driven the public and private sectors to engage in technological developments to tackle food security issues in the future. Additionally, IoT approaches significantly improved agricultural productivity, the quality of agricultural products, lower workforce expenses, enhanced growers' income, and modernised agricultural activities (Xu et al., 2022).

In the context of plant disease, the application of IoT as a based technology is possible to be used for disease detection and recognition, disease diagnosis and identification, disease monitoring, disease controlling and disease prediction. For example, using IoT and machine

learning, disease prediction has become a powerful tool in identifying, classifying and recognising plant disease with the latest development and upgraded simulation software such as MATLAB and other software. The rapid growth of the internet and communication has also accelerated the research on insects and integrated pest management by detecting the insect, identifying them, and proposing the solution to overcome infection by introducing robotics and drones in precision agriculture. Ampatzidis et al. (2017) summarise robotic applications in plant pathology based on the integration of IoT and WSN. At the same time, the development of IoT technology can lead to beneficial applications for drones as well as Global Positioning Systems (GPS) and Geographical Information Systems (GIS). Therefore, the integrated-based IoT system could provide aerial crop monitoring and plant disease mapping. For instance, Shafi et al. (2020) have utilised IoT-based system technology and remote sensing to gather various information, including drone data, IoT data, multisource data integration, Vegetation Indices data, health maps, and IoT data maps.

Plant disease detection from crop images and agro-environmental variables has attracted considerable automation and mechanisation to simplify disease recognition. Khan et al. (2020) used an image processing framework for plant disease analysis in their IoT system, where the leaf disease detection analysis was applied using MATLAB simulation software. Due to the novel design of Wisekar as a generic centralised IoT respiratory for sensor networks, Sarangi et al. (2016) implemented the Wisekar concept to propose and implement a distributed Automated Crop-disease Advisory Service (ACAS). The authors incorporated Wisekar as a communication link between the advisory system and software to recognise plant disease. Furthermore, few scholars have established their plant disease machinery or platform, such as sCrop (Udutalapally et al., 2021), modified ride-NN (Mishra et al., 2021), Smart Palm (Koubaa et al., 2020), KrishiAl (Chavan et al., 2020), RiceTalk (Chen et al., 2019), FARM EASY (Ramesh et al., 2020), I^2MS – Intelligent Insect Monitoring System (Sobreiro et al., 2019), PLANTAE (Hossam et al., 2018), and VineSens (Pérez-Expósito et al., 2017). Despite the plant disease mechanisation, Lin et al. (2019) proposed SensorTalk to detect sensor failures and semi-automatically calibrate ageing sensors automatically.

Figure 7 explains the evolution of trend topics based on the keywords and abstract. The straight line represents the timeline, whereas the circle size shows word frequency per year. The result interpretation can be made from a different angle. Based on the author's keyword, the terms internet of things, deep learning, artificial intelligence, machine learning, and sensor proved to be among the trending term nowadays. Rice, grape, and cucumber are the commonly researched crops on the subject field based on a single word in an abstract if referring to the trend of more than two abstract words, agricultural devices such as sensors, uncrewed aerial vehicles, and support vector machines are the popular tools in plant disease detection together with precision agriculture practices primarily via internet communication.

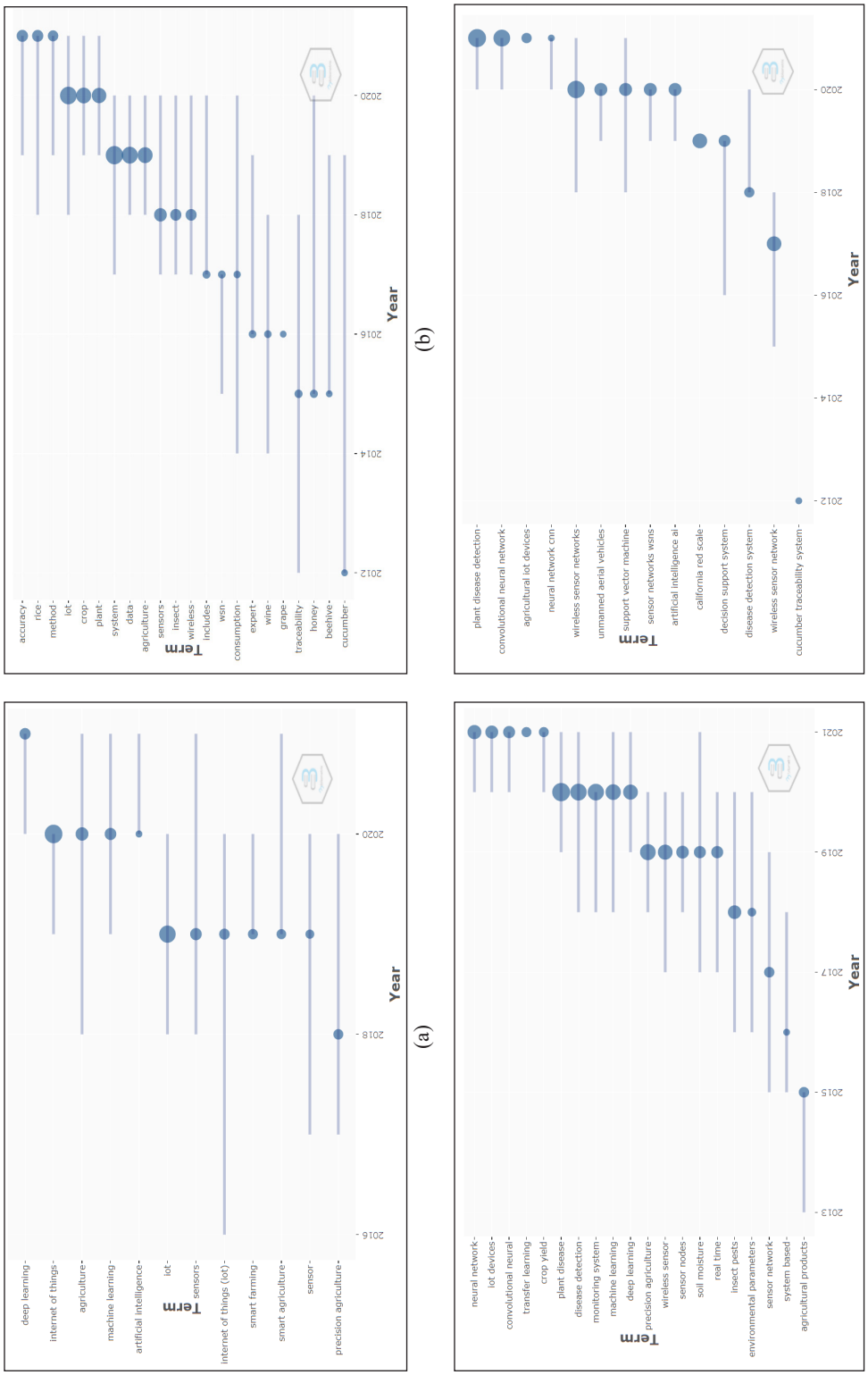

Figure 7. Trend topics based on (a) keywords, (b) abstract with a single word, (c) abstract with two words and (d) abstract with three words

Thematic evolution of IoT and plant disease and insect pest study are represented in Figure 8. A thematic map is used to analyse themes on the words and placed in the quadrant based on development degree (density) and relevance degree (centrality). Density and centrality properties indicated the development and important degree of the topic (Agbo et el., 2021). There are four quadrants: quadrant 1 (motor theme), quadrant 2 (basic theme), quadrant 3 (niche theme) and quadrant 4 (emerging or declining theme). Quadrant 1 is characterised by high density and centrality, which means that the themes are developed and vital in the research field. Notably, from Figure 8, the neural network theme connected to the components of machine learning, convolutional neural, and disease prediction is more developed in the literature, and it becomes a driving theme to the body of knowledge. Quadrant 2 is expressed by high centrality and low density. The themes of yield, crop disease and precision agriculture are considered basic and general topics transversal to the different research areas of the field. Quadrant 3 is described by the theme, which is a highly developed and isolated or niche area. The theme has low centrality (limited importance for the field) and high density (well-developed internal but unimportant external links). Thematic map reveals that wireless sensors (agricultural internet, sensor network, solar insecticidal) and monitoring systems (artificial intelligence, crop yield, environmental monitoring) are the niche themes for the topic studied. Integrating machine learning, artificial intelligence, deep learning, convolutional network, and sensor network with IoT technology for time series could help farmers to obtain detailed information about crop health (Shafi et al., 2020).

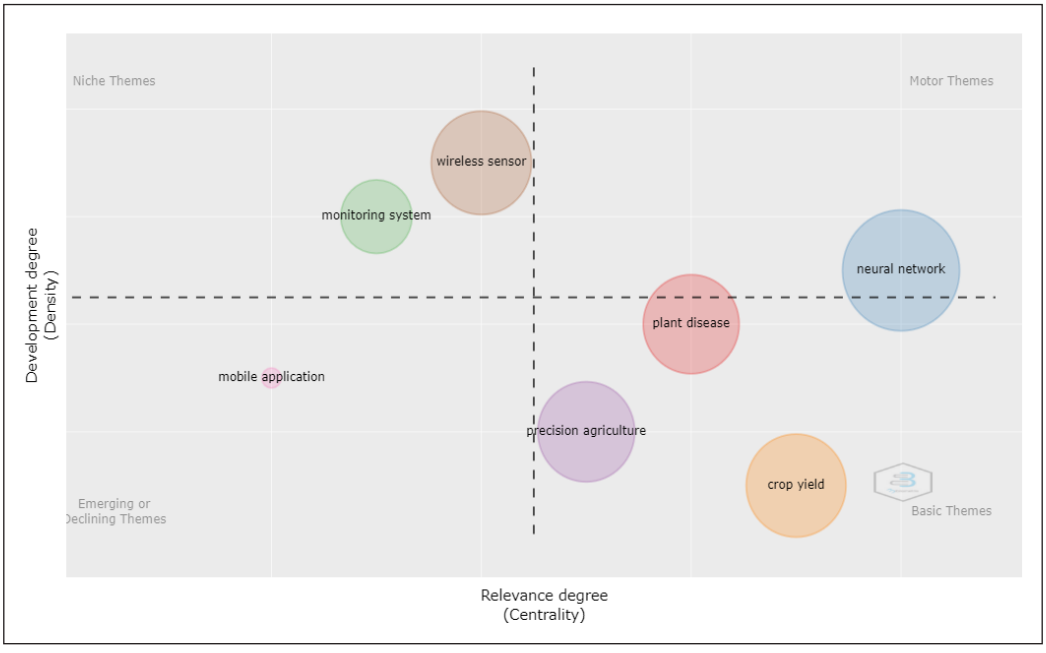

Figure 8. Thematic evolution of the field of IoT and plant disease and insect pest study based on words in abstract

Quadrant 4 is drawn at the lower-left quadrant with low centrality and density. The theme could be an emerging or declining topic since it is weakly developed and marginal. Mobile application theme is expected to be emerging trends, and it is connected to plant health, IoT-based, modern technologies, IoT innovation and smart greenhouse components. Precision agriculture and wireless sensor themes are located at the border of the centrality line, indicating that wireless sensors have become a niche area of precision agriculture and can be used differently in crop monitoring systems through mobile applications. Furthermore, it is a promising technology supporting IoT approaches (Kavitha et al., 2020). By connecting a network, farmers could retrieve real-time data via smartphones to help farmers with contingency plans or crop maintenance (Ali et al., 2020). Locally, Padi2U mobile app was developed by Roslin et al. (2021) to monitor paddy health status in a paddy plot study at Ladang Merdeka, Ketereh, Kelantan. Additionally, the authors highlighted that the future crop monitoring status using IoT and mobile apps is one of the effective ways for farmers to monitor and manage their crops.

CONCLUSION

The present study explored the knowledge mapping trends and identified the related hot topics on IoT application in plant disease and insect pest study worldwide via VOSviewer and R programming. Although a considerable amount of research is available in the target subject area, there is incomplete information on bibliometric analysis. Using bibliographical information extracted from peer-reviewed articles in the WoS database, research questions developed at the beginning stage of this study have been answered. Publication trends, knowledge growth and keyword co-occurrence analysis, were conducted to investigate and explore the current and future direction of the subject field.

A few highlights can be drowned from this study. First, global IoT application publication trends in plant disease and insect pest studies have shown positive growth for 12 years. This subject area is still an emerging topic with an annual scientific production growth rate of 48.74%. Second, the most productive country, such as India and China, produced 52% of the scientific document in the studied field. Collaboration among different countries in publishing research articles increases the published materials' visibility and quality. Third, integration between cross-multidisciplinary knowledge domains such as machine learning, deep learning, image processing, and artificial intelligence for crop monitoring and decision support systems can produce excellent crop yield and reduce dependency on human resources. For example, undiscovered research projects like the application of IoT in Fusarium wilt disease detection in bananas can be explored and further developed to become an effective monitoring system. Besides, the relationship between soil properties and environment parameters by sensor and IoT approach is interesting to be investigated

as it considers the media conditions and relates to soil and plant health. The application and development of such a system are relevant to future food demand, food security and climatic change adaptation.

The main limitation of the present study is the selection and attention to certain aspects of bibliometric analysis, which are highly related to research questions. There are still different angles or directions of data analysis, such as comprehensive conceptual, intellectual and social structure analysis, that should be addressed for future research. This study also focuses on full research articles in the WoS database, where other documents such as review articles, book chapters, and other publication types are not considered. The main barrier to getting and combining different databases is difficulty integrating different databases since some of the recorded methods vary between database providers. Different bibliographical information processed by different visualisation software will produce a different interpretation. Therefore, it would be interesting if future scholars could identify and resolve the knowledge gap in future publications.

ACKNOWLEDGEMENT

The authors thank the research fund and financial support from Fundamental Research Grant (FRGS/1/2020/WAB04/UMK/02/7) and Skim Latihan Akademik Bumiputera, SLAB (No: 474/2019/8). We also acknowledge the reviewers for their efforts, time allocation, and fruitful comments to improve and enhance the quality of the manuscript. We also would like to thank UPM-Kyutech International Symposium on Applied Engineering and Sciences 2021 (SAES2021) and Universiti Putra Malaysia for supporting the publication fee of this article.

REFERENCES

Agbo, F. J., Oyelere, S. S., Suhonen, J., & Tukiainen, M. (2021). Scientific production and thematic breakthroughs in smart learning environments: A bibliometric analysis. *Smart Learning Environments, 8*(1), 1-25. https://doi.org/10.1186/s40561-020-00145-4

Ale, L., Sheta, A., Li, L., Wang, Y., & Zhang, N. (2019, December 9-13). *Deep learning based plant disease detection for smart agriculture.* [Paper presentation]. 2019 IEEE Globecom Workshops (GC Wkshps), Waikoloa, Hawaii. https://doi.org/10.1109/GCWkshps45667.2019.9024439

Alexandratos, N., & Bruinsma, J. (2012). *World agriculture towards 2030/2050: The 2012 revision*. https://ageconsearch.umn.edu/record/288998/files/a-ap106e.pdf

Ali, M., Kanwal, N., Hussain, A., Samiullah, F., Iftikhar, A., & Qamar, M. (2020). IoT based smart garden monitoring system using NodeMCU microcontroller. *International Journal of Advances in Applied Sciences*, *7*(8), 117-124.

Ampatzidis, Y., De Bellis, L., & Luvisi, A. (2017). iPathology: Robotic applications and management of plants and plant diseases. *Sustainability, 9*(6), Article 1010. https://doi.org/10.3390/su9061010

Araújo, S. O., Peres, R. S., Barata, J., Lidon, F., & Ramalho, J. C. (2021). Characterising the agriculture 4.0 landscape-Emerging trends, challenges and opportunities. *Agronomy, 11*(4), Article 667. https://doi.org/10.3390/agronomy11040667

Aria, M., & Cuccurullo, C. (2017). Bibliometrix: An R-tool for comprehensive science mapping analysis. *Journal of Informetrics*, *11*(4), 959-975. https://doi.org/10.1016/j.joi.2017.08.007

Babu, T. G., & Babu, G. A. (2020). Identification of crop health condition using IoT based automated system. In S. Borah, V. E. Balas & Z. Polkowski (Eds.), *Advances in Data Science and Management* (pp. 421-433). Springer. https://doi.org/10.1007/978-981-15-0978-0_41

Back, M. A., Haydock, P. P. J., & Jenkinson, P. (2002). Disease complexes involving plant parasitic nematodes and soilborne pathogens. *Plant Pathology, 51*(6), 683-697. https://doi.org/10.1046/j.1365-3059.2002.00785.x

Börner, K., Chen, C., & Boyack, K. W. (2005). Visualising knowledge domains. *Annual Review of Information Science and Technology, 37*(1), 179-255. https://doi.org/10.1002/aris.1440370106

Chavan, S. V., Gopalani, D. M., Heda, R. R., Israni, R. G., & Sethiya, R. B. (2020, May 13-15). *KrishiAI-An IoT and machine learning based mobile application for farmers*. [Paper presentation]. 4th International Conference on Intelligent Computing and Control Systems (ICICCS), Madurai, India. https://doi.org/10.1109/ICICCS48265.2020.9120952

Chen, S., Xu, H., Liu, D., Hu, B., & Wang, H. (2014). A vision of IoT: Applications, challenges, and opportunities with China perspective. *IEEE Internet of Things Journal, 1*(4), 349-359. https://doi.org/10.1109/JIOT.2014.2337336

Chen, W. L., Lin, Y. B., Ng, F. L., Liu, C. Y., & Lin, Y. W. (2019). RiceTalk: Rice blast detection using Internet of Things and artificial intelligence technologies. *IEEE Internet of Things Journal, 7*(2), 1001-1010. https://doi.org/10.1109/JIOT.2019.2947624

de Oliveira, O. J., da Silva, F. F., Juliani, F., Barbosa, L. C. F. M., & Nunhes, T. V. (2019). Bibliometric method for mapping the state-of-the-art and identifying research gaps and trends in literature: An essential instrument to support the development of scientific projects. In S. Kunosic & E. Zerem (Eds.), *Scientometrics Recent* Advances (pp. 47-64). IntechOpen. https://doi.org/10.5772/intechopen.85856

Ding, X., & Yang, Z. (2020). Knowledge mapping of platform research: A visual analysis using VOSviewer and CiteSpace. *Electronic Commerce Research, 22,* 787-809. https://doi.org/10.1007/s10660-020-09410-7

Donthu, N., Kumar, S., Mukherjee, D., Pandey, N., & Lim, W. M. (2021). How to conduct a bibliometric analysis: An overview and guidelines. *Journal of Business Research*, *133*, 285-296. https://doi.org/10.1016/j.jbusres.2021.04.070

Fox, R. T. V, & Narra, H. P. (2006). Plant disease diagnosis. In B. M. Cooke, D. G. Jones & B. Kaye (Eds.), *The Epidemiology of Plant Diseases* (pp. 1-42). Springer. https://doi.org/10.1007/1-4020-4581-6_1

Ghazali, M. H. M., Teoh, K., & Rahiman, W. (2021). A systematic review of real-time deployments of UAV-based Lora communication network. *IEEE Access, 9*, 124817-124830. https://doi.org/10.1109/ACCESS.2021.3110872

Gupta, A. K., Gupta, K., Jadhav, J., Deolekar, R. V., Nerurkar, A., & Deshpande, S. (2019, March 13-15). Plant disease prediction using deep learning and IoT. [Paper presentation]. 6th International Conference on Computing for Sustainable Global Development (INDIACom), New Delhi, India.

Hadi, M. K., Kassim, M. S. M., & Wayayok, A. (2021). Development of an automated multidirectional pest sampling detection system using motorised sticky traps. *IEEE Access, 9*, 67391-67404. https://doi.org/10.1109/ACCESS.2021.3074083

Harun, A. N., Ani, N. N., Ahmad, R., & Azmi, N. S. (2013, December 02-04). *Red and blue LED with pulse lighting control treatment for Brassica chinensis in indoor farming.* [Paper presentation]. IEEE Conference on Open Systems (ICOS), Kuching, Malaysia. https://doi.org/10.1109/ICOS.2013.6735080

Hassan, S. I., Alam, M. M., Illahi, U., Al Ghamdi, M. A., Almotiri, S. H., & Su'ud, M. M. (2021). A systematic review on monitoring and advanced control strategies in smart agriculture. *IEEE Access, 9*, 32517-32548. https://doi.org/10.1109/ACCESS.2021.3057865

He, Y., Zeng, H., Fan, Y., Ji, S., & Wu, J. (2019). Application of deep learning in integrated pest management: A real-time system for detection and diagnosis of oilseed rape pests. *Mobile Information Systems, 2019*, 1-14. https://doi.org/10.1155/2019/4570808

Hossam, M., Kamal, M., Moawad, M., Maher, M., Salah, M., Abady, Y., Hesham, A., & Khattab, A. (2018, December 17-19). PLANTAE: An IoT-based predictive platform for precision agriculture. [Paper presentation]. *International Japan-Africa Conference on Electronics, Communications and Computations (JAC-ECC),* Alexandria, Egypt. https://doi.org/10.1109/JEC-ECC.2018.8679571

Hu, X., Sun, L., Zhou, Y., & Ruan, J. (2020). Review of operational management in intelligent agriculture based on the Internet of Things. *Frontiers of Engineering Management, 7*(3), 309-322. https://doi.org/10.1007/s42524-020-0107-3

Jaishetty, S. A., & Patil, R. (2016). IoT sensor network based approach for agricultural field monitoring and control. *IJRET: International Journal of Research in Engineering and Technology*, *5*(6), 45-48.

Jarial, S. (2022). Internet of things application in Indian agriculture, challenges and effect on the extension advisory services-A review. *Journal of Agribusiness in Developing and Emerging Economies,* 1-15. https://doi.org/10.1108/JADEE-05-2021-0121

Jawad, H. M., Nordin, R., Gharghan, S. K., Jawad, A. M., & Ismail, M. (2017). Energy-efficient wireless sensor networks for precision agriculture: A review. *Sensors, 17*(8), 1781. https://doi.org/10.3390/s17081781

Jusoh, M. F., Muttalib, M. F. A., Krishnan, K. T., & Katimon, A. (2021). An overview of the internet of things (IoT) and irrigation approach through bibliometric analysis. *IOP Conference Series: Earth and Environmental Science 756*(1), Article 012041. https://doi.org/10.1088/1755-1315/756/1/012041

Karnati, R., Rao, H. J., PG, O. P., & Maram, B. (2022). Deep computation model to the estimation of sulphur dioxide for plant health monitoring in IoT. *International Journal of Intelligent Systems, 37*(1), 944-971. https://doi.org/10.1002/int.22653

Kavitha, B. C., Vallikannu, R., & Sankaran, K. S. (2020). Delay-aware concurrent data management method for IoT collaborative mobile edge computing environment. *Microprocessors and Microsystems, 74*, Article 103021. https://doi.org/10.1016/j.micpro.2020.103021

Khan, F. A., Ibrahim, A. A., & Zeki, A. M. (2020). Environmental monitoring and disease detection of plants in smart greenhouse using internet of things. *Journal of Physics Communications, 4*(5), Article 055008. https://doi.org/10.1088/2399-6528/ab90c1

Khanna, A., & Kaur, S. (2019). Evolution of Internet of Things (IoT) and its significant impact in the field of Precision Agriculture. *Computers and Electronics in Agriculture, 157*, 218-231. https://doi.org/10.1016/j.compag.2018.12.039

Kim, S., Lee, M., & Shin, C. (2018). IoT-based strawberry disease prediction system for smart farming. *Sensors, 18*(11), Article 4051. https://doi.org/10.3390/s18114051

Koubaa, A., Aldawood, A., Saeed, B., Hadid, A., Ahmed, M., Saad, A., Alkhouja, H., Ammar, A., & Alkanhal, M. (2020). Smart Palm: An IoT framework for red palm weevil early detection. *Agronomy, 10*(7), Article 987. https://doi.org/10.3390/agronomy10070987

Kundu, N., Rani, G., Dhaka, V. S., Gupta, K., Nayak, S. C., Verma, S., Ijaz, M. F., & Woźniak, M. (2021). IoT and interpretable machine learning based framework for disease prediction in pearl millet. *Sensors, 21*(16), Article 5386. https://doi.org/10.3390/s21165386

Lee, M., Hwang, J., & Yoe, H. (2013, December 03-05). *Agricultural production system based on IoT*. [Paper presentation]. IEEE 16Th International Conference on Computational Science and Engineering, Sydney, Australia. https://doi.org/10.1109/CSE.2013.126

Lin, Y. B., Lin, Y. W., Lin, J. Y., & Hung, H. N. (2019). SensorTalk: An IoT device failure detection and calibration mechanism for smart farming. *Sensors, 19*(21), Article 4788. https://doi.org/10.3390/s19214788

Linnenluecke, M. K., Marrone, M., & Singh, A. K. (2020). Conducting systematic literature reviews and bibliometric analyses. *Australian Journal of Management*, *45*(2), 175-194. https://doi.org/10.1177/031289621987767

Magdama, F., Monserrate-Maggi, L., Serrano, L., Sosa, D., Geiser, D. M., & Jiménez-Gasco, M. D. M. (2019). Comparative analysis uncovers the limitations of current molecular detection methods for Fusarium oxysporum f. sp. cubense race 4 strains. *PLoS One*, *14*(9), Article e0222727. https://doi.org/10.1371/journal.pone.0222727

Materne, N., & Inoue, M. (2018, March 12-13). *IoT monitoring system for early detection of agricultural pests and diseases*. [Paper presentation]. 12th South East Asian Technical University Consortium (SEATUC), Yogyakarta, Indonesia. https://doi.org/10.1109/SEATUC.2018.8788860

Mishra, M., Choudhury, P., & Pati, B. (2021). Modified ride-NN optimiser for the IoT based plant disease detection. *Journal of Ambient Intelligence and Humanized Computing, 12*(1), 691-703. https://doi.org/10.1007/s12652-020-02051-6

Mohamed Shaffril, H. A., Samsuddin, S. F., & Abu Samah, A. (2021). The ABC of systematic literature review: The basic methodological guidance for beginners. *Quality & Quantity, 55*(4), 1319-1346. https://doi.org/10.1007/s11135-020-01059-6

Mongeon, P., & Paul-Hus, A. (2016). The journal coverage of Web of Science and Scopus: A comparative analysis. *Scientometrics, 106*(1), 213-228. https://doi.org/10.1007/s11192-015-1765-5

Nasir, I. M., Bibi, A., Shah, J. H., Khan, M. A., Sharif, M., Iqbal, K., Nam, Y., & Kadry, S. (2021). Deep learning-based classification of fruit diseases: An application for precision agriculture. *Computers, Materials & Continua, 66*(2), 1949-1962. https://doi.org/10.32604/cmc.2020.012945

Nawaz, M. A., Khan, T., Rasool, R. M., Kausar, M., Usman, A., Bukht, T. F. N., Ahmad, R. & Ahmad, J. (2020). Plant disease detection using Internet of Thing (IoT). *International Journal of Advanced Computer Science and Applications*, *11*(1), 505-509. https://doi.org/10.14569/ijacsa.2020.0110162

Oerke, E. C. (2006). Crop losses to pests. *The Journal of Agricultural Science, 144*(1), 31-43. https://doi.org/10.1017/s0021859605005708

Olivares, B. O., Rey, J. C., Lobo, D., Navas-Cortés, J. A., Gómez, J. A., & Landa, B. B. (2021). Fusarium wilt of bananas: A review of agro-environmental factors in the Venezuelan production system affecting its development. *Agronomy, 11*(5), Article 986. https://doi.org/10.3390/agronomy11050986

Omar, N., Zen, H., Anak Aldrin, N. N. A. A., Waluyo, W., & Hadiatna, F. (2020). Accuracy and reliability of data in IoT system for smart agriculture. *International Journal of Integrated Engineering, 12*(6), 105-116. https://doi.org/10.30880/ijie.2020.12.06.013

Ostertagová, E. (2012). Modelling using polynomial regression. *Procedia Engineering, 48*, 500-506. https://doi.org/10.1016/j.proeng.2012.09.545

Page, M. J., McKenzie, J. E., Bossuyt, P. M., Boutron, I., Hoffmann, T. C., Mulrow, C. D., Shamseer, L. Tetzlaff, J. M., Akl, E. A., Brennan, S. E., Chou, R. Glanville, J., Grimshaw, J. M., Hrobjartsson, A., Lalu, M. M., Li, T., Loder, E. W., Wilson, E. M., McDonald, S., … & Moher, D. (2021). The PRISMA 2020 statement: An updated guideline for reporting systematic reviews. *International Journal Of Surgery, 88*, Article 105906. https://doi.org/10.1016/j.ijsu.2021.105906

Patil, S. S., & Thorat, S. A. (2016, August 12-13). *Early detection of grapes diseases using machine learning and IoT.* [Paper presentation]. Second International Conference on Cognitive Computing and Information Processing (CCIP), Mysuru, India. https://doi.org/10.1109/CCIP.2016.7802887

Pawara, S., Nawale, D., Patil, K., & Mahajan, R. (2018, April 06-08). *Early detection of pomegranate disease using machine learning and internet of things*. [Paper presentation] 3rd International Conference for Convergence in Technology (I2CT), Pune, India. https://doi.org/10.1109/I2CT.2018.8529583

Pérez-Expósito, J. P., Fernández-Caramés, T. M., Fraga-Lamas, P., & Castedo, L. (2017). VineSens: An eco-smart decision-support viticulture system. *Sensors, 17*(3), Article 465. https://doi.org/10.3390/s17030465

Ramesh, B., Divya, M., & Revathi, G. P. (2020, November 12-13). *Farm easy-IoT based automated irrigation, monitoring and pest detection using thingspeak for analysis of ladies finger plant*. [Paper presentation]. International Conference on Recent Trends on Electronics, Information, Communication & Technology (RTEICT), Bangalore, India. https://doi.org/10.1109/RTEICT49044.2020.9315688

Ratnaparkhi, S., Khan, S., Arya, C., Khapre, S., Singh, P., Diwakar, M., & Shankar, A. (2020). Smart agriculture sensors in IoT: A review. *Materials Today: Proceedings*. https://doi.org/10.1016/j.matpr.2020.11.138

Rawi, R., Hasnan, M. S. I., & Sajak, A. A. S. (2020). Palm oil soil monitoring system for smart agriculture. *International Journal of Integrated Engineering, 12*(6), 189-199. https://doi.org/10.30880/ijie.2020.12.06.022

Rochester, E., Ma, J., Lee, B., & Ghaderi, M. (2019, April 15-18). *Mountain pine beetle monitoring with IoT*. [Paper presentation]. IEEE 5th World Forum on Internet of Things (WF-IoT), Limerick, Ireland. https://doi.org/10.1109/WF-IoT.2019.8767291.

Roslin, N. A., Che'Ya, N. N., Rosle, R., & Ismail, M. R. (2021). Smartphone application development for rice field management through aerial imagery and Normalised Difference Vegetation Index (NDVI) analysis. *Pertanika Journal of Science & Technology, 29*(2), 809-836. https://doi.org/10.47836/pjst.29.2.07

Saleem, R. M., Kazmi, R., Bajwa, I. S., Ashraf, A., Ramzan, S., & Anwar, W. (2021). IOT-Based cotton whitefly prediction using deep learning. *Scientific Programming, 2021,* 1-17. https://doi.org/10.1155/2021/8824601

Sarangi, S., Umadikar, J., & Kar, S. (2016). Automation of agriculture support systems using wisekar: Case study of a crop-disease advisory service. *Computers and Electronics in Agriculture, 122*, 200-210. https://doi.org/10.1016/j.compag.2016.01.009

Seo, Y., & Umeda, S. (2021). Evaluating farm management performance by the choice of pest-control sprayers in rice farming in Japan. *Sustainability, 13*(5), Article 2618. https://doi.org/10.3390/su13052618

Sethy, P. K., Behera, S. K., Kannan, N., Narayanan, S., & Pandey, C. (2021). Smart paddy field monitoring system using deep learning and IoT. *Concurrent Engineering, 29*(1), 16-24. https://doi.org/10.1177/1063293X21988944

Shafi, U., Mumtaz, R., Iqbal, N., Zaidi, S. M. H., Zaidi, S. A. R., Hussain, I., & Mahmood, Z. (2020). A multi-modal approach for crop health mapping using low altitude remote sensing, internet of things (IoT) and machine learning. *IEEE Access, 8*, 112708-112724. https://doi.org/10.1109/ACCESS.2020.3002948

Singh, V., & Misra, A. K. (2017). Detection of plant leaf diseases using image segmentation and soft computing techniques. *Information Processing in Agriculture, 4*(1), 41-49. https://doi.org/10.1016/j.inpa.2016.10.005

Sobreiro, L. F., Branco, S., Cabral, J., & Moura, L. (2019, October 14-17). *Intelligent insect monitoring system (I2MS): Using internet of things technologies and cloud based services for early detection of pests of field crops*. [Paper presentation]. IECON 2019 - 45th Annual Conference of the IEEE Industrial Electronics Society, Lisbon, Portugal. https://doi.org/10.1109/IECON.2019.8927085

Uddin, M. A., Mansour, A., Le Jeune, D., Ayaz, M., & Aggoune, E. H. M. (2018). UAV-Assisted dynamic clustering of wireless sensor networks for crop health monitoring. *Sensors, 18*(2), Article 555. https://doi.org/10.3390/s18020555

Udutalapally, V., Mohanty, S. P., Pallagani, V., & Khandelwal, V. (2020). Scrop: A novel device for sustainable automatic disease prediction, crop selection, and irrigation in internet-of-agro-things for smart agriculture. *IEEE Sensors Journal, 21*(16), 17525-17538. https://doi.org/10.1109/JSEN.2020.3032438

Van den Berg, W., Vos, J., & Grasman, J. (2012). Multimodel inference for the prediction of disease symptoms and yield loss of potato in a two-year crop rotation experiment. *International Journal of Agronomy, 2012*, Article 438906. https://doi.org/10.1155/2012/438906

Van Eck, N. J., & Waltman, L. (2021). *VOSviewer Manual Version 1.6.17*. Universiteit Leiden.

Varandas, L., Faria, J., Gaspar, P. D., & Aguiar, M. L. (2020). Low-cost IoT remote sensor mesh for large-scale orchard monitorization. *Journal of Sensor and Actuator Networks, 9*(3), Article 44. https://doi.org/10.3390/jsan9030044

Vazquez, J. P. G., Torres, R. S., & Perez, D. B. P. (2021). Scientometric analysis of the application of artificial intelligence in agriculture. *Journal of Scientometric Research, 10*(1), 55-62. https://doi.org/10.5530/jscires.10.1.7

Verma, S., Chug, A., & Singh, A. P. (2018, September 19-22). *Prediction models for identification and diagnosis of tomato plant diseases*. [Paper presentation]. International Conference on advances in computing, communications and informatics (ICACCI), Bangalore, India. https://doi.org/10.1109/ICACCI.2018.8554842.

Wang, K. Q., & Cai, K. (2011). On design of sensor nodes in the rice planthopper monitoring system based on the internet of things. *PIAGENG 2010: Photonics and Imaging for Agricultural Engineering, 7752*, 74-81. https://doi.org/10.1117/12.887423

Wang, X., Wang, Z., Zhang, S., & Shi, Y. (2015, September). *Monitoring and discrimination of plant disease and insect pests based on agricultural IoT*. [Paper presentation]. 4th International Conference on Information Technology and Management Innovation, Shenzhen, China. https://doi.org/10.2991/icitmi-15.2015.21

Wei, X., Aguilera, M., Walcheck, R., Tholl, D., Li, S., Langston Jr, D. B., & Mehl, H. L. (2021). Detection of soilborne disease utilizing sensor technologies: Lessons learned from studies on stem rot of peanut. *Plant Health Progress*, *22*(4), 436-444. https://doi.org/10.1094/PHP-03-21-0055-SYN

Xie, H., Zhang, Y., & Duan, K. (2020). Evolutionary overview of urban expansion based on bibliometric analysis in Web of Science from 1990 to 2019. *Habitat International, 95*, Article 102100. https://doi.org/10.1016/j.habitatint.2019.102100

Xu, J., Gu, B., & Tian, G. (2022). Review of agricultural IoT technology. *Artificial Intelligence in Agriculture*, *6,* 10-22. https://doi.org/10.1016/j.aiia.2022.01.001

Zhang, J., Liu, J., Chen, Y., Feng, X., & Sun, Z. (2021). Knowledge mapping of machine learning approaches applied in agricultural management - A scientometric review with CiteSpace. *Sustainability, 13*(14), Article 7662. https://doi.org/10.3390/su13147662

Zhang, J., Rao, Y., Man, C., Jiang, Z., & Li, S. (2021). Identification of cucumber leaf diseases using deep learning and small sample size for agricultural internet of things. *International Journal of Distributed Sensor Networks, 17*(4), 1-13. https://doi.org/10.1177/15501477211007407

Pertanika J. Sci. & Technol. 31 (4): 1645 - 1667 (2023)

PERTANIKA JOURNALS

SCIENCE & TECHNOLOGY

Journal homepage: http://www.pertanika.upm.edu.my/

Properties of Sustainable Concrete Containing Different Percentages and Particles of Oil Palm Ash as Partial Sand Replacement

Farah Nora Aznieta Abdul Aziz[1]*, Al-Ghazali Noor Abbas[1], Law Kay Min[2], Kalaiyarasi Aramugam[2], Noor Azline Mohd Nasir[1] and Teik Hua Law[3]

[1]Housing Research Centre, Department of Civil Engineering, Faculty of Engineering, Universiti Putra Malaysia, 43400 UPM, Serdang, Selangor, Malaysia

[2]Department of Civil Engineering, Faculty of Engineering, Universiti Putra Malaysia, 43400 UPM, Serdang, Selangor, Malaysia

[3]Road Safety Research Centre, Department of Civil Engineering, Faculty of Engineering, Universiti Putra Malaysia, 43400 UPM, Serdang, Selangor, Malaysia

ABSTRACT

Oil palm shell (OPS) in concrete is well studied as an alternative material of fine aggregate in concrete, as a way to use agricultural waste, and helps to contribute to environmental sustainability and economical construction cost. However, OPS addition will lead to lower properties of the concrete, and much research focuses on treating the OPS to overcome it. Many previous works focused on replacement without examining the effect of different particle sizes of OPS. Hence, this study focuses on the performance of concrete with different particle sizes of OPS as sand replacers in concrete at 25% and 50%. The physical and permeability properties of concrete prepared with OPS particle sizes in the ranges between 600μm to 4.75mm (L), 300μm to 1.18mm (M), and of less than 600μm (S) and two different percentages of 25% and 50% by weight as sand replacement are examined. More than 200 cubes, cylinders, and prisms were tested to determine their physical, mechanical, and permeability properties. The workability was measured by the slump height, the mechanical properties by the compressive strength test, flexural strength test, splitting tensile test, ultrasonic pulse velocity (UPV) test, and rebound hammer test. While the permeability properties by the water penetration test, sorptivity test, and rapid chloride permeability test. The findings showed that increasing the particle sizes of OPS would reduce concrete's physical and

ARTICLE INFO

Article history:
Received: 27 April 2022
Accepted: 05 July 2022
Published: 24 May 2023

DOI: https://doi.org/10.47836/pjst.31.4.03

E-mail addresses:
farah@upm.edu.my (Farah Nora Aznieta Abdul Aziz)
na706050@gmail.com (Noor Abbas Al-Ghazali)
kaymin96@gmail.com (Law Kay Min)
kalai2807@yahoo.com (Kalaiyarasi Aramugam)
lawteik@upm.edu.my (Teik Hua Law)
nazline@upm.edu.my (Noor Azline Mohd Nasir)
* Corresponding author

ISSN: 0128-7680
e-ISSN: 2231-8526

permeability properties. The optimum OPS particle size for structural concrete grade 30 is less than 600μm. With OPS particles of 600um, green concrete using OPS can be made for medium to low-strength applications in the construction industry.

Keywords: Different sieve size, oil palm shell (OPS), permeability properties, physical properties, sand replacement, sustainability

INTRODUCTION

Malaysia is the second-largest oil palm producer in the world, producing more than 52% of the world's total palm oil (Tripathi et al., 2015). Malaysia's oil palm tree land area has grown from 54,000 hectares in 1960 to 5.90 million in 2019 (Ting et al., 2020). At the same time, this industry generates an increasing number of by-products that are disposed of as waste. OPS is a by-product of palm oil mills produced after the fruit's oil is extracted. Using this substance as one of the mixing ingredients in concrete would increase the waste's functionality, reducing the quantity of OPS, which would otherwise end up in landfills. The open burning of OPS to eliminate solid waste also contributed to environmental pollution. The construction industry, on the other hand, is developing at a fast pace, and the demand for concrete for construction has greatly increased (Qasem et al., 2021). The high demand for concrete in construction leads to natural resource depletion, particularly sand. The sand formation takes thousands of years of erosion and rock breaking down, but it is used relatively quickly. In 2012, the yearly aggregate usage was predicted to be between 25 and 29 billion tonnes, with demands expected to reach 50 billion in 2019 (UNEP, 2019). The extensive usage of natural sand has negatively impacted the environment and ecosystem, threatening species (Sutherland et al., 2017). Numerous studies have been carried out on recycled materials for replacing aggregates in concrete to overcome these issues.

Substitution of aggregates with agricultural waste is an environmental-friendly option as agricultural waste is a type of sustainable material. Since OPS is cheap and easily available in Malaysia, it can replace the aggregate (Rahman et al., 2020). Huda et al. (2016) stated that the utilization of OPS as a replacement for the aggregates in concrete could solve the issue of natural aggregate depletion and air pollution resulting from the aggregate production process. Moreover, according to Olanipekun et al. (2006), the substitution of the aggregate with OPS has the potential to reduce the cost by 42%. The cost of concrete production is a crucial component in construction as it influences the construction cost of a project. In the last decade, extensive work has been conducted on using OPS as a replacement for the coarse aggregate in the production of concrete (Mo et al., 2017; Mannan & Ganapathy, 2002; Mannan & Ganapathy, 2004).

Maghfouri et al. (2018) reported on the performance of concrete containing different percentages of OPS to replace the coarse aggregates with percentages from zero to 100% with an interval of 20%. The authors reported that the percentage of OPS should not exceed 60% of the total volume of coarse aggregate. At the same time, Mo et al. (2015) studied the performance of concrete mixes containing the OPS as coarse aggregate lightweight concrete with different percentages of ground granulated blast slag (GGBS) on the mechanical and bond properties of OPS concrete (OPSC). The findings demonstrate that although a higher GGBS percentage reduced strength, the OPSC with GGBS as a 60% cement replacement material had compressive and splitting tensile strengths of 25 and 2.3 MPa, respectively, which were higher than the minimum stated strength required for lightweight structural concrete.

Mannan et al. (2006) investigated several pre-treatment techniques for increasing the quality of OPS aggregates to achieve higher OPSC strength. Their techniques were comparable to how wood is treated with preservatives. The authors achieved OPS concrete with compressive strength of 33 MPa, around 39% greater than the control concrete (with untreated OPS aggregate). However, no specific grading of OPS is recorded. Similarly, Nadh et al. (2021) also found that OPSC prepared with treated OPS exhibited higher strength than concrete with untreated OPS. Besides, the SEM images showed fewer gaps between the treated OPS and the cement matrix, which refer to better bonding between the constituents of the concrete.

The literature shows that several investigations on OPSC have been conducted, particularly for lightweight structures. However, there was insufficient information about the effect of grading the OPS particles on the mechanical characteristics, permeability, unit weight, and other attributes of the OPSC when utilized as a partial replacement for the fine aggregates. Studies mainly focused on the impacts of OPS content, the pre-treatment methods, curing conditions, and adding supplementary cementitious materials like the GGBS and fly ash.

The grading of the particles is one of the most important factors in evaluating the sand's quality. It directly impacts workability and paste requirements and may have an economic impact. Guan et al. (2020) reported that the size of sand particles significantly affects the strength and permeability of concrete.

The novelty of this work is to study the effect of OPS percentage and grading on the engineering properties of the concrete using this by-product as a partial replacement for the sand. Hence, the impact of OPS percentage and grading on various properties of OPSC was examined and compared with the control mix prepared with normal sand. The proportions of OPS with sizes ranging between 600μm to 4.75mm (L), 300μm to 1.18mm (M), and of less than 600μm (S) were used to form three categories of gradings.

MATERIALS AND METHOD

Materials

Cement, OPS, water, and aggregates produce concrete. All materials are carefully selected in accordance with the rules of practice that apply to all materials. Ordinary Portland Cement (OPC) is used to produce the samples, which are widely available locally. The coarse aggregates used in this research were with a maximum size of 10mm and a specific gravity of 2.7, while the specific gravity of the fine aggregates was 2.58. For this research, the OPS is sieved using a shaker machine according to their respective ranges of sizes of 600μm to 4.75mm, 300μm to 1.18mm, and less than 600μm forming three categories of gradings. The water absorption and the specific gravity of OPS were 25.31% and 1.14, respectively.

Mix Proportions and Preparation of Concrete

Seven batches of concrete mixtures were prepared. Variables in each mix are the percentage of OPS replacement, which are 25% and 50%, and the particle size of the OPS, between 600μm to 4.75mm, 300μm to 1.18mm, and of less than 600μm. The description of each batch of concrete is tabulated in Table 1.

The proportion of the coarse aggregates, fine aggregate, cement, and water is determined using British Mix Design Method (DOE Method) with a design concrete characteristic strength at 28 days is 30 N/mm^2, while the target slump height is in the range of 30mm to 60mm. Table 1 displays the mixed proportions of concrete materials with various ratios of sand replacement in OPS concrete. The 0% replacement is the control sample.

In the mixing process, the aggregates and the OPS were dry mixed for 4 minutes, and then the OPC was added and mixed for another 3 minutes. After that, the required water was added and mixed for 6 min before being poured into oiled moulds and vibrating. In total, more than 200 cubes, cylinders, and prisms were made using different batches of

Table 1
Mix Proportions in kg/m^3

Mix ID	OPS percentage %	Range of OPS particle size	Cement	Water	Coarse aggregate	Sand	OPS
OPSC 0	0	-	390	230	1130	660	0
OPSC L25	25	600μm to 4.75mm	390	230	1130	495	165
OPSC M25	25	300μm to 1.18mm	390	230	1130	495	165
OPSC S25	25	less than 600μm	390	230	1130	495	165
OPSC L50	50	600μm to 4.75mm	390	230	1130	330	330
OPSC M50	50	300μm to 1.18mm	390	230	1130	330	330
OPSC S50	50	less than 600μm	390	230	1130	330	330

concrete. Three repetitive samples were prepared for each test, and average testing results were calculated.

Sample Preparations

A total of 63 concrete cubes with dimensions of 100 mm were prepared to determine the compressive strength at 7, 28, and 56 days. For the tensile strength, sorptivity, and chloride tests, 84 concrete cylinders with dimensions of 100 mm × 200 mm were prepared. Furthermore, 21 concrete prism beams of 100 mm × 100 mm × 500 mm dimensions were cast for flexural strength test at 28 days. In order to determine the water penetration depth under pressure at 28 and 56 days, 56 big cubes of 150mm dimensions were also prepared.

Test Method

The workability of the fresh concrete was performed using the slump test according to ASTM C1437, as displayed in Figure 1(a). The compressive, flexural, and tensile strength tests were conducted following BS EN 12390-3 (2009), BS EN 12390-5 (2009) BS EN 12390-6 (2009), respectively, as shown in Figures 1(b), 1(c) and 1(d). For the Non-Destructive Tests (NDT), the UPV and the rebound hammer tests were performed according to ASTM C597-09 (2010) and ASTM C 805-02 (2002) guidelines, respectively, as presented in Figures 1(e) and 1(f). For the durability properties, BS EN 12390-8 (2009), ASTM C1585-13 (2013), and ASTM C1202 (2012) were followed to conduct the water penetration, sorptivity, and rapid chloride permeability test (RCPT) tests, respectively, as shown in Figures 1(g) and 1(h).

RESULTS AND DISCUSSION

Slump

The slump test is used to examine the fresh concrete's consistency and workability. The slump is set to fall from 30mm to 60mm. The slump height of various mixtures is presented in Figure 2. The inclusion of OPS in the mixtures decreased the workability by 34%. The slump height of the mixes containing OPS decreased gradually with increasing OPS percentage; however, including finer particles of OPS increased the slump.

The percentage of sand replacement in concrete with OPS influences the slump height. The highest slump of OPS concrete is 55 mm for the mixtures prepared with 25% OPS, while the lowest was obtained when the percentage of OPS increased to 50%. This trend might be associated with OPS's increased water absorption capacity when a higher amount is included in the mixtures. The decreasing slump height of OPS concrete with the increment in the OPS percentage is in line with Khan et al. (2016), who observed a decline of 44% in slump height of concrete with OPS when the percentage increased from 10% to 40%.

Figure 1. Test setup of (a) slump, (b) compressive strength, (c) flexural strength, (d) splitting tensile strength, (e) UPV, (f) rebound hammer, (g) water penetration, and (h) RCPT

The results also show that increasing the particle size of the OPS decreased the workability of the concrete mixtures. OPSC with smaller particle sizes (OPSC S25, OPSC, and S50) achieved a higher slump than OPSC with a larger particle size (OPSC L25 and OPSC L50) of all percentages. It could be justified by the fact that decreasing the OPS particles increased the packing of concrete and decreased the amount of entrapped air.

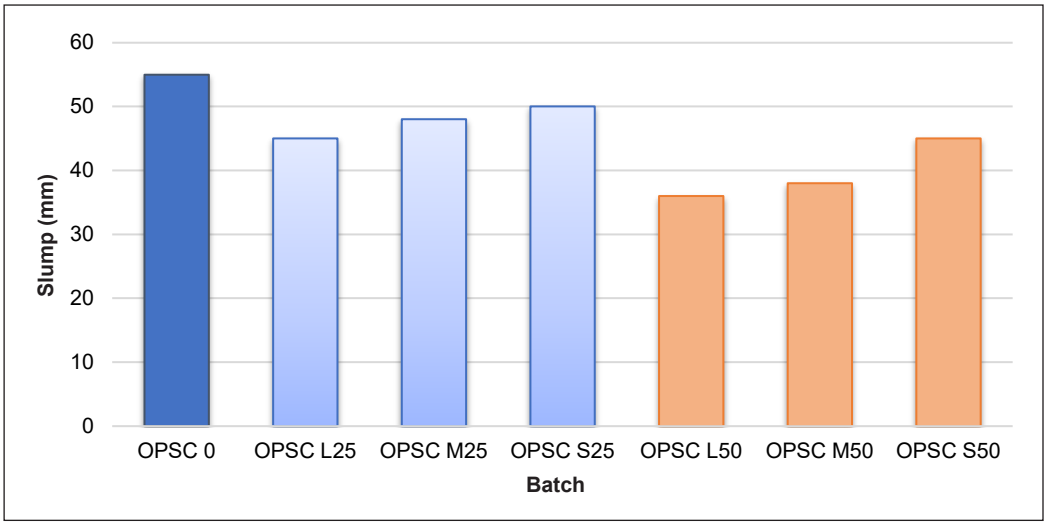

Figure 2. Slump height of concrete mixtures

Density

The density was measured by the dried density method. Concrete density is the ratio of weight to its unit volume. Concrete with a density of lower than 2000kg/m^3 is lightweight concrete (LWC), while concrete with a density of 2400 kg/m^3 is normal-weight concrete (NWC) (Teo et al., 2006). Figure 3 shows the average density of all concrete mixes at 28 days. The density of concrete decreased with the inclusion of OPS. Besides, increasing the percentage of OPS from 25% to 50% resulted in a higher reduction because the specific gravity of OPS is half of the sand, which is 1.14 and 2.58, respectively. Replacing the sand with OPS in concrete increased the void content of the mixture. Similar findings of density reduction were achieved by Babafemi & Olusola (2012), who reported that densities of concrete samples with 100% sand and 25% palm shell ranged between 2000 and 2400 kg/m^3, respectively classifying them as NWC. However, at 50%, 75%, and 100% palm shell replacement levels, the density values were between 1340 and 1900 kg/m^3, classifying them as LWC.

Figure 3 shows that the concrete changed from NWC for 25% OPS concrete to LWC for 50% OPS concrete due to the higher percentage of OPS with low specific gravity and higher porosities.

In terms of the grading effect, the findings show that increasing the particle size of the OPS decreased the density of the OPSC mixtures. OPSC with smaller particle sizes, OPSC M25, and OPSC S25 are considered NWC, while the other mixes are categorized as LWC. The lower density of OPSC with larger particles could be attributed to the air-entrapping impact, causing the formation of tiny air bubbles in the concrete structure (Abbas et al., 2022).

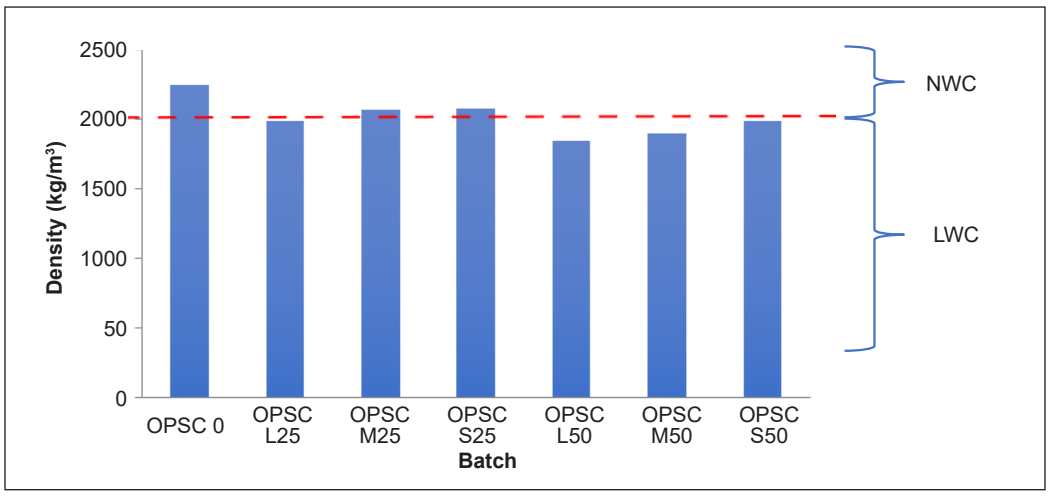

Figure 3. Average concrete density at 28 days

Compressive Strength

The average compressive strength of mixes is presented in Figure 4. The control specimen (OPSC 0) achieved the design concrete compressive strength of 30 MPa. The strength of concrete increases as the days of curing increase, except two mixtures exhibited a decrease in strength at 56 days compared to their values in 28 days, which are OPSC M50 and OPSC S50 mixes. The dimensional instability due to the high water absorption capacity of the OPS particles during curing contributes to this strength loss. It is evidenced by the high water absorption of OPS found in this study, which was 25.31%. As a result, the bond strength between OPS and the surrounding concrete matrix is weakened (Momoh & Osofero, 2019).

The compressive strength of OPSC is lower than the control sample at all testing ages. Also, an increasing percentage of OPS as a sand replacement caused a higher reduction in strength. A similar trend has been reported by other researchers (Muthusamy et al., 2013), confirming the best performance of concrete with 25% OPS. Mannan & Ganapathy (2002) also reported that the compressive strength development in concrete mixtures prepared with OPS was almost 49%–55% lower than in the reference sample. The compressive strength is affected by porosity. The OPS concrete showed a lower density (Figure 3), indicating a larger porosity than the control concrete, thus, lower compressive strength.

Figure 4 also shows that increasing the OPS particle size at both replacement percentages decreased the OPS compressive strength of the OPSC. The OPSC with finer particle size achieved higher compressive strength at all ages (OPSC S25 and OPSC S50). It could be attributed to finer particles' better filling and packing features (Lim et al., 2013). For OPSC with 25% of sand replacement, the compressive strength of OPSC S25 is the highest, while the compressive strength of OPSC L25 is the lowest. A similar trend for OPSC with 50% sand replacement can be observed.

In this research, all batches of OPSC with 25% sand replacement achieved the minimum structural concrete compressive strength of 17 MPa. While for OPS concrete with 50% sand replacement, the compressive strength of OPSC M50 and OPSC S50 is higher than 17 MPa. Only OPSC L50 does not achieve the minimum structural concrete compressive strength.

Thus, these findings indicate that the value of the compressive strength of OPSC highly depends on the percentage of the OPS in the mixtures in addition to the OPS particle size. The maximum amount of sand replacement in OPS concrete while achieving the structural concrete compressive strength is 50%, provided that small OPS particle sizes are used.

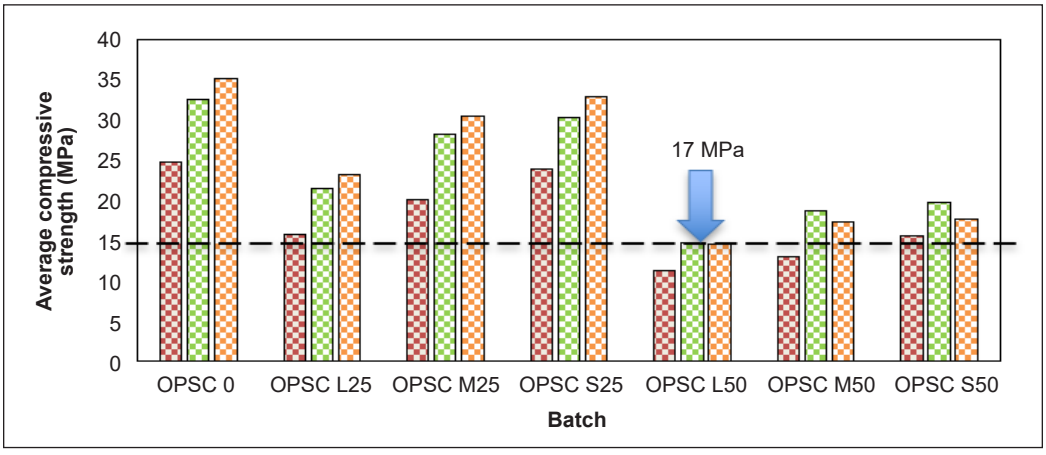

Figure 4: Average concrete compressive strength

The results are also analyzed by a two-way Analysis of Variance (ANOVA). The analysis used the composite strength as the dependent variable during the OPS and time as the explanatory variable. This statistical technique examined the effect of OPS and time and their interaction on the composite strength. An interaction effect happens when one explanatory variable's effect relies on another's level. Additionally, a post hoc Tukey test was utilized to detect significant differences between the levels of explanatory variables. The analysis results are in Table 2, indicating significant main effects of both the OPS and time on the composite strength at the significance level of 0.05. Also, a significant interaction effect was found between the OPS and time, suggesting that the differences in the effect of OPS depend on time (Figure 5).

Table 2
The effects of OPS and time on the composite strength

Source	Sum of Squares	Degree of Freedom	Mean Square	F-value	Level of Significance
OPS	2406.77	6	401.13	199.53	$P < 0.01$
TIME	548.75	2	274.38	136.48	$P < 0.01$
OPS*TIME	104.01	12	8.67	4.31	$P < 0.01$

The boxplot in Figure 6 shows no significant difference between OPSC0 and OPSCS25, as well as between OPSCM50 and OPSCS50. The boxplot indicates 28 days has no significant difference compared to 56 days (Figure 7). The post hoc Tukey test also supports these results. It means replacing 25% of 600µm fine particles of sand with OPS and 50% of less than 600µm to 1.18mm sand particles with OPS gives no significant differences in strength. It also proves that replacing 25% of sand with small particles of OPS will give similar strength. While at 50% replacement, small and medium particles of OPS give the same reduction effect to the strength.

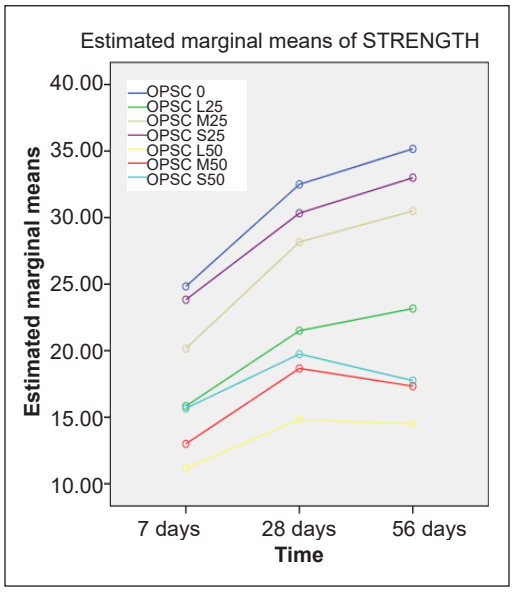

Figure 5. Interaction effect between OPS and time

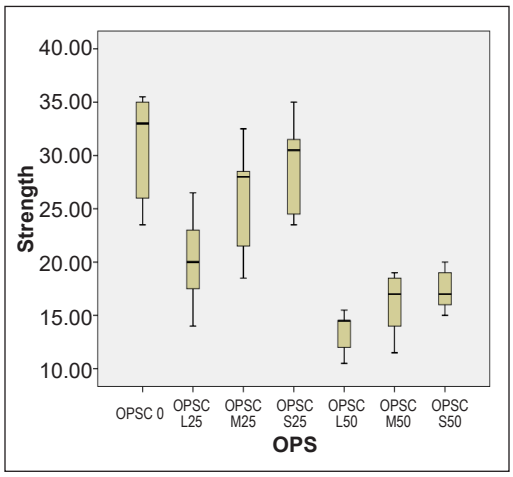

Figure 6. Boxplot of composite strength against OPS

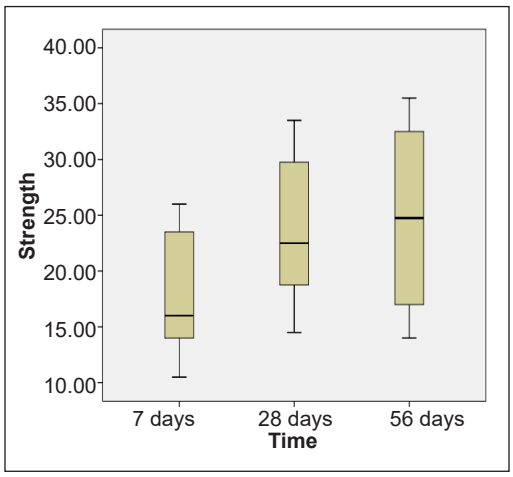

Figure 7. Boxplot of composite strength against time

Splitting Tensile Strength

The average splitting tensile strength is shown in Figure 8, and the relative changes in the strength of other concrete mixes than the control mixture are presented in Table 3. The results show that the tensile strength values range from 1.50–2.75 MPa. Besides, the samples containing OPS exhibited a loss in tensile strength ranging from 12% to 45% than that of the control sample (Table 3).

Similar to compressive strength results, including the OPS in the concrete mixtures decreased the tensile strength of the concrete. The tensile strength of OPSC S25 was close to that of the control specimen, which was 2.42 MPa. At the same time, the concrete samples containing 50% OPS recorded the lowest splitting tensile strength of 1.50 MPa. The reduction in strength is due to the porous nature of OPS that allows micro-cracks to spread during testing; hence lower strength is recorded (Karakoç et al., 2016). Alengaram et al. (2010) also reported that the concrete samples prepared with OPS achieved 30% lower tensile strength than that prepared with normal aggregates. The authors attributed the strength reduction to the weaker bond between the OPS particles and the concrete matrix.

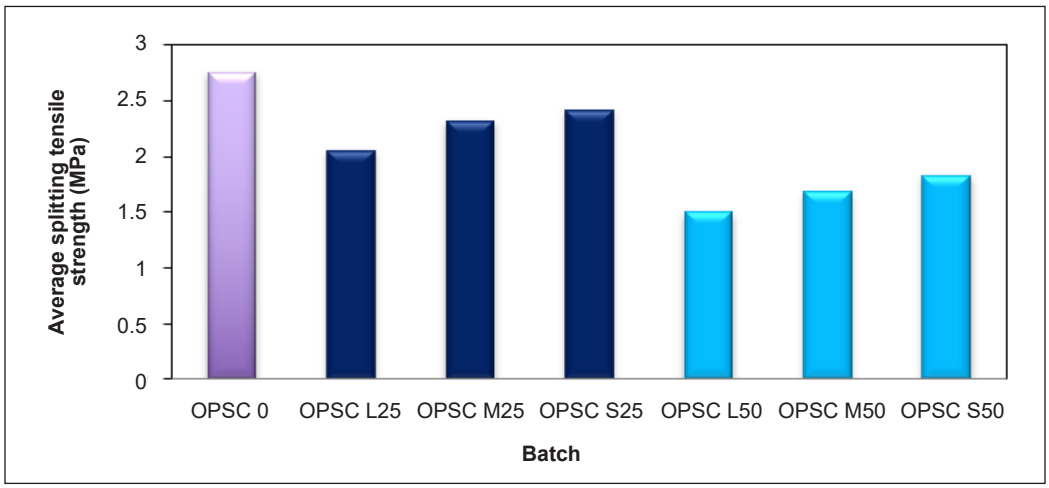

Figure 8. Average splitting tensile strength at 28 days

Table 3
Relative change in compressive, splitting tensile and flexural strength of concrete mixes

Batch	Compressive strength (MPa)	Splitting Tensile Strength (MPa)	Flexural Strength (MPa)
OPSC 0	32.5 (-)	2.75 (-)	4.6 (-)
OPSC L25	21.5 (-33.8%)	2.05 (-25%)	3.47 (-24.5%)
OPSC M25	28.17 (-13.3%)	2.32 (-15.6)	3.8 (-17%)
OPSC S25	30.33 (-6.6%)	2.42 (-12%)	4.2 (8.6)
OPSC L50	14.67 (-54.8%)	1.5 (-45%)	2.57 (-44%)
OPSC M50	18.67 (-42.5%)	1.68 (-38%)	2.8 (-39%)
OPSC S50	19.83 (-38.9)	1.83 (-33.4)	3.27 (-28%)

The results also show that decreasing the particle size of OPS enhanced the tensile strength for both percentages of OPS. For OPS concrete with 25% of sand replacement, OPSC S25 gained the highest splitting tensile strength with a strength reduction of 12%, while the OPSC L25 achieved the lowest splitting tensile strength and highest strength reduction of about 25%. OPS concrete with 50% sand replacement demonstrated a similar pattern. Hence, it shows that higher splitting tensile strength can be achieved when a smaller particle size of OPS is used in concrete.

Flexural Strength

The flexural strength of different concrete mixes is presented in Figure 9. The results show that replacing sand with OPS decreased the flexural strength of concrete, and increasing the OPS percentage caused a further reduction. A reduction of about 8.6%–24.5% and 28.9%–44.0% are recorded when 25% and 50% of OPS were included, respectively, as presented in Table 3 above. Although OPSC S50 has double the amount of sand replacement than OPSC S25, the strength reduction is three times higher, 28% and 8.6%, respectively. At the same time, the flexural strength reduction of OPSC M50 is 39% which is two times lower than OPSC M25 of 17%. The strength reduction is due to the weak interfacial bond between the binder and the OPS when a higher percentage of OPS is included in the mixture. As a result, flexural load-initiated cracks in the weaker location at the interfacial zone, resulting in flexural failure.

From the aspect of the OPS particle sizes, the results indicate that decreasing the particle size of the OPS increased the flexural strength by 21% and 27.23% for OPS with 25% OPS and 50% OPS concrete, respectively, for concrete samples prepared with 25% OPS, the highest value of flexural strength is attained by OPSC S25, which is 4.20 MPa,

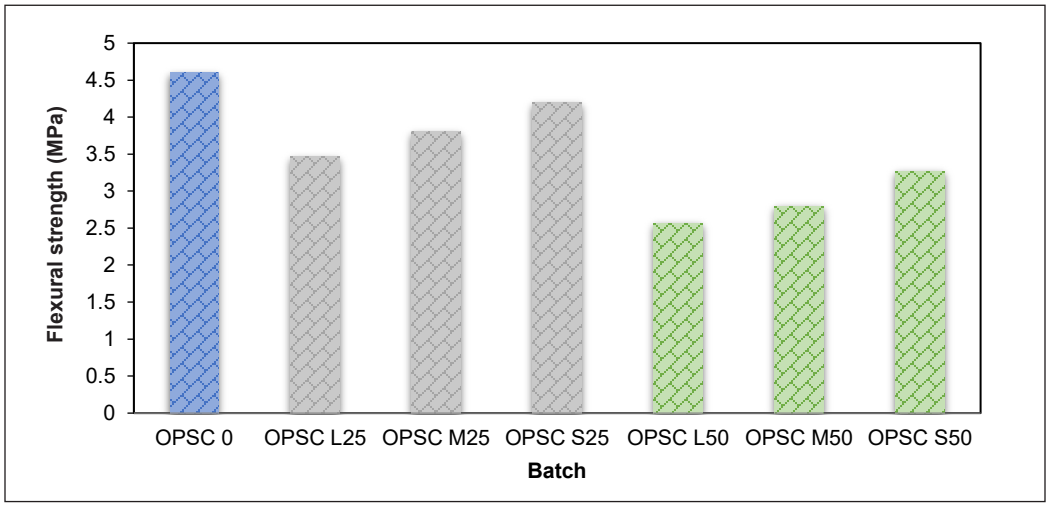

Figure 9. Average flexural strength at 28 days

while OPSC L25 achieved the lowest flexural strength, with a value of 3.47 MPa. OPS concrete with 50% sand replacement demonstrated a similar trend. The smaller particle of OPS in concrete can bond more effectively with the other concrete materials, which in turn aids in increasing the concrete flexural strength for resisting the applied tension. Thus, the smaller particle sizes of OPS are suitable for replacing sand in concrete as it does not reduce flexural strength.

Ultrasonic Pulse Velocity (UPV)

Ultrasonic Pulse Velocity (UPV) test is conducted to evaluate the quality of concrete, including its uniformity and the presence of cracks. Figure 10 displays the average UPV readings of specimens at 28 days. The results show that all the mixes are good quality concrete with UPV values between 3650m/s–4099m/s (Awal & Mohammadhosseini, 2016). Using OPS to replace the sand has decreased the UPV values of the samples. The replacement of sand with 25% of fine OPS (OPSC S25) produces an insignificant impact on the UPV results of less than 6%. Hence, it shows that decreasing the particle size of OPS impacts compactness positively and increases the UPV values to a certain percentage. OPSC S25 and OPSC M25 attained UPV of 4288m/s and 4245m/s, respectively, which are very close to the control sample.

However, further increases in the OPS percentage to 50% decreased the UPV values. This reduction in velocity is often attributed to the presence of microcracks in the samples, which decrease the homogeneity of the concrete. Besides, the porous features of OPS aggregate that are unable to create a good bond with the binder for the development of a highly packed concrete structure contribute to the reduction of UPV readings. The lack

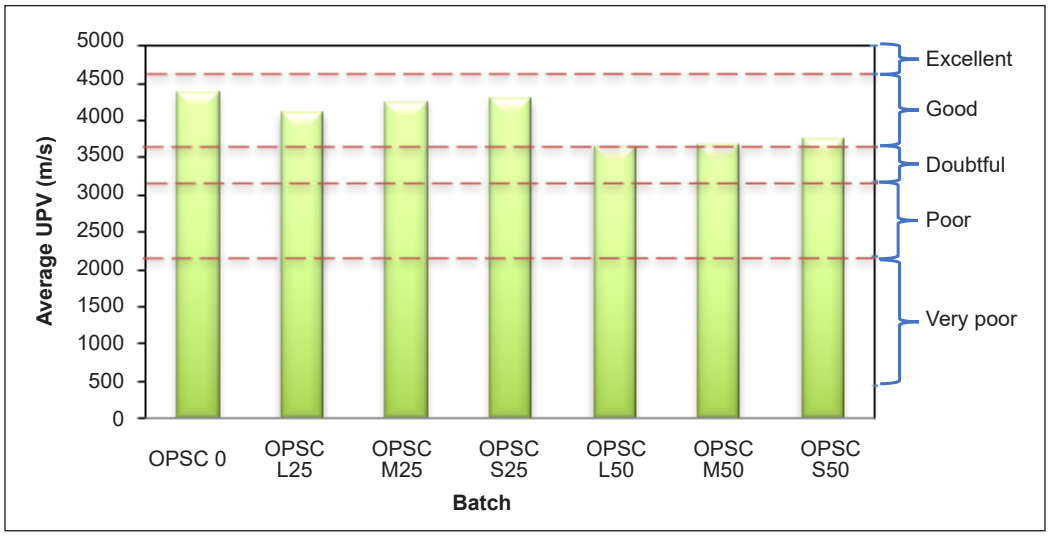

Figure 10. Average UPV of concrete at 28 days

of a strong interlocking action results in the formation of voids has resulted in a reduced pulse travel rate of UPV. Figure 11 displays the correlation between compressive strength and UPV, showing an average coefficient (R^2) of 0.89.

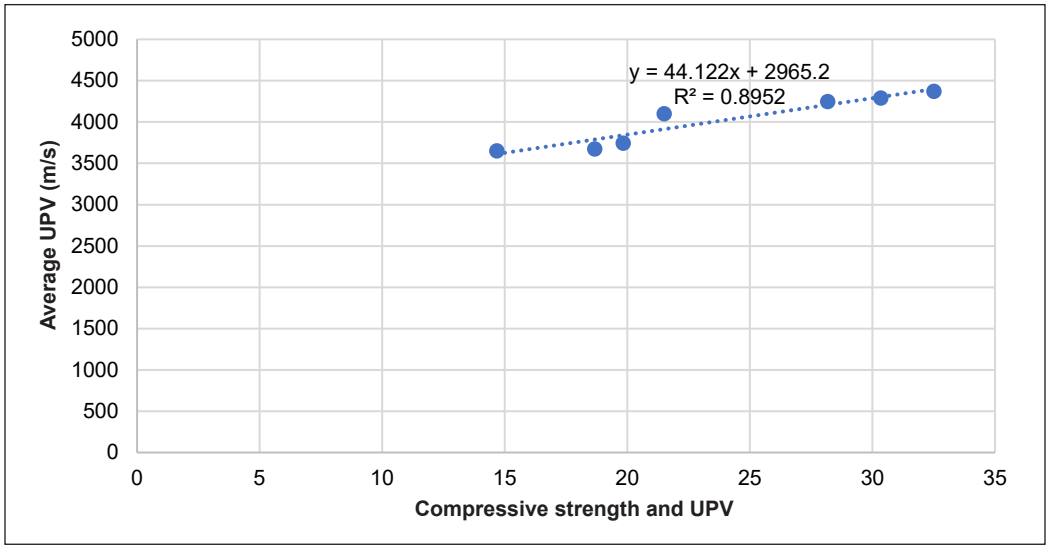

Figure 11. Relationship between compressive strength and UPV

Rebound Number

The other NDT test for concrete is the rebound hammer, tested to evaluate the concrete uniformity and quality in terms of its surface hardness at 28 days. The findings are illustrated in Figure 12. The OPS concrete displayed a lower rebound number than the control sample. Besides, the rebound number of OPSC concrete with 25% sand replacement ranges from 24 to 29, while samples with 50% OPSC range from 18 to 23.

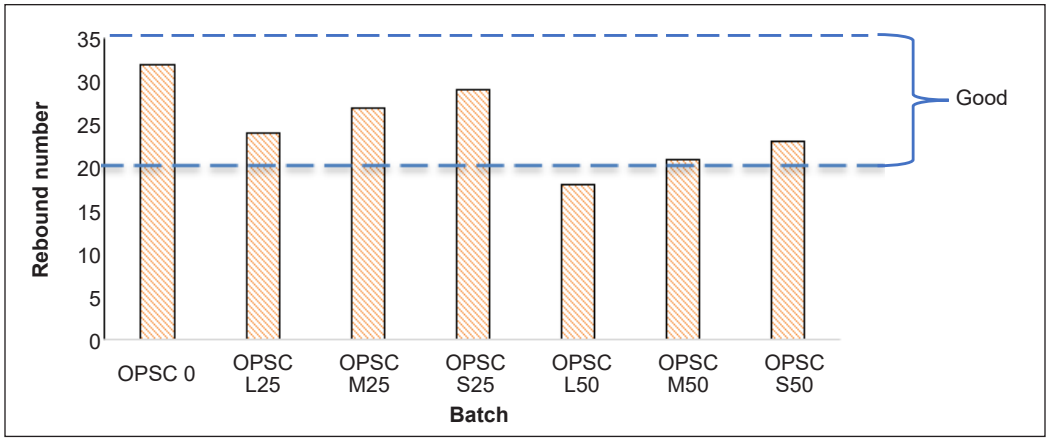

Figure 12. Average rebound number of concretes at 28 days

When smaller particle sizes of OPS are used, concrete density is higher, producing higher surface hardness concrete, i.e., rebound number. It is also observed that smooth surfaces of OPS affected the bonding between the cement matrix and OPS, which increased the porosity and reduced the surface hardness, i.e., the rebound number of concretes. The results show that all mixes attained higher than 20, an average rebound number accepted for structural application, except OPSC L50, which is 18.

The correlation of rebound number, UPV, and compressive strength is illustrated in Figure 13. The rebound number exhibits a positive relationship with compressive strength and UPV. It is also observed that the concrete compressive strength evaluated through the rebound hammer test is lower than the compressive strength measured through the compressive strength test. The percentage difference between the compressive strength values measured through the rebound hammer test and the compressive strength test is shown in Table 4. The differences between the compressive strength values measured from

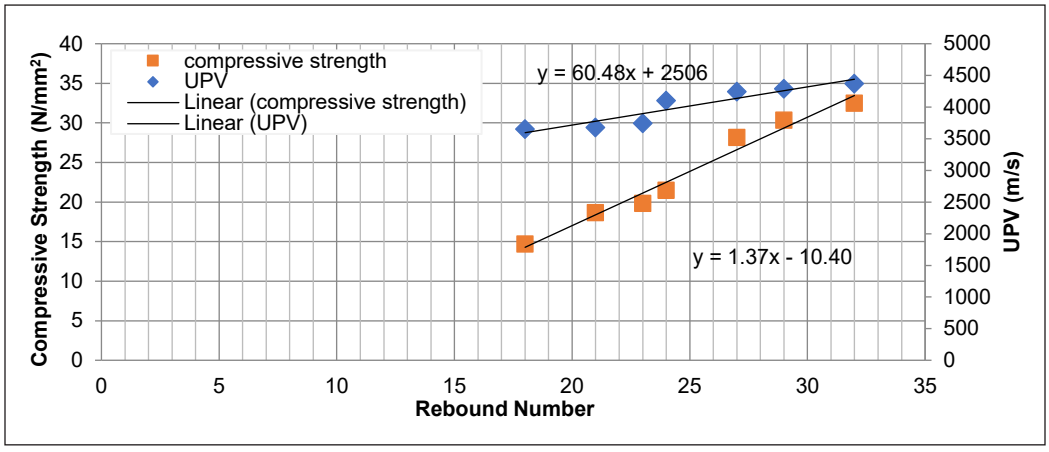

Figure 13. Correlation of rebound number with compressive strength and UPV

Table 4
Percentage difference of the compressive strength measured through rebound hammer test and compressive strength test

Batch	Average compressive strength measured from rebound hammer test (N/mm²)	Average compressive strength measured from compressive strength test (N/ mm²)	Percentage difference between both tests (%)
OPSC 0	30.33	32.50	6.67
OPSC L25	18.67	21.50	13.16
OPSC M25	23.66	28.17	16.01
OPSC S25	27.66	30.33	8.80
OPSC L50	<15	14.67	-
OPSC M50	15.67	18.67	16.07
OPSC S50	18.00	19.83	9.23

both tests range from 6.67% to 16.07%. The average compressive strength of concrete estimated through the rebound hammer correlation curves is lower than its actual value. However, the rebound hammer test still serves as a quick method to assess the concrete compressive strength, where concrete with a higher rebound number indicates that the concrete has a higher surface hardness. Hence, it can resist a higher amount of compressive force without failure.

Water Penetration Depth

The strength of concrete predominantly relies on the water capacity to infiltrate the solid microstructure, also known as permeability (Manjunath et al., 2019). The findings of water penetration depth under the pressure of the OPSC 0, concrete with 25% and 50% of OPS after 28 and 56 days are presented in Figure 14. All concrete show a similar trend: the water penetration depth increases from the 28th to the 56th day. The comparison of values indicates that the lowest penetration depth is obtained in the control specimens, and the penetration depth increases with increasing the percentage of OPS.

At 28 days, the control sample OPSC 0 and OPSC S25 obtained the lowest penetration depth of 31mm and 33mm, respectively. As the OPS replacement percentages increased, the water penetration depth increased. Higher percentages of OPS are associated with larger interconnected pores that produce a high surface area and allow more water penetration, and this effect is observed to be more severe with increasing time. Khan et al. (2016) found a similar phenomenon for concrete containing OPS, where increasing the OPS percentage from 10% to 40% as coarse aggregate replacement increased the water absorption of the concrete from 1.48% to 4.75%.

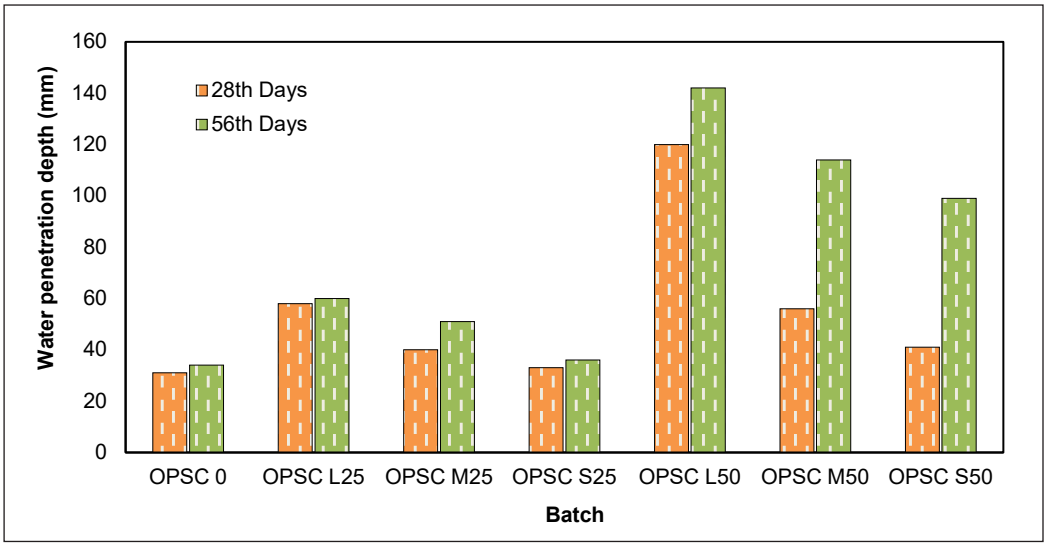

Figure 14. Water penetration test at 28 days and 56 days

In terms of OPS particle size, decreasing the particle size of OPS leads to better results in terms of water penetration. For the 25% replacement of OPS, the values of depth obtained for the sizes OPSC S25, OPSC M25, and OPSC L25 are 33mm, 40mm, and 58mm, respectively, while for the 56th day, the depths were 36mm, 51mm, and 60mm respectively. It could be attributed to the enhanced packing of OPS concrete with finer particle size. The 50% replacement of sand with OPS shows poor bonding between OPS and the matrix, allowing more water to penetrate the sample. It also witnesses more voids forming between the particles and cement matrix, hence providing a higher level of water permeability, as shown in Figure 14.

Sorptivity Test

One of the essential characteristics that determine the durability of concrete is the sorptivity (rate of water absorption), which refers to the ability of concrete to absorb and transmit water and other fluids by capillarity action. The sorptivity results after 28 and 56 days are displayed in Figures 15 and 16, respectively.

The results demonstrated that concrete samples prepared with OPS showed a higher water absorption rate than the control sample. Besides, the mixes prepared with 25% OPS exhibited lower water absorption than that with 50% OPS at the same grading, which aligns with the findings obtained from the water permeability test. The sorptivity levels for both produced a slight increase trend when time increased. Mannan and Ganapathy (2002) observed a similar pattern: the OPS mixes showed higher water absorption capacity than the control sample. The authors concluded that this behavior is due to the high absorption capacity of OPS particles, which increased the porosity of the concrete sample.

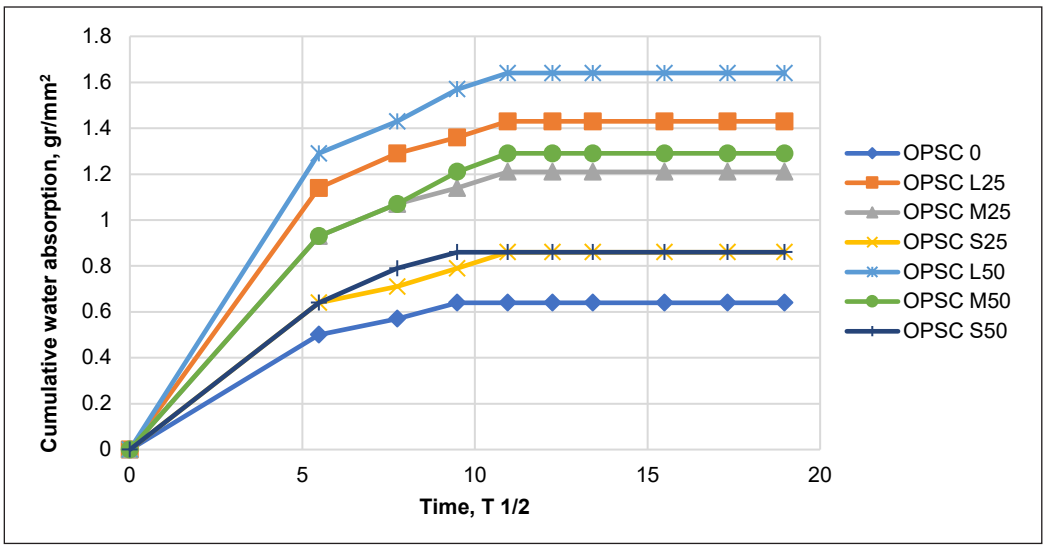

Figure 15. Water absorption versus square root of time at 28 days

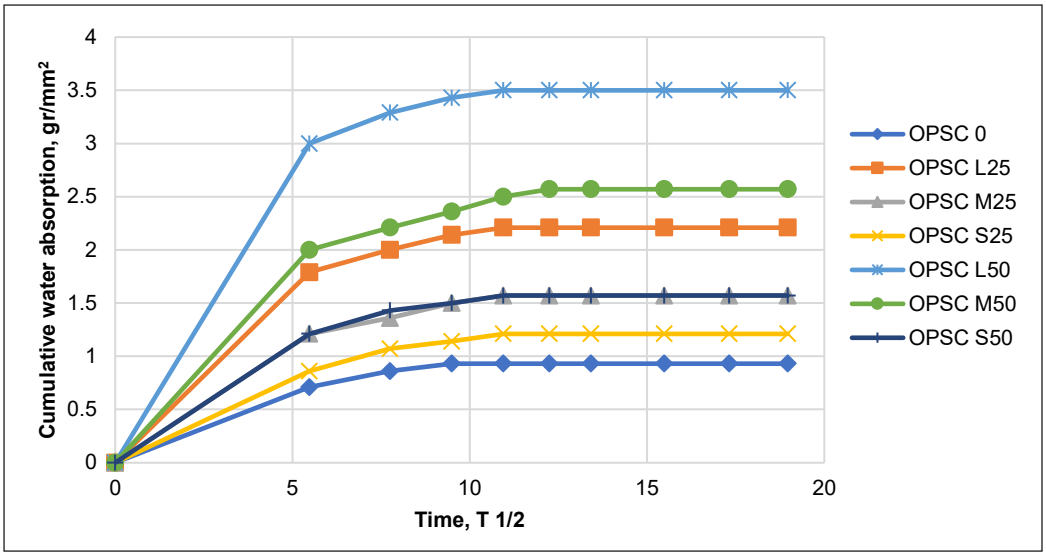

Figure 16. Water absorption versus square root of time at 56 days

The sorptivity level for OPSC M25 and OPSC L25 is higher than that of OPSC S25. It shows that when the size range increases, the sorptivity level also increases. It is similar to the results by Teo et al. (2007). According to Figure 16, the rate of water absorption at 56 days was similar to the results of 28 days for 25% and 50% OPS replacements. The sorptivity level for all mixes slightly increased until 120 minutes and remained constant afterward. The sorptivity level for OPS concrete with larger particle sizes was greater than those with smaller particles for both percentages of OPS. The lowest value of sorptivity level was achieved by using finer particles of OPS at both ages.

Rapid Chloride Permeability Test

The RCPT findings of concrete mixtures are shown in Figure 17. The chloride resistance of concrete decreased when the sand was partially replaced by the OPS, especially with using 50% of OPS. It is due to the increase in the internal connectivity of voids and capillary porosity in concrete produced with OPS.

Decreasing the particle size of OPS for both percentages showed about a 13% decrease in the total charge passed through the samples. OPSC S25, OPSC M25, and OPSC L25 produced a charge of 2593, 2684, and 2729 coulombs, respectively. A similar trend has also been observed for 50% OPS concrete. This result indicates that the smaller particles of OPS have lower permeability because the matrix became well connected and produced more compact concrete, so the current passed through the concrete decreased. While for OPSC L25, the current increased because it contains high levels of porosity. The level of chloride ions in concrete depends on the internal pore structure (Joshi & Chan, 2002). Factors such

as mixed design, construction methods, and hydration conditions can increase the pores in concretes. As discussed earlier in slump test results, the lowest quality of concrete consists of more pores and porosity levels. Therefore, a bigger range of 600µm–4.75mm size observed a high level of chloride permeability.

All the concrete mixtures used in this research are classified as moderate chloride ion permeability concrete (Akid et al., 2021). From the studies by Stanish et al. (1997), the lower the quality of concrete, the greater the current passed at a given voltage to the concretes. Thus, this shows the greater heat energy produced in the lowest quality concrete, which consists of the OPS range for a larger size of 600µm–4.75mm.

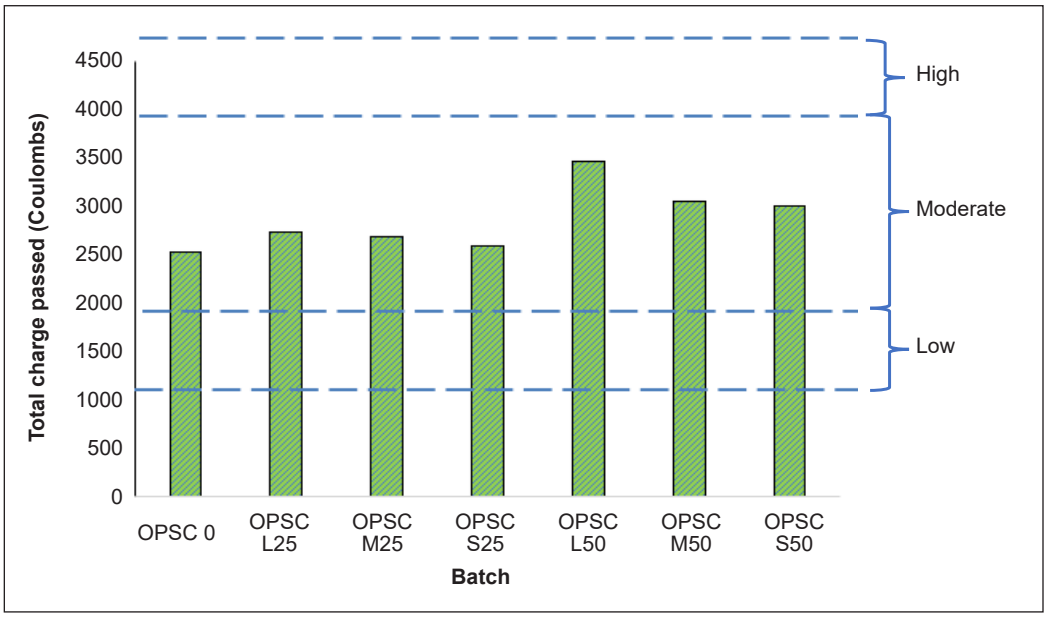

Figure 17. RCPT results of concrete mixes

CONCLUSION

Based on the experimental investigation, the following conclusion can be derived:

1. The partial replacement of the sand with the OPS decreased the workability of the concrete. Moreover, this reduction was higher for the samples containing larger particle sizes of OPS.
2. Increasing the OPS percentages and its particle size decreased the density of the concrete. OPS concrete with 0% and 25% sand replacement can be classified as normal weight concrete (NWC), while OPS concrete with 50% sand replacement is categorized as lightweight concrete (LWC). A higher density is achieved when a smaller particle size of OPS is used.

3. OPS concrete has a lower compressive strength than that of the control samples. However, the reduction in the strength can be overcome by including finer OPS particles due to the better compaction of the samples. OPSC S25 mix achieved a compressive strength of 30.33 MPa at 28 days, which was very close to the strength of the control sample.
4. The partial replacement of the sand with the OPS reduced the performance of concrete under the flexural and tensile loads. However, decreasing the particle size of the OPS increased the tensile and flexural strength by 18% and 17.38%, respectively, for OPS by 25% OPS. OPSC L50 achieved the lowest concrete tensile and flexural strengths of 1.5 and 2.57 MPa, respectively.
5. The UPV results indicate that all OPS mixes are characterized as good quality concrete with UPV values between 3650m/s–4099m/s.
6. The concrete with bigger particles with higher OPS percentage has more penetration depth. The sorptivity level also increased gradually when the dosage and size range increased.
7. All the OPS concretes are classified as moderate chloride ion permeability in 28 days. Decreasing the particle sizes and percentages of OPS improved the chloride resistance, and the lowest chloride permeability was achieved by using 25% OPS with a particle size of less than 600μ.

ACKNOWLEDGEMENT

The authors gratefully acknowledge the financial support for this publication by UPM-Kyutech International Symposium on Applied Engineering and Sciences 2021 (SAES2021) and Universiti Putra Malaysia.

REFERENCES

Akid, A. S. M, Hossain, S., Munshi, M. I. U., Elahi, M. M. A., Sobuz, M. H. R., Tam, V. W. Y., & Islam, M. S. (2021). Assessing the influence of fly ash and polypropylene fiber on fresh, mechanical and durability properties of concrete. *Journal of King Saud University - Engineering Sciences*, *33*, 1-11. https://doi.org/10.1016/j.jksues.2021.06.005

Abbas, A. G. N., Aziz, F. N. A. A., Abdan, K., Nasir, N. A. M., & Huseien, G. F. (2022). A state-of-the-art review on fibre-reinforced geopolymer composites. *Construction and Building Materials*, *330*, Article 127187. https://doi.org/10.1016/j.conbuildmat.2022.127187

Alengaram, U. J., Mahmud, H., & Jumaat, M. Z. (2010). Comparison of mechanical and bond properties of oil palm kernel shell concrete with normal weight concrete. *International Journal of Physical Sciences*, *5*(8), 1231-1239.

ASTM C 805-02. (2002). *Standard test method for rebound number of hardened concrete C 805.* United States: American Society for Testing and Material. https://www.academia.edu/14787775/Standard_Test_Method_for_Rebound_Number_of_Hardened_Concrete

ASTM C1202. (2012). *Standard test method for electrical indication of concrete's ability to resist chloride ion penetration*. American Society for Testing and Materials https://doi.org/10.1520/C1202-12.2

ASTM C1585-13. (2013). Standard test method for measurement of rate of absorption of water by hydraulic cement concretes. *ASTM International*, *41*(147), 1-6. https://doi.org/10.1520/C158513.2

ASTM C597-09. (2010). *Standard test method for pulse velocity through concrete*. *Annual Book of ASTM Standards*. American Society for Testing and Materials. https://www.studocu.com/row/document/dogu-akdeniz-universitesi/civil-engineering/kupdfnet-astm-c-597-02-ultrasonic-pulse-velocity/36387906

Awal, A. S. M. A., & Mohammadhosseini, H. (2016). Green concrete production incorporating waste carpet fiber and palm oil fuel ash. *Journal of Cleaner Production*, *137*, 157-166. https://doi.org/10.1016/j.jclepro.2016.06.162

Babafemi, A. J., & Olusola, K. O. (2012). Influence of curing media on the compressive strength of Palm Kernel Shell (PKS) concrete. *International Journal of Recent Research and Applied Studies*, *13*(1), 180-185.

BS EN 12390-3. (2009). *Testing hardened concrete - Part 3 : Compressive strength of test specimens*. https://www.thenbs.com/PublicationIndex/documents/details?Pub=BSI&DocID=288816

BS EN 12390-5. (2009). *Testing hardened concrete - Part 5 : Flexural strength of test specimens*. https://kupdf.net/download/bs-en-12390-5-2009-part-5-flexural-strength-of-test-specimens_58caa120dc0d60ab1033902f_pdf

BS EN 12390-6. (2009). *Testing hardened concrete - Part 6 : Tensile splitting strength of test specimens*. https://pdfcoffee.com/bs-en-12390-6-2009-testing-hardened-concrete-part-6-tensile-splitting-strength-of-test-specimens-pdf-free.html

BS EN 12390-8. (2009). *Testing hardened concrete - Part8: Depth of penetration of water under pressure*. British Standard. https://pdfcoffee.com/bs-en-12390-8-3-pdf-free.html

Guan, W., Qi, Q., Zhang, Z., & Nan, S. (2020). Effect of sand particle size on microstructure and mechanical properties of gypsum-cemented similar materials. *Materials*, *13*(3), 1-16. https://doi.org/10.3390/ma13030765

Huda, M. N., Jumat, M. Z. Bin, & Islam, A. B. M. S. (2016). Flexural performance of reinforced oil palm shell & palm oil clinker concrete (PSCC) beam. *Construction and Building Materials*, *127*, 18-25. https://doi.org/10.1016/j.conbuildmat.2016.09.106

Joshi, P., & Chan, C. (2002). Rapid chloride permeability testing. *Concrete Construction - World of Concrete*, *47*(12), 37-43.

Karakoç, M. B., Türkmen, I., Maraş, M. M., Kantarci, F., & Demirboğa, R. (2016). Sulfate resistance of ferrochrome slag based geopolymer concrete. *Ceramics International*, *42*(1), 1254-1260. https://doi.org/10.1016/j.ceramint.2015.09.058

Khan, M. M. H., Guong Wei, L., Deepak, T. J., & Nair, S. (2016). Use of oil palm shell as replacement of coarse aggregate for investigating properties of concrete. *International Journal of Applied Engineering Research*, *11*(4), 2379-2383.

Lim, S. K., Tan, C. S., Chen, K. P., Lee, M. L., & Lee, W. P. (2013). Effect of different sand grading on strength properties of cement grout. *Construction and Building Materials*, *38*, 348-355. https://doi.org/10.1016/j.conbuildmat.2012.08.030

Maghfouri, M., Shafigh, P., & Aslam, M. (2018). Optimum oil palm shell content as coarse aggregate in concrete based on mechanical and durability properties. *Advances in Materials Science and Engineering*, *2018*, Article 4271497. https://doi.org/10.1155/2018/4271497

Manjunath, R., Narasimhan, M. C., & Umesha, K. M. (2019). Studies on high performance alkali activated slag concrete mixes subjected to aggressive environments and sustained elevated temperatures. *Construction and Building Materials*, *229*, Article 116887. https://doi.org/10.1016/j.conbuildmat.2019.116887

Mannan, M. A., Alexander, J., Ganapathy, C., & Teo, D. C. L. (2006). Quality improvement of oil palm shell (OPS) as coarse aggregate in lightweight concrete. *Building and Environment*, *41*(9), 1239-1242. https://doi.org/10.1016/j.buildenv.2005.05.018

Mannan, M. A., & Ganapathy, C. (2004). Concrete from an agricultural waste-oil palm shell (OPS). *Building and Environment*, *39*(4), 441-448. https://doi.org/10.1016/j.buildenv.2003.10.007

Mannan, M. A., & Ganapathy, C. U. (2002). Engineering properties of concrete with oil palm shell as coarse aggregate. *Construction and Building Materials*, *16*, 29-34. https://doi.org/10.1016/S0950-0618(01)00030-7

Mo, K. H., Alengaram, U. J., Jumaat, M. Z., & Yap, S. P. (2015). Feasibility study of high volume slag as cement replacement for sustainable structural lightweight oil palm shell concrete. *Journal of Cleaner Production*, *91*, 297-304. https://doi.org/10.1016/j.jclepro.2014.12.021

Mo, K. H., Yeoh, K. H., Bashar, I. I., Alengaram, U. J., & Jumaat, M. Z. (2017). Shear behaviour and mechanical properties of steel fibre-reinforced cement-based and geopolymer oil palm shell lightweight aggregate concrete. *Construction and Building Materials*, *148*, 369-375. https://doi.org/10.1016/j.conbuildmat.2017.05.017

Momoh, E. O., & Osofero, A. I. (2019). Behaviour of oil palm broom fibres (OPBF) reinforced concrete. *Construction and Building Materials*, *221*, 745-761. https://doi.org/10.1016/j.conbuildmat.2019.06.118

Muthusamy, K., Zulkepli, N. A., & Mat Yahaya, F. (2013). Exploratory study of oil palm shell as partial sand replacement in concrete. *Research Journal of Applied Sciences, Engineering and Technology*, *5*(7), 2372-2375. https://doi.org/10.19026/rjaset.5.4667

Nadh, V. S., Krishna, C., Natrayan, L., Kumar, K. M., Nitesh, K. J. N. S., Raja, G. B., & Paramasivam, P. (2021). Structural behavior of nanocoated oil palm shell as coarse aggregate in lightweight concrete. *Journal of Nanomaterials*, *2021*, Article 4741296. https://doi.org/10.1155/2021/4741296

Olanipekun, E. A., Olusola, K. O., & Ata, O. (2006). A comparative study of concrete properties using coconut shell and palm kernel shell as coarse aggregates. *Building and Environment*, *41*(3), 297-301. https://doi.org/10.1016/j.buildenv.2005.01.029

Qasem, A. A., Almekhlafi, M. A., & Yahaya, F. M. (2021). The effect of palm oil fuel clinker powder and cockleshell powder as cement replacement on durability properties of the concrete mortar. *IOP Conference Series: Earth and Environmental Science*, *682*(1), Article 012037. https://doi.org/10.1088/1755-1315/682/1/012037

Rahman, F. F., Prakoso, W. A., Tjahjono, E., Sentosa, B. O. B., & Orentilize, M. (2020). Load-displacement response of oil palm shell concrete compressive test using digital image correlation. *IOP Conference Series: Earth and Environmental Science*, *498*(1), 012037. https://doi.org/10.1088/1755-1315/498/1/012037

Stanish, K. D., Hooton, R. D., & Thomas, M. D. (1997). *Testing the chloride penetration resistance of concrete : A literature review*. Transportation Research Board. https://trid.trb.org/view/690568

Sutherland, W. J., Barnard, P., Broad, S., Clout, M., Connor, B., Cote, I. M., Dicks, L. V., Doran, H., Entwistle, A. C., Fleishman, E., Fox. M., Gaston, K. J., Gibbons, D. W., Jiang, Z., Keim, B., Lickorish, F. A., Markillie, P., Monk, K. A., Pearce-Higgins. J. W., … & Ockendon, N. (2017). A 2017 horizon scan of emerging issues for global conservation and biological diversity. *Trends in Ecology and Evolution*, *32*(1), 31-40. https://doi.org/10.1016/j.tree.2016.11.005

Teo, D. C. L., Mannan, M. A., & Kurian, V. J. (2006). Structural concrete using oil palm shell (OPS) as lightweight aggregate. *Turkish Journal of Engineering and Environmental Sciences*, *30*(4), 251-257.

Teo, D. C. L., Mannan, M. A., Kurian, V. J., & Ganapathy, C. (2007). Lightweight concrete made from oil palm shell (OPS): Structural bond and durability properties. *Building and Environment*, *42*(7), 2614-2621. https://doi.org/10.1016/j.buildenv.2006.06.013

Ting, T. Z. H., Rahman, M. E., & Lau, H. H. (2020). Sustainable lightweight self-compacting concrete using oil palm shell and fly ash. *Construction and Building Materials*, *264*, Article 120590. https://doi.org/10.1016/j.conbuildmat.2020.120590

Tripathi, M., Sahu, J. N., Ganesan, P., Monash, P., & Dey, T. K. (2015). Effect of microwave frequency on dielectric properties of oil palm shell (OPS) and OPS char synthesized by microwave pyrolysis of OPS. *Journal of Analytical and Applied Pyrolysis*, *112*, 306-312. https://doi.org/10.1016/j.jaap.2015.01.007

UNEP. (2019). *Sand and sustainability: Finding new solutions for environmental governance of global sand resources.* United Nations Environment Programme. https://wedocs.unep.org/20.500.11822/28163

Pertanika J. Sci. & Technol. 31 (4): 1669 - 1684 (2023)

PERTANIKA JOURNALS

SCIENCE & TECHNOLOGY

Journal homepage: http://www.pertanika.upm.edu.my/

Effect of Low Loading Biodegradable Poly(Ethylene Carbonate) to Physicochemical and Mechanical Properties of Melt-Blended Poly(Lactic Acid)

Norkhairun Nisa' Abdul Rahman[1], Nur Fadilah Abdul Jabar[1] and Nur Azrini Ramlee[1,2]*

[1]School of Chemical Engineering, College of Engineering, Universiti Teknologi MARA, 40450 UiTM, Shah Alam, Selangor, Malaysia

[2]Circular + Industrial Research Laboratory, School of Chemical Engineering, College of Engineering, Universiti Teknologi MARA, UiTM 40450, Shah Alam, Selangor, Malaysia

ABSTRACT

Poly(lactic acid)/poly(ethylene carbonate) (PLA/PEC) blends with a low ratio range of PEC contents were successfully prepared via the melt blending technique. The objectives of this study are to evaluate the effect of low content of PEC on the PLA and further characterize the blend using torque analysis, Thermogravimetric Analysis (TGA), Differential Scanning Calorimetry (DSC) analysis, Fourier Transform Infra-Red (FTIR) analysis, and mechanical properties. The PLA/PEC samples with different ratios, which is PLA98/PEC2, PLA96/PEC4, PLA94/PEC6, PLA92/PEC8, and PLA90/PEC10, are selected in this research. The addition of PEC content in PLA reduced the torque value. The PLA90/PEC10 blends degraded first, and 5 wt% weight loss (Td_5) of the PEC/PLA blends was decreased with PEC, which influences the thermal stability of the blends. The crystallinity of PLA has changed with the addition of 10% of PEC, resulting in the highest crystallinity up to 48.81%, thus influencing the toughness of the blends, giving the PLA a better modulus of toughness, and increasing the elongation at the break due to the plasticizing effect. Slight changes in the absorbance peaks of carbonyl and ether groups have confirmed the interaction between PLA and PEC even at a low loading of PEC. Due to the low loading of PEC content to PLA, the absorbance peak of PLA/PEC blends for the carbonyl group tends to shift towards a neat PLA peak. Thus, low PEC loading is strongly suggested as an alternative to PLA modification in various applications.

Keywords: Biodegradable, low loading, poly(ethylene carbonate), poly(lactic acid), polymer blend

ARTICLE INFO

Article history:
Received: 09 June 2022
Accepted: 07 September 2022
Published: 24 May 2023

DOI: https://doi.org/10.47836/pjst.31.4.04

E-mail addresses:
khairunnisa5314@gmail.com (Norkhairun Nisa' Abdul Rahman)
diela151129@gmail.com (Nur Fadilah Abdul Jabar)
azrini@uitm.edu.my (Nur Azrini Ramlee)
* Corresponding author

ISSN: 0128-7680
e-ISSN: 2231-8526

INTRODUCTION

Polymers are large macromolecules containing "monomers," which can be classed based on chain branching, molecular weight, functional groups, and physical properties. Synthetic polymers are common polymers, also known as "biopolymers" (Russell, 2003). Controversies about plastics production and usage are created due to synthetic polymer's production and large-scale use. It is reported that only 10% of all plastic products have been recycled, and the majority of them end up in landfills or are assembled as waste in the environment (Geyer et al., 2017). According to research done by Fushimi & Gaffney (2014), up to 10 billion tonnes of garbage from plastics can be created worldwide every year. It is estimated that the time for decomposition of this plastic waste is 200-400 years. Reducing environmental waste leads to the interest in replacing plastic with more eco-friendly and biodegradable synthetic polymers. The potential solution to minimizing the pollution of plastic and controlling the carbon footprint is by using biodegradable plastic, which is produced by using biodegradable polyesters such as poly(hydroxyalkanoate) (PHA) and poly(lactic acid) (PLA). Poly(lactic acid) (PLA) is a common biodegradable thermoplastic polyester made from the monomers lactic acid and lactide by polycondensation and ring-opening polymerization (ROP) (Wang et al., 2017). PLA has several advantages, such as good physical and mechanical behavior, other than better clarity and barrier properties. However, the limitation of PLA comes into brittleness due to its low toughness, and it also has poor physicochemical and biodegradability properties that need to modify (Nofar et al., 2020). The methods for modification of PLA are chemical copolymerization, plasticization, and polymer mixture. The addition of thermoplastic polyurethane (TPU) improves mechanical strength, resistance impact, and shape memory property (Chen et al., 2017). Moreover, approaches to blending PLA with another type of aliphatic polycarbonate have caught the interest of many researchers. Aliphatic polycarbonate is biodegradable and has better strain hardening in mechanical properties that can help improve PLA properties. One of the attractive aliphatic polycarbonate types is poly(ethylene carbonate) (PEC). PEC is a biodegradable polymer made from carbon dioxide (CO_2) reacting with epoxides through a copolymerization method, having strong biodegradability and biocompatibility (Ramlee & Tominaga, 2019a).

The most used technique in the preparation of polymer blending is physical blending by the extrusion technique. Melt blending of poly(lactide) (PLA) and poly(butylene succinate) (PBS) blends was used to create a new type of biodegradable material with high toughness and strength for fused deposition modeling (FDM) technology (Ou-Yang et al., 2018). Lyu et al. (2020) studied polymer blending for 3D printing applications combining poly (lactic acid) (PLA) and poly(butylene-adipate-co-tere-phthalate) (PBAT).

Polymer blends have also become the most popular thermoplastic filament materials for 3D printing technology. Alternative materials for 3D printing were produced using PLA, PBAT, and nano talc (Prasong et al., 2020). Other than that, the polymer blends of poly(lactic acid) and poly(butylene adipate-co-terephthalate) were examined by Pivsa-Art et al. (2013), with the addition of poly(butylene succinate) (PBS) as a compatibilizer.

The preparation of PLA/PEC blends using the melt blending technique still needs further investigation. The previous research study for this blend was done at the high ratio range for PEC using solvent-based casting. Their research study found that phase separation occurred in the PLA50/PEC50. Therefore, this study focuses on preparing PLA/PEC blends via the melt blending technique with the effect of low-loading PEC on the phase separation of the blends. Since the PEC has limited stock availability due to the high cost, the low loading of PEC has been used in the research. The characterizations, including the torque analysis, Thermogravimetric Analysis (TGA), Differential Scanning Calorimetry (DSC) analysis, Fourier Transform Infra-Red (FTIR) analysis, and mechanical properties of the PEC/PLA blends, were investigated.

MATERIALS AND METHOD

Materials

A commercial grade poly(lactic acid) (PLA), grade 3001D pellets (MFI: 22 g/10min) were used, and poly(ethylene carbonate) (PEC) (QPAC®25) with molecular weight, Mw=131,000 was purchased from Empower Materials, USA also being used. Both materials were used without chemical treatment for the preparation of the blends. Before processing, PLA pellets were vacuum dried at 60 ºC for 24 hours to eliminate the moisture content and weighed on a high precision scale. Both polymers were kept in a desiccator prior to the preparation of the blends.

Methods

The melt blending technique was used to prepare the samples of PEC/PLA blends. The PLA/PEC samples at different weight percentage ratios, PLA98/PEC2, PLA96/PEC4, PLA94/PEC6, PLA92/PEC8, and PLA90/PEC10, were premixed prior to melting blending. The melt blending method was prepared using Thermo Scientific (Haake Rheonix OS) with a temperature process of 150°C and 60 rpm for the speed of the screw. All blends were palletized using a granulator after the mixing process. By maintaining 4.29 g of the weight of each pallet's samples, the samples were prepared by hot pressing technique (Model: ComeTech) at a temperature of 160°C for pre-heating and compressed and 50°C for a cooling process under 5 MPa pressure for 10 min. The film was kept in a desiccator before being analyzed.

Characterization

Torque analysis is characterized using Thermo Scientific (Haake Rheomix OS) internal mixer for the melt blending technique. The multiple polymers, PEC and PLA, were mixed using rolls within a closed chamber. The thermogravimetric analyzer (TGA) was used to determine the degradation temperatures of the PLA/PEC blend film (Model: Mettler Toledo). The temperature was characterized by the mass of the sample being measured over time as the temperature changed. All film samples had the same dimensions of 5mm x 5mm x 3mm and were heated at 10°C/min from 30°C to 600°C. The thermal characteristics of the PLA/PEC blend film samples were measured using a Differential Scanning Calorimeter (DSC) (Model: Mettler Toledo). DSC was used to observe enthalpy changes in samples as a function of temperature or time due to changes in physical and chemical characteristics. It was subjected to DSC processes at temperatures ranging from -40°C to 200°C, with a heating rate of 10°C/min. The blends' value of glass transition temperature (T_{g1}) was determined using the heating method. The melting temperature (T_m) of PEC, PLA, and all PLA/PEC blend samples was observed using the temperature at the melting peak's maximum values. The blends' cold crystallization can also be determined by using DSC analysis. The crystallinity of PLA (X_c) is calculated using Equation 1, which is normalized by the PLA weight fraction (X_{PLA}),

$$X_c(\%) = \frac{\Delta H_m}{\Delta H_m^\circ} x \frac{100}{X_{PLA}} \quad (1)$$

where ΔH_m (J/g) is the melting enthalpy of PLA and ΔH^o_m is the theoretical melting enthalpy of a 100 percent crystalline PLA, which is 107 J/g, according to Ramlee and Tominaga (2018). Fourier Transform Infra-Red (FTIR) Perkin Elmer (Model: Spectrum One) was used to observe the FTIR measurement of the PLA/PEC blends film samples. The FTIR readings were taken between 4000 cm^{-1} and 515 cm^{-1}. The tensile strength of materials or all PLA/PEC blends film samples was determined using Universal Tensile Machine Tinius Olson (Model: H50KT). The Universal Tensile Machine was fitted with a 2 kN load cell with ± 0.5% accuracy with the design of the tensile specimens according to the ASTM D882-10. The crosshead speed for the tensile machine ranges from 1 to 500 mm/min. Therefore, the crosshead speed is set to 25 mm/min in this study. A sample from each blend was used to determine the tensile properties. The width of the sample was 25 mm, and the thickness was 0.3 mm, with an area of 7.5 mm^2. After that, the elastic modulus was calculated in the stress-strain curve by taking the slope of the initial linear region.

RESULTS AND DISCUSSION

Torque Analysis

Figure 1 shows the mixing torque analysis as a function of time, and Figure 2 indicates the mixing torque as a function of the composition of PEC.

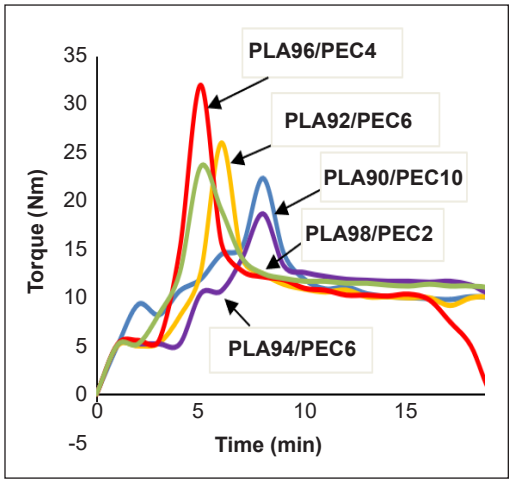

Figure 1. Mixing torque as a function of mixing time at 60 rpm and 150°C

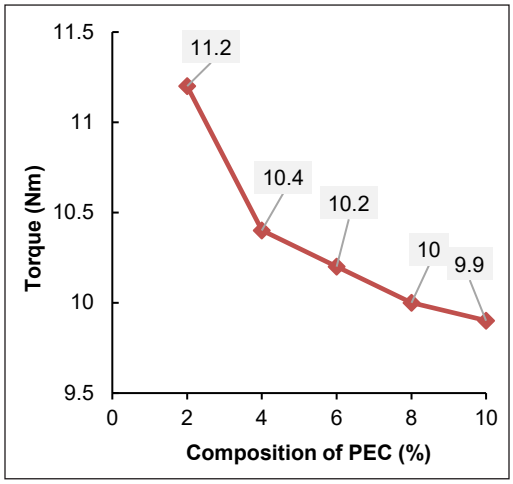

Figure 2. Mixing torque as a function of the composition of PEC in the blends at 15 min

The torque for the blends develops significantly initially due to the input of PLA and PEC pellets into the mixer, then decreases due to the melting of the pellets, and finally remains rather constant, as shown in Figure 1. Zhang et al. (2020) found a similar result in their research of the torque analysis since they found that the melting of PLA pellets and the addition of PUDA-co-BUDA are responsible for the initial peaks and abrupt drops on the torque curves. As demonstrated in Figure 2, the torque values for all blends were obtained based on Figure 1 at a constant time of 15 min (black circle). The torque value for all PLA/PEC blends dropped as the percentage of PEC in the blends increased. It is probably due to the friction caused by the increase in PEC composition, which resulted in a higher resistance on the rotor blades. It can be shown in Figure 1 that PLA96/PEC4 mixed well at 7 min compared to the PLA94/PEC6, which mixed well at 10 min. The initial peaks and abrupt declines on torque curves show the melting of PLA pellets and adding PEC components to the blends.

Based on Figure 2, the torque values decreased with increasing PEC content. According to Gigante et al. (2019), the trend of the torque reduced when the plasticizer, which is poly(butylene succinate) (PBS), was mixed with the PLA. It is also reported by Patti et al. (2020) that the torque value reduction by increasing cellulose composition by 35%, 55%, 68%, and 77%, and the processing time recorded was 25 minutes. Due to the melting of PLA, the torque decreases dramatically, resulting in a fall in melt viscosity (Kamaludin et al., 2020). Thus, the selection processing time was 15 minutes which the PLA and PEC were thoroughly melted and uniformly mixed. According to Xie et al. (2019), PLA and polypropylene glycol (PPG) were melted entirely in the mixer after 15 to 20 minutes of processing. This behavior indicates that the torque will decrease when another material

is mixed with PLA, even though the processing time differs. The significance of torque analysis reveals that PEC can help process PLA, especially for mechanical processing such as extrusion to produce filament for 3D printing applications.

Thermogravimetric Analysis (TGA)

The thermogravimetric analysis (TGA) curves for PEC/PLA blends are shown in Figure 3, and the thermogravimetric data for all samples are listed in Table 1. Table 1 shows the temperature at 5 wt% weight loss (T_{d5}) and the maximum decomposition temperature (T_{max}) of the PLA/PEC blends. The 5 wt% weight loss (T_{d5}) of the PLA/PEC blends was decreased with the added PEC. However, adding 6 wt% PEC to the PLA shows an insignificant decrease of T_{d5} from 244.39°C, showing by PLA98/PEC2, to 238.29°C showing by PLA94/PEC6, which is only 6°C. It is probably due to the PLA94/PEC6 blend that maintains stability with the added 6 wt% PEC. The thermal stability of PLA is insignificantly affected by the addition of 6 wt% PEC. PEC shows lower thermal stability than PLA; therefore, the blends with a higher PLA content, PLA98/PEC2, show better thermal stability. Contrary to Wacharawichanant et al. (2019), it is reported that the addition of polyethylene co-polymer content to PLA could not enhance thermal stability. Even though the degradation temperature of polyethylene co-polymer shows a higher value of around 429.48°C, while PLA is at 337.82°C, when polyethylene co-polymer was added to PLA, the degradation temperature of this blend was found to be lower than PLA and polyethylene co-polymer which was 334.26°C. However, the increase of PEC content in the blends makes the sample degrade faster (Figure 3), and PLA90/PEC10 was the fastest to degrade at 500°C compared to others blends fully. Similar results have been reported by Ramlee and Tominaga (2018), the addition of 10%, 30%, 70%, and 90% of PEC to PLA reducing the temperature 5% weight loss (T_{d5}) with the T_{d5} for pure PLA and PEC was 294°C and 198°C, respectively.

The maximum decomposition temperature (T_{max}) obtained from derivative weight loss (DTG) diagrams was used to determine the thermal stability of the PLA/PEC blends. The decomposition temperature is the temperature at which the maximum rate of weight loss occurs (Yayshahri et al., 2019). According to Ramlee and Tominaga (2018), PLA can improve the thermal stability of the PEC. PLA98/PEC2 and PLA96/PEC4 have only one value for T_{max}, indicating that PLA decomposes in a single step, with decomposition temperatures of 364.83°C and 364.87°C, respectively. Adding 2% and 4% of PEC to PLA shows no separated degradation since the difference between PEC and PLA degradation was insignificant. According to Table 1, with the addition of 6 wt% of PEC composition, the PLA and PEC start to decompose separately, causing the degradation of PEC to occur at a lower temperature than the one showed by PLA92/PEC8 and PLA94/PEC6, which around 320°C to 330°C.

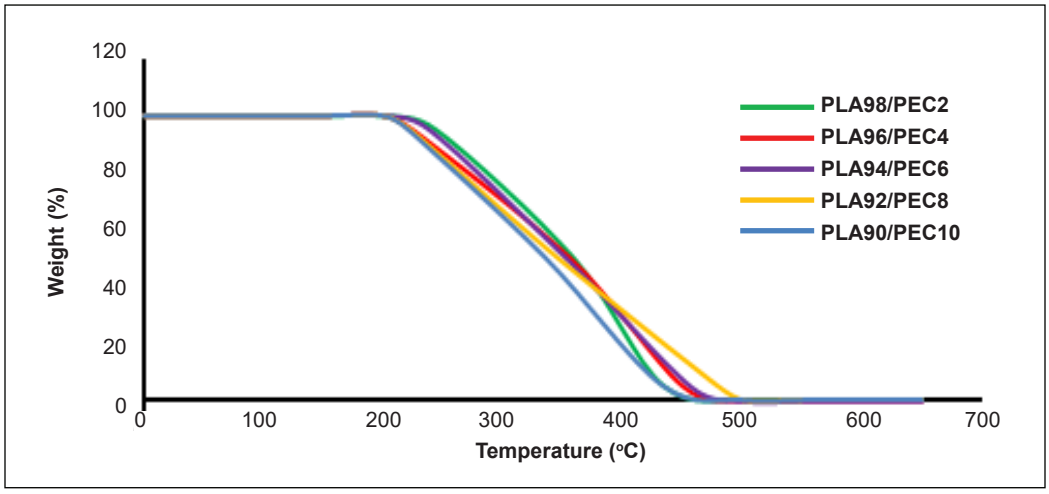

Figure 3. TGA curves for PLA/PEC blends

Table 1
Thermogravimetric data for PLA/PEC blends

Sample	T_{d5} [°C]	T_{max} of PEC [°C]	T_{max} of PLA [°C]
PLA98/PEC2	244.39	364.83	364.83
PLA96/PEC4	224.39	364.87	364.87
PLA94/PEC6	238.29	330	364.53
PLA92/PEC8	222.47	320	362.80
PLA90/PEC10	220.64	331.69	370

Differential Scanning Calorimetry (DSC) Analysis

Using Differential Scanning Calorimetry (DSC), the glass transition temperature (T_g), degree of crystallinity of PLA, and melting temperature (T_m) of PLA/PEC blends made by the melt blending process were determined. The observed value of T_g is usually explained by the strong molecular chain mobility of polymers above T_g and the significantly reduced chain mobility of polymers below T_g (Ramlee & Tominaga, 2018). As in the characterization section, the degree of crystallinity (X_c) is computed using Equation 1. Table 2 shows the DSC data for PLA/PEC blends, Figure 4a indicates the DSC curve of the blend, and Figure 4b shows the melting temperature curve of the blend. The red circle allocated at the curve in Figure 4b refers to the melting temperature peak for each blend. Table 2 and Figure 4b show that when PEC is added to PLA, the melting temperature of the PLA/PEC blends does not vary significantly. Ramlee and Tominaga (2019b) also reported that for the melt-quenched PEC/PLA technique, the melting temperature of PLA crystals is unaffected by the presence of PEC. Other than that, according to Sonseca et al. (2020), T_m values were not showing any significant difference for PLA/OLA blends, where OLA stands for lactic

acid oligomer with the addition of chitosan-based silver nanoparticles (AgCH-NPs). The result for melting temperature obtained by Tao et al. (2017) shows the melting temperature was 167°C for both PLA filament and the composite of WF/PLA can clarify that adding any materials to pure PLA will not cause any different changes in melting temperature of the blends.

The glass transition temperature of a composite is determined by its molecular properties, composition, and compatibility (Tao et al., 2017). According to Table 2, adding 6%, 8% and 10% of PEC decreased T_g values for PLA from 59°C to 56°C. Adding PEC from 6% to 10% leads to this reduction related to macromolecule polymer with high mobility due to an increase in the matrix's free volume (Sonseca et al., 2020). The increase of T_{g1} from 15°C

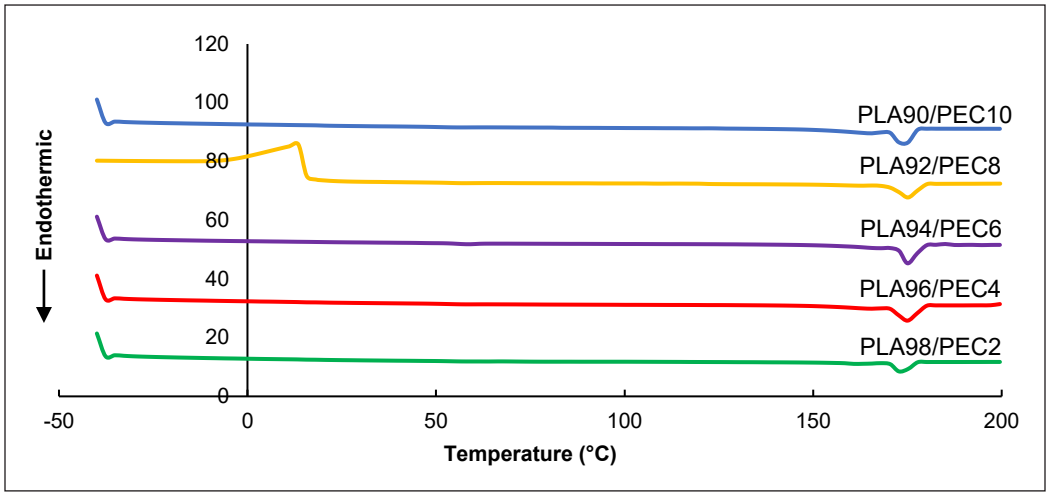

(a)

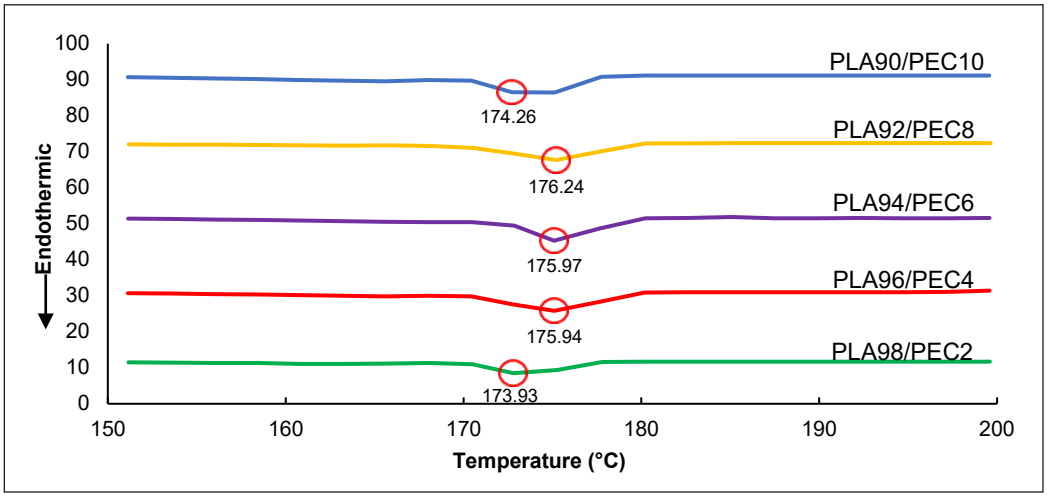

(b)

Figure 4. (a) DSC curves for PLA/PEC blends; (b) DSC melting temperature curves for PLA/PEC blends

Table 2
DSC data for PLA/PEC blends

Sample	Tg_1 (PEC) [°C]	Tg_2 (PLA) [°C]	T_m [°C]	ΔH_m [J/g]	X_c [%]
PLA98/PEC2	15	56	173.93	14.16	**13.50**
PLA96/PEC4	16	58	175.94	42.78	**41.65**
PLA94/PEC6	15	59	175.97	40.59	**40.36**
PLA92/PEC8	16	56	176.24	28.8	**29.26**
PLA90/PEC10	18	56	174.26	47	**48.81**

to 18°C and T_{g2} value from 59°C to 56°C for 6 wt% to 10 wt % PEC shows that PLA/PEC blends are partially miscible, which may be due to the intermolecular interaction between the carbonyl oxygen of PEC and PLA system (Ramlee & Tominaga, 2018). At high PLA content, the presence of PLA in the PEC matrix may act as a barrier to the polymer chains' mobility, increasing the T_{g2} value. Furthermore, with the addition of PEC, the crystallinity of PLA/PEC blends increases, as shown in Table 2. Interestingly, only 4 wt% PEC increased the crystallinity to 41.65%, giving the highest crystallinity of 48.81% with 10 wt% PEC. Similar results were obtained by Ramlee and Tominaga (2018), who stated that the crystallinity of PLA90/PEC10 was 42%. It is due to the flexible PEC in the blends, which improves the polymer's chain mobility (Ramlee & Tominaga, 2018; 2019b). Therefore, the crystallinity of PLA increased with the addition of PEC into the PLA matrix.

Fourier Transform Infra-Red (FTIR) Analysis

Fourier Transform Infra-Red (FTIR) analysis observed the interaction between PLA and PEC in the blend samples. Figure 5 displays the infrared spectrum for the carbonyl group for PLA/PEC film blends, and Figure 6 shows the FTIR curve of the ether group for the blends. The different wavenumbers at each peak are related to the carbonyl groups, including (–C=O) and ether groups (–O–C–O). As illustrated in Figure 5, the extended vibrational mode of the (–C=O) group in the 1700-1800 cm^{-1} was visible. Line a indicates the value of neat PLA, which is 1754 cm^{-1} (Chen et al., 2005), and 1738 $cm^{-1,}$ indicated by Line b, where the peak of neat PEC appeared in the infrared spectrum (Ma et al., 2006). Figure 5 illustrates that the absorbance peaks for PLA/PEC blends are between lines a and b, indicated by the arrow for each blend. It is observed that both PLA90/PEC10 and PLA92/PEC8 have a peak at 1752 cm^{-1}. PLA94/PEC6, PLA96/PEC4, and PLA98/PEC2 recorded the same peak value for the carbonyl group, 1753 cm^{-1}. Due to the low loading of PEC content to PLA, the absorbance peak of PLA/PEC blends for the carbonyl group tends to shift towards a neat PLA peak.

Similar research on poly(ethylene carbonate) (PEC) blends with PLA also being observed by Ramlee and Tominaga (2018), and it showed similar carbonyl peak shifts of

the (–C=O) group. Other than that, a similar result for carbonyl peaks was also obtained by Ma et al. (2006) in their study of blending between PLA and poly(propylene carbonate) (PPC). Line c in Figure 6 indicates the value for the (–O–C–O) group in PEC, which is 1207 cm^{-1} (Ramlee & Tominaga, 2018). The peaks between Line a and Line b show the active peaks compared to others, proving that the molecular interaction bonding of both polymers for PLA and PEC occurred at this point. Furthermore, it can be supported by

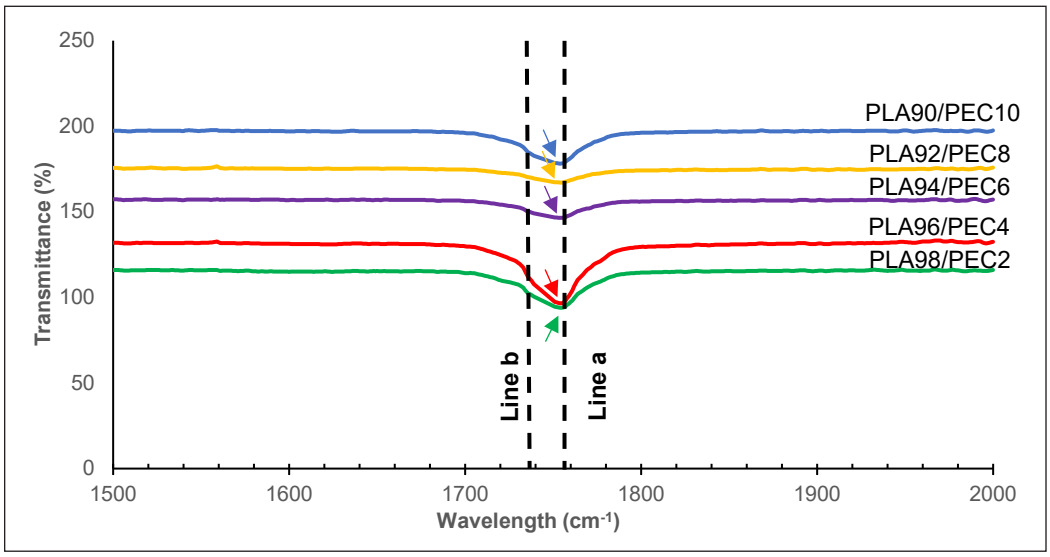

Figure 5. FTIR curves for the carbonyl group

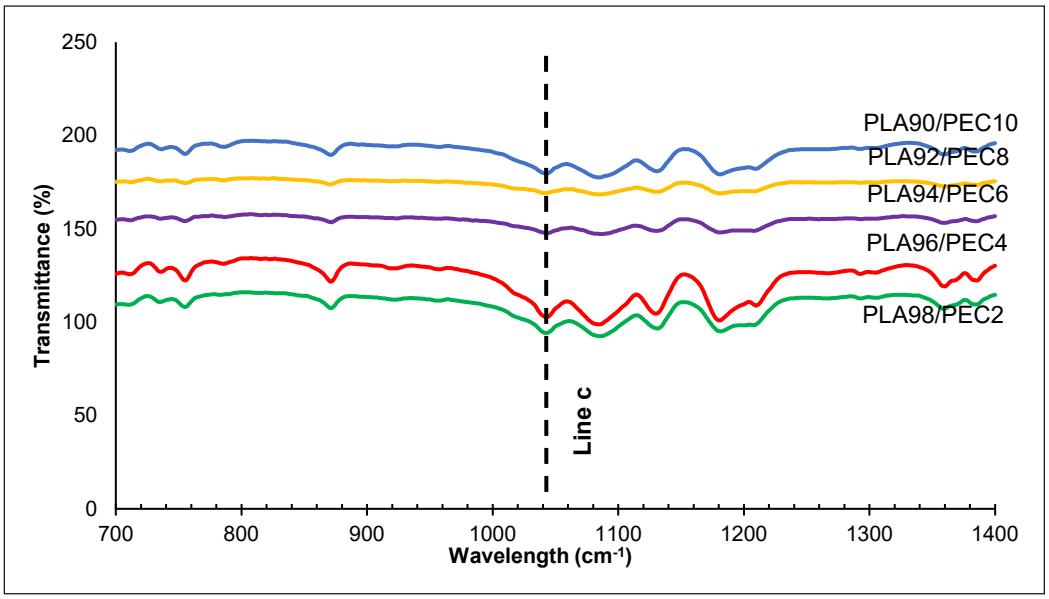

Figure 6. FTIR curves for ether group

observing Line c, which is the absorbance of the (–O–C–O) ether group. Line c shows a slight shift for all the blends, confirming that molecular interaction occurred between PLA and PEC. Figure 7 depicts the structural image of PLA and PEC interactions for –O–C in –O–C=O of PLA and carbonyl –C=O of PEC. As a result, there is an interaction between the PLA and PEC since it showed a significant change in the absorbance peak when the low ratio range of PEC was added to the PLA/PEC blends.

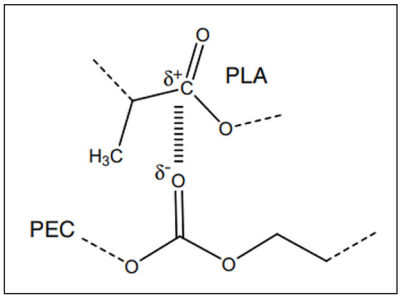

Figure 7. Structural image of interactions between PLA and PEC (Ramlee & Tominaga, 2018)

Mechanical Properties

Figure 8 shows the Young's Modulus values at different compositions of PEC in the PLA matrix. The mechanical parameters of PLA/PEC blends, such as Young's Modulus, tensile strength, and elongation at break, are shown in Table 3. Furthermore, Figure 9 shows the stress-strain (S-S) curve for PLA/PEC blends, and the tensile strength and elongation at break curves for each blend of film samples are shown in Figure 10. The Young's Modulus does not clearly depend on the low PEC content, although the tensile strength and elongation at break do.

According to Ramlee and Tominaga (2019a), it exhibits normal brittle behavior when tensile deformation is applied to neat PLA. In contrast, in its natural form, PEC has a normal ductile stress-strain profile and can endure elongation of more than 400% without rupturing. From Table 3, PLA92/PEC8 recorded the highest Young's Modulus value, 1.79 GPa. On the contrary, PLA90/PEC10 recorded the highest value of Young's Modulus and tensile

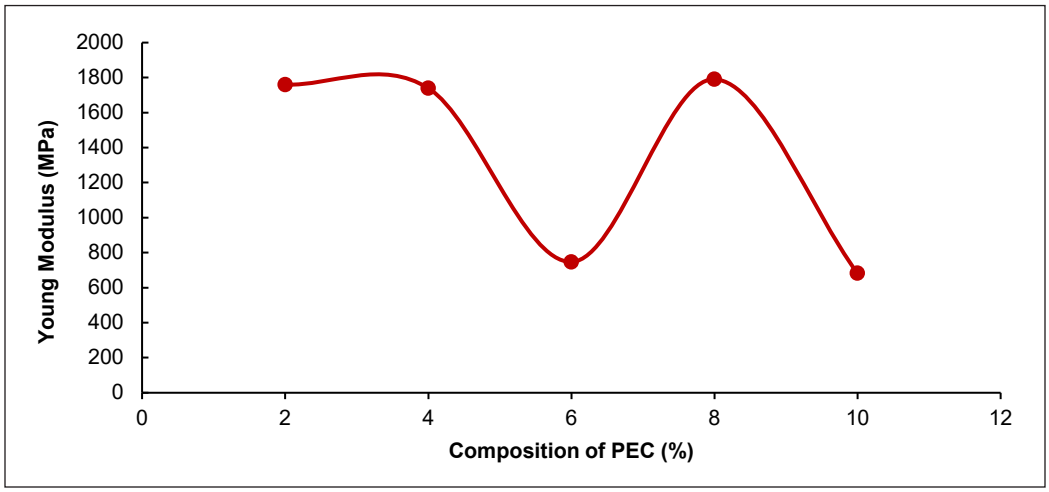

Figure 8. Young's Modulus of PLA/PEC blends for 2, 4, 6, 8, and 10 wt% PEC

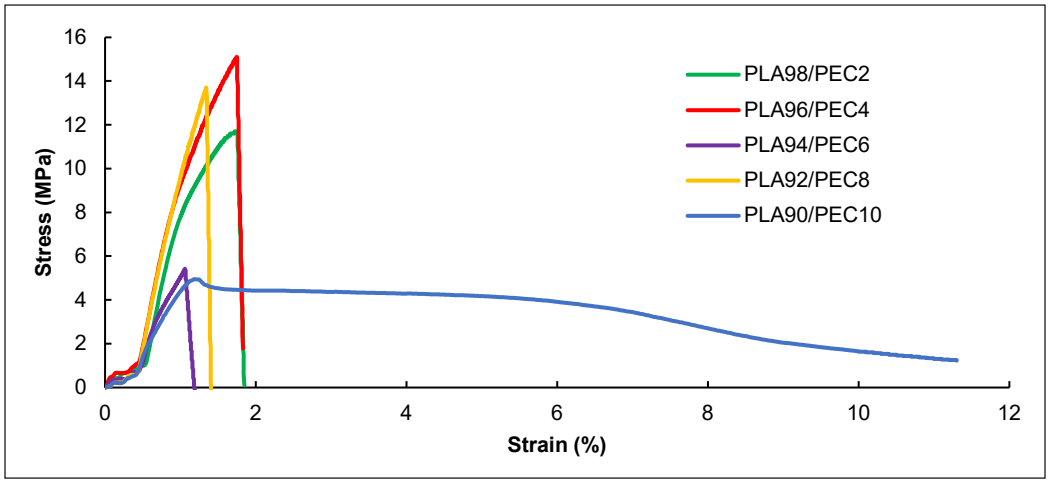

Figure 9. Stress-Strain curve of PLA/PEC blends

strength using the solution casting method reported by Ramlee and Tominaga (2019a). Polymer with high tensile strength and Young's Modulus results in a lower elongation at break value (Hedayati et al., 2020). The elongation at break (ε) of PLA92/PEC8 was 1.34% when the highest value of Young's Modulus was recorded. However, PLA94/PEC6 has the lowest elongation at break, which is 1.06%, but the Young's Modulus (E) and tensile strength (σ) recorded little higher values compared to PLA90/PEC10 blend. It is probably due to the morphology of the film sample, which influences the sample's mechanical characteristics. The lowest value of modulus of toughness (U_t) resulted from PLA94/PEC6, which is 19900 MJ/m^3 due to the lowest value of Young's Modulus, low tensile strength, and low elongation at break. The highest modulus of toughness in this study was recorded by PLA90/PEC10, which is 362000 MJ/m^3. It is shown that the highest composition of PEC will result in the highest modulus of toughness. Similar to Ramlee and Tominaga's (2019b) work, they stated that PEC90/PLA10, which has the highest PEC composition, resulted in the highest modulus of toughness, which is 16.3 MJ/m^3.

The interplay of various elements, including phase morphology, relative modulus of the phases, chain structure, and interfacial adhesion, determines the toughness or breaking energy (Ma et al., 2006). The highest value of toughness is also affected by the blends' crystallinity with increasing crystallinity, resulting in a higher value of toughness. It is due to the intermolecular interaction between PEC and PLA in the blends that resulted in layer structure in the morphology of the blends (Ramlee & Tominaga, 2019a). It is proved from DSC analysis that PLA90/PEC10 has the highest value of crystallinity, which is 48.81 %. Therefore, it results in the highest value of toughness in mechanical properties for this blend. From Figure 8, the tensile strength for PLA/PEC blends with 2 to 8 wt % PEC is above 11.7 MPa, except for PLA94/PEC6, which could not be explained further in this

study. Meanwhile, the tensile strength of PLA has decreased tremendously to 1.23 MPa and reaches the maximum elongation at a break of about 11.3% with 10 wt% PEC, giving the highest modulus of toughness to the PLA/PEC blends. This observation is associated with the result of tensile toughness for PLA/PEC blends prepared by solution casting, in which the PLA toughness was improved from 5.1 MJ/m^3 to 5.5 MJ/m^3 when 10 wt% of PEC was added to the PLA matrix, due to the ductility of PEC that helps in improving the toughness of PLA (Ramlee & Tominaga, 2019a).

Table 3
Mechanical data for PLA/PEC blends

Film Samples	Young's Modulus, E [GPa]	Tensile Strength, σ [MPa]	Elongation at Break, ε [%]	Modulus of Toughness, U_t [MJ/m^3]
PLA98/PEC2	1.76	11.7	1.76	**92100**
PLA96/PEC4	1.74	15	1.75	**115000**
PLA94/PEC6	0.75	5.4	1.06	**19900**
PLA92/PEC8	1.79	13.6	1.34	**63700**
PLA90/PEC10	0.68	1.23	11.3	**362000**

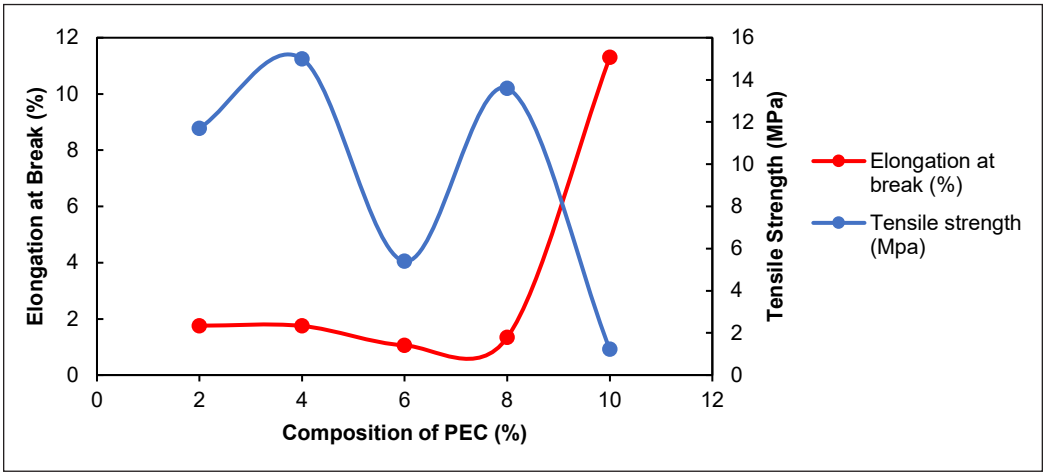

Figure 10. Elongation at break and tensile strength of PLA/PEC blends

CONCLUSION

The blends of PLA/PEC with different PLA and PEC ratios were successfully prepared using the melt blending technique. Despite the different processing times, the torque decreased when PEC was added to PLA. The increasing PEC content in the blends makes the sample degrade faster, as PLA90/PEC10 blends were the fastest to degrade at 500°C compared to other full blends observed in TGA analysis. In addition, 5 wt% weight loss (T_{d5}) of the PLA/PEC blends was decreased with PEC, which influences the thermal stability of

the blends. However, shifting in both T_g for PEC and PLA revealed that the chain mobility induces the crystallinity of PLA that reaches the highest, resulting in 10 wt% PEC, with crystallinity up to 48.81%. The higher toughness value also supports PLA90/PEC10, 362000 MJ/m^{3,} and high elongation at break 11.3%. Molecular interaction between PEC and PLA blends showed slight changes in the absorbance peaks for the carbonyl group when the low ratio range of PEC was added to the PLA/PEC blends. Adding PEC at more than 6 wt% could ease the melt blending process due to the low torque. However, the blend showed less thermal stability. Nevertheless, it gives a significant toughness property, as shown by PLA90/PEC10 blend. Due to this, low PEC loading is strongly suggested to be an alternative to the PLA modification in various applications such as fused deposition modeling (FDM) in 3D printing and as a compatibilizer.

ACKNOWLEDGEMENT

This research was funded by University Teknologi MARA Grant, 600-RMC/GPK 5/3 (199/200). The authors thank University Teknologi MARA for its financial support.

REFERENCES

Chen, C., Dong, L., & Cheung, M. K. (2005). Preparation and characterization of biodegradable poly(l-lactide)/chitosan blends. *European Polymer Journal*, *41*(5), 958-966. https://doi.org/10.1016/j.eurpolymj.2004.12.002

Chen, Q., Mangadlao, J. D., Wallat, J., Leon, A. D., Pokorski, J. K., & Advincula, R. C. (2017). 3D printing biocompatible polyurethane/poly(lactic acid)/graphene oxide nanocomposites: Anisotropic properties. *ACS Applied Materials and Interfaces*, *9*(4), 4015-4023. https://doi.org/10.1021/acsami.6b11793

Fushimi, R., & Gaffney, A. M. (2014). The new ChemPren process for the conversion of waste plastic to chemicals and fuel. *Topics in Catalysis*, *57*(17-20), 1412-1418. https://doi.org/10.1007/s11244-014-0312-6

Geyer, R., Jambeck, J. R., & Law, K. L. (2017). Production, use, and fate of all plastics ever made. *Science Advances*, *3*(7), Article e1700782. https://doi.org/10.1126/sciadv.1700782

Gigante, V., Coltelli, M. B., Vannozzi, A., Panariello, L., Fusco, A., Trombi, L., Donnarumma, G., Danti, S., & Lazzeri, A. (2019). Flat die extruded biocompatible poly(lactic acid) (PLA)/poly(butylene succinate) (PBS) Based Films. *Polymers*, *11*(11) Article 1857. https://doi.org/10.3390/polym11111857

Hedayati, F., Moshiri-Gomchi, N., Assaran-Ghomi, M., Sabahi, S., Bahri-Laleh, N., Mehdipour-Ataei, S., Mokhtari-Aliabad, J., & Mirmohammadi, S. A. (2020). Preparation and properties of enhanced nanocomposites based on PLA/PC blends reinforced with silica nanoparticles. *Polymers for Advanced Technologies*, *31*(3), 566-573. https://doi.org/10.1002/pat.4797

Kamaludin, N. H. I., Ismail, H., Rusli, A., Sam, S. T., & Gunny, A. A. N. (2020). Processing, tensile and morphological characteristics of polylactic acid/ Chitosan biocomposites prepared by melt compounding technique. In *AIP Conference Proceedings*, *2267*(1) Article 020002. https://doi.org/10.1063/5.0016532

Lyu, Y., Chen, Y., Lin, Z., Zhang, J., & Shi, X. (2020). Manipulating phase structure of biodegradable PLA/PBAT system: Effects on dynamic rheological responses and 3D printing. *Composites Science and Technology*, *200* Article 108399. https://doi.org/10.1016/j.compscitech.2020.108399

Ma, X., Jiugao, Y., & Wang, N. (2006). Compatibility characterization of poly(lactic acid)/ poly(propylene carbonate) blends. *Journal of Polymer Science, Part B: Polymer Physics*, *44*(1), 94-101. https://doi.org/10.1002/polb.20669

Nofar, M., Mohammadi, M., & Carreau, P. J. (2020). Effect of TPU hard segment content on the rheological and mechanical properties of PLA/TPU blends. *Journal of Applied Polymer Science*, *137*(45), Article 49387. https://doi.org/10.1002/app.49387

Ou-Yang, Q., Guo, B., & Xu, J. (2018). Preparation and Characterization of Poly(butylene succinate)/Polylactide Blends for Fused Deposition Modeling 3D Printing. *ACS Omega*, *3*(10), 14309-14317. https://doi.org/10.1021/acsomega.8b02549

Patti, A., Acierno, D., Latteri, A., Tosto, C., Pergolizzi, E., Recca, G., Cristaudo, M., & Cicala, G. (2020). Influence of the processing conditions on the mechanical performance of sustainable bio-based PLA compounds. *Polymers*, *12*(10) Article 2197. https://doi.org/10.3390/POLYM12102197

Pivsa-Art, W., Chaiyasat, A., Pivsa-Art, S., Yamane, H., & Ohara, H. (2013). Preparation of polymer blends between poly(lactic acid) and poly(butylene adipate-co-terephthalate) and biodegradable polymers as compatibilizers. *Energy Procedia*, *34*, 549-554. https://doi.org/10.1016/j.egypro.2013.06.784

Prasong, W., Muanchan, P., Ishigami, A., Thumsorn, S., Kurose, T., & Ito, H. (2020). Properties of 3D printable Poly(lactic acid)/Poly(butylene adipate-co-terephthalate) blends and nano talc composites. *Journal of Nanomaterials*, *2020* Article 8040517. https://doi.org/10.1155/2020/8040517

Ramlee, N. A., & Tominaga, Y. (2018). Preparation and characterization of poly (ethylene carbonate)/ poly (lactic acid) blends. *Journal of Polymer Research*, *25*(2), Article 54.

Ramlee, N. A., & Tominaga, Y. (2019a). Mechanical and degradation properties in alkaline solution of poly(ethylene carbonate)/poly(lactic acid) blends. *Polymer*, *166*, 44-49. https://doi.org/10.1016/j.polymer.2019.01.043

Ramlee, N. A., & Tominaga, Y. (2019b). Structural and physicochemical properties of melt-quenched poly (ethylene carbonate)/ poly (lactic acid) blends. *Polymer Degradation and Stability*, *163*, 35-42.

Russell, E. B. (2003). Book review: Book review. *Journal of Cutaneous Pathology*, *30*(2), 158-158. https://doi.org/10.1034/j.1600-0560.2003.00021.x

Sonseca, A., Madani, S., Rodríguez, G., Hevilla, V., Echeverría, C., Fernández-García, M., Muñoz-Bonilla, A., Charef, N., & López, D. (2020). Multifunctional PLA blends containing chitosan mediated silver nanoparticles: Thermal, mechanical, antibacterial, and degradation properties. *Nanomaterials*, *10*(1) Article 22. https://doi.org/10.3390/nano10010022

Tao, Y., Wang, H., Li, Z., Li, P., & Shi, S. Q. (2017). Development and application ofwood flour-filled polylactic acid composite filament for 3d printing. *Materials*, *10*(4) Article 339 https://doi.org/10.3390/ma10040339

Wacharawichanant, S., Opasakornwong, P., Poohoi, R., & Phankokkruad, M. (2019). Morphology, mechanical and thermal properties of poly(Lactic acid)/propylene-ethylene copolymer/cellulose composites. *Materials Science Forum*, *972*, 172-177. https://doi.org/10.4028/www.scientific.net/MSF.972.172

Wang, M., Wu, Y., Li, Y. D., & Zeng, J. B. (2017). Progress in toughening poly(lactic acid) with renewable polymers. *Polymer Reviews*, *57*(4), 557-593. https://doi.org/10.1080/15583724.2017.1287726

Xie, D., Zhao, Y., Li, Y., LaChance, A. M., Lai, J., Sun, L., & Chen, J. (2019). Rheological, thermal, and degradation properties of PLA/PPG Blends. *Materials*, *12*(21) Article 3519. https://doi.org/10.3390/ma12213519

Yayshahri, A. M., Peighambardoust, S. J., & Shenavar, A. (2019). Impact , thermal and biodegradation properties of high impact polystyrene / corn starch blends processed via melt extrusion. *Polyolefins Journal*, *6*(2), 151-158. https://doi.org/10.22063/poj.2019.2390.1130

Zhang, Y., Chen, J., Peng, Q., Song, L., Wang, Z., & Wang, Z. (2020). Hydrogen bonding assisted toughness enhancement of poly(lactide) blended with a bio-based polyamide elastomer of extremely low amounts. *Applied Surface Science*, *506,* Article 144684. https://doi.org/10.1016/j.apsusc.2019.144684

Pertanika J. Sci. & Technol. 31 (4): 1685 - 1693 (2023)

PERTANIKA JOURNALS

SCIENCE & TECHNOLOGY

Journal homepage: http://www.pertanika.upm.edu.my/

Review Article

Graphene Functionalized Carbon Felt/Graphite Felt Fabrication as Electrodes for Vanadium Redox Flow Batteries (VRBs): A Review

Ellie Yi Lih Teo[1,2]*, Omar Faruqi Marzuki[1,2] and Kwok Feng Chong[3]

[1]Department of Science and Technology, Faculty of Humanities, Management and Science, Universiti Putra Malaysia, Jalan Nyabau, 97008 UPM, Bintulu, Sarawak, Malaysia
[2]Institut EkoSains Borneo, Universiti Putra Malaysia, Jalan Nyabau, 97008 UPM, Bintulu, Sarawak, Malaysia
[3]Faculty of Industrial Sciences & Technology, Universiti Malaysia Pahang, Lebuhraya Tun Razak, Gambang, 26300 UMP, Kuantan, Pahang, Malaysia

ABSTRACT

The growth in the development of renewable energy sources has led to tremendous attention to the research in energy storage systems. One of the electrochemical energy storage systems that have shown great potential to be used on a large scale is vanadium redox flow batteries (VRBs), as they possess flexible designs, long life cycles, and high energy density. Carbon felts (CF), and graphite felts (GF) have commonly been used as electrodes in VRBs. To improve market penetration using VRB technology, researchers have focused on electrode modifications to increase the power density and rate capabilities of VRBs. One of the carbon-based modifications which have shown significant improvements in the performance of VRBs is the use of graphene, which has outstanding electrochemical and physical characteristics as an electrocatalyst. In this review, electrochemical, physical, and other methods which have been reported in the graphene functionalization of graphite felt/carbon felt are discussed. The working principle and limiting methods were elaborated on and discussed for each method. Finally, recommendations for future developments are also highlighted.

Keywords: Carbon felt, electrode fabrication, graphene, vanadium redox flow battery

ARTICLE INFO

Article history:
Received: 13 June 2022
Accepted: 16 August 2022
Published: 24 May 2023

DOI: https://doi.org/10.47836/pjst.31.4.05

E-mail addresses:
ellie_teo@upm.edu.my (Ellie Yi Lih Teo)
omar_faruqi@upm.edu.my (Omar Faruqi Marzuki)
ckfeng@ump.edu.my (Kwok Feng Chong)
* Corresponding author

INTRODUCTION

The widespread use of fossil fuels has caused various environmental drawbacks. To avoid this, various renewable energy sources, such as solar and wind, are being

ISSN: 0128-7680
e-ISSN: 2231-8526

developed and implemented worldwide. However, their volatility and intermittent problems pose a barrier to the large-scale application of clean energy. Hence, a reliable energy storage system is required.

Electrical energy storage systems can be divided into geological energy storage technologies, flywheels and supercapacitors, and battery storage technologies. Geological energy storage technologies (compressed air and pumped hydro energy storage) are suited for large-scale energy storage but are costly. At the same time, flywheels and supercapacitors have high and low energy densities, which are more suitable for power management. Lead acid, lithium-ion, and redox flow batteries (RFBs) are examples of battery storage technologies that are potential candidates for large-scale energy storage. Compared to other commercial batteries, RFBs have the advantage of design flexibility as the energy and power density can be decoupled. It also merits high energy density, a long life cycle, and rapid response.

The vanadium redox flow battery (VRB) is an electrochemical energy storage system with the following components, electrolytes, a membrane, and electrodes. The electrolytes (both anolyte and catholyte) are stored in tanks and circulated through the cell using pumps. An example of the VRB setup is shown in Figure 1.

The VRB electrode reactions are as given in Equations 1 to 3:

Reaction on negative side: $V^{2+} \leftrightarrows V^{3+} + e^{-}$ [1]

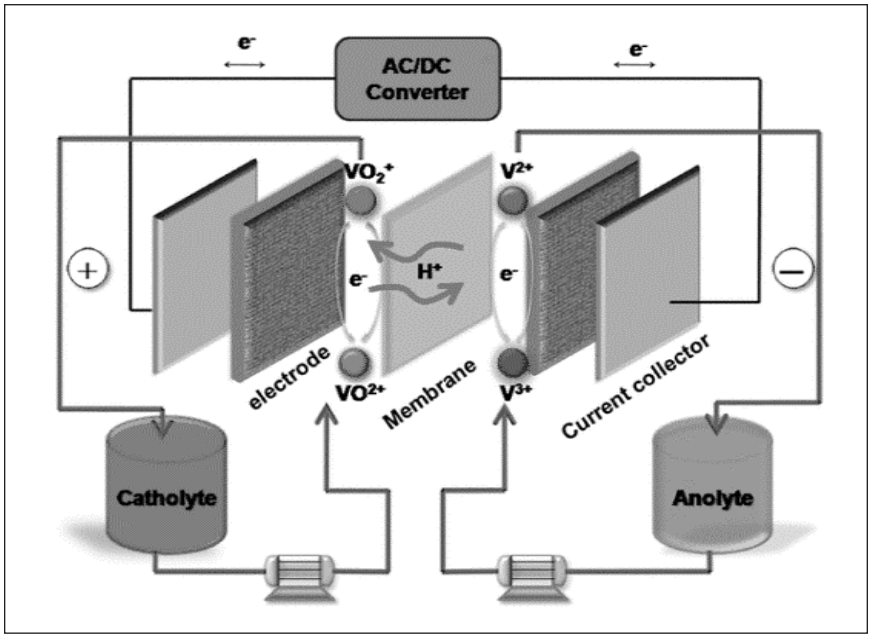

Figure 1. Schematic of vanadium redox flow battery setup (Ding et al., 2013). Reprinted (adapted) with permission from Ding et al., 2013. Copyright 2013 American Chemical Society

Reaction on the positive side: $VO_2^+ + 2H^+ + e^- \leftrightarrows VO^{2+} + H_2O$ [2]

Overall cell reaction: $VO_2^+ + V^{2+} + 2H^+ \leftrightarrows VO^{2+} + V^{3+} + H_2O$ [3]

The reaction shows that as VRB is discharged, V^{2+} is oxidized to V^{3+} on the negative electrode while VO_2^+ is reduced to VO^{2+} on the positive electrode, and only one electron is involved in this process. Apart from the one-electron transfer, water and two protons are exchanged to maintain the charge balance. The analysis shows that the positive electrode reaction is the one that is limiting the performance of VRB. Hence, researchers are focused on developing materials with high electrochemical kinetics towards VO_2^+/VO^{2+} to enhance the overall performance of VRB.

Carbon felts (CF) and graphite felts (GF) have been commonly used as the electrodes in the VRBs due to their three-dimensional structure, their high conductivity as well as their chemical stability (González et al., 2017; Moghim et al., 2017). However, they are hydrophobic, resulting in poor wettability and low electrochemical activity. This results in severe polarization and low device efficiency which requires the development of catalyst materials to enhance its performance.(González et al., 2017; Moghim et al., 2017; Xia et al., 2019).

Among the carbonaceous electrocatalyst, graphene has attracted wide interest due to its outstanding properties, such as large specific surface area (~2600 m^2/g), high electrical conductivity (~200,000 cm^2/V s), chemical stability and high thermal conductivity (~5000 W/m K). These properties are crucial to enhance the active reaction sites and electron transportation. Due to the potentials demonstrated by graphene, researchers have worked extensively on the fabrication process of graphene-modified carbon felt/graphite felt with the aim of further enhancing the electrochemical activity of the electrode towards the vanadium ion couples via two key aspects, which are (1) to maximize the effective surface area of the electrodes by reducing the stacking of graphene layers and (2) by improving the bond between the graphene coating and the carbon felt which will promote the electrode's stability. This article reviewed and summarized the literature on the fabrication of graphene-functionalized graphite felt/carbon felt for vanadium redox flow batteries (VRBs).

Physical Method

One of the general methods in preparing graphene-coated carbon felt is the dipping-drying process. In this process, carbon felt (CF) is dipped into a suspension of graphene or graphene oxide and allowed to dry before it is ready for use. This process is based on the inherent solid-liquid interaction between the surface tension of the graphene oxide solution and carbon felt/graphite felt substrate (Tang & Yan, 2017). Li et al. (2013) dipped CF into a suspension of GO and dried it. Subsequently, the GO-coated CF was reduced

electrochemically at different potentials in phosphate buffer solution (PBS) before using it as the electrodes in the VRB (Li et al., 2013). It was found that the prepared graphene-coated CF demonstrated lower electrochemical polarization, and its energy efficiency was approximately 82%. Moghim et al. (2017) and Opar et al. (2020) prepared graphene-coated carbon felt using this dipping-drying process using graphene ink and three-dimensional graphene, respectively. By dipping CF into different concentrations of graphene ink (1–5 mg/mL) to load different amounts of graphene on the CF, Moghim et al. (2017) found that 2 mg/mL was the optimum concentration. Loading beyond 2 mg/mL did not significantly improve peak current (Moghim et al., 2017). Meanwhile, Opar et al. (2020) coated CF with three-dimensional graphene to reduce the restacking and agglomeration of graphene layers due to the strong π-π interactions. The graphene layers were covalently bonded to CF as the triblock polymer (P123) was used. After the dip and dry process, the CFs were weighed to determine the amount of graphene loaded.

Meanwhile, Xia et al. (2019) dipped CF into graphene by adding a Nafion binder to obtain graphene-coated CF. The study by Xia et al. (2019) focused on the correlation between the number of dipping times and the electrochemical performance of the VRB. As the dipping times increased, the amount of Nafion deposited also increased. The Nafion has no contribution to the electrochemical activity; therefore, a higher amount deposited is detrimental to the electrochemical performance. (Xia et al., 2019).

Preparing graphene-coated CF by dipping is relatively simple and requires no special equipment. However, the authors did not report whether the graphene layers suffer from peeling from the CF over long cycles. It is slightly trickier to determine the amount of graphene loaded when a binder such as Nafion is used. The use of binders in this process also increases the fabrication cost and reduces the surface area and conductivity of the electrodes (Opar et al., 2020; Zhang et al., 2016).

Sankar et al. (2018) prepared graphene-coated CF using electrostatic assembly. In the layer-by-layer assembly, a cationic polyelectrolyte is used as a binder between the two graphene layers (Sankar et al., 2018). As the porosity and thickness can be obtained for each layer, the total deposited layers can be tailored to the specific peak currents required. Compared to the physical dipping method, electrostatic layer-by-layer assembly provided better control over the electrode surface morphology and electrocatalytic activity. This technique also demonstrated scale-up potential as the number of reaction active sites can be systematically calculated.

With the aim of preparing an electrode that is suitable for practical implementation, Bellani et al. (2021) incorporated graphene prepared from wet jet milling of graphite onto CF, which was plasma treated using an infiltration method with the assistance of polyvinylidene fluoride (PVDF) binder (Bellani et al., 2021). Electrodes prepared without the PVDF binder were also tested, and the graphene flakes peeled off easily, resulting in fast deterioration of the VRFB performance (Bellani et al., 2021).

Electrochemical Method

Besides the physical methods of fabricating graphene-coated carbon felts discussed earlier, researchers have also explored electrochemical methods as they are economical, controllable, and scalable. Gonzalez et al. (2017) and Nia et al. (2018) demonstrated the use of electrophoretic deposition (EPD) and electrodeposition to simultaneously deposit and reduce graphene oxide (GO) produced by the Hummers' method.

The EPD process is usually conducted in a two-electrode system where the electric potential (direct or modulated mode) is applied to the graphene oxide solution. GO produced by the Hummers' method contained various oxygen functional groups (hydroxyl and epoxide on the basal planes, carboxylate, and carbonyl on the edges). When the electric field is applied, negatively charged GO moves to the oppositely charged electrode, transferring it from the suspension and depositing it on the electrodes (Diba et al., 2016) (Ma et al., 2018).

Using the EPD method at 10 V for 3 hours, Gonzalez et al. (2017) prepared reduced graphene oxide (rGO) coated CF, while the study by Nia et al. (2018) used the cyclic voltammetry method in the potential range of 0 to -1.5 V. A schematic diagram of the EPD process is illustrated in Figure 2. Besides physical adsorption, chemical bonds formed also helped the graphene layers formed to adhere to CF surfaces. Simultaneously, during the EPD and electrodeposition process, the GO was reduced, which enabled the recovery of π-π bonds (An et al., 2010; González et al., 2017; Nia et al., 2018). The stability of the graphene-coated CF prepared through the EPD process was tested over 20 cycles, and a high energy efficiency of 95.8% remained, showing no graphene peeling was evident. Like the electrodeposited graphene-coated CF, the energy efficiency remained unchanged after 20 cycles. When the cycles were increased to 80, the energy efficiency decreased slightly.

Apart from using GO from Hummers' method as the source to deposit graphene on CF, Gürsu et al. (2018) have also demonstrated a one-step procedure to coat CF using cyclic voltammetry (CV) from pencil graphite in sulfuric acid solution (Gürsu et al., 2018). In this one-step procedure, the pencil graphite was oxidized through electrochemical in-situ oxidation, and it was then electrochemically reduced to rGO, which can be observed through the cyclic voltammograms. The intensities of the anodic and cathodic peaks were found to have increased proportionally with the number of cycles. The stability of the electrodes was studied using cyclic voltammetry for 500 cycles, and it did not show any significant changes in the cyclic voltammogram.

As the studies show, electrochemical procedures are simple, controllable, and scalable to fabricate graphene-coated carbon felt. Despite the significant advantages, literature on forming graphene-coated carbon felt/graphite felt through electrochemical procedures is limited.

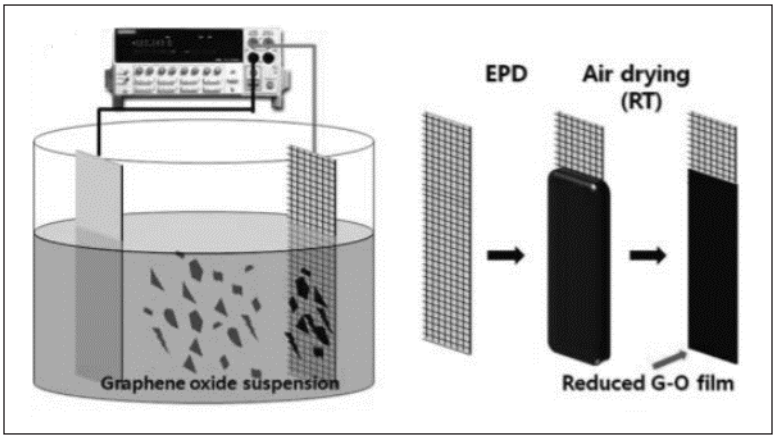

Figure 2. A schematic diagram of the EPD process (An et al., 2010). Reprinted (adapted) with permission from An et al., 2010. Copyright 2010 American Chemical Society

Other Methods

Besides the physical and electrochemical methods elaborated above, other methods such as electrospinning, chemical vapor deposition (CVD), and microwave plasma-enhanced CVD have been reported. Jing et al. (2019) proposed an electrospinning method to fabricate graphene-coated CF. The electrospinning technique relies on the electrostatic repulsion between the surface charges to continuously synthesize various scalable assemblies (Al-Dhahebi et al., 2022). It is also known as a cost-effective, simple, and versatile technique. The partially reduced GO-coated CF was successfully prepared by introducing GO into the electrospinning solution, followed by a carbonization process (Jing et al., 2019). The oxygen content in the partially reduced GO formed has significantly enhanced the hydrophilicity of the CF and the electrochemical performance of the VRB (increased by 9.0% in energy efficiency).

An in-situ microwave plasma-enhanced chemical vapor deposition method synthesized 3D graphene nanowell decorated carbon felts (Li et al., 2016). The graphene sheets were vertically grown and wrapped in the fibers in CF. It increases the electrode's surface area, promoting the vanadium ions' electrocatalytic activity. The prepared electrodes showed no morphological changes after 100 charge and discharge cycles.

Meanwhile, Long et al. (2021) studied the large-scale (20 cm x 20 cm) preparation of graphene-modified carbon felt using the chemical vapor deposition method (CVD). The electrodes enhanced electrical conductivity and redox catalytic performance. The prepared electrodes endured over 500 cycles of charge-discharge with only slight decay observed (Long et al., 2021). Both the microwave plasma-enhanced chemical vapor deposition and chemical vapor deposition (CVD) methods have successfully demonstrated the preparation of graphene-modified carbon felt. Long et al. (2021) was the first study on the large-scale

preparation of graphene-modified carbon felt and is another step toward the practical use of graphene-modified carbon felts as electrodes in VRBs. However, using CVD requires a highly expensive instrument, and the reaction process emits by-products in the form of toxic gases.

OUTLOOK

A suitable electrode for VRBs requires high electrical conductivity, specific surface area, and inertness to strong acids. Carbon felt/graphite felt met all the requirements, which makes it, thus far, the best material to be used. However, its low chemical activity towards the vanadium ion couple results in severe polarization and low device efficiency. Modifications with noble metals (Ru, Pt & Au) are not cost-effective at a large scale. Intrinsic control of morphologies is required when low-cost metals are used to guarantee high VRB performance and metal oxides (PbO_2, NiO & CeO_2) decompose in strong acids, which are used as VRBs electrolytes. As graphene-based materials have a high specific surface area, high conductivity, and abundant active groups, graphene-modified CF/GF has shown superior performance to pristine CF/GF. However, several interesting challenges need to be overcome for the large-scale application of graphene-coated CF/GF in VRBs. Firstly, control over the graphene loading is crucial as it provides the electroactive sites which enhance the electrochemical performance of the VRB. Controlling the graphene loaded on CF/GF, the amount required can be tailored to the desired VRB performance. Secondly, the cycling life of the graphene coating is also key to applying graphene-modified CF practically. Peeling of the graphene layers is detrimental to the energy efficiency of the VRB. The number of cycles tested in the literature is limited and is insufficient to conclude the performance of graphene-modified CF/GF over long cycles. Thirdly, large-scale preparation of the graphene-modified CF is important as it is necessary to ensure that the procedure can be applied at the industrial scale. To our knowledge, limited large-scale preparation of graphene-modified CF was reported. We are convinced that with more research, graphene-modified carbon felt can be applied in a large-scale use of vanadium redox flow battery.

CONCLUSION

This study has reviewed various methods to prepare graphene-modified carbon felt/graphite felt (CF/GF) as the electrode material for vanadium redox flow batteries and discussed the advantageous and disadvantageous of each method reported. The methods have successfully prepared graphene-modified CF/GF, which performed superiorly compared to pristine CF/GF, demonstrating its potential to be integrated into large-scale vanadium redox flow battery deployment. The challenges which need to be overcome are also discussed. Further research conducted can overcome these barriers and realize the full potential of graphene-coated CF/GF in large-scale VRBs applications.

ACKNOWLEDGEMENTS

The authors thank the Ministry of Higher Education for Fundamental Research Grant Scheme (FRGS) (FRGS/1/2020/STG05/UPM/02/3), Universiti Putra Malaysia for Geran Inisiatif Putra Muda (GP-IPM) (9683600) and UPM-Kyutech International Symposium on Applied Engineering and Sciences 2021 (SAES 2021) and Universiti Putra Malaysia for supporting the publication fee.

REFERENCES

Al-Dhahebi, A. M., Ling, J., Krishnan, S. G., Yousefzadeh, M., Elumalai, N. K., Saheed, M. S. M., Ramakrishna, S., & Jose, R. (2022). Electrospinning research and products: The road and the way forward. *Applied Physics Reviews*, *9*(1), Article 011319. https://doi.org/10.1063/5.0077959

An, S. J., Zhu, Y., Lee, S. H., Stoller, M. D., Emilsson, T., Park, S., Velamakanni, A., An, J., & Ruoff, R. S. (2010). Thin film fabrication and simultaneous anodic reduction of deposited graphene oxide platelets by electrophoretic deposition. *The Journal of Physical Chemistry Letters, 1*(8), 1259-1263. https://doi.org/10.1021/jz100080c

Bellani, S., Najafi, L., Prato, M., Oropesa-Nuñez, R., Martín-Garciá, B., Gagliani, L., Mantero, E., Marasco, L., Bianca, G., Zappia, M. I., Demirci, C., Olivotto, S., Mariucci, G., Pellegrini, V., Schiavetti, M., & Bonaccorso, F. (2021). Graphene-based electrodes in a vanadium redox flow battery produced by rapid low-pressure combined gas plasma treatments. *Chemistry of Materials*, *33*(11), 4106-4121. https://doi.org/10.1021/acs.chemmater.1c00763

Diba, M., Fam, D. W. H., Boccaccini, A. R., & Shaffer, M. S. P. (2016). Electrophoretic deposition of graphene-related materials: A review of the fundamentals. *Progress in Materials Science, 82*, 83-117. https://doi.org/10.1016/j.pmatsci.2016.03.002

Ding, C., Zhang, H., Li, X., Liu, T., & Xing, F. (2013). Vanadium flow battery for energy storage: Prospects and challenges. *The Journal of Physical Chemistry Letters*, *4*(8), 1281-1294. https://doi.org/10.1021/jz4001032

González, Z., Flox, C., Blanco, C., Granda, M., Morante, J. R., Menéndez, R., & Santamaría, R. (2017). Outstanding electrochemical performance of a graphene-modified graphite felt for vanadium redox flow battery application. *Journal of Power Sources*, *338*, 155-162. https://doi.org/10.1016/j.jpowsour.2016.10.069

Gürsu, H., Gençten, M., & Şahin, Y. (2018). Cyclic voltammetric preparation of graphene-coated electrodes for positive electrode materials of vanadium redox flow battery. *Ionics*, *24*(11), 3641-3654. https://doi.org/10.1007/s11581-018-2547-x

Jing, M., Xu, Z., Fang, D., Fan, X., Liu, J., & Yan, C. (2019). Anchoring effect of the partially reduced graphene oxide doped electrospun carbon nanofibers on their electrochemical performances in vanadium flow battery. *Journal of Power Sources*, *425*, 94–102. https://doi.org/10.1016/j.jpowsour.2019.04.003

Li, W., Liu, J., & Yan, C. (2013). Reduced graphene oxide with tunable C/O ratio and its activity towards vanadium redox pairs for an all vanadium redox flow battery. *Carbon*, *55*, 313-320. https://doi.org/10.1016/j.carbon.2012.12.069

Li, W., Zhang, Z., Tang, Y., Bian, H., Ng, T. W., Zhang, W., & Lee, C. S. (2016). Graphene-nanowall-decorated carbon felt with excellent electrochemical activity toward VO_2^+/VO^{2+} couple for all vanadium redox flow battery. *Advanced Science*, *3*(4), 1-7. https://doi.org/10.1002/advs.201500276

Long, T., Long, Y., Ding, M., Xu, Z., Xu, J., Zhang, Y., Bai, M., Sun, Q., Chen, G., & Jia, C. (2021). Large scale preparation of 20 cm × 20 cm graphene modified carbon felt for high performance vanadium redox flow battery. *Nano Research*, *14*(10), 3538-3544. https://doi.org/10.1007/s12274-021-3564-z

Ma, Y., Han, J., Wang, M., Chen, X., & Jia, S. (2018). Electrophoretic deposition of graphene-based materials: A review of materials and their applications. *Journal of Materiomics, 4*(2), 108-120. https://doi.org/10.1016/j.jmat.2018.02.004

Moghim, M. H., Eqra, R., Babaiee, M., Zarei-Jelyani, M., & Loghavi, M. M. (2017). Role of reduced graphene oxide as nano-electrocatalyst in carbon felt electrode of vanadium redox flow battery. *Journal of Electroanalytical Chemistry*, *789*, 67-75. https://doi.org/10.1016/j.jelechem.2017.02.031

Nia, P. M., Abouzari-lotf, E., Woi, P. M., Alias, Y., Ting, T. M., Ahmad, A., & Jusoh, N. W. C. (2018). Electrodeposited reduced graphene oxide as a highly efficient and low-cost electrocatalyst for vanadium redox flow batteries. *Electrochimica Acta*, *297*, 31-39 https://doi.org/10.1016/j.electacta.2018.11.109

Opar, D. O., Nankya, R., Lee, J., & Jung, H. (2020). Three-dimensional mesoporous graphene-modified carbon felt for high-performance vanadium redox flow batteries. *Electrochimica Acta*, *330*, Article 135276. https://doi.org/10.1016/j.electacta.2019.135276

Sankar, A., Michos, I., Dutta, I., Dong, J., & Angelopoulos, A. P. (2018). Enhanced vanadium redox flow battery performance using graphene nanoplatelets to decorate carbon electrodes. *Journal of Power Sources*, *387*, 91-100. https://doi.org/10.1016/j.jpowsour.2018.03.045

Tang, X., & Yan, X. (2017). Dip-coating for fibrous materials: mechanism, methods and applications. *Journal of Sol-Gel Science and Technology, 81*(2), 378-404. https://doi.org/10.1007/s10971-016-4197-7

Xia, L., Zhang, Q., Wu, C., Liu, Y., Ding, M., Ye, J., Cheng, Y., & Jia, C. (2019). Graphene coated carbon felt as a high-performance electrode for all vanadium redox flow batteries. *Surface and Coatings Technology*, *358*, 153-158. https://doi.org/10.1016/j.surfcoat.2018.11.024

Zhang, C., Liang, P., Yang, X., Jiang, Y., Bian, Y., Chen, C., Zhang, X., & Huang, X. (2016). Biosensors and bioelectronics binder-free graphene and manganese oxide coated carbon felt anode for high-performance microbial fuel cell CF GO / CF rGO / CF. *Biosensors and Bioelectronic*, *81*, 32-38. https://doi.org/10.1016/j.bios.2016.02.051

Pertanika J. Sci. & Technol. 31 (4): 1695 - 1716 (2023)

PERTANIKA JOURNALS

SCIENCE & TECHNOLOGY

Journal homepage: http://www.pertanika.upm.edu.my/

Hybridised Intelligent Dynamic Model of 3-Satisfiability Fuzzy Logic Hopfield Neural Network

Farah Liyana Azizan[1,2], Saratha Sathasivam[1]* and Majid Khan Majahar Ali[1]

[1]School of Mathematical Sciences, Universiti Sains Malaysia, Penang, 11800, USM, Malaysia
[2]Centre for Pre-University Studies, Universiti Malaysia Sarawak, 94300 UNIMAS, Kota Samarahan, Sarawak, Malaysia

ABSTRACT

This study presents a new way of increasing 3SAT logic programming's efficiency in the Hopfield network. A new model of merging fuzzy logic with 3SAT in the Hopfield network is presented called HNN-3SATFuzzy. The hybridised dynamic model can avoid locally minimal solutions and lessen the computing burden by utilising fuzzification and defuzzification techniques in fuzzy logic. In addressing the 3SAT issue, the proposed hybrid approach can select neuron states between zero and one. Aside from that, unsatisfied neuron clauses will be changed using the alpha-cut method as a defuzzifier step until the correct neuron state is determined. The defuzzification process is a mapping stage that converts a fuzzy value into a crisp output. The corrected neuron state using alpha-cut in the defuzzification stage is either sharpening up to one or sharpening down to zero. A simulated data collection was utilised to evaluate the hybrid techniques' performance. In the training phase, the network for HNN-3SATFuzzy was weighed using RMSE, SSE, MAE and MAPE metrics. The energy analysis also considers the ratio of global minima and processing period to assess its robustness. The findings are significant because this model considerably impacts Hopfield networks' capacity to handle 3SAT problems with less complexity and speed. The new information and ideas will aid in developing innovative ways to gather knowledge for future research in logic programming. Furthermore, the breakthrough in dynamic learning is considered a significant step forward in neuro-symbolic integration.

Keywords: 3SAT, alpha-cut, defuzzification, fuzzification, fuzzy logic, Hopfield network

ARTICLE INFO

Article history:
Received: 16 June 2022
Accepted: 13 September 2022
Published: 24 May 2023

DOI: https://doi.org/10.47836/pjst.31.4.06

E-mail addresses:
afliyana@unimas.my (Farah Liyana Azizan)
saratha@usm.my (Saratha Sathasivam)
majidkhanmajaharali@usm.my (Majid Khan Majahar Ali)
* Corresponding author

ISSN: 0128-7680
e-ISSN: 2231-8526

INTRODUCTION

Artificial Intelligence (AI) is the impetus for today's technological advancement. Thus, it leads to the advanced development of machine learning techniques to solve those problems. Artificial Neural Networks (ANNs) can be categorised as a sub-domain of AI widely used to improve decision-making in various disciplines. An ANN comprises interconnected neurons with discrete input and output layers inspired by the biological neuron model. The system is an aligned computing system created by simulating the human's instinctive thinking while investigating the biological brain's network in terms of biological neurons (Garcez & Zaverucha, 1999). The Hopfield Network (HNN) is a single-level recursive neural network (RNN) in which every single neuron output is linked to every other neuron response (Hopfield & Tank, 1985). HNN uses a particular symbolic learning model to efficiently coordinate the propagation of the input and output neurons in solving problems. The capacity of the HNN to resolve to the closest minimal solution determines the neuron state's dynamic behaviour. Abdullah (1992) proposes a method for logic programming on the HNN.

After defining the connection strengths, or mostly called the synaptic weight with logic programming, that is, by comparing cost and energy functions, the network performed a logical inconsistency reduction in programming. Abdullah (1993) introduces the learning phase in the HNN directly. The logic paradigm of Abdullah has become the most prominent and has lately been employed (Mansor & Sathasivam, 2021; Sathasivam et al., 2020). A mathematical framework can describe various scientific and technological challenges in daily life. However, one must first create methods for resolving some mathematical issues to do so. Many crucial problems, such as categorising or finding an ordered list, can be solved with realistic solutions. Nevertheless, a mathematical problem is the Satisfiability Problem (SAT). Unravelling these difficulties is possible with the aid of a computer. The Satisfiability Problem, or SAT, is one of the most well-known issues. It is described as an approach for achieving the best task utilising Boolean quantities to verify that the 3SAT formula is met. A large number of NP issues can be simplified via SAT.

In earlier research, the HNN model and 3SAT logic programming were combined to characterise the innovation as a singular data mining method. This model has been tested with a real-life dataset to assess its efficiency of the model. The method assesses various data sets related to cardiovascular disorders (Mansor et al., 2018). More logic mining strategies, including 3SAT in HNN, have been presented using real-life datasets such as the Bach Choral Harmony and German Credit (Zamri et al., 2020). However, the existing work's 3SAT problem in the Hopfield network only considers zero and one neuron values. Hence, to resolve this problem, this model is further improved by incorporating fuzzy logic techniques to create a hybridised intelligent dynamic model

that can choose between zero and one neuron states. Traditional logic, as well as logic programming languages, are incapable of dealing with uncertainty. Crisp relations are nonfuzzy relations that use the basic two-valued Boolean logic connectives to define their operations, a mathematical system based on true and false statements. Fuzzy logic connectives are extensions that substitute two-valued Boolean logic connectives with many-valued logic connectives.

The Boolean relations and sets that are crisp and nonfuzzy are essentially particular examples of fuzzy relational structures, thanks to a unified approach to relations.

MATERIALS AND METHODS

Satisfiability Problem

The challenge of establishing the exposition of an assignment using a specified Boolean formula that assesses it as true or false is known as Boolean Satisfiability (SAT). Every variable is denoted by $X_1, X_2, \ldots, X_n$ for any $n \in \mathbb{N}$ in a propositional formula, θ. Each value from the set $\{0,1\}$, signifying false and true, can be assigned to these variables. If a variable has not yet been assigned a truth value, it is a free variable (Maandag, 2012). A propositional Boolean formula can also include the Boolean connectives of AND $(\wedge)$, OR $(\vee)$, NOT $(\neg)$ as well as parentheses to denote precedence.

If a propositional expression contains one or more clauses, it is understood as conjunctive normal form (CNF). A clause is a disjunction with one or many literals from the set *L*, including all literals. Each *L* represents whether it is a variable ω_i or its negation, $\neg\omega_i$. The following is an example of a propositional formula, θ. An *i*-CNF formula is a CNF formula in which each sentence has at most *i* different literals. For example, Equation 1 below is a 2-CNF formula.

$$\theta = (\omega_1 \vee \omega_2) \wedge (\neg\omega_1 \vee \omega_3) \wedge (\neg\omega_2 \vee \neg\omega_3) \quad [1]$$

This work will emphasise 3-CNF satisfiability or 3SAT in abbreviated form. The 3SAT problem examines whether a 3-CNF formula has a valuation that evaluates the formula as true or if a particular 3-CNF formula is satisfactory.

The structure of SAT will be described below:

1. The *i* variables in the Boolean SAT formula as given in Equation 2:

   $$\omega_1, \omega_2, \ldots, \omega_i \text{ for every } \omega \in \{-1,1\} \quad [2]$$

   Every variable of the clause is related to function OR $(\vee)$. Because this study will focus on 3SAT, it will consist of 3 literals per clause.
2. In a 3SAT formula, a set of a clause, β_m joined by AND $(\wedge)$ as given in Equation 3

$$\beta_1 \wedge \beta_2 \wedge \ldots \wedge \beta_m \quad [3]$$

where if $m = 3$, the Boolean SAT will have three clauses.

3. The literal's status can then be either the negative or the positive of the variables.

The logical formula is derived from the randomised 3SAT formula in this study. The propositional logic formula, including the 3SAT formula, can be translated into logic programming notations (Abdullah, 1992; Kowalski & Sergot, 1986). The ideal performance measures define and evaluate the 3SAT problem in the HNN. The example of 3SAT logic programming is shown in Equation 4.

$$\begin{aligned} \theta = \omega_1 &\leftarrow \omega_2, \omega_3 \\ \wedge \quad \omega_4, \omega_5 &\leftarrow \omega_6 \\ \wedge \quad \omega_7, \omega_8, \omega_9 &\leftarrow . \end{aligned} \quad [4]$$

Given the goal as Equation 5,

$$\leftarrow \vartheta \quad [5]$$

where $\omega_1, \omega_2 \ldots\ldots \omega_n$ for any $n \in \mathbb{N}$ refers to the literals in the clauses and $\leftarrow$ describes the implication and the given goal is ϑ.

The general formula for 3SAT is expressed in Equation 6.

$$\theta = \wedge_{i=1}^{n} \beta_m \quad [6]$$

where β_m signifies a set of a clause and *i* indicates the number of the clause.

The 3SAT logical representation in Boolean algebraic form with strictly three literals per sentence is known as discrete logic representation, as demonstrated in Equation 7.

$$\theta_{3SAT} = (\omega_1 \vee \neg\omega_2 \vee \neg\omega_3) \wedge (\omega_4 \vee \omega_5 \vee \neg\omega_6) \wedge (\omega_7 \vee \omega_8 \vee \omega_9) \quad [7]$$

where θ_{3SAT} will be fulfilled if $\theta_{3SAT} = 1$, the capacity to store information in Bipolar states, in which each state represents a significant structure for the dataset, is one of the critical reasons for encoding the variable in the form Equation 6. The logic program's primary goal is to find an interpretation of the structure that satisfies the whole clause. The hybridised dynamic model of HNN will have the 3SAT logical rule encoded in it. As a result, finding the logical inconsistencies transforms Equation 7 into the negation of θ_{3SAT} as presented in Equation 8.

$$\neg\theta_{3SAT} = (\neg\omega_1 \wedge \omega_2 \wedge \omega_3) \vee (\neg\omega_4 \wedge \neg\omega_5 \wedge \omega_6) \vee (\neg\omega_7 \wedge \neg\omega_8 \wedge \neg\omega_9) \quad [8]$$

Logic Programming in Hopfield Neural Network

HNN maintains the discrete nature of the difficulty and resolves it by minimising the energy function related to the outcome. HNNs are particularly good at pattern recognition (Fung et al., 2019) and defect identification (Pan et al., 2020). According to Little (1974), the dynamics of this model are asynchronous, with each neuron changing its state deterministically. According to most studies, HNN is regarded to have good properties, such as parallel execution for quick calculation and outstanding stability. Considering the structure of HNN is non-symbolic, the logical concept of 3SAT can enhance its ability with exceptional storage. The neuron's activation can be mathematically formulated as Equation 9:

$$\omega_i = \begin{cases} 1 & if \sum_j \varphi_{ij}\, \omega_i > \gamma \\ -1 & else \end{cases} \quad [9]$$

where φ_{ij} denotes the weight for part j to i, along with γ implies the threshold value. This paper executes 3SAT in HNN called HNN-3SAT, where we only incorporate three neurons for each clause. The local field efficiently suppressed the obtained output before producing the final state. Equation 10 shows the formulation for the local field with $m = 3$.

$$h_i = \sum_k \varphi_{ijk}\ \delta_{\omega_j} \delta_{\omega_k} + \sum_j \varphi_{ij}\ \delta_{\omega_j} + \varphi_i \quad , \text{for } m = 3 \quad [10]$$

These local fields will determine the functionality as well as the flexibility of the last states. As a result, the last interpretation will decide whether the result is overfitted. The updating rule remains as Equation 11.

$$\delta_{\omega_i}(t+1) = sgn[h_i(t)] \quad [11]$$

The neuron connection is symmetric and zeroes diagonal. Such cases are as given in Equation 12:

$$\varphi_{ii}^{(2)} = \varphi_{jj}^{(2)} = \varphi_{kk}^{(2)} = \varphi_{iii}^{(3)} = \varphi_{jjj}^{(3)} = \varphi_{kkk}^{(3)} = 0 \quad [12]$$

The structure of the generalised Lyapunov final energy of each variation of HNN-3SAT is in Equation 13:

$$E = -\frac{1}{3}\sum_i \sum_j \sum_k \varphi_{ijk}\ \delta_{\omega_i} \delta_{\omega_j} \delta_{\omega_k} - \frac{1}{2}\sum_i \sum_j \varphi_{ij}\ \delta_{\omega_i} \delta_{\omega_j} - \sum_i \varphi_i\, \delta_{\omega_i} \quad [13]$$

The Lyapunov energy function is always minimised when HNN is used. The HNN energy landscape comprises a high-level-dimensional formation with hills and valleys (Lee & Gyvez, 1996).

Fuzzy Logic

The fuzzy logic development is built on fuzzy set theory, the development of classical set theory. A fuzzy clause is when each variable is true to a certain degree, which can be any real integer between zero and one. Fuzzy logic is a multivalued logic that allows for intermediate numbers within typical classification evaluations like correct or incorrect, yes or no, high or low, and so on (Badawi et al., 2022). As a result, when dealing with inconsistency and vagueness, fuzzy logic allows us to be more adaptable in our argument (Halaby & Abdalla, 2016). The truth numbers in Boolean can only be the binary numbers of zero or one, $x \in \{0,1\}$ (Novák et al., 1999). Meanwhile, fuzzy logic offers truth numbers between zero and $\mu \in (0,1)$.

A fuzzy set A is a function on universe X that matches into the range [0,1] and is probably bound to fit into a group such $\mu_A: X \to [0,1]$. As seen in Equation 14, the membership function of A is symbolised by the symbol μ_A:

$$A = \{(x, \mu_A(x)) | x \in X\} \quad [14]$$

in which $0 \leq \mu_A(x) \leq 1$. The notation can be used for discrete universe X, as stated in Equation 15, to illustrate the set (Zadeh, 1973).

$$A = \frac{\mu_A(x_1)}{x_1} + \frac{\mu_A(x_2)}{x_2} + \cdots + \frac{\mu_A(x_n)}{x_n} = \sum_{x \in X} \frac{\mu_A(x)}{x} \quad [15]$$

where $\sum$ implies union across all $x \in X$. The degree of membership of x in A is known as the value of $\mu_A(x)$.

Traditional formal logic has been effectively applied for computations problems such as in Horn clause form (Sathasivam & Abdullah, 2008) and has shown to be a powerful reasoning technique. While this type of logic is solid, it is also restricted and lacks expression. It is especially true when there is much ambiguity. Fuzzy logic provides an intriguing result to this dilemma because it allows for manipulating propositions containing ambiguity (Zadeh, 1974, 1979). Therefore, its clause needs the equivalent common structure as a standard clause, excluding its vagueness (Rhodes & Menani, 1992). Because of the complexity of many computation problems and the difficulty of coping with uncertainty, researchers have turned to fuzzy logic theory to solve optimisation problems (Nasir et al., 2021). Furthermore, the distinctive and valuable characteristics of fuzzy logic and the Hopfield network have caused each of these ways to reinforce itself by leveraging the strengths of both methods.

In fuzzy logic, connectives from classical logic are often linked to operators like conjunction, disjunction, implication, and negation (Brys et al., 2012). Table 1 shows the operands of fuzzy logic.

Table 1
Operators in fuzzy logic

Operators	Formula
Negation, NOT (¬)	$F_{\neg}(\omega_i) = 1 - \mu_{\omega_i}$
Disjunction, OR (∨)	$F_{\vee}(\omega_i, \omega_j) = max\{\omega_i, \omega_j\}$
Conjunction, AND (∧)	$F_{\wedge}(\omega_i, \omega_j) = min\{\omega_i, \omega_j\}$
Implication	$F_{\rightarrow}(\omega_i, \omega_j) = min\{1,1 - \omega_i, \omega_j\}$

A fuzzy logic system's basic design consists of a fuzzifier, rule evaluator, and defuzzifier. In the fuzzifier step, it converts crisp inputs into fuzzy sets. For OR and AND, fuzzy set operations assess Max and Min rules, respectively. The defuzzifier is a mapping stage in a fuzzy system that converts a fuzzy set into a crisp output. In the defuzzification process, the crisp production is generated using the alpha-cut form of a fuzzy collection. Because the alpha-cut method may extract the crisp value of a fuzzy set (Bodjanova, 2002), the theory of alpha-cut is crucial in combining fuzzy sets and crisp sets. Figure 1 shows the fundamental model of a fuzzy logic structure.

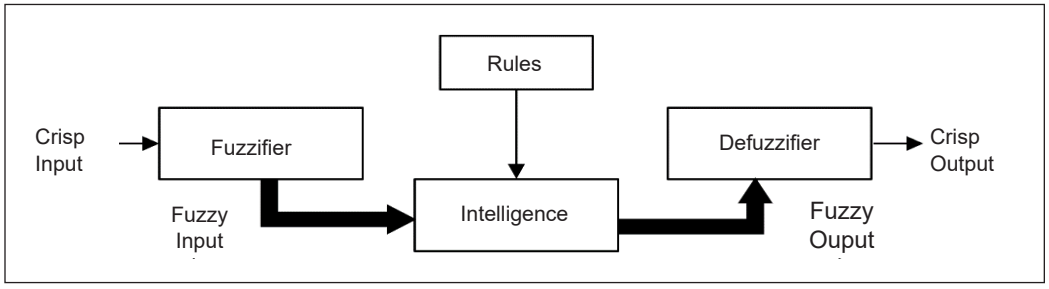

Figure 1. Fuzzy logic structure's fundamental design

3-Satisfiability Fuzzy Logic Hopfield Neural Network Using Abdullah (1992) Method

To assess synaptic weight methodically, we use a solid training strategy. According to Abdullah (1992), logic programming may be integrated into a neural network. When Abdullah's technique seeks the optimum solutions for the logic program's clauses, the subsequent results may shift as new clauses are introduced. As a result, we train the 3SAT using the Abdullah approach. The method was the first in formal synaptic weight derivation of superficial logical contradictions (Abdullah, 1992). Following that, Abdullah (1993) introduced a logic programming paradigm for Horn clauses in a neural network. Sathasivam (2010) expanded the work by introducing neural symbolic integration in HNN. Velavan et al. (2015) published the result on logic programming, which focused on logic programming for higher-order clauses using mean-field theory.

It is an excellent way to train the HNN, especially when accumulating synaptic weight. A set of systematic approaches are used in the training phase of 3SAT logic programming. The selection logic formula is critical for providing the neural network with good instructions. Synaptic weight will be computed using Abdullah (1992). A comprehensive learning approach calculates the corresponding synaptic weight using Boolean logical inconsistencies. The fuzzification and defuzzification algorithms will be connected with the network in the 3SAT programming to link a neuron's membership function to its identity. The 3SAT problem will be treated as an optimisation problem that HNN will solve. The clauses have a cost function that removes logical inconsistencies.

With the third-degree network, we created an HNN-3SAT method using the Abdullah approach during the training phase. The proposed method included a fuzzy logic technique to the network to improve the algorithm and name it HNN-3SATFuzzy. An HNN-3SATFuzzy algorithm is an integrated framework created using the fuzzification and defuzzification procedures until it achieves its final state. The last condition's stability was analysed to achieve a global minimum solution.

Fuzzification. The fuzzification technique connects a neuron's identity to its membership function. The function μ_{ω_X} defines a fuzzy set by pairing each component of the universe of discourse by its membership degree (Equation 16):

$$\mu_{\omega_i}(i): I \rightarrow [0,1] \quad [16]$$

where $\mu_{\omega_i} = 0$ signifies that a part *i* does not belong to a fuzzy set, and $\mu_{\omega_i} = 1$ denotes that *i* is a component of a fuzzy set (Zadeh, 1974).

Fuzzy Rules. Union, intersection, and complement are all characterised and linked to membership functions for fuzzy sets. Allow the membership function of μ_{ω_i} where $i = 1,2 \ldots$ n for $n = 9$ to express the fuzzy logical sets.

The membership function in Equation 17 is an example of one definition of the fuzzy union.

$$\mu_{\omega_1 \cup \omega_2}(x) = max\left[\mu_{\omega_1}(x), \mu_{\omega_1}(x)\right] \quad [17]$$

Equation 18 implies the membership function of one definition of fuzzy intersection.

$$\mu_{\omega_1 \cap \omega_2}(x) = min\left[\mu_{\omega_1}(x), \mu_{\omega_1}(x)\right] \quad [18]$$

Moreover, the membership function in Equation 19 implies a fuzzy complement.

$$\mu_{\overline{\omega_1}}(x) = 1 - \mu_{\omega_1} \quad [19]$$

We can assess rules using fuzzy logic properties by transforming the 3SAT problem in Equation 5 into a fuzzy logic structure. Then, consider Equation 21 as the negation of Equation 20. The formulas are as follows:

$$\theta_{3SAT} = min\left[max\left(\mu_{\omega_1}, 1-\mu_{\omega_2}, 1-\mu_{\omega_3}\right), max\left(\mu_{\omega_4}, \mu_{\omega_5}, 1-\mu_{\omega_6}\right), max\left(\mu_{\omega_7}, \mu_{\omega_8}, \mu_{\omega_9}\right)\right] \quad [20]$$

$$\neg\theta_{3SAT} = max\left[min\left(1-\mu_{\omega_1}, \mu_{\omega_2}, \mu_{\omega_3}\right), min\left(1-\mu_{\omega_4}, 1-\mu_{\omega_5}, \mu_{\omega_6}\right), min\left(1-\mu_{\omega_7}, 1-\mu_{\omega_8}, 1-\mu_{\omega_9}\right)\right] \quad [21]$$

If the program allocates value $\mu_{\omega_i} \geq \alpha$ to be accurate and $\mu_{\omega_i} < \alpha$ to be false, then $\neg\theta_{3SAT} < \alpha$ indicates a consistent interpretation and $\neg\theta_{3SAT} > \alpha$ implies the clauses in the structure are not fulfilled.

Defuzzification. Aside from that, the HNN-3SATFuzzy algorithm will use the alpha-cut approach in the defuzzification phase to adjust the unsatisfied neuron clauses until the proper neuron state is determined. The defuzzifier is a mapping stage that converts a fuzzy value into a crisp output. It is referred to as a stable state when the state acquired is constant across both algorithms. The alpha-cut defuzzification technique, which is used to make the estimation, is stated in Equations 22 and 23:

$$\text{if } \mu_{\omega_i} \geq \alpha, then\ \delta_{\omega_{i\alpha}} = 1 \quad [22]$$

$$\text{if } \mu_{\omega_i} < \alpha, then\ \delta_{\omega_{i\alpha}} = 0 \quad [23]$$

Alpha-Cut. A subset of the universe with membership grades, μ which are greater than or equal to alpha, α for any $\alpha \in [0,1]$ is called an alpha-cut (Wang, 1996). The idea of alpha-cut is critical in connecting fuzzy and crisp sets. Sharpening produces a clean set, which is dependent on the alpha value. During defuzzification, neuron clauses will be adjusted using the alpha-cut method until the right neuron state is obtained (Pourabdollah et al., 2020). Equation 24 is the modified alpha-cut defuzzification:

$$\text{alpha-cut} = \frac{\sum_i \alpha_i \overline{[\mu_{\omega_i}]}}{\sum_i \alpha_i} \qquad i = 1, \ldots L \quad [24]$$

where $[\mu_{\omega_i}]$ represents the average of the membership value of neurons, and L is the number of discretisation stages along the vertical axis.

The learning algorithm of the hybridised intelligent dynamic model of 3SAT using fuzzy logic in HNN is shown in Figure 2. The initial stage is constructing a 3SAT logic programming that must demonstrate inconsistency to prove a certain objective. After that,

the process continues to convert the logic structure into a Boolean algebraic structure and negation. The advanced model includes the fuzzification method, which links a neuron's identity to its membership function. We can evaluate rules using fuzzy logic attributes by changing the Boolean model into a fuzzy structure. Next, we employ the alpha-cut defuzzification technique. The principle of alpha-cut is critical in the connection between fuzzy and crisp sets. The cost function is then required to determine the synaptic weights. The estimates of synaptic weights are then obtained by analysing the cost function in conjunction with the energy function. Finally, let the neural networks evolve until they reach a minimum energy state.

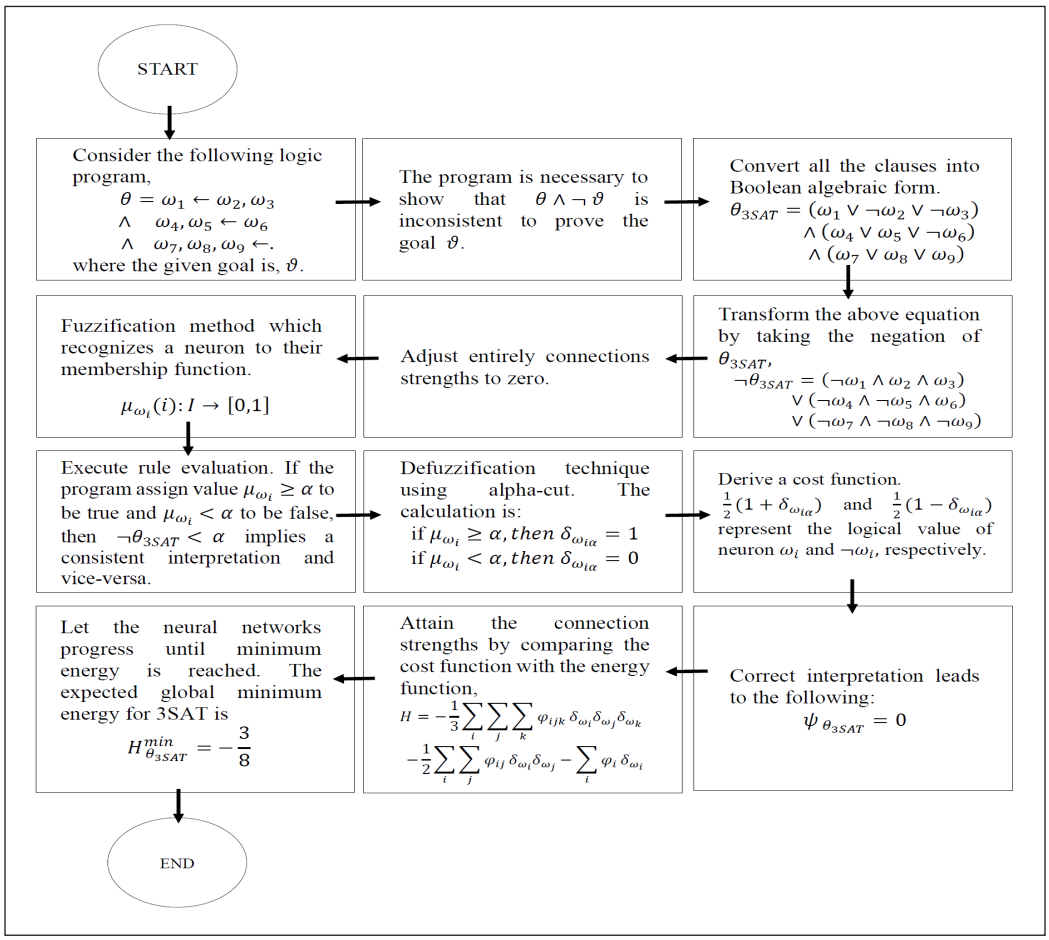

Figure 2. Algorithm in the learning phase for HNN-3SATFuzzy

Implementation and Experimental Setup

The discussion will cover the HNN-3SATFuzzy experimental simulation and algorithm descriptions (Table 2).

Table 2
Listing of related factors utilised in HNN-3SATFuzzy

Parameter	Value
Number of neurons	$9 \leq NN \leq 135$
Total of combinations	100
Tolerance measurement	0.001
CPU time threshold	24H
Activation function	HTAF
The initialisation of fuzzy membership neuron	$\mu_{\omega i} \epsilon [0,1]$
Finalised neuron states	$\delta_{\omega i} \epsilon [-1,1]$

The performance of the fuzzy logic techniques in training HNN to execute 3SAT is carried out using Matlab 2020b software in this experimental simulation. HNN-3SAT models integrated with fuzzy logic algorithm (HNN-3SATFuzzy) are the hybrid HNN models investigated in this work. The HNN models in this study used simulated datasets to generate 3SAT clauses with varying difficulty levels. The simulations of this experiment are carried out with varying numbers of neurons (NN) ranging from 9 to 135. The CPU time cutoff for generating data will be 24 hours (Kho et al., 2020), and if the CPU time exceeds 24 hours, the experiment will be aborted. Aside from that, we employed HTAF in this work because HTAF is regarded as an example of good quality activation functions to be developed in HNN based on its stability. Furthermore, the suggested network operates even if no activation function is used. The final energy execution requirements were set to 0.001 since this reduced statistical errors better (Sathasivam, 2010). The success of this study will be evaluated by comparing the accuracy and efficiency of two models: HNN-3SAT and HNN-3SATFuzzy.

The experiment is divided into three phases to validate the success of the suggested approach: training phase, retrieval phase, and energy analysis. As noted below, each subsection represents a distinct purpose. The list of the three subsections and their metrics may be found in Table 3.

Table 3
List of the phases and metrics used in all performance evaluation measures

Phases	Description	Metrics
Learning phase	to achieve ideal weight management through well-structured training programming.	$RMSE_{Learn}$ MAE_{Learn} SSE_{Learn} $MAPE_{Learn}$
Retrieval phase	to assess the quality of the HNN-3SATFuzzy generated solution	$RMSE_{Retrieve}$ $MAE_{Retrieve}$ $SSE_{Retrieve}$ $MAPE_{Retrieve}$
Energy analysis	to investigate the energy difference obtained by HNN-3SATFuzzy	N_{Local} N_{Global}

Figure 3 shows the summary flowchart of the successful integration of HNN-3SAT with fuzzy logic. Figure 3 shows how the HNN-3SATFuzzy is distributed into the learning and retrieval phases, with the fuzzy logic being implemented in the learning phase. The goal of the proposed network is to achieve the final global states of HNN-3SAT.

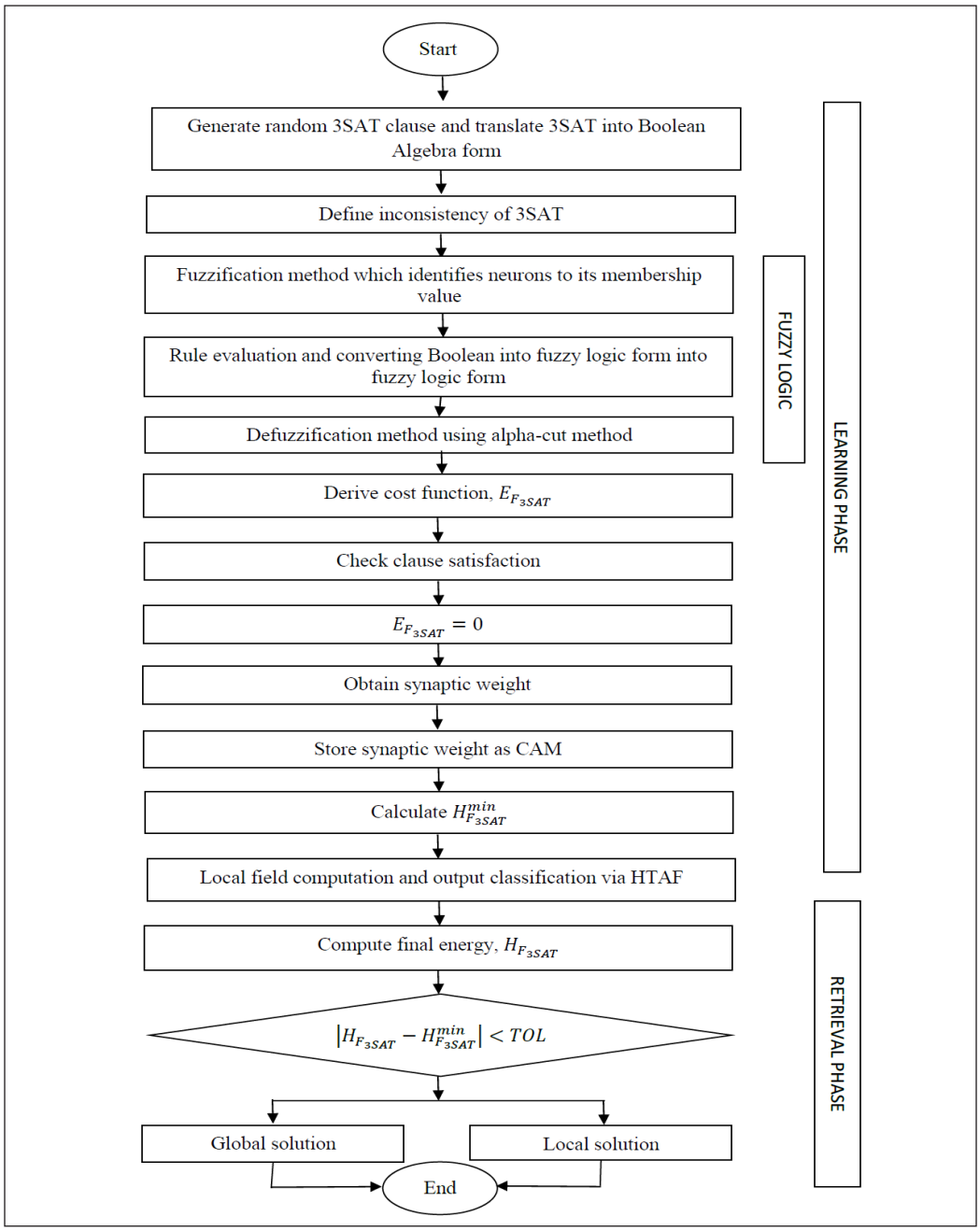

Figure 3. Flowchart of HNN-3SATFuzzy

Performance Evaluation Metrics for HNN-3SATFuzzy

Two measurement methods will be used to assess the competence of HNN-3SATFuzzy models, such as error analysis and energy analysis. The explanations for each metric will be discussed further down in greater detail.

Root Mean Square Error (RMSE). RMSE reports the actual divergence of the anticipated amounts and the computed value (Equation 25) (Willmott & Matsuura, 2005)

$$RMSE = \sum_{i=1}^{n} \sqrt{\frac{1}{n}\left(I_{highest} - I_x\right)^2} \quad [25]$$

where I_x is the network's computed value, $I_{highest}$ is the network's highest value, and n is the total number of iterations.

Mean Absolute Error (MAE). By computing the disparity of the average gap between the calculated values and the expected values, MAE proves to be a good metric for analysing the model (Equation 26) (Alzaeemi & Sathasivam, 2021).

$$MAE = \sum_{i=1}^{n} \frac{1}{n}\left|I_{highest} - I_x\right| \quad [26]$$

where I_x stands for the generated values, n for the number of iterations, and $I_{highest}$ for the most significant values by the network, which describes the number of clauses in the kSAT.

Sum Squared Error (SSE). SSE is a statistical technique for calculating how much the data deviates from expected values (Equation 27) (Bilal et al., 2012)

$$SSE = \sum_{i=1}^{n} \left(I_{highest} - I_x\right)^2 \quad [27]$$

where I_x denotes the computed values, and $I_{highest}$ is the largest number, which relates to the value of the kSAT logic clauses.

Mean Absolute Percentage Error (MAPE). MAPE is a modified form of the MAE in which the results are normalised to a percentage (De Myttenaere et al., 2016). MAPE's formulation is given as Equation 28:

$$MAPE = \sum_{i=1}^{n} \frac{100}{n} \frac{\left|I_{highest} - I_x\right|}{\left|I_x\right|} \quad [28]$$

where I_x is the network's computed value, $I_{highest}$ is the network's highest value, and n is the total number of iterations.

Global Minima Ratio (Zm). In prior research, global minima are employed to thoroughly investigate energy analysis (Alzaeemi et al., 2021; Mansor & Sathasivam, 2021). The energy process is also an indicator of the program's efficacy (Equation 29).

$$Global\ Minima = \frac{1}{NT.COMBMAX}\sum_{i=1}^{n} N \quad [29]$$

where NT is the total of testing, $COMBMAX$ is the combination of neurons, N is the number of global minima of the network. A network is believed to be strong if the amount of global minima is close to one.

CPU (Central Processing Unit) Time. Processing time generally refers to the total time to finish a simulation. The processing time is used to determine the robustness and stability. This investigation will employ the second SI unit for processing time. When the model's CPU period is reduced, the simulation's productivity is believed to be improved. Equation 30 shows the CPU time calculation:

Processing time = Training phase time + Retrieval phase time [30]

RESULTS AND DISCUSSION

Figures 4 to 9 show the performance of HNN-3SAT and HNN-3SATFuzzy in terms of RMSE, MAE, SSE, MAPE, global minima and CPU time, respectively.

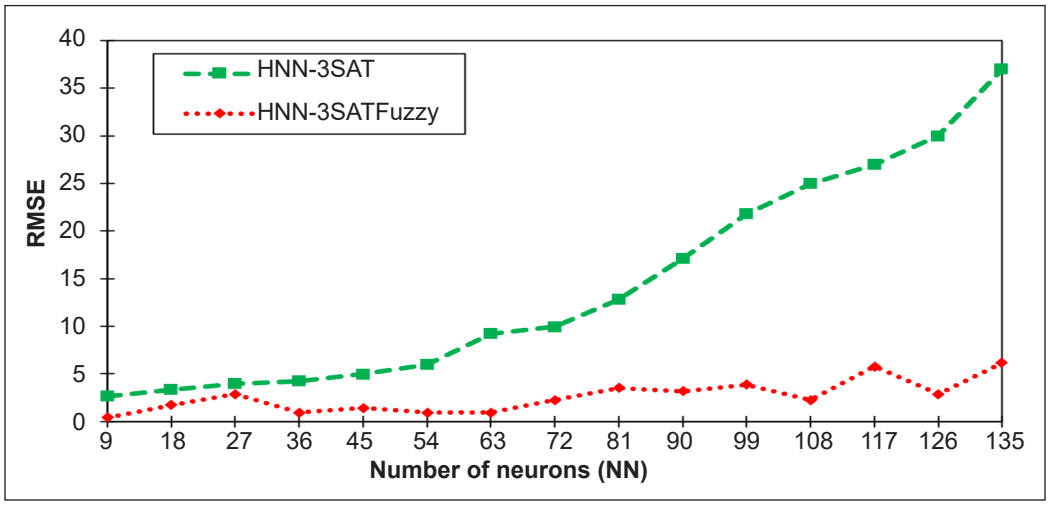

Figure 4. Root Mean Square Error (RMSE)

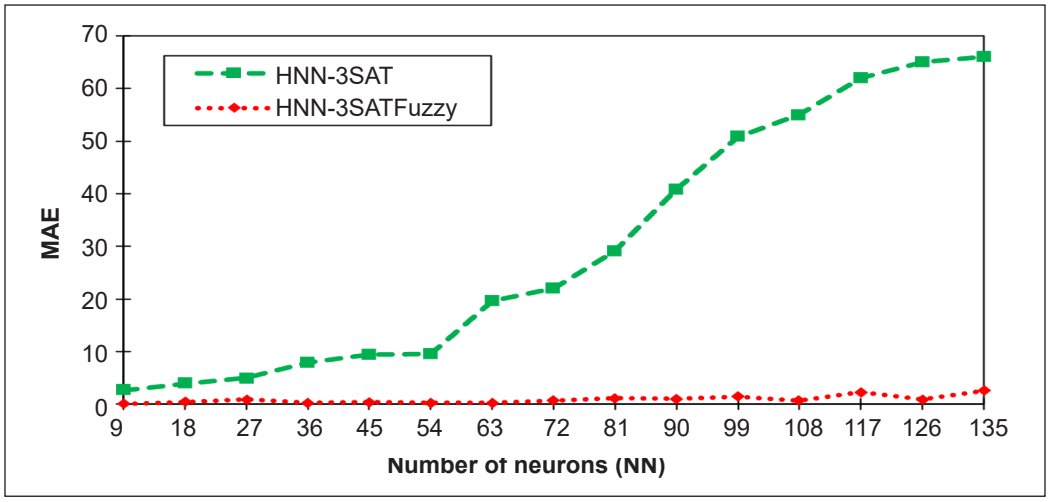

Figure 5. Mean Absolute Error (MAE)

The output of RMSE and MAE in the training stage for HNN-3SAT and HNN-3SATFuzzy are shown in Figures 4 and 5, respectively. During the training phase, HNN-3SATFuzzy beat its equivalent, HNN-3SAT, as per RMSE and MAE indicators. The results show that the RMSE and MAE values for HNN-3SATFuzzy are lower than the HNN-3SAT network, even as the total of neurons (NN) increases. As a result, the HNN-3SATFuzzy solutions diverged less from the potential solutions. At the start of the simulations, the outcomes for both networks appeared to have close results during $9 \leq NN \leq 45$. The performance for RMSE and MAE in HNN-3SAT seemed to rise once it reached $NN = 54$ slowly, and subsequently, the results rose significantly to about 600% and 2000%, respectively, towards the end of the simulations. The suggested technique, HNN-3SATFuzzy, achieves $\psi_{\theta_{3SAT}} = 0$ at lower results than HNN-3SAT, based on RMSE and MAE calculation. The fundamental reason is that 3SAT's fuzzy logic technique partitions solution is better, allowing $\psi_{\theta_{3SAT}} = 0$ to be obtained in fewer rounds. The fuzzy logic algorithm's increased likelihood of exploring for accurate interpretations during training is owing to it. Similarly, the HNN-3SATFuzzy used a systematic strategy using the fuzzification and defuzzification methods throughout the searching neuron stage. Furthermore, HNN-3SATFuzzy could check the correct interpretation efficiently and handle additional limitations compared to the other network.

Figures 6 and 7 show that HNN-3SATFuzzy has a lower SSE and MAPE value than HNN-3SAT. HNN-3SATFuzzy has a more robust capability to train the simulated data set than HNN-3SAT since it has a lower SSE value. It was clear that HNN-3SATFuzzy was found to have good quality results with a lower SSE value for all hidden neuron counts. Although at the beginning of the simulations, when $9 \leq NN \leq 45$ of SSE for both networks seemed to obtain almost similar results, the results for HNN-3SAT dramatically increased

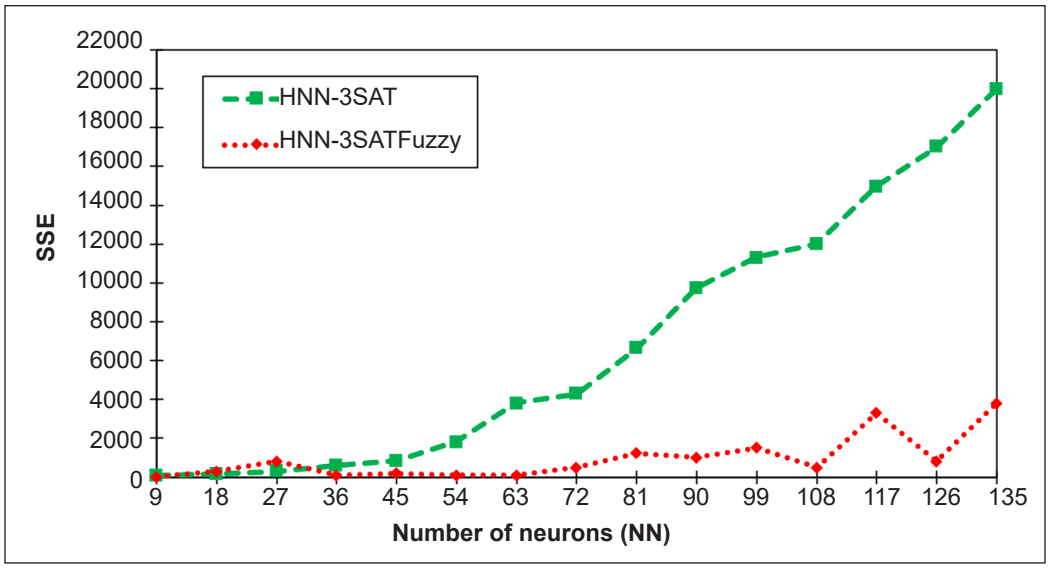

Figure 6. Sum Squared Error (SSE)

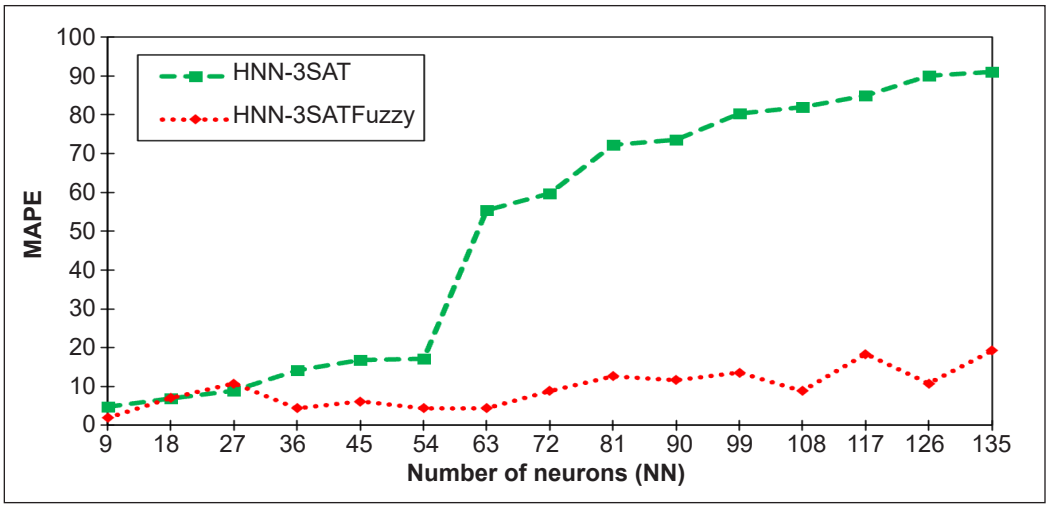

Figure 7. Mean Absolute Percentage Error (MAPE)

when it reached $NN = 54$ till the last simulations. The results of HNN-3SAT increased by about 500% compared to HNN-3SATFuzzy at the final NN, which makes it a poor network. Compared to HNN-3SAT and HNN-3SATFuzzy, a comparable output was obtained for the MAPE values. The MAPE value also has offered strong evidence of fuzzy logic's ability to work well with HNN-3SATFuzzy. The outcomes for HNN-3SAT significantly rose after it hit $NN = 54$. At $NN = 135$, the outcomes of HNN-3SAT converged by roughly 400% compared to HNN-3SATFuzzy. In conclusion, compared to the two results, the HNN-

3SATFuzzy method performs substantially better. It is owing to the efficient operators in the training phase, such as the fuzzification and defuzzification features of fuzzy logic, which increased the compatibility of the solutions. HNN-3SATFuzzy can recover a more accurate end state than HNN-3SAT.

For varied numbers of neurons, Figure 8 illustrates the global minima ratio recorded by HNN-3SAT and HNN-3SATFuzzy. Sathasivam (2006) discovered a link between the global minima value and the type of energy gained at the last part of the program. Given that the suggested hybrid network's global minima ratio is reaching value one, the results in the system have tentatively achieved minimum global energy except for HNN-3SAT. Compared to HNN- 3SATFuzzy have the potential to provide more exact and correct states. It is because the fuzzy logic algorithm's searching technique is very efficient. The HNN-3SATFuzzy solution has achieved the best minimum global energy of value 1. It is due to HNN's use of the fuzzy logic approach in conjunction with the 3SAT network. The proposed method can accept additional neurons since fuzzy logic reduces computing load by fuzzifying and defuzzifying the state of the neurons to find the appropriate states. Aside from that, during the defuzzification process, unsatisfied neuron clauses will be refined using the alpha-cut method until the correct neuron state is identified. Compared to the other network, this property effectively causes fuzzification and defuzzification techniques to converge to global minima. The network in HNN-3SAT becomes stuck in a suboptimal state when the number of neurons increases. The fuzzy logic algorithm has been shown to reduce the network's complexity, and in comparison to HNN-3SAT, the global minimum solutions of the HNN-3SATFuzzy converged to optimal solutions with beneficial results.

The calculation time is a critical metric or indicator for evaluating the effectiveness of our suggested algorithm. The efficacy of the entire calculation process can be used to

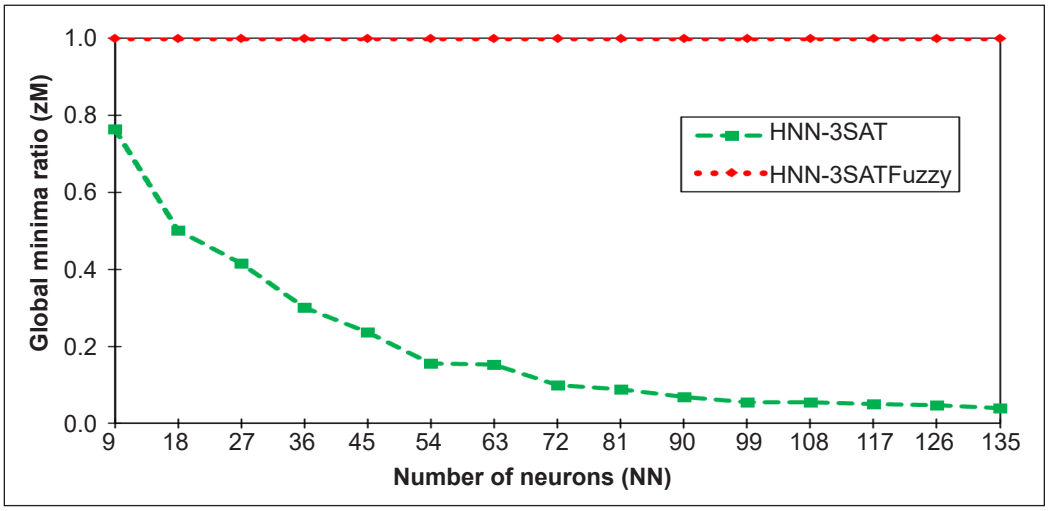

Figure 8. Global Minima Ratio (zM)

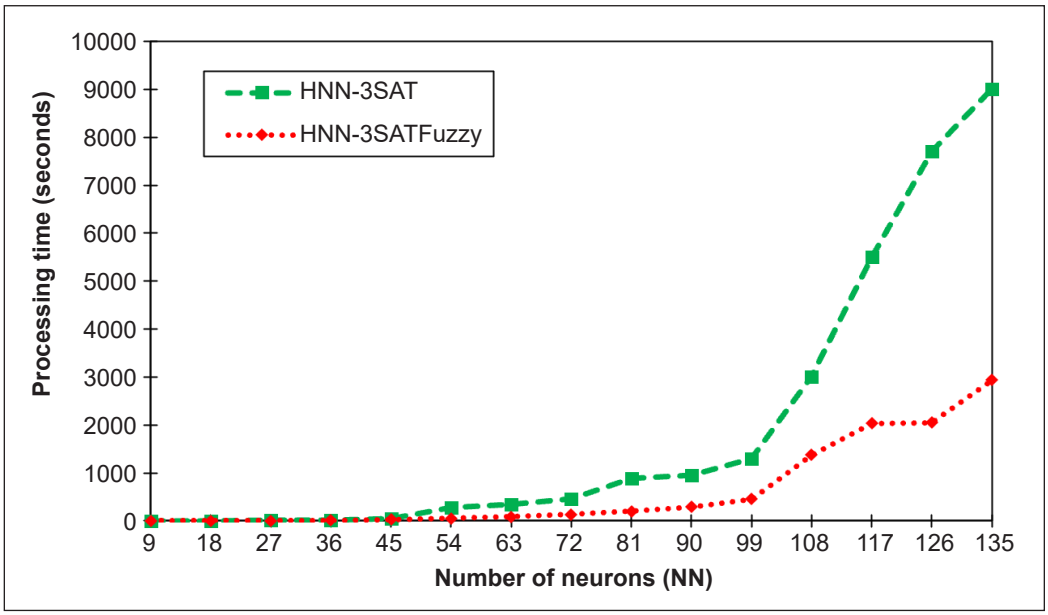

Figure 9. Processing time

indicate our techniques' robustness roughly. The computing time sometimes called the CPU period, can be described as the point it took our system to finish the entire calculation procedure in the investigation (Kubat, 1999). The computation method uses our suggested framework to train and generate the most satisfying phrases. The computing time for the HNN-3SAT and HNN-3SATFuzzy is displayed in Figure 9. As the number of neurons rose, the possibility of the identical neuron being implicated in an additional phrase increased (Sathasivam & Abdullah, 2008). As the network grew more extensive and complex, it was more likely to become stuck in local minima and consume more processing time. For all hybrid networks, the CPU moment rises as the number of neurons increases. Since the logical contradictions have been resolved, the HNN's rigorous search process will examine the appropriate option. As a result, a system that accelerates the training process is required. Furthermore, Figure 9 clearly shows that HNN-3SATFuzzy surpasses its contemporary HNN-3SAT. Even though the time spent by all networks for fewer clauses is not much different, the HNN-3SATFuzzy improved faster than the other network as the number of clauses for each amount of neurons rose. Due to the efficiency of the fuzzification and defuzzification methods, the CPU time was faster when the fuzzy logic technique was used. HNN-3SATFuzzy is slightly quicker than the HNN-3SAT network due to the potential to improve interpretations using fuzzy logic. The computation time was lowered when fuzzy logic was applied because the state of the fuzziness neurons was provided before starting the defuzzification process, which methodically turned the dissatisfied clause into a satisfied clause.

CONCLUSION

The findings proved that HNN-3SATFuzzy is a unique approach to increasing the efficiency of logic programming that integrates fuzzy logic and 3SAT in the Hopfield network. Fuzzification and defuzzification techniques with the alpha-cut approach were applied to improve the strategies of avoiding local minimum solutions and reducing the computer handling load of constructing the best results. When employing the HNN-3SATFuzzy to compute stability, the strength of this technique outperformed HNN-3SAT in terms of the error analysis, as stated in this publication. Furthermore, the suggested paradigm provides a global minima ratio of roughly one. The CPU time of the hybrid method is more rapidly compared to HNN-3SAT. As a result, the HNN-3SATFuzzy has proven to be more potent than the HNN-3SAT in 3SAT logic programming elements, such as better global minima ratio, constant lower error analysis values, and faster CPU time. The discoveries are crucial because the hybrid model considerably impacts Hopfield networks' capacity to solve difficulties with less complexity rapidly. The new knowledge and ideas will aid in developing creative approaches for extracting information in logic programming. Furthermore, dynamic learning advancement is considered a significant breakthrough in the neuro-symbolic field. The results of the suggested model have shown that the network is stable, making it clear that it is a long-lasting hybrid network. In the future, HNN-3SATFuzzy can be further improved to solve satisfiability problems by integrating with a metaheuristic algorithm.

ACKNOWLEDGEMENT

This research was supported by the Ministry of Higher Education Malaysia (MOHE) through the Fundamental Research Grant Scheme (FRGS), FRGS/1/2022/STG06/USM/02/11 and Universiti Sains Malaysia.

REFERENCES

Abdullah, W. A. T. W. (1992). Logic programming on a neural network. *International Journal of Intelligent Systems*, *7*(6), 513-519. https://doi.org/10.1002/int.4550070604

Abdullah, W. A. T. W. (1993). The logic of neural networks. *Physics Letters A*, *176*(3-4), 202-206. https://doi.org/10.1016/0375-9601(93)91035-4

Alzaeemi, S. A., & Sathasivam, S. (2021). Examining the forecasting movement of palm oil price using RBFNN-2SATRA metaheuristic algorithms for logic mining. *IEEE Access*, *9*, 22542-22557. https://doi.org/10.1109/ACCESS.2021.3054816

Alzaeemi, S. A., Sathasivam, S., & Velavan, M. (2021). Agent-based modeling in doing logic programming in fuzzy hopfield neural network. *International Journal of Modern Education and Computer Science*, *13*(2), 23-32. https://doi.org/10.5815/IJMECS.2021.02.03

Badawi, M. B., Awad, T. H., & Fahham, I. M. E. (2022). Application of artificial intelligence for the prediction of plain journal bearings performance. *Alexandria Engineering Journal*, *61*(11), 9011-9029. https://doi.org/10.1016/j.aej.2022.02.041

Bilal, M., Masud, S., & Athar, S. (2012). FPGA design for statistics-inspired approximate sum-of-squared-error computation in multimedia applications. *IEEE Transactions on Circuits and Systems II: Express Briefs*, *59*(8), 506-510. https://doi.org/10.1109/TCSII.2012.2204841

Bodjanova, S. (2002). A generalized α-cut. *Fuzzy Sets and Systems*, *126*(2), 157-176. https://doi.org/10.1016/S0165-0114(01)00062-8

Brys, T., Hauwere, Y. M. D., Cock, M. D., & Nowé, A. (2012, August 6-8). *Solving satisfiability in fuzzy logics with evolution strategies*. [Paper presentation]. 2012 Annual Meeting of the North American Fuzzy Information Processing Society (NAFIPS), Berkeley, California. https://doi.org/10.1109/NAFIPS.2012.6290998

Fung, C. H., Wong, M. S., & Chan, P. W. (2019). Spatio-temporal data fusion for satellite images using hopfield neural network. *Remote Sensing*, *11*(18), Article 2077. https://doi.org/10.3390/rs11182077

Garcez, A. S. A., & Zaverucha, G. (1999). Connectionist inductive learning and logic programming system. *Applied Intelligence*, *11*(1), 59-77. https://doi.org/10.1023/A:1008328630915

Halaby, M. E., & Abdalla, A. (2016, May 9-11). Fuzzy maximum satisfiability. [Paper presentation]. INFOS '16: The 10th International Conference on Informatics and Systems, Giza, Egypt. https://doi.org/10.1145/2908446.2908476

Kubat, M. (1999). Neural networks: A comprehensive foundation by Simon Haykin, Macmillan, 1994, ISBN 0-02-352781-7. *The Knowledge Engineering Review, 13*(4), 409-412. https://doi.org/10.1017/s0269888998214044

Hopfield, J. J., & Tank, D. W. (1985). "Neural" computation of decisions in optimization problems. *Biological Cybernetics*, *52*(3), 141-152. https://doi.org/10.1007/BF00339943

Kho, L. C., Kasihmuddin, M. S. M., Mansor, M. A., & Sathasivam, S. (2020). Logic mining in league of legends. *Pertanika Journal of Science and Technology*, *28*(1), 211-225.

Kowalski, R., & Sergot, M. (1986). A logic-based calculus of events. *New Generation Computing*, *4*(1), 67-95. https://doi.org/10.1007/BF03037383

Lee, C. C., & Gyvez, J. P. (1996). Color image processing in a cellular neural-network environment. *IEEE Transactions on Neural Networks*, *7*(5), 1086-1098. https://doi.org/10.1109/72.536306

Little, W. A. (1974). The existence of persistent states in the brain. *Mathematical Biosciences*, *19*(1-2), 101-120. https://doi.org/10.1016/0025-5564(74)90031-5

Maandag, P. (2012). *Solving 3-SAT* [Bachelor dissertation]. Radboud University Nijmegen, Netherlands. https://www.cs.ru.nl/bachelors-theses/2012/Peter_Maandag___3047121___Solving_3-Sat.pdf

Mansor, M. A., & Sathasivam, S. (2021). Optimal performance evaluation metrics for satisfiability logic representation in discrete hopfield neural network. *International Journal of Mathematics and Computer Science*, *16*(3), 963-976.

Mansor, M. A., Sathasivam, S., & Kasihmuddin, M. S. M. (2018). 3-satisfiability logic programming approach for cardiovascular diseases diagnosis. *AIP Conference Proceedings*, *1974*(1), Article 020022. https://doi.org/10.1063/1.5041553

De Myttenaere, A., Golden, B., Le Grand, B., & Rossi, F. (2016). Mean absolute percentage error for regression models. *Neurocomputing*, *192*, 38-48. https://doi.org/10.1016/j.neucom.2015.12.114

Nasir, M., Sadollah, A., Grzegorzewski, P., Yoon, J. H., & Geem, Z. W. (2021). Harmony search algorithm and fuzzy logic theory: An extensive review from theory to applications. *Mathematics*, *9*(21), 1-46. https://doi.org/10.3390/math9212665

Novák, V., Perfilieva, I., & Močkoř, J. (1999). *Mathematical principles of fuzzy logic*. Springer. https://doi.org/10.1007/978-1-4615-5217-8

Pan, J., Pottimurthy, Y., Wang, D., Hwang, S., Patil, S., & Fan, L. S. (2020). Recurrent neural network based detection of faults caused byparticle attrition in chemical looping systems. *Powder Technology*, *367*, 266-276. https://doi.org/10.1016/j.powtec.2020.03.038

Pourabdollah, A., Mendel, J. M., & John, R. I. (2020). Alpha-cut representation used for defuzzification in rule-based systems. *Fuzzy Sets and Systems*, *399*, 110-132. https://doi.org/10.1016/j.fss.2020.05.008

Rhodes, P. C., & Menani, S. M. (1992). Towards a fuzzy-logic programming system: A 1st-order fuzzy logic. *Knowledge-Based Systems*, *5*(2), 106-116. https://doi.org/10.1016/0950-7051(92)90001-V

Sathasivam, S. (2006). *Logic mining in neural networks*. [Unpublished Doctoral Dissertation] Universiti Malaya, Malaysia.

Sathasivam, S. (2010). Upgrading logic programming in hopfield network. *Sains Malaysiana*, *39*(1), 115-118.

Sathasivam, S., & Abdullah, W. A. T. W. (2008). Logic learning in hopfield networks. *Modern Applied Science*, *2*(3), 57-63. https://doi.org/10.5539/mas.v2n3p57

Sathasivam, S., Mamat, M., Kasihmuddin, M. S. M., & Mansor, M. A. (2020). Metaheuristics approach for maximum k satisfiability in restricted neural symbolic integration. *Pertanika Journal of Science and Technology*, *28*(2), 545-564.

Velavan, M., Yahya, R. Z., Halif, M. N. A., & Sathasivam, S. (2015). Mean field theory in doing logic programming using hopfield network. *Modern Applied Science*, *10*(1), 154-160. https://doi.org/10.5539/mas.v10n1p154

Wang, L. X. (1996). *A course in fuzzy systems and control*. Prentice-Hall Inc.

Willmott, C. J., & Matsuura, K. (2005). Advantages of the mean absolute error (MAE) over the root mean square error (RMSE) in assessing average model performance. *Climate Research*, *30*(1), 79-82. https://doi.org/10.3354/cr030079

Zadeh, L. A. (1973). Outline of a new approach to the analysis of complex systems and decision processes. *IEEE Transactions on Systems, Man and Cybernetics*, *SMC-3*(1), 28-44. https://doi.org/10.1109/TSMC.1973.5408575

Zadeh, L. A. (1974). The concept of a linguistic variable and its application to approximate reasoning. In K. S. Fu & J. T. Tou (Eds.), *Learning Systems and Intelligent Robots* (pp. 1-10). Springer. https://doi.org/10.1007/978-1-4684-2106-4_1

Zadeh, L. A. (1979). A theory of approximation reasoning. In J. E. Hayes, D. Mishie & L. I. Mikulish (Eds.), *Machine Intelligence* (pp. 149-194). Elservier.

Zamri, N. E., Alway, A., Mansor, M. A., Kasihmuddin, M. S. M., & Sathasivam, S. (2020). Modified imperialistic competitive algorithm in hopfield neural network for boolean three satisfiability logic mining. *Pertanika Journal of Science and Technology*, *28*(3), 983-1008.

Pertanika J. Sci. & Technol. 31 (4): 1717 - 1729 (2023)

PERTANIKA JOURNALS

SCIENCE & TECHNOLOGY

Journal homepage: http://www.pertanika.upm.edu.my/

Effect of Transition Metals Addition on the Nickel Oxide Catalyst Toward Reduction Behaviour in Carbon Monoxide Atmosphere

Norliza Dzakaria[1], Azizul Hakim Lahuri[2]*, Fairous Salleh[3], Tengku Shafazila Tengku Saharuddin[4], Alinda Samsuri[5] and Mohd Ambar Yarmo[3]

[1]Advanced Material for Environmental Remediation (AMER) Research Group, Faculty of Applied Science, University Teknologi MARA, Cawangan Negeri Sembilan, 72000 UiTM, Kuala Pilah, Negeri Sembilan, Malaysia

[2]Department of Science and Technology, Universiti Putra Malaysia Bintulu Campus, 97008 UPM, Bintulu, Sarawak, Malaysia

[3]Catalysis Research Group, Department of Chemical Sciences, Faculty of Science and Technology, Universiti Kebangsaan Malaysia, 43600 UKM, Bangi, Selangor, Malaysia

[4]Faculty of Science and Technology, Universiti Sains Islam Malaysia, 71800 USIM, Nilai, Negeri Sembilan, Malaysia

[5]Department of Chemistry, Centre for Defence Foundation Studies, Universiti Pertahanan Nasional Malaysia, 57000 UPNM, Kuala Lumpur, Malaysia

ABSTRACT

The chemical reduction progression behaviour of transition metals (Mo, Zr, W, Ce, and Co) doped on NiO was studied using temperature programmed reduction (TPR) analysis. A wet impregnation method was applied to synthesise the doped NiO series catalysts. The reduction progress of the catalysts was attained by using a reductant gas at the concentration of 40% v/v CO/N_2. X-ray diffraction (XRD) was employed to determine the composition of the reduced phases. Undoped NiO was reduced at 384°C to obtain a cubic phase of NiO. It was observed that Ce/NiO exhibited the lowest reduction temperature of 370°C among all catalysts. This phenomenon might be due to a higher surface area of Ce/NiO compared to undoped NiO, which facilitated a faster reduction reaction. The rest of the doped NiO series catalysts (Co/NiO, Mo/NiO, W/NiO and Zr/NiO) demonstrated a higher reduction temperature compared to undoped NiO. New peaks in the XRD pattern were observed only for the reduced catalysts of Mo/NiO and W/NiO, which were associated with monoclinic MoO_2 and $WO_{2.72}$ phases, respectively. The formation of new compounds or more stable nickel

ARTICLE INFO

Article history:
Received: 16 June 2022
Accepted: 16 August 2022
Published: 24 May 2023

DOI: https://doi.org/10.47836/pjst.31.4.07

E-mail addresses:
norliza864@uitm.edu.my (Norliza Dzakaria)
azizulhakim@upm.edu.my (Azizul Hakim Lahuri)
fairoussalleh@gmail.com (Fairous Salleh)
tengkushafazila@usim.edu.my (Tengku Shafazila Tengku Saharuddin)
alinda@upnm.edu.my (Alinda Samsuri)
ambar_y@gmail.com (Mohd Ambar Yarmo)
* Corresponding author

ISSN: 0128-7680
e-ISSN: 2231-8526

alloys led to a slower reduction reaction than undoped NiO. Therefore, Ce/NiO was the most efficient catalyst in promoting the formation of Ni under the CO atmosphere.

Keywords: Carbon monoxide, metal oxide, nickel oxide, nickel, reduction

INTRODUCTION

The transition-metal oxides (TMOs) fascinate the materials chemists ascribed to the interesting class of inorganic metals (Ahmad et al., 2022). Their magnetic (Farber et al., 2014), electrical (Rebello & Adeyeye, 2016), optical (Pandey et al., 2020), catalytic (Zheng et al., 2013) and mechanical properties (Vazinishavan et al., 2018) are the significant features in various applications. TMOs are compounds of oxygen atoms bound to transition metals, commonly utilised in several electronic applications due to their superior semiconducting properties (Parkinson et al., 2010; Kaiser, 2004). TMOs have important physical properties in which the spinal oxides show comparably good, interesting magnetic and electrical properties (Cho et al., 2017). These features make TMOs very attractive for several novel applications.

Recently, nanostructured materials have been noticed by researchers owing to their unique and fascinating properties. Specifically, metal oxide nanomaterials, such as NiO, have attracted interest and are applied in various technologies and industries. Nickel oxide is a prominent example of TMO. It is also used as a catalyst in CO_2 capture (Hakim, Tahari et al., 2015; Hakim, Isahak et al., 2015; Lahuri et al., 2022) and as antiferromagnetic layers in lightweight structural components in the aerospace, in active optical filters, in cathode materials for alkaline batteries and materials for gas or temperature sensors, such as CO sensor, H sensor, and formaldehyde sensors (Khan et al., 2019). Besides, the performance of the TMOs, namely CeO_2 and Co_3O_4, was also proven in other applications, such as CO_2 capture (Lahuri et al., 2020). Meanwhile, MoOx, ZrOx and WoOx catalytic activities in hydrogen production were also explored (Sun et al., 2020; Fakeeha et al., 2020; Oudejans et al., 2022; Wondimu et al., 2022).

The performance of Ni-based catalysts is significant as metal oxide support (Charisiou, Papageridis et al., 2019; Charisiou, Tzounis et al., 2019; Papageridis et al., 2020). For instance, alkali and alkaline earth metals (Tsiotsias et al., 2020), transition metals (Lv et al., 2020) and rare-earth metals (Siakavelas et al., 2021) have proven their suitability as promoters through modification of physicochemical properties of metal oxide support (Anastasios et al., 2021). The co-deposition of CeO_2 and NiO can improve the corrosion resistance compared to pure Ni (Hasannejad et al., 2012). A comparison from previous work showed that NiO as bimetal catalysts of nickel oxide exhibited a high reduction temperature in the CO atmosphere as the percentage of zirconia and cobalt increased (Dzakaria, Samsuri et al., 2020; Dzakaria, Tahari et al., 2020).

Therefore, this work attempted to study the influence of the reduction behaviour of NiO doped with transition metals such as Ce, Co, Mo, W and Zr. The catalysts were reduced using carbon monoxide to obtain the reduction pattern with their reduction temperature.

MATERIALS AND METHODS

Catalyst Preparation

The NiO (97.0%) and $(NH_4)_2Ce(NO_3)_6$ (99.0%) were purchased from Acros Organics and Merck. $Co(NO_3)_2{\cdot}6H_2O$ (99.0%), $(NH_4)_6Mo_7O_{24}{\cdot}4H_2O$ (99.98%), $(NH_4)_{10}H_2(W_2O_7)_6{\cdot}xH_2O$ (99.99%) and $ZrOCl_2{\cdot}8H_2O$ (98.0%) were purchased from Merck, Sigma-Aldrich, Aldrich Chemistry and Acros Organics respectively. The ethanol was obtained from Systerm®. The wet impregnation method prepared the Ce/NiO, Co/NiO, Mo/NiO, W/NiO, and Zr/NiO catalysts. Three per cent wt./wt. Ce, Co, Mo, W and Zr of the total metal cation were dissolved in 5 mL distilled water and 5 mL ethanol. The NiO powder was added corresponding to the metal cation additives in the above proportion. The mixture was stirred aggressively for 2 hours at room temperature. The mixtures were dried at 120°C overnight and subsequently calcined at 400°C for 4 hours. The catalysts were denoted as Mo/NiO, Zr/NiO, W/NiO, Ce/NiO and Co/NiO.

Characterisation

The TPR analysis was performed by using a Micromeritic Autochem 2920 Chemisorption Analyzer. The 50 mg of catalysts were heated up with non-isothermal reduction until 700°C at 10 °C/min and followed by isothermal reduction at 700°C for 60 minutes with 40% CO in N_2 flow at 20 mL/min (STP) was introduced as reducing gas. The CO consumption was detected by a thermal conductivity detector (TCD) in the instrument. The structures' lattices and phases were identified using the XRD Bruker AXS D8 Advance type. The X-ray radiation source was Cu K_α (40 kV, 40 mA), and the 2θ diffraction was recorded at the angle of 10-80º with the wavelength of $\lambda = 0.154$ nm. The XRD patterns were matched with standard diffraction (JCPDS) to determine the crystalline phase composition.

The N_2 adsorption-desorption isotherms and textural properties were obtained using a static volumetric technique instrument (Gas sorption analyser, Micromeritics ASAP 2020). The Brunauer-Emmett-Teller (BET) surface area was calculated from the isotherms. Approximately 500 mg of catalysts were outgassed at 300°C for 4 hours under vacuum to remove moisture content and humidity gases before measurement. The measurement was conducted in a circulating bath of liquid N_2 of nitrogen (77 K).

RESULTS AND DISCUSSION

Temperature Programmed Reduction

The reduction process of Mo/NiO, Zr/NiO, W/NiO, Ce/NiO, Co/NiO and NiO catalysts in the CO atmosphere was studied by using CO-TPR (Figure 1) under a flow of 40% CO in N_2 (20 mL·min^{-1}) in a non-isotherm (40-700°C, 10°C·min^{-1}). TPR analysis profile was obtained from the reduction process of NiO catalysts added with various transition metals compared with undoped NiO catalysts. The reduction reaction for undoped NiO occurred at the temperature of 384°C. Referring to the study by Sharma et al. (1997), Alizadeh et al. (2007) and Krasuk & Smith (1972), responses to NiO catalyst reduction using C, H_2 and CO as reducing agents occurred through only one step of the reduction reaction, i.e., $NiO \rightarrow Ni^0$.

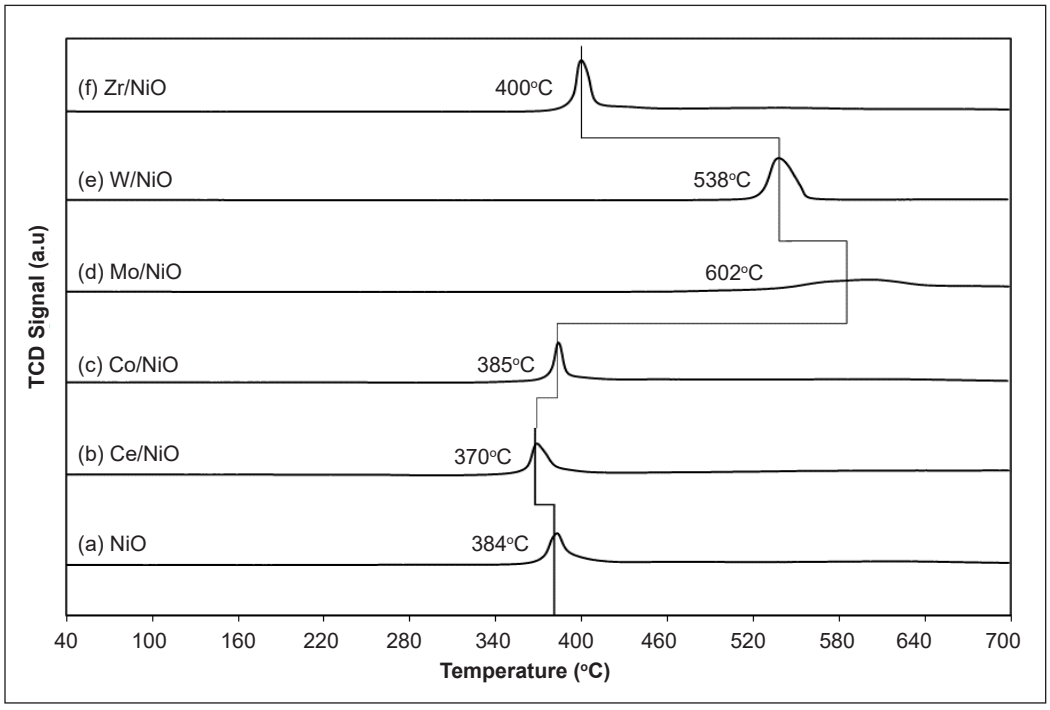

Figure 1. The TPR profile for 3% bt. various other metals upward of NiO is modified under a flow of 40% CO in N_2 (20 mL·min^{-1}) in a non-isotherm (40-700°C, 10°C·min^{-1})

The results of the TPR analysis shown in Figure 1 describe a change in the position of the decreased peak for all 3% of the metal loads to NiO. The 3% wt./wt. metal loading is chosen to screen the effectiveness of transition metal doped NiO and observe whether this percentage is sufficient to reduce temperature/behaviour. Although the 3% metal loads of the transition metal doped NiO was small, it gave a very significant reduction effect. It was found that only Ce/NiO gave the lowest reduction temperature of 370°C compared

to the NiO catalyst of 384°C. It is most likely due to the metal-metal interaction between Ce and NiO because Ce particles are more likely to disperse evenly on the NiO surfaces (Dzakaria et al., 2021), and the increase in surface area on a Ce/NiO catalyst facilitates the reduction reaction to occur quickly. At the same time, other metal loads such as W/NiO, Mo/NiO, Co/NiO and Zr/NiO showed a higher reduction temperature than NiO catalysts. It is due to the formation of new compounds or more stable nickel alloys and, in turn, can further slow down the action counter-decline.

Crystallinity Analysis Using XRD

XRD analysis was performed in the 2θ range between 10° - 80° for NiO and modified catalysts consisting of Mo/NiO, Zr/NiO, W/NiO, Ce/NiO and Co/NiO at 3% loads, respectively (Figures 2). The XRD pattern for NiO indicates a stoichiometric cubic-shaped phase (JCPDS 00-047-1049). The addition of Ce, Co and W at 3% (wt./wt.) showed no significant changes in crystal structure due to the addition of a small amount of Ce, Co and W metals or the Ce, Co and W compounds existed in amorphous form so that they could not be detected using XRD techniques. Moreover, the addition of Ce, Co and W may make these metals completely dispersed on the surface of NiO. Subsequently, adding Mo to NiO indicates a new diffraction pattern of MoO_3 as the orthorhombic phase (JCPDS 01-878-4613). At the same time, the addition of W showed a slight presence of WO_3 as the triclinic phase (JCPDS 00-020-1323) in addition to the major peak of NiO.

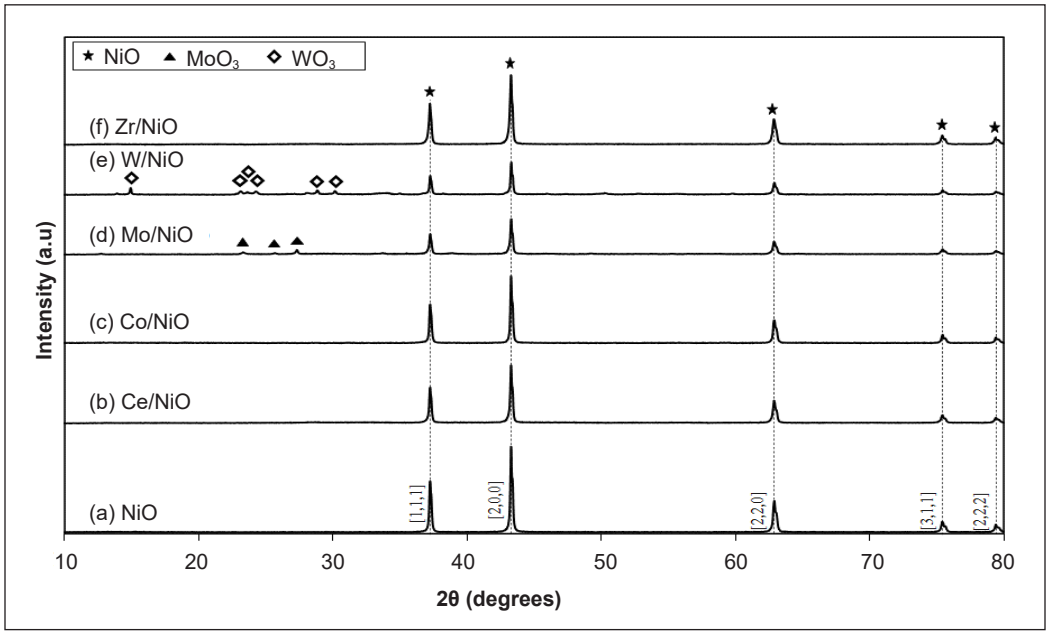

Figure 2. XRD diffractogram of (a) NiO; (b) Ce/NiO; (c) Co/NiO; (d) Mo/NiO; (e) W/NiO/SiO2 and (f) Zr/NiO after calcined at 400ºC for 4 hours

After the reduction reaction, the samples were collected for analysis using the XRD technique to understand the crystallinity properties of the modified NiO catalyst. This XRD analysis was performed on a modified NiO catalyst that underwent a reduction reaction using CO gas as the reduction agent under non-isothermal reduction conditions (40–700°C, 10°C·min^{-1}) under a flow of 40% CO in N_2 (20 mL·min^{-1}). XRD diffractograms were performed in the 2θ range between 10°–80° for NiO catalysts and modified NiO catalysts at 3% wt. The various metals doped NiO after the reduction reaction are shown in Figure 3. The XRD diffraction pattern of the NiO catalyst after the reduction reaction shows a change in which the cubic-shaped NiO (JCPDS 00-047-1049) is completely reduced to cubic-shaped NiO (JCPDS 01-087-9414) with a 2θ value of 44.5°, 51.9°, 76.4° representing the lattice plane (1,1,0), (2,0,0), (2,2,0) and no other compound. When the addition of 3% bt. multi-metal loading was performed on the NiO catalyst, and the XRD diffraction pattern showed only Mo/NiO and W/NiO small peak formation for MoO_2 (JCPDS 01076-1807) and $WO_{2.72}$ (JCPDS 01-084-1516). At the same time, other modified NiO catalysts did not show any formation of new phase peaks other than Ni phase peaks of different intensities. Due to the low content of the metals, peaks from other metals are expected to be scattered on the surface of the NiO catalyst in the form of an amorphous or nano-shaped structure.

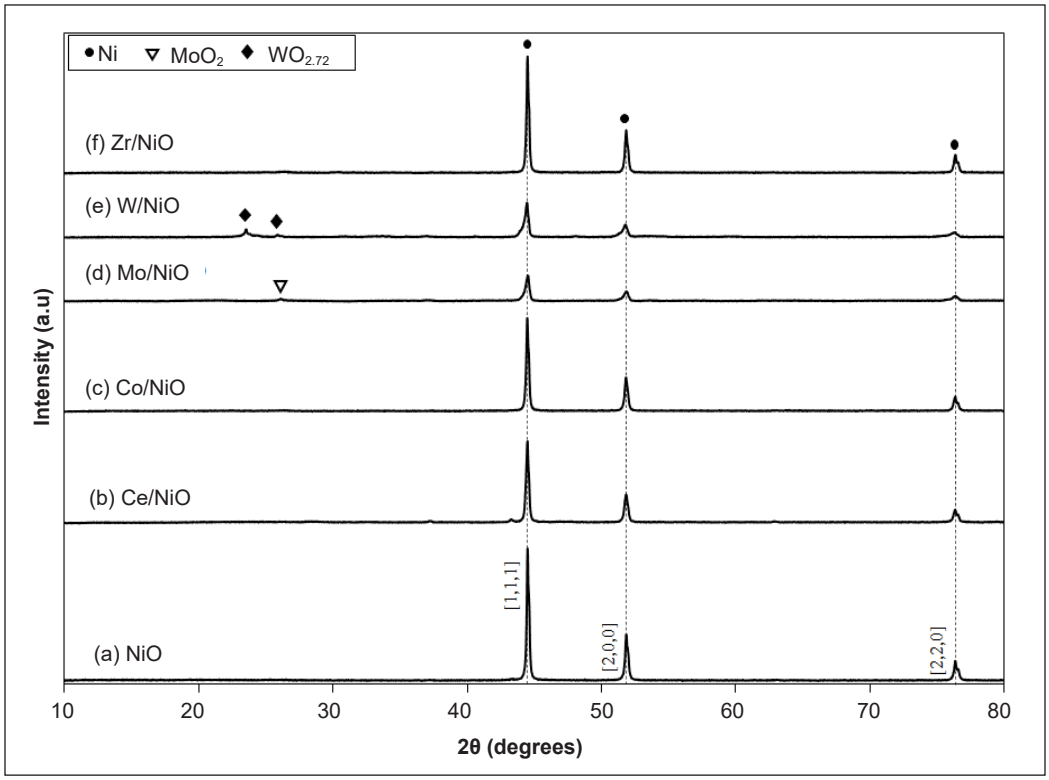

Figure 3. XRD diffractograms (a) NiO; (b) Ce/NiO; (c) Co/NiO; (d) Mo/NiO; (e) W/NiO and (f) Zr/NiO after reduction at 40-700ºC, 10°C·min^{-1}

Physical Surface Analysis

The textural properties of the catalysts were studied through N_2 adsorption-desorption isotherms (Figure 4) and its parameters, such as BET surface area, pore volume and average pore diameter (Table 1). The adsorption isotherms are associated with type III according to IUPAC adsorption isotherms of classification, whereas hysteresis H4 type is characteristic of macroporous materials. The hysteresis, proven based on the isotherms associated with narrow slit pores, is observed (Sing et al., 1985; Othman, 2012).

The parameters of BET surface area, pore volume and average pore diameter for the catalysts are shown in Table 1. The plot of the isotherm of N_2 adsorption for 3% wt. transition metals doped NiO are shown in Figure 4. Based on the IUPAC classification, the shape of the NiO catalyst isothermal curve is a type III mesoporous isotherm with H4 hysteresis. This type III isotherm shows that NiO catalysts have multilayer adsorption properties on non-porous or macroporous materials. Catalysts having this type of isotherm are characterised as adsorption occurs when the interaction between the adsorbed material and the first adsorbent layer is stronger than the interaction of the adsorbed material with the surface of the adsorbent material. Meanwhile, the hysteresis property of H4 has the characteristic of a wide slope between the adsorption and desorption plots that is wide

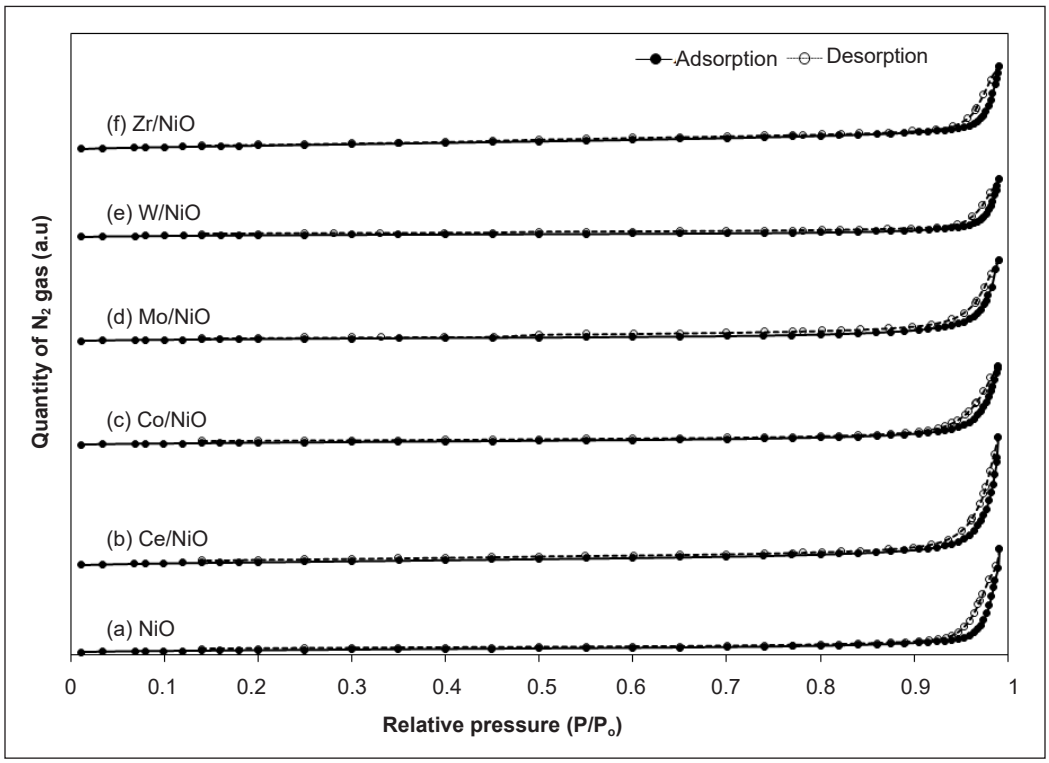

Figure 4. N_2 adsorption-desorption isotherms for (a) NiO, (b) Ce/NiO, (c) Co/NiO, (d) Mo/NiO, (e) W/NiO and (f) Zr/NiO

and covers a large part of the relative pressure area range (P/P_0). The 3% metal loading of various metals shows the same type of isotherm and hysteresis. Apart from this isothermal plot, it was found that all the modified NiO catalyst materials were mesoporous with the addition of 3% metal loading.

Table 1 shows the values of surface area (S_{BET}), pore diameter (D_{pore}) and modified volume (V_{pore}) and NiO catalysts. The results showed significant changes in the surface area, volume and diameter of the pores from the samples studied. It was because each addition of a different metal to the NiO catalyst surfaces had a different particle size, resulting in different textural properties. The surface area of the NiO catalyst was 4.5 m^2/g with pore diameter and volume of 40.6 nm and 0.030 cm^3/g, respectively. The NiO catalysts with such surface area value are considered a material with a very low surface area. NiO samples are highly crystalline due to having a low surface area. In Table 1, Zr/NiO has a higher surface area than other metals doped NiO but a slightly higher reduction temperature than Ce/NiO. Salleh et al. (2015) and Vazinishayan et al. (2018) stated that ZrO_2 has higher BET surface areas than NiO. It suggests that more active sites may be attributed to the higher temperature reduction of NiO after doping.

Overall, the addition of different metals, namely Ce, Co, Mo, W and Zr, showed a slight increase in the surface area compared to undoped NiO. The increase in surface area is likely due to the increase in the surface area contributed by the effect of metal oxides added via impregnation. Some additional metal oxides were expected to have partially filled the NiO mesopores and partially formed a new surface outside the NiO pores. This phenomenon is due to the larger additional cluster metal size and the higher quantity of metal than the pore volume. Metallic materials outside the pores can usually add to the surface area of the catalyst material (Zurina, 2015). Nevertheless, the volume and diameter of the pores showed less significant changes after adding other metals.

Table 1
Surface area, pore size and pore volume of NiO catalyst and various transition metal doped NiO

Catalyst	**S_{BET} (m^2/g)**	**D_{pore} (nm)**	**V_{pore} (cm^3/g)**
NiO	4.5	40.6	0.030
Ce/NiO	6.8	32.1	0.038
Co/NiO	4.8	29.0	0.027
Mo/NiO	4.8	33.1	0.033
W/NiO	5.2	29.2	0.017
Zr/NiO	8.9	16.1	0.027

The pore size distribution was computed using N_2 adsorption-desorption isotherm data to apply with the Barrett-Joyner-Halenda (BJH) model. Figure 5 shows the pore size distribution of the various metals doped NiO catalysts, with the inset picture showing

the enlarged scale at 20 to 60 Å (2-6 nm). The catalysts showed a significant change in pore size distribution after being doped with various metals. The inset figure in Figure 5 indicates that Mo/NiO has the highest pore size distribution in the 30 to 42 Å (3-4.2 nm) compared to the rest of the NiO-doped catalysts. Undoped NiO was not observed in the pore size distribution of the 20-60 Å (2-6 nm) region. Thus, the additive metals contribute to the changes in pore size distribution at the mesopore region. In general, the presence of additive metals contributes to a higher surface area than NiO (Table 1). It is due to each metal particle having its pores as well.

Various pore size distribution patterns were observed at the 300 to 1800 Å (30-180 nm) region. The undoped NiO only exhibited pore size distribution at mesopore to macropore region around 300 to 1800 Å (30-180 nm). A mesopore region is found in the range of 20 to 500 Å (2-50 nm), whereas a macropore region is located in the range larger than 500 Å (50 nm) (Hakim, Tahari et al., 2015; Hakim et al., 2016). The undoped NiO has a larger pore size distribution at 300 to 1100 Å (30-110 nm) compared to Co/NiO, W/NiO, Mo/NiO and Zr/NiO. It could be attributed to additive metals in smaller sizes that are partially embedded into NiO pores of this region. Meanwhile, the Ce/NiO possesses Ce particles of larger sizes, which possibly makes Ce particles the only particles deposited on NiO surfaces. Furthermore, at 600 to 1500 Å (60-150 nm), the Ce/NiO showed the highest and broadest distribution. Therefore, the high surface area of the Ce/NiO catalyst is attributed to the mesopore and macropore regions.

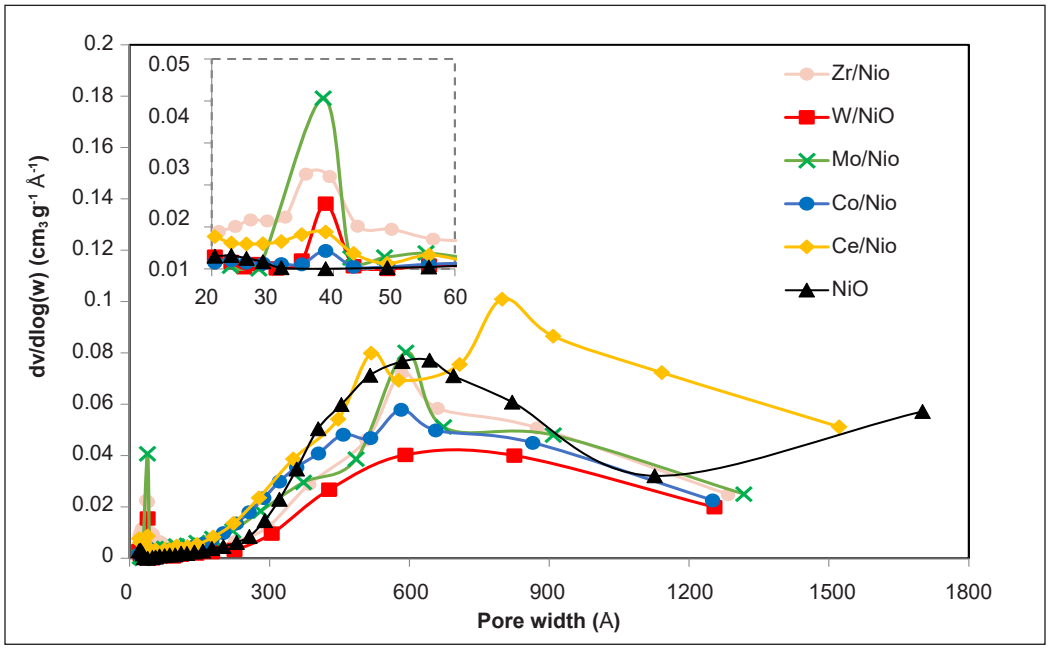

Figure 5. Pore size distribution of the various metals doped NiO catalysts with the inset picture showing the enlarged scale at 20 to 60 Å (2-6 nm)

CONCLUSION

The reduction behaviour of Mo/NiO, Zr/NiO, W/NiO, Ce/NiO, Co/NiO and undoped NiO catalysts in the CO atmosphere was investigated and compared using the TPR technique and characterised by XRD and N_2 gas adsorption-desorption analysis (BET). This research revealed that the reduction reaction obeyed the consecutive mechanism, and NiO was reduced to Ni completely. The 3% Ce/NiO possessed a higher surface. Furthermore, adding Ce to NiO enhanced a lower reduction temperature compared to adding Co, Mo, W and Zr. Adding Ce to the NiO shifted the TPR peaks to the lower temperature. It can be concluded that the reduction temperature of NiO decreases by the Ce with 3% Ce loading, which is sufficient to reduce NiO to Ni at 370°C. It is mainly ascribed to ceria's intricate redox and O^{2-} -defect chemistry capable of transporting oxygen species and exhibiting a strong metal-support interaction favouring a higher Ni dispersion. The Ce changes the coordination environment of nickel and the strength of Ni-O bonds, leading to a decrease in the reduction temperature of doped NiO.

ACKNOWLEDGEMENT

The publication fee is supported by UPM-Kyutech International Symposium on Applied Engineering and Sciences 2022 (SAES2022) and Universiti Putra Malaysia.

REFERENCES

Ahmad T., Pandey V., Saddam Husain M., Adiba, & Munjal S. (2022). Structural and spectroscopic analysis of pure phase hexagonal wurtzite ZnO nanoparticles synthesized by sol-gel. *Materials Today Proceeding. 49,* 1694-1697. https://doi.org/10.1016/j.matpr.2021.07.456

Alizadeh, R., Jamshidi, E., & Ale-Ebrahim, H. (2007). Kinetic study of nickel oxide reduction by methane. *Chemical Engineering and Technology 30*(8), 1123-1128. https://doi.org/10.1002/ceat.200700067

Anastasios I. T., Nikolas D. C., Ioannis V. Y., & Maria A. G. (2021). Bimetallic Ni-Based Catalysts for CO_2 Methanation: A Review. *Nanomaterials*, *11*(28), 1-34.

Charisiou, N. D., Papageridis, K. N., Tzounis, L., Sebastian, V., Hinder, S. J., Baker, M. A., AlKetbi, M., Polychronopoulou, K., & Goula, M. A. (2019). Ni supported on CaO-MgO-Al_2O_3 as a highly selective and stable catalyst for H_2 production via the glycerol steam reforming reaction. *International Journal of Hydrogen Energy*, *44*(1), 256-273. https://doi.org/10.1016/j.ijhydene.2018.02.165

Charisiou, N. D., Tzounis, L., Sebastian, V., Hinder, S. J., Baker, M. A., Polychronopoulou, K., & Goula, M. A. (2019). Investigating the correlation between deactivation and the carbon deposited on the surface of Ni/Al_2O_3 and Ni/La_2O_3 -Al_2O_3 catalysts during the biogas reforming reaction. *Applied Surface Science*, *474*, 42–56. https://doi.org/10.1016/j.apsusc.2018.05.177

Cho D. Y., Luebben M., Wiefels S., Lee K. S., & Valov. I. (2017). Interfacial metal-oxide interactions in resistive switching memories. *ACS Applied Materials & Interfaces*, *9*(22), 19287-19295. https://doi.org/10.1021/acsami.7b02921

Dzakaria, N., Lahuri, A. H., Tengku Saharuddin, T. S., Samsuri, A, Salleh, F., Wan Isahak, W. N. R., Yusop, M. R., & Yarmo, M. A. (2021). Preparation of cerium doped nickel oxide for lower reduction temperature in carbon monoxide atmosphere. *Malaysian Journal of Analytical Sciences, 25*(3), 521-531.

Dzakaria, N., Tahari, M. N. A., Samidin, S., Tengku Saharuddin, T. S., Salleh, F., Lahuri, A. H., & Yarmo, M. A. (2020). Effect of cobalt on nickel oxide toward reduction behaviour in hydrogen and carbon monoxide atmosphere. *Material Science Forum*, *1010*, 373-378. https://doi.org/10.4028/www.scientific.net/MSF.1010.373

Dzakaria, N., Samsuri, A., Halim, A., M. A., Saharuddin, T. S. T., Tahari, M. N. A., Salleh, F., Yusop, M. R., Isahak, W. N. R. W., Hisham, M. W. M., & Yarmo, M. A. (2020). Chemical reduction behavior of zirconia doped to nickel at different temperature in carbon monoxide atmosphere. *Indonesian Journal of Chemistry*, *20*(1), 105-112. https://doi.org/10.22146/ijc.40891

Fakeeha A., Ibrahim A. A., Aljuraywi H., Alqahtani Y., Alkhodair A., Alswaidan S., Abasaeed A. E, Kasim S. O., Mahmud S., & Al-Fatesh A. S. (2020). Hydrogen production by partial oxidation reforming of methane over Ni catalysts supported on high and low surface area alumina and zirconia. *Processes*, *8*(5), Article 499. https://doi.org/10.3390/pr8050499

Farber S., Ickowicz D. E., Melnik K., Yudovin-Farber I., Recko D., Rampersaud A., & Domb A. J. (2014). Surface functionalization of magnetic nanoparticles formed by self-associating hydrophobized oxidized dextrans. *Journal of Nanoparticle Research*, *16*, Article 2425. https://doi.org/10.1007/s11051-014-2425-z

Hasannejad, H., Shahrab, T., & Jafarian, M. (2012). Synthesis and properties of high corrosion resistant Ni-cerium oxide nano-composite coating. *Material Corrosion*, *64*(12), 1104-1113. https://doi.org/10.1002/maco.201106484

Hakim. A., Tahari, M. N. A., Marliza, T. S., Wan Isahak, W. N. R., Yusop, M. R., Hisham, W. W. M., & Yarmo, M. A. (2015). Study of CO_2 adsorption and desorption on activated carbon supported iron oxide by Temperature Programmed Desorption. *Jurnal Teknologi (Sciences & Engineering)*, *77*(33), 75-84. https://doi.org/10.11113/jt.v77.7010

Hakim, A., Isahak, W. N. R. W., Yusop, M. R., Tahari, M. N. A., Hisham, M. W. M., & Yarmo, M. A. (2015). Temperature programmed desorption of carbon dioxide for activated carbon supported nickel oxide: The adsorption and desorption studies. *Advanced Materials Research*. *1087*, 45-49. https://doi.org/10.4028/www.scientific.net/AMR.1087.45

Hakim, A., Yarmo, M. A., Marliza, T. S., Tahari, M. N. A., Samad, W. Z., Yusop, M. R., Hisham, W. W. M., & Dzakaria, N. (2016). The influence of calcination temperature on iron oxide (α-Fe_2O_3) towards CO_2 adsorption prepared by simple mixing method. *Malaysian Journal of Analytical Sciences*, *20*(6), 1286-1298. http://dx.doi.org/10.17576/mjas-2016-2006-07

Kaiser M. (2004). Semiconductor-to-metallic transition in Cu-substituted Ni - Mn ferrite. *Physica Status Solidi*, *201*(14), 3157-3165. https://doi.org/10.1002/pssa.200406861

Khan, I., Saeed, K., & Khan I. (2019), Nanoparticles: Properties, applications and toxicities. *Arabian Journal of Chemistry, 12*(7)*,* 908-931. https://doi.org/10.1016/j.arabjc.2017.05.011

Krasuk, J. H., & Smith, J. M. (1972). Kinetics of reduction of nickel oxide with carbon monoxide. *AIChE Journal 18*(3), 506-512. https://doi.org/10.1002/aic.690180308

Lahuri, A. H., Ling, N. K. M., Rahim, A. A., & Nordin, N. (2020). Adsorption kinetics for CO_2 capture using cerium oxide impregnated on activated carbon. *Acta Chimica Slovenica*, *67*(2), 570-580. http://dx.doi.org/10.17344/acsi.2019.5572

Lahuri, A. H., Yusuf, A. M., Adnan, R., Rahim, A. A., Tajudee, N. F. W., & Nordin, N. (2022). Kinetics and thermodynamic modeling for CO_2 capture using NiO supported activated carbon by temperature swing adsorption. *Biointerface Research in Applied Chemistry*, *12*(3), 4200-4219. https://doi.org/10.33263/BRIAC123.42004219

Lv, C., Xu, L., Chen, M., Cui, Y., Wen, X., Li, Y., Wu, C.E., Yang, B., Miao, Z., & Hu, X. (2020). Recent progresses in constructing the highly efficient Ni based catalysts with advanced low-temperature activity toward CO_2 methanation. *Frontiers in Chemistry*, *8*, Article 269. https://doi.org/10.3389/fchem.2020.00269

Othman, Z. A. (2012). A review: Fundamental aspects of silicate mesoporous materials. *Materials, 5*(12), 2874-2902. https://doi.org/10.3390/ma5122874

Oudejans D., Offidani M., Constantinou A., Albonetti S., Dimitratos N., & Bansode A. (2022). A comprehensive review on two-step thermochemical water splitting for hydrogen production in a redox cycle. *Energies*, *15*(9), Article 3044. https://doi.org/10.3390/en15093044

Pandey V., Adiba, Munjal S., & Ahmad T. (2020). Optical properties and spectroscopic investigation of single phase tetragonal Mn_3O_4 nanoparticles. *Material Today Proceeding*, *26*, 1181-1183. https://doi.org/10.1016/j.matpr.2020.02.238

Papageridis, K. N., Charisiou, N. D., Douvartzides, S., Sebastian, V., Hinder, S. J., Baker, M. A., AlKhoori, S., Polychronopoulou, K., & Goula, M. A. (2020). Promoting effect of CaO-MgO mixed oxide on Ni/γ-Al_2O_3 catalyst for selective catalytic deoxygenation of palm oil. *Renewable Energy*, *162*, 1793-1810. https://doi.org/10.1016/j.renene.2020.09.133

Parkinson, G. S., Mulakaluri, N., Losovyj, Y., Jacobson, P., Pentcheva, R., & Diebold, U. (2010). Semiconductor-half metal transition at the Fe_3O_4 (001) surface upon hydrogen adsorption. *Physical Review B*, *82*, Article 125413. https://doi.org/10.1103/PhysRevB.82.125413

Rebello, A., & Adeyeye, A. O. (2016). Robust electric-field tunable opto-electrical behavior in Pt-NiO-Pt planar structures. *Scientific Reports*, *6*, Article 28007. https://doi.org/10.1038/srep28007

Salleh, F., Saharuddin, T. S. T., Samsuri, A., Othaman, R., & Yarmo, M. A. (2015). Effect of zirconia and nickel doping on the reduction behavior of tungsten oxide in carbon monoxide atmosphere. *International Journal of Chemical Engineering Application*, 6(*6*), 389-394. https://doi.org/10.7763/ijcea.2015.v6.516

Sharma, K., Vastola, F. J., & Walker, P. L. 1997. Reduction of nickel oxide by carbon: III. Kinetic studies of the interaction between nickel oxide and natural graphite. *Carbon, 35*(4), 535-541. https://doi.org/10.1016/S0008-6223(97)83728-1

Siakavelas, G. I., Charisiou, N. D., AlKhoori, S., AlKhoori, A. A., Sebastian, V., Hinder, S. J., Baker, M. A., Yentekakis, I. V., Polychronopoulou, K., & Goula, M. A. (2021). Highly selective and stable nickel catalysts supported on ceria promoted with Sm_2O_3, Pr_2O_3 and MgO for the CO_2 methanation reaction. *Applied Catalysis B: Environmental*, *282*, Article 119562. https://doi.org/10.1016/j.apcatb.2020.119562

Sing, K. S. W., Everett, D. H., Haul, R. A. W., Moscou, L., Pierotti, R. A., & Rouquerol, J. (1985). Reporting physisorption data for gas/solid systems with special reference to the determination of surface area and porosity. *Pure and Applied Chemistry, 57*(4), 603-619. https://doi.org/10.1351/pac198557040603

Sun, J., Zhang, X., Jin, M., Xiong, Q., Wang, G., Zhang, H., & Zhao, H. (2020). Robust enhanced hydrogen production at acidic conditions over molybdenum oxides-stabilized ultrafine palladium electrocatalysts. *Nano Research*, *14*, 268-274. https://doi.org/10.1007/s12274-020-3083-3

Tsiotsias, A. I., Charisiou, N. D., Yentekakis, I. V., & Goula, M. A. (2020). The role of alkali and alkaline earth metals in the CO_2 methanation reaction and the combined capture and methanation of CO_2. *Catalysts*, *10*(7), Article 812. https://doi.org/10.3390/catal10070812

Vazinishayan, A., Lambada, D. R., Yang, S., Zhang, G., Cheng, B., Woldu, Y. T., Shafique, S., Wang, Y., & Anastase, N. (2018). Effects of mechanical strain on optical properties of ZnO nanowire. *AIP Advances*, *8*(2), Article 025306. https://doi.org/10.1063/1.5016995

Wondimu, T. H., Bayeh, A. W., Kabtamu, D. M., Xu, Q., Leung, P., & Shah, A. A. (2022). Recent progress on tungsten oxide-based materials for the hydrogen and oxygen evolution reactions. *International Journal of Hydrogen Energy*, *47*(47), 20378-20397. https://doi.org/10.1016/j.ijhydene.2022.04.226

Zheng, J., Dong, Y., Wang, W., Ma, Y., Hu, J., Chen, X., & Chen, X. (2013). In situ loading of gold nanoparticles on Fe_3O_4@SiO_2 magnetic nanocomposites and their high catalytic activity. *Nanoscale*, *5*(11), 4894-4901. https://doi.org/10.1039/C3NR01075A

Zurina, S. W. (2015). Conversion of glycerol to 1,2-propanadiol and methanol by hydrogenolysis and sub-critical fluid techniques using fluorine-doped tin oxide (FTO) catalyst. Universiti Kebangsaan Malaysia.

Pertanika J. Sci. & Technol. 31 (4): 1731 - 1754 (2023)

PERTANIKA JOURNALS

SCIENCE & TECHNOLOGY

Journal homepage: http://www.pertanika.upm.edu.my/

Design of a Smart Portable Farming Kit for Indoor Cultivation Using the Raspberry Pi Platform

Muhammad Izzad Ramli[1], Muhammad Azizi Mohd Ariffin[1]*, Zarina Zainol[1], Mohd Nazrul Mohd Amin[1], Dedeng Hirawan[2], Irfan Dwiguna Sumitra[2] and Nursuriati Jamil[1]

[1]National Autism Resource Centre, Faculty of Computer and Mathematical Sciences, 40450 UiTM, Shah Alam, Malaysia

[2]Department of Informatic Engineering, Universitas Komputer Indonesia, Bandung, West Java, 40132 Indonesia

ABSTRACT

The global crisis and climate change have resulted in severe food shortages worldwide. One of the solutions is self-farming by using smart farming technology. Smart and efficient agricultural production or smart farming using IoT sensors, big data, and cloud service has proven its value for a decade, but the effect depends on the agricultural environment of the country or society. Hence self-farming is likely the most feasible solution to avoid food scarcity. The smart farming system monitors and maintains essential growth parameters like light, temperature, and humidity to ensure maximum yield. In this paper, we propose a Smart Portable Farming Kit design, which is simple, lightweight, and durable to be placed indoors in an urban area. This prototype design uses the Internet of Things (IoT) based system for cultivating short-duration vegetables and mushrooms in an urban area with minimal user attention. The proposed design proved better than the traditional setup by increasing the mushroom yield. With Smart Portable Farming Kit, urban farming becomes a more viable alternative to increase food security, making oyster mushroom cultivation in the urban area easier and more profitable.

ARTICLE INFO

Article history:
Received: 22 June 2022
Accepted: 20 September 2022
Published: 24 May 2023

DOI: https://doi.org/10.47836/pjst.31.4.08

E-mail addresses:
izzad@fskm.uitm.edu.my (Muhammad Izzad Ramli)
mazizi@fskm.uitm.edu.my (Muhammad Azizi Mohd Ariffin)
zarina@fskm.uitm.edu.my (Zarina Zainol)
nazrul@fskm.uitm.edu.my (Mohd Nazrul Mohd Amin)
dedeng@email.unikom.ac.id (Dedeng Hirawan)
irfan.dwiguna@email.unikom.ac.id (Irfan Dwiguna Sumitra)
lizajamil@computer.org (Nursuriati Jamil)
* Corresponding author

ISSN: 0128-7680
e-ISSN: 2231-8526

Keywords: Food security, indoor farming, internet of things (IoT), remote farming, single board computer, smart farming, urban farming

INTRODUCTION

The global food demand has affected households worldwide, especially in food consumption and security due to climate change (Ballais et al., 2021). The demand will lead to rising food costs and affect low-

income families across 53 countries (Antonaci et al., 2022), especially in the urban area (Laborde et al., 2021; Rudolfsen, 2020). Based on Tan et al. (2020), the population will reach 9.8 billion by 2050, and most are expected to live in urban areas. Nowadays, smart agriculture technology is needed, especially in urban areas with limited space, to increase family food security by allowing households to grow nutritious food in their own homes. Therefore, urban smart vertical farming (USVF) (Jayasekara et al., 2021; Rajermani et al., 2020; Saad et al., 2021; Zulqarnain et al., 2020) and portable smart farming (Sutono & Selvia, 2020; Rajermani et al., 2020) are the potential solutions to help meet the demand without additional farmland. The main advantage of a portable smart farming system is that it can be relocated, installed easily in a building, and utilized by small families at home or offices.

Mushrooms are suitable for urban farming as it requires small space, do not require direct sunlight and require a shorter time for harvest. It is also sustainable and environmentally friendly and uses agricultural waste for its growing medium (Rosmiza et al., 2016). Mushroom also has commercial value as it is always in high demand (Rosmiza & Hussin, 2017). However, mushroom cultivation has specific growing conditions (e.g., humidity) to produce a high yield; therefore, an IoT system is needed to aid the cultivation process.

Indoor farming has gained much interest in urban areas because it is compact and movable to any available indoor space. However, the designs of portable smart farming kits for mushroom cultivation (Ibrahim et al., 2018; Kassim et al., 2019; Mat et al., 2019; Najmurrokhman et al., 2020; Shakir et al., 2019; Hendrawan et al., 2019) are still inadequate. Furthermore, the existing designs of indoor, portable smart farming (Ahmmad et al., 2020; Sutono & Selvia Lorena, 2020; Rankothge et al., 2022) are usually modelled specifically to the cultivated plant. Many factors should be considered when designing an indoor, portable smart farming kit, including the size, the materials used, the shape and the hardware installation. An inappropriate interior design of the portable kit could lead to the ruin of the plants and difficulty in operating and maintenance.

Therefore, this paper proposes a design of a Smart Portable Farming Kit (SPFK) for mushroom cultivation in urban areas where land is limited. The SPFK must be easy to install, lightweight, and developed on open-source platforms with cost-effective hardware components. The design automates growing vegetables in an urban indoor residential. A portable farming kit is a container designed to mimic a small agricultural land that can be moved to another location without any changes to the physical system. On the other hand, the design of the SPFK must have aesthetic values suitable for an indoor showcase.

The contribution of this paper is twofold: (1) This paper demonstrates the proposed design of a Smart Portable Farming Kit for mushroom cultivation using an IoT climate control system in an indoor environment, and (2) This paper proves that the implementation

of smart farming technology in a portable farming kit provides a better environment, management and resulted in a higher yield of harvested mushroom as compared to the traditional method in an indoor environment.

RELATED WORK

Indoor cultivation refers to farming in an enclosed space environment. Since it is isolated from external environmental influences, the plant yields are unaffected by the weather or any climatic ailment. Furthermore, Sutono & Selvia Lorena (2020) mentioned that indoor plants could be grown even when the soil is barren. Our study excludes indoor aquaponics and hydroponics system because plants in these environments used different growing systems and technologies.

A design of indoor portable farming was built using steel, wood, and acrylic by Sutono & Selvia Lorena (2020) to utilize home yards in the urban area. The container did not have direct contact with the ground to avoid corrosion and had wheels to allow portability. The system was equipped with IoT technology using Arduino Mega 2560, 3 Stepper Motor and 12 Soil Moisture Sensors. Ahmmad et al. (2020) developed a portable Automatic Gardening Portable Plant with an automated watering system using a DHT22 humidity and temperature sensor and LED illumination using Light Intensity Sensor. Ample lighting was provided to the plants to undergo an appropriate photosynthesis process. The user is alerted if the water level or light intensity is low through Wi-Fi access using the Blynk app. Despite the success of testing the functionalities of their systems, no real-life implementation of plant cultivation was presented in both work.

In Rankothge et al. (2021), an indoor microgreen sprouts portable unit was developed to provide optimum growing conditions for mung-bean sprouts. Fuzzy inference engines and DHT-11 sensors were used to control the temperature and humidity, and ultrasonic sensors were utilized to monitor the plants' heights. Different temperatures, lighting durations, and watering frequencies were tested using the prototype for five days, and the optimum conditions for the sprouts were concluded. While IoT-based farming system is not new, the design of a portable IoT-based system for indoor farming is scarce. In a systematic review of IoT in smart farming (Terence & Purushothaman, 2020), the authors investigated which agriculture functions were commonly automated, whether the implementation was conducted in real-time, what IoT components were mostly used and how evaluations were done. There was no study on the design of the IoT-based system, whether for small- or large-scale cultivations.

Kassim et al. (2019), Mat et al. (2019) and Shakir et al. (2019) proposed a system using a wireless sensor network and a real-time embedded system to control the growing environment for shitake mushroom cultivation. The system provided an automated corrective action based on a pre-defined threshold of the growing variables to control

the actuators. Shakir et al. (2019) also added a light intensity parameter to light up the environment. They observed increased CO_2 levels in artificial light, indicating that the mushrooms produced more CO_2 when the light was turned on. Their results showed an increase of 192.9% in mushroom yields. In another similar setting using a miniature enclosed house, Cruz-del Amen & Villaverde (2019) have used fuzzy logic to control temperature and humidity for oyster mushroom cultivations. They grew 30 blocks of oyster mushrooms in three separate houses to compare the conventional method, an IoT-based system, and an IoT-based system with thunderstorm audio sounds. While the results showed that an IoT-based system with thunderstorm audio produced more yields, no discussion was done on the significance and justifications of using the audio.

Other studies on IoT-based mushroom cultivation deployed indoor portable farming kits to encourage urban farming. Najmurrokhman et al. (2020) and Hendrawan et al. (2019) implemented IoT systems using closed plastic boxes to grow oyster mushrooms and monitored light, humidity, and temperature levels. Both papers detailed the design of their portable IoT-based farming kits. While Najmurrokhman et al. (2019) only tested the functionalities of their portable system. Hendrawan et al. (2019) proved that their fuzzy-based portable IoT system produced more mushroom yields compared to threshold-based methods. Nasution et al. (2019) did another indoor, portable mushroom cultivation where a wooden container for six mushrooms was equipped with an IoT-based system to monitor the growing environment. The design of their sensor, control and monitoring system was described, and the experiments concluded that the cultivation of oyster mushrooms with IoT is more effective by comparing the mushroom growth rate. However, all studies did not consider the aesthetic elements of the design for their indoor portable farming kits. A summary of these selected IoT-based mushroom cultivation systems is presented in Table 1.

Table 1 shows the two cultivation setups preferred for mushroom farming. Most medium-scale farming is done in specially built mushroom houses or rooms in a building. The other setup, which is the focus of our paper, is the indoor, portable IoT-based system designed for urban dwellers so that it can be moved around to utilize the unused space. There are two important variables which are temperature and humidity. However, the work of Mat et al. (2019) and Shakir et al. (2019) stated that CO_2 and air quality levels also play a role, especially in a growing environment where air circulation is stagnant. Cruz-del Amen & Villaverde (2019) recommended that the growing environment of oyster mushrooms must be clean from any emissions due to its sensitivity to environmental changes. To our knowledge, no portable smart farming design for mushroom cultivation has considered this factor. Thus, our proposed SPFK is equipped with a gas quality sensor to monitor the presence of harmful gases. Furthermore, our SPFK kit provides the end-user with a web dashboard and real-time camera feed so that they can monitor their plants remotely to cater for the busy lifestyle of urban dwellers.

Table 1
Summary of selected IoT-based mushroom cultivation system

Authors	Parameters			Cultivation setup	Environment	Real-time implementation
	Temperature	Humidity	CO_2			
Ibrahim et al. (2018)	✓	✓	✓	Mushroom house	Indoor	✓
Cruz-del Amen & Villaverde (2019)	✓	✓		Enclosed space	Indoor	✓
Kassim et al. (2019) Mat et al. (2019)	✓	✓	✓	Building room	Indoor	✓
Shakir et al. (2019)	✓	✓	✓	Building room	Indoor	✓
Hendrawan et al. (2019)	✓	✓		Plastic container	Indoor	✓
Nasution et al., (2019)	✓	✓		Mini wooden container	Indoor	✓
Najmurrokhman et al. (2020)	✓	✓		Plastic container	Indoor	X

We also noted that all portable smart farming listed employed Arduino-based microcontrollers. However, our SPFK is powered by the Raspberry Pi 4 computer to process the sensor data, regulate the growing condition, and display the monitoring data. Raspberry Pi is a single-board computer powered by the Linux operating system and capable of performing the general computational task and embedded low-powered processing tasks, as demonstrated by the work of Almalki et al. (2021) and Baqer et al. (2023). Almalki et al. (2021) proposed a low-cost method of monitoring farming parameters using a drone powered by a Raspberry Pi and LoRaWAN module for communication. The sensor data, such as soil moisture, were processed in the cloud. The works show a low-cost solution to help farmers monitor the farming area, but it does not discuss further how corrective action can be taken to regulate the growing environment.

METHODOLOGY

The proposed SPFK for the oyster mushroom cultivation system was designed and implemented at Universiti Teknologi MARA, Malaysia, for evaluation. During the evaluation, the oyster mushroom yield was compared to the control system and the SPFK. The primary data, such as temperature, humidity and harmful gas concentration, were captured from the sensors for analysis.

System Design

The design of the portable IoT-Based system was divided into three sections: portable and smart cultivation system using Raspberry Pi platform, control system algorithm and interface.

Portable Smart Cultivation System Using Raspberry Pi Platform

The system was designed to be portable and smart to control the growing environment effectively. The system was designed as portable to support urban farming requirements (Salim et al., 2019) to optimize the urban space. Moreover, the system must be moved around easily in urban homes. Therefore, the build material for the system housing must be lightweight, and all the electronic components must be miniaturized. The system needs to be "Smart" to control the oyster mushroom's growing condition effectively. The oyster mushroom has a specific growing condition to produce a good yield, and the temperature must be maintained within the range of 28–30°C and humidity within the range of 80%–90% (Cikarge & Arifin, 2018).

Furthermore, the quality of the oyster mushroom can also degrade if exposed to harmful aerosols found in insect repellent (Tarigan et al., 2017); therefore, the system needs to be able to detect harmful particles in the air. Manually maintaining the growing condition of the oyster mushroom is tedious and may not be possible for urban dwellers as they are not always available at home. Thus, the system was developed on the Raspberry Pi 4 platform, which allows the programmability of the system to automatically control and monitor the growing condition based on inputs of the sensors. It also allows the system to have a database to store data in a structured manner and display the data dashboard via a web server and the internet via a built-in Wi-Fi module. Figure 1 shows the overall system design diagram.

Based on Figure 1, the mushroom growing medium was placed vertically inside a custom housing built using lightweight 3mm acrylic glass. Inside the housing, an IoT system automatically monitors and regulates the growing condition. The system's brain is the Raspberry Pi 4 computer equipped with a Quad-Core 64bit 1.5Ghz ARM processor, 1GB DDR4 RAM, 256GB Flash Storage, dual-band 2.4 and 5 GHz Wi-Fi interface and 40 pin GPIO interface. The operating system was Raspbian Linux and was installed with Python3 interpreter, MySQL database and Apache2 web server software. The Raspberry Pi was powered by 5.1V 3A USB type C and was placed inside the system housing. In order to gauge the environmental condition inside the housing, the system was equipped with two sensors, a DHT22 sensor for capturing temperature and humidity values and an MQ135 for determining the presence of harmful gas in the housing. The data collected by the sensors were then sent to the Raspberry Pi via 3C 22AWG to be processed by the control system algorithm implemented in Python 3 script. The script is responsible for

storing the sensor data in the MySQL database, and an alert email will be sent using SMTP if a certain exceeds the pre-determined threshold.

The system was equipped with a two-channel 5V relay which acts as an actuator to control motor or electrical devices to regulate the growing condition. In the proposed system, the relay was used to control the humidifier to increase humidity when the level was below a predetermined threshold. The humidifier can be filled with 10 litres of water to regulate the humidity level and is powered by an 18V 500mA power outlet and placed at the top level of the housing. The system was not equipped with an external fan to regulate the temperature as the setup was placed inside a building in Malaysia where the average room temperature ranges from 23°C to 30°C (Jamaludin et al., 2015); thus, it is not necessary to regulate the temperature. Nevertheless, the system can be equipped with an external fan. The system was designed to send an alert if the temperature exceeds the pre-determined threshold, and the user can move it to the area without direct sunlight. Moreover, the proposed system was also equipped with a mini 8 megapixels camera on top of the housing to allow the user to monitor the growth remotely. The camera was connected to the Raspberry Pi 4 using an FFC cable, and the user can view the video stream in real-time via a web interface served by Apache2. The IoT system was connected to the Internet via a Wi-Fi access point installed in the room using the Wi-Fi module. The end-user can access the web dashboard

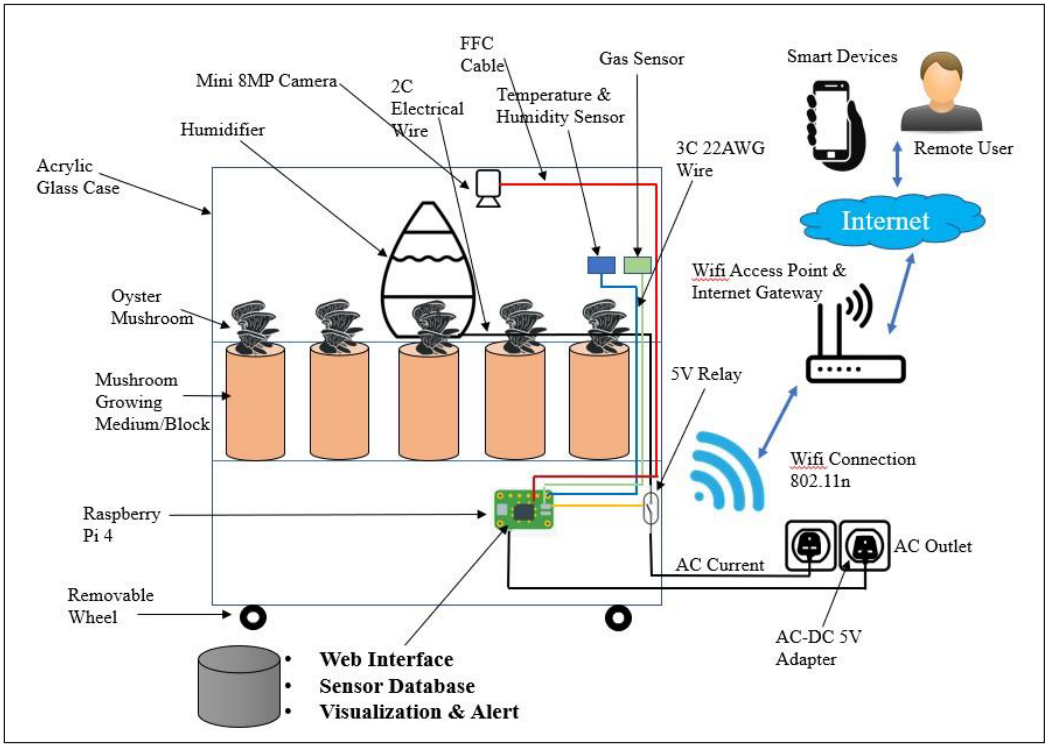

Figure 1. Overall portable smart farming system design diagram

and camera to monitor their plant remotely from anywhere. All the electronic components used in the IoT were small and could fit in the internal housing. Figure 2 shows the system's physical arrangement diagram.

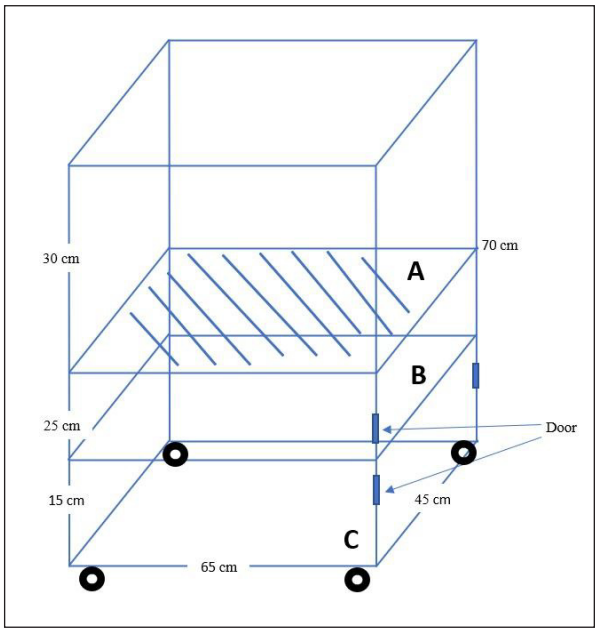

Figure 2. System physical arrangement diagram

Based on the physical arrangement shown in Figure 2, the housing size was 70cm x 65cm x 45cm, equipped with four sets of wheels for portability. The housing of the system consists of three parts. Part A provided an area for the oyster mushroom to grow; there are eight holes to place the growing medium. Part A also housed the humidifier, sensors, and camera to monitor the growing environment. The top was left open during the cultivation and can be closed with rolled blind if not used. Meanwhile, the mushroom growing medium consisting of sawdust and other agriculture by-product wrapped into a block was placed in Part B. The medium block was placed vertically in line with holes reaching Part A's area. The Raspberry Pi board is placed in Part B. The circuit diagram for the proposed IoT system is shown in Figure 3. Lastly, part C was a compartment to store miscellaneous items such as unused mushroom blocks and a cleaning cloth.

The system circuit diagram in Figure 3 shows that the Raspberry Pi 4 was the system's centre, which integrates different components. The Raspberry Pi 4 had 40 general-purpose input/output (GPIO) pins for external connection. The DHT22 sensor, which was used to capture the temperature and humidity value, has three pins: the DOUT pin was connected to GPIO 17 pin, the VCC pin was connected to GPIO 3.3v power pin and the GND pin was connected to the GPIO ground pin. The data from the DHT22 sensor was sent to the Raspberry Pi 4 in a digital signal. Meanwhile, the MQ135 sensor was used to detect the presence of harmful gas particles in the air, and it has three pins. The DOUT pin was connected to GPIO 14 pin, the VCC pin to GPIO 3.3v power pin, and the GND pin to the GPIO ground pin. The MQ135 sent a digital signal to the Raspberry Pi 4 in Boolean data form. If harmful gas was detected, it sent a True value; otherwise, a False value was sent.

For corrective action, the IoT system used a two-channel 5v relay for controlling the humidifier. The relay IN 1 pin was connected to GPIO 21 pin, VCC to GPIO 5v power

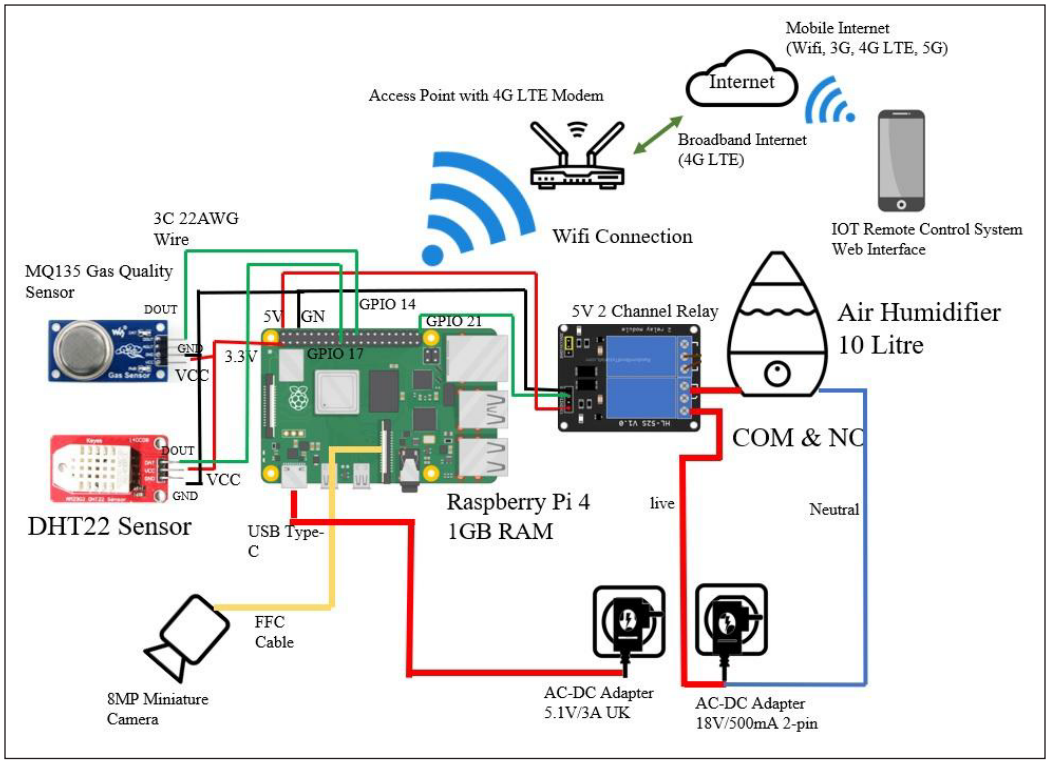

Figure 3. System circuit diagram

pin, and GND to the GPIO ground pin. The relay is a switch to turn on/off the humidifier; by default, the humidifier is always turned off. If the Raspberry Pi decided to turn on the humidifier, it sent a signal to the relay, which activated the relay. The sensors and relay were connected to the GPIO pin via a 40cm 3C 22AWG jumper wire. Meanwhile, the 8MP mini camera used to capture the growth was connected to the Raspberry Pi 4 via the FFC cable to the camera I/O port. The Raspberry pi board has an 802.11n Wi-Fi module which operates at 2.4 and 5Ghz bands. The Wi-Fi module was used to connect to the Internet, which allows it to send alert emails via SMTP protocol and allows end-users to monitor the system in real time via a web dashboard. The Raspberry Pi processes the sensor's data and takes corrective action based on the process defined in the control system algorithm.

Control System Algorithm

The control system algorithm defined the processing of data and actions taken by the Raspberry Pi 4 platform. The growing environment of the oyster mushroom was monitored and regulated based on pre-determined thresholds. The algorithm was implemented in Python 3, and several modules were used to access the MySQL database (pymysql), GPIO port (RPi.GPIO), DHT22 sensors (Adafruit_DHT), Raspberry Pi Camera (picamera) and

SMTP protocol (smtplib). Figure 4 shows the flowchart of the algorithm. To support the operation of the control script, all necessary software, as listed in Table 2, was installed on the Raspberry Pi 4.

Based on Figure 4 starts by initializing the database connection, web service, SMTP connection and GPIO port. This step was important to ensure all the essential dependencies were ready. If one of the components failed to initiate, the script exited the process and logged the error. Next, the script entered an infinite loop; if there was no interruption, the script continued to repeat the step in a loop. At the start of the loop, the script obtained the current time using the time library and read the current temperature, humidity, and gas

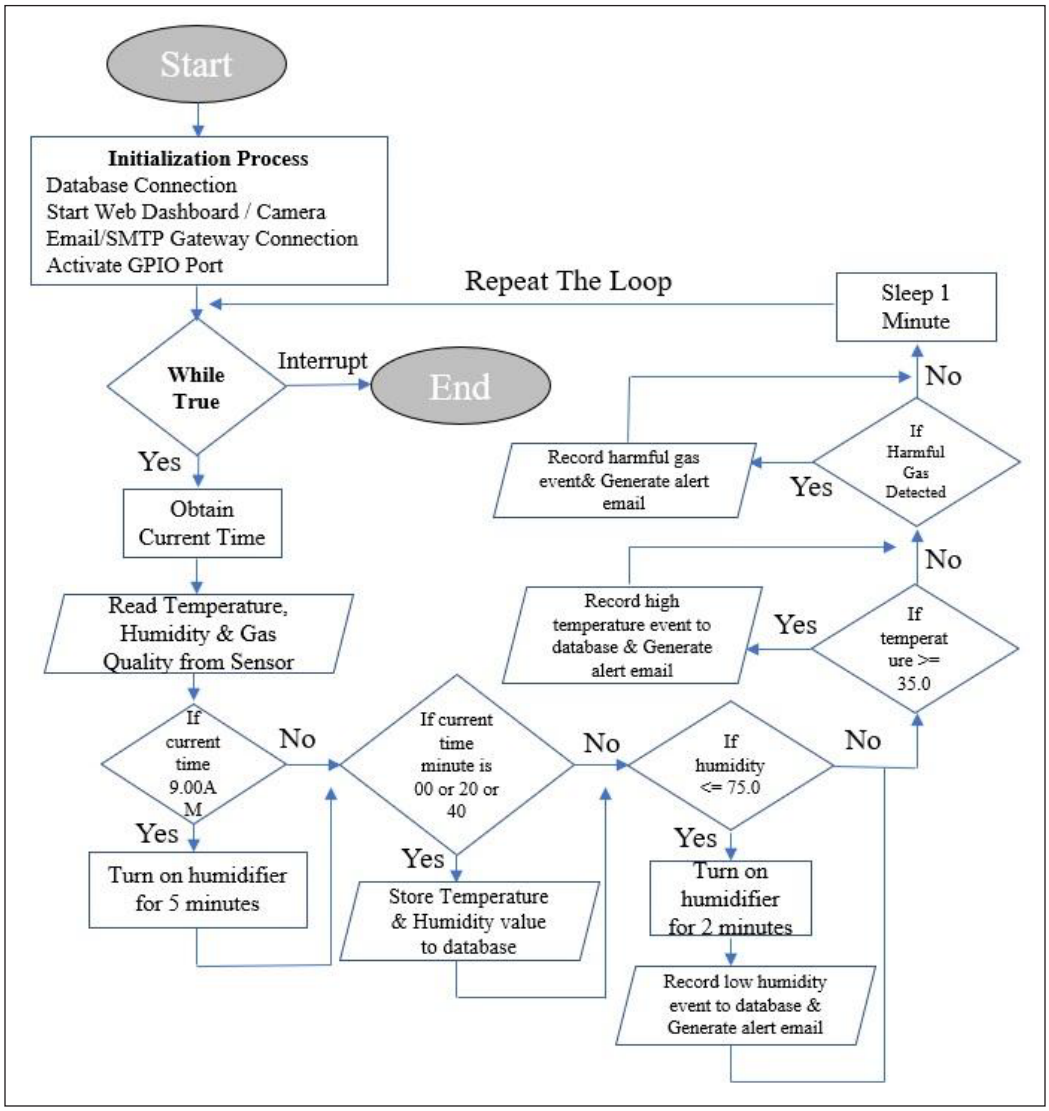

Figure 4. Control system process flowchart

Table 2
List of installed software

No	Software	Version	Description
1.	Raspberry Pi OS (Raspbian) 64bit	10 Buster	A Debian-based GNU/Linux operating system for the Raspberry Pi 4. Manage hardware and resources of the platform. Pre-Installed with all essential UNIX libraries.
2.	Python 3	3.7.3	Python 3 interpreter for running Python script.
3.	Pip Tools	18.1	Tool for installing and managing Python packages or modules.
4.	Adafruit DHT sensor library	-	A library for DHT22 sensors.
5.	Apache2	2.4.38	Server for serving Web service used for the dashboard and viewing camera stream.
6.	PHP7	7.3.31-1	Use alongside Apache2 web server for serving dynamic web content.
7.	MySQL	10.3.31	Open-Source relational database. The sensor's data and events were stored structurally in this database.

quality level from the sensors. If the current time was 9.00 am, the script sent a signal to the relay to turn on the humidifier for 5 minutes. It is to ensure that the growing environment is humid every morning. After that, the script checks the minute for every hour. If the minute is 00, 20 or 40, the script stores the temperature and humidity in the database.

The data from the database was displayed on the dashboard and stored. After that, the script checked the current reading of humidity. If it is less than 75.0%, the script instructs the humidifier to be turned on, alerts the user, and stores the record of the events in the database. The 75% threshold is chosen based on the optimal range identified in the work of Cikarge & Arifin (2018). The user can later use the record to identify the frequency of low-humidity events. Then the script checked the current temperature value. If the value was more than 35°C, the script sent an email alert to the user, and the high-temperature event was recorded in the database. After that, the script checked for the presence of harmful gases. If the gas sensor detects harmful gases, it sends an alert to the user and records the event in the database. Then the script remained idle for one minute before repeating the loop. The algorithm was implemented as a Python 3 script and continuously ran on the Raspberry Pi. The pseudocode of the algorithm is elaborated in Algorithm 1.

Algorithm 1: Control System Algorithm Implementation

Input: *temperature*, *humidity, currentTime, gasQuality,* temperature (float), humidity (float), Current Time (datetime) and Gas Quality (Boolean) reading from two sensors.
DatabaseObject = StartDatabaseConnection()
StartWebDashboard()
StartWebCamera()
EmailObject = StartSMTPConnection()

```
GPIOObject = initializeGPIO()
while True:
    currentTime = getCurrentTime()
    temperature = GPIOObject.getTemperature()
    humidity = GPIOObject.getHumidity()
    gasQuality= GPIOObject.getGasQuality()
    if currentTime == 0900:
            GPIOObject.startHumidifier()
            Sleep(300)
            GPIOObject.stopHumidifier()
      minute = getMinute(currentTime);
      if minute == 00 or minute == 20 or minute == 40:
              DatabaseObject.storeValue(currentTime, temperature, humidity)
      if humidity <= 75.0:
            GPIOObject.startHumidifier()
            Sleep(120)
            GPIOObject.stopHumidifier()
            DatabaseObject.storeValue(currentTime, humidity, “Low Humidity”)
            EmailObject.sendEmail(“Low Humidity, Check your plant”)
       if temperature >= 35.0:
            DatabaseObject.storeValue(currentTime, temperature, “High Temperature”)
            EmailObject.sendEmail(“High Temperature, Check your plant”)
        if gasQuality == True:
            DatabaseObject.storeValue(currentTime, gasQuality, “Harmful gas detected”)
            EmailObject.sendEmail(“Harmful gas detected, Check your plant”)
```

IoT System Interface

The proposed system has several interfaces, such as a web dashboard, web camera, and database, which the end user can access. The end-user can access the web dashboard remotely via a web browser anywhere. Figure 5 shows the screenshot of the web dashboard interface. The dashboard displayed real-time information to end-users, such as an ongoing alert event, a total alert for harmful gas detection, and low-humidity and high-temperature events. Moreover, the dashboard also displayed a time-series graph for daily humidity and temperature value. The graph provides useful insights regarding humidity and temperature pattern. Besides, the proposed system can display a live feed from the camera, which can be used to monitor the condition remotely. Figure 6 shows the web camera interface. The live camera feed can also be used to verify the email alert sent by the system. For example, after receiving an alert regarding harmful gas detection, use the live feed to verify whether there is smoke or any harmful gases near the cultivation area.

Figure 5. System web dashboard interface

Figure 6. System web camera interface

To access the sensors and event data stored in the database, the user can access the MySQL database via SQL software. Figure 7 shows the database data interface via Heidi SQL software. To connect to the MySQL interface, the SQL client needs to connect to TCP port 3306 with TLS enabled to ensure data security while in transit. Users will be prompted to provide valid database credentials for authentication and authorization purposes.

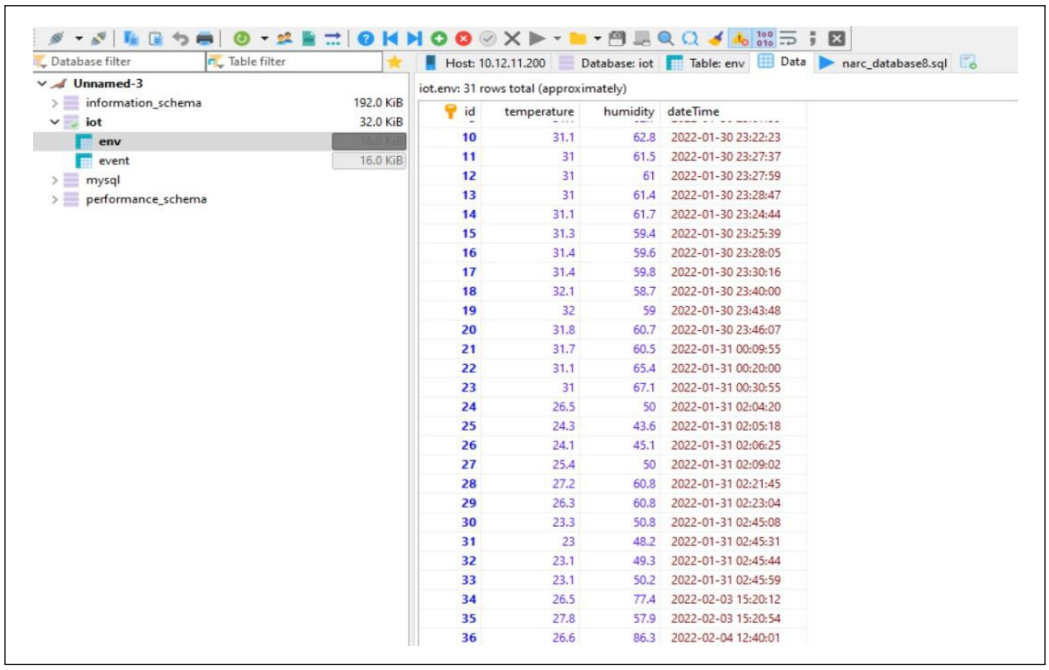

id	temperature	humidity	dateTime
10	31.1	62.8	2022-01-30 23:22:23
11	31	61.5	2022-01-30 23:27:37
12	31	61	2022-01-30 23:27:59
13	31	61.4	2022-01-30 23:28:47
14	31.1	61.7	2022-01-30 23:24:44
15	31.3	59.4	2022-01-30 23:25:39
16	31.4	59.6	2022-01-30 23:28:05
17	31.4	59.8	2022-01-30 23:30:16
18	32.1	58.7	2022-01-30 23:40:00
19	32	59	2022-01-30 23:43:48
20	31.8	60.7	2022-01-30 23:46:07
21	31.7	60.5	2022-01-31 00:09:55
22	31.1	65.4	2022-01-31 00:20:00
23	31	67.1	2022-01-31 00:30:55
24	26.5	50	2022-01-31 02:04:20
25	24.3	43.6	2022-01-31 02:05:18
26	24.1	45.1	2022-01-31 02:06:25
27	25.4	50	2022-01-31 02:09:02
28	27.2	60.8	2022-01-31 02:21:45
29	26.3	60.8	2022-01-31 02:23:04
30	23.3	50.8	2022-01-31 02:45:08
31	23	48.2	2022-01-31 02:45:31
32	23.1	49.3	2022-01-31 02:45:44
33	23.1	50.2	2022-01-31 02:45:59
34	26.5	77.4	2022-02-03 15:20:12
35	27.8	57.9	2022-02-03 15:20:54
36	26.6	86.3	2022-02-04 12:40:01

Figure 7. Database data interface

The proposed system will send an alert if low humidity, high temperature and harmful gas are detected in the growing environment. The alert was sent via email using SMTP protocol. Figure 8 shows an example of the system's alert notification to the end user.

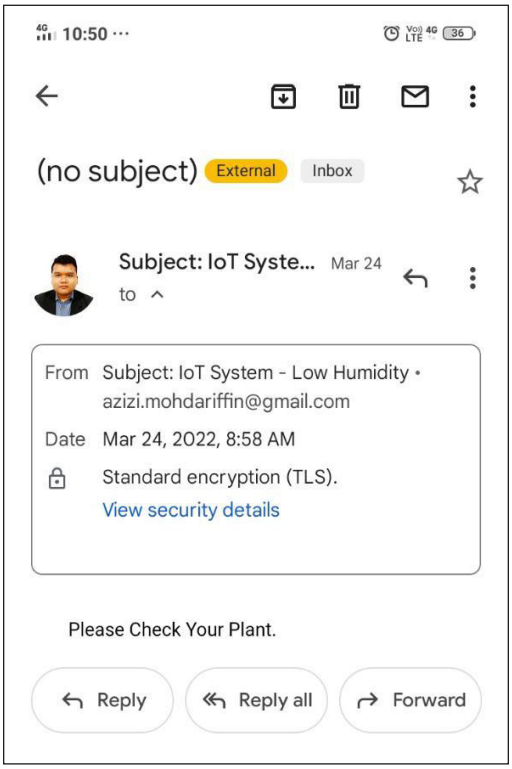

Figure 8. Alert notification from IoT system

Summary of System Design

As this paper is improving the previous IoT-based system for mushroom cultivation proposed by Ariffin et al. (2020) and Ariffin et al. (2021), comparisons of features and specifications are presented in Table 3.

The first two designs in 2020 and 2021 were for a mushroom house, and the oyster mushroom cultivations were for small, home business purposes. The design for the proposed Smart Portable Farming system was scaled down and revamped to cater for

Table 3
Summary of improved features and specifications compared to Ariffin et al., 2020 and Ariffin et al., 2021

No	Features / Specification	(Ariffin et al., 2020)	(Ariffin et al., 2021)	Portable IoT-Based Smart System
1.	Platform	Arduino NodeMCU	Arduino NodeMCU	Raspberry Pi 4
2.	Microcontroller Logic	Threshold-based Logic	Fuzzy Logic	Threshold-based Logic
3.	Power & Connection	Two 5V External power sources and connection were via Breadboard	Single External power source powering the NodeMCU Baseboard with 5V voltage regulator	Single External power source
4.	Rack Arrangement	Vertical arrangement	Horizontal arrangement to allow optimal airflow and to avoid wetting the mushroom block during rainfall	Do not use a rack
5.	Water Nozzle Placement	The nozzle was not installed to spray the roof	Installed nozzle to spray water on the roof	Using Humidifier
6.	Portability	No	No	Yes
7.	Operating Size	Large, Fixed Mushroom House	Large, Fixed Mushroom House	Small and Lightweight
8	Harmful Gas Detection	No	No	Able to Detect

portability. Another feature is harmful gas detection was also added to the system to optimize plant yield further. Figure 9 shows that the IoT system sends an alert when harmful gas is detected.

System Implementation

It discusses how the Smart Portable Farming Kit for oyster mushroom cultivation system was implemented in Universiti Teknologi MARA as a proof of concept and to validate its functionality via experiments.

Deployment of Portable IoT-Based Smart Mushroom Cultivation System

The proposed portable IoT-based smart mushroom cultivation system was implemented at the National Autism

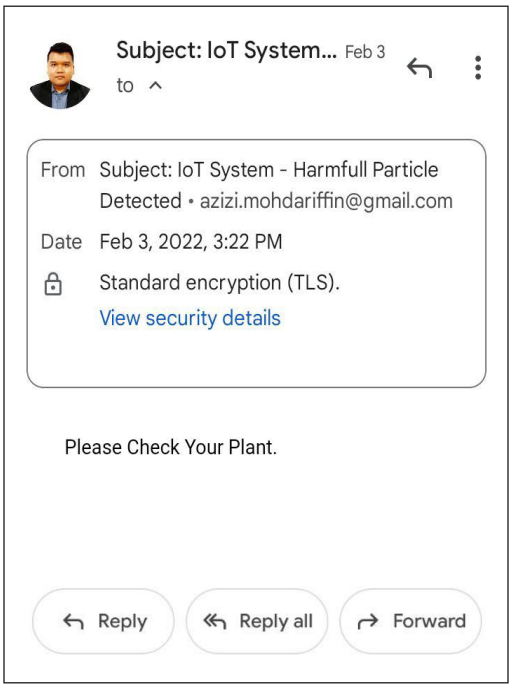

Figure 9. Harmful gas detection alert

Resource Centre (NARC), Faculty of Computer and Mathematical Sciences, Universiti Teknologi MARA (UiTM), Malaysia. The system was placed in an unused space inside the room equipped with a central air conditioner (only turned on in the daytime), and the windows are tinted and installed with sunlight shade. Thus, the room did not receive direct sunlight, and the temperature varied between 23°C and 30°C. Figure 10 shows the IoT-based portable system deployment in UiTM.

Figure 10 shows that the oyster mushroom growing block or medium was placed in Part B (middle) of the housing, with the exposed part of the block placed at the corresponding hole, which went into Part A (top). The oyster mushroom grew in Part A, where the system automatically monitored and regulated the environment . The humidifier used to regulate the humidity was placed inside Part A with DHT22 and MQ135 sensors. Figure 11 shows that the humidifier is turned on. The 8MP mini camera was placed at the top overlooking Part A to ensure a clear view of the growth of the oyster mushroom.

Figure 10. Portable system deployment in Universiti Teknologi MARA

Figure 11. Humidifier operation

Meanwhile, Figure 12 shows the side of the housing with an open cover. The Raspberry Pi 4 with relay and other electronic components were inside part B. The mushroom block was placed vertically inside Part B. Figure 12 also shows that Part C can store other miscellaneous items, such as power extension.

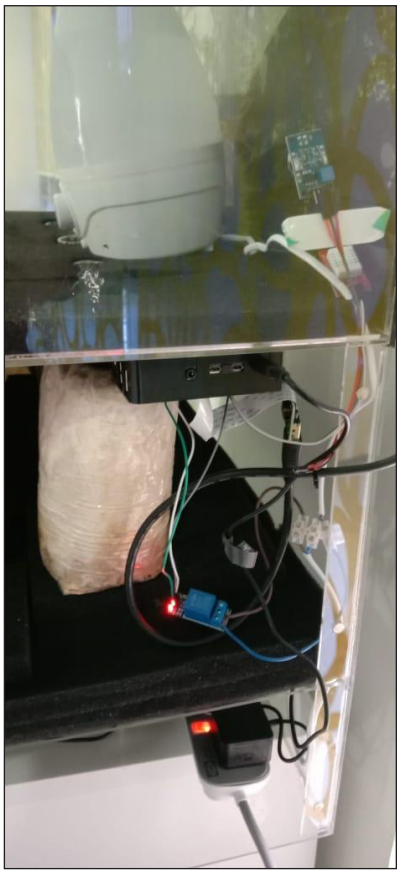

Figure 12. Raspberry Pi 4 platform and sensors for the portable system

System Testing and Evaluation

Two oyster mushroom cultivation experiments were set up simultaneously inside a room in the National Autism Resource Centre (NARC), Faculty of Computer and Mathematical Sciences, Universiti Teknologi MARA (UiTM), Malaysia, to test and evaluate the effectiveness of the proposed system. Both cultivation setups used eight mushroom medium blocks, and the duration of the experiments was one week. The first experiment was the controlled experiment where the oyster mushroom was cultivated without the IoT-based system. Figure 13 shows the setup for the controlled experiment. Based on Figure 13, a wet towel was used to keep the controlled environment humid. The towel was changed and soaked with water every two days. An electronic thermometer was used to record the temperature and humidity of the control experiment, and the value was recorded daily throughout the one week of experimenting.

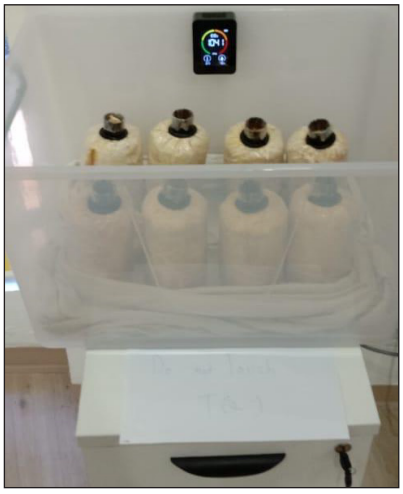

Figure 13. Control experiment setup

Meanwhile, the second experiment used the proposed Smart Portable Farming Kit. The first and second experiments were placed in the same room, as seen in Figure 14. At the end of a week, the oyster mushroom yield weight was measured quantitatively using a digital weighing device, and the quality of the oyster mushroom produced was verified qualitatively using visual inspection. Besides that, the pattern of the temperature and humidity recorded for one week will be compared between the two experiments.

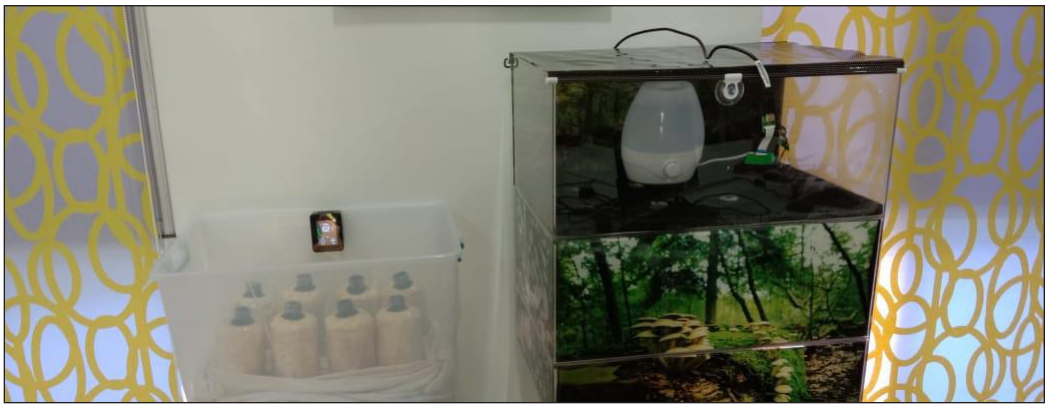

Figure 14. Control and IoT-based experiments in the same room

RESULTS AND DISCUSSION

Comparisons of the control experiment and SPFK were made based on four parameters:

(i) Temperature
(ii) Humidity
(iii) Weight of mushroom yield
(iv) Quality of mushroom yield

Temperature and Humidity Control

Figures 15 and 16 show the average temperature and humidity monitored for seven days. The temperature and humidity readings were taken three times a day, specifically at 10.00 am, 3.00 pm, and 8.00 pm from 17 to 23 March 2022 and were then averaged.

The line graph in Figure 15 shows that the average temperature is lowermost days in the SPFK as the temperature was kept at the preferred value for cultivation between 28°–30°C.

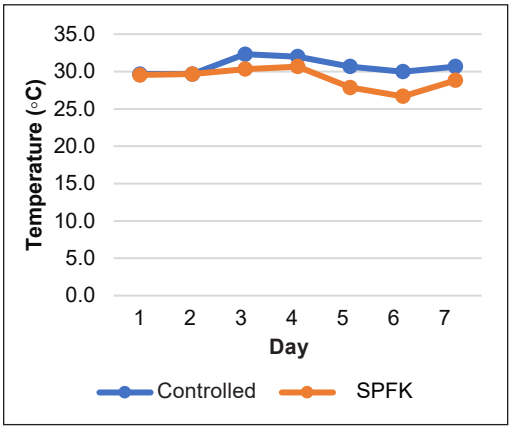

Figure 15. Comparisons of average temperature of controlled and Smart Portable Farming (SPFK)

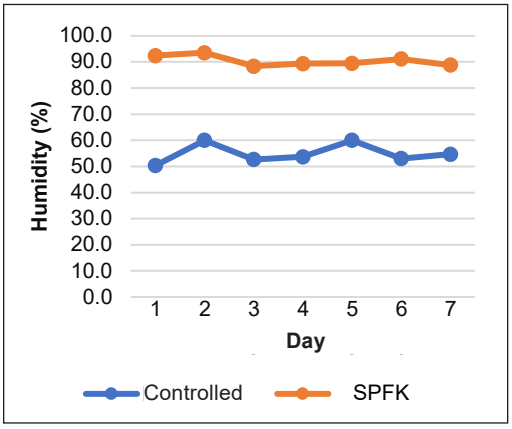

Figure 16. Comparisons of average humidity of controlled and Smart Portable Farming (SPFK)

The temperature of the controlled experiment averages slightly above 30°C depending on the weather. A check at AccuWeather (2022) recorded the lowest temperature of 24°C and the highest temperature of 35°C during the stated week. The temperature of the control setup was higher because it was placed in a closed room, and the central air conditioner was turned on for an average of only four hours during the daytime.

The average humidity in March 2022, as reported in Weather (2022), was 77%. The humidity readings for the stated week in March for the SPFK, as shown in Figure 16, range from a minimum of 78.5% to a maximum of 97.7%. The humidity was kept within the optimum range of cultivation (Cikarge & Arifin, 2018) between 80% to 90%. However, the humidity recorded by the controlled experiment was as low as 47% and highest at 71%. The air conditioning caused the low humidity readings, which are known to reduce humidity levels.

Weight of Mushroom Yield

Three mushroom yield cycles were recorded from the SPFK and the control setup. One cycle took seven days, beginning with taking off the medium block cover and harvesting the mushroom. Table 4 shows the weight of the oyster mushroom's yield.

Table 4
Percentage of mushroom yield difference

Date	Weight (gm)		Difference (gm)	Difference (%)
	Smart Portable Farming Kit	Controlled Setup		
24 March	584	428	156	26.7
4 April	200	0	200	100.0
27 April	167	152	15	8.98

In the first cycle, 584gm of oyster mushroom was harvested compared to 428gm for the controlled setup. The SPFK produced 26.7% more yield, equivalent to 156gm. For the second cycle, 200 grams were collected from SPFK, while the controlled setup failed to produce any yield. The third cycle harvested from the same eight mushroom blocks only produced 167gm for the SPFK and 152gm for the controlled setup. The proposed SPFK still produced higher mushroom yields of 8.98% (15gm) compared to the controlled setup. These results demonstrate that SPFK facilitates maintaining and controlling the environmental requirement for better mushroom cultivation.

Quality of Mushroom Yield

In the Malaysian Standard of mushroom quality (MS 2515: 2012) by FAMA (2012), the grade specification for oyster mushrooms is divided into premium grades, Grades 1 and 2, as detailed in Table 5. For premium grade, if the percentage of freshness, size

uniformity, matureness and defect of the mushroom is above 95%, the mushroom's grade is considered premium. Furthermore, if the damage is less than 3%, the pile of mushrooms is categorized as a premium class. A pile of mushrooms is classified as Grade 1 when the freshness, matureness and non-damages are above 95%. While the size uniformity must be at least 90%, and the defect percentage must be less than 10%. The third class of Grade 2 is required to attain freshness, uniformity of matureness and non-defect of above 90%. Meanwhile, the mushroom must have more than 80% of size uniformity, and less than 5% of the mushrooms be damaged.

Table 5
Oyster mushroom grade specification by FAMA, Malaysia

Grade	Specification	Criteria	Tolerance (%)
Premium	Oyster mushrooms in this class must have a uniformity of size and maturity, fresh and clean, and free of defects and damage	Fresh	≤5
		Size uniformity	≤5
		Uniformity of matureness	≤5
		Defect	≤5
		Damage	≤3
1	Oyster mushrooms in this class must have a uniformity of size and maturity, fresh and clean, and free of defects and damage	Fresh	≤5
		Size uniformity	≤10
		Uniformity of matureness	≤5
		Defect	≤10
		Damage	≤5
2	Oyster mushrooms in this class must have a uniformity of size and maturity, fresh and clean, and be unobvious of defects and damage	Fresh	≤10
		Size uniformity	≤20
		Uniformity of matureness	≤10
		Defect	≤10
		Damage	≤5

Based on Figure 17, the mushroom produced from SPFK displays all characteristics of Premium grade. The freshness, size uniformity and matureness uniformity are above

Figure 17. Mushroom yields by SPFK (left) and controlled setup (right)

95%. Only 5% of mushroom defects and less than 3% damage are observed in one pile of mushrooms.

Furthermore, research done by Khan et al. (2016) highlighted that the quality of mushrooms could be measured based on physic-chemical analysis (moisture, protein, and sensory evaluation). Therefore, we focus on the sensory evaluation based on texture and manual observation. The texture of the mushroom from the SPFK was better, and the size was larger than the control system. It can be concluded that the SPFK produces higher quality mushrooms compared to the controlled system.

CONCLUSION

This paper proposed a design of a Smart Portable Farming Kit to ease oyster mushroom cultivation in the urban area. Up to the writing, the most portable smart farming system used Arduino-based IoT setups and did not consider harmful gases in the air, such as CO_2. In our SPFK, we used the Raspberry Pi 4 platform to process the sensor data such as temperature, humidity and air quality value stored in the MYSQL database. Our design also incorporates aesthetic elements because the portable system will be used indoors. Unlike the common usage of sprinkler that requires water pumps to regulate the humidity, our SPFK utilized a humidifier that simplifies maintenance and provides a much more pleasant visual misty effect. Moreover, SPFK was also installed with a webcam and dashboard for a better UI/UX experience for the users. The dashboard can display the sensor data and real-time camera feed to enable the user to monitor their plant remotely. The design of a portable smart farming system for indoor use needs to be compact, pleasant-looking, and lightweight. We have detailed the designs by presenting the overall system architecture, physical arrangement, system circuit, control system flowchart, fuzzy algorithm pseudocode, and the user interfaces to be used as guidelines.

To demonstrate SFK effectiveness, the mushroom yields of SFK and the conventional method setup were presented, and a cumulative of 951gm and 580gm of oyster mushroom was collected over three cycles, respectively. Overall, SFK has been shown to produce more than 39% oyster mushrooms compared to the conventional method. However, SFK has more room for improvement and can be refined with more features. Since the deployment system was conducted in Malaysia, the system has only been tested in a tropical climate with constant indoor temperatures. Our next step is to investigate the performance of SFK in different climates and explore other technologies to add more features, such as image recognition or using artificial intelligence techniques to automatically track the mushroom's growth phase based on the live camera feed. There are also some limitations to the evaluations of SFK's performance. Due to time allocation, and financial resources, only sixteen mushroom blocks are used in this study, and the results of mushroom yield are based on three times of cultivation. More cycles should be done over a longer period to test the robustness of SFK.

ACKNOWLEDGEMENT

The authors thank Universiti Teknologi MARA, Malaysia, for providing a research grant (100-TNCPI/INT 16/6/2 (039/2021)) to complete this project.

REFERENCES

AccuWeather. (2022, June 6). AccuWeather, Shah Alam, Selangor. https://www.accuweather.com/en/my/shah-alam/230464/june-weather/230464

Ahmmad, S. N. Z., Jaafar, M. M., Muchtar, F., & Yusof, M. A. (2020). Automated gardening portable plant using IoT. *International Journal of Advanced Trends in Computer Science and Engineering*, *9*(1.1), 205-211. https://doi.org/10.30534/ijatcse/2020/3691.12020

Almalki, F. A., Soufiene, B. O., Alsamhi, S. H., & Sakli, H. (2021). A low-cost platform for environmental smart farming monitoring system based on IoT and UAVs. *Sustainability, 13*(11), Article 5908. https://doi.org/10.3390/SU13115908

Antonaci, L., Atieno, I., Baoua, I., Chotard, S., Difrancesco, P., Gayford, M., Goetschal, N., Hamadoun, M., Herwanger, N., Hoffine, T., Hohfeld, L., Hoover, S., Husain, A., Hussein, P., Jama, A., Jayasekaran, D., Joud, D., Kabuyaya, J., Khosravi, A., … & Verstraeten, R. (2022). *Global Report on Food Crises*. Food Security Information Network.

Ariffin, M. A. M., Ramli, M. I., Amin, M. N. M., Ismail, M., Zainol, Z., Ahmad, N. D., & Jamil, N. (2020). Automatic climate control for mushroom cultivation using IoT approach. In *2020 IEEE 10th International Conference on System Engineering and Technology (ICSET)* (pp. 123-128). IEEE Publishing. https://doi.org/10.1109/ICSET51301.2020.9265383

Ariffin, M. A. M., Ramli, M. I., Zainol, Z., Amin, M. N. M., Ismail, M., Adnan, R., Ahmad, N. D., Husain, N., & Jamil, N. (2021). Enhanced IoT-based climate control for oyster mushroom cultivation using fuzzy logic approach and NodeMCU microcontroller. *Pertanika Journal of Science and Technology*, *29*(4), 2863-2885. https://doi.org/10.47836/PJST.29.4.34

Ballais, L. J., Sharma, T. N., Thu, H. W., Sanadeera, S. D. A. P., Taparugssanagorn, A., & Dailey, M. N. (2021). IoT-Based terrace farming system for cities. In *25th International Computer Science and Engineering Conference (ICSEC)* (pp. 11-16). IEEE Publishing. https://doi.org/10.1109/ICSEC53205.2021.9684609

Baqer, N. S., Mohammed, H. A., & Albahri, A. S. (2023). Development of a real-time monitoring and detection indoor air quality system for intensive care unit and emergency department. *Signa Vitae*, *19*(1), 77-92. https://doi.org/10.22514/sv.2022.013

Cikarge, G. P., & Arifin, F. (2018). Oyster mushrooms humidity control based on fuzzy logic by using Arduino ATMega238 microcontroller. *Journal of Physics: Conference Series, 1140*, Article 012002. https://doi.org/10.1088/1742-6596/1140/1/012002

Cruz-del Amen, J. d., & Villaverde, J. F. (2019). Fuzzy logic-based controlled environment for the production of oyster mushroom. In *2019 IEEE 11th International Conference on Humanoid, Nanotechnology, Information Technology, Communication and Control, Environment, and Management, HNICEM 2019* (pp. 1-5). IEEE Publishing. https://doi.org/10.1109/HNICEM48295.2019.9072902

FAMA. (2012). *Kualiti Cendawan Tiram Kelabu MS2515:2012* [Oyster Mushroom Quality Malaysia Standard MS2515:2012]. Federal Agricultural Marketing Authority. https://www.fama.gov.my/documents/20143/0/cendawan+red.pdf/63676187-392a-48ce-4405-6d4090cb5568?fbclid=IwAR2YUzItHgpd6zhCs0BaoFaIttLRhkXOKySrrym6j9o6DpH1-G7my7p3eo

Hendrawan, Y., Anta, D. K., Ahmad, A. M., & Sutan, S. M. (2019). Development of fuzzy control systems in portable cultivation chambers to improve the quality of oyster mushrooms. *IOP Conference Series: Materials Science and Engineering*, *546*(3), Article 032013. https://doi.org/10.1088/1757-899X/546/3/032013

Ibrahim, N. H. N., Brahim, A. R., Mat, I., Harun, A. N., & Witjaksono, G. (2018). IR 4.0 using IoT and LORAWAN to accelerate lentinula edodes growth. In *2018 2nd International Conference on Smart Sensors and Application, ICSSA 2018* (pp. 28-32). IEEE Publishing. https://doi.org/10.1109/ICSSA.2018.8535954

Jamaludin, N., Mohammed, N. I, Khamidi, M. F., & Wahab, S. N. A. (2015). Thermal comfort of residential building in Malaysia at different micro-climates. *Procedia-Social and Behavioral Sciences*, *170*, 613-623. https://doi.org/10.1016/j.sbspro.2015.01.063

Jayasekara, C., Banneka, S., Pasindu, G., Udawaththa, Y., Wellalage, S., & Abeygunawardhane, P. K. W. (2021). Automated crop harvesting, growth monitoring and disease detection system for vertical farming greenhouse. In *ICAC 2021 - 3rd International Conference on Advancements in Computing, Proceedings* (pp. 228-233). IEEE Publishing. https://doi.org/10.1109/ICAC54203.2021.9671074

Kassim, M. R. M., Mat, I., & Yusoff, I. M. (2019). Applications of internet of things in mushroom farm management. In *2019 13th International Conference on Sensing Technology (ICST)* (pp. 1-6). IEEE Publishing. https://doi.org/10.1109/ICST46873.2019.9047702

Khan, S. H., Rani, S., Shah, A. S., Javeria, S., Hasham, M., & Amin, S. (2016). Quality evaluation of oven dried and fresh oyster mushroom store at room temperature. *The Open Agriculture Journal*, *1*(1), 18-22.

Laborde, D., Martin, W., & Vos, R. (2021). Impacts of COVID-19 on global poverty, food security, and diets: Insights from global model scenario analysis. *Agricultural Economics*, *52*(3), 375-390. https://doi.org/10.1111/AGEC.12624

Mat, I., Kassim, M. R. M., Harun, A. N., & Yusoff, I. M. (2019). Smart agriculture using internet of things. In *2018 IEEE Conference on Open Systems (ICOS)* (pp. 54-59). IEEE Publishing. https://doi.org/10.1109/ICOS.2018.8632817

Najmurrokhman, A., Kusnandar, Daelami, A., Nurlina, E., Komarudin, U., & Ridhatama, H. (2020). Development of Temperature and humidity control system in internet-of-things based oyster mushroom cultivation. In *2020 3rd International Seminar on Research of Information Technology and Intelligent Systems (ISRITI)* (pp. 551-555). IEEE Publishing. https://doi.org/10.1109/ISRITI51436.2020.9315426

Nasution, T. H., Yasir, M., Fahmi, & Soeharwinto. (2019). Designing an IoT system for monitoring and controlling temperature and humidity in mushroom cultivation fields. In *2019 International Conference on Electrical Engineering and Computer Science (ICECOS)* (pp. 326-331). IEEE Publishing. https://doi.org/10.1109/ICECOS47637.2019.8984446

Rajermani, T., Sarasvathi, N., & Eng, J. H. (2020). Smart vertical farming using IoT. *Inti Journal*, *2020*(49), 1-6.

Rankothge, W., Kehelella, P., Perera, D., Kanchana, B., Madushan, K., & Peiris, R. (2022). IOT based smart

microgreen sprouter. In K. Arai (Ed.), Proceedings of the Future Technologies Conference (FTC) 2021. Lecture Notes in Networks and Systems, (Vol 358, pp. 321-329). Springer. https://doi.org/10.1007/978-3-030-89906-6_22

Rosmiza, M. Z., & Hussin, J. M. (2017). Kecenderungan penglibatan agropreneur dalam industri tanaman cendawan di Johor [Agropreneurs' inclination to participate in the Johor mushroom industry]. *Malaysian Journal of Society and Space*, *13*(4), 37-46. https://doi.org/10.17576/GEO-2017-1304-04

Rosmiza, M., Davies, W., Aznie, R. C., Jabil, M., & Mazdi, M. (2016). Prospects for increasing commercial mushroom production in Malaysia: Challenges and opportunities. *Mediterranean Journal of Social Sciences*, *7*(1 S1), 406-415. https://doi.org/10.5901/MJSS.2016.V7N1S1P406

Rudolfsen, I. (2020). Food price increase and urban unrest: The role of societal organizations. *Journal of Peace Research, 58*(2), 215-230. https://doi.org/10.1177/0022343319899705

Saad, M. H. M., Hamdan, N. M., & Sarker, M. R. (2021). State of the art of urban smart vertical farming automation system: Advanced topologies, issues and recommendations. *Electronics, 10*(12), Article 1422. https://doi.org/10.3390/electronics10121422

Salim, S. A., Alaa, M., Yusof, Z. M., Ibharim, L. F. M., Salim, S. H., & Hashim, F. (2019). Urban farming activities in Southeast Asia: A Review and future research direction. *MATEC Web of Conferences*, *266*, Article 02010. https://doi.org/10.1051/MATECCONF/201926602010

Shakir, A. A., Hakim, F., Rasheduzzaman, M., Chakraborty, S., Ahmed, T. U., & Hossain, S. (2019). Design and implementation of SENSEP ACK: An IoT based mushroom cultivation monitoring system. In *2019 International Conference on Electrical, Computer and Communication Engineering (ECCE)* (pp. 1-6). IEEE Publishing. https://doi.org/10.1109/ECACE.2019.8679183

Sutono, & Lorena, B. R. G. S. (2020). Portable farming. *IOP Conference Series: Materials Science and Engineering*, *879*, Article 879. https://doi.org/10.1088/1757-899X/879/1/012099

Tan, E. K., Chong, Y. W., Niswar, M., Ooi, B. Y., & Basuki, A. (2020). An IoT platform for urban farming. In *Proceedings. 2020 International Seminar on Intelligent Technology and Its Application: Humanification of Reliable Intelligent Systems (ISITIA)* (pp. 51-55). IEEE Publishing. https://doi.org/10.1109/ISITIA49792.2020.9163781

Tarigan, Y. G., Chen, R. Y., Lin, H. C., Jung, C. Y., Kallawicha, K., Chang, T. P., Hung, P. C., Chen, C. Y., & Chao, H. J. (2017). Fungal bioaerosol exposure and its effects on the health of mushroom and vegetable farm workers in Taiwan. *Aerosol and Air Quality Research*, *17*(8), 2064-2075. https://doi.org/10.4209/AAQR.2016.09.0401

Terence, S., & Purushothaman, G. (2020). Systematic review of internet of things in smart farming. *Transactions on Emerging Telecommunications Technologies*, *31*(6), Article e3958. https://doi.org/10.1002/ETT.3958

Weather, A. (2022). *Shah Alam, Malaysia - Climate & Monthly weather forecast*. Weather Atlas. https://www.weather-atlas.com/en/malaysia/shah-alam-climate#humidity_relative

Zulqarnain, Man, N., Sharifuddin, J., Roslan, M., & Hassan, S. (2020). Factors influencing attitude towards technology adoption among permanent food production park (PFPP) program participants in West Malaysia. *Journal of Agricultural Science and Technology B*, *10*(2), 89-97. https://doi.org/10.17265/2161-6264/2020.02.004

Pertanika J. Sci. & Technol. 31 (4): 1755 - 1766 (2023)

PERTANIKA JOURNALS

SCIENCE & TECHNOLOGY

Journal homepage: http://www.pertanika.upm.edu.my/

Perception of the Current Situation of Urban Solid Waste in the Municipality of Quelimane, Mozambique

Rodrigo Florencio da Silva[1]*, Felizardo Bernardo Camões[2] and Alma Delia Torres-Rivera[3]

[1]Superior School of Mechanical and Electrical Engineering - ESIME Ticomán, Instituto Politécnico Nacional, Ticomán Ave. 600, Mexico City, Mexico
[2]Polytechnic University of Maputo, Paulo Samuel Kankhomba Ave., Maputo, Mozambique
[3]Interdisciplinary Professional Unit of Energy and Mobility, Instituto Politécnico Nacional, Instituto Politécnico Nacional Ave. 2508, Mexico City, Mexico

ABSTRACT

This paper analyzed the solid waste management process in the municipality of Quelimane, Mozambique. The methodology of this study is based on reviewing the scientific literature through fieldwork and observations on how urban solid waste management reaches its final destination. For that purpose, the population selected for this article was interviewed for a better perspective. As a result, it was possible to obtain answers that impacted the public management of the municipality since the level of attention to control depends on the location of the houses and also lacks a great deal of training for the workers who collect solid waste in the Quelimane region, along with awareness, environmental education programs for the population.

Keywords: Quelimane, Mozambique, sustainability, urban solid waste, waste management

ARTICLE INFO

Article history:
Received: 27 June 2022
Accepted: 20 September 2022
Published: 24 May 2023

DOI: https://doi.org/10.47836/pjst.31.4.09

E-mail addresses:
rflorencio@ipn.mx (Rodrigo Florencio da Silva)
felizardocamoes@hotmail.com (Felizardo Bernardo Camões)
atorresri@ipn.mx (Alma Delia Torres-Rivera)
* Corresponding author

INTRODUCTION

The economy of Quelimane, a municipality with a population of 349.842 inhabitants, relies on commerce, the fishing industry, and the storage of agricultural products (Moçambique, 2017). The city is considered vital for the region's development, and its natural conditions favor the growth of palm trees, orange and lemon trees, and other fruit varieties (Fews Net, 2014). It also has a maritime port, and the infrastructure is

ISSN: 0128-7680
e-ISSN: 2231-8526

adapted for the marine sailing of large-sized ships. Figure 1 shows the map of Mozambique and the location of Quelimane.

Figure 1. Map of Mozambique, Quelimane (Google Maps, 2022)

Taking as a point of reference some of the current weaknesses in the management and treatment of solid waste in the municipality of Quelimane, some alternatives are recommended to improve the collection and disposal of solid waste, as well as for the reduction of expenses related to the large labor force of the municipal public company that is responsible for providing services in Quelimane.

Firstly, the urban cleaning systems, together with the rupturing of the wastewater ducts, and storm drains, part of the essential sanitary services in Quelimane (Deutsche Welle, 2021), represent a high interest in public health and the preservation of the environment since they all guarantee a better quality of life for the people in the municipality.

Municipal authorities are responsible for urban waste management. Therefore, even though the rules have the legal scope of guaranteeing urban sanitary services based on the legal budget, there is a need to verify if the resources can deal with the burden of fulfilling the need to provide these essential services to the people and for health promotion purposes, for the local development, and a healthy town (Moçambique, 2008).

Many countries are facing managing urban solid waste problems. Africa is a continent where the challenges associated with waste management are high, and it is expected to worsen due to its high demographic growth (Kanhai et al., 2021). Mozambique is not an exception, as this problem arises in Quelimane. It is in addition to the risk of an inadequate capacity to collect and treat waste, which increases daily (Ayeleru et al., 2020). As a result, countries worldwide are striving to improve their solid domestic waste management practices since there will be an increase in the percentage of residues (Azevedo et al., 2021).

It is expected that, in the following 30 years, due to population growth, rapid urbanization, and economic growth, there will be a 70% increase in global waste, which means that 3.4 tons of residues will be generated per year (World Bank, 2022).

The unplanned growth of many cities caused by rapid urbanization has led to infrastructure challenges that exceeded the capacities of national and municipal governments to increase the levels of service in managing waste to keep up with the demand (Guerrero et al., 2013).

The people of Quelimane generate solid waste in homes, commerce, and industries and send it to the SWM plants (Villa et al., 2022). Based on the types of products they purchase, they conditioned the trash that must be presented at the voluntary delivery posts to be collected by the trucks and tractors intended solely for that purpose.

According to the UN report on Urban Solid Waste, around 99% of the goods purchased originally to be used by consumers will become waste after the first six months. It has been one of the main factors that have led to the increase in solid waste generated worldwide every year (IISD, 2018).

As a result, the urban cleaning systems to be implemented, operated, and maintained within the patterns require financial resources and community involvement.

The deposit of urban domestic and industrial solid waste in Quelimane is made outdoors due to a lack of a container. This problem began to reach extreme and alarming levels when the waste dumpsite was closed along the Quelimane Madal road in early 1997 (Moçambique, 2016). Due to the rural exodus, the population began to get closer to the cities to find better ways of life. In the last decades, due to rapid urban growth, the increase in the population (Das et al., 2019; Dos Muchangos et al., 2015) and its transformation, there was a spike in the generation of urban solid waste (Tan et al., 2014).

Therefore, the areas reserved to deposit solid waste, even though they did not have the conditions to manage it adequately, were occupied, thus generating new problems. The homes were close to the waste dumping sites, causing uncomfortable situations for those people. In addition to polluting the surrounding saltworks and mangroves, the proliferation of flies, mosquitoes, and disgusting odors, began to pose a risk to public health, especially in the area where the waste was deposited. These generated endemic diseases such as malaria, diarrhea, and cholera. Bad waste management leads to public health risks, environmental problems, and reduced quality of life, particularly among those most vulnerable (Kazuva & Zhang, 2019; Ziraba et al., 2016).

Currently, urban solid waste removal in Quelimane is deficient, and its management is differentiated. In paved neighborhoods and the central part of the city, trash is collected daily from the containers in the defined spots. In markets, garbage is collected three times a week, such as in the case of Brandão, Central, and Aeroporto markets. Smaller markets get their trash collected twice a week. Efficient urban solid waste management is an essential

issue in cities worldwide. However, this is particularly worse in developing countries due to rapid urbanization (Perteghella et al., 2020).

Depending on availability and mechanical conditions, waste transportation is done through trucks and tractors. The area chosen as a waste deposit in Quelimane is 5km away despite the precarious conditions (Moçambique, 2016). However, it is essential to mention that urban solid waste is dumped without any prior treatment, thus polluting the underground water sources in the area.

Due to the lack of space and the existing ideological and political conflict in Quelimane, opening a sanitary landfill is far from solving this problem.

The efficiency of solid waste management relies on how it is posed in the environmental, social, economic, and political spaces. Therefore, it requires establishing an efficiency guarantee in waste collection, treatment, and disposal (Fratta et al., 2019).

Abandoning the waste, significantly located next to the markets and suburban areas, together with the sewage system, obstructs solid waste management even more. Even though there was an increase in the efforts and awareness to implement solid waste management in African cities, this continues to be a chronic problem (Mbiba, 2014). However, sanitation services and solid waste management are among the services in developing countries that have received more noticeable attention through the United Nations Millennium Development Objectives (Tukahirwa et al., 2013).

Figures 2, 3, and 4 show this study's impact on the region and the people in the area, which has motivated the study of the situation.

As the generation of unsustainable amounts of solid waste increases worldwide, the concern for excessive consumerism and its consequences has increased significantly in the last decades (Da Silva, 2019). In addition to this, the few existing consumers are not enough to cover the entire city. The situation worsens even more with a population that does not respect the dates and times of voluntary waste delivery. As a result, they overfill the containers and incinerate trash in them, thus damaging their metallic structure.

Figure 2. Waste container in Quelimane

Figure 3. Broken glasses around the lake in Quelimane are used as a landfill

Even though solid waste management is an essential component of sustainability, it rarely gets any attention in most places (Burns et al., 2021). Waste deposits in mangroves are another factor that endangers life as well as the existing aquatic species in the area (Van Bijsterveldt et al., 2021), together with water pollution (Zeng et al., 2021), the sanitary situation of the populations which rely on these species, the local environment, and other related problems (Torell et al., 2012).

The main focalized problem in this study is the lack of sanitation associated with the inefficient solid waste management system. It is justified because Quelimane shows weakness as far as coverage of the urban solid waste sanitation system since the collection is concentrated more on certain regions with easier access. Hence, leaving the suburban area unprotected as far as trash collection is concerned, even though the people in those areas also pay the taxes. Nevertheless, solid waste management plays an important role (Tong et al., 2021; Chithra et al., 2016), and its correct application is motivated by international pressure in developed and undeveloped countries (Costa & Dias, 2020).

Figure 4. A man collecting reusable objects in Quelimane

Although plenty of regulations exist (Alzamora & Barros, 2020), compliance is still weak (Seror & Portnov, 2020). Also, to Bui et al. (2020), the lack of financial and human resources threatens the local management system, thus compromising the delivery of those essential services in Mozambique and many other parts of the world.

METHODOLOGY

The methodology in this research was based on three steps: literature revision, fieldwork and observation, and survey.

The first was based on the revision of scientific articles that report on the SWM in countries with the same issues as Mozambique, regulations, and laws from Mozambique

and Quelimane where the "state of the art" was determined. This research found the existing literature on solid waste management and the existing gaps in the matter, and this allowed the identification of the main theoretical and methodological obstacles to have a better understanding and analyze the Urban Solid Waste Management Bylaws (Decreto 94/2014, dated December 31, 2014) and the Hazardous Solid Waste Management Bylaws (Decreto 83/2014, dated December 2014), and to assess the weaknesses and the application of these legal documents.

The bibliographical revision contributed to obtaining information about the matter's current situation and the problems that are the subject of this research. It is to insert the investigation within a theoretical reference framework to explain why these problems are theoretical rather than generated or presented by a particular theory. However, even in the bibliographical revision stage, it proceeded to conduct a historical revision and track the evolution of waste management and its handling locally and worldwide in Mozambique and Quelimane since the establishment of local state authorities, powers, and/or entities.

A list of problems related to urban solid waste management was created and consulted in the different institutional documents and sanitation guides, reports and waste inventories, judicial actions, and sanitation guides in scientific publications to develop the survey for the municipal managers. In the case of the people of Quelimane, the intention was to collect information related to the awareness of waste management services provided by the municipal government.

The second stage was composed of fieldwork. It was conducted a thorough analysis of the object of the study. Contact was made with the local authorities, such as managers, town assembly members, and neighborhood secretaries in close contact with the municipal authorities and the administrators.

The municipal management of urban solid waste in Quelimane is done by the Municipal Sanitation Company, which is responsible for urban sanitation, collection, transportation, and final disposal of urban waste.

The interviews with the municipal administrators were done individually, and they all had management positions within the hierarchical municipal structure.

Before conducting the surveys and interviews, the purpose of the research was clarified. At this stage, it was possible to level the issues on sustainability and its terminology, and the list of problems was presented to the interviewed subjects. They were asked about their opinion and to point out the specific problems in Quelimane and identify other issues in case those were not on the list presented to them.

The third stage deals with the analysis of the results and the interpretation of the interviews. An intentional sample was selected, and people who worked directly in the Municipal Council and those most affected by the waste management problems were chosen. For this, 219 individuals of both sexes were selected and classified: Municipal

Council President/advisor (1), members of the Municipal Assembly (4), Chief of Urban Services of the Quelimane Municipal Council (1), Councilmember from sanitation and environmental affairs (1), Technician of the Municipal Sanitation Company (4), Non-government organizations where a member of each organization was chosen (4), and Administrators of the city of Quelimane (204), where two from the 51 existing neighborhoods were chosen.

The following elements to collect data were used within the research instrument: (1) observation sheets recorded the types of local solid waste deposited, the collection times, and the frequency, and (2) semi-structured interviews were adapted to exploit all verbalizations, including those with affective content. Interview guides were addressed to the administrators and the Public Entities and NGOs.

Interviews were directed to the following social role players: (1) Members of the Municipal Assembly, (2) Technicians of the Municipal Sanitation Company, (3) The Advisor of the Municipal Council President, and (4) Council Member on Sanitation and Environmental Affairs.

The objectives of the interviews contained the following aspects for each area:

(1) Municipal Council: To evaluate the urban solid waste management process in the town of Quelimane and get insight into the urban solid waste management public policies.

(2) Municipal Assembly: To verify the regulations' enforcement and the relations between the legislators or enforcers and the city administrators.

(3) The Municipal Sanitation Company: To verify the concept of environmental education adopted by the Municipal Sanitation Company to mobilize a social change of attitude and behavior, identify the educational and technical procedures for urban solid waste management, as well as to point out the restrictions that the transportation sector faces when collecting waste and the status of the infrastructure through the eyes of the technicians. Figure 5 shows an interview with the inhabitants of Quelimane.

The knowledge in the area of study was taken into consideration to select the parties that would be interviewed: A range of ages higher than 30 years old and the profession of the interviewed person.

Figure 5. Interview with inhabitants in Quelimane

RESULTS AND DISCUSSION

To analyze and interpret the data, three questions that were considered to be important in urban waste management were applied: the organizational structure of the Quelimane Municipal Council, the deposit sites of urban solid waste at the voluntary delivery posts, and economic and financial sustainability to provide basic services for the administrators in the city of Quelimane.

In the question regarding the structure of the Quelimane Municipal Council for urban solid waste management, the study tried to understand the responsibility of environmental sanitation in the town. This question was answered by the Public Branch, where two out of the four municipal council members answered that a company in Quelimane was created within the Municipal Council and is responsible for solid waste management. In contrast, of the four members of the Municipal Assembly, three have acknowledged the existence of the Municipal Sanitation Company, but they affirmed that the service provided to the population is deficient. It can also be highlighted that one member of the Municipal Assembly stated that he did not know of a company dedicated to solid waste management. If there were one, the city would not be filled with trash and foul odors.

Analyzing the answers of the four Assembly Members, it is possible to say that despite the divergence between the structure of solid waste management in Quelimane, they were unanimous when affirming that the town is facing many challenges and that the means available to the city are not sufficient to provide solutions to the real sanitation needs. Additionally, they emphasized that everyone working at the Municipal Sanitation Company requires training on the matter.

Regarding the existence of a voluntary solid waste deposit and the hours established for the delivery, the Advisor for the Municipal Council President stated that, most positively, the Municipal Council has sent efforts so that the trash is deposited in a safe place and that the current City Mayor of Quelimane was very adamant about ordering the construction of voluntary trash delivery posts in the areas where there were no containers. Nevertheless, the situation in the city needs to be analyzed holistically. The citizens of the town are not prepared to live in an urban environment, and many of them arrived during the armed period. They were living in the housing centers, and after that period, they did not return to their places of origin; they stayed in the suburban area. With the city expansion, these areas are part of the city, and the people still keep the bad habit of throwing trash irresponsibly.

The Advisor for the Municipal Council President talked about the trash reception hours that the municipality established in the period from 18–20h for trash reception but that the administrators never upheld the schedule. He also stated that people threw the trash when the trash collecting truck was about to collect the garbage and that many people from the town threw the garbage outside the container, thus making the job more difficult for the people in charge of the collection.

The third question concerns economic and financial sustainability in providing essential services for the administrators of Quelimane. Eight members of the Public Branch, four Municipal Council Members, and four Municipal Assembly Members agreed to say that the municipality gets money from the Central Government from the so-called autarchic compensation fund. They also stated that Quelimane has funded through the payment fees of trash collection, Mozambique's electrical energy, and water consumption.

Out of the 204 administrators that were interviewed about the trash collection fee, 150 answered that this fee does not satisfy the administrators since there are times when the garbage is not collected and that indigents light the containers on fire, that the collection favors the paved and easy to access areas, and there is no discount for the areas that are affected by the collection. The remaining 54 citizens said they did their part and deposited the trash in the allocated times and containers. However, they lack the human and material means to cover the entire city, and the town has to double the efforts to fulfill the population's basic needs.

With this study, it was possible to identify different problems related to urban solid waste management in Quelimane. Due to the lack of direction and the deficiencies in the legislation for urban sustainability, people in the area do not have the correct guidance and tools to follow a protocol that reduces solid waste generation, allowing sanitation promotion for a healthy town.

CONCLUSION

It was possible to verify that urban waste management in Quelimane poses a somber scenario regarding coverage in the provision of essential urban sanitation services, and solid waste collection in the paved areas was considered the most privileged in the suburban area.

The issues mentioned earlier are due to a lack of efficient management mechanisms and an organizational structure that responds to the expectations of the administrators. In addition, the voluntary delivery posts built in the neighborhoods were not enough since the waste should be separated before they were sent to landfills.

Regarding solid waste management, this study corroborated that the people who live in the central areas are more privileged regarding trash collection. In contrast, most people bury their trash in their backyards.

In the town of Quelimane, there is no landfill, and the trash is deposited outdoors, thus creating public health risks during the rainy season. The city suffers from diseases such as malaria, diarrhea, and cholera.

Also, in addition to the trash containers, it is common to find trash in abandoned lots where animals fight over food with indigent people.

It is essential to create a multisectoral technical group to aid the Municipal Council in creating action plans regarding urban solid waste management, train the Environmental

Municipal Sanitation Company workers, as well as to implement a monitoring system of urban solid waste management, its collection, treatment, transportation, and final destination. The participation of all actors to establish a correct SWM group, such as the government, waste collection companies, and the inhabitants, is required because the problem cannot be solved by only one of the actors. It is necessary to revise the regulations on fines and penalties for those who fail to dispose of the trash in the allocated places, revise the trash collection fee, and follow up on the correct usage of the resources obtained from it to create a management plan for urban solid waste for the people.

Finally, Quelimane needs a sanitary landfill that complies with current regulations so that it does not generate a risk to the health of its population, especially during heavy rains, since there is a high rate of malaria, cholera, and diarrhea in the region, which is fatal to the infected people. The results of this study are a precedent for the challenges that many regions in the world, such as Quelimane's, will face nowadays derived from social exclusion, intensive exploitation of natural resources, and the spiral of environmental degradation associated with water management.

ACKNOWLEDGEMENT

The authors thank the National Polytechnic Institute (IPN), and the Polytechnic University of Maputo for supporting the research, especially the people who participated in the interviews.

REFERENCES

Alzamora, B. R., & Barros, R. T. D. V. (2020). Review of municipal waste management charging methods in different countries. *Waste Management*, *115*, 47-55. https://doi.org/10.1016/j.wasman.2020.07.020

Ayeleru, O. O., Dlova, S., Akinribide, O. J., Ntuli, F., Kupolati, W. K., Marina, P. F., Blencowe, A., & Olubambi, P. A. (2020). Challenges of plastic waste generation and management in sub-Saharan Africa: A review. *Waste Management*, *110*, 24-42. https://doi.org/10.1016/j.wasman.2020.04.017

Azevedo, B. D., Scavarda, L. F., Caiado, R. G. G., & Fuss, M. (2021). Improving urban household solid waste management in developing countries based on the German experience. *Waste Management*, *120*, 772-783. https://doi.org/10.1016/j.wasman.2020.11.001

Bui, T. D., Tsai, F. M., Tseng, M. L., & Ali, M. H. (2020). Identifying sustainable solid waste management barriers in practice using the fuzzy Delphi method. *Resource Conservation and Recycling, 154*, Article 104625. https://doi.org/10.1016/j.resconrec.2019.104625

Burns, C., Orttung, R. W., Shaiman, M., Silinsky, L., & Zhang, E. (2021). Solid waste management in the Arctic. *Waste Management*, *126*, 340-350. https://doi.org/10.1016/j.wasman.2021.03.021

Chithra, K., Anilkumar, P. P., & Naseer, M. A. (2016). Municipal solid waste management, a major impacted sector of urban environment due to residential land use activities-study of Kozhikode City. *Procedia Environment Science, 35*, 110-118. https://doi.org/10.1016/j.proenv.2016.07.055

Costa, I. M., & Dias, M. F. (2020). Evolution on the solid urban waste management in Brazil: A portrait of the Northeast Region. *Energy Reports*, *6*, 878-884. https://doi.org/10.1016/j.egyr.2019.11.033

Da Silva, L., Prietto, P. D. M., & Korf, E. P. (2019). Sustainability indicators for urban solid waste management in large and medium-sized worldwide cities. *Journal of Cleaner Production*, *237*, Article 117802. https://doi.org/10.1016/j.jclepro.2019.117802

Das, S., Lee, S. H., Kumar, P., Kim, K. H., Lee, S. S., & Bhattacharya, S. S. (2019). Solid waste management: Scope and the challenge of sustainability *Journal of Cleaner Production*, *228*, 658-678. https://doi.org/10.1016/j.jclepro.2019.04.323

Deutsche Welle. (2021). *Varredoras de Quelimane: Trabalho arriscado e mal pago*. [Quelimane sweepers: Risky and poorly paid work]. https://www.dw.com/pt-002/varredoras-de-quelimane-trabalho-arriscado-e-mal-pago/g-57391972

Dos Muchangos, L. S., Tokai, A., & Hanashima, A. (2015). Analyzing the structure of barriers to municipal solid waste management policy planning in Maputo city, Mozambique. *Environment Development 16*, 76-89. https://doi.org/10.1016/j.envdev.2015.07.002

Fews Net. (2014). *Moçambique: Descrição das zonas de Formas de Vida* [Description of Life Forms zones]. Famine Early Warning Systems Network. https://fews.net/sites/default/files/documents/reports/MZ%20LHdescriptions%202013%20pt.pdf

Fratta, K. D. D. S. A., Toneli, J. T. D. C. L., & Antonio, G. C. (2019). Diagnosis of the management of solid urban waste of the municipalities of ABC Paulista of Brasil through the application of sustainability indicators. *Waste Management*, *85*, 11-17. https://doi.org/10.1016/j.wasman.2018.12.001

Guerrero, L. A., Maas, G., & Hogland, W. (2013). Solid waste management challenges for cities in developing countries. *Waste Management*, *33*, 220-232. https://doi.org/10.1016/j.wasman.2012.09.008

IISD. (2018, October 9). *UN urges tackling waste management on world habitat day. The International Institute for Sustainable Development*. https://sdg.iisd.org/news/un-urges-tackling-waste-management-on-world-habitat-day/

Kanhai, G., Fobil, J. N., Nartey, B. A., Spadaro, J. V., & Mudu, P. (2021). Urban municipal solid waste management: Modeling air pollution scenarios and health impacts in the case of Accra, Ghana. *Waste Management*, *123*, 15-22. https://doi.org/10.1016/j.wasman.2021.01.005

Kazuva, E., & Zhang, J. (2019). Analyzing municipal solid waste treatment scenarios in rapidly urbanizing cities in developing countries: The case of Dar es Salaam, Tanzania. *International Journal Environment Research Public Health*, *16*(11), Article 2035. https://doi.org/10.3390/ijerph16112035

Mbiba, B. (2014). Urban solid waste characteristics and household appetite for separation at source in Eastern and Southern Africa. *Habitat International*, *43*, 152-162. https://doi.org/10.1016/j.habitatint.2014.02.001

Moçambique. (2008). *Publicação Oficial da República* [Official Publication of the Republic]. http://www.portaldogoverno.gov.mz/por/content/download/3813/29186/version/1/file/BR+51+III+SERIE+SUPLEMENTO+3.pdf

Moçambique. (2016). *Conselho Municipal da Cidade de Quelimane: Relatório Anual de Actividades* [Quelimane City Council: Annual Activitities Report]. http://www.portaldogoverno.gov.mz/por/content/download/5565/39958/version/1/file/BR_46_III_SERIE_2016.pdf

Moçambique. (2017). *Instituto Nacional de Estadística* [National Institute of Statistics]. http://www.ine.gov.mz/operacoes-estatisticas/censos/censo-2007/censo-2017/divulgacao-os-resultados-preliminares-iv-rgph-2017/view

Perteghella, A., Gilioli, G., Tudor, T., & Vaccari, M. (2020). Utilizing an integrated assessment scheme for sustainable waste management in low and middle-income countries: Case studies from Bosnia-Herzegovina and Mozambique. *Waste Management*, *113*, 176-185. https://doi.org/10.1016/j.wasman.2020.05.051

Seror, N., & Portnov, B. A. (2020). Estimating the effectiveness of different environmental law enforcement policies on illegal C&D waste dumping in Israel. *Waste Management*, *102*, 241-248. https://doi.org/10.1016/j.wasman.2019.10.043

Tan, S. T., Lee, C. T., Hashim, H., Ho, W. S., & Lim, J. S. (2014). Optimal process network for municipal solid waste management in Iskandar Malaysia. *Journal of Cleaner Production*, *71*, 48-58. https://doi.org/10.1016/j.jclepro.2013.12.005

Tong, Y. D., Huynh, T. D. X., & Khong, T. D. (2021). Understanding the role of the informal sector for sustainable development of municipal solid waste management system: A case study in Vietnam. *Waste Management*, *124*, 118-127. https://doi.org/10.1016/j.wasman.2021.01.033

Torell, E., Redding, C. A., Blaney, C. L., Hernandez, E., Sison, O., Dyegula, J., & Robadue Jr. D. D. (2012). Population, health, and environment situational analysis for the Saadani National Park Area, Tanzania. *Ocean & Coast Management*, *66*, 1-11. https://doi.org/10.1016/j.ocecoaman.2012.05.005

Tukahirwa, J. T., Mol, A. P. J., & Oosterveer, P. (2013). Comparing urban sanitation and solid waste management in East African metropolises: The role of civil society organizations. *Cities*, *30*, 204-211. https://doi.org/10.1016/j.cities.2012.03.007

Van Bijsterveldt, C. E. J., van Wesenbeeck, B. K., Ramadhani, S., Raven, O. V., van Gool, F. E., Pribadi, R., & Bouma, T. J. (2021). Does plastic waste kill mangroves? A field experiment to assess the impact of macro plastics on mangrove growth, stress response and survival. *Science of the Total Environment*, *756*, Article 143826. https://doi.org/10.1016/j.scitotenv.2020.143826

Villa, F., Vinti, G., & Vaccari, M. (2022). Appropriate solid waste management system in Quelimane (Mozambique): Study and design of a small-scale center for plastic sorting with wastewater treatment. *Waste Disposal & Sustainable Energy, 4*, 49-62. https://doi.org/10.1007/s42768-022-00091-6

World Bank. (2022, February 11). *Solid waste management. The World Bank*. https://www.worldbank.org/en/topic/urbandevelopment/brief/solid-waste-management

Zeng, D., Chen, G., Zhou, P., Xu, H., Qiong, A., Duo, B., & Han, Z. (2021). Factors influencing groundwater contamination near municipal solid waste landfill sites in the Qinghai-Tibetan plateau. *Ecotoxicology and Environmental Safety*, *211*, Article 111913. https://doi.org/10.1016/j.ecoenv.2021.111913

Ziraba, A. K., Haregu, T. N., & Mberu, B. (2016). A review and framework for understanding the potential impact of poor solid waste management on health in developing countries. *Archives of Public Health*, *74*, Article 55. https://doi.org/10.1186/s13690-016-0166-4

Pertanika J. Sci. & Technol. 31 (4): 1767 - 1781 (2023)

PERTANIKA JOURNALS

SCIENCE & TECHNOLOGY

Journal homepage: http://www.pertanika.upm.edu.my/

Curve Fitting Using Genetic Algorithm and its Application in Craniofacial Reconstruction

Nurul Hafiza Rahamathulla and Md Yushalify Misro*

School of Mathematical Sciences, Universiti Sains Malaysia, 11800 USM, Gelugor, Pulau Pinang, Malaysia

ABSTRACT

A best-fit curve is required to reconstruct craniofacial fracture to ensure the preciseness of the reconstructed contour. A genetic algorithm (GA) is applied to get the best-fit curve in reconstructing the fractured part. This method provides a fast decision in obtaining suitable sets of control points to interpolate both boundary regions to form a reconstructed part without any try-and-error approach that requires altering the control points several times. The optimised sets of control points with different degrees of continuity are used to develop the reconstructed part using the quintic Bézier curve to generate a smooth curve. The best-fit curvature value of the quintic Bézier curve for each degree of continuity is compared, and the curve with the lowest absolute error of curvature is chosen as the inner and outer parts of the craniofacial fracture reconstruction.

Keywords: Best-fit curve, continuity Quintic Bézier curve, craniofacial reconstruction, genetic algorithm

INTRODUCTION

A curve is a line that does not need to be straight, and it is called a curved line (Adnan et al., 2020). Curves are commonly used in the alignment of road, railway, and highway design (Eliou et al., 2014; Misro et al., 2017). Two types of curves that are commonly used in computer graphics: the Bézier curve and the B-spline curve. Bézier and B-spline curves are similar in control points and degree of the curve, but a Bézier curve does not involve knot vectors. One of the applications of B-spline curves has been hand recognition (Ma et al., 2004), while the Bézier curve is suitable for reconstructing medical images (Abdel-Aziz et al., 2021; Amorim et al., 2020).

ARTICLE INFO

Article history:
Received: 27 June 2022
Accepted: 20 September 2022
Published: 24 May 2023

DOI: https://doi.org/10.47836/pjst.31.4.10

E-mail addresses:
nurulhafiza391@gmail.com (Nurul Hafiza Rahamathulla)
yushalify@usm.my (Md Yushalify Misro)
* Corresponding author

ISSN: 0128-7680
e-ISSN: 2231-8526

Curve fitting is a process of constructing a best-fit curve to a set of data points via interpolation technique. The approximation process of the data points is very difficult. Therefore, some researchers use artificial intelligence techniques (Loucera et al., 2014). Ueda et al. (2018) used a piecewise cubic Bézier curve to approximate the point cloud boundary using the curve fitting technique. Another important aspect that needs to be considered when combining all the data points through interpolation is curve continuity.

Continuity usually accompanies curve fitting, especially when constructing a smooth curve. Ibrahim et al. (2017) used curvature continuity to connect two quintic Bézier curves into a piecewise quintic Bézier curve before applying it on the road, while Adnan et al. (2020) used continuity with a suitable degree to connect the curves and construct the outline of key and spoon. Ibrahim et al. (2017) and Misro et al. (2018) used curvature information to estimate the maximum safe speed. Curvature is the value from which a curve deviates from being a straight line. In this research, the curvature value will be used to calculate the errors in a constructed curve.

Virtual craniofacial construction using computer vision technologies is arising, but the best-fit curve is required to reconstruct the original structure. Craniofacial is a medical term related to the skull and face bones. Craniofacial studies and treatments are important for congenital malformations or facial injuries. Craniofacial reconstruction is also a basic subject in plastic surgery, Chen et al. (2017) shares various experience of craniofacial reconstruction that relate to plastic surgery.

Craniofacial reconstruction is commonly used to reconstruct facial appearance based on the analysis of skull morphology, as mentioned in Lee & Shin (2020). Many researchers have applied various approaches to construct the missing parts of the craniofacial, such as performing craniofacial reconstruction using landmark points and skull face/(tissue) skin features.

A hybrid evolutionary computing scheme containing Particle Swarm Optimization (PSO) and Differential Evolution is performed to extract the feature point and landmark count reduction by Mansour (2020). An optimal solution of curve fitting can be evaluated using various optimisation methods. PSO is one of the optimisation methods used to obtain curve fitting by generating control points for NURBS (Adi et al., 2009).

Majeed et al. (2020) constructed the missing craniofacial parts in a 3D structure using 2D CT scan contours. They also constructed the surface using a bi-cubic rational Ball surface with C^2 continuity. Craniofacial reconstruction is also developed using Radial Basis Function and bootstrap error as in Ali et al. (2020). Majeed et al. (2022) also did a comparative study using an existing technique that uses a Bezier-like function to construct craniofacial reconstruction. Moreover, Moiduddin et al. (2020) used lightweight scaffolds in craniofacial reconstruction for facial implants, which was mentioned to be useful for orthopaedic and complicated surgical procedures.

METHODOLOGY

Bézier Curve

Bézier curve is a parametric curve given by Equation 1:

$$B(t) = \sum_{i=0}^{n} b_{i,n}(t)P_i \ , \qquad t \in [0,1] \tag{1}$$

where P_i represents the control points, and $b_{i,n}(t)$ is the basic functions of Bézier known as Bernstein basis polynomials of degree n. The polynomials coefficient is in Equation 2:

$$b_{i,n}(t)=\binom{n}{i} t^i \ (1-t)^{n-i} \quad i = 0, 1, \ldots, n \tag{2}$$

and the binomial coefficient is in Equation 3:

$$\binom{n}{i} = \frac{n!}{i!(n-i)!}. \tag{3}$$

Continuity

Continuity is important and helpful in creating a smooth curve. In this research, parametric continuity will be used. Parametric continuity is the simplest way to connect two or more curves. There are three degrees for parametric continuities, namely C^0, C^1, and C^2. Each degree of continuity has its geometric interpretation (Said et al., 2021; Ammad et al., 2022).

C^0 is a position continuity, the connecting point of two curves, where the endpoint of the first curve $B_L(t)$ is connected to the first point of the second curve, $B_R(t)$. Thus, by solving $B_L(1) = B_R(0)$, the C^0 continuity condition will be satisfied.

C^1 continuity is tangent continuity at a common point, requiring the C^0 continuity condition to be satisfied first. By solving $B_L(1) = B_R(0)$, and $B_L'(1) = B_R'(0)$, continuity condition of C^1 can be satisfied.

Second order continuity at the common point is called C^2 continuity. C^0 and C^1 need to be satisfied before applying the C^2 continuity condition. C^2 continuity can be achieved when solving $B_L(1) = B_R(0)$, $B_L'(1) = B_R'(0)$, and $B_L''(1) = B_R''(0)$.

Genetic Algorithm

GA is a class of search techniques inspired by evolutionary biology. GA is chosen because of its computational robustness in the metaheuristic method. Previously, researchers have employed GA in constructing the craniofacial parts, as discussed and mentioned in the introduction. The flexibility in GA that can set suitable parameters based on a particular scenario is the main reason why GA has become a favourite among researchers. In this research, GA is used in curve fitting to reconstruct craniofacial fracture parts using the quintic Bézier curve.

Figure 1 shows the process of GA. Firstly, sets of the initial population need to be generated. Then, each population will undergo selection, crossover, and mutation to create a set of new populations, and each new population's fitness value will be calculated. The process will be repeated until all the criteria are satisfied, then GA stops, and the best solution is obtained.

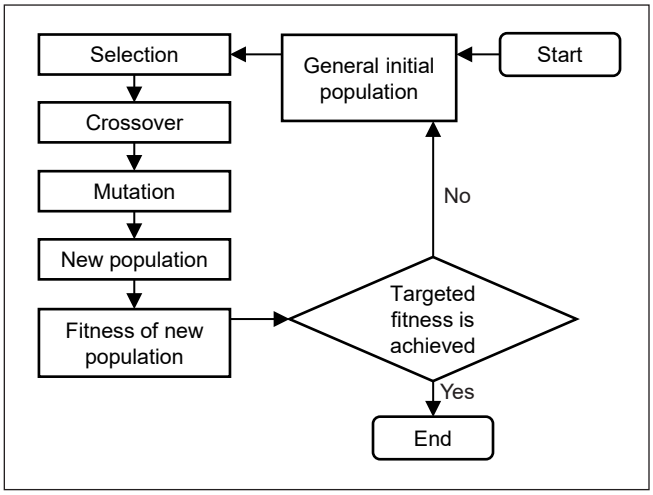

Figure 1. Flowchart of GA

Initial Population. The initial population in this research are set of coordinates to construct the fractured part. The number of coordinates or points (gene) in a solution (chromosome) depends on the degree of the Bézier curve. This research will reconstruct the fractured part using a quintic Bézier curve with degree five. Thus, a set of the solution has six coordinates $(P_0, P_1, \dots, P_5)$, while both boundary curves of the craniofacial skull use cubic Bézier curves.

Two types of the initial population used in this research are sets of C^0 and C^1 continuity solutions. These two types of curves will be used to develop the fractured part with different levels of smoothness. The set of coordinates for the initial population of C^0 continuity (P_0, P_5) and for C^1 continuity(P_0, P_1, P_4, P_5) can be determined using the idea of continuity from the previous discussion.

Therefore, the missing coordinates between these two initial populations were obtained randomly and optimised using GA, which involved four points for C^0 continuity and two points for C^1 continuity. The range of the *x*-coordinate and *y*-coordinate was set to ensure the random coordinates were still in the range set of solutions.

For the inner layer, the range of *x*-coordinates and *y*-coordinates of the control points for C^0 continuity is $x \in [152,180]$ and $y \in [155,157]$ respectively, while for C^1 continuity, the range of coordinates for the inner layer is $x \in [160,175]$ and $y \in [155,156]$. However, for the outer layer, the *x*-coordinates and *y*-coordinates of the control points for C^0 continuity are $x \in [150,190]$ and $y \in [160.5,164]$, while for curve with C^1 continuity, the range is $x \in [160,180]$ and $y \in [160.5,164]$.

Selection. Selection is a process of selecting parents to produce offspring. The total number of offspring must be equal to the original number of populations. Two solutions (parent) will be randomly selected for pairing. If there are *m* population, there will be *m/2* pairs of

parents when *m* is even. If *m* is odd, *n* odd numbers of solutions with the best fitness value will advance to the next without undergoing the remaining process. Since the number of offspring is required to be equal to the population, *(m-n)*/2 pairs of parents are needed to produce the solutions. The *(m-n)*/2 pairs of parents will be selected from *n* populations chosen to advance, as Carr (2014) suggested. In this study, 10 solutions (parent) will be generated before they undergo the crossover and mutation process.

Crossover. Crossover is an important phase in GA where variations of offspring are created by exchanging the parent's gene from the crossover point. In this research, the crossover process may provide better control points to construct a best-fit curve for the fractured part compared to the original solution. Crossover points are determined randomly in this research. Figure 2 shows the crossover process, where the orange line is the crossover point. Parents 1 and 2 contained a set of six coordinates (genes) each. During the crossover, the genes are exchanged between Parents 1 and 2. There will be 5 pairs of parents in this study as 10 populations are used; thus, these pairs will undergo the crossover process.

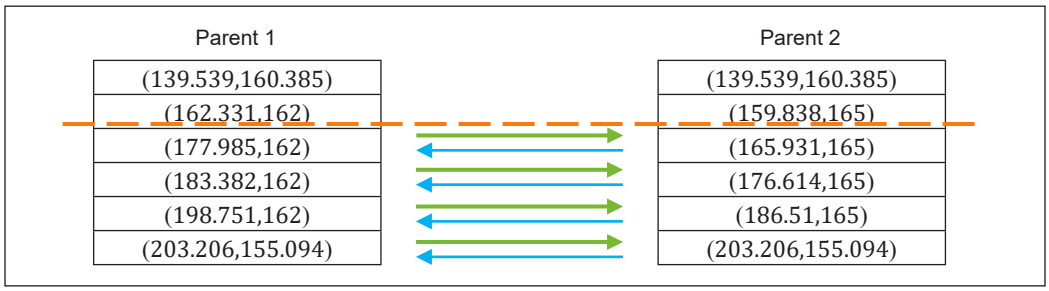

Figure 2. Crossover occurs

Mutation. The mutation is important to maintain the original population's diversity and prevent premature convergence. Premature convergence occurs when a set of coordinates (solution) with the best fitness value dominates the population. Mutation occurs in the new offspring, where two genes or coordinates will be switched. Figure 3 shows that the gene in positions two and four are switched when the mutation occurs.

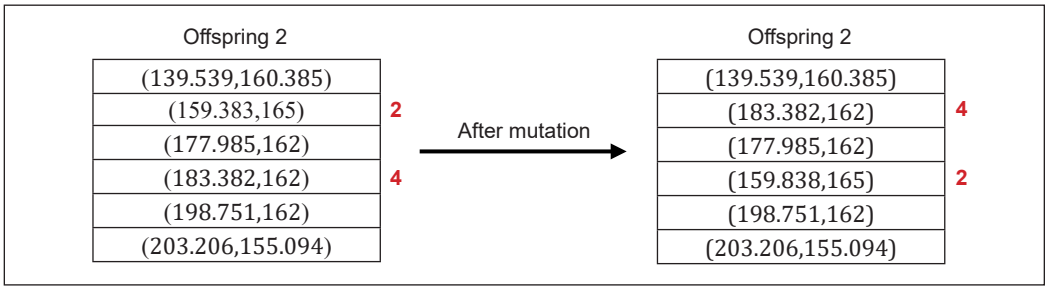

Figure 3. Mutation

Fitness Function. The fitness function is one of the crucial parts of GA. It determines the best solution compared to other solutions based on their fitness value. In this research, the fitness value of a solution will be determined using the arc length of the curve. The arc length of the curve will provide the total length of the curve. Thus, a smooth and shortest reconstructed part can be developed. Let a parametric curve $B(t) = (x(t), y(t))$ on the interval of $[a, b]$ has the length, s (Equations 4 and 5),

$$s = s(t) = \int_a^t \|B'(t)\| \, dt \tag{4}$$

where

$$\|B'(t)\| = \sqrt{x'(t)^2 + y'(t)^2} \, . \tag{5}$$

A good solution needs a good fitness value. The lower the arc length, the better the fitness value. Therefore, the solution with the lowest arc length will reconstruct the fractured part. Hence, the constructed curve does not overfit or wiggle.

Cubic-Quintic-Cubic Piecewise Continuity Curve

The reconstruction of craniofacial structure in this research involves connected curves between cubic (A_0, A_1, A_2, A_3) – quintic (P_0, P_1, P_2, P_3, P_4 and P_5) – cubic (B_0, B_1, B_2, B_3). The cubic curves or boundary curves regarded as Curve 1 and Curve 2 were constructed using the extracted data points from the craniofacial structure of the CT scan image. For a quintic curve, three different levels of continuity will be used to construct the fractured part, which are C^0, C^1 and C^2.

The first type of curve is the quintic Bézier curve with C^0 continuity, where the curve is connected to boundary Curves 1 and 2. Thus, the control points P_0 and P_5 are the same as A_3 and B_0 such that $A_3 = P_0$ and $P_5 = B_0$. Thus, the remaining 4 control points (P_1, P_2, P_3 and P_4) of the quintic Bézier curve will be determined and optimised using GA.

The second type of curve is the quintic Bézier curve with C^1 continuity. Thus, the first and last two control points of the quintic Bezier curve, which are P_0, P_1 and P_4, P_5 will connect with A_2, A_3, and B_0, B_1, respectively. Hence, fewer control points (P_2, P_3) must be generated and optimised using GA.

The third or last type of curve is the quintic Bézier curve with C^2 continuity. C^2 continuity requires 3 control points from the first curve to connect with another curve. Since the quintic Bézier curve is an intermediate curve between both boundary curves, 3 control points from each boundary curve are enough to construct a quintic Bézier curve with 6 control points. Hence, for this type of curve, the control points do not need to be generated or optimised using GA. Therefore, this type of curve will become this study's benchmark or indicative curve.

Curvature and Surface Curvature

The curvature of the constructed curve with C^0 and C^1 continuity will be compared with the C^2 continuity curve to determine the minimum error in curve fitting. Curvature of a Bézier curve $B(t) = (x(t), y(t))$ is given by Equation 6:

$$\kappa(t) = \frac{x'(t)y''(t) - y'(t)x''(t)}{(x'(t)^2 + y'(t)^2)^{\frac{3}{2}}}, \quad (6)$$

where the primes are the derivative for t.

Error in curvature is computed using the absolute error of the measured and model values of curvatures. The choice of the model value varies depending on the smoothness criteria. Assuming there is no prior record of the CT scan image of a patient's skull, the C^2 continuity curve will be chosen as our model curve and the measured value for this research is the curvature value of the quintic Bézier curve with C^0 and C^1 continuities (Equation 7).

$$\text{Absolute Curvature Error} = |\ \text{measured value} - \text{model value}\ | \quad (7)$$

RESULTS AND DISCUSSION

This research aims to obtain the best-fit curve using GA to reconstruct the craniofacial region. Figure 4 shows the original CT scan of a patient with a head injury from Majeed et al. (2015). The inner and outer layers of boundary curves are constructed as shown in Figure 5 using a cubic Bézier curve.

Normally, a CT scan is a diagnostic imaging procedure that uses a combination of X-rays and computer technology to produce images of the internal body part. Any body part, including the skull that undergoes a CT scan is a two-dimensional image representing a three-dimensional physical object. Therefore, the image of the skull can be imported into advanced computational software such as Mathematica to get the boundary points (data) of the fractured skull. Four data points from each opposite boundary are required to construct Curves 1 and 2 of the fractured part, respectively. The selected data points should produce curves aligned with the craniofacial structure on both sides, as shown in Figure 5.

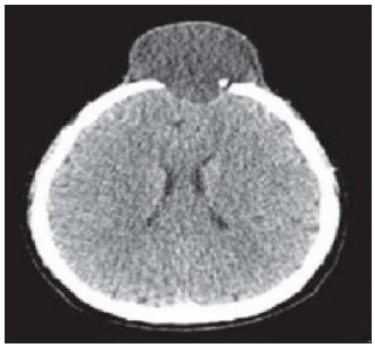

Figure 4. Original CT scan

Table 1 displays the values of the selected data points of Curves 1 and 2 of the outer and inner layers from Figure 5. Curves 1 and 2 of both layers act as boundary curves of the craniofacial region constructed using the cubic Bézier curve, where four control points

are required. The data points in Table 1 are used as control points, and the curve can be obtained using Equation 1 when n is 3.

Based on Figure 5(a), Curve 1 is cyan, while the green curve is Curve 2 of the outer layer. Then, from Figure 5(b), the blue curve is Curve 1, while the pink curve is Curve 2 of the inner layer. The curves only interpolate at the endpoints from Curves 1 and 2 of both layers. Curves 1 and 2 of both layers will be used in constructing the curve of missing parts with parametric continuity.

Table 1
Data points of outer layer and inner layer of boundary curves

Points	Data points
Curve 1 of outer layer (cyan)	((102.02,143.48), (113.25,153.34), (124.27,157.68), (142.38,160.39))
Curve 2 of outer layer (green)	((194.93,158.14), (210.40,154.61), (224.38,146.34), (229.46,136.81))
Curve 1 of inner layer (blue)	((115.81,142.56), (124.76,150.57), (135.58,154.33), (148.765,155.27))
Curve 2 of inner layer (pink)	((187.3,153.76), (201.28,150.79), (212.73,142.74), (222.05,131.72))

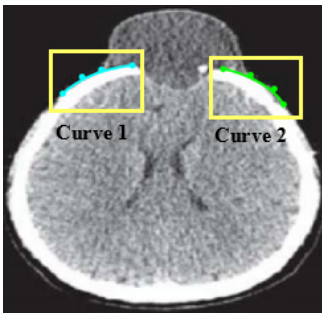

(a)

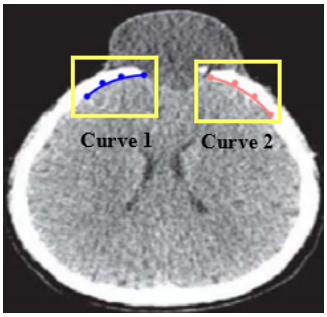

(b)

Figure 5. Positions of data points and Curve 1 and Curve 2 of (a) outer layer and (b) inner layer

Construction of the Missing Parts

In this research, the population size is 10, and the mutation rate is 0.5. The mutation rate is 0.5, which indicate that half of the offspring will undergo the mutation process, while the crossover process will occur only at any point between point 1 and 5 with the rates of 0.6 and 0.2 for C^0 and C^1 continuity, respectively. The optimised population were constructed using the quintic Bézier curve to reconstruct the craniofacial region. The smooth connectivity of the reconstructed part will be guaranteed by imposing the continuity conditions at both ends of the reconstructed part with boundary curves. The inner and outer curves are constructed in the same way, where the only difference is their data points.

Usually, researchers that applied GA in their studies will have a fixed set value of chromosomes and a population size that only differs in chromosome combinations. This population will undergo the GA process and could provide the best solution for each generation until the fitness value is converged. However, in this research, if the set value of the chromosome is fixed, there are only four genes for C^0 continuity and two different genes for C^1 continuity. It is because some of the points will stay the same even after imposing continuity conditions. Therefore, the solution will be very limited, and the geometric continuity will not be guaranteed. This study aims to automatically generate

the intermediate control points for the reconstructed curve, given the condition and limit range of the coordinates.

In this study, each population contains different sets of coordinates (chromosomes) with 6 control points for each chromosome. The remaining control points will be randomly generated and optimised using GA to complete the set of control points based on different types of continuity. Hence, the usual convergence graph is not available in this study.

Moreover, the lowest arc length from GA will be used as stopping criteria, and the GA is stopped when the quintic Bézier curve (reconstructed part) has a similar shape and lowest arc length value with the model curve value. It applies to both C^0 and C^1 continuities. The best-fit curvature value of the quintic Bézier curve for each degree of continuity is compared, and the curve with the lowest absolute error of curvature is chosen as the inner and outer parts of the craniofacial fracture reconstruction.

Quintic Bézier curve needs to get six control points (Table 2) to connect both Curve 1 and Curve 2 with C^2 continuity. Therefore, the quintic Bézier curve with C^2 continuity will be the model curve for the fractured part of the craniofacial region. C^2 continuity contains enough information to reconstruct the smooth fracture part. Next, the quintic Bézier curve with C^0 and C^1 continuity will be compared with the model curve.

A yellow curve in Figure 6(a) and 6(b) are the outer and inner layers of the quintic Bézier curve with C^2 continuity, where the control points are taken from Table 2. Figure 6(c) shows the model curve for the

Table 2
Control points of quintic Bézier curve with C^2 continuity

Layer		Control Points	Length
Outer layer	P_0	(142.38,160.39)	52.8980
	P_1	(153.25,162.02)	
	P_2	(166.24,163.15)	
	P_3	(175.93,160.96)	
	P_4	(185.65,160.26)	
	P_5	(194.93,158.14)	
Inner layer	P_0	(148.76,155.27)	38.6597
	P_1	(156.68,155.84)	
	P_2	(165.30,155.56)	
	P_3	(169.77,155.80)	
	P_4	(178.91,155.54)	
	P_5	(187.30,153.76)	

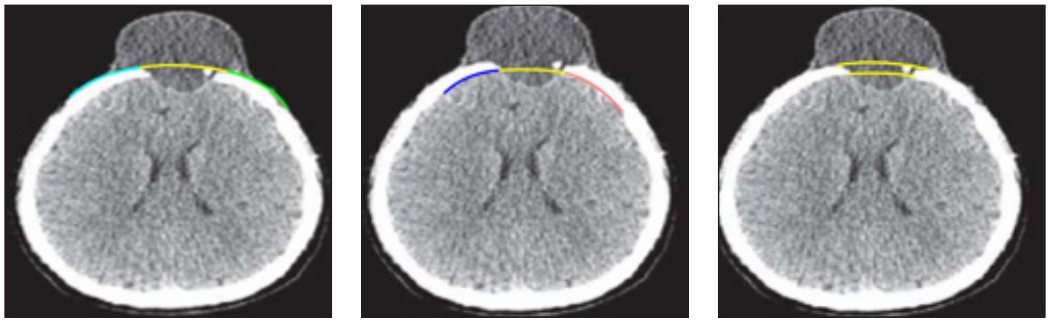

(a) (b) (c)

Figure 6. Quintic Bézier curve with C^2 continuity for (a) outer layer, (b) inner layer and (c) both layers

inner and outer layers of craniofacial, where the reconstructed part can smoothly reattach the fractured part.

Now, the quintic Bézier curve for the inner layer and outer layer is constructed with C^0 and C^1 continuity using GA where the optimisation occurs, while the quintic Bézier curve with C^2 continuity was constructed without any optimisation taking place.

Best Fit Curve Using Genetic Algorithm (GA)

A best-fit curve with C^0 continuity and C^1 continuity was acquired using GA for inner and outer curves. By implementing this technique, medical practitioners or surgeons do not have any obligation to manually figure out the exact position (data points) to patch the broken part, as GA will automatically provide the best set of coordinates for the quintic Bézier curve that has the lowest arc length compared to another set of coordinates.

The curve with C^0 continuity and C^1 continuity evaluated using GA will be compared with the model curve, the quintic Bézier curve with C^2 continuity from Figure 6(c) for the outer and inner layers. Tables 3 and 4 show the control points of the quintic Bézier curve for the outer and inner curves and their curve length with C^0 and C^1 continuity obtained using GA, respectively. The red curve in Figures 7 and 8 are quintic Bézier curves with C^0 and C^1 continuity constructed using the control points from Tables 3 and 4, respectively.

In Figure 9, quintic Bézier curves with C^0 and C^1 continuity (red curve) are compared with the model curve (yellow curve). Based on Figure 9, there is not much difference in

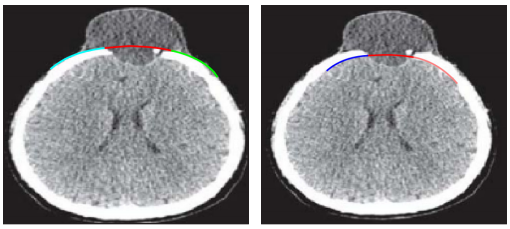

(a) (b)

Figure 7. Quintic Bézier curve with C^0 using GA for: (a) outer and (b) inner layers

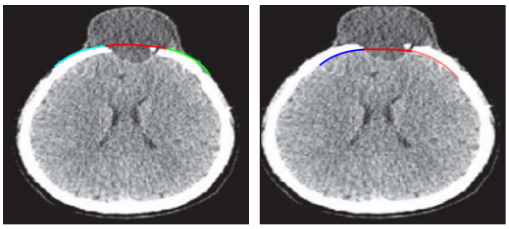

(a) (b)

Figure 8. Quintic Bézier curve with C^1 using GA for: (a) outer and (b) inner layers

Table 3
Control points and length of quintic Bézier curve with C^0 using GA

Outer Layer	Control points	((142.38,160.39), (170.07,162.60), (162.69,162.36), (163.88,160.52), (173.69,163.73), (194.93,158.14))
	Length	52.9327
Inner layer	Control points	((148.77,155.27), (154.29,155.65), (152.30,155.05), (163.06,156.39), (171.25,156.58), (187.30,153.76))
	Length	38.6781

Table 4
Control points and length of quintic Bézier curve with C^1 using GA

Outer Layer	Control points	((142.38,160.39), (163.18,162.54), (153.25,162.02), (178.06,161.01), (185.65,160.26), (194.93,158.14))
	Length	52.8443
Inner layer	Control points	((148.77,155.27), (156.68,155.84), (162.05,155.11), (178.91,155.54), (172.22,155.34), (187.30,153.76))
	Length	38.6218

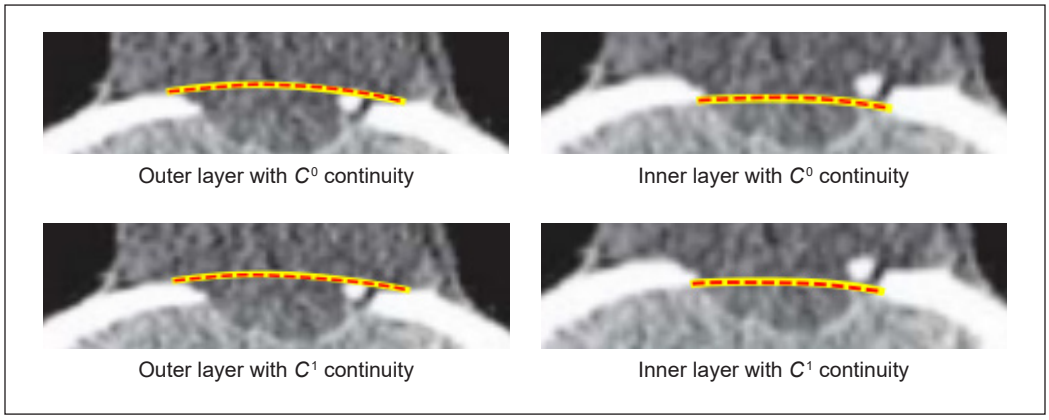

Figure 9. Overlapping of quintic Bézier curve with C^0 and C^1 continuity using GA (red) and model curve (yellow) of outer and inner layer

overlapping the red and yellow curves in both layers with C^0 and C^1 continuity. It shows that the control points obtained from GA provide a good fit curve, which is highly identical to the model curve.

Comparison of Errors in Curvature Between C^0, C^1 and C^2 Continuity

The curvature value of the best-fit curve with C^0 and C^1 continuity for both layers will be calculated. Then, the curvature error for each curve will be calculated and compared with the model curve (C^2) to determine which continuity gives the best curve for both layers.

Figures 10 and 11 show the curvature plot of the quintic Bézier curve with C^0, C^1 and C^2 continuity of outer and inner layers, respectively. The quintic Bézier curve with C^2 continuity (purple curve) in Figures 10 and 11 will be the indicator curve or benchmark curve used in this research, as the quintic Bézier curve with C^2 continuity preserves the geometric properties that are derived from boundary curves on both sides.

The curvature values from Tables 5 and 6 were used to calculate the absolute error at each t value using Equation 6. Based on Table 5, the highest error for the outer layer curve is between C^0 and C^2 continuity, where $t = 1.0$, while the lowest is between C^1 and

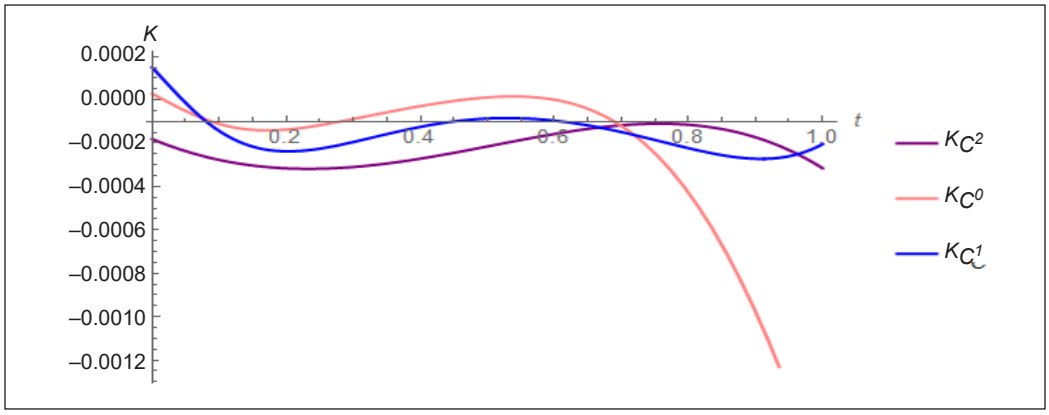

Figure 10. Quintic Bézier curve with C^0 and C^1 using GA for outer layers

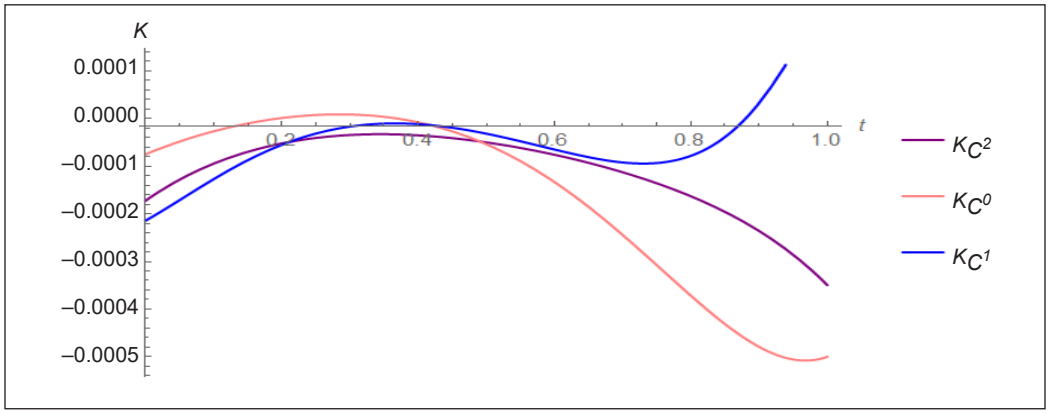

Figure 11. Quintic Bézier curve with C^0 and C^1 using GA for inner layers .

C^2 continuity, where $t = 0.6$. For the inner layer, the highest and lowest errors are between C^1 and C^2 continuity, where $t = 1.0$ and $t = 0.2$, respectively.

Based on Table 5, the average absolute error in curvature between the quintic Bézier curve with C^2 and C^1 is less than that between the quintic Bézier curve with C^2 and C^0 for the outer layer. Meanwhile, in Table 6, the average absolute error in curvature between the quintic Bézier curve with C^2 and C^0 is less than that between the quintic Bézier curve with C^2 and C^1 for the inner layer. Thus, the quintic Bézier curve with C^1 continuity from Figure 8 is the best-fit curve for the outer layer, while for the inner layer, the quintic Bézier curve with C^0 continuity from Figure 7 is the best-fit curve for the fractured part in the craniofacial region. Hence, this research proves that the GA is useful in determining the best-fit curve for the inner and outer layers of the craniofacial reconstruction. A lower degree of continuity can mimic the same features as C^2 and preserve the curvature continuity at both boundary curves.

Table 5
Curvature value of quintic Bézier curve with C^0, C^1 and C^2 continuity and the absolute error of outer layer

t	Curvature value of quintic Bézier curve			Absolute error	
	C^0	C^1	C^2	$\|\| C^2-C^0 \|\|$	$\|\| C^2-C^1 \|\|$
0	2.855×10^{-5}	1.4980×10^{-4}	-1.8064×10^{-4}	2.092×10^{-4}	3.304×10^{-4}
0.2	-1.3702×10^{-4}	-2.3745×10^{-4}	-3.1578×10^{-4}	1.788×10^{-4}	7.833×10^{-5}
0.4	-2.896×10^{-5}	-1.2451×10^{-4}	-2.7122×10^{-4}	4.423×10^{-4}	1.467×10^{-4}
0.6	5.83352×10^{-7}	-9.591×10^{-5}	-1.5734×10^{-4}	1.579×10^{-4}	6.143×10^{-5}
0.8	-4.2754×10^{-4}	-2.2279×10^{-4}	-1.1487×10^{-4}	3.127×10^{-4}	1.079×10^{-4}
1.0	-1.77593×10^{-3}	-2.0421×10^{-4}	-3.1519×10^{-4}	1.461×10^{-3}	1.110×10^{-4}
			Average	4.603×10^{-4}	1.393×10^{-4}

Table 6
Curvature value of quintic Bézier curve with C^0, C^1 and C^2 continuity and absolute error of inner layer

t	Curvature value of quintic Bézier curve			Absolute error	
	C^0	C^1	C^2	$\|\| C^2-C^0 \|\|$	$\|\| C^2-C^1 \|\|$
0	-7.488×10^{-5}	-2.1409×10^{-4}	-1.7226×10^{-4}	9.738×10^{-5}	4.183×10^{-5}
0.2	1.13496×10^{-6}	-5.498×10^{-5}	-5.211×10^{-5}	5.0975×10^{-5}	2.870×10^{-6}
0.4	-7.910×10^{-6}	-1.180×10^{-5}	-3.527×10^{-5}	2.736×10^{-5}	2.347×10^{-5}
0.6	-1.333×10^{-4}	-6.502×10^{-5}	-7.597×10^{-5}	5.733×10^{-5}	1.095×10^{-5}
0.8	-3.717×10^{-4}	-7.829×10^{-5}	-1.6303×10^{-4}	2.0867×10^{-4}	8.474×10^{-5}
1.0	-5.002×10^{-4}	2.7044×10^{-4}	-3.4918×10^{-4}	1.5102×10^{-4}	6.1962×10^{-4}
			Average	9.879×10^{-5}	1.3058×10^{-4}

CONCLUSION

This paper aims to present a new method that helps to develop fractured craniofacial parts using different types of continuity by matching the boundary curves (cubic Bézier curve) with the constructed curve (quintic Bézier curve). This method can be extended by applying a higher degree of curve. After satisfying the continuity conditions, the remaining control points can be calculated using GA with the lowest arc length as the fitness function while preserving the curvature continuity at both ends.

On the other hand, the size of the fractured region is an important factor in deciding the suitable degree of the curve in reconstructing the fractured part. In this study, the fractured region is considered small. Thus, C^0 and C^1 are enough to reconstruct the craniofacial region. Hence, the results are compared with C^2 continuity to validate the finding. GA is used to find the remaining control points after it undergoes a different order of continuity since moving or changing the control points will be time-consuming.

For future works, the surface of the fractured part in the craniofacial region could be reconstructed if CT scan images from different heights are available. Thus, the surface of

the fractured part can be precisely constructed, and the curve can be combined to form a surface patch. Furthermore, a 3D surface can be used as a template fitting in craniofacial reconstruction is suggested to be investigated further.

ACKNOWLEDGEMENT

This research was supported by the Ministry of Higher Education Malaysia through the Fundamental Grant Scheme (FRGS/1/2020/STG06/USM/03/1) and the School of Mathematical Sciences, Universiti Sains Malaysia. The authors are very grateful to the anonymous referees for their valuable suggestions.

REFERENCES

Abdel-Aziz, H. S., Zanaty, E. A., Ali, H. A., & Saad, M. K. (2021). Generating Bézier curves for medical image reconstruction. *Results in Physics, 23*, Article 103996. https://doi.org/10.1016/j.rinp.2021.103996

Adi, D. I. S., Shamsuddin, S. M., & Ali, A. (2009). Particle swarm optimization for NURBS curve fitting. In *2009 Sixth International Conference on Computer Graphics, Imaging and Visualization* (pp. 259-263). IEEE Publishing. https://doi.org/10.1109/CGIV.2009.64

Adnan, S. B. Z., Ariffin, A. A. M., & Misro, M. Y. (2020). Curve fitting using quintic trigonometric Bézier curve. In *AIP Conference Proceedings* (Vol. 2266, No. 1, Article 040009). AIP Publishing LLC. https://doi.org/10.1063/5.0018099

Ali, N. S. S., Ramli, A., & Rahman, N. A. (2020), October. Searching an optimum parameter value for radial basis function by bootstrap error analysis for 2D craniofacial reconstruction. In *AIP Conference Proceedings* (Vol. 2266, No. 1, Article 050008). AIP Publishing LLC. https://doi.org/10.1063/5.0018115

Ammad, M., Misro, M. Y., & Ramli, A. (2022). A novel generalized trigonometric Bézier curve: Properties, continuity conditions and applications to the curve modeling. *Mathematics and Computers in Simulation*, *194,* 744-763. https://doi.org/10.1016/j.matcom.2021.12.011

Amorim, P. H., Moraes, T. F., Silva, J. V., Pedrini, H., & Ruben, R. B. (2020). Reconstruction of panoramic dental images through Bézier function optimization. *Frontiers in Bioengineering and Biotechnology, 8*, 794. https://doi.org/10.3389/fbioe.2020.00794

Carr, J. (2014). An introduction to genetic algorithms. *Senior Project, 1*(40), 1-40.

Chen, B., Gao, Q., Song, H., & Xu, M. (2017) Retrospective study of experience of craniofacial reconstruction. *International Wound Journal, 14*(2)*,* 399-407. https://doi.org/10.1111/iwj.12613

Eliou, N., & Kaliabetsos, G. (2014). A new, simple and accurate transition curve type, for use in road and railway alignment design. *European Transport Research Review, 6*, 171-179. https://doi.org/10.1007/s12544-013-0119-8

Ibrahim, M. F., Misro, M. Y., Ramli, A., & Ali, J. M. (2017). Maximum safe speed estimation using planar quintic Bézier curve with C^2 continuity. In *AIP Conference Proceedings* (Vol. 1870, No. 1, Article 050006). AIP Publishing LLC. https://doi.org/10.1063/1.4995916

Lee, W. J., & Shin, D. H. (2020). Craniofacial reconstruction in mummy studies. In D. H. Shin & R. Bianucci (Eds.), *The Handbook of Mummy Studies* (pp. 1-14). Springer. https://doi.org/10.1007/978-981-15-1614-6_5-1

Loucera, C., Gálvez, A., & Iglesias, A. (2014). Simulated annealing algorithm for Bézier curve approximation. In *2014 International Conference on Cyberworlds* (pp. 182-189). IEEE Publishing. https://doi.org/10.1109/CW.2014.33

Ma, Y., Pollick, F., & Hewitt, W. T. (2004). Using b-spline curves for hand recognition. In *17th International Conference on Pattern Recognition, 2004 (ICPR)* (Vol. 3, pp. 274-277). IEEE Publishing. https://doi.org/10.1109/ICPR.2004.1334520

Majeed, A., Abbas, M., & Miura, K. T. (2022). A comparative study of different schemes based on Bézier-like functions with an application of craniofacial fractures reconstruction. *Mathematics*, *10*(8), Article 1269. https://doi.org/10.3390/math10081269

Majeed, A., Abbas, M., Miura, K. T., Kamran, M., & Nazir, T. (2020). Surface modeling from 2D contours with an application to craniofacial fracture construction. *Mathematics, 8*(8), Article 1246. https://doi.org/10.3390/math8081246

Majeed, A., Piah, A. R. M., Gobithaasan, R. U., & Yahya, Z. R. (2015). Craniofacial reconstruction using rational cubic ball curves. *PLOS One, 10*(4), Article e0122854. https://doi.org/10.1371/journal.pone.0122854

Mansour, R. F., (2020). Evolutionary computing enriched ridge regression model for craniofacial reconstruction. *Multimedia Tools and Applications, 79*, 22065-22082. https://doi.org/10.1007/s11042-017-5015-0

Misro, M. Y., Ramli, A., & Ali, J. M. (2017). S-shaped and c-shaped transition curve using cubic trigonometric Bézier. In *AIP Conference Proceedings* (Vol. 1870, No. 1, Article 050005). AIP Publishing LLC. https://doi.org/10.1063/1.4995915

Misro, M. Y., Ramli, A., & Ali, J. M. (2018). Quintic trigonometric Bézier curve and its maximum speed estimation on highway designs. In *AIP Conference Proceedings* (Vol. 1974, No. 1, Article 020089). AIP Publishing LLC. https://doi.org/10.1063/1.5041620

Moiduddin, K., Mian, S. H., Elseufy, S. M., Abdo, B. M. A., Aboudaif, M. K., & Alkhalefah, H. (2022). Craniofacial reconstruction with personalized lightweight scaffold fabricated using electron-beam additive manufacturing. *Metals*, *12*(4), Article 552. https://doi.org/10.3390/met12040552

Ueda, E. K., Tsuzuki, M. S. G., & Barari, A. (2018). Piecewise Bézier curve fitting of a point cloud boundary by simulated annealing. In *2018 13th IEEE International Conference on Industry Applications (INDUSCON)* (pp. 1335-1340). IEEE Publishing. https://doi.org/10.1109/INDUSCON.2018.8627161

Zain, S. A. A. A. S. M., Misro, M. Y. & Miura, K. T. (2021). Generalized fractional Bézier curve with shape parameters. *Mathematics, 9*(17), Article 2141. https://doi.org/10.3390/math9172141

Pertanika J. Sci. & Technol. 31 (4): 1783 - 1805 (2023)

PERTANIKA JOURNALS

SCIENCE & TECHNOLOGY

Journal homepage: http://www.pertanika.upm.edu.my/

Evaluation the Situation of Heavy Metal Contamination on a Sandy Beach in the Eastern Provinces of Thailand

Patarapong Kroeksakul[1]*, Pakjirat Singhaboot[2], Sujit Pokanngen[1], Kitsakorn Suksamran[1] and Channaphat Klansawang[1]

[1]Faculty of Environmental Culture and Ecotourism, Srinakharinwirot University, Bangkok, 10110 Thailand
[2]Agricultural Product Innovation and Technology, Srinakharinwirot University, Ongkharak, Nakhon Nayok, 26120 Thailand

ABSTRACT

Thailand's eastern provinces are essential as a hub for industry and tourism, effect to the study has purposed for heavy metal contamination of a beach in the Thai Gulf area in the east of Thailand was monitored and focuses on the use of the enrichment factor (*EF*) and geoaccumulation index (*Igeo*) to indicate the environmental condition of beaches. The 30 sample sites were in Chonburi (CHR), Rayong (RY), Chanthaburi (CB), and Trad (TR) provinces, along a sandy beach of about 320 kilometers in length. An inductively coupled plasma technique (ICP-OES) was used to analyze the heavy metals present in the samples. The sand of the range with granulometries greater than 0.85 (18%), between 0.85–0.25 (77%), or less than 0.25 mm (5%). The most common heavy metal found in the samples was Fe at 1632±931 mg/kg dry weight, and the number of heavy metals found in the samples did not exceed the Pollution Control Department of Thailand standards. Principle Component Analysis (PCA) indicated that land use activities influence Hg content. The *Igeo* of Hg was 1–1.99 (moderately polluted) in sample location 4th of the Rayong province, which has an industrial zone and a port. The *EF* was mainly within the range of 2–5 in the four provinces studied (indicating deficiency to minimal enrichment), except for one location in Trad and Rayong province, which had an *EF* of over 5; a possible reason for this is that the area is close to agricultural and aquacultural zones, the government organizations can use the data to plan, monitor, and promote tourism in the future.

ARTICLE INFO

Article history:
Received: 28 June 2022
Accepted: 14 November 2022
Published: 25 May 2023

DOI: https://doi.org/10.47836/pjst.31.4.11

E-mail addresses:
patarapong@g.swu.ac.th (Patarapong Kroeksakul)
pakjirat@g.swu.ac.th (Pakjirat Singhaboot)
sujit.pokanngen@g.swu.ac.th (Sujit Pokanngen)
kanokphon.ssr@g.swu.ac.th (Kitsakorn Suksamran)
channaphat.kla@g.swu.ac.th (Channaphat Klansawang)
*Corresponding author

Keywords: Beach, Eastern provinces of Thailand, Enrichment Factor (*EF*), geoaccumulation index (*Igeo*), heavy metals, Thai Gulf

ISSN: 0128-7680
e-ISSN: 2231-8526

INTRODUCTION

There is a long history of studies of heavy metal contamination. Around 1959, mercury (Hg) was toxicology tested on a rat, which developed symptoms similar to Minamata disease in humans (Yorifuji & Harada, 2011). In the era of Hippocrates, lead (Pb) was found to give laborers in steel smelting factories stomach cramps. The present distribution of contamination by heavy metals such as cadmium (Cd), Pb, and Hg differs from previous eras. Exposure is often caused by smoke from combustion processes in industry and transportation (WHO, 2007). It is also possible for contamination to be caused by agriculture, as Cd, Pb, and Hg are components in chemical fertilizer (Zhao & Wang, 2010), and manganese (Mn), zinc (Zn), and copper (Cu) are components of pesticides (Chopra & Phathak, 2009; Alvers et al., 2016). Soils, sediments, air, and water can be contaminated by heavy metals present in rainwater (Maanan et al., 2004; Khayan et al., 2019). The ocean is at the end of the mineral and biogeochemical cycle and is the base of the pollution transfer cycle (Ilyina et al., 2006; Gioia et al., 2011; Foteinis et al., 2013), and this can result in the contamination of sand and organisms on beaches (Alshahri, 2017; Cabrini et al., 2017). Because many people travel to the beach to relax, this can lead to human health risks (Khaled et al., 2017; Benssa et al., 2021; Kim & Choi, 2016). However, the research focuses on the beach around the eastern provinces zone of Thailand because it is essential to the country's industrial zone and has the beach for tourism supported together. The beaches around the eastern region of Thailand are popular with tourists. About 13.7 million internal and foreign tourists visited the four eastern provinces of Thailand in 2009, and in 2015 this Figure increased by about 51% from 2009, with more than 26.9 million persons visiting the eastern region (National Statistic Office Thailand, 2021). This tourism is focused on the sea beaches in the Thai Gulf area. A geochemical survey of heavy metals provides a framework for assessing sources and mechanisms of element entry and enrichment distribution in beaches and sediments (Magesh et al., 2011). In 2021, it was reported that the Amazonian oceanic beaches were contaminated with Cd and Hg at moderate to very high levels (Vilhena et al., 2021), and Greek beaches were contaminated with Cu, Zn, and Pb (Foteinis et al., 2013). However, the amount of heavy metal is almost concentrated in the sediments, but the differences in studies focus on the beach to support people may rest and travel.

Environmental pollution monitoring involves using indicators to show the presence and amount of human pathogenic pollutants deposition on soil surfaces, and the purpose of this research is to examine the quality of sandy beaches by utilizing the enrichment factor (*EF*) and geoaccumulation index (*Igeo*) to measure the contamination of heavy metals on the beaches in Thailand's eastern regions. The enrichment ratio of heavy metals in the environment of eastern Thai beaches is ascribed to human activities, and the study focuses on Hg, Cd, Pb, Zn, Cu, Mn, nickel (Ni), and iron (Fe). The results of this environmental

monitoring will support the unpolluted beaches and protection from heavy metal poisoning in beach around the eastern provinces of Thailand.

MATERIALS AND METHODS

Sample Collection Area

The sand samples were collected from beaches in the eastern provinces of Thailand, which include Chonburi (CHR), Rayong (RY), Chanthaburi (CR), and Trad (TR). These provinces have about 320 kilometers of beaches. The samples were collected at the 30 locations indicated in Figure 1 within the supratidal. Samples were collected by placing quadrats (1.5 x 1.5 m^2) on the sample area and collecting about 50g of soil at a depth of about 0–5 cm in the beach around 300–400 m. The total sample weight was about 1.3 kilograms from each of the 30 locations, and each of these 30 samples was homogenized by mixing in a polypropylene bag (Chen et al., 2019).

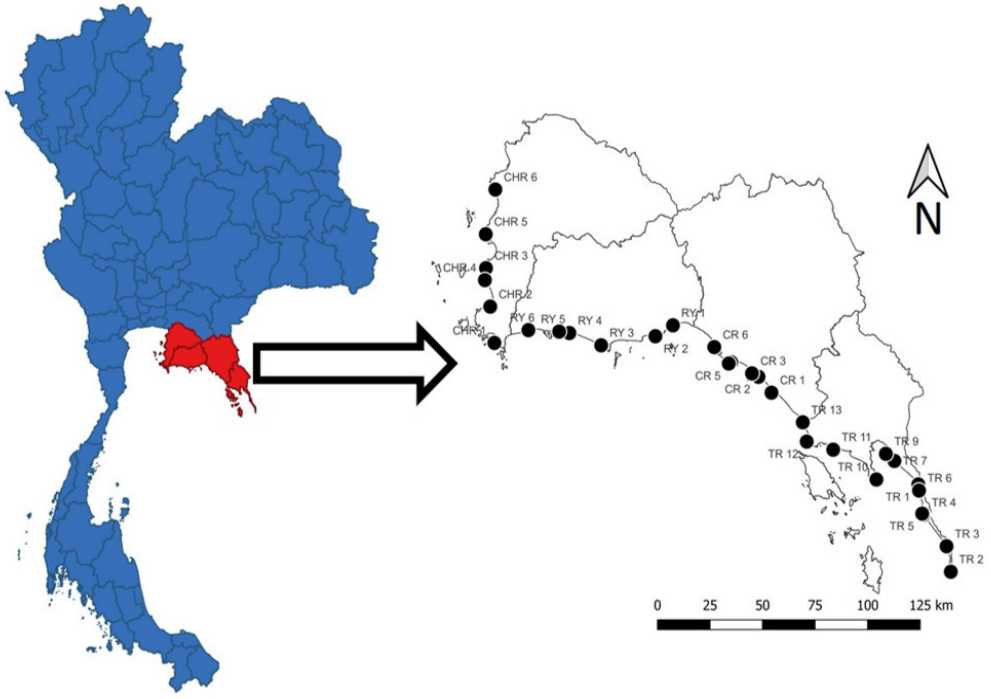

Figure 1. Sample collection areas in the beach of the eastern provinces of the Thai Gulf region

Sample Preparation and Heavy Metal Analysis

In the laboratory, the samples were air-dried on a plastic tray, and each sample was then sieved through a No. 20 sieve with a 0.85 mm mesh size and a No. 60 sieve with a 0.25 mm mesh size to separate the gravel fraction from grains below 1 mm in size, and to separate

larger grains from smaller grains, for analysis. Samples of 5 g were then combined with a solution of 3% (v/v) hydrogen peroxide (H_2O_2) for 48 hours to remove most of the organic matter (Sanz-Prada et al., 2020). These samples were then dried in a hot air oven at 105°C for three days (until they were dry), and samples were taken for continuous extraction. These 2 g samples were mixed with 50 ml of acid (HF: HNO_3: $HClO_4$ ratio 1:1:1), heated to 180°C on a hot plate until the samples were dry, and re-dissolved with 50 ml 1% HNO_3. The samples were left for 24 hours before being filtered using a Whatman No. 5 filter and collected in PP tubes for analysis. The heavy element analysis used the inductively coupled plasma (ICP) technique in a PlasmaQuant 9100 series (Germany), and the sample references material with the AccuTrace™ standard (USA.). The concentration of heavy metals in the samples was calculated in Equation 1:

$$\text{Element concentration (mg/kg)} = Cx\ (v/w) \quad (1)$$

where Cx is the concentration value given by the instrument (µg/L), v represents the volume of the sample that is soluble (L), and w is the weight of the sample after extraction (g).

The Enrichment Factor (EF) and Geoaccumulation Index (Igeo)

The enrichment factor (EF) was derived from Equation 2:

$$EF=(C/RE)_{sample}/(C/RE)_{background} \quad (2)$$

where C/RE_{sample} is the value of element concentration (C) to a reference element (RE) in the samples, and $C/RE_{background}$ is the value of element concentration (C) to a reference element (RE) present in the background (Bern et al., 2019). Aluminum (Al) was used as the reference element because it is a major component of clay, and the background element concentration references for Pb, Cd, Cu, Zn, Fe, and Ni were taken from Looi et al. (2019). The geoaccumulation index ($Igeo$) was originally formulated by Muller (1980) and is a quantitative measure of pollution in aquatic sediment (Nobi et al., 2010) and was worked out on the basis of an understanding of the lithogenic effect. $Igeo$ was derived using the formula in Equation 3:

$$Igeo = \log 2\ ([\text{sediment}]/\ 1.5^*\ [\text{reference sample}]). \quad (3)$$

where factor 1.5 is introduced to minimize the effect of possible variations in the background values, which might be attributed to lithologic variations in the sediments. Reference values for Cd, Pb, and Cu (0.3, 20, and 50 mg/kg, respectively) were taken from Brandl et al. (2013), reference values for Fe (43.4g/kg) and Zn (159 mg/kg) were taken from Potipat et

al. (2015), and Hg (0.02 mg/kg) and Ni (25 mg/kg) reference values were taken from Guan et al. (2014). However, the meaning of indicates with *EF* and *Igeo* is present in Table 1.

Table 1
The meaning of EF and Igeo indicator

EF		*Igeo*	
<1	does not indicate enrichment	≤0	Unpolluted
<3	is slight enrichment	0–1	Unpolluted to moderately polluted
3–5	is moderate enrichment	1–2	Moderately polluted
5–10	is moderately severe enrichment	2–3	Moderately to highly polluted
12–25	is severe enrichment	3–4	Highly polluted
25–50	is very severe enrichment	4–5	Highly to extremely polluted
>50	is extremely severe enrichment	>5	Extremely polluted

Statistical Analysis

Data were analyzed using one-way ANOVA for variance. Differences in the data were compared using a Least Significant Difference (LSD) test at $p<0.05$ between data components. Principal Component Analysis (PCA) was used to evaluate the correlation matrix components, with factors of influence related to heavy metals on the beach and activity in the area, and the correlation analysis used Pearson correlation ($p<0.05$). All analyses were performed using the SPSS V.22 and Sigmaplot 12.0 programs (free trial versions).

RESULTS AND DISCUSSION

Sample Collection Locations and Grain Size of Samples

Human activities such as agriculture, fishing, and tourism affect the sample collection areas. As shown in Table 1S, these areas contain fishing and travel piers, agricultural regions, rest zones, industrial zones, and fish markets. There are differences in sand grain size between the different sample sites. Figure 2 presents the differences in grain size between the samples, which are categorized as over 0.85 mm, between 0.25 and 0.85 mm, or less than 0.25 mm (average proportions were 18, 77, and 5%, respectively). However, the analysis of heavy metals uses the size of the grain of sand between 0.25–0.85 mm, so its general grain size is in the range around the eastern provinces of Thailand.

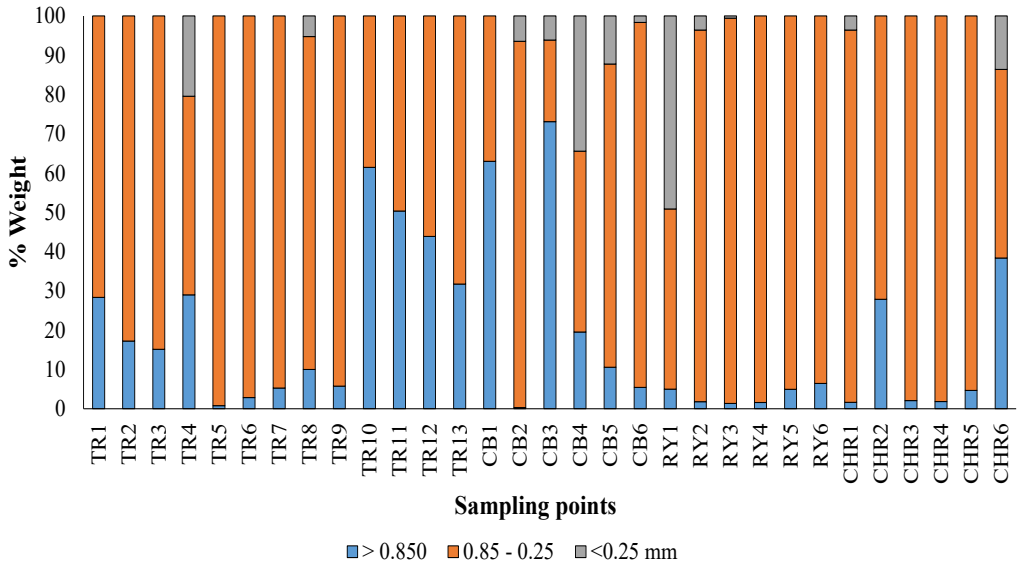

Figure 2. Grain sizes of sand samples along the eastern coastline of Thailand

Heavy Metal Content in Sandy Beach

Fe was the most common heavy metal in the samples, with an average content of 1632±931 mg/kg by dry weight, or 88% of the heavy metals in the sand samples. In descending order, the most common heavy metals on average in the samples were Fe, Mn, Zn, Cu, Pb, Cd, Ni, and Hg. The quantities of heavy metal contaminants found in the sand samples are presented in Table 2, and the spatial distribution of heavy metal contaminants is presented in Figure 3. Cd contamination was found to be significantly higher in the beaches of RY province than in the beaches of TR and CB provinces ($p<0.05$), and Fe contamination was significantly higher in the beaches of CB province than the beaches of TR, RY, and CHR provinces ($p<0.05$), and the Pb contamination in CB province was significantly higher ($p<0.05$) than in the TR, RY, and CHR provinces. However, no significant differences were found between the Cu, Hg, Ni, and Zn contamination levels between the four provinces. These data are presented in Table 3. Figure 4 shows the ratio of all heavy metal contaminants to Fe contamination and the distribution of heavy metal contamination in the four studied provinces.

Levels of heavy metal contamination in the beaches of the eastern region were not found to have reached emergency levels of contamination. The scale provided by the Pollution Control Department for agricultural and residential areas (Pollution Control Department, 2021) requires that heavy metal content must not exceed the following levels: Cd <67 mg/kg, Cu <2.9 g/kg, Mn<1.7 g/kg, Ni 140.4 mg/kg, Pb <400 mg/kg, and Hg <22 mg/kg. The average heavy metal content in the samples did not exceed this standard in any case, nor

did it exceed World Health Organization (WHO) requirements the Hg <0.5 mg/kg, Cd<30 mg/kg, Pb<30mg/kg (WHO,2007).

Table2

Average heavy metal contamination in sampled beaches (mg/kg)

	Cd	Cu	Fe	Mn	Ni	Pb	Zn	Hg
Average	13.6	17.2	1632.6	140.6	12.2	15.3	20.5	0.005
SD	3.19	19.2	931.8	147.7	1.64	2.45	6.56	0.018
%	0.734	0.93	88.1	7.59	0.661	0.828	1.10	0.0002

Note. Pb=lead, Fe=iron, Cd=cadmium, Ni=nickel, Mn=manganese, Zn=zinc, Cu=copper, and Hg=mercury

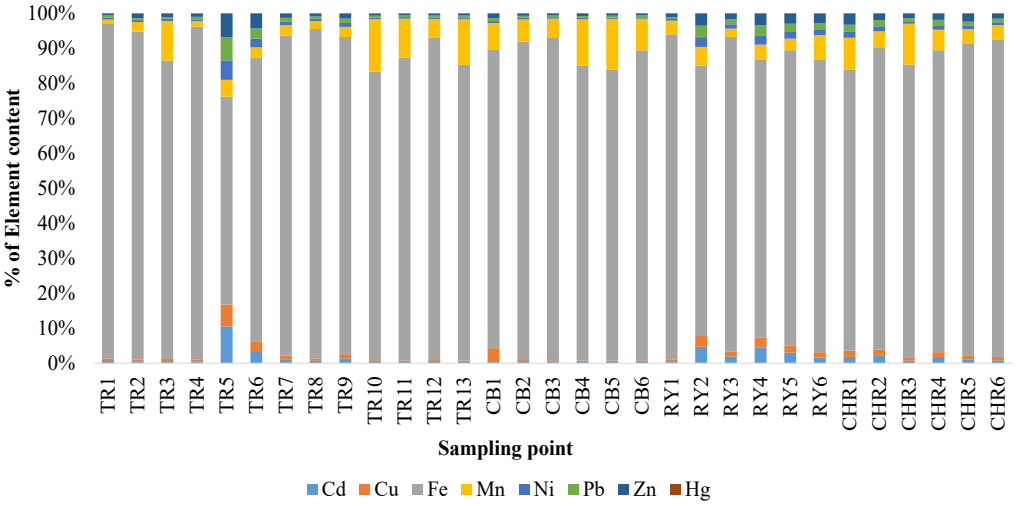

Figure 3. Heavy metal content classified by sampling point

Table 3

The volume of heavy metal contamination classified by province

Element (mg/kg)	Trad	Chanthaburi	Rayong	Chonburi
Cd	13.08±3.142^{acd}	10.92±0.417^{ac}	16.71±3.211^{bd}	14.33±2.317^{ad}
Cu	14.85±3.854	31.34±43.51	12.50±0.104	13.07±0.653
Fe	1864.7±908.1^{a}	2607.5±6.32^{b}	802.8±694.8^{c}	985±371.8^{c}
Hg	0.002±0.006	0.001	0.017±0.041	0.002±0.003
Mn	151.8±169.9^{a}	281.9±0.417^{a}	37.95±29.28^{ab}	77.64±60.97^{ac}
Ni	12.73±2.140	12.88±1.582	11.32±0.193	11.54±0.235
Pb	15.26±2.180^{a}	17.75±3.654^{b}	13.95±0.757^{a}	14.45±0.566^{a}
Zn	19.87±6.267	23.28±9.920	17.98±4.315	21.65±5.284

Note. Pb=lead, Fe=iron, Cd=cadmium, Ni=nickel, Mn=manganese, Zn=zinc, Cu=copper, and Hg=mercury

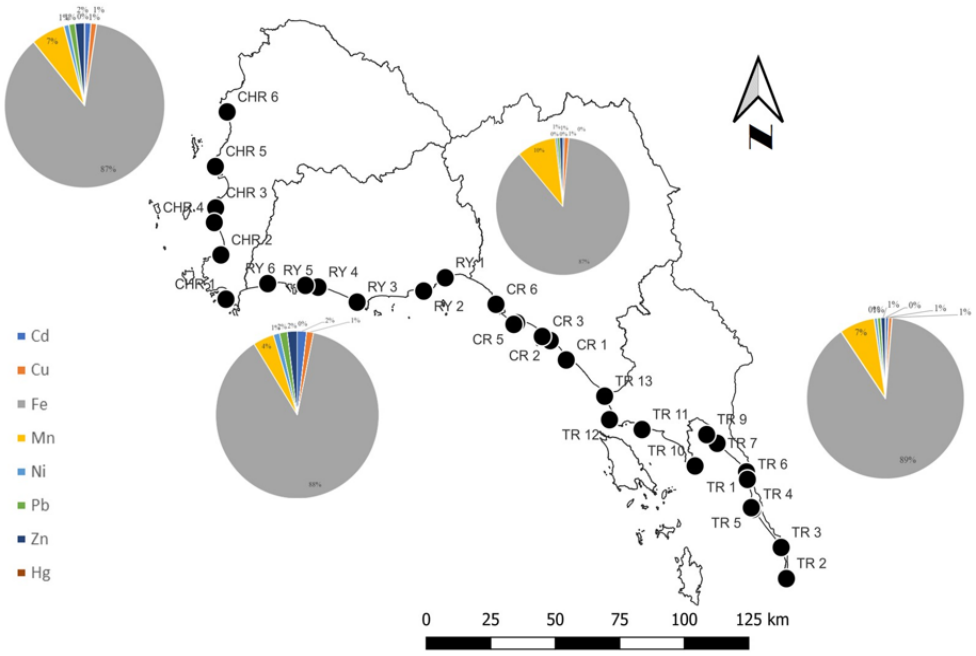

Figure 4. Spatial distribution of heavy metal contamination

Factor Analysis

The factor analysis used 10 components as parameters in a PCA. Prior to this, heavy metal contamination components were tested using the Kaiser-Meyer-Olkin (KMO) and Bartlett tests. The KMO Measure of Sampling Adequacy was 0.698 (Table 4), and there was a significant difference between the eigenvalues (p<0.001). The three principal components (PCs) found had eigenvalues over 1 and explained 74.589% of the total variance in the dataset (Table 5). A variance of over 10% was found for PC1, PC2, and PC3. PC1 explained 44.153% of the variance (Table 4 & Figure 5). Pb was the most important contributor to PC1, with a factor loading of 0.853. For PC2, the factor loading of Cu was 0.637, so the two primary components of PC2 were Cu and the province. For PC3, local utilization was the most important factor, while Hg had a factor load of 0.883. It was interesting to note that despite the proximity of RY4 to an industrial zone and harbor, the Hg contamination level was only 0.1 mg/kg, which did not exceed the standard of the Pollution Control Department, which is 22 mg/kg (Pollution Control Department, 2021).

Table 4

Results of KMO and Bartlett tests of heavy metal contamination distribution

Kaiser-Meyer-Olkin Measure of Sampling Adequacy	0.698
Bartlett's Test of Sphericity Approx. Chi-Square	181.244
df	45
Sig.	.000

(a)

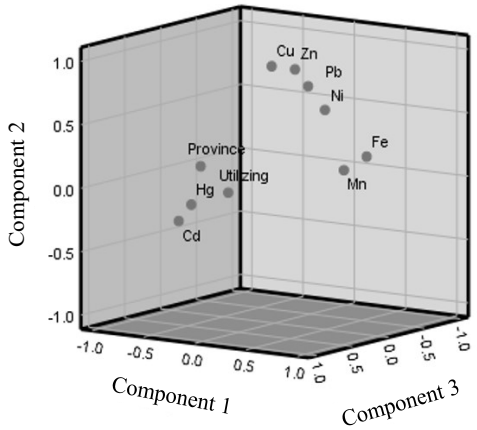

(b)

Figure 5. Results of the PCA for heavy metal contamination distribution: (a) the eigenvalue of components in the principal analysis; and (b) the loading of PC components: for PC1, various heavy metals, for PC2 is Cu and province, and for PC3 the local utilization and Hg

Table 5

Results of PCA of the statistical significance of heavy metal contamination distribution

PCs	Component		
	PC1	PC2	PC3
% of variance	44.153	15.839	14.589
Cumulative %	44.153	59.991	74.580
Eigenvalue	4.415	1.584	1.459
Pb	.843	-	-
Fe	.838	-	-
Cd	-.834	-	-
Ni	.790	-	-
Mn	.739	-	-
Zn	.698	-	-
Cu	.624	.637	-
Province	-	.504	-
Located utilization	-	-	.853
Hg	-	-	.640

Note. PC=Principal component; underlying factor loading is weighted higher when within 10% of the variation of the absolute value of the highest factor loading for each PC; Pb=Lead; Fe=Iron; Cd=Cadmium; Ni=Nickle; Mn=Manganese; Zn=Zinc; Cu=Copper; and Hg=Mercury

EF and *Igeo* Heavy Metal Contamination in A Sandy Beach of the Eastern Provinces, Thailand

The study sites almost all had *EF* values below 2 (deficiency to minimal enrichment), but the *EF* value for Mn was higher than 2 (mean deficiency to moderate enrichment) in locations TR6, RY2, RY4, and RY5, and the *EF* value for Mn in TR5 was 6 (significant enrichment). *EF* values classified by element and location are presented in Table 2S, *EF* values by element and location are shown in Table 6, and the

spatial distribution of *EF* values is presented in Figure 6. However, the ratio with *EF* sediments in the Gulf of Thailand presents an average Cu of 0.80, average Cd of 0.91, average Pb of 1.32, and average Hg of 1.16 (Liu et al., 2016), so the *EF* value is almost below 2 is mean to deficiency to mineral enrichment.

Differences between the *EF* values of Cd between CB and RY provinces were found to be significant (p<0.05), differences between the *EF* values of Cu were not found to be significant, the *EF* values of Fe were not found to be significant (p<0.05) between RY and CHR provinces, and the *EF* values of Hg, Mn, Pb, and Zn were found to be significantly different (p<0.05) between CB and RY provinces. These data are presented in Figure 7, and Table 7 presents *EF* values by heavy metal and province. Mn *EF* values were found to be at levels of 2–5 and 6–20 in locations close to a community, restaurant, and a population of green mussels (*Perna viridus*) culture, so it is possible that Mn levels are related to community activity and transportation in the area (Pavilonis et al., 2015; Choi et al., 2020), and also to the soil parent material in the area (Sanz-Prada et al., 2020).

Table 6

EF by element and location

Element	*EF*<2	*EF* 2-5	*EF* 6-20
Cd	TR1-13/ CB1-6/RY1-6/CHR1-6		
Cu	TR1-13/ CB1-6/RY1-6/CHR1-6		
Fe	TR1-13/ CB1-6/RY1-6/CHR1-6		
Hg	TR1-13/ CB1-6/RY1-6/CHR1-6		
Pb	TR1-13/ CB1-6/RY1-6/CHR1-6		
Ni	TR1-13/ CB1-6/RY1-6/CHR1-6		
Mn	TR1,2,3,4,7,8,9,10,11,12,13/CB1-6/ RY1,3,6/CHR1-6	TR6, RY2, RY4, RY5	TR5
Zn	TR1-13/ CB1-6/RY1-6/CHR1-6		

Note. EF=Enrichment Factors, Pb=lead, Fe=iron, Cd=cadmium, Ni=nickel, Mn=manganese, Zn=zinc, Cu=copper, and Hg=mercury

Table 7

EF by heavy metal and province

		EF-Cd	EF-Cu	EF-Fe	EF-Hg	EF-Pb	EF-Ni	EF-Mn	EF-Zn
TR	Min	.030	.000	.002	.000	.007	.004	.115	.023
	Max	1.71	.094	.060	.000	.420	.253	6.42	1.30
	Average	.290	.010	.042	.000	.071	.042	1.087	.220
	SD	.451	.025	.020	.000	.110	.066	1.69	.344

Table 7 *(Continue)*

		EF-Cd	EF-Cu	EF-Fe	EF-Hg	EF-Pb	EF-Ni	EF-Mn	EF-Zn
CB	Min	.029	.000	.059	.000	.007	.004	.109	.022
	Max	.141	.003	.060	.000	.034	.020	.531	.107
	Average	.029	.001	.060	.000	.020	.012	.317	.064
	SD	.141	.000	.000	.000	.009	.005	.148	.030
RY	Min	.172	.001	.007	.000	.042	.025	.645	.131
	Max	.890	.009	.049	.000	.218	.131	3.33	.678
	Average	.172	.005	.018	.000	.129	.077	1.97	.400
	SD	.890	.003	.016	.000	.073	.044	1.12	.228
CBR	Min	.212	.002	.012	.000	.052	.031	.797	.161
	Max	.529	.005	.033	.000	.130	.078	1.985	.403
	Average	.212	.004	.022	.000	.095	.057	1.45	.296
	SD	.529	.001	.008	.000	.029	.017	.455	.092

Note. EF=Enrichment Factors, TR=Trad province, CB=Chanthaburi, RY=Rayong, CHR=Chonburi, *EF*=Enrichment Factor, Cd=cadmium, Cu=copper, Fe=iron, Hg=mercury, Pb=lead, Ni=nickel, Mn=manganese, Zn=zine

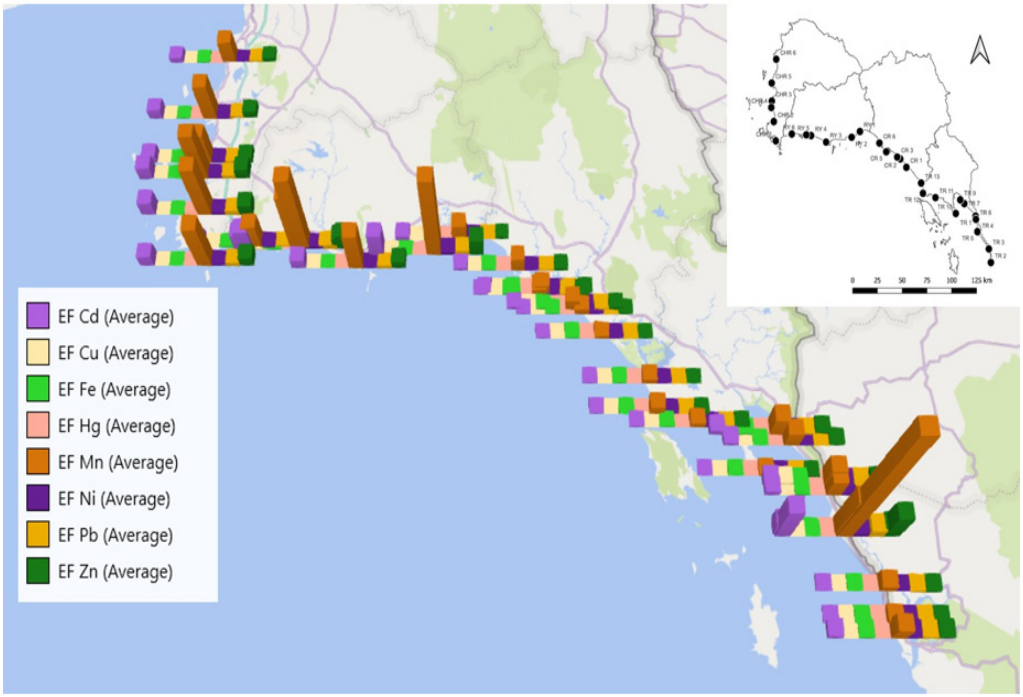

Figure 6. EF distribution in the sandy beach of eastern provinces groups, Thailand

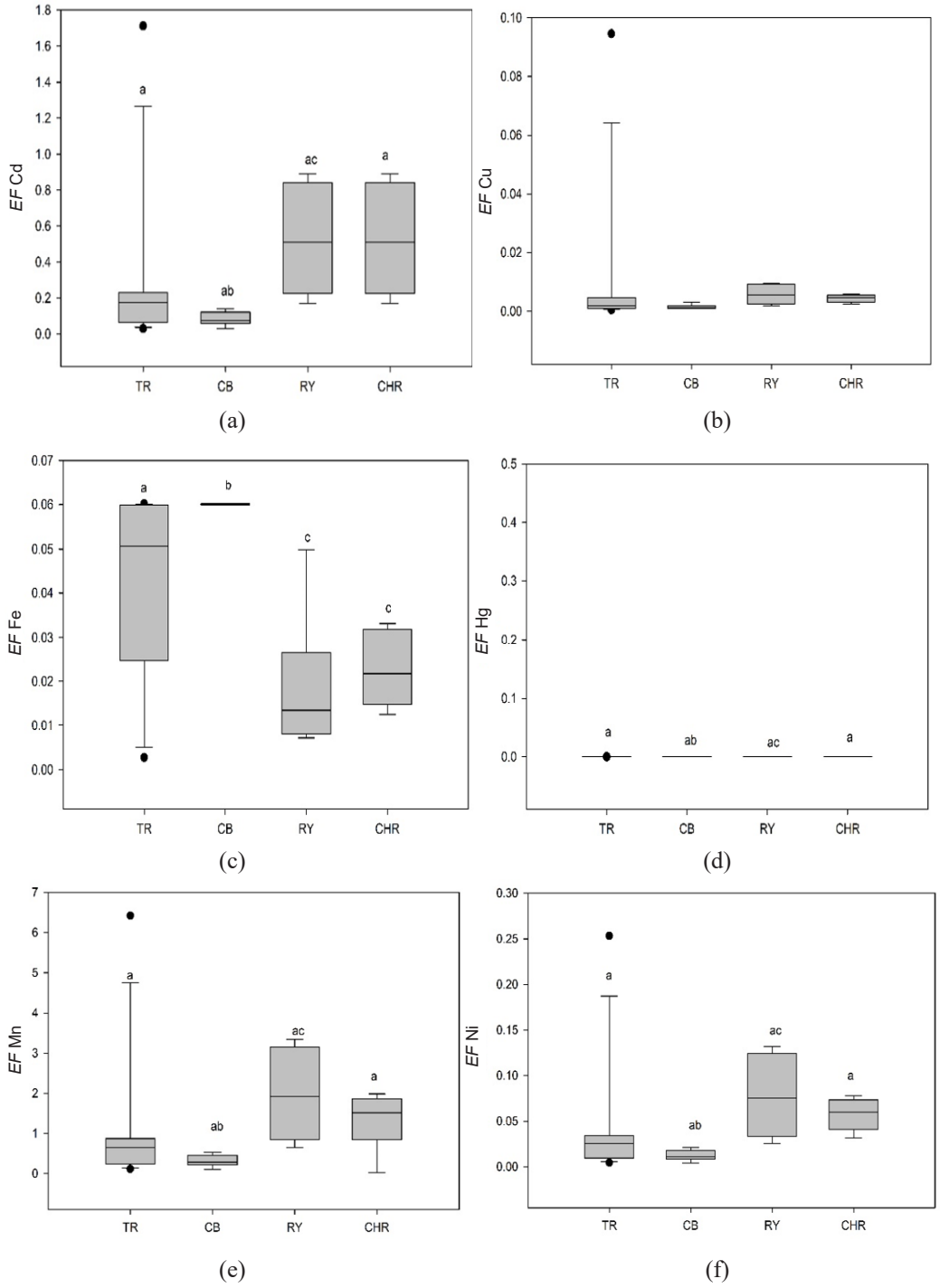

Figure 7. The *EF* results classified by provinces and heavy metals. (a) value *EF* of Cd, (b) value *EF* of Cu, (c) value *EF* of Fe, (d) value *EF* of Hg, (e) value *EF* of Mn, (f) value *EF* of Ni, (g) value *EF* of Pb, (h) value *EF* of Zn

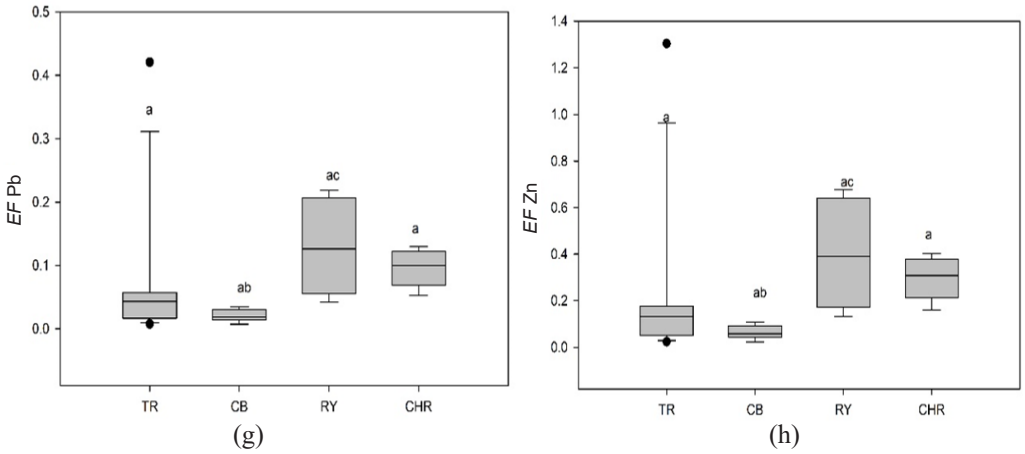

Figure 7. (Continue)
Note. [a, b, c,] and [d] indicate that the difference is significant at the 0.05 level (*LSD*)

As shown in Table 8, almost no *Igeo* values were over 0 (<0 = unpolluted). *Igeo* values for each heavy metal are presented by location in Figure 8 (Table 3S). The *Igeo* of Cd was over 0 in every location, and the *Igeo* values of Fe, Pb, Mn, and Zn did not exceed 0 at any location. However, the *Igeo* of Hg was found to be 1.00–1.99 at location RY4, meaning that the area is moderately polluted. Thongra-ar et al. (2008) have reported *Igeo* values of below 0 for Hg, Cd, and Ni, but our study found an *Igeo* of Hg of over 0 (1.76) in one location because the location was close to an industrial zone and a large pier. The *Igeo* of Cd was over 0 but not over 2, meaning the beaches were moderately polluted with Cd. However, the value with *Igeo* sediments in the Gulf of Thailand presents the average Cu -1.23, average Cd -1.08, average Pb -0.57, and average Hg -0.76 (Liu et al., 2016), so the *Igeo* value almost below 0 is not polluted.

The categorization of *Igeo* by province is shown in Table 9 shows that Cd and Fe levels were significantly different between TR and RY provinces (p<0.05) but not between RY and CHR provinces. Mn and Pb levels in the CB province significantly differed from those in TR, RY, and CHR provinces (p<0.05). No significant differences between provinces existed between Hg, Ni, and Zn levels. These relationships are presented in Figure 9.

Although our study demonstrates that the east coast beaches of Thailand have safe levels of heavy metal contamination, the *Igeo* of Cd, Ni, and Hg was found to be higher than 0 but not over 2. It means that concentrations of these heavy metals are between the 'non-polluted' and 'moderately polluted' categories, and it is very important that the monitoring and protection of the conserved environment of the beaches continues. The *Igeo* level and high *EF* values are associated with soil parent material, possible enrichment due to human activity (Barbieri, 2016), and the related character of the sea (Nowrouzi & Pourkhabbaz, 2014) the nearby seawater in the Gulf of Thailand will be high in some minerals as a result of the gravitational transfer of heavy metals from the land to the sea, especially in delta zones (Pellinen et al., 2021).

Table 8

Igeo by element and location

Element	*Igeo*	Location
Cd	<0	-
	0.01–0.99	TR1,2,3,4,10,11,12,13, CB1,2,3,4,5,6, RY1,6, CHR1,6
	1.00–1.99	TR5,6,7,8,9, RY2,3,4,5, CHR2,3,4,5
Cu	<0	TR1-13, CB2-6, RY1-6, CHR 1-6
	0.01–0.99	-
	1.00–1.99	CB1
Fe	<0	TR1-13, CB1-6, RY1-6, CHR 1-6
Hg	<0	TR1-13, CB 1-6, RY1,2,3,5,6, CHR1-6
	0.01–0.99	-
	1.00–1.99	RY4
Pb	<0	TR1-13, CB1-6, RY1-6, CHR 1-6
Ni	<0	TR1,2,3,5,6,7,8,9,10,11,13, CB1-6, RY1-6, CHR 1-6
	0.01–0.99	TR4,12
Mn	<0	TR1-13, CB1-6, RY1-6, CHR 1-6
Zn	<0	TR1-13, CB1-6, RY1-6, CHR 1-6

Note. Igeo= Geoaccumulation index, Pb=lead, Fe=iron, Cd=cadmium, Ni=nickel, Mn=manganese, Zn=zinc, Cu=copper, and Hg=mercury

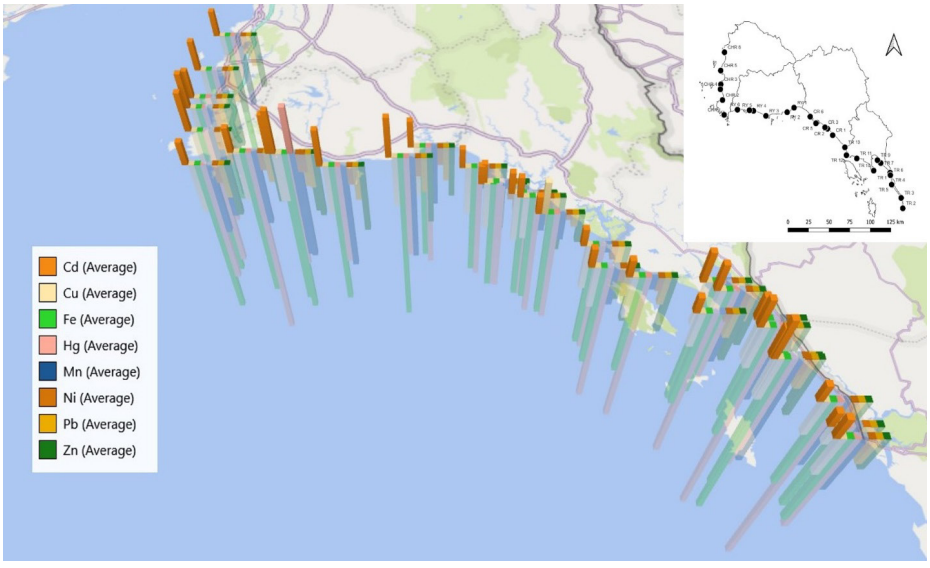

Figure 8. Igeo distribution in the sandy beach of eastern provinces groups, Thailand

Table 9

Igeo results from heavy metal and province

Province		*Igeo*							
		Cd	Cu	Fe	Hg	Pb	Ni	Mn	Zn
TR	Min	.66	-2.02	-9.10	-10.88	-1.47	-.77	-5.66	-3.05
	Max	1.69	-0.92	-4.64	-.28	-.82	.01	-.04	-1.64
	Average	.966	-1.80	-5.48	-5.92	-1.25	-.596	-2.72	-2.36
	SD	.316	.297	1.36	2.82	.193	.208	1.92	.428
CB	Min	.68	-1.99	-4.65	-5.40	-1.30	-.68	-1.69	-2.62
	Max	.82	1.24	-4.64	-4.65	-.53	-.25	-.08	-1.19
	Average	.739	-1.38	-4.64	-4.86	-1.04	-.572	-.893	-2.15
	SD	.054	1.28	.003	.28	.264	.163	.636	.509
RY	Min	.95	-2.04	-7.71	-8.88	-1.45	-.77	-4.66	-2.80
	Max	1.65	-2.00	-4.91	1.77	-1.23	-.72	-2.42	-2.05
	Average	1.11	-2.02	-6.68	-4.37	-1.37	-.750	-3.96	-2.48
	SD	.224	.012	1.01	3.44	.076	.020	.957	.335
CBR	Min	.66	-2.01	-6.90	-6.05	-1.38	-.75	-3.75	-2.74
	Max	1.69	-1.86	-5.50	-1.76	-1.22	-.68	-1.27	-1.74
	Average	1.02	-1.96	-6.13	-4.77	-1.32	-.72	-2.89	-2.21
	SD	.318	.070	.57	1.54	.055	.029	.848	.364

Note. Igeo=Geoaccumulation index, TR = Trad province, CB=Chanthaburi, RY=Rayong, CHR=Chonburi, *EF*=Enrichment Factor, Cd=cadmium, Cu=copper, Fe=iron, Hg=mercury, Pb=lead, Ni=nickel, Mn=manganese, Zn=zine

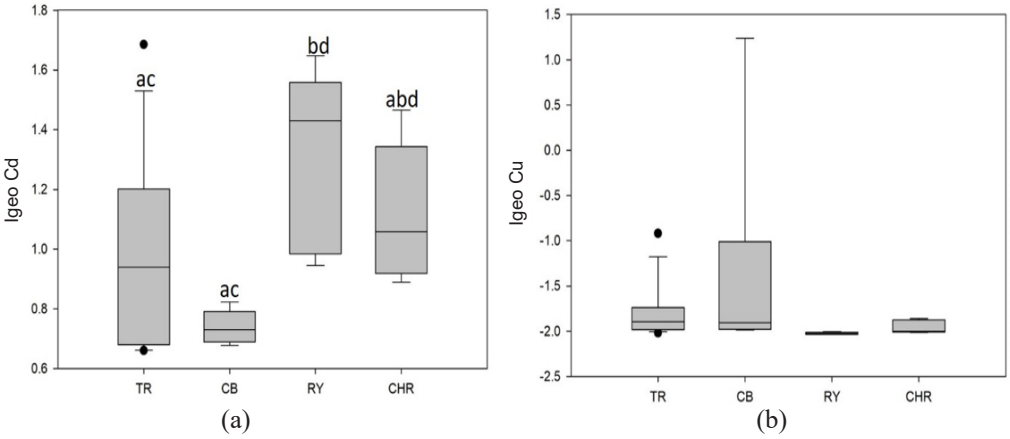

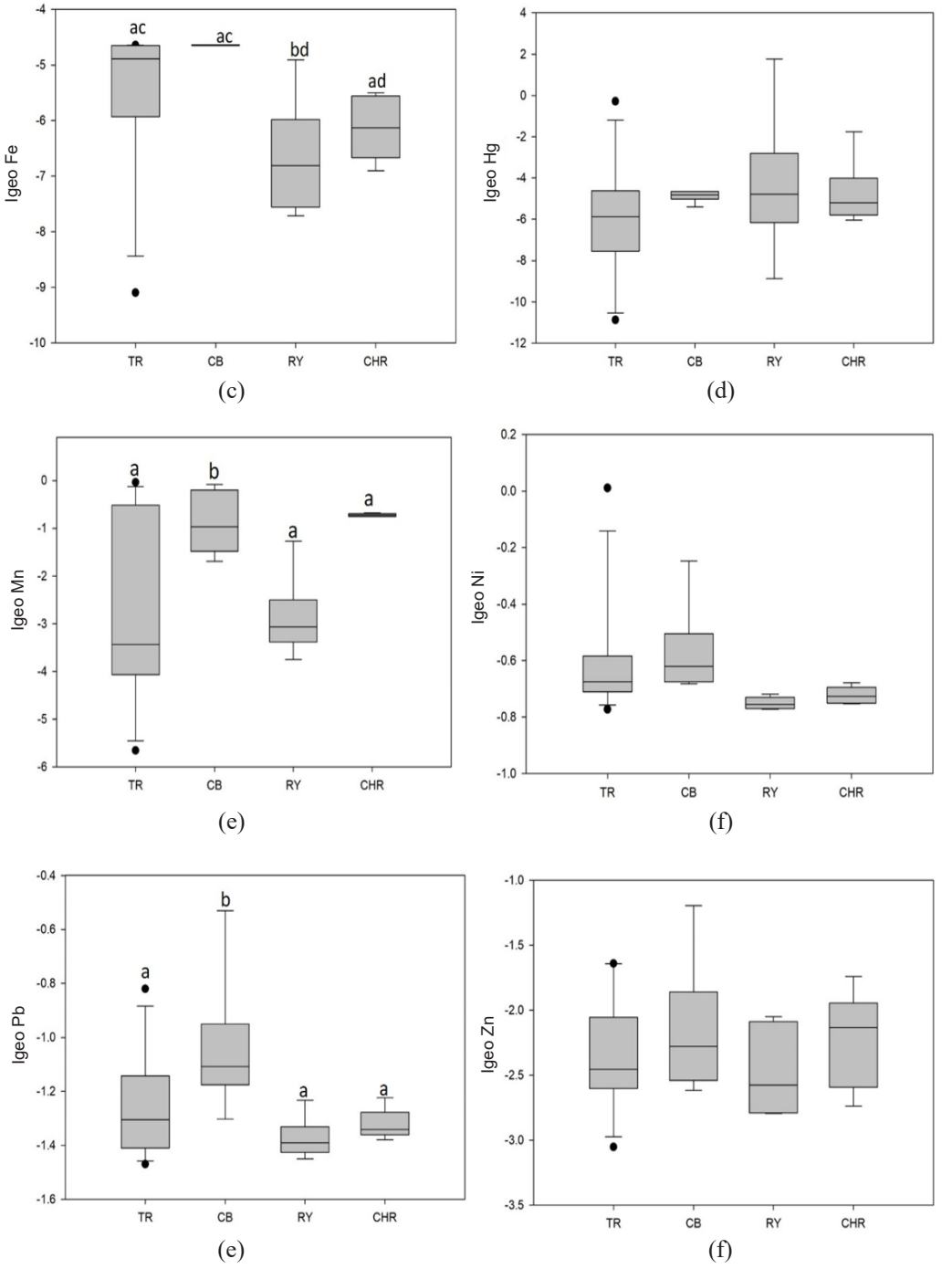

Figure 9. The *Igeo* results are classified by provinces and heavy metals. (a) value *Igeo* of Cd, (b) value *Igeo* of Cu, (c) value *Igeo* of Fe, (d) value *Igeo* of Hg, (e) value *Igeo* of Mn, (f) value *Igeo* of Ni, (g) value *Igeo* of Pb, (h) value *Igeo* of Zn

Note. The letters [a, b, c], and [d] indicate significant differences at the 0.05 level (*LSD*).

CONCLUSION

Overall, sand particles in the beaches of the east coast of Thailand were found to range in size between 0.25–0.85 mm, and the most common heavy metals on average in the samples in descending order were Fe, Mn, Zn, Cu, Pb, Cd, Ni, and Hg (the ratio was 88: 7.74: 0.9312: 0.8283: 0.7347: 0.6582: 0.0002). The volume of Cd contamination in the beaches of RY province was significantly higher than in TR and CB provinces ($p<0.05$), Fe contamination in the beaches of CB province was significantly different ($p<0.05$) to that in the beaches of TR, RY and CHR provinces, and Pb concentration in CB province was significantly different ($p<0.05$) to that in TR, RY, and CHR provinces. None of the contamination levels in the studied beaches exceeded national or international standards. Principle component analysis demonstrated that land use activities influence Hg. The *Igeo* of Hg (1–1.99, moderately polluted) in location RY4 results from the industrial zone and harbor. The *EF* of Mn was within the range of 2–5 in each of the four locations (indicating deficiency to minimal enrichment) and was over 5 (indicating significant enrichment) in one region in Trad and Rayong province. A possible reason for this high Mn *EF* is that the area is near farming and raises aquatic animals of a villager to live around the beach. This study indicates that human activity and land use around beaches can have an impact on the quality of the environment in terms of heavy metal contamination and that soil parent material has an influence on background heavy metal levels, so it is important to calculate background values to perform *EF* and *Igeo* analyses.

The results of this study show that heavy metal contamination in the beaches around the east coast of Thailand is at present within safety levels from the heavy metal, but the *Igeo* and *EF* values signal the possibility that pollution may occur in some areas to relate to human activity which may affect the environment. This information implies that the local and central governments should continue to monitor the environmental impact of human activity and land use around the east coast of Thailand.

ACKNOWLEDGMENTS

This research was supported by a generous scholarship from the Faculty of Environmental Culture and Ecotourism at Srinakharinwirot University (Cord; 203/2564), Bangkok, Thailand. I would like to thank the Faculty of Environmental Culture and Ecotourism at Srinakharinwirot University of Thailand for their analysis tools.

REFERENCES

Alshahri, F. (2017). Heavy metal contamination in sand and sediments near to disposal site of reject brine from desalination plant, Arabian Gulf: Assessment of environmental pollution. *Environmental Science Pollution Research, 24*, 1821-1831. https://doi.org/10.1007/s11356-016-7961-x

Alvers, L. R., Reis, R. A., & Gratao, P. L. (2016). Heavy metals in agricultural soils: from plants to our daily life (a review). *Cientifica*, *44*(3), 346-361. https://doi.org/10.15361/1984-5529.2016V44N3P346-361

Barbieri, M. (2016). The importance of enrichment factor (*EF*) and geoaccumulation index (*Igeo*) to evaluate the soil contamination. *Journal Geology & Geophysics*, *5*(1), Article 1000237.

Benssa, A. Z. E., Ngueutchoua, G., Janpou, A. K., El-Amier, Y. A., Nguetnga, O. A. N. N. Kayou, U. R. K., Bisse, S. B., Mapuna, E. C. N., & Armstrong-Altrin, J. S. (2021). Heavy metal contamination and its ecological risks in the beach sediments along the Atlantic Ocean (Limbe coastal fringes, Cameroon). *Earth Systems and Environment*, *5*, 433-444. https://doi.org/10.1007/s41748-020-00167-5

Bern, C. R., Walton-Day, K., & Naftz, D. L. (2019). Improved enrichment factor calculations through principal component analysis: Examples from soils near breccia pipe uranium mines, Arizona, USA. *Environmental Pollution*, *248*, 90-100. https://doi.org/10.1016/j.envpol.2019.01.122

Brandl, P., Regelous, M., Beler, C., & Haase, K. (2013). High mantle temperatures following rifting caused by continental insulation. *Nature Geoscience*, *6,* 391-394. https://doi.org/10.1038/ngeo1758

Cabrini, T. M. B., Barboza, C. A. M., Skinner, V. B., Hauser-Davis, R. A., Rocha, R. C., Saint'Pierre, T. D., Valentin, J. L., & Cardoso, R. S. (2017). Heavy metal contamination in sandy beach macrofauna communities from the Rio de Janeiro coast, Southeastern Brazil. *Environmental Pollution*, *221*, 116-129. https://doi.org/10.1016/j.envpol.2016.11.053.

Chen, L., Larson, S. L., Ballard, J. H., Ma, Y., Zhang, Q., Li, J., Wu, L., Arslan, Z., & Han, F. X. (2019). Laboratory spiking process of soil with various uranium and other heavy metals. *MethodsX*, *6*, 737-739. https://doi.org/10.1016/j.mex.2019.03.026

Choi, J. Y., Jeong, H., Choi, K., Hong, G. H., Yang, D. B., Kim, K., & Ra, K. (2020). Source identification and implications of heavy metals in urban roads for the coastal pollution in a beach town, Busan, Korea. *Marine Pollution Bulletin*, *161,* Article 111724. https://doi.org/10.1016/j.marpolbul.2020.111724

Chopra, K. A., & Phathak, C. (2009). Scenario of heavy metal contamination in agricultural soil and its management. *Journal of Applied and Natural Science*, *1*(1), 99-108. https://doi.org/10.31018/jans.v1i1.46

Foteinis, S., Kallithrakas-Kontos, K. G., & Synolakis, C. (2013). Heavy metal distribution in opportunistic beach nourishment: A case study in Greece. *The Scientific World Journal*, *2013*, Article 472149. https://doi.org/10.1155/2013/472149

Gioia, R., Dachs, J., Nizzetto, L., Berrojalbiz, N., Galban, C., Vento, D. S., MeJanell, L., & Jone, C. K. (2011). Sources, transport and fate of organic pollutants in the oceanic environment. In M. Quante, R. Ebinghaus & G. Flöser (Eds.), *Persistent Pollution - Past, Present and Future: School of Environmental Research* (pp.111-139). Springer. https://doi.org/10.1007/978-3-642-17419-3_8

Guan, Y., Shao, C., & Ju, M. (2014). Heavy metal contamination assessment and partition for industrial and mining gathering areas. *International Journal of Environmental Research and Public Health*, *11*(7), 7286-7303. https://doi.org/10.3390/ijerph110707286

Ilyina, T., Pohlmann, T., Lammel, G., & Sundermann, J. (2006). A fate and transport ocean model for persistent organic pollutants and its application to the North Sea. *Journal of Marine Systems*, *63*(1-2), 1-19. https://doi.org/10.1016/j.jmarsys.2006.04.007

Khaled, A., Abdel-Halim, A., El-Sherif, Z., & Mohamed, L. (2017). Health risk assessment of some heavy metals in water and sediment at Marsa-Matrouh, Mediterranean Sea, Egypt. *Journal of Environmental Protection*, *8*(1), 74-97. http://doi: 10.4236/jep.2017.81007

Khayan, K., Husodo, H. A., Astuti, I., Sudarmadji, S., & Djohan, S. T. (2019). Rainwater as a source of drinking water: health impacts and rainwater treatment. *Journal of Environmental and Public Health*, *2019*, Article 760950. https://doi.org/10.1155/2019/1760950

Kim, S., & Choi, Y. (2019). Mapping heavy metal concentrations in beach sands using GIS and portable XRF data. *Journal of Marine Science and Engineering*, *7*(2), Article 42. http://doi:10.3390/jmse7020042

Liu, S., Shi, X., Yang, G., Khokiattiwong, S., & Kornkanitnan, N. (2016). Concentration distribution and assessment of heavy metals in the surface sediment of the western Gulf of Thailand. *Environmental Earth Science*, *75*, Article 346. https://doi.org/10.1007/s12665-016-5422-y

Looi, L. J., Aris, A. Z., Yusoff, F. M., Isa, N. M., & Haris, H. (2018). Application of enrichment factor, geoaccumulation index, and ecological risk index in assessing the elemental pollution status of surface sediments. *Environmental Geochemistry and Health*, *41*, 27-42. https://doi.org/10.1007/s10653-018-0149-1

Maanan, M., Zourarah, B., Carruesco, C., Aajjane, A., & Naud, J. (2004). The distribution of heavy metals in the Sidi Moussa lagoon sediments (Atlantic Moroccan Coast). *Journal of African Earth Sciences*, *39*(3-5), 473-483. https://doi.org//10.1016/j.jafrearsci.2004.07.017

Magesh, N. S., Chandrasekar, N., & Vetha-Roy, D. (2011). Spatial analysis of trace element contamination in sediments of Tamiraparani estuary, southeast coast of India. *Estuarine, Coastal and Shelf Science*, *92*(4), 618-628. https://doi.org/10.1016/j.ecss.2011.03.001

Muller, G. (1980). Schwermetalle in Sedimenten des staugeregelten Neckars [Heavy metals in sediments of the impounded]. *Naturwissenschaften, 67*, 308-309. https://doi.org/10.1007/bf01153502

National Statistic Office Thailand. (2021). *Tourism-Statistics*. http://service.nso.go.th/nso/web/statseries/statseries23.html

Nobi, E. P., Dilipan, E., Thangaradjou, T., Sivakumar, K., & Kannan, L. (2010). Geochemical and geo-statistical assessment of heavy metal concentration in the sediments of different coastal ecosystems of Andaman Islands, India. *Estuarine, Coastal and Shelf Science*, *87*(2), 253-264. https://doi.org/10.1016/j.ecss.2009.12.019

Nowrouzi, M., & Pourkhabbaz, A. (2014). Application of geoaccumulation index and enrichment factor for assessing metal contamination in the sediments of Hara biosphere reserve, Iran. *Chemical Speciation & Bioavailability*, *26*(2), 99-105. https://doi.org/10.3184/095422914x13951584546986

Pavilonis, B. T., Lioy, P. J., Guazzetti, S., Bostick, B. C., Donna, F., Peli, M., Zimmerman, N. J., Bertrand, P., Lucas, E., Smith, D. R., Georgopoulos, P. G., Mi, Z., Royce, S. G., & Lucchini, R. G. (2015). Manganese concentrations in soil and settled dust in an area with historic ferroalloy production. *Journal of Exposure Science & Environmental Epidemiology*, *25*, 443-450. https://doi.org/10.1038/jes.2014.70

Pellinen, V. A., Cherkashina, T. Y., Ukhova, N. N., & Komarova, A. V. (2021). Role of gravitational processes in the migration of heavy metals in soils of the Priolkhonye mountain-steppe landscapes, Lake Baikal: Methodology of research. *Agronomy*, *11*(10), Article 2007. https://doi.org/10.3390/agronomy11102007

Pollution Control Department. (2021). *Quantity Standard Control in Soil*. http://www.envimtp.com/info_pic/TT.PDF

Potipat, J., Tanglrock-olan, N., & Helander, H. F. (2015). Distribution of selected heavy metals in sediment of the river basin of coastal area of Chanthaburi province, Gulf of Thailand. *EnvironmentAsia*, *8*(1), 166-143.

Sanz-Prada, L., García-Ordiales, E., Roqueñí, N., Grande Gil, J. A., & Loredo, J. (2020). Geochemical distribution of selected heavy metals in the Asturian coastline sediments (North of Spain). *Marine Pollution Bulletin*, *156*, Article 111263. https://doi.org/10.1016/j.marpolbul.2020.111263

Thongra-ar, W., Musika, C., Wongsudawan, W. & Munhapol, A. (2008). Heavy metals contamination in sediments along the eastern coast of the Gulf of Thailand. *EnvironmentAsia*, *1*(1), 37-45. https://doi.org/10.14456/ea.2008.5

Vilhena, J. C. E., Amorim, A., Ribeiro, L., Duarte, B., & Pombo, M. (2021). Baseline study of trace element concentrations in sediments of the intertidal zone of Amazonian oceanic beaches. *Frontiers in Marine Science*, *8*, Article 671390. https://doi.org/10.3389/fmars.2021.671390

WHO. (2007). *Health Risks of Heavy Metals from Long-Range Transboundary Air Pollution*. WHO Regional Office for Europe. https://apps.who.int/iris/handle/10665/107872

Yorifuji, T., & Harada, M. (2011). Environmental health research implications of methylmercury. *Environmental Health Perspectives*, *119*(7), Article A284. https://doi.org/10.1289/ehp.1103580

Zhao, X., & Wang, D. (2010). Mercury in some chemical fertilizers and the effect of calcium superphosphate on mercury uptake by corn seedlings (*Zea mays* L.). *Journal of Environmental Sciences*, *22*(8), 1184-1188. https://doi.org/10.1016/S1001-0742(09)60236-9

SUPPLIMENTARY DATA

Table 1S

The sampling location and coordinates, including the description of the sample spaces collected

ID	Limit point		Located near the beach to collect
	N	***E***	
TR1	12.0221134	102.76605800	Nearly estuary, and close local restaurant and resort.
TR2	11.6533522	102.90784420	Community
TR3	11.6879430	102.90128350	Community and local fishery pier.
TR4	11.7612855	102.88920890	Nearby the pier (Fish market) and community
TR5	11.8932093	102.78807520	Community and restaurant.
TR6	11.8988673	102.78306920	Community and restaurant.
TR7	11.9968267	102.76926490	Community
TR8	12.1217879	102.66205500	Restaurant
TR9	12.1520733	102.62421470	Community
TR10	12.0434036	102.58364800	Empty area
TR11	12.1691575	102.39527110	Community
TR12	12.2035554	102.27991430	Estuary and community
TR13	12.2851977	102.26292050	Aquaculture zone and community
CB1	12.4102581	102.12649630	Community and local fishery pier.
CB2	12.4777700	102.07000000	Estuary and community
CB3	12.4919145	102.04136630	Pier (Fish market)
CB4	12.5390000	101.95053000	Estuary and community
CB5	12.5336800	101.94046000	Estuary
CB6	12.6032149	101.87718030	Estuary and agriculture zone.
RY1	12.6950931	101.69717390	Estuary and community
RY2	12.6490500	101.62057000	Estuary
RY3	12.6108000	101.38428000	Community and resort
RY4	12.6676500	101.21545000	Neary by industrial zone.
RY5	12.6687729	101.20109160	Aquaculture zone
RY6	12.6750000	101.06728000	Community
CHR1	12.6209150	100.91894900	Tourism space and pier (travel)
CHR2	12.7742808	100.90095440	Estuary and community
CHR3	12.9368950	100.88236810	Tourism space and pier (travel)
CHR4	12.8864152	100.87751200	Restaurant and resort
CHR5	13.0803218	100.88141120	Tourism space and pier (travel)
CHR6	13.2694363	100.92309310	Tourism space and community (in city)

Table 2S

The EF classification by location and element

	EF							
	Cd	Cu	Fe	Hg	Pb	Ni	Mn	Zn
TR1	.239	.094	.045	.000	.058	.035	.898	.182
TR2	.174	.001	.050	.000	.042	.025	.653	.132
TR3	.049	.001	.059	.000	.012	.007	.185	.037
TR4	.101	.001	.060	.000	.024	.015	.381	.077
TR5	1.7	.018	.002	.000	.420	.253	6.42	1.30
TR6	.597	.006	.008	.000	.146	.088	2.23	.454
TR7	.218	.002	.026	.000	.053	.032	.818	.166
TR8	.186	.002	.042	.000	.045	.027	.698	.141
TR9	.224	.002	.022	.000	.055	.033	.842	.171
TR10	.030	.000	.059	.000	.007	.004	.115	.023
TR11	.067	.000	.059	.000	.016	.009	.251	.051
TR12	.105	.001	.060	.000	.026	.015	.397	.080
TR13	.063	.000	.059	.000	.015	.009	.239	.048
CB1	.029	.003	.059	.000	.007	.004	.109	.022
CB2	.067	.000	.060	.000	.016	.010	.254	.051
CB3	.116	.001	.060	.000	.028	.017	.436	.088
CB4	.082	.000	.060	.000	.020	.012	.309	.062
CB5	.070	.000	.059	.000	.017	.010	.264	.053
CB6	.141	.001	.060	.000	.034	.020	.531	.107
RY1	.172	.001	.049	.000	.042	.025	.645	.131
RY2	.890	.009	.007	.000	.218	.131	3.33	.678
RY3	.400	.004	.018	.000	.098	.059	1.50	.305
RY4	.823	.008	.008	.000	.202	.121	3.08	.627
RY5	.622	.006	.011	.000	.152	.091	2.33	.473
RY6	.245	.002	.015	.000	.060	.036	.919	.186
CHB1	.456	.005	.012	.000	.112	.067	1.71	.347
CHB2	.529	.005	.015	.000	.130	.078	1.98	.403
CHB3	.299	.003	.033	.000	.073	.044	1.12	.228
CHB4	.484	.005	.018	.000	.119	.071	1.81	.369
CHB5	.352	.004	.025	.000	.086	.052	1.32	.268
CHB6	.212	.002	.031	.000	.052	.031	.797	.161
Max	.029	.000	.002	.00001	.007	.004	.109	.022
Min	1.71	.094	.060	.00040	.420	.253	6.42	1.30
Average	.315	.006	.037	.00007	.077	.046	1.18	.239
SD	.346	.016	.021	.00008	.085	.051	1.30	.264

Table 3S

The Igeo value of location to collect sample

	Igeo							
Location	Cd	Cu	Fe	Hg	Pb	Ni	Mn	Zn
TR1	.981	-1.89	-5.03	-.282	-1.46	-.725	-4.20	-3.05
TR2	.938	-1.97	-4.88	-5.40	-1.35	-.697	-2.88	-1.63
TR3	.660	-.919	-4.65	-2.53	-1.16	.011	-0.495	-1.64
TR4	.734	-1.70	-4.64	-10.04	-.821	-.639	-3.47	-1.86
TR5	1.68	-2.01	-9.09	-5.00	-1.43	-.772	-5.65	-2.85
TR6	1.29	-1.99	-7.44	-6.04	-1.43	-.734	-5.14	-2.30
TR7	1.17	-1.96	-5.81	-10.8	-1.30	-.675	-3.66	-2.60
TR8	1.08	-1.98	-5.14	-4.33	-1.38	-.691	-3.44	-2.55
TR9	1.23	-1.97	-6.04	-5.87	-1.38	.684	-3.93	-2.59
TR10	.662	-1.56	-4.65	-7.70	-1.12	-.374	-0.037	-2.23
TR11	.697	-1.85	-4.64	-7.40	-1.21	-.596	-0.53	-2.51
TR12	.759	-1.76	-4.64	-6.64	-1.26	.599	-1.65	-2.45
TR13	.661	-1.88	-4.65	-4.90	-.980	-.570	-0.265	-2.40
CB1	.677	1.24	-4.64	-4.87	-.530	-.247	-1.08	-1.19
CB2	.779	-1.75	-4.63	-5.4	-1.09	-.590	-1.41	-2.27
CB3	.823	-1.98	-4.63	-4.64	-1.30	-.681	-1.68	-2.51
CB4	.736	-1.97	-4.64	-4.76	-1.13	-.602	-0.239	-2.07
CB5	.692	-1.87	-4.64	-4.64	-1.11	-.639	-0.082	-2.27
CB6	.724	-1.94	-4.63	-4.87	-1.10	-.672	-0.853	-2.61
RY1	.997	-2.01	-4.90	-5.26	-1.37	-.718	-2.42	-2.04
RY2	1.52	-2.03	-7.71	-4.43	-1.45	-.772	-4.48	-2.79
RY3	1.38	-2.03	-6.33	-4.33	-1.41	-.756	-4.51	-2.78
RY4	1.64	-2.02	-7.50	1.76	-1.41	-.769	-4.66	-2.67
RY5	1.47	-2.03	-7.01	-5.12	-1.36	-.753	-4.60	-2.47
RY6	.945	-2.00	-6.59	-8.87	-1.23	-.734	-3.11	-2.09
CHR1	.889	-2.00	-6.90	-5.26	-1.37	-.750	-2.96	-2.15
CHR2	1.46	-1.99	-6.58	-6.04	-1.35	-.753	-3.74	-2.73
CHR3	1.02	-2.01	-5.49	-4.76	-1.33	-.678	-1.26	-2.01
CHR4	1.30	-2.00	-6.37	-5.12	-1.34	-.734	-3.17	-2.54
CHR5	1.08	-1.86	-5.88	-5.70	-1.29	-.718	-3.26	-1.73
CHR6	.927	-1.87	-5.57	-1.75	-1.22	-.700	-2.91	-2.11
Max	1.68	1.24	-4.63	1.76	-.53	.011	-0.037	-1.19
Min	.66	-2.03	-9.09	-10.8	-1.46	-.772	-5.65	-3.05
Average	1.01	-1.79	-5.67	-5.19	-1.24	-.644	-2.63	-2.31
SD	.315	.601	1.19	2.44	.200	0.165	1.67	0.413

Pertanika J. Sci. & Technol. 31 (4): 1807 - 1825 (2023)

PERTANIKA JOURNALS

SCIENCE & TECHNOLOGY

Journal homepage: http://www.pertanika.upm.edu.my/

Measuring the Learning Effectiveness in the Cognitive, Affective, and Psychomotor (CAP) Domains in Electrical Engineering Laboratory Courses Using Online Delivery Mode: Universiti Teknologi MARA

A'zraaAfhzan Ab Rahim[1], Ng Kok Mun[1]*, Azilah Saparon[1], Ahmad Fadzli Nizam Abdul Rahman[2] and Norlida Buniyamin[1]

[1]*School of Electrical Engineering, College of Engineering, Universiti Teknologi MARA, 40450 Shah Alam, Selangor, Malaysia*

[2]*Faculty of Information and Communication Technology, Universiti Teknikal Malaysia Melaka, Hang Tuah Jaya, 76100 UTeM, Durian Tunggal, Melaka, Malaysia*

ABSTRACT

Online laboratories have been conducted in Malaysian universities using video demonstrations, virtual or simulation tools, or/and remote laboratories. Recent studies on online engineering labs mainly focused on the student learning experience, facilities, and teaching quality. The literature review indicated that the effectiveness of online laboratory learning should be approached from the cognitive, affective, and psychomotor (CAP) domains. The perceived effectiveness of these learning domains will help practitioners identify learning gaps in current practices. This study aims to measure learning effectiveness in CAP using the perceived CAP tool in electrical engineering online laboratory courses in a Malaysian public university. Three electrical and electronics online laboratory courses were selected. A survey questionnaire based on perceived CAP was distributed to 273 students and received 139 responses, a 50.92% response rate. The measured data were analyzed using descriptive statistics and reliability analysis in SPSS. The survey results suggest that affective learning is enhanced. However, psychomotor learning efficiency is badly affected when the delivery mode of the laboratory course content is changed from physical face-to-face to total online delivery. The evaluation of the effectiveness of cognitive learning was inconclusive due to the limitation of sample size in this area to enable accurate measurement.

Keywords: Online laboratories, perceived affective, perceived cognitive, perceived psychomotor

ARTICLE INFO

Article history:
Received: 06 July 2022
Accepted: 05 October 2022
Published: 25 May 2023

DOI: https://doi.org/10.47836/pjst.31.4.12

E-mail addresses:
azraa@uitm.edu.my (A'zraaAfhzan Ab Rahim)
ngkokmun@uitm.edu.my (Ng Kok Mun)
azilah574@uitm.edu.my (Azilah Saparon)
fadzli@utem.edu.my (Ahmad Fadzli Nizam Abdul Rahman)
nbuniyamin@uitm.edu.my (Norlida Buniyamin)
*Corresponding author

ISSN: 0128-7680
e-ISSN: 2231-8526

INTRODUCTION

In December 2019, an unknown virus (now called COVID-19) in Wuhan, China, started spreading worldwide, leading to a worldwide pandemic ("Coronavirus:the first three months as it happened", 2020). The pandemic has caused more than 191 million infections and more than 4 million deaths worldwide ("COVID live update:179,937,394 cases",2021). The COVID-19 pandemic quickly led to the closure of universities and colleges to curb the spread of the disease (Murphy, 2020). Consequently, educational institutions in Malaysia quickly adopted e-learning under the online distance learning (ODL) mode in all institutes of higher learning (Tan, 2021).

In the Malaysian Institution of Higher Learning (IHLs), engineering laboratory sessions normally conducted in a traditional face-to-face setting were no longer viable as students were no longer on campus during the pandemic period. March 2020 marks students' first semester to migrate to an online delivery method compared to traditional physical presence at the labs. This migration occurred worldwide, where laboratory courses were made online to replace the conventional offline mode during the pandemic (Monash University, 2021). Before the pandemic, online laboratories were conducted in some institutions via virtual labs, remote control labs, or video-based labs (Zhai et al., 2012). For virtual labs, simulation tools and virtual reality are used. Online laboratories enable students to access and perform the experiments in the lab remotely. On the other hand, video-based activities provide a step-by-step overview of a real lab so that students can visualize the whole experimental process and its outputs through a video demonstration. These methods have now been widely adopted during the pandemic period.

Gamage et al. (2020) reviewed the transition of offline laboratory courses to online methods during the pandemic. The authors presented the challenges of online laboratories and the impact on assessment activities and student experiences. One of the immediate challenges with online laboratories is the difficulty of achieving hands-on practical skills effectively. Lewis (2014) reported that the performance of examinations of the virtual laboratory tools in biological sciences was equally effective as traditional laboratories in increasing student knowledge and understanding as they facilitate active, inquiry-based learning. However, the main pitfall is their inability to provide individual hands-on experience in using lab equipment. Based on the findings of (Gamage et al., 2020; Lewis, 2014), it can be assumed that learning outcomes that will most be affected when an engineering laboratory course is delivered online will be the loss of psychomotor skills and competencies.

The effectiveness of these online courses has been measured in terms of technology readiness, learning experience, quality of teaching, and communication (Khanna & Prasad, 2020; Lau & Sim, 2020). Chan and Fok (2015) evaluated student learning experience in the virtual laboratory through a perception survey. A survey questionnaire with both closed

and open-ended questions was designed, and data were collected to compare students' perceptions of virtual and traditional laboratories. Similarly, Kapilan et al. (2020) developed and circulated a survey among students to gather feedback on their learning experiences after completing their fluid mechanics virtual lab. Based on the survey, 90 percent of the participants were happy about the virtual laboratory and expressed that their learning process improved with virtual laboratory experiments.

Davies (2008) reported that laboratories enable students to (a) develop experimental, design, problem-solving, and analysis skills; (b) develop data-recording and analysis skills; (c) develop communication and interpersonal skills; (d) develop technical judgment and professional practice and (e) integrate theory and practice. These learning attributes can be categorized into the cognitive, affective, and psychomotor (CAP) domains introduced by Bloom (1956). A more recent elaboration of CAP domains can be found in Tomei (2010). The cognitive domain involves the learning and application of knowledge (Bloom, 1956; Bennett et al., 2016). The affective domain addresses the acquisition of attitudes and values (Kratwohl et al., 1956; Taneri, 2017), and the psychomotor domain focus on the development of the body and the skills it performs (Jewett et al., 1971; Ahmad et al., 2018). Hence, it would be more sensible to measure the effectiveness of learning using the CAP learning domains in online laboratory courses.

Perceived CAP learning domains are a good way to measure CAP attainments independent of course content, grades, institution, and other factors. The method is solely based on students' perception of how much they have learned. The measurement and evaluation of CAP domains are usually conducted using students' grades (Cooper & Higgins, 2014; Mohd Nor et al., 2020). This is the current practice in many online and offline courses. However, this method may not reflect what students learned, and the evaluation is constrained by institution, course content, and inconsistencies of instructors (Rovai et al., 2009). Rovai et al. (2009) introduced a perceived CAP that measures the attainment of these learning domains from the students' perception, independent of limitations imposed by course content, instructor assessments, and institution. In 2018, this instrument was used by Horning (2018) to examine the perceived CAP learning of students using open educational resources in face-to-face and distance education courses at nine community colleges in the southeastern United States. It has been used to evaluate CAP learning in the clinical skills training conducted via ODL (Kawasaki et al., 2021) and assess bakery skills required by students during industrial training (Rachmawati et al.,2019). Khidzir et al.(2016) used perceived CAP learning to study the viability of implementing virtual learning in various fields.

However, based on the review, it can be observed that perceived CAP learning in online laboratory courses related to the teaching of engineering, science, and technology during the pandemic has not been conducted extensively. Most CAP perception surveys

focused on non-technology fields and were more general (Rovai et al., 2009; Horning, 2018; Kawasaki et al., 2021; Rachmawati et al., 2019; Khidzir et al., 2016). Other perception surveys concentrate only on the technology readiness, facilities, and quality of teaching (Khanna & Prasad, 2020). Though evaluation of online laboratory courses in engineering has been done (Chan & Fok, 2015 & Kapilan et al., 2020), it mainly focuses on the student learning experiences. They did not assess the perceived CAP domains of learning.

It is believed that investigating CAP domains for online laboratory courses may help practitioners evaluate whether their online laboratory courses can achieve the CAP domains' learning outcomes. The cognitive, affective, and psychomotor learning domains include knowledge of the subject matter, experimental design, problem solving and analysis skills, hands-on competencies, data collection and analysis, interpersonal and communication skills, ability to relate theory and practice, valuing of occupational safety, and health, professional attitudes, and ethics and ability to collaborate with others**.** These attributes have not been studied in-depth by others. They could reveal whether students have learned the CAP effectively in the online laboratory course, particularly in engineering, science, and technology. Given the need to evaluate the perceived CAP achievement of learning in engineering, science, and technology online laboratories, this study aims to measure and evaluate the perceived effectiveness in the CAP domains of learning in electrical engineering online laboratory courses in a Malaysian public university.

METHODOLOGY

After the objective has been identified, the next step is to identify the sample selection to evaluate the achievement of CAP learning domains. A quantitative study was conducted to answer the research questions posed in this study.

Sampling Technique

An online survey questionnaire (non-experimental design) was designed and administered to 273 students in the EE241 Electronics Engineering and EE242 Electrical Engineering degree program at the School of Electrical Engineering, Universiti Teknologi MARA, Shah Alam, Malaysia for the Semester March-August 2021. The online survey was emailed to the chosen respondents in July 2021. The survey is anonymous, and participation is voluntary. The survey questionnaire is explained in the next subsection.

Due to the COVID-19 pandemic, many students have not previously experienced being in a face-to-face lab session at the university. Students from semesters 2, 3, and 4 who were chosen as the respondents for this research are students from three laboratory courses, which are Electrical Engineering Laboratory II (EPO423), Electrical Engineering Laboratory III (EEE430), and Electrical Engineering Laboratory III (EPO562). The laboratory courses

enhanced students' theoretical knowledge and practical skills in using basic electronic and electrical components, handling equipment, and measurement techniques. However, due to the pandemic, the content of these courses was delivered using videos and simulation software.

For example, during a normal face-to-face lab session, one of the experiments was Printed Circuit Board (PCB) Fabrication. Students underwent a complete PCB fabrication process, such as transferring the PCB layout to a transparent sheet, preparing an FR4 board, and fabricating the PCB using an ultraviolet (UV) light exposer, developer, and etching machine. Nevertheless, due to the pandemic, the hands-on exposure to the PCB process was replaced by a video demonstration. A question arises, will the students be aware of health and safety issues by watching an experiment via a video? Online experiments allow multiple runs and extreme variable settings without physical consequences. It might decrease students' perception of risk and danger to themselves or operating equipment wrongly, which may lead to danger or destroy the equipment in an actual physical laboratory. Another example is a student physically in the labs who could be triggered to switch on vents if there are fumes and put on safety glasses if they feel the vibration. As the labs were conducted online, other experiments involving physical measurement from real equipment have been substituted with various simulations using software such as MATLAB and Simulink, Scilab, PSIM, and FEMM.

Data Collection Instrument

A closed-ended survey questionnaire was designed to address the gaps in the literature review. The survey questionnaire was deployed to the chosen sample of respondents using Google Forms to collect responses from students on their perceived attainment in cognitive, affective, and psychomotor (CAP) learning during these online laboratory sessions.

The survey questionnaire consists of two sections. The first section consists of basic demographic questions such as gender, year of study, experience in a physical lab, students' literacy, and communication proficiency. The second section consists of CAP questions developed by adapting and improvising existing, proven perceived CAP questions (Rovai et al., 2009; Chowdury et al., 2019; Kapilan et al., 2020; Chan & Fok, 2015; Rachmawati et al., 2019), and some questions were added to address certain CAP based on expert advice. Originally, there were twenty-two questions for evaluating CAP perception using a 5-point Likert scale (where scores of 1 to 5 were used to indicate levels of agreement with the statements). However, nine questions were removed after the reliability and validation process using SPSS. In the end, 13 questions remain, as listed in Table 1, after performing Principal Component Analysis (PCA) and Exploratory Factor Analysis (EFA) using SPSS. Items reliability was verified using Cronbach Alpha and achieved a reliability value exceeding 0.7.

Table 1

Questionnaire of student CAP perception on online laboratory

Questions	Survey Items	Label
I1	I cannot produce a course study guide (compilation of topics, exercises, and learning activities) for future students	C1r
I2	I cannot organize my tasks, apply appropriate methods and solve related problems to achieve the desired outputs	C2r
I3	I cannot relate the online lab experiments to fundamental concepts and theories	C3r
I4	I cannot complete the online lab independently	C4r
I5	I cannot complete all the required group tasks effectively and timely	C5r
I6	I am actively involved in the learning process through the online lab.	A1
I7	I can communicate my findings and results through reports and oral presentations	A2
I8	I can collaborate well with others in my group	A3
I9	I am aware of the safety requirements when working in a physical lab compared to an online lab	A4
I10	I can perform the online lab experiments multiple times, unrestricted by laboratory space, rules, and safety concerns	P1
I11	I can visualize the procedure for using the lab's equipment through the online lab videos	P2
I12	I can demonstrate to others the physical/technical skills learned in this course	P3
I13	I can operate actual equipment confidently after conducting online lab experiments using simulated/ virtual equipment	P4

Items I1 to I5 are negatively worded to ensure students respond to the survey honestly and have more reliability in terms of measurement after being reverse coded. The questions (Table 2) used in this instrument were mapped to the closest attributes in one of the three CAP learning domains, as shown in Table 2. Each domain is represented by questions that refer to the domain's lower and higher learning levels.

Table 2

Attributes of CAP domains of learning for online laboratory

Cognitive	Affective	Psychomotor
• Ability to relate theory and practice (**I3**)*	• Ability to regulate attitude of learning (**I6**)*	• Ability to demonstrate the practical skills learned (**I12**)**
• Ability to collect and analyze data (**I2, I4, I5**)*	• Ability to collaborate with others (**I8**)*	• Ability to perform laboratory work safely (**I10**)***
• Ability to analyze and solve problems (**I2, I3, I5**)	• Ability to communicate results and findings (**I7**)*	• Ability to handle actual equipment after learning simulated/video-based experiments (**I13**)***
• Ability to understand and apply knowledge independently (**I3, I4**)**	• Ability to communicate effectively with instructor/peers (**I7**)*	• Ability to conduct experiments via guided responses (**I10, I11, I12**)*
• Ability to organize knowledge (**I1, I2**) **	• Ability to evaluate learning experience (**I6, I9**)*	
	• Ability to value safety and ethics (**I9**)***	

Referred and elaborated from: * (Davies, 2008) **(Rovai, 2009) ***New attributes

Data Handling and Analysis

The data collected from the approved questions were stored securely in Google Drive, which requires secure access. As the questions were all set as compulsory, all respondents answered all the questions. Hence, there are no outliers in the data. Subsequently, the data were exported for further analysis.

Reliability tests were conducted to ensure the consistency of the data collection instrument. Confidence interval and margin of error were checked to ensure that the data obtained and the estimation of the location of a statistical parameter was true for the population (Taherdoost, 2017).

Lastly, descriptive and inferential statistics were used to analyze the collected data. The data were analyzed by the median, lower and upper quartile of each item and the distribution of responses, i.e. (percentage (%) that agree, disagree). Data on the number of students with experience in a physical lab and students who do not have physical lab experience were compared. Mann-Whitney U-test was conducted to investigate whether a significant statistical difference exists in students' confidence to operate actual equipment between those with and without physical lab experience (I13). Other demographic data such as gender, year of study, students' literacy, and communication proficiency are not used in this study and are reserved for future studies.

RESULTS AND DISCUSSION

This section discusses the results in greater detail for the research questions concerning the achievement of CAP attributes in the online laboratory courses of our case study.

Respondents' Demographics

A total of 139 students (98 males and 41 females) out of 273 from three different laboratory courses and semesters participated in the survey. The sample size gives a 95% confidence level and a 5.80% margin of error, which means the survey results are acceptable and representative of the engineering student population who took the courses. Figure 1 indicates that only 22.30% (31 out of 139 students) have attended physical laboratory at the university, while others only attended online courses because they were from the lower semesters and the online courses started in 2020.

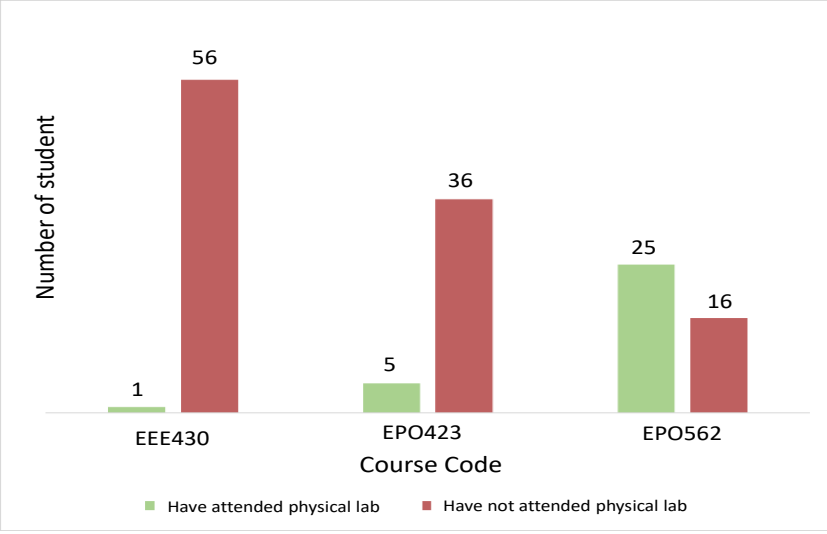

Figure 1. Respondents' demographic profiles data

Reliability Test

The data were analyzed using SPSS version 28. The reliability statistics for the survey items are shown in Table 3. On average, the students responded positively to the thirteen items with good reliability, from 0.7 to 0.85 for Cronbach's Alpha (Taber, 2018). It confirms that all the questions have high internal consistency.

Salient Outcomes from CAP analysis

For CAP analysis, data from the survey are considered ordinal categorical data since the survey questions were based on the level of agreement, from strongly agree to strongly

disagree (Chen & Wang, 2014). Hence, the data were analyzed by the median, lower and upper quartile of each item and the distribution of responses, i.e., the percentage that agrees or disagrees. Some responses are not uniformly distributed; hence, the median as central tendency and interquartile range (IQR) is used to measure the dispersion of data (Kostoulas, 2014).

Table 3

Reliability (Cronbach's Alpha) statistics

Domains of Learning	Cronbach's Alpha
Cognitive*	0.815
Affective	0.726
Psychomotor	0.852

**Note*. Negatively worded items were reverse-scored

Cognitive Learning

Table 4 shows the descriptive statistics for assessing students' cognitive learning perception. It shows the number of respondents, *n,* and the percentage of respondents who strongly agree, agree, is neutral, disagree, or strongly disagree with each question. The quartiles show that not more than 25% of the sample is below 2, and not more than 25% is above 4. Thus, the data are concentrated in the center except for item I5, which is positively skewed.

Findings for the cognitive domain show that 41.00% agreed they could not produce a course study guide for future students (I1). Neutral is 30.94% and those who were sure they could produce a study guide are 28.06%. It suggests that most students (41.00% vs. 28.06%) may not be competent to independently organize knowledge and their learning process in the form of a personal course study guide. This suggestion is further strengthened by findings for I2 and I3, where for both questions, most students agreed that they are not competent to organize their tasks or relate to experiments. It could thus be concluded that the learning process delivered online was not effective. As for I4*,* more students think they could complete the experiment individually (35.25% vs. 30.93%); for I5, the majority could complete the group task.

Table 4

Descriptive statistics of cognitive learning

Cognitive	Median	Q1	Q3	Strongly disagree *n* (%)	Disagree *n* (%)	Neutral *n* (%)	Agree *n* (%)	Strongly agree *n* (%)
I cannot produce a course study guide (compilation of topics, exercises, and learning activities) for future students. (**I1**)	3	2	4	4 (2.88)	35 (25.18)	43 (30.94)	47 (33.81)	10 (7.19)

Table 4 *(Continue)*

Cognitive	Median	Q1	Q3	Strongly disagree *n* (%)	Disagree *n* (%)	Neutral *n* (%)	Agree *n* (%)	Strongly agree *n* (%)
I cannot organize my tasks, apply appropriate methods and solve related problems to achieve the desired outputs (**I2**)	3	2	4	7 (5.04)	33 (23.74)	53 (38.13)	36 (25.90)	10 (7.19)
I cannot relate the online lab experiments with fundamental concepts and theories (**I3**)	3	2	4	6 (4.32)	31 (22.30)	49 (35.25)	40 (28.78)	13 (9.35)
I cannot complete the online lab independently (**I4**)	3	2	4	11 (7.91)	38 (27.34)	47 (33.81)	27 (19.42)	16 (11.51)
I cannot complete all the required group tasks effectively and timely **(I5)**	2	2	4	17 (12.23)	53 (38.13)	27 (19.42)	34 (24.46)	8 (5.76)

Our findings differ from the perceived opinion of academics (with a mean score of 3.78 out of 5) that cognitive learning can be attained in online courses based on the survey (Khidzir et al., 2016). It also contradicts the findings of Kawasaki et al. (2021) that cognitive learning was not affected in an online nursing course. Overall, the perceived cognitive learning was unsatisfactory for the online laboratory. An adequate performance should reveal a median score of at least 2 and below if most students disagreed/strongly disagreed that they could not do the tasks in I1 to I4. Hence, it can be said that some aspects of cognitive learning were lost in online labs. Factors that contributed to this should be identified and further investigated.

Affective Learning

Table 5 shows the descriptive statistics for the items assessing affective learning, the number of respondents, *n,* and the percentage (%) of respondents who strongly agree, agree, are neutral, disagree, or strongly disagree with each question. Contrary to the results of the cognitive domain, responses for all four items are negatively skewed in the affective

domain, as seen in Table 6. Most respondents show agreement with all statements, i.e., I6 to I9. About 74% of the respondents agreed they were actively involved in the learning process (I6), whereas 84.17% agreed they could collaborate well with others in their lab group (I7). However, only 58.99% agreed they could communicate results and findings through reports and demonstrations. It indicates that the online laboratory courses provided space to interact with their peers or instructors, which helps the learning process. However, respondents who disagree or are neutral about these aspects of the online lab may be affected by internet connectivity and their motivation to learn in an online environment.

As for I9, surprisingly, 86.30% agreed with the statement, agreeing that they are aware of the safety requirements when working in a physical lab compared to an online lab, even though only 22.30% of the respondents had experienced being in a physical lab before the pandemic. It could be attributed to the explanation of safety by instructors or provided in the lab manual. In addition, those who may not have entered the lab due to the pandemic, i.e., semester 1 to semester 3 students, may have responded to this question based on their safety awareness in previous physical labs experienced in their secondary/diploma studies. These may be some factors that can be further investigated. Overall, the results of the affective domain reveal that the students have good attitudes and values. They could evaluate their own learning experiences quite well. It can be observed that this aspect of learning is preserved in an online setting. It can be supported by the findings of (Kawasaki et al., 2021) that affective learning in online labs is as effective as in face-to-face labs. In addition, it is shown that affective learning is not affected when students use digital resources compared to traditional textbooks (Horning, 2018).

Table 5
Descriptive statistics of affective learning

Affective	Median	Q1	Q3	Strongly Disagree *n* (%)	Disagree *n* (%)	Neutral *n* (%)	Agree *n* (%)	Strongly Agree *n* (%)
I am actively involved in the learning process through the online lab (**I6**)	4	3	5	0 (0)	12 (8.63)	25 (17.99)	64 (46.04)	38 (27.34)
I can collaborate well with others in my group (**I7**)	4	4	5	0 (0)	5 (3.60)	17 (12.23)	49 (35.25)	68 (48.92)

Table 5 *(Continue)*

Affective	Median	Q1	Q3	Strongly Disagree *n* (%)	Disagree *n* (%)	Neutral *n* (%)	Agree *n* (%)	Strongly Agree *n* (%)
I can communicate my findings and results through reports and oral presentations (**I8**)	4	3	4	1 (0.72)	8 (5.76)	48 (34.53)	62 (44.60)	20 (14.39)
I am aware of the safety requirements when working in a physical lab compared to an online lab (**I9**)	4	4	5	2 (1.44)	5 (3.60)	12 (8.63)	64 (46.04)	56 (40.29)

Psychomotor Learning

Table 6 shows the descriptive statistics of psychomotor learning, and it portrays different types of distribution with an IQR score of 1. It means most of the answers are concentrated at the 'neutral.' As for the psychomotor domain, 65.47% of the students agreed/strongly agreed that they could perform the online lab experiments multiple times, unrestricted by laboratory space, rules, and safety concerns (I10). Response to (I11) showed that more than half of the samples could visualize the procedure to use the lab's equipment through the online lab video. It indicates that the delivery method, such as video demonstrations, instructor explanations, and lab manuals, have satisfactorily instilled students' knowledge and understanding of guided responses.

As for items I12 and I13, 42.45% indicated they could demonstrate the skills learned (I12) to others, whereas 34.53% agree/strongly agree they could operate actual equipment. However, approximately 42 to 45% of the students were neutral with the statement that they could demonstrate the physical/technical skills learned and operate the equipment confidently. The relevance of experience in the physical lab with the ability to demonstrate technical skills and operate actual equipment confidently is portrayed in the bar graphs in Figure 2.

Figure 2(a) shows that 25.81% (8 out of 31 students) who have attended physical lab perceive that they could not demonstrate the skills they have learned. Figure 2(b) shows a similar trend where 29.03% (9 out of 31 students) with physical lab experience rate themselves as incapable of confidently operating actual equipment. It is probably based on their experience that they knew the difficulty of handling the actual equipment compared to

Table 6

Descriptive statistic of psychomotor learning

Psychomotor	Median	Q1	Q3	Strongly Disagree *n* (%)	Disagree *n* (%)	Neutral *n* (%)	Agree *n* (%)	Strongly agree n (%)
I can perform the online lab experiments multiple times, unrestricted by laboratory space, rules, and safety concerns (**I10**)	4	3	4	3 (2.16)	5 (3.60)	40 (28.78)	62 (44.60)	29 (20.86)
I can visualize the procedure to use the lab's equipment through the online lab videos (**I11**)	3	3	4	3 (2.16)	20 (14.39)	49 (35.25)	50 (35.97)	17 (12.23)
I can demonstrate to others the physical/ technical skills learned in this course (**I12**)	3	3	4	8 (5.75)	14 (10.07)	58 (41.73)	52 (37.41)	7 (5.04)
I can operate actual equipment confidently after conducting online lab experiments using simulated/ virtual equipment (**I13**)	3	3	4	12 (8.63)	16 (11.51)	63 (45.32)	38 (27.34)	10 (7.19)

the virtual simulations. Taking the analysis a step further, we performed the Mann-Whitney U-test on item I13 to investigate if there is any significant difference between students who have and have not attended physical lab before. The Mann-Whitney U-test is chosen as the alternative to the independent t-test since, in this research, the Likert scale is considered ordinal data, as discussed earlier, Salient Outcomes from CAP analysis. Hence the suitable inferential statistic is the nonparametric Mann-Whitney U-test. The result is seen in Table 8.

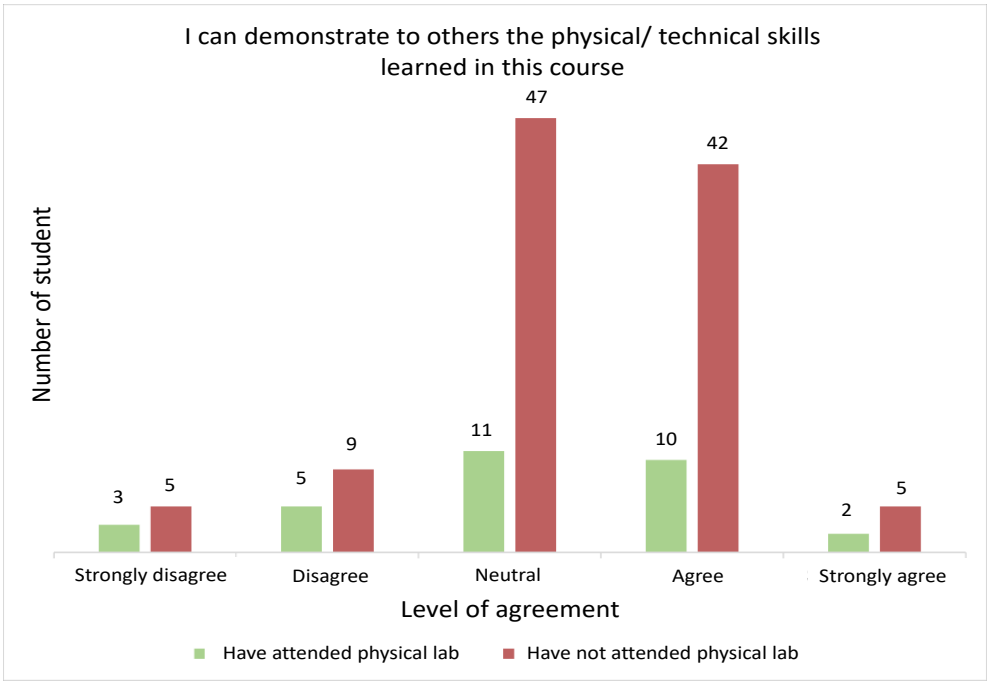

(a)

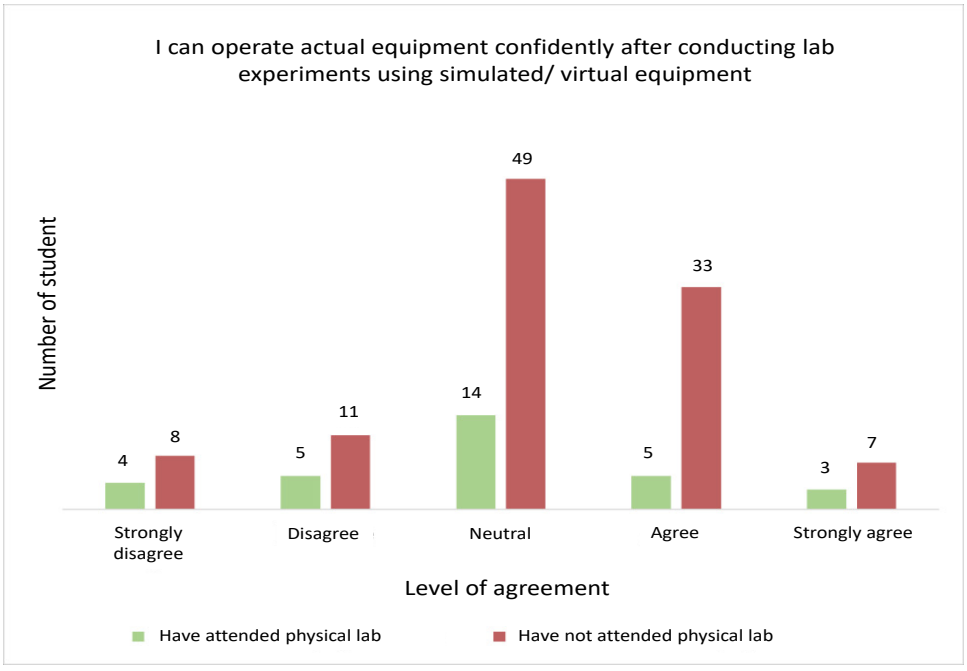

(b)

Figure 2. Difference of perception between students who have and have not attended physical lab for items I12 (a) and I13 (b)

With a non-significant p-value of 0.186 (p>0.05) for the Mann-Whitney U-Test shown in Table 7, we can conclude that there is no statistically significant difference (p>0.05) between students who have or have not been in a physical lab before when it comes to their confidence in operating lab equipment after conducting online lab experiments using simulated/virtual equipment.

Table 7

Mann-Whitney U-test

	Test Statistics[a]
	I can operate actual equipment confidently after conducting online lab experiments using simulated/virtual equipment
Mann-Whitney U	1428.500
Wilcoxon W	1924.500
Z	-1.321
Asymp. Sig. (2-tailed)	.186

a. Grouping Variable: Have or have not attended physical lab

In addition, as seen in Table 8, the mean rank for the group that has not attended physical lab is 72.27, while the mean rank for the group that has attended physical lab is 62.08. It illustrates that the scores between both groups tend to be similar, indicating that the confidence level in handling equipment after online simulations is independent of the student's physical lab experience.

Overall, those who indicated they could handle actual equipment were lower at 34.53% (48 out of 139 students) compared to those who were confident to demonstrate the skills (i.e., software/simulations) learned, which is much higher at 42.45% (59 out of 139 students). Furthermore, the simulation does not reflect real issues because symbols or icons of components do not emulate the real components in true behavior. Hence, the 42.45% who agree/strongly agree with I12 believe they could demonstrate to others that the physical/technical skills learned in the course were mostly software.

Table 9

Rank of students who have and have not attended physical lab for item item I13

	Have or have not attended physical lab	N	Mean Rank	Sum of Ranks
I can operate actual equipment confidently after conducting online lab experiments using simulated/virtual equipment	No	108	72.27	7805.50
	Yes	31	62.08	1924.50
	Total	139		

The beauty of online courses is that students can perform experiments multiple times without restrictions. However, students cannot properly visualize the lab procedures without good video demonstrations or visualization ability. As for those who have not attended any physical lab, more than 40.00% were neutral on their ability to operate the equipment (I13) or demonstrate the physical skills (I12), as presented in Table 7, which could be because they had not been exposed to handling actual equipment. The hands-on aspect of the psychomotor domains suffers the most loss in an online lab, where only 34.53% of respondents indicated they could confidently handle actual equipment. This finding can be somewhat supported by the perceived opinion from academics that psychomotor skills may be the most poorly attained in online distance learning (Khidzir, 2016). Lewis (2014) also concurred that virtual labs could not provide students with actual hands-on experience. However, it is interesting to note that Kawasaki et al. (2021) stated that psychomotor learning in online labs is as effective in face-to-face settings for nursing students. Perhaps hands-on learning may not be ineffective in an online environment depending on the level of difficulty of the psychomotor skill that needs to be imparted and the complexity of the required equipment. It can be further explored and analyzed in future research.

CONCLUSION

This research aims to measure and evaluate students' learning efficiency in electrical and electronics engineering online laboratory courses in the CAP learning domains. The findings indicate the advantages of teaching laboratory courses online, especially in the affective learning domain. Though conducted online, the laboratory courses seem capable of attracting students' enthusiasm for learning through interactivity, encouraging collaboration, and offering a safe environment by maximizing time and space flexibilities through simulated experiments. Hence, the affective learning domain is still preserved.

On the other hand, it was discovered that safety awareness and ethics are best instilled in a physical lab. The major disadvantage is that teaching laboratory courses online affects learning in the psychomotor domain. Students become unfamiliar with physical instruments and real devices, which may affect their confidence level when faced with the actual equipment in the future. Simulated experiments and video demonstrations could not help students attain hands-on skills effectively. So, transferable hands-on skills cannot be achieved. In addition, attributes in the cognitive domain are unattainable because of the limitation of the sample size of experienced students in the physical lab since only 22.30% (31 out of 139 students) have attended the physical lab before. The cognitive learning which was averagely attained can also be attributed to various factors such as the delivery methods of the instructors, the clarity of the video demonstrations, and lab manuals. Poor design and implementation of the delivery method could lead to the ineffective impartation of knowledge and understanding. It is good that further works should scrutinize and evaluate

online lab delivery methods and other contributing factors such as internet connectivity and student self-learning ability in an online environment.

ACKNOWLEDGEMENT

The authors thank the College of Engineering, Universiti Teknologi MARA, Shah Alam, Malaysia for financial support.

REFERENCES

Ahmad, A., Kamin, Y., & Nasir, A. N. M. (2018). Applying psychomotor domain for competency-based teaching in Vocational Education. *Journal of Physics: Conference Series*, *1049*, Article 012049. https://doi.org/10.1088/1742-6596/1049/1/012049

Bennett, R. E., Deane, P., & van Rijn, P. W. (2016). From cognitive-domain theory to assessment practice. *Educational Psychologist*, *51*(1), 82-107. https://doi.org/10.1080/00461520.2016.1141683

Bloom, B. S. (Ed.). (1956). *Taxonomy of Educational Objectives*, *Handbook I: Cognitive Domain*. David McKay.

Bloom, B. S., Englehart, M. D., Furst, E. J., Hill, W. H., & Krathwohl, D. R. (1956). *Taxonomy of Educational Objectives*, *Handbook II: Affective Domain*. David McKay Company.

Chan, C., & Fok, W. (2015). Evaluating learning experiences in virtual laboratory training through student perceptions: A case study in electrical and electronic engineering at the University of Hong Kong. *Engineering Education*, *4*(2), 70-75. https://doi.org/10.11120/ened.2009.04020070

Chen, H. C., & Wang, N. S. (2014). The assignment of scores procedure for ordinal categorical data. *Scientific World Journal*, *2014*, Article 304213. https://doi.org/10.1155/2014/304213

Chowdury, H., Alam, F., & Mustary, I. (2019). Development of an innovative technique for teaching and learning of laboratory experiments for engineering courses. *Energy Procedia*, *160*, 806-811. https://doi.org/10.1016/j.egypro.2019.02.154

Cooper, H., & Higgins, S. (2015). The effectiveness of online instructional videos in the acquisition and demonstration of cognitive, affective, and psychomotor rehabilitation skills. *British Journal of Educational Technology*, *46*(4), 768-779. https://doi.org/10.1111/bjet.12166

Worldometer. (2021). COVID live update:179,937,394 cases: Coronavirus Statistics. https://www.worldometers.info/coronavirus/

Davies, C. (2008). *Learning and Teaching in Laboratories*. Higher Education Academy Engineering Subject Centre, Loughborough University.

Gamage, K. A. A., Wijesuriya, D. I., Ekanayake, S. Y., Rennie, A. E. W., Lambert, C. G., & Gunawardhana, N. (2020). Online delivery of teaching and laboratory practices: Continuity of university programmes during covid-19 pandemic. *Education Sciences*, *10*(10), Article 291. https://doi.org/10.3390/educsci10100291.

Jewett, A. E., Jones, L. S., Luneke, S. M., & Robinson, S. M. (1971). Educational change through a taxonomy for writing physical education objectives. *Ques*t, *15*(1), 32-38. https://doi.org/10.1080/00336297.1971.10519699

Kapilan, N., Vidhya, P., & Gao, X-Z (2020). Virtual laboratory: A boon to the mechanical engineering education during Covid-19 pandemic. *Higher Education for the Future*, *8*(1), 31-46. https://doi.org/10.1177/2347631120970757

Kawasaki, H., Yamasaki, S., Masuoka, Y., Iwasa, M., Fukita, S., & Matsuyama, R. (2021). Remote teaching due to COVID-19: An exploration of its effectiveness and issues. *International Journal of Environmental Research and Public Health*, *18*(5), Article 2672. https://doi.org/10.3390/ijerph18052672

Khanna, D., & Prasad, A. (2020). Problems faced by students and teachers during online education due to covid-19 and how to resolve them. In *2020 6th International Conference on Education and Technology (ICET)* (pp. 32-35). IEEE Publishing. https://doi.org/10.1109/ICET51153.2020.9276625

Khidzir, N. Z., Daud, K. A. M., & Ibrahim, M. A. H. (2016). The relationship among student's domain of learning development implementing virtual learning in higher learning institutions. *International Journal of Information and Education Technology*, *6*(6), 418-422. http://dx.doi.org/10.18178/ijiet

Kostoulas, A. (2014). How to summarize Likert Scale data using SPSS. https://achilleaskostoulas.com/2014/12/15/how-to-summarise-likert-scale-data-using-spss/

Lau, S. L., & Sim, T. Y. (2020). Feedback of university students on online delivery learning during the covid-19 pandemic period. In *2020 IEEE Conference on e-Learning, e-Management, and e-Services (IC3e)* (pp.13-18). IEEE Publishing https://doi.org/10.1109/IC3e50159.2020.9288409

Lewis, L. D. (2014). *The Pedagogical Benefits and Pitfalls of Virtual Tools for Teaching and Learning Laboratory Practices in the Biological Sciences.* The Higher Education Academy.

Monash University. (2020). Remote labs ensure continuity of lab exercises. *University News*. https://www.monash.edu.my/news-and-events/pages/latest/articles/2021/remote-lab-ensures-ontinuity-of-lab-exercises.

Murphy, M. P. A. (2020). Covid-19 and emergency e-Learning: Consequences of the securitization of higher education for post-pandemic pedagogy. *Contemporary Security Policy*, *41*, 492-505. https://doi.org/10.1080/13523260.2020.1761749

Nature. (2022, April 17). Coronavirus: The first three months as it happened. *Nature*. https://doi.org/10.1038/d41586-020-00154-w

Noor, N. A. M., Saim, N. M., Alias, R., & Rosli, S. H. (2020). Students' performance on cognitive, psychomotor and affective domain in the course outcome for embedded course. *Universal Journal of Educational Research*, *8*(8), 3469-3474. https://doi.org/10.13189/ujer.2020.080821

Rachmawati, E., Mufidah, L., Sulistiyani, T., & Ab-Latif, Z. (2019). Examining the students' cognitive, affective and psychomotor abilities in the bakery industry. *Journal of Technology and Operations Management*, *14*(2), 1-9. https://doi.org/10.32890/jtom2019.14.2.1

Rovai, A., Wighting, M., Baker, J., & Grooms, L. (2009). Development of an instrument to measure perceived cognitive, affective, and psychomotor learning in traditional and virtual classroom higher education settings. *The Internet and Higher Education*, *12*(1), 7-13. https://doi.org/10.1016/j.iheduc.2008.10.002

Taherdoost, H. (2017). Determining sample size: How to calculate survey sample size. *International Journal of Economics and Management Systems*, *2*, 237-239.

Tan, P. L. (2021, June 1). Online learning: Leave no student behind. *The Star*. https://www.thestar.com.my/opinion/letters/2021/06/01/online-learning-leave-no-student-behind

Taber, K. S. (2018) The use of Cronbach's alpha when developing and reporting research instruments in science education. *Research in Science Education*, *48*, 1273-1296. https://doi.org/10.1007/s11165-016-9602-2

Taneri, P. O. (2017). The viewpoints of instructors about the effects of teacher education programs on prospective teachers' affective characteristics. *Eurasian Journal of Educational Research*, *17*(70), 105-120. http://dx.doi.org/10.14689/ejer.2017.70.6

Tomei, L. (2010). The cognitive, affective, and psychomotor domains: The taxonomy of the traditional learner. IGI Global. https://doi.org/10.4018/978-1-60566-824-6.ch004

Zhai, G., Wang, Y., & Liu, L. (2012). Design of electrical online laboratory and E-learning. *IERI Procedia*, *2*, 325-330. https://doi.org/10.1016/j.ieri.2012.06.096

Pertanika J. Sci. & Technol. 31 (4): 1827 - 1845 (2023)

PERTANIKA JOURNALS

SCIENCE & TECHNOLOGY

Journal homepage: http://www.pertanika.upm.edu.my/

Spectral Correction and Dimensionality Reduction of Hyperspectral Images for Plant Water Stress Assessment

Lin Jian Wen[1], Mohd Shahrimie Mohd Asaari[1]* and Stijn Dhondt[2]

[1]School of Electrical and Electronic Engineering, Universiti Sains Malaysia, Nibong Tebal, 14300 USM, Penang, Malaysia
[2]Ghent University, Department of Plant Biotechnology and Bioinformatic, Ghent 9000, Belgium

ABSTRACT

Hyperspectral Imaging (HSI) is one of the emerging techniques used in plant phenotyping as it carries abundant information and is non-invasive to plants. However, factors like illumination effect and high-dimensional spectral features need to be solved to attain higher accuracy of plant trait analysis. This research explored and analysed spectral normalisation and dimensionality reduction methods. The focus of this paper is twofold; the first objective was to explore the Standard Normal Variate (SNV), Least Absolute Deviations (L1) and Least Squares (L2) normalisation for spectral correction. The second objective was to explore the feasibility of Principal Component Analysis (PCA) and Analysis of Variance Fisher's Test (ANOVA F-test) for spectral dimensionality reduction in spectral discriminative modelling. The analysis techniques were validated with HSI data of maise plants for early detection of water deficit stress response. Results showed that SNV performed the best among the three normalisation methods. Besides, ANOVA F-test outperformed PCA for the band selection method as it improved the trait assessment on the water deficit response of maise plants.

Keywords: Analysis of variance fisher's test, hyperspectral imaging, plant phenotyping, principal component analysis, standard normal variate

ARTICLE INFO

Article history:
Received: 14 July 2022
Accepted: 05 October 2022
Published: 25 May 2023

DOI: https://doi.org/10.47836/pjst.31.4.13

E-mail addresses:
jianwenapp1996@gmail.com (Lin Jian Wen)
mohdshahrimie@usm.my (Mohd Shahrimie Mohd Asaari)
stdho@psb.vib-ugent.be (Stijn Dhondt)
*Corresponding author

INTRODUCTION

The advanced technology in plant genomics is important for breeding more sustainable crops. However, the ability to dissect traits' genetics depends on plant phenotyping development. Among the techniques developed for plant phenotyping are visible,

ISSN: 0128-7680
e-ISSN: 2231-8526

fluorescence imaging, infrared imaging, hyperspectral Imaging (HSI), and 3D structural tomography.

Visible imaging was performed to plant phenotyping by analysing digital images with spectral information from 400 nm–700 nm. The advantage of this technique is low implementation cost and maintenance fee. Despite that, there are limitations like restricted analysis of plant physiology and difficulty caused by overlapping leaves. Fluorescence imaging contradicts visible imaging by detecting fluorescence signals (250 nm–700 nm) emitted from plants after exposure to visible or UV light. This method detects plant diseases (Balachandran et al., 1997; Lohaus et al., 2000). In general, every object emits infrared radiation, allowing infrared imaging possible for plant phenotyping (Kastberger & Stachl, 2003). Infrared radiation ranges from 700 nm to 1000 nm. The wide range will require a high computational cost. Therefore, many implementations of infrared imaging only focus on a certain band range. For instance, thermal imaging utilises spectra from 3–5 μm and 7–14 μm for detecting biotic and abiotic stresses (Chaerle & van der Straeten, 2000; Nilsson, 1995). Near-infrared (NIR) is another way to utilise infrared radiation. It ranges from 700 nm–1400 nm and has a higher reflective intensity on healthy green plants (Yang et al., 2013). The benefit of NIR imaging is that radiation can be transmitted through leaves that overcome difficulties visible imaging faces.

Hyperspectral imaging (HSI) is a technique that combines both visible and NIR imaging methods. The downside of visible and NIR imaging can be overcome mutually. Furthermore, HSI can divide images into bands, enabling analysis of the plant's condition using Vegetation Indices (VI). Ihuoma and Madramootoo (2019) compared a few vegetation indices extracted from hyperspectral images to monitor the water stress level in tomato plants and found that Water Index (WI), Photochemical Reflectance Index centred at 550 nm (PRI550), and Optimised Soil Adjusted Vegetation Index (OSAVI) are the most sensitive indices in distinguishing plants with 80% or less available water content (AWC). Besides, the popular NDVI and RENDVI were studied by Andaryani et al. (2019) to investigate the drought level in the agriculture field. These studies show that water-sensitive VIs can detect drought stress to a certain extent. However, these studies do not consider linearity and scattering of illumination. Thus, solely computing VIs from hyperspectral data might not be the most optimum method for identifying water-stressed plants. In different studies, HSI has been used to estimate leaf water content (LWC) and the result is compared with LWC value measured destructively (Ge et al., 2016; Pandey et al., 2017). However, this approach is undesirable as many samples will be destroyed for long-duration studies. In contrast, the comparison is made between hyperspectral images of the control and water-deficit groups (Asaari et al., 2019) by computing the Euclidean Distance (ED) of the hyperspectral spectrum with reference from the control group.

Although HSI has many edges over other imaging techniques, it is still far from perfection. The illumination effect is still one of the difficulties faced by plant phenotyping.

Besides, the high dimension of hyperspectral images also leads to high computational costs. This study performs quantitative analysis for eliminating the illumination effect using SNV, L1, and L2 normalisation techniques to tackle these concerns. SNV is considered the effective method to reduce the illumination effect (Asaari et al., 2018). Even though SNV shows prominent results in mitigating linear illumination effect (Mohd Asaari et al., 2018; Vigneau et al., 2011). One of the downsides is the inability to extract VIs from SNV spectra as the values are not bounded in the positive range, thus preventing direct linkage between the normalised wavelength and the biophysical properties of the plant. It is worth mentioning that, apart from SNV, Savitzky-Golay (SG) filter (Fletcher & Turley, 2018; Liu et al., 2019) and Multiple Scattering Correction (MSC) (Geladi et al., 1985; Isaksson & Næs, 1988) are other popular spectral pre-treatment methods. SNV and MSC are both spectral pre-processing inspired by chemometrics. The difference between SNV and MSC is that MSC requires a reference spectrum deemed unaffected by noises (Li et al., 2018). In most HSI analyses, the performance of MSC is very dependent on the average spectrum as it is used as the reference spectrum, which is difficult to excess, especially on articulated plant structures. In this context, SNV performs better than MSC (Mishra, Lohumi, et al., 2020) as the average spectrum is not out of the noise. On the other hand, the SG filter is used to smoothen hyperspectral data from the data aspect without considering chemometrics. Thus, pure smoothing ignores the multiplicative and additive effect when illumination is reflected from the plant surface.

Another popular method in pre-processing of hyperspectral data is L1 and L2. In a recent study (Zhuang & Ng, 2020), L1 normalisation was used to remove Gaussian noise from hyperspectral images. On the other hand, Feng et al. (2022) used L2 normalisation to improve feature robustness towards impulse noise before feeding data into the deep learning model. Even though these studies show satisfactory results for respective objectives, the data used are remote sensing hyperspectral images. To the author's knowledge, no study has been done using L1 and L2 normalisation on proximal hyperspectral images thus far. In recent work (Abenina et al., 2022), HSI analysis was performed to study plant traits by comparing the SG filter, MSC and SNV. The results showed that SNV performs best among all. Thus, only SNV is implemented here to compare with L1 and L2 to see if the proposed normalisation method works better than the current best method.

Besides the illumination issues, another common difficulties researchers face when dealing with a hyperspectral image is the curse of dimensionality, also known as Hughes Phenomenon (Hughes, 1968). The high number of bands carried by hyperspectral images always requires high computational power and time for analysis. To tackle these concerns, two dimension reduction methods, PCA and ANOVA F-test (Asaari et al., 2019; Calzone et al., 2021; Pandey et al., 2017), are explored to quantify their feasibility for improving spectral discrimination. Even though these two methods serve the same purpose, the

dimensionally reduced data characteristic differs. Principal Components (PCs) generated by PCA are non-interpretable, whereas ANOVA F-test works more directly by selecting the most varied bands. This study compares the effectiveness of the two methods in dimension reduction and determines if they can be used as an alternative to each other.

This study aims to address two objectives. The first objective involves evaluating the suitability of two proposed normalization methods, L1 and L2 in comparison to the current best method, SNV normalization, for HSI analysis. The second objective entails comparing the water stress detection efficiency of two dimension reduction methods, namely PCA and ANOVA F-test. The more effective normalization and dimension reduction method will be determined via computation of Euclidean Distance (ED) between spectra of two different groups of maise plants; healthy and water deficit groups.

METHODOLOGY

In this work, the images of maise plants were obtained from Asaari et al. (2018), in which imaging was done in the VIB-UGent Center greenhouse in Ghent, Belgium. Pushbroom hyperspectral camera with visible to NIR detection range was coupled with an array of 3x3 halogen lamps, each placed at the same level as the camera. During image acquisition, maise plants were transferred via a high-throughput phenotyping platform (HTPPP) and individually snapped in dedicated enclosed cabins.

The obtained data were separated into two sets, where the first dataset contains hyperspectral images of five maise plants captured at five different platform heights. Meanwhile, the second dataset contains hyperspectral images of ten maise plants, categorised into control and water-deficit groups, followed consecutively for nine days. Hyperspectral images captured have resolutions of 510 x 328 pixels, and each pixel has 194 spectral bands ranging from 400 nm to 1000 nm.

After the images dataset was prepared, white and dark reference was carried out to convert reflectance intensities into values between 0 and 1 followed by removal of bands with inconsistent values. After that, vegetation pixels were segmented by calculating every pixel's Normalised Difference Vegetation Index (NDVI). Pixels with NDVI values lower than 0.3 were removed.

To achieve the first objective spectral normalisation was performed after the pre-processing steps to reduce the illumination effects. SNV, L1, and L2 normalisations were carried out separately on both datasets. For the first dataset, clustering was used to classify normalised spectra into clusters. Five graphs representing different platform heights were studied for each spectra type. For the second dataset, spectra similarity measurement was computed between the mean spectra of maise plants and daily reference. Results were presented in error bar graphs to determine the duration for complete discrimination between control and water-deficit groups. In achieving the second objective, the normalised

spectra of the second dataset were further processed by dimension reduction using PCA and ANOVA F-test separately. Then, spectra similarity measurement was performed again to determine the duration of attaining the complete separation of control and water-deficit groups. Figures 1 and 2 show the flowchart from image acquisition to plant discrimination.

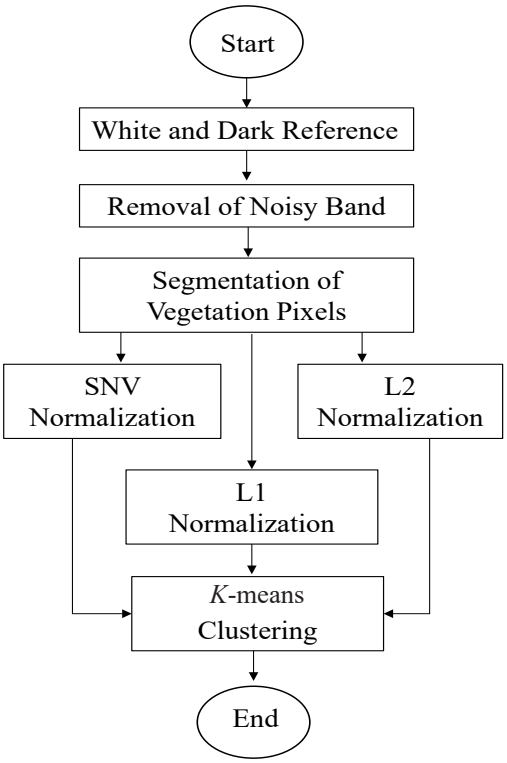

Figure 1. Process flow for the first dataset

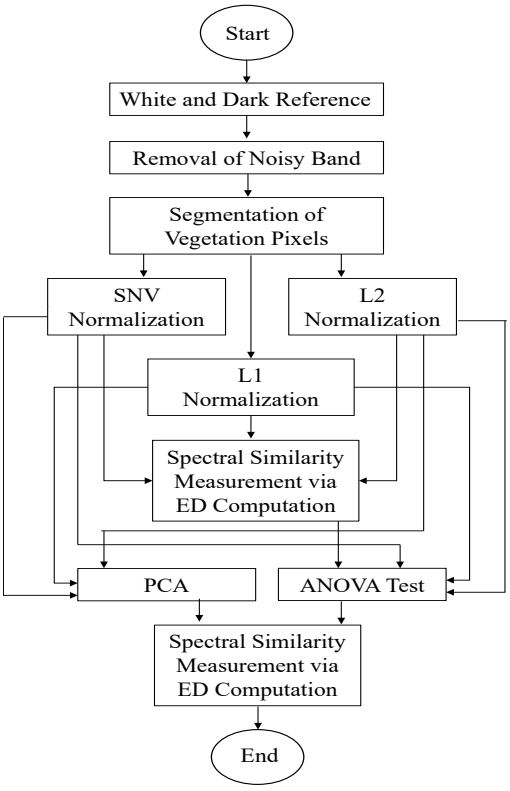

Figure 2. Process flow for the second dataset

Image Pre-processing

There were three steps in this stage. The first was a white and dark reference, a standardisation method common in hyperspectral images study (Geladi et al., 2004; Ortaç et al., 2016; Shaikh et al., 2021). White reference is obtained by capturing an image when placing a high reflectance (~99%) board perpendicularly opposite the camera. On the other hand, dark reference is the image captured when the shutter or light is off. Reflectance was calculated using Equation 1:

$$R = \frac{I-D}{W-D} \quad (1)$$

where R is reflectance, I is original image intensity, D is a dark reference, and W is a white reference.

Noisy bands fluctuate inconsistently due to different kinds of noise like thermal, instrumental, and photon noise, thus containing more outlying values. In this work, the bands below 500 nm and above 810 nm are visibly noisy and were removed, leaving spectra with 111 spectral bands after the process.

Since leaves of maise plants did not just form the original hyperspectral image but also unnecessary components like pots and platforms, segmentation of vegetation pixels was required. NDVIs of all pixels were calculated. Then, the threshold was set to 0.3. It means pixels with NDVI of more than 0.3 were deemed to belong to the maise plant's leaves. Therefore, only leaves remain for further analysis after segmentation.

Spectral Normalisation

After the above pre-processing steps, normalisation was needed to reduce the illumination effect. The ideal intensity of light received was when the whole object's surface was perpendicular to the sensor. However, in real life, the leaves of maise plants face different directions. In addition, leaf surfaces were not smooth, causing light to scatter in all directions.

When doing vector (L1 and L2) normalisation, all spectra were treated as vectors with values of all bands as components. Equations 2 and 3 are norm computations for L1 and L2, respectively. Vector normalisation changed the spectrum into a unit vector by Equation 4, and only the magnitude of the spectrum was transformed. All normalised spectra had uniform magnitude, thus minimising the illumination effect.

$$norm = |s_1| + |s_2| + \cdots + |s_N| \tag{2}$$

$$norm = \sqrt{{s_1}^2 + {s_2}^2 + \cdots + {s_N}^2} \tag{3}$$

$$(s_i)_{normalized} = \frac{s_i}{norm} \tag{4}$$

Other than vector normalisation, SNV normalisation was also applied in this research to compare the performances of different normalisation methods. SNV normalisation has been implemented in recent hyperspectral studies (Abenina et al., 2022; Mishra et al., 2020; Polder, et al., 2020) and is deemed the effective way to mitigate the scattering effect. It is aimed to transform the spectrum to have a mean of 0 and a standard deviation of 1 using Equation 5:

$$(X_i)_{SNV} = \frac{X_i - \overline{X_i}}{\sigma_i} \tag{5}$$

where $\overline{X_i}$ is the mean, and σ_i is the standard deviation of data, respectively.

The noise on received spectra can be illustrated as Equation 6, where $s_{reference}(\lambda)$ is said to be light reflectance at a reference. Besides, β refers to the illumination effect caused by the inclination of leaves and the distance between the camera and the maise plant. Moreover, α refers to specular reflectance, the additive effect on the reference spectrum.

$$s_{reference}(\lambda) = \beta \cdot s_{reference}(\lambda) + \alpha \quad (6)$$

By some rearrangement, Equation 7 was obtained. By comparing Equations 5 and 7, it was not hard to notice that α refers to the spectrum mean, and β refers to the standard deviation. Therefore, from this theory, SNV normalisation can be used to yield noiseless spectra.

$$s_{reference}(\lambda) = \frac{s_{received}(\lambda) - \alpha}{\beta} \quad (7)$$

Spectral Discrimination

The classification was performed on normalised spectra to determine if a spectra type has high efficiency in water stress detection. For the first dataset, the classification method performed was *k*-means clustering (Ranjan et al., 2017). Built-in *k*-means function was used, and the algorithm takes in a few parameters: the number of clusters (*k*) and maximum iterations. After referring to (Asaari et al., 2019), the *k* value was set to 6. Maximum iteration was set to 500 as well to prevent the infinite running of code. A bar graph with the number of pixels in each cluster was presented for each platform height. The variation across different bar graphs was studied to see if platform heights affect normalisation performance.

For the second normalised dataset, spectra similarity was measured between daily reference and mean spectrum of each maise plant by calculating the ED between them. The formula for ED is shown in Equation 8. After the ED was computed, the daily mean and standard deviation were calculated from the daily ED obtained according to control and water-deficit groups. Then, the result was shown as error bar graphs in which no overlapping of the error bar indicates complete discrimination of maise plants experiencing water stress.

$$ED(q,r) = \sqrt{\sum_{\lambda=1}^{B}(q(\lambda) - r(\lambda))^2} \quad (8)$$

Dimensionality Reduction

In this work, each hyperspectral image has around 10000 vegetation pixels, and each pixel has 111 bands. The computational cost was very high for such a large amount of data. Therefore, PCA and ANOVA F-test were applied on the normalised second dataset to see if improvement in the duration of water stress detection happened after the spectra dimension was reduced.

Each day's plant was represented by its mean spectrum when implementing PCA. Besides, the daily reference spectrum will also be computed for the control and water-deficit groups. All these spectra will be combined as samples for PCA. There are a total of 108 rows with 111 columns. In MATLAB, PCA was applied using the built-in PCA function. The first few PCs were used to check the effect of PCA.

In this work, the spectral band used for analysis was from 400 nm to 810 nm with a bandwidth of 3.1 nm. Even though information can be extracted from every band, not all bands contributed the same to water stress detection. ANOVA F-test uses the average daily spectrum as input. The built-in function, anova1, was used to compute the daily F-value for each band. Bands with the highest 10% of F-value were elected for each day. The selected bands were used for spectra similarity measurement to determine the duration taken for discrimination between control and water-deficit groups.

RESULTS AND DISCUSSION

The effect of SNV, L1, and L2 normalisation on different platform heights was evaluated to satisfy the first objective. *K*-means clustering was used to segregate results into different clusters displayed in the bar graph. Besides, the outcome of water stress detection using different spectra types was evaluated by calculating ED between spectra. The error bar was displayed for all nine days of the experiment. However, only the first seven days were studied for water stress detection as maise plants in the water-deficit group were not irrigated in these seven days.

PCA and ANOVA F-test were applied on normalised spectra separately to realise the second objective. Then, spectra similarity measurement with ED has performed again on the dimensionally reduced data. The same procedure of water stress analysis for the first objective was done again to determine the effect of each dimension reduction method.

Image Processing

Figure 3 shows spectra where bands below 500 nm and above 810 nm were removed. The variance of spectra decreases from 500 nm to around 650 nm, and after 700 nm, the variance of spectra increases and remains constant after around 750 nm. The number of spectral involved is 111, with 3.1 nm as the width of each band.

Figures 4 and 5 show the hyperspectral image before and after segmentation using threshold NDVI of 0.3, as stated in (Gandhi et al., 2015) as best for vegetation analysis. Figure 4's image background includes soil, pots, and a platform base. Therefore, the NDVI of these pixels will be lower than 0.3, representing non-vegetative pixels. The remaining spectra are around 10000 pixels for each maise plant, as shown in Figure 5. These pixels will be considered for further analysis.

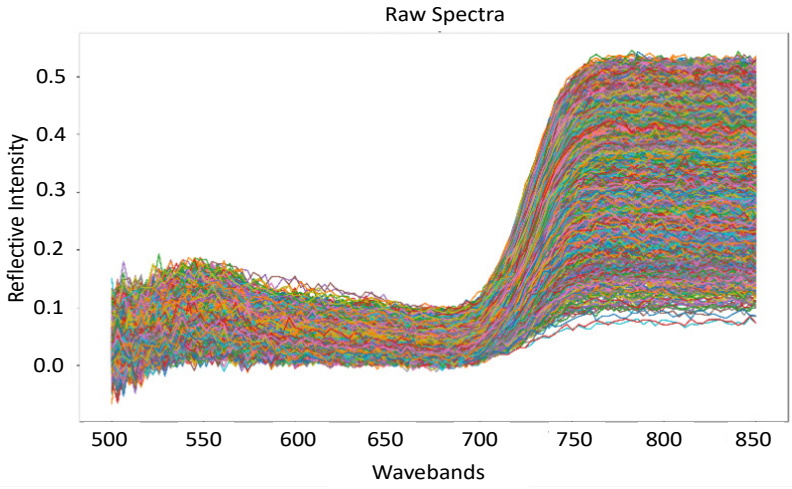

Figure 3. Spectra after removal of noisy bands

Figure 4. Hyperspectral image presented in RGB

Figure 5. Hyperspectral image after segmentation

Analysis of Spectral Normalisation of HSI of Maize Plant at Different Imaging Platform Heights

After normalisation using SNV, L1, and L2, the normalised spectra underwent classification using k-means clustering to determine if normalisation performs differently according to platform heights. MATLAB built-in *k*-means function has a parameter of 6 as the *k* value and 500 as the maximum iteration. Results of *k*-means clustering on SNV, L1, and L2 spectra are shown in Figures 6, 7, and 8, respectively. From Figures 6 and 8, it is observed that cluster 5 and 6 has the greatest number of pixels. Figure 7 shows that most pixels belong to clusters 3, 4, and 5. Besides, the graph pattern is consistent across four heights for all three spectrum types. It proves normalisation has consistent efficiency from 0 mm to 450 mm platform heights. The findings align with the study conducted by (Witteveen et al., 2022), which also observed normalization is not impacted by variations in distance.

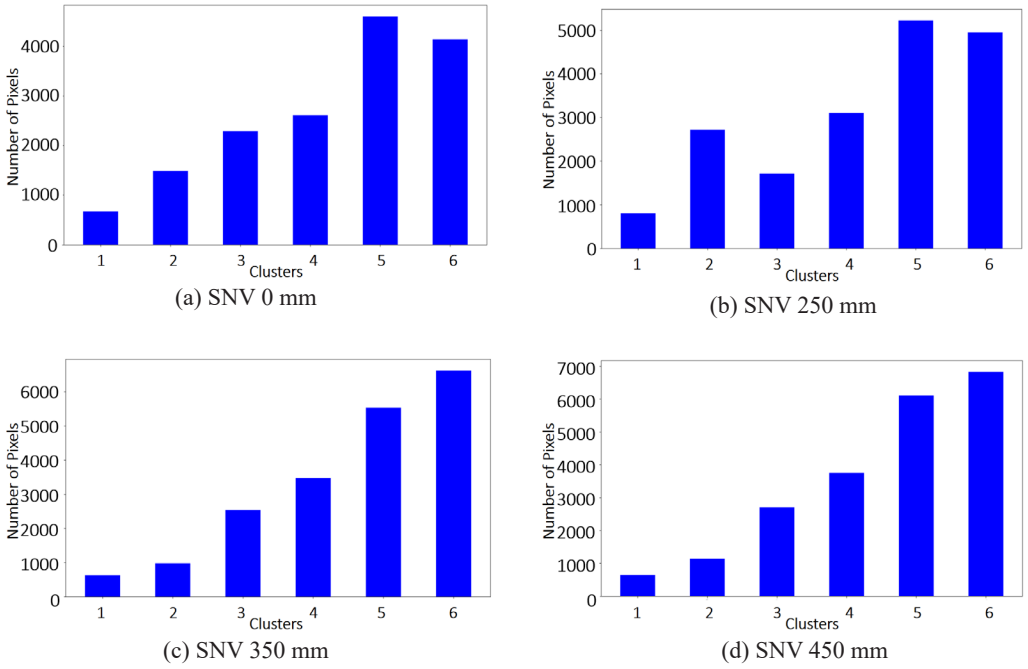

(a) SNV 0 mm (b) SNV 250 mm

(c) SNV 350 mm (d) SNV 450 mm

Figure 6. K-means clusters shown in the bar graph for SNV normalised spectra at different imaging platforms: (a) 0 mm, (b) 250 mm, (c) 350 mm, and (d) 450 mm

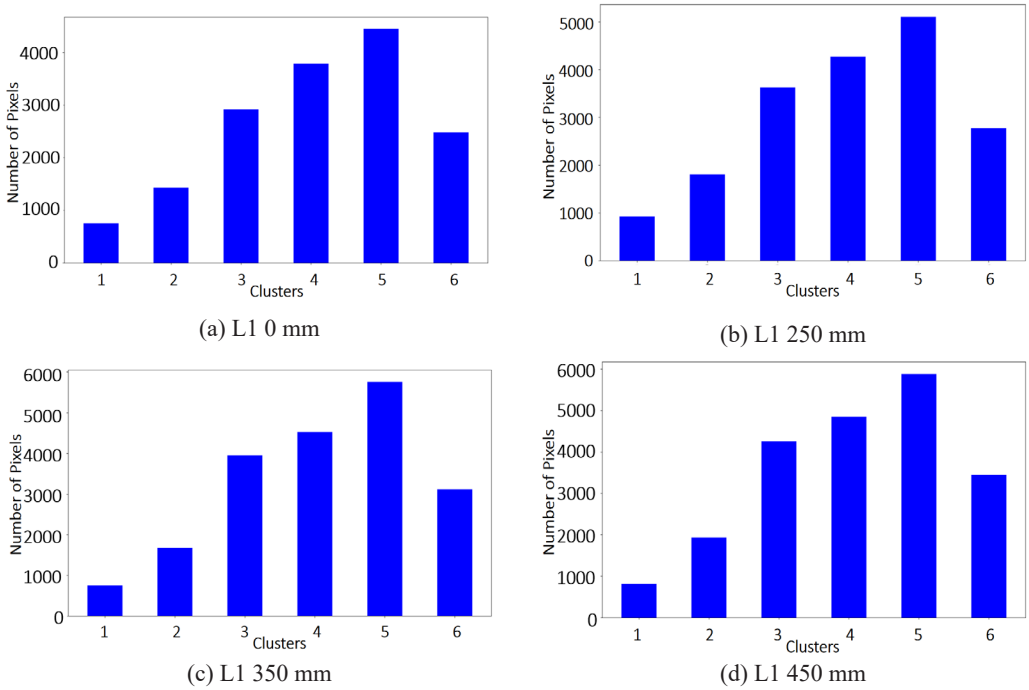

(a) L1 0 mm (b) L1 250 mm

(c) L1 350 mm (d) L1 450 mm

Figure 7. *K*-means clusters shown in the bar graph for L1 normalised spectra at different imaging platforms: (a) 0 mm, (b) 250 mm, (c) 350 mm, and (d) 450 mm

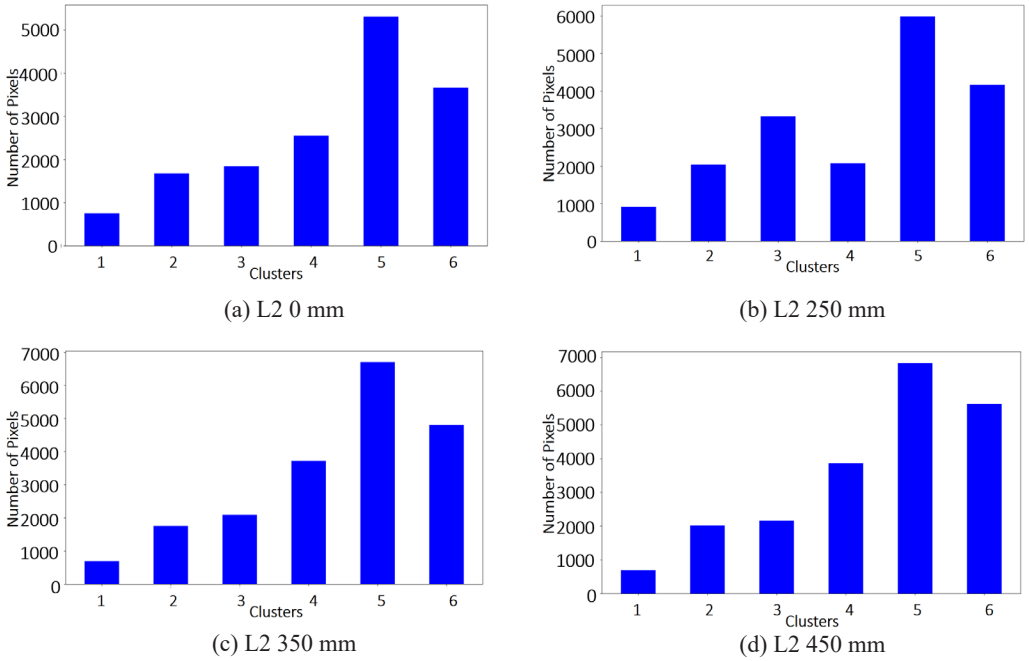

Figure 8. K-means clusters shown in the bar graph for L2 normalised spectra at different imaging platforms: (a) 0 mm, (b) 250 mm, (c) 350 mm, and (d) 450 mm

Analysis of Spectral Normalisation on Water Deficit Response in Maize Plants

After proving that normalisation works the same at different platform heights, spectra similarity measurement was performed for raw, SNV, L1, and L2 normalised spectra. Daily reference was first computed by getting the mean of maise plants in the control group. Then, the ED between the mean spectrum of maise plants and daily reference was calculated. Daily ED values were categorised according to control and water-deficit groups. Then, daily mean and standard deviation were obtained from these ED values and presented in an error bar graph. Note that in this study, no Cross-Validation (CV) is performed as only computation of ED between mean reference spectrum is done without any parameter tuning required. CV is generally used when developing a machine learning model, which requires the dataset to be split into training and testing sets. After the CV's k-folds are performed, each fold's parameter will be averaged and used as model parameters. In the ED calculation, the error bars' lower and upper boundaries represent the minimum and maximum of each sample group, respectively. Thus, the complete separation of the error bar is sufficient to indicate drought plants among samples.

From Figure 9(a), error bar analysis similar to (Asaari et al., 2019) has been conducted. The duration taken for raw spectra to separate control and water-deficit groups is 7 days, while for SNV spectra, it takes 4 days. On the contrary, both vector normalisations, L1 and

L2, fail to detect maise plants experiencing water stress within the first 7 days. It can be noticed that the red error bar, which represents the difference between water-deficit maise plants and daily reference, increases consistently from day 2 to day 7 for SNV. It shows that SNV-normalised spectra respond according to the plant's water level. However, a closer observation of Figure 9 (c-d) shows an unusually large increment of the control error bars from day 4 to day 6. It causes the error bar of both groups to "stick" with each other and not be able to discriminate in the first 7 days completely. Therefore, from Figure 9, it can be concluded that spectra after being SNV normalised are better compared to L1 and L2 normalised spectra in detecting water deficit stress response in maise plants.

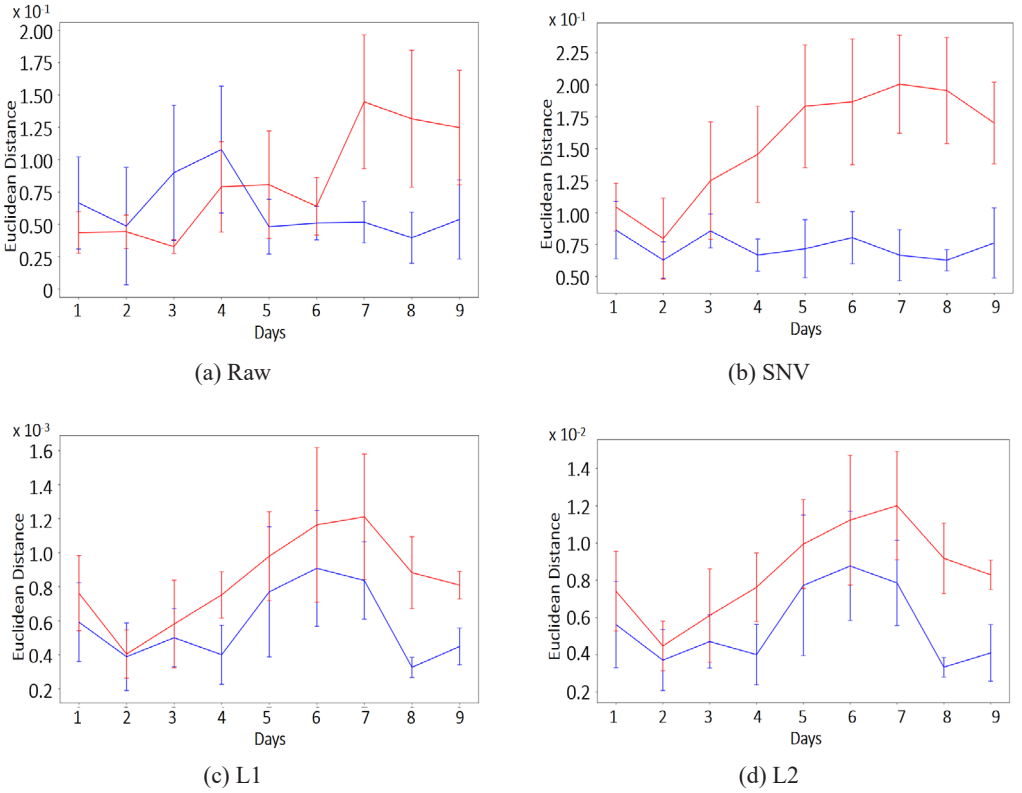

Figure 9. Spectra similarity result on (a) raw, (b) SNV, (c) L1 and (d) L2 spectra with blue error bar representing the control group and red error bar representing the water deficit group.

Analysis of Dimensionality Reduction

The second objective of this work studies the effect of dimension reduction methods, PCA and ANOVA F-test in water stress detection. Both methods have different ways of implementation. However, they serve the same purpose: to reduce the computational cost of analysis.

Results of spectra similarity measurement after PCA is applied and shown in Figures 10 and 11 for each spectra type when 1 and 10 PCs were selected. When comparing with Figure 9, graphs with 10 PCs are very similar to the spectra similarity result before dimension reduction. On the other hand, graphs using only 1 PC show worse results when compared with spectra similarity results before dimension reduction. Therefore, it can be deduced that PCA does not affect the duration taken for water stress detection when enough PCs are used. A closer look at Figure 10 shows that when 1 PC is used for spectra similarity measurement, the result is not as good as another two. It is due to the variance in the first PC being insufficient "replicate" that of the whole data set. Similar scenarios have been observed in studies conducted by (Fernández et al., 2022; Ren et al., 2020; Vu et al., 2016) where multiple PCs were utilized for machine learning computation. Therefore, the optimum number of PCs used in this work is 10.

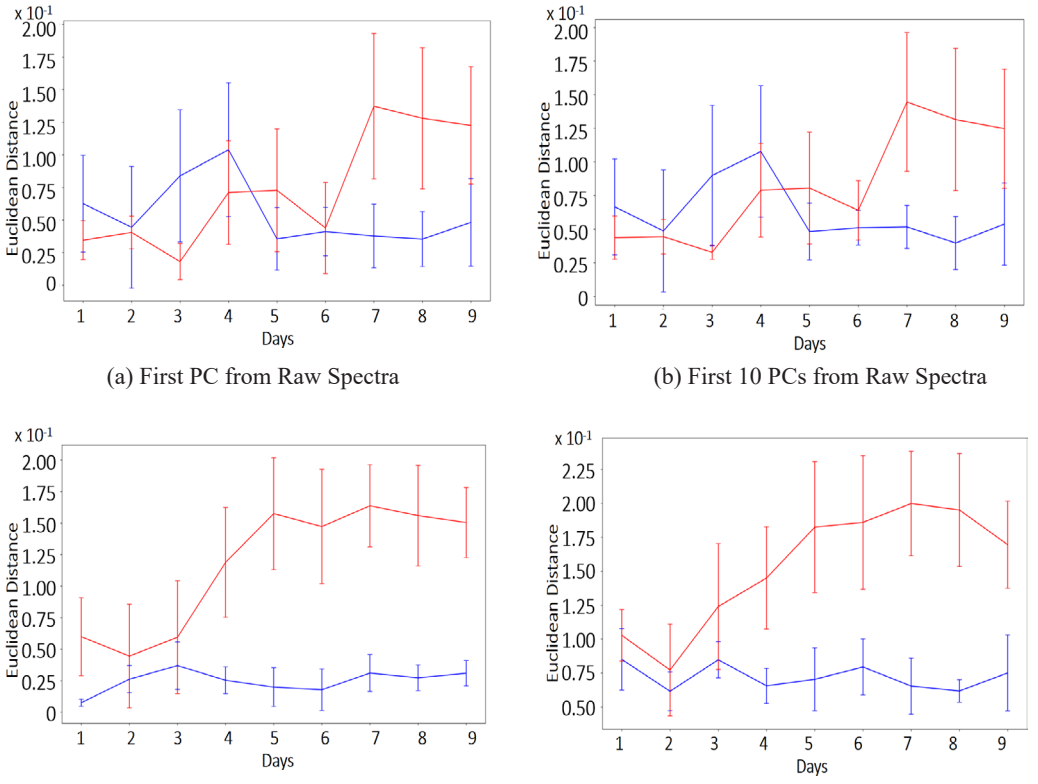

(a) First PC from Raw Spectra

(b) First 10 PCs from Raw Spectra

(c) First PC from SNV Spectra

(d) First 10 PCs from SNV Spectra

Figure 10. Spectra similarity result-based PCA with 1 and 10 PCs of raw spectra (a-b) and 1 and 10 PCs of SNV normalised spectra (c-d). The blue error bar represents the control group, and the red represents the water deficit group.

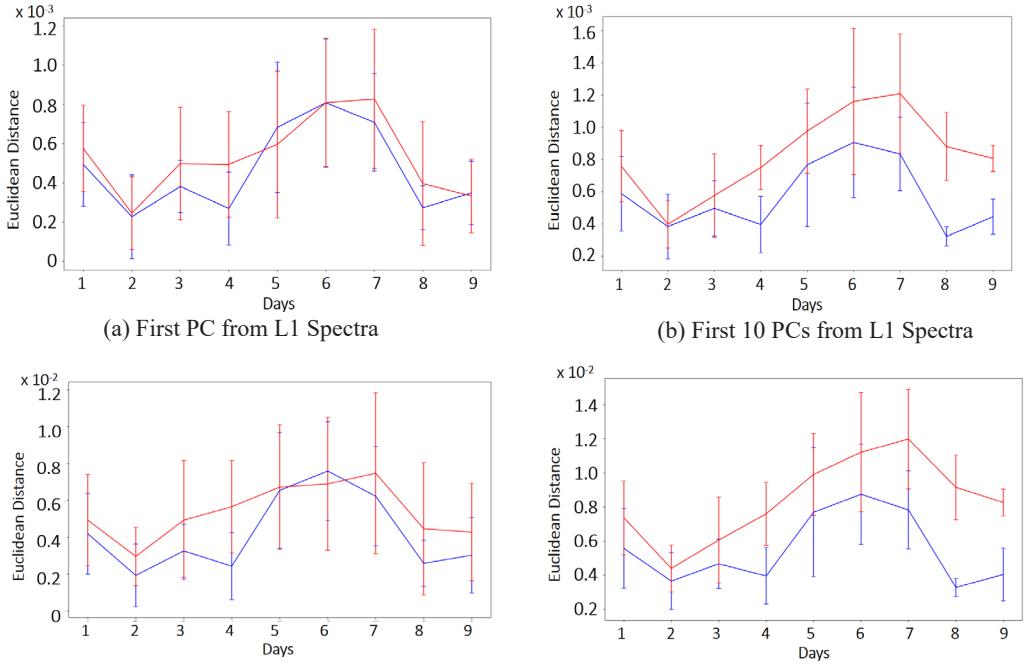

Figure 11. Spectra similarity based on PCA with 1 and 10 PCs of L1 normalised spectra (a-b) and 1 and 10 PCs of L2 normalised spectra. The blue error bar represents the control group, and the red represents the water deficit group.

Spectra, which have been dimensionally reduced using ANOVA F-test, were processed with the same spectra similarity measurement method used for objective one. Results for raw, SNV, L1, and L2 spectra are shown in Figure 12. Improvement happens for all normalised spectrum types when comparing these results with the spectral discrimination in Figure 9. For SNV spectra, the duration taken for water stress detection was reduced from 4 days to just 4 days. Besides, even though the result on L1 spectra shows that water stress detection still fails in the first 7 days, a further separation between error bars can be observed. Different from L1 to L2 spectra show the successful separation of control and water deficit on the fourth day. The improvement from failure to success in just 4 days for water stress detection gives ANOVA F-test the highest efficiency when applied to L2 spectra. From the results from PCA and ANOVA F-test, it can be deduced that ANOVA F-test works better in improving the performance of HSI analysis in terms of duration to detect water-deficit maise plants. Conversely, PCA can reduce the computational cost, but it does not affect the result of water stress detection.

A comparison was made with several well-known vegetation indices as used in the previous studies to quantify the effectiveness of the analysis method of HSI performed in this study for the use case of early drought stress detection in the plant (Andaryani et al.,

2019; Ihuoma & Madramootoo, 2019). Figure 13 shows the result of separating samples from control and drought groups using NDVI, OSAVI, PRI 550 and RENDVI. All four VIs considered sensitive to water content cannot distinguish drought plants completely from the control group throughout the 9 days of the experiment. It further highlights the importance of normalisation to minimise collinear and scattering effects before analysis.

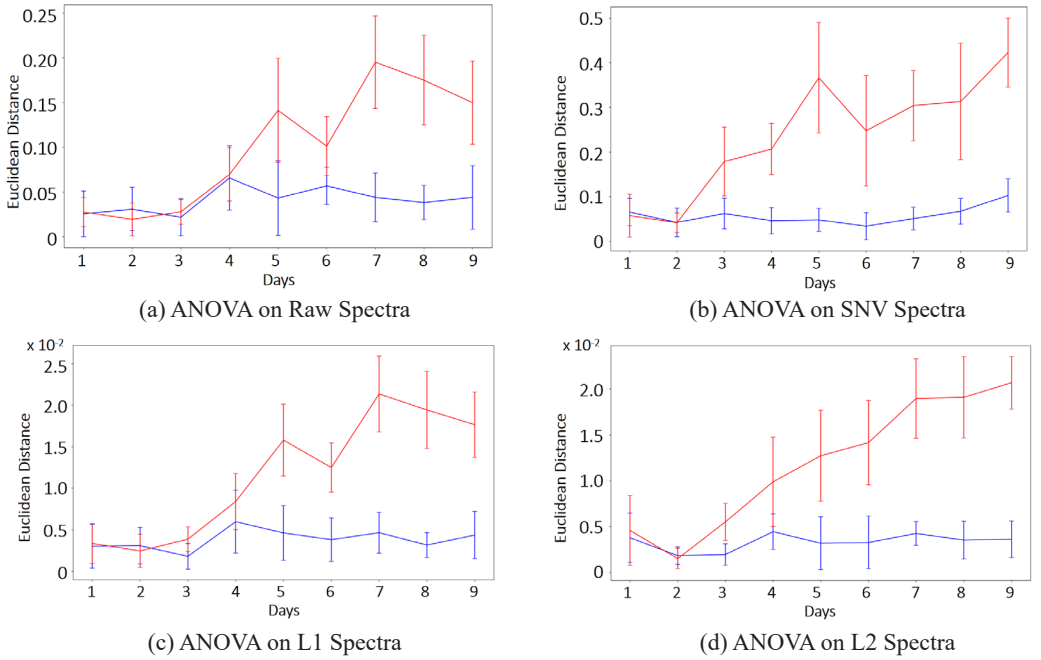

Figure 12. Spectra similarity result on (a) raw (b) SNV (c) L1 and (d) L2 spectra after performing ANOVA F-test with blue error bar representing the control group and red error bar representing water deficit group.

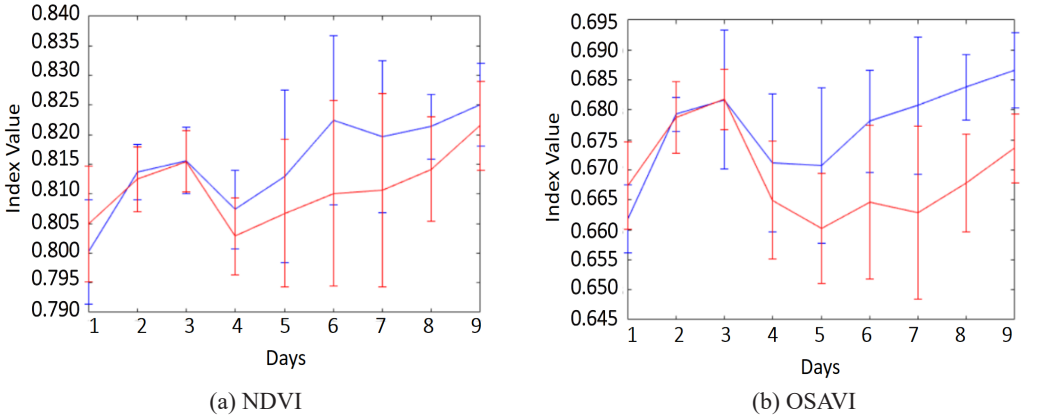

Figure 13. Vegetation indices value (a) NDVI, (b) OSAVI, (c) PRI 550 and (d) RENDVI for drought plants detection on raw spectra.

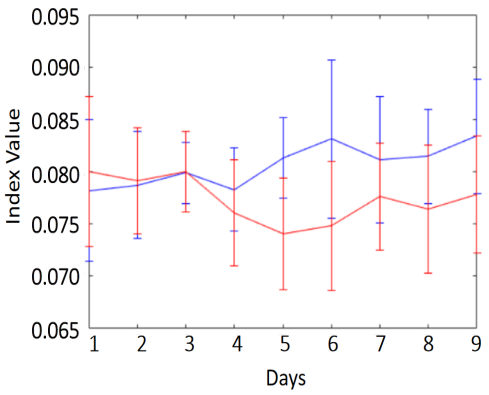

(c) PRI 550

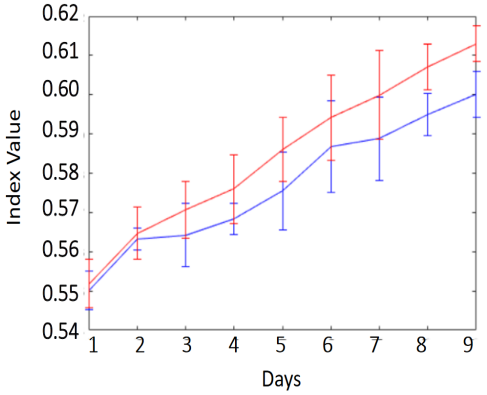

(d) RENDVI

Figure 13. Continue

CONCLUSION

In this paper, two comparisons have been carried out: the performances between the effect of SNV, L1, and L2 normalisation and between PCA and ANOVA F-test in water stress detection. The first objective was achieved with spectra similarity measurement performed on SNV spectra which successfully separated control and water-deficit groups in 4 days, while L1 and L2 spectra showed failure in water stress detection. Furthermore, the second objective was achieved by showing that similarity measurement on spectra after treatment using ANOVA F-test showed better performance in water stress detection. On the other hand, spectra similarity measurement after PCA showed the same result as in the non-dimensionally reduced one.

ACKNOWLEDGMENTS

The authors acknowledged the Ministry of Higher Education (MOHE) Malaysia for the Fundamental Research Grant Scheme with Project Code: FRGS/1/2020/TK0/USM/02/13. The author also fully acknowledged the VIB-UGent Center for Plant Systems Biology of Ghent University Belgium research team for help in preparing the Hyperspectral images.

REFERENCES

Abenina, M. I. A., Maja, J. M., Cutulle, M., Melgar, J. C., & Liu, H. (2022). Prediction of potassium in peach leaves using hyperspectral imaging and multivariate analysis. *AgriEngineering*, *4*(2), 400-413. https://doi.org/10.3390/agriengineering4020027

Andaryani, S., Trolle, D., & Asl, A. M. (2019). *Application of hyperion data for investigating agriculture field stress to drought conditions*. EasyChair.

Asaari, M. S. M., Mishra, P., Mertens, S., Dhondt, S., Inzé, D., Wuyts, N., & Scheunders, P. (2018). Close-range hyperspectral image analysis for the early detection of stress responses in individual plants in a high-throughput phenotyping platform. *ISPRS Journal of Photogrammetry and Remote Sensing*, *138*, 121-138. https://doi.org/10.1016/j.isprsjprs.2018.02.003

Asaari, M. S. M., Mertens, S., Dhondt, S., Inzé, D., Wuyts, N., & Scheunders, P. (2019). Analysis of hyperspectral images for detection of drought stress and recovery in maize plants in a high-throughput phenotyping platform. *Computers and Electronics in Agriculture*, *162*, 749-758. https://doi.org/10.1016/j.compag.2019.05.018

Balachandran, S., Hurry, V. M., Kelley, S. E., Osmond, C. B., Robinson, S. A., Rohozinski, J., Seaton, G. G. R., & Sims, D. A. (1997). Concepts of plant biotic stress. Some insights into the stress physiology of virus-infected plants, from the perspective of photosynthesis. *Physiologia Plantarum*, *100*(2), 203-213. https://doi.org/10.1111/j.1399-3054.1997.tb04776.x

Behmann, J., Steinrücken, J., & Plümer, L. (2014). Detection of early plant stress responses in hyperspectral images. *ISPRS Journal of Photogrammetry and Remote Sensing*, *93*, 98-111. https://doi.org/10.1016/j.isprsjprs.2014.03.016

Calzone, A., Cotrozzi, L., Lorenzini, G., Nali, C., & Pellegrini, E. (2021). Hyperspectral detection and monitoring of salt stress in pomegranate cultivars. *Agronomy*, *11*(6). https://doi.org/10.3390/agronomy11061038

Chaerle, L., & van der Straeten, D. (2000). Imaging techniques and the early detection of plant stress. *Trends in Plant Science*, *5*(11), 495-501. https://doi.org/10.1016/S1360-1385(00)01781-7

Feng, F., Zhang, Y., Zhang, J., & Liu, B. (2022). Small sample hyperspectral image classification based on cascade fusion of mixed spatial-spectral features and second-order pooling. *Remote Sensing*, *14*(3), Article 505. https://doi.org/10.3390/rs14030505

Fernández, C. I., Leblon, B., Wang, J., Haddadi, A., & Wang, K. (2022). Cucumber powdery mildew detection using hyperspectral data. *Canadian Journal of Plant Science*, *102*(1), 20–32. https://doi.org/10.1139/cjps-2021-0148

Fletcher, R. S., & Turley, R. B. (2018). Comparing Canopy Hyperspectral Reflectance Properties of <i>Palmer amaranth</i> to Okra and Super-Okra Leaf Cotton. *American Journal of Plant Sciences*, *09*(13), 2708–2718. https://doi.org/10.4236/ajps.2018.913197

Gandhi, G. M., Parthiban, S., Thummalu, N., & Christy, A. (2015). Ndvi: Vegetation Change Detection Using Remote Sensing and Gis – A Case Study of Vellore District. *Procedia Computer Science*, *57*, 1199–1210. https://doi.org/10.1016/j.procs.2015.07.415

Ge, Y., Bai, G., Stoerger, V., & Schnable, J. C. (2016). Temporal dynamics of maize plant growth, water use, and leaf water content using automated high throughput RGB and hyperspectral imaging. *Computers and Electronics in Agriculture*, *127*, 625-632. https://doi.org/10.1016/j.compag.2016.07.028

Geladi, P., Burger, J., & Lestander, T. (2004). Hyperspectral imaging: Calibration problems and solutions. *Chemometrics and Intelligent Laboratory Systems*, *72*(2), 209-217. https://doi.org/10.1016/j.chemolab.2004.01.023

Hughes, G. F. (1968). On the mean accuracy of statistical pattern recognizers. *IEEE Transactions on Information Theory*, *14*(1), 55-63. https://doi.org/10.1109/TIT.1968.1054102

Ihuoma, S. O., & Madramootoo, C. A. (2019). Sensitivity of spectral vegetation indices for monitoring water stress in tomato plants. *Computers and Electronics in Agriculture*, *163*, Article 104860. https://doi.org/10.1016/j.compag.2019.104860

Isaksson, T., & Næs, T. (1988). The Effect of Multiplicative Scatter Correction (MSC) and Linearity Improvement in NIR Spectroscopy. *Applied Spectroscopy*, *42*(7), 1273–1284. https://doi.org/10.1366/0003702884429869

Kastberger, G. & Stachl, R. (2003). Infrared imaging technology and biological applications. *Behaviour Research Methods, Instruments & Computers*, *35*(3), 429-439. https://doi.org/10.3758/BF03195520

Li, X., Li, R., MengyuWang, Liu, Y., Zhang, B., & Zhou, J. (2018). Hyperspectral Imaging and Their Applications in the Nondestructive Quality Assessment of Fruits and Vegetables. *Hyperspectral Imaging in Agriculture, Food and Environment*, 28–63. https://doi.org/10.1016/j.colsurfa.2011.12.014

Liu, J., Han, J., Chen, X., Shi, L., & Zhang, L. (2019). Nondestructive detection of rape leaf chlorophyll level based on Vis-NIR spectroscopy. *Spectrochimica Acta Part A: Molecular and Biomolecular Spectroscopy*, *222*, 117202. https://doi.org/10.1016/j.saa.2019.117202

Lohaus, G., Heldt, H. W., & Osmond, C. B. (2000). Infection with phloem limited abutilon mosaic virus causes localized carbohydrate accumulation in leaves of abutilon striatum: relationships to symptom development and effects on chlorophyll fluorescence quenching during photosynthetic induction. *Plant Biology*, *2*(2), 161-167. https://doi.org/10.1055/s-2000-9461

Mishra, P., Lohumi, S., Ahmad Khan, H., & Nordon, A. (2020). Close-range hyperspectral imaging of whole plants for digital phenotyping: Recent applications and illumination correction approaches. *Computers and Electronics in Agriculture*, *178*, Article 105780. https://doi.org/10.1016/j.compag.2020.105780

Mishra, P., Polder, G., Gowen, A., Rutledge, D. N., & Roger, J. M. (2020). Utilising variable sorting for normalisation to correct illumination effects in close-range spectral images of potato plants. *Biosystems Engineering*, *197*, 318–323. https://doi.org/10.1016/j.biosystemseng.2020.07.010

Mohd Asaari, M. S., Mishra, P., Mertens, S., Dhondt, S., Inzé, D., Wuyts, N., & Scheunders, P. (2018). Close-range hyperspectral image analysis for the early detection of stress responses in individual plants in a high-throughput phenotyping platform. *ISPRS Journal of Photogrammetry and Remote Sensing*, *138*, 121–138. https://doi.org/10.1016/j.isprsjprs.2018.02.003

Nilsson, H. E. (1995). Remote sensing and image analysis in plant. *Annual Review Phytopathol*, *15*, 489-527.

Ortaç, G., Bilgi, A. S., Taşdemir, K., & Kalkan, H. (2016). A hyperspectral imaging based control system for quality assessment of dried figs. *Computers and Electronics in Agriculture*, *130*, 38-47. https://doi.org/10.1016/j.compag.2016.10.001

Pandey, P., Ge, Y., Stoerger, V., & Schnable, J. C. (2017). High throughput in vivo analysis of plant leaf chemical properties using hyperspectral imaging. *Frontiers in Plant Science*, *8*, Article 1348. https://doi.org/10.3389/fpls.2017.01348

Ranjan, S., Nayak, D. R., Kumar, K. S., Dash, R., & Majhi, B. (2017). Hyperspectral image classification: A k-means clustering based approach. *2017 4th International Conference on Advanced Computing and Communication Systems (ICACCS)*, 1–7. https://doi.org/10.1109/ICACCS.2017.8014707

Ren, G., Wang, Y., Ning, J., & Zhang, Z. (2020). Using near-infrared hyperspectral imaging with multiple decision tree methods to delineate black tea quality. *Spectrochimica Acta - Part A: Molecular and Biomolecular Spectroscopy*, *237*, 118407. https://doi.org/10.1016/j.saa.2020.118407

Sensing, R., Analysis, I., & Plant, I. N. (1995). REMOTE SENSING AND IMAGE ANALYSIS IN PLANT. *Annual Review Phytopathol*, *15*, 489–527.

Shaikh, M. S., Jaferzadeh, K., Thörnberg, B., & Casselgren, J. (2021). Calibration of a hyper-spectral imaging system using a low-cost reference. *Sensors*, *21*(11), Article 3738. https://doi.org/10.3390/s21113738

Vigneau, N., Ecarnot, M., Rabatel, G., & Roumet, P. (2011). Potential of field hyperspectral imaging as a non destructive method to assess leaf nitrogen content in Wheat. *Field Crops Research*, *122*(1), 25–31. https://doi.org/10.1016/j.fcr.2011.02.003

Vu, H., Tachtatzis, C., Murray, P., Harle, D., Dao, T. K., Le, T. L., Andonovic, I., & Marshall, S. (n.d.). *Rice Seed Varietal Purity Inspection using Hyperspectral Imaging*.

Witteveen, M., Sterenborg, H. J. C. M., van Leeuwen, T. G., Aalders, M. C. G., Ruers, T. J. M., & Post, A. L. (2022). Comparison of preprocessing techniques to reduce nontissue-related variations in hyperspectral reflectance imaging. *Journal of Biomedical Optics*, *27*(10). https://doi.org/10.1117/1.JBO.27.10.106003

Yang, W., Duan, L., Chen, G., Xiong, L., & Liu, Q. (2013). Plant phenomics and high-throughput phenotyping: Accelerating rice functional genomics using multidisciplinary technologies. *Current Opinion in Plant Biology*, *16*(2), 180-187. https://doi.org/10.1016/j.pbi.2013.03.005

Zhuang, L., & Ng, M. K. (2020). Hyperspectral mixed noise removal by ℓ1-norm-based subspace representation. *IEEE Journal of Selected Topics in Applied Earth Observations and Remote Sensing*, *13*, 1143-1157. https://doi.org/10.1109/JSTARS.2020.2979801

Pertanika J. Sci. & Technol. 31 (4): 1847 - 1860 (2023)

PERTANIKA JOURNALS

SCIENCE & TECHNOLOGY

Journal homepage: http://www.pertanika.upm.edu.my/

Adaptive Density Control Based on Random Sensing Range for Energy Efficiency in IoT Sensor Networks

Fuad Bajaber

Department of Information Technology, Faculty of Computing and Information Technology, King Abdulaziz University, Jeddah, Kingdom of Saudi Arabia

ABSTRACT

IoT sensor networks enable long-term environmental monitoring. Most environmental applications require sensor node data gathering to satisfy application objectives. Therefore, sensing range optimization is a significant element in prolonging the lifetime of IoT sensor networks and saving energy. This study proposes an adaptive density control based on random sensing range (ADCR). It can reduce data redundancy by selecting several active and hybrid nodes in a sensing field. Thus, reducing redundancy power consumption will maximize the network lifetime. The simulation results demonstrate the effectiveness of density control based on the random sensing range.

Keywords: Density control, energy efficiency, IoT, sensing range, wireless sensor network

INTRODUCTION

Sensor nodes are small devices with sensors, transceivers, CPU, and storage capabilities. Sensor nodes form networks and work together to complete bigger sensing jobs. An IoT sensor network (WSN) is distinguished by its limited resources, vast and dense networks, and dynamic topology. In general, more sensors are deployed than are necessary to complete the planned job, which enhances fault tolerance. A WSN might include hundreds or even thousands of sensor nodes. The density control problem is an important issue addressed in the literature (Dong et al., 2020; Bar-Noy & Baumer, 2015; Dolas & Ghosh, 2018; Das & Kapelko,2021; Gulati et al., 2022). This challenge revolves around a fundamental question: arranging sensor node activity so that the redundant nodes can enter passive mode to save energy. Because battery resources are limited in WSNs, energy efficiency is a critical concern.

ARTICLE INFO

Article history:
Received: 14 August 2022
Accepted: 02 November 2022
Published: 25 May 2023

DOI: https://doi.org/10.47836/pjst.31.4.14

E-mail address:
fbajaber@kau.edu.sa (Fuad Bajaber)

ISSN: 0128-7680
e-ISSN: 2231-8526

Batteries provide the only energy source for the sensor nodes, and it is frequently impossible to recharge batteries, especially in severe conditions. Density control methods can save energy and solve this problem by keeping a subset of sensor nodes active while switching the rest of the sensor nodes to passive mode (Liu, 2016; Puneeth & Kulkarni, 2020; Singh et al., 2019; Luomala & Hakala, 2022; Merabtine et al., 2021). Energy-saving mechanisms are very desirable since they directly influence WSN lifetime. "Network lifetime" is generally defined as the time interval the network can conduct the sensing functions and transmit data to the base station. Some nodes may become inaccessible over the network's lifetime, or others may be installed. A widely used approach is to arrange the sensor node activity to allow redundant nodes to enter the passive mode as often and for as long as possible (Al-Shalabi, 2018; Cheng et al., 2017; Nkomo et al., 2018; Zhang et al., 2011; Piran et al., 2021; Singh et al., 2021). In order to create such a system, the following questions must be addressed: Which rule should each node use to determine whether to enter passive mode? When should nodes make this choice? Moreover, for how long should a sensor be in passive mode?

Randomizing the sensor range is another way to minimize power usage. If it is possible to randomize the sensing range, the sensing region of one sensor node is covered by another. As a result, the sensor node enters passive mode to conserve energy. Numerous investigations have been carried out and assume that a node's sensing range is fixed (Seah et al., 2009; Yang & Heinzelman, 2009; Walker et al., 2015; Raja, 2022; Sinha & Rajeshwari, 2021). This paper tackles the problem of scheduling sensor nodes to conserve energy. Assume that a network of sensor nodes has been set up to gather information from the forest. The network should be able to gather data from numerous points throughout the area being watched and transmit it to the base station. Sensing range and energy efficiency are crucial factors in ensuring that applications can be fulfilled.

Two strategies were suggested by Dhawan et al. (2006) to optimize the lifespan of a target-covering sensor network. The active sensors are scheduled in the first method, and it is specified which sensors fall into sleep mode, whereas the detecting range is adjusted in the second method by the protocol. Since energy increases with distance, a sensor can choose the ideal sensing range to cover targets and conserve energy. The suggested technique utilizes the greedy algorithm for the tiniest weight Sensor. Nayak et al. (2011) suggested a mechanism for power conservation. Sensors switch between the active and sleep modes to regulate power and modify the communication and sensor range. This technique uses a greedy heuristic and genetic algorithm to identify the ideal sensing range for effective energy management in a sensor network. Wannachai et al. (2015) devised the A-TRED protocol to adapt the communication range based on the sensing data level. There are two communication modes in this protocol. The first option, short-range communication, enables sensor nodes to convey data over a short distance utilizing low-power transmission

to conserve energy. Long-range communication is the second mode. When sensor nodes find urgent data, the second method is used. The nodes can communicate at high power across great distances to convey data.

Dynamic power management was first introduced by Raza et al. (2016) by putting a node into an energy-saving inactive mode. This work proposes a combination of hardware and software strategies to reduce energy consumption activities and the number of transitions. The plan involves gathering sensor data and running a data reduction algorithm to reduce energy use. The transmission unit is turned on to transfer the data when it is necessary to do so. Experimental findings demonstrate that the suggested approach provides power savings. To solve the issue of maximizing lifetime in directed sensor networks with variable sensing ranges, Liu et al. (2017) developed a hybrid strategy. The directed sensor nodes can change the sensing ranges to cover targets. A sensor node has several movable directions. The index of the sensor node, the sensing orientation, and the sensing range are all included in an adjusted direction. In order to extend the network lifetime, the directional sensors can modify their sensing ranges. The outcomes demonstrate that the suggested approach achieves a more extended network lifetime. The immune genetic algorithm also needs less calculation time than other protocols.

Debnath et al. (2018) established an effective sensing radius for probabilistic sensing models. The network planning of sensor networks can be done using this protocol. It can consider the signal's fading and propagation losses. An adaptive compressive sensing-based sample scheduling approach was proposed by Hao et al. (2015). This methodology determines the minimal sample rate necessary for a particular sensor quality. Based on hash data that shows the correlation between the sample rate and the degree of sparsity, this protocol first gathers sensing data from the sensing field. In the second phase, the node can set its sample rate. The hash table is being formed now, and the sensor node can choose to adjust its intensity or base its sample rate decision on the degree of sparsity. The findings demonstrate that, in comparison to existing protocols, the suggested technique can perform well using a significantly lower sample rate.

A method for maximizing lifespan that allows for the adjustment of node sensing ranges was put forth by Rossi et al. (2012). The sensor can modify its detection range to cover targets. The node can modify the sensing ranges in the first type of node up to the maximum sensing range, whereas in the second type of node, the node can modify the sensing ranges up to a set of specified values. The findings demonstrate this scheme's adaptability to various lifetime maximization scenarios. According to Cerullia et al. (2012), this system specifies a subset of sensors to cover the set of targets and establishes optimal schedule times for each node to conserve energy. Furthermore, each sensor node has a variety of power levels that can be used to switch it on, allowing it to choose between various detecting ranges and power requirements.

Heinzelman et al. (2000) established an energy-efficient communication protocol for wireless microsensor networks. LEACH is a crucial protocol for energy-efficient homogeneous WSNs that introduces a dynamic cluster-building method. A hierarchical, probabilistic, one-hop protocol randomly rotates the cluster heads' duty to distribute the network energy burden among the sensors. It further enhances energy efficiency by conducting data aggregation at the cluster head level. LEACH operates in rounds, each consisting of two phases: setup and steady state. Cluster heads are chosen randomly during the setup phase, and clusters are established for the current round. The stochastic approach assures that each node has an equal chance of becoming the cluster head in the long term. Data is transported from nodes to the base station during the steady-state phase.

Most density control methods assume that all sensors have the same sensing range. The issue they are attempting to solve is how to make the model operate when various sensor nodes have varying sensing ranges while not utilizing the randomized sensing ranges to obtain better performance.

We are inspired to design a protocol for adaptive density control based on random sensing range to make IoT sensor networks more energy efficient. The proposed protocol divides the entire operation into rounds. The sensor node randomly chooses its sensing range at the start of each round. A sample is shown in Figure 1. Assume that a field of sensors (s_1, s_2, s_3 ..., s_i) has been randomly distributed. A sensing range is chosen at random by each sensor node.

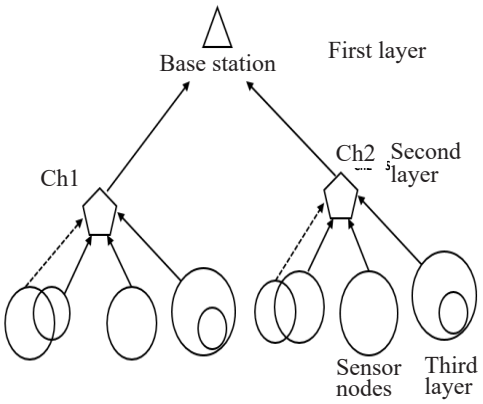

Figure 1. Three layers of IoT sensor network

METHODOLOGY

Network Model

The wireless sensor network applied the scheduling algorithm to prevent resource depletion and set up the nodes to work in succession. As a result, there are three modes for sensor nodes: Active, Passive, and Hybrid. In active mode, the sensor nodes are working to sense their surroundings and transmit the data they have collected. The nodes operating in passive mode are disabled. In hybrid mode, the sensor nodes combine active and passive sensor types to increase energy efficiency. The sensor network is made up of a set of nodes S in which $S = \{s_1, s_2, s_3, \ldots \ldots .. s_i\}$, and the wireless network is made up of a set of nodes CH in which $CH = \{ch_1, ch_2, ch_3, \ldots \ldots .. ch_i\}$, where S is the sensor network, and CH is the cluster head. The sensor node s_i gathers information from the environment and transmits it to the cluster head ch_i. This plan is built on a network

concept with three levels. The network model's three layers comprise the base station, cluster heads, and sensor nodes.

The base station is the first layer, where data from sensor nodes is stored. The cluster heads are the second layer for gathering and averaging data from member nodes. They transmit data to the base station and are in charge of topology control. The third layer consists of the sensor nodes. The sensor nodes sense their surroundings, gather information, and send it to the base station by cluster heads. Data transmission between sensor nodes, cluster heads, and the base station affects energy consumption. Heinzelman et al. (2000; 2002) define the energy required to transmit an n-bit over a distance *d* in Equation 1.

$$E_t = n * E_{el} + n * \epsilon_{fs} * d^2 \quad (1)$$

E_{el} stands for the electronic energy the bit uses, and ϵ_{fs} stands for free space's power loss. For each sensor node, the energy required to receive n-bit data across a distance d is given by Equation 2.

$$E_r = \mathrm{n} * E_{el} \quad (2)$$

The energy consumption for data aggregation is given by Equation 3.

$$E_{a} = 5\ nJ/bit/signal \quad (3)$$

The placement of the sensor nodes is random--The traffic flow between sensor nodes and cluster heads, as well as between cluster heads and the base station. Each sensor node's overall energy usage is defined in Equation 4.

$$E = RE_r + TE_t + AEa \quad (4)$$

Where R, T, $\wedge$ A are arrival rates of received, transmitted, and aggregated data packets, respectively.

To calculate the remaining energy E_{rm} for each node using Equation 5.

$$E_{rm} = E_{\mathrm{i}} - (RE_r + TE_{\mathrm{t}} + AE_a) \quad (5)$$

Where E_i is the initial energy of the sensor node.

Adaptive Density Control

ADCR assumes that the sensing field is a square area whose length and width are L and W, respectively. The sensor network is divided into clusters to reduce the redundant data collected by the sensor nodes. According to Wannachai and Champrasert (2015), Raza et al. (2016), Liu et al. (2017), Debnath et al. (2018) and Hao et al. (2015), Lata and Verma (2022), Williams et al. (2021), Zagrouba and Kardi (2021) data gathered by sensor nodes close to each other often show some similarities. Thus, to decrease the amount of redundant data, this work proposed adaptive density control based on random sensing range protocol (ADCR)

The sensor nodes keep the energy balance by exchanging the responsibility to address the adaptive density control problem in IoT sensor networks with random sensing range. Figure 2 shows an example with four sensor nodes $s1$, $s2$, $s3$, ∧ $s4$. Each sensor node has a random sensing range $r1$, $r2$, $r3$, ∧ $r4$, and three operations modes: Active, Passive, and Hybrid. A node, In addition, can switch to another mode depending on the status of neighboring nodes.

The strategy of protocol for network monitoring includes two phases executed sequentially. The first phase operates when the wireless network is initialized. Then, the node turns Active and sends an update message with its ID, residual energy, current mode, and sensing range to the base station. Then, all nodes can define their location information using localization techniques or GPS. After the exchange of location information and energy information with the base station, the second phase starts. ADCR protocol will calculate each sensor node's coverage contribution within the sensing area.

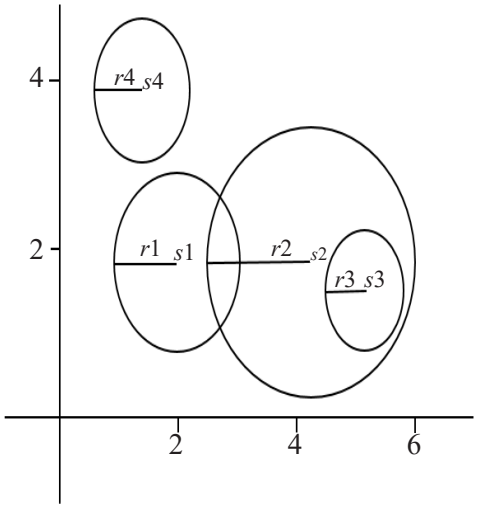

Figure 2. An example of four sensor nodes

Initialization Phase

All sensor nodes will be activated in Active mode. As shown in Figure 2, there are four sensor nodes ($s1$, $s2$, $s3$, $s4$), and their locations are listed in Table 1, where x represents the horizontal coordinates, and y represents the vertical coordinates of node s in a sensing field.

Table 1

Four nodes in the sensing field

s	1	2	3	4
(x,y)	2,1.8	4.3,1.8	5.2,1.6	1.8,3.9

As illustrated in Figure 2, assume that a sensing radius is a random number. ADCR considers the intersection sensing area and distances between nodes.

As illustrated in Figure 3, suppose d is the distance between nodes s_1 and s_2. Then the shared area is covered by both nodes, s_1, and s_2. This area is called the typical coverage area *CR* calculated using Equation 6:

$$CR_{s1s2} = SR(s_1) \cap SR(s_2) \quad (6)$$

where *SR* is the sensing range, the wireless sensor network has many Active, Passive, and Hybrid nodes. In Figure 3(a), two sensor nodes with $d(s_1, s_2)$, the shared area can be sensed

by both nodes s_1 and s_2, if and only if $d(s_1, s_2) < r_1 + r_2$. While in Figure 3(b), two sensor nodes can communicate with each other but without a typical coverage area where $d(s_1, s_2) > r_1 + r_2$. In Figure 3(c), two sensor nodes with $d(s_1, s_2) \leq (max(r_1, r_2) - min(r_1, r_2))$. The typical coverage area is covered by the sensor node, which has $max(r_1, r_2)$.

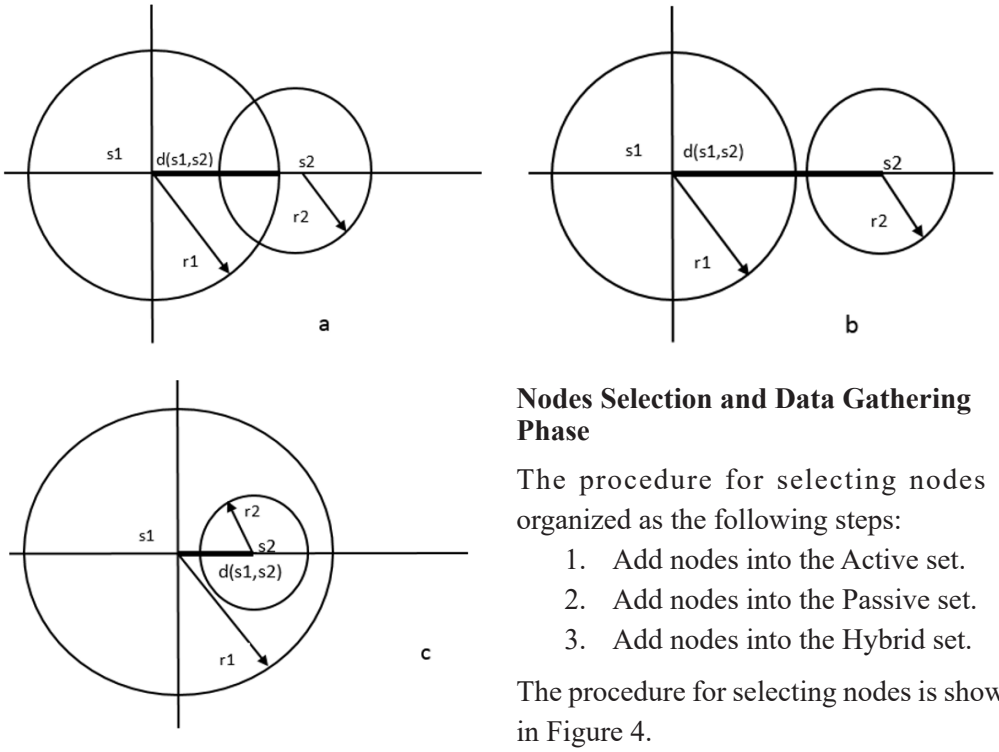

Figure 3. Two sensor nodes with $d(s_1, s_2)$

Nodes Selection and Data Gathering Phase

The procedure for selecting nodes is organized as the following steps:

1. Add nodes into the Active set.
2. Add nodes into the Passive set.
3. Add nodes into the Hybrid set.

The procedure for selecting nodes is shown in Figure 4.

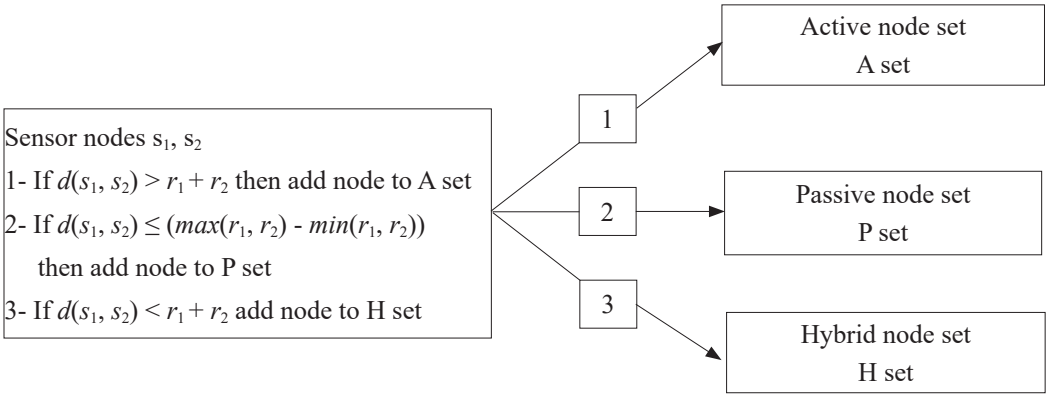

Figure 4. The procedure of adding nodes in sets

Step 1. Add nodes into the Active node-set

According to Figure 4, if $d(s_1, s_2) > r_1 + r_2$, the nodes belong to A set. Hence, ADCR put these nodes into an Active node set.

Step 2. Add nodes into the Passive node-set

If $d(s_1, s_2) \leq (max(r_1, r_2) - min(r_1, r_2))$, the node belongs to the P set. Hence, ADCR put these nodes into Passive and Active node sets. According to Figure 3(c), it is considered that the sensing area of s_2 is entirely covered by other node s_1. Thus, s_2 goes into the Passive node-set while s_1 goes into the Active node-set.

Step 3. Add nodes into the Hybrid node-set

If $d(s_1, s_2) < r_1 + r_2$, as shown in Figure 3(a), the part of the sensing area of s_2 is covered by the sensor node s_1. In this case, these nodes belong to the H set. Hence, ADCR put these nodes into a Hybrid node set. These sensor nodes s_1 and s_2 work together; alternatively, when the sensor node s_1 is Active, the sensor node s_2 is Passive, and vice versa. It is because node s_1 has an overlapping area with node s_2. The passive node set whose sensing areas are entirely covered by other Active nodes goes into Passive mode. While the Hybrid node set, whose sensing areas are partially covered by other nodes, goes into Hybrid mode.

Therefore, the redundancy of data gathered from the Passive and Hybrid node-set will be decreased. Repeat, adding nodes into the sensor nodes' A, P, and H sets.

Once the sensor node collects data from the environment, transmitting the relevant data to the base station is necessary. First, the cluster head creates a TDMA schedule for the nodes. Next, the cluster head allocates a separate time slot for each node. Then each node starts transmitting data to the cluster head in its time slot. Finally, cluster heads perform the aggregation task on the received data. The data is then forwarded to the base station through single-hop communication.

RESULTS AND DISCUSSION

In this section, the performance of the ADCR protocol is evaluated. The WSN with a set of sensor nodes is in a 100 m × 100 m region. Several experiments were carried out to evaluate parameters such as network lifetime, energy dissipation, and network stability. The results were compared to the LEACH protocol (OMNeT; Heinzelman et al., 2000). Table 2 gives the parameters used in the simulation. The experiments are performed in the OMNeT simulator.

The simulation scenarios were executed ten times. Also, the result is obtained from the average of ten independent runs. ADCR has considered up to five levels of random sensing range for simulation purposes. Also, the simulation uses various values of *LR* that determine the level of random sensing range in the network, where *LR* = 2,3,4,5,v 6.

Table 2
Simulation parameters

Parameter	Value
Size of sensing field	100 m × 100 m
Number of sensor nodes	50~100 nodes
Initial energy of each node	0.2~0.9 Joule
Initial sensing range	5 m
Base station location	50×175
$\boldsymbol{E_{el}}$	50 *nJ*/*bit*
$\boldsymbol{\varepsilon_{fs}}$	10 $pJ/bit/m^2$
Size of a data packet	500 bytes
Size of info packet	25 bytes
Level of randomization (***LR***)	2~6

For $LR = 2$, the model describes the two levels of the random sensing range. The node generates a random number *rnd* for each round where $0 < rnd \leq 2$. The sensor nodes can adjust their sensing range as follows by using Equation 7:

$$R_{rng} = I_{rng} + rnd \quad (7)$$

where R_{rng} is the random sensing range, and I_{rng} is the initial sensing range.

For $LR = 3$, the model describes the three levels of the random sensing range. The node generates a random number *rnd* for each round where $0 < rnd \leq 3$. The sensor nodes can adjust their sensing range using Equation 7.

For $LR = 4$, the model describes the four levels of the random sensing range. The node generates a random number *rnd* for each round where $0 < rnd \leq 4$. The sensor nodes can adjust their sensing range using Equation 7.

For $LR = 5$, the model describes the five levels of the random sensing range. The node generates a random number *rnd* for each round where $0 < rnd \leq 5$. The sensor nodes can adjust their sensing range using Equation 7.

For $LR = 6$, the model describes the six levels of the random sensing range. The node generates a random number *rnd* for each round where $0 < rnd \leq 6$. The sensor nodes can adjust their sensing range using Equation 7.

Experiment 1 examined the effects of energy and round count. The number of rounds varied from 20 to 100. The outcomes are shown in Figures 5 and 6. According to Figure 5, the nodes use more energy as the number of rounds increases because each sensor node collects data from the sensing field and sends it to the cluster head. Compared to LEACH, the rate of energy dissipation is substantially slower. When the number of rounds is set to 20, the energy dissipation in ADCR increases gradually, making it equivalent to the LEACH protocol. However, when the number of rounds is set to 100, the ADCR protocol extends the network lifetime using less energy than the LEACH protocol, as shown in Figure 6.

Experiment 2 examined the influence of the random sensing range and network lifetime. The level of randomization ranged from 2 to 6 with incremental step 1. The stability period has been used as a performance measure to evaluate the protocols, as the stability period represents the number of rounds from the network initialization to the death of the first

node, as shown in Figure 7. For example, in the randomization level = 2, the first node dies in 98 rounds. In randomization level = 6, the first node becomes dead in 122 rounds, while in LEACH protocol, the first node becomes dead in 39 rounds. Figure 8 represents the network lifetime from initialization until 80% of the sensor nodes die. The eighty dead sensor nodes for LR = 2, 3, 4, 5, or 6 die at 147, 161, 174, 193, and 207 rounds, respectively, while the eighty dead sensor nodes for LEACH protocol die at 55 rounds. As presented in Figures 7 and 8, with an increase in the level of randomization, the number of rounds increases, leading to increases in the network lifetime.

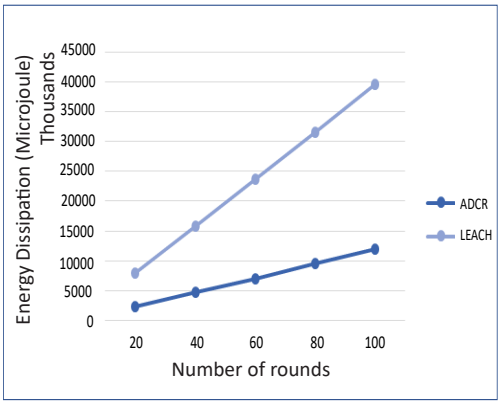

Figure 5. The energy dissipation versus the number of rounds

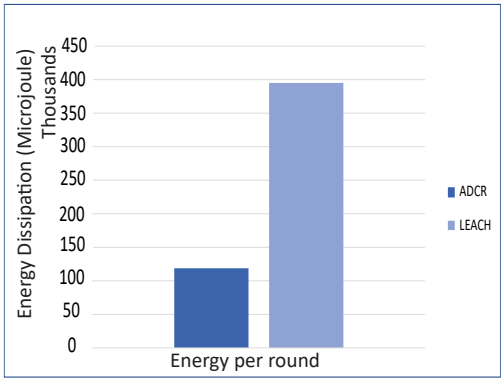

Figure 6. Average energy spent per round

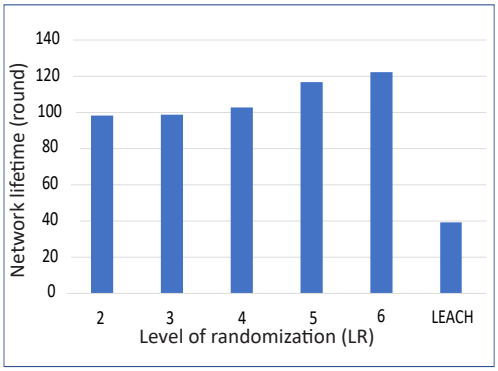

Figure 7. Stability period

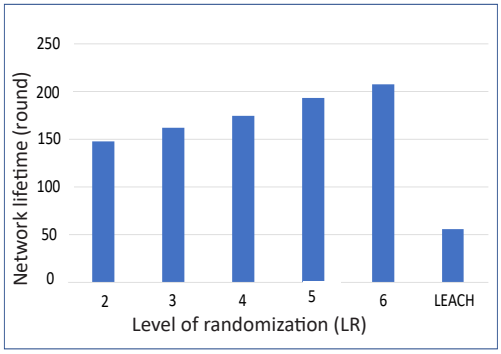

Figure 8. Network lifetime – eighty dead sensor nodes

Experiment 3 investigated how the random sensing range affected the quantity of data received. With incremental step 1, the amount of randomization was incrementally increased from 2 to 6. The experiment's measurement is the quantity of data gathered from the sensing field and transmitted to the base station. Figure 9 displays the findings. For LR = 2, 3, 4, 5, or 6, respectively, 7352, 8061, 8706, 9603, and 10308 packets of data were sent to the base station using the ADCR protocol, whereas 2771 packets were sent using the LEACH protocol. The findings show that the amount of received data increases when the random sensing range expands.

Experiment 4 examined the effects of the number of Active, Passive, and Hybrid nodes and the random sensing range. There were 50 to 100 sensor nodes, each with a 25-step increase. Figure 10's findings reveal that when the number of deployed nodes rises, the proportion of hybrid and passive nodes increases while the proportion of active nodes decreases. The cause is that when the random sensing range expands, some sensor nodes cover nearby nodes, which causes a decrease in active nodes and an increase in passive and hybrid nodes. Figure 11 shows a randomization level that varied from 2 to 6. It is understood that the sensor node whose detecting range is encircled by other sensor nodes will operate in either a passive or hybrid mode. As a result, as seen in Figure 11, as the level of randomization increases, the number of Active nodes decreases while the number of hybrid nodes increases. All investigations indicate that the ADCR protocol outperforms the LEACH protocol in terms of extending network lifetime, boosting network stability, and boosting throughput by catching more data packets at the base station.

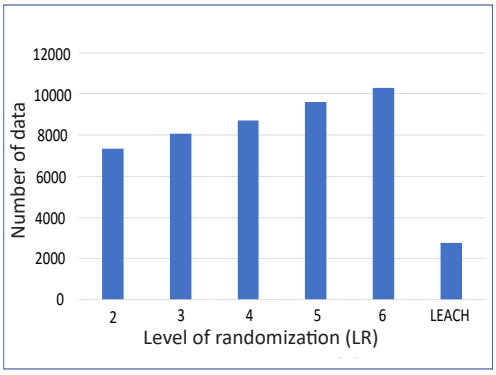

Figure 9. The number of data packets sent to the base station

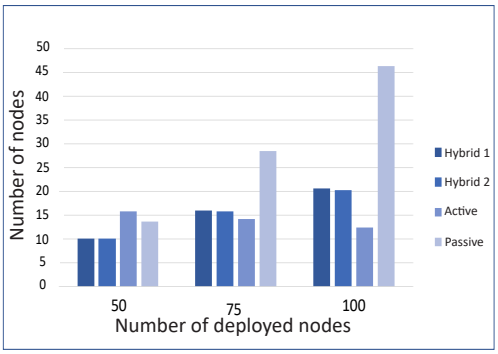

Figure 10. Active, Passive, and Hybrid nodes versus the number of deployed nodes

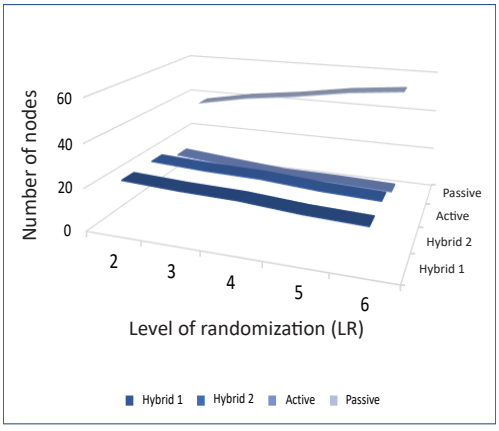

Figure 11. Active, Passive, and Hybrid nodes versus the level of randomization

CONCLUSION

In IoT sensor networks, each sensor node must not always be active. In this study, an adaptive density control is proposed by using a random sensing range. Several experiments have assessed the performance of the ADCR protocol were conducted. The first experiment started by evaluating the influence of the number of rounds and energy, while the second experiment investigated the impact of the random sensing range and network lifetime. This research observed the influence of the

random sensing range on the number of received data. Finally, the last experiment investigated the impact of the random sensing range and the number of Active, Passive, and Hybrid nodes. Simulation results confirm that ADCR can extend the network lifetime and save energy. As a part of future work, the mobility of the nodes can be used to expand this work. The sensor nodes' positions may change depending on the necessity of the WSN's goal. The node's mobility could improve network performance while adding flexibility to the WSN.

ACKNOWLEDGMENTS

This work was funded by the Deanship of Scientific Research (DSR), King Abdulaziz University, Jeddah, Saudi Arabia under grant No. (G-621-611-39). The authors, therefore, gratefully acknowledge the DSR's technical and financial support.

REFERENCES

Al-Shalabi, M., Anbar, M., Wan, T.C., & Khasawneh, A. (2018). Variants of the low-energy adaptive clustering hierarchy protocol: Survey, issues and challenges. *Electronics*, *7*(8), Article 136. https://doi.org/10.3390/electronics7080136

Bar-Noy, A., & Baumer, B. (2015). Average case network lifetime on an interval with adjustable sensing ranges. *Algorithmica*, *72*(1), 148-166. https://doi.org/10.1007/s00453-013-9853-5

Cerulli, R., De Donato, R., & Raiconi, A. (2012). Exact and heuristic methods to maximize network lifetime in wireless sensor networks with adjustable sensing ranges. *European Journal of Operational Research*, *220*(1), 58-66. https://doi.org/10.1016/j.ejor.2012.01.046

Cheng, S., Cai, Z., & Li, J. (2017). Approximate sensory data collection: A survey. *Sensors*, *17*(3), Article 564. https://doi.org/10.3390/s17030564

Debnath, S., Hossain, A., Chowdhury, S. M., & Singh, A. K. (2018). Effective sensing radius (ESR) and performance analysis of static and mobile sensor networks. *Telecommunication Systems*, *68*(1), 115-127. https://doi.org/10.1007/s11235-017-0379-z

Dhawan, A., Vu, C. T., Zelikovsky, A., Li, Y., & Prasad, S. K. (2006). Maximum lifetime of sensor networks with adjustable sensing range. In *Seventh ACIS International Conference on Software Engineering, Artificial Intelligence, Networking, and Parallel/Distributed Computing (SNPD'06)* (pp. 285-289). IEEE Publishing. https://doi.org/10.1109/snpd-sawn.2006.46

Dolas, P., & Ghosh, D. (2018). Compressed Sensing Based Network Lifetime Enhancement in Wireless Sensor Networks. In V. Janyani, M. Tiwari, G. Singh & P. Minzioni (Eds.), *Optical and Wireless Technologies* (pp. 465-471). Springer. https://doi.org/10.1007/978-981-10-7395-3_52

Dong, Z., Shang, C., Chang, C. Y., & Roy, D. S. (2020). Barrier coverage mechanism using adaptive sensing range for renewable WSNs. *IEEE Access*, *8*, 86065-86080. https://doi.org/10.1109/access.2020.2992867

Hao, J., Zhang, B., Jiao, Z., & Mao, S. (2015). Adaptive compressive sensing based sample scheduling mechanism for wireless sensor networks. *Pervasive and Mobile Computing*, *22,* 113-125. https://doi.org/10.1016/j.pmcj.2015.02.002

Heinzelman, W. B., Chandrakasan, A. P., & Balakrishnan, H. (2002). An application-specific protocol architecture for wireless microsensor networks. *IEEE Transactions on Wireless Communications*, *1*(4), 660-670. https://doi.org/10.1109/twc.2002.804190

Heinzelman, W. R., Chandrakasan, A., & Balakrishnan, H. (2000). Energy-efficient communication protocol for wireless microsensor networks. In *Proceedings of the 33rd Annual Hawaii International Conference on System Sciences* (pp. 1-10). IEEE Publishing. https://doi.org/10.1109/hicss.2000.926982

Liu, S., Gao, S., Bao, T., & Zhang, Y. (2017). A hybrid approach to maximize the lifetime of directional sensor networks with smoothly varying sensing ranges. *Chinese Journal of Electronics*, *26*(4), 703-709. https://doi.org/10.1049/cje.2017.06.001

Liu, X. (2016). A novel transmission range adjustment strategy for energy hole avoiding in wireless sensor networks. *Journal of Network and Computer Applications*, *67*, 43-52. https://doi.org/10.1016/j.jnca.2016.02.018

Nayak, A. K., Misra, B. B., & Rai, S. C. (2011). Energy efficient adaptive sensing range for sensor network. In *2011 International Conference on Energy, Automation and Signal* (pp. 1-6). IEEE Publishing. https://doi.org/10.1109/iceas.2011.6147143

Nkomo, M., Hancke, G. P., Abu-Mahfouz, A. M., Sinha, S., & Onumanyi, A. J. (2018). Overlay virtualized wireless sensor networks for application in industrial internet of things: A review. *Sensors*, *18*(10), Article 3215. https://doi.org/10.3390/s18103215

Puneeth, D., & Kulkarni, M. (2020). Data aggregation using compressive sensing for energy efficient routing strategy. *Procedia Computer Science*, *171*, 2242-2251. https://doi.org/10.1016/j.procs.2020.04.242

Raza, U., Bogliolo, A., Freschi, V., Lattanzi, E., & Murphy, A. L. (2016). A two-prong approach to energy-efficient WSNs: Wake-up receivers plus dedicated, model-based sensing. *Ad Hoc Networks*, *45*, 1-12. https://doi.org/10.1016/j.adhoc.2016.03.005

Rossi, A., Singh, A., & Sevaux, M. (2012). An exact approach for maximizing the lifetime of sensor networks with adjustable sensing ranges. *Computers & Operations Research*, *39*(12), 3166-3176. https://doi.org/10.1016/j.cor.2012.04.001

Seah, W. K., Eu, Z. A., & Tan, H. P. (2009). Wireless sensor networks powered by ambient energy harvesting (WSN-HEAP)-Survey and challenges. In *2009 1st International Conference on Wireless Communication, Vehicular Technology, Information Theory and Aerospace & Electronic Systems Technology* (pp. 1-5). IEEE Publishing. https://doi.org/10.1109/wirelessvitae.2009.5172411

Singh, N., Kumar, S., Kanaujia, B. K., Choi, H. C., & Kim, K. W. (2019). Energy-efficient system design for internet of things (IoT) devices. In M. Mittal, S. Tanwar, B. Agarwal, & L. M. Goyal, (Eds.), *Energy Conservation for IoT Devices* (pp. 49-74). Springer. https://doi.org/10.1007/978-981-13-7399-2_3

Walker, C., Sivakumar, S., & Al-Anbuky, A. (2015). Data flow and management for an IoT based WSN. In *2015 IEEE International Conference on Data Science and Data Intensive Systems* (pp. 624-631). IEEE Publishing. https://doi.org/10.1109/dsdis.2015.29

Wannachai, A., & Champrasert, P. (2015). Adaptive transmission range based on event detection for WSNs. In *2015 IEEE Tenth International Conference on Intelligent Sensors, Sensor Networks and Information Processing (ISSNIP)* (pp. 1-6). IEEE Publishing. https://doi.org/10.1109/issnip.2015.7106944

Yang, O., & Heinzelman, W. (2009). A better choice for sensor sleeping. In *European Conference on Wireless Sensor Networks* (pp. 134-149). Springer Berlin Heidelberg. https://doi.org/10.1007/978-3-642-00224-3_9

Zhang, H., Li, L., Yan, X. F., & Li, X. (2011). A load-balancing clustering algorithm of WSN for data gathering. In *2011 2nd International Conference on Artificial Intelligence, Management Science and Electronic Commerce (AIMSEC)* (pp. 915-918). IEEE Publishing. https://doi.org/10.1109/aimsec.2011.6010559

Pertanika J. Sci. & Technol. 31 (4): 1861 - 1879 (2023)

PERTANIKA JOURNALS

SCIENCE & TECHNOLOGY

Journal homepage: http://www.pertanika.upm.edu.my/

Design Requirement of Bathroom and Toilet for the Elderly in Malaysia

Mohd Rizal Hussain[1], Nuzul Azam Haron[2], Raja Ahmad Azmeer Raja Ahmad Effendi[3], Fakhrul Zaman Rokhani[1]*, Siti Anom Ahmad[1], Asmidawati Ashari[4], Mohd Khair Hassan[5], Mohd Shahrizal Dolah[3] and Saiful Hasley Ramli[3]

[1]Malaysian Research Institute on Ageing, Universiti Putra Malaysia, 43400 UPM, Serdang, Selangor, Malaysia
[2]Department of Civil Engineering, Faculty of Engineering, Universiti Putra Malaysia, 43400 UPM, Serdang, Selangor, Malaysia
[3]Department of Industrial Design, Faculty of Design and Architecture, Universiti Putra Malaysia, 43400 UPM, Serdang, Selangor, Malaysia
[4]Department of Human Development and Family Studies, Faculty of Human Ecology, Universiti Putra Malaysia, 43400 UPM, Serdang, Selangor, Malaysia
[5]Department of Electrical and Electronic Engineering, Faculty of Engineering, Universiti Putra Malaysia, 43400 UPM, Serdang, Selangor, Malaysia

ABSTRACT

According to previous research, the toilet and bathroom are the most common locations where injuries and accidents involving elderly people occur. Thus, the purpose of this paper is to investigate the issues and challenges of existing toilets and bathrooms among the Malaysian elderly and to identify appropriate solutions for them. The Focus Group Discussion (FGD) and Quality Function Deployment (QFD) sessions were implemented in this study, which involved a total of nineteen respondents, including elderly aged 60 years and above, their caregivers/family members, and agencies/authorities related to housing planning/development and technologies as well as researchers/experts. The recorded data were transcribed into text and organized systematically in the House of Quality (HoQ) for technical analysis. The focus group findings revealed that the four categorized issues raised by respondents in this study were quality, design, cost, and function. Furthermore, based on the HoQ analysis, it indicated that the top five highest ranks of customer requirements (CRs) for a

ARTICLE INFO

Article history:
Received: 12 May 2022
Accepted: 11 October 2022
Published: 25 May 2023

DOI: https://doi.org/10.47836/pjst.31.4.15

E-mail addresses:
mrizal@upm.edu.my (Mohd Rizal Hussain)
nuzul@upm.edu.my (Nuzul Azam Haron)
azmeer@upm.edu.my (Raja Ahmad Azmeer Raja Ahmad Effendi)
fzr@upm.edu.my (Fakhrul Zaman Rokhani)
sanom@upm.edu.my (Siti Anom Ahmad)
asmidawati@upm.edu.my (Asmidawati Ashari)
khair@upm.edu.my (Mohd Khair Hassan)
shahrizal@upm.edu.my (Mohd Shahrizal Dolah)
shr@upm.edu.my (Saiful Hasley Ramli)
*Corresponding author

ISSN: 0128-7680
e-ISSN: 2231-8526

new bathroom and toilet design requirement were comfortable (Rank 1), safety (Rank 2), affordable price (Rank 3), easy to enter bathroom/toilet (Rank 4) and anti-slippery floor (Rank 5). Meanwhile, the top five highest rank of technical requirements (TRs) refer to the existing OKU toilet design (Rank 1), anti-slip ramp & small drain under toilet door (Ranks 2 and 3), relocating existing toilet accessories, e.g., sink bow (Rank 4) and categories the cost according to the minor, major or new design (Rank 5). The information gathered could be used to develop appropriate bathrooms and toilets for the elderly in Malaysia.

Keywords: Bathroom, design requirement, elderly, focus group discussion, Malaysia, quality function deployment, toilet

INTRODUCTION

Elderly people are defined in a variety of ways. The chronological age of 65 has been accepted as a definition of "elderly" or older person in most developed countries worldwide (Kowal & Dowd, 2001). In Japan, "elderly" has traditionally been defined as being 65 years old or older, with those 65 to 74 years old referred to as "early elderly" and those over 75 years old referred to as "late elderly" (Orimo et al., 2006). The National Policy on Older Persons in India, on the other hand, defines "senior citizen" or "elderly" as a person 60 years of age or older (Amarya et al., 2015). At the moment, the United Nations does not have a standard numerical criterion for 'elderly'. However, when referring to the elderly, the UN-agreed-upon cut-off is 60 or older (Swaminathan & Audisio, 2012). In Malaysia, elderly people are defined as those aged 60 and above. This definition is based on the definitions made at the 1982 World Aging Conference in Vienna (DOSM, 2019). The elderly is one of the fastest-growing segments of the population, and the world's population is aging. The number of people aged 60 and up is expected to more than double by 2050 and triple by 2100, rising from 962 million in 2017 to 2.1 billion in 2050 and 3.1 billion in 2100, up from 962 million in 2017 (United Nations, 2017).

According to Jacob (2005), increasing longevity as well as declining fertility and mortality rates (Rashid et al., 2014) result in a higher proportion of elderly people in the population over time as well as more advanced healthcare and treatment facilities, improved infectious disease prevention and a significant improvement in nutritional status have all contributed to this situation. Malaysia also has a rapidly growing elderly population. According to the Department of Statistics Malaysia's 2018 census, approximately 3.23 million (9.97 percent) of the total population of 32.38 million are elderly people aged 60 and over, with men and women having life expectancies at birth 72.7 and 77.4 years, respectively. By 2034, the number of elderly is expected to exceed 5.1 million, accounting for 15% of the total population, with Malaysia expected to achieve aged nation status at that time (Tyng & Hamid, 2015).

Physiological changes are associated with decreased muscular strength, movement, and postural balance (Haus et al., 2007; Trappe, 2009). It is due to changes in joints and muscles that reduce mobility and strength. Muscle mass and strength usually decline as individuals age (Hasegawa et al., 2008). The aging process causes a loss of muscle mass and strength, where muscle strength declines between 16.6 percent and 40.9 percent between people aged 40 and those over 40 (Keller & Engelhardt, 2013). Furthermore, reduced muscle mass and strength contribute to a higher risk of fractures, fatigue, lower quality of life, and a loss of independence (Faulkner et al., 2007). Besides muscle, aging also influences some body postures, particularly those in the upper and lower body, because it is a key indicator for assessing health and quality of life, especially for the elderly (Gong et al., 2019). Furthermore, poor posture leads to decreased movement and a reduced ability to respond appropriately to external and internal stimuli (Bellomo et al., 2009). According to previous studies, good posture alignment and muscle quality are critical for elderly people's balance control (Hsu et al., 2014). As people get old, their vision and hearing abilities also deteriorate. Thus, physiological changes associated with aging reduce elderly people's autonomy and functional independence, which can lead to falls, either directly or indirectly (Terroso et al., 2014). At the same time, psychological issues such as dementia, agitation, anxiety, loneliness, and social exclusion have a negative impact on the health of elderly people due to the aging process (Kourkouta et al., 2015). People will experience physiological and psychological changes as they age, resulting in challenges in interacting with their environment due to functional decreases or declines in these aspects.

Elderly people frequently spend more time at home (Krantz-Kent & Stewart, 2007; Reinhardt et al., 2021). The environment is an important factor in an older person's self-sufficiency (Illario et al., 2016). Environmental hazards were as prevalent in the elderly homes, where the bathroom reported had the most home environmental hazards except for the lack of grab bars in the tub/shower (Gill et al., 1999), no slip-resistant mats, and a toilet that was not close to the bedroom (Zuniga et al., 2011). For the elderly, bathing is the most difficult daily activity (Guay et al., 2019). Home hazards are significant predictors of falls among elderly people (Sophonratanapokin et al., 2012), where most falls occur in the bathroom/toilet (Carling et al., 2018; D'souza et al., 2008; Rose et al., 2020). According to Hanba et al. (2017), a significant proportion of elderly traumatic injuries are caused by bathroom falls. Home injuries are a significant public health issue resulting in frequent hospitalizations and high fatalities (Camilloni et al., 2011). Furthermore, the rates of injury and hospitalization both increased with age. A study by Stevens et al. (2011) estimated that 234,094 non-fatal bathroom injuries were treated in EDs in 2008, and which majority of injuries were caused by falls and occurred while bathing, showering, or getting out of the tub or shower. While during the period 2002–2010, 13,175 toilet-related injuries were reported to ERs, which most common mechanism involved a crush caused by an accidental

fall of the toilet seat (Glass et al., 2013). In terms of toilet usage, according to Panek et al. (2017), standard toilets frequently fail to meet the needs of a significant number of elderly and disabled people. Besides, toileting difficulties were three times more common among the elderly who used assistive devices. Furthermore, non-flush toilet users in rural areas were almost two times more likely to have difficulty toileting than flush toilet users (Fong & Feng, 2021). Musculoskeletal problems caused by aging and lifestyle changes make it difficult for the elderly to defecate in a squatting or semi-squatting posture (Hari Krishnan, 2019).

Therefore, modifications to products, systems, and environments for daily use and use should be considered to accommodate these age-related changes in functional capabilities (Pennathur et al., 2003). It is because the built environment influences people's ability to live healthy lives, and elderly people require high-quality built environments that meet their needs throughout their lives—a building stock and infrastructure that supports independent living and improves the quality of life for the elderly (Tobi et al., 2017). This study examined the issues and challenges that the elderly face in their current bathroom and toilet, as well as identified potential solutions for improvements. However, several previous studies have been conducted on similar issues (Lim et al., 2014; Rosnah et al., 2008; Zaid et al., 2019); this study is seen as an additional finding but highlighted in a technical solution using QFD and HoQ. The findings are expected to enable the development of suitable bathrooms and toilets that are tailored to the needs of the elderly.

METHODOLOGY

In the social sciences, Focus Group Discussion (FGD) is a common qualitative research technique typically carried out in person to generate research insights through group discussion and interaction (Chen & Neo, 2019). FGD is simple, inexpensive, requires a small number of participants, and can be completed in a short amount of time (Zacharia et al., 2021). Thus, the purposive sampling method, such as FGD, was used in this study to obtain information involving six older persons aged 60 years old and above from the Association for Lifelong Learning of Older Persons (U3A) Kuala Lumpur and Selangor, Malaysia members and living in community-dwelling, one of their carer/family members and three agencies/authorities person related to housing planning and development. They were divided into groups of 2–5 people each. Participants were given written information about the purpose of the study prior to the session, and they signed an agreement form to ensure the confidentiality of the entries. This study has also received ethical approval from the UPM Ethics Committee for Human Subjects Research (reference no: JKEUPM-2018-123). FGD sessions were led by trained moderators assisted by rapporteurs (note-taker). The moderator begins the discussion session by greeting participants and explaining the purpose of the research. Participants/respondents were asked to introduce

themselves before being asked questions about the research topic. The moderator guides the discussion, encouraging all participants to share and ensuring everyone has enough time to express their opinions. Each session was recorded with a digital voice recorder, and the notes were later reviewed, analyzed, and transcribed into text form. The focus group lasted between one and a half or two hours. The information gained was structured systematically and categorized into a particular classification based on issues and challenges, ways to solve issues, as well as important criteria for consideration in developing friendly bathrooms and toilets for the elderly in the future.

Then, the Quality Function Deployment (QFD) session was conducted in the second stage involving two carers/family members for the elderly and seven researchers/experts to generate a new design solution for bathrooms and toilets that considers the needs of the elderly people. QFD is an effective and powerful tool in product design, development, and planning, where the primary function is to convert the voice of the customer (VoC) to technical characteristics or the designer's voice (Iranmanesh et al., 2014). According to Leppänen et al. (2000), QFD has features similar to participatory ergonomics and can be used to improve the ergonomics and usability of products. Both methods and approaches tend to include the end user in the design process. Starting with the initial matrix, commonly known as the House of Quality (HoQ) (Figure 1), the QFD methodology focuses on the most important product or service attributes or qualities. However, the correlation matrix (Roof of the HoQ or interrelationship between technical descriptors) was not considered or applied for this project. VoC or Customer Requirements (CRs) or WHATs are data collected from respondents during the FGD relating to their needs and requirements.

These are given a weighted priority rating. The information was then converted into technical descriptors or Technical Requirements (TRs) or HOWs, which are engineering considerations and specifications (product characteristics). This step was challenging because it required specific people, such as researchers/experts, elderly caregivers, and industry persons involved in the marketing and sale of walking frames/walkers, to work in teams to identify the variables that may have the greatest impact on the customer requirements. Furthermore, variables must be meaningful and measurable, and TRs must be synchronized with CRs. Based on Cudney and Elrod (2011), the correlation or strength of CRs and TRs can be represented on a value scale using the relationship matrix; 0 (no correlation), 1 (weak correlation), 3 (moderate correlation), and 9 (strong correlation). Data was then technically analyzed using specific Equations 1, 2 and 3 to determine importance value, Design Priority (DP), and Percent Priority (PP). This matrix identifies the technical requirements that satisfy most customer consequences. The obtained values are then displayed in order of rank. The design process should prioritize the technical requirements that address the most customer consequences to ensure that a product or service meets customer expectations.

$$\text{Average CRs importance value} = \frac{\Sigma \text{ of all points from each CR given by the respondent}}{\Sigma \text{ of maximum point value for each CR}} \quad [1]$$

$$\text{Design Priority (DP)} = \Sigma \text{ (Correlation Value x CRs Importance Value)} \quad [2]$$

$$\text{Percent Priority (PP)} = \frac{\Sigma \text{ (Correlation Value x CRs Importance Value)}}{} \times 100 \quad [3]$$

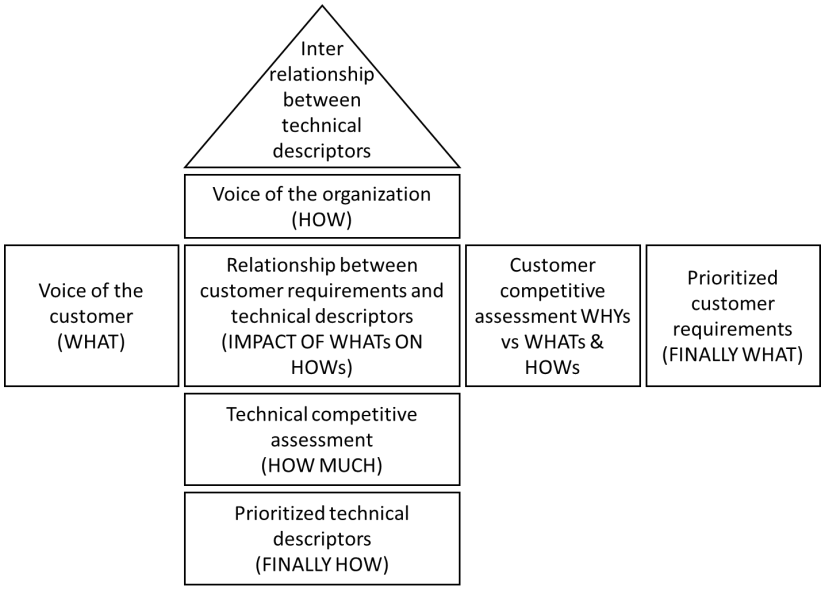

Figure 1. QFD house of quality (Kiran, 2017)

RESULTS AND DISCUSSION

Focus Group Discussion (FGD)

Some issues were reported by respondents regarding the current design of bathrooms and toilets in the home based on discussions conducted. Hence, researchers have categorized them into four issues: quality, design, cost, and function.

Quality. On the quality aspect, some of the issues and challenges highlighted by respondents were slippery bathtub base and floor when wet as well as slippery steel bar holder when covered with soap. The information shared by the respondents during the discussion was summarized in the statements below.

Elderly (M): Most people put a slippery tile style, right? Very dangerous. Sometimes bring water; a little spill can fall.

Elderly (M): I think the practice is in this bathroom. Our people like to use a lot of soap. Wet is ok. But if there is soap, it is slippery. So, it is very dangerous when you slip. It is a problem.

Elderly (F): Grab bar also has to be selected. If it is stainless steel, it is slippery, especially when covered by soap.

The feedback of respondents in this FGD was found to be supportive of some findings from previous studies regarding quality aspects such as slippery/wet floors in bathrooms or toilets (Hignett et al., 2010; Rosnah, Norazizan, Aizan & Rizal, 2008; Vaccari, Lenardt, Willi, Betiolli & de Oliveira, 2014). Because aging is associated with a decline in several body systems' strength and senses, slippery floors may contribute to the elderly's loss of balance (Sophonratanapokin et al., 2012). As a suggestion by Mazloomy Mahmoodabad et al. (2018), promoting a culture of non-slippery flooring, as well as using public media and education, can help prevent elderly people from falling. Furthermore, separating dry and wet spaces can help the elderly avoid slipping, prevent splashing, and maintain heat (Han et al., 2020).

Design. The finding discovered the issues on design were bathroom size bigger/smaller, toilet door width too small for wheelchair access, toilet/bathroom far from bedroom, squat toilet/toilet seat too low, water pipe too low, and non-lever type water tap. The statements below summarize the information shared by the respondents during the discussion.

Elderly (M): Some bathrooms are large, while others are small. My wife has a little bit of bathroom experience. She could fall if the area is too large for her to grasp.

Agency/authorities person (M): Because of the narrowness of the door, it is difficult for the current wheelchair to enter the toilet.

Elderly (F): In some village houses, the bathroom is far from the bed. It is not located in the bedroom but occasionally in the kitchen. Then there are stairs that you must descend.

Elderly (F): There is one location where all the toilets are squat. If I sit down, I won't be able to get up. I need to cling to something.

Elderly (F): For me, the water pipe I am currently using needs to be slightly bent. However, neither is it very high nor very low.

Elderly (M): As I previously stated, the floor was covered in vinyl. Most people use a slick tile style. It is extremely dangerous. Bring water on occasion, as a small spill can cause a fall or slip. Slips are hazardous because falling is extremely dangerous.

Some previous research findings were also found to be similar to the issues and challenges of design that have been raised in this study. As mentioned by Nagananda et al. (2010), the lack of a bidirectional door and insufficient door width made the bathroom entrance unsafe for the elderly and difficult for those who needed ambulatory or mobility aids. Besides, inadequate bathroom size is also viewed as a potential hazard and discomfort to users (Joshi & Dsouza, 2015). A previous study also shows that the elderly who had outside bathrooms or toilets were likelier to fall than those who did not, possibly due to inadequate lighting, uneven floors, and the path to the toilet (Sophonratanapokin et al., 2012). Thus, the bathroom should be reserved enough from the start of the design process so that the elderly can stay as long as they want (Ju & Lee, 2017). Creating a new approach to designing and optimizing the layout of bathroom facilities is also recommended (Wang et al., 2018). Toilets are typically located at the back or outside the house, whereas squatting toilets are common in traditional houses. Some are typically not well-maintained, with unpaved outdoor areas and improvised kitchens, which may contribute to hazards and risk of falls (Romli et al., 2018). Therefore, changing the sole position in a squatting-type toilet and its sloping design can effectively make users more comfortable (Mououdi et al., 2020). It also discovered that the low water faucet height from the lowest floor level makes it difficult for wheelchair users with permanent or temporary back injuries to operate (Dawal et al., 2016). Thus, using anthropometric data to design products and living facilities is critical for increasing the comfort, safety, and health of the elderly (Kaewdok et al., 2020).

Cost. According to feedback from respondents on cost, some of them stated that if an item's price or cost is relatively high, they are unlikely to purchase it. The following are some of the respondents' responses to the cost-related discussion.

Elderly (M): For the safety and well-being of the elderly. That is valuable. That is what developers have to think about. It involves cost. So, we have to find a way that does not cost that much.

Elderly (F): We sometimes buy because it is beautiful. But we do not know its safety. Sometimes when we buy something, we do not even think about it. Then look at the price, right? If it is too expensive, do not buy it either.

According to the study, most elderly did not have enough money in their later years (Yin-Fah et al., 2010). As a result, it will indirectly affect their purchasing power and represent a significant economic and social issue (Jakimovski, 2010). This study's findings in terms of cost and price were found to support the previous study. In terms of functionality, there have been previous studies that show similar results. Most respondents did not have

bathtub grab bars installed in their homes (Sveistrup et al., 2006), and toilets always had no handrails or other supporters (Yuan et al., 2021). Therefore, related issues should be given full attention to ensure this environment is safe and comfortable for the elderly.

Function. The respondents' feedback on the functionality issue revealed that several related issues were highlighted, such as no safety railing in the toilet, a grab bar to enter the bathtub, and a two-way door lock. Some of the issues raised by respondents are listed below.

Elderly (F): Handrails are only found in public restrooms. There are not in any homes yet.

Elderly (F): At home, I also have a bathtub. It is a bit hassle when you want to go in and out because you have to step up one level to get inside. There is no rail/handrail to grab. I am concerned because it is slick.

Elderly (F): When it comes to doors, I always tell them. If someone needs to use the restroom, do not lock the door from the inside. Because if it is locked and something unexpected happens inside, it takes time to save or assist someone inside.

Some previous studies were similar to the issues and challenges raised in this study regarding functionality. As Chacko et al. (2017) mentioned, handrails were absent in most of the toilets in rural houses of elders. Past researchers have also voiced issues related to grab bars. The basic function of the grab bar is to maintain balance during transfers and allow safe movement in the bathtub (Morales et al., 2017). However, the study also shows that most respondents did not have bathtub grab bars installed in their homes (Edwards et al., 2006; Sveistrup et al., 2006).

QFD House of Quality

Based on the FGD session, CRs were classified into three categories: quality, design, cost, and function, as shown in Figure 2. Under Quality, the CRs' list was anti-slippery bathtub base, floor and hand bar/railing, higher safety, and comfort. For Design, the CRs identified were suitable size for the bathroom, easy to enter toilet/bathroom, location of the toilet near bedroom, enough lighting lux, toilet flush level at both hand sides, and suitable color. Under Cost, affordable price is the CRs' list. While for Function, two-way door lock, emergency button's switch, and fall/movement detector were CRs' list suggested by respondents.

Thus, some of the previous study's findings are consistent with respondents' suggestions or Customer Requirements (CRs) for improvements. On the quality aspect, floor tiles may be treated with an anti-slip coating to prevent slips and fall. If the floor cannot be treated, use a rubber or anti-slip mat (Salam & Shams El-din, 2019; Lago et al., 2018; Mulliner et

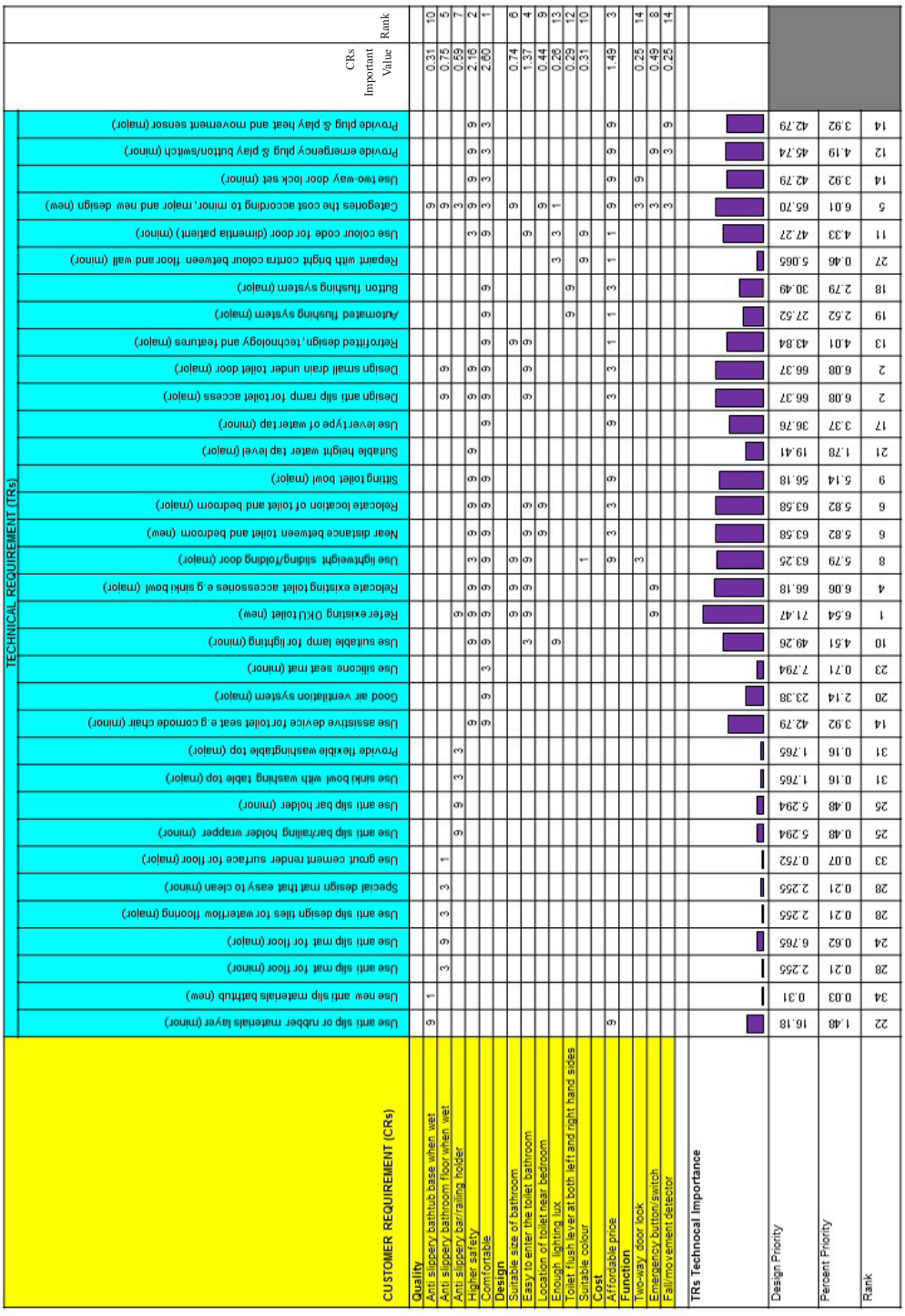

Figure 2. QFD House of Quality (HoQ) for toilet and bathroom design requirement

al., 2020), handrail or grab handle (Blanchet & Edwards, 2018; Rousseau, 2018). While in the design aspect, recommendations for the distance between the rooms that support the activities of daily living for elderly residents should be shortened to improve the QoL of the elderly in the home, including locating bedrooms near bathrooms/toilets (Yu et al., 2017). Furthermore, as mentioned by Leung et al. (2016), the route between the bedroom and the toilet should be short and free of obstacles, there should be adequate artificial lighting, and doors should be wide enough to allow elders in wheelchairs to pass through to ensure the elderly's safety.

Therefore, appropriate support features/facilities are required to create a safe and comfortable environment, which is critical for meeting the psychological and social needs of the elderly (Ma et al., 2016) as well as one of the most important fall prevention interventions used to reduce the risk of falling in the home setting (Hamm et al., 2019). For the cost aspect, the higher-priced product should be carefully considered based on scientific support or user feedback before being produced or marketed. In terms of functionality, as suggested by Kam and Chan (2015), the locked door must be easily opened from the outside if there may have collapsed or fallen incident inside the bathroom or toilet. Besides, a qualified emergency calling device or emergency button in the bedroom and bathroom is also recommended (Huang & Ho, 2012). At the same time, some researchers emphasize using devices/sensors to detect emergencies such as falls and injuries involving the elderly in the home (Meng et al., 2017; Rachuy et al., 2013; Thapliyal et al., 2017; Tsuchiyama & Kajiwara, 2019).

The requirement obtained for TRs according to the CRs list. Some of the TRs that were discovered included using anti-slip tiles for the floor, a good air ventilation system, relocating the location of the toilet and bathroom, a sitting toilet bowl, suitable height water tab level, and use of lightweight sliding/folding door. Table 1 shows the example detailed calculation for TR16. Finally, the rank for the TRs was determined accordingly based on the value of PP, starting from the highest (Rank No.1) to the lowest (Rank No. 33).

The Technical Requirements (TRs) analysis findings were also compared to previous research recommendations. Several studies have suggested that the toilet and bathroom should be installed with a non-slip mat or floor (Afifi et al., 2015; Kamei et al., 2015; Mahmoodabad et al., 2018), air ventilation system (Leung et al., 2017; Savchenko et al., 2017), relocation of toilet or bathroom (Granbom et al., 2019), sitting toilet bowl type (Dawal et al., 2015; Zaid et al., 2019), the suitable height of water tab/faucet (Sukadarin et al., 2021) and use sliding/folding door (Lee et al., 2007).

Table 1

The detailed calculation for TR 16

(CR)	TR16: Refer to Existing OKU Toilet	CRs Importance Value (IV)
CR 4	Strong correlation = 9	0.59
CR 5	Strong correlation = 9	2.16
CR 6	Strong correlation = 9	2.60
CR 9	Strong correlation = 9	0.74
CR 10	Strong correlation = 9	1.37
CR 21	Strong correlation = 9	0.49
	DP = (9 x 0.59) + (9 x 2.16) + (9 x 2.60) + (9 x 0.74) + (9 x 1.37) + (9 x 0.49) = 71.47	
	PP $= \frac{\text{Design Priority}}{\Sigma \text{ Design Priority}} x\ 100 \frac{\text{Design Priority}}{\Sigma \text{ Design Priority}} x\ 100$ $= \frac{71.47}{1093} x100 \frac{71.47}{1093} x100$ $= 6.54$	

Note. CR = Customer's Requirement, TR = Technical Requirement, IV = Importance Value, DP = Design Priority and PP = Percent Priority

CONCLUSION

In conclusion, it has been discovered that there are issues and challenges with the existing bathroom and toilet facilities among Malaysia's elderly, which have been classified into three categories: quality, design, cost, and function. Based on the findings, the authors created a House of Quality (HoQ) for bathroom and toilet design requirements. Using the results of the Design Priority (DP) and Percent Priority (PP) of the technical requirements in HoQ (Figure 2), the design team can prioritize the TRs for an appropriate bathroom and toilet design recommendation, which may meet the CRs as the elderly user. It shows that the highest rank of CRs for a bathroom and toilet design requirements are comfortable (Rank 1), higher safety (Rank 2), affordable price (Rank 3), easy to enter bathroom/toilet (Rank 4), and anti-slippery bathroom floor when wet (Rank 5). Meanwhile, the highest rank of TRs refers to the existing OKU toilet design (Rank 1), the design anti-slip ramp for toilet access and drain under the toilet door (Ranks 2 & 3), relocating existing toilet accessories, e.g., sink bowl (Rank 4) and categories the cost according to the minor, major and new design (Rank 5). Thus, this information is hoped to be useful in designing bathrooms and toilets that may provide more safety features, stability, and user-friendliness for the elderly.

ACKNOWLEDGEMENTS

We thank all respondents for this study. We also thank any person or organization involved directly or indirectly in this study. This study was supported by the Putra Research Grant Scheme (reference: GP/2018/9625700), Universiti Putra Malaysia. The Universiti Putra Malaysia Research Ethics Committee has approved this study (Reference Letter ID: JKEUPM-2018-123 dated 9 July 2018).

REFERENCES

Afifi, M., Al-Hussein, M., & Bouferguene, A. (2015). Geriatric bathroom design to minimize risk of falling for older adults - A systematic review. *European Geriatric Medicine*, *6*(6), 598-603. https://doi.org/10.1016/j.eurger.2015.05.004

Amarya, S., Singh, K., & Sabharwal, M. (2015). Changes during aging and their association with malnutrition. *Journal of Clinical Gerontology Geriatrics*, *6*(3), 78-84. https://doi.org/10.1016/j.jcgg.2015.05.003

Bellomo, R., Iodice, P., Savoia, V., Saggini, A., Vermiglio, G., & Saggini, R. J. (2009). Balance and posture in the elderly: An analysis of a sensorimotor rehabilitation protocol. *International Journal of Immunopathology and Pharmacology 22*(3_suppl), 37-44.

Blanchet, R., & Edwards, N. (2018). A need to improve the assessment of environmental hazards for falls on stairs and in bathrooms: Results of a scoping review. *BMC Geriatrics*, *18*(1), 1-16. https://doi.org/10.1186/s12877-018-0958-1

Camilloni, L., Farchi, S., Rossi, P. G., Chini, F., Di Giorgio, M., Molino, N., Iannone, A., Borgia, P. & Guasticchi, G. (2011). A case-control study on risk factors of domestic accidents in an elderly population. *International Journal of Injury Control Safety Promotion*, *18*(4), 269-276. https://doi.org/10.1080/17457300.2011.562615

Carling, A., Forsberg, A., & Nilsagård, Y. (2018). Falls in people with multiple sclerosis: Experiences of 115 fall situations. *Clinical Rehabilitation*, *32*(4), 526-535. https://doi.org/10.1177/026921551773059

Chacko, T. V., Thangaraj, P., & Muhammad, G. M. (2017). How fall-safe is the housing for the elderly in rural areas? A cross sectional study using fall prevention screening checklist. *Journal of the Indian Academy of Geriatrics*, *13*(3), 124-130.

Chen, J., & Neo, P. (2019). Texting the waters: An assessment of focus groups conducted via the WhatsApp smartphone messaging application. *Methodological Innovations*, *12*(3). https://doi.org/10.1177/2059799119884276

Cudney, E. A., & Elrod, C. C. (2011). Quality function deployment in continuous improvement. In A. Coskun, T. C. Inal & M. Serteser (Eds.), *Six Sigma Projects Personal Experiences* (pp. 45-78). InTech.

Dawal, S. Z. M., Ismail, Z., Yusuf, K., Abdul-Rashid, S. H., Shalahim, N. S. M., Abdullah, N. S., & Kamil, N. S. M. (2015). Determination of the significant anthropometry dimensions for user-friendly designs of domestic furniture and appliances–Experience from a study in Malaysia. *Measurement*, *59*, 205-215. https://doi.org/10.1016/j.measurement.2014.09.030

Dawal, S. Z. M., Mahadi, W. N. L., Mubin, M., Daruis, D. D. I., Mohamaddan, S., Razak, F. A. A., Abd Rahman, N. I., Abd Wahab, M. H. N., Adnan, N., Anuar, S. A. & Hamsan R. (2016). Wudu'workstation design for elderly and disabled people in Malaysia's mosques. *Iranian Journal of Public Health*, *45*(Supple 1), 114-124.

DOSM. (2019). *Definition of 'Elderly'*. Department of Social Welfare. http://www.jkm.gov.my/jkm/index.php?r=portal/left&id=VEpUUXV3THFURkZETmxWNjZpQ1BXdz09

D'souza, S. A., Shringarpure, A., & Karol, J. (2008). Circumstances and consequences of falls in Indian older adults. *Indian Journal of Occupational Therapy*, *40*(1), 3-11.

Edwards, N., Birkett, N., Nair, R., Murphy, M., Roberge, G., & Lockett, D. (2006). Access to bathtub grab bars: Evidence of a policy gap. *Canadian Journal on Aging/La Revue canadienne du vieillissement*, *25*(3), 295-304. https://doi.org/10.1353/cja.2007.0002

Faulkner, J. A., Larkin, L. M., Claflin, D. R., & Brooks, S. V. (2007). Age-related changes in the structure and function of skeletal muscles. *Clinical and Experimental Pharmacology and Physiology*, *34*(11), 1091-1096. https://doi.org/10.1111/j.1440-1681.2007.04752.x

Fong, J. H., & Feng, Q. (2021). Toileting disability among older adults in china and role of environmental factors. *Journal of Aging Health*, *33*(10), 852-864. https://doi.org/10.1177/0898264321101502

Gill, T. M., Robison, J. T., Williams, C. S., & Tinetti, M. E. (1999). Mismatches between the home environment and physical capabilities among community-living older persons. *Journal of the American Geriatrics Society*, *47*(1), 88-92. https://doi.org/10.1111/j.1532-5415.1999.tb01906.x

Glass, A. S., Bagga, H. S., Tasian, G. E., McGeady, J. B., McCulloch, C. E., Blaschko, S. D., McAninch, J. W. & Breyer, B. N. (2013). No small slam: Increasing incidents of genitourinary injury from toilets and toilet seats. *BJU International*, *112*(3), Article 398. https://doi.org/10.1111/bju.12173

Gong, H., Sun, L., Yang, R., Pang, J., Chen, B., Qi, R., Gu, X., Zhang, Y. & Zhang, T. M. (2019). Changes of upright body posture in the sagittal plane of men and women occurring with aging–a cross sectional study. *BMC Geriatrics*, *19*(1), 1-11. https://doi.org/10.1186/s12877-019-1096-0

Granbom, M., Perrin, N., Szanton, S., Cudjoe, T. K. M., & Gitlin, L. N. (2019). Household accessibility and residential relocation in older adults. *The Journals of Gerontology: Series B*, *74*(7), e72-e83. https://doi.org/10.1093/geronb/gby131

Guay, M., D'Amours, M., & Provencher, V. (2019). When bathing leads to drowning in older adults. *Journal of Safety Research*, *69*, 69-73. https://doi.org/10.1016/j.jsr.2019.02.003

Hamm, J., Money, A. G., Atwal, A., & Ghinea, G. (2019). Mobile three-dimensional visualisation technologies for clinician-led fall prevention assessments. *Health Informatics Journal*, *25*(3), 788-810. https://doi.org/10.1177/1460458217723170

Han, R., Shao, D., & Wang, Y. (2020). Design of senior family bathroom system based on demand theory. *E3S Web of Conferences*, *179*, Article 02080. https://doi.org/10.1051/e3sconf/202017902080

Hanba, C., Gupta, A., Svider, P. F., Folbe, A. J., Eloy, J. A., Zuliani, G. F., & Carron, M. A. (2017). Forgetful but not forgotten: Bathroom-related craniofacial trauma among the elderly. *The Laryngoscope*, *127*(4), 820-827. https://doi.org/10.1002/lary.26111

Hasegawa, R., Islam, M. M., Lee, S. C., Koizumi, D., Rogers, M. E., & Takeshima, N. (2008). Threshold of lower body muscular strength necessary to perform ADL independently in community-dwelling older adults. *Clinical Rehabilitation*, *22*(10-11), 902-910. https://doi.org/10.1177/0269215508094713

Haus, J. M., Carrithers, J. A., Trappe, S. W., & Trappe, T. A. (2007). Collagen, cross-linking, and advanced glycation end products in aging human skeletal muscle. *Journal of Applied Physiology*, *103*(6), 2068-2076. https://doi.org/10.1152/japplphysiol.00670.2007

Hignett, S., Sands, G., Youde, J., & Griffiths, P. L. (2010, July 17-20). *Targeting environmental factors to reduce elderly in-patient falls.* [Paper presentation]. 1st International Conference on Human Factors and Ergonomics in Healthcare, Miami, USA.

Hsu, W. L., Chen, C. Y., Tsauo, J. Y., & Yang, R. S. (2014). Balance control in elderly people with osteoporosis. *Journal of the Formosan Medical Association*, *113*(6), 334-339. https://doi.org/10.1016/j.jfma.2014.02.006

Huang, C. H., & Ho, Z. S. (2012). A discussion on the environmental evaluation tools of care institutions for the elderly. In P. Israsena, J. Tangsantikul & D. Durling (Eds.), *Research: Uncertainty Contradiction Value - DRS International Conference 2012* (pp. 765-775) Chulalongkorn University. https://dl.designresearchsociety.org/drs-conference-papers/drs2012/researchpapers/56

Illario, M., Vollenbroek-Hutten, M. M., Molloy, D. W., Menditto, E., Iaccarino, G., & Eklund, P. (2016). Active and healthy ageing and independent living 2016. *Journal of Aging Research*, *2016*, Article 8062079. https://doi.org/10.1155/2016/8062079

Iranmanesh, S. H., Rastegar, H., & Mokhtarani, M. H. (2014). An intelligent fuzzy logic–based system to support quality function deployment analysis. *Concurrent Engineering*, *22*(2), 106-122. https://doi.org/10.1177/1063293X14522080

Jacob, R. (2005). Aging and current trends in Malaysia. *International Journal of Social Work and Human Services Practice*, *4*(3), 57-61.

Jakimovski, J. (2010). The socio-demographic context of rural poverty. *Eastern European Countryside*, *16*, 131-156. https://doi.org/10.2478/v10130-010-0007-3

Joshi, R., & Dsouza, S. (2015). Bathroom hazards among older adults in western India: A cross-sectional study. *Asian Journal Gerontology Geriatric*, *10*(2), 83-91.

Ju, H., & Lee, H. (2017). The bathroom plan for the impaired elderly with caregiver-focus on the size of bathroom needed for behaviours. *Korean Institute of Interior Design Journal*, *26*(5), 3-15. https://doi.org/10.14774/JKIID.2017.26.5.003

Kaewdok, T., Sirisawasd, S., Norkaew, S., & Taptagaporn, S. (2020). Application of anthropometric data for elderly-friendly home and facility design in Thailand. *International Journal of Industrial Ergonomics*, *80*, Article 103037. https://doi.org/10.1016/j.ergon.2020.103037

Kam, W. K., & Chan, Y. T. (2015). Human factor and operating considerations for door lockset design for patient bathrooms in a tertiary acute hospital. *Procedia Manufacturing*, *3*, 216-218. https://doi.org/10.1016/j.promfg.2015.07.131

Kamei, T., Kajii, F., Yamamoto, Y., Irie, Y., Kozakai, R., Sugimoto, T., Chigira, A. & Niino, N. (2015). Effectiveness of a home hazard modification program for reducing falls in urban community-dwelling

older adults: A randomized controlled trial. *Japan Journal of Nursing Science*, *12*(3), 184-197. https://doi.org/10.1111/jjns.12059

Keller, K., & Engelhardt, M. (2013). Strength and muscle mass loss with aging process. Age and strength loss. *Muscles, Ligaments Tendons Journal, 3*(4), 346-350.

Kiran, D. R. (2017). Total quality management: An overview. In D. R. Kiran (Ed.), *Total Quality Management* (pp. 1-14) Elsevier. https://doi.org/10.1016/B978-0-12-811035-5.00001-5

Kourkouta, L., Iliadis, C., & Monios, A. (2015). Psychosocial issues in elderly. *Progress in Health Sciences*, *5*(1), 232-237.

Kowal, P., & Dowd, J. E. (2001). Definition of an older person. Proposed working definition of an older person in Africa for the MDS Project. *World Health Organization, Geneva, 10*(2.1), 5188-9286.

Krantz-Kent, R., & Stewart, J. (2007). How do older Americans spend their time. *Monthly Labor Review*, *130*(5), 8-26.

Krishnan, R. H. (2019). A review on squat-assist devices to aid elderly with lower limb difficulties in toileting to tackle constipation. *Proceedings of the Institution of Mechanical Engineers, Part H: Journal of Engineering in Medicine*, *233*(4), 464-475. https://doi.org/10.1177/095441191983864

Lago, E., Barkokébas, B., da Cruz, F., Martins, A., Vasconcelos, B., Zlatar, T., Manta, R. & Porto, S. (2018) Accidents prevention at home with elderly. In P. M. Arezes, J. S. Baptista, M. P. Barroso, P. Carneiro, P. Cordeiro, N. Costa, R. B. Melo A. S. Miguel & G. Perestrelo (Eds.),. *Occupational Safety and Hygiene VI*, (pp. 137-142). CRC Press. https://doi.org/10.1201/9781351008884

Lee, S., Dilani, A., Morelli, A., & Byun, H. (2007). Health supportive design in elderly care homes: Swedish examples and their implication to Korean counterparts. *Architectural Research*, *9*(1), 9-18.

Leppänen, M., Mattila, M., & Kivistö-Rahnasto, J. (2000). Designing the ergonomic properties of pruning shears using Quality Function Deployment (QFD). *Proceedings of the Human Factors and Ergonomics Society Annual Meeting*, *44*(22), 647–650. https://doi.org/10.1177/154193120004402240

Leung, M. Y., Yu, J., & Chong, M. L. (2017). Impact of facilities management on the quality of life for the elderly in care and attention homes - Cross-validation by quantitative and qualitative studies. *Indoor and Built Environment*, *26*(8), 1070-1090. https://doi.org/10.1177/1420326X1666269

Leung, M. Y., Yu, J., & Memari, A. (2016). Managing indoor facilities in public housing to improve elderly quality of life. *International Journal for Housing Science & Its Applications*, *40*(2), 85-99.

Lim, K. H., Jasvindar, K., Normala, I., Ho, B. K., Yau, W. K., Mohmad, S., Lai, W.Y., & Sherina, M. S. (2014). Risk factors of home injury among elderly people in Malaysia. *Asian Journal of Gerontology & Geriatrics*, *9*(1), 16-20.

Ma, G. X., Yu, J., & Jiang, X. (2016). Investigation on satisfaction among elderly residents of senior homes in China from a social marketing perspective. *Public Policy and Administration Research*, *6*(1), 15-20.

Mahmoodabad, S. S. M., Zareipour, M., Askarishahi, M., & Beigomi, A. (2018). Effect of the living environment on falls among the elderly in Urmia. *Open Access Macedonian Journal of Medical Sciences*, *6*(11), 2233-2238. https://doi.org/10.3889/oamjms.2018.434

Meng, L., Kong, X., & Taniguchi, D. (2017). Dangerous situation detection for elderly persons in restrooms using center of gravity and ellipse detection. *Journal of Robotics and Mechatronics*, *29*(6), 1057-1064. https://doi.org/10.20965/jrm.2017.p1057

Morales, E., Pilon, M. A., Doyle, O., Gauthier, V., Gamache, S., Routhier, F., & Rousseau, J. (2017). Which grab bar do you prefer in the bathroom? *Journal of Enabling Technologies*, *11*(4), 123-137.

Mououdi, M. A., Razzaghi Pahnehkolai, S. F., Qhaempanah, F., Mahdavi, A., & Veisi, A. R. (2020). An ergonomic approach to designing an Iranian-Islamic toilet in a sample of Iranian society. *Iranian Journal of Ergonomics*, *8*(2), 8-16. https://doi.org/10.30699/jergon.8.2.8

Mulliner, E., Riley, M., & Maliene, V. (2020). Older people's preferences for housing and environment characteristics. *Sustainability*, *12*(14), 5723. https://doi.org/10.3390/su12145723

Nagananda, M. S., Sengupta, A., Santhosh, J., Anand, S., Rehman, S. M. K., Khan, A. M., Rautray, P., Gharai, D. & Das, L. K. (2010). Design and pragmatic studies of bathroom for elderly people in India. *WSEAS Transaction on Biology Biomedicine*, *7*(4), 287-305.

Orimo, H., Ito, H., Suzuki, T., Araki, A., Hosoi, T., & Sawabe, M. (2006). Reviewing the definition of "elderly". *Geriatrics Gerontology International*, *6*(3), 149-158. https://doi.org/10.1111/j.1447-0594.2006.00341.x

Panek, P., Fazekas, G., Lüftenegger, T., Mayer, P., Pilissy, T., Raffaelli, M., Rist, A., Rosenthal, R., Savanovic, A., Sobjak, A. & Sonntag, F. (2017). On the prototyping of an ICT-enhanced toilet system for assisting older persons living independently and safely at home. In D. Hayn & G. Schreier (Eds.), *Health Informatics Meets eHealth* (pp. 176-183). IOS Press.

Pennathur, A., Magham, R., Contreras, L. R., & Dowling, W. (2003). Daily living activities in older adults: Part I - A review of physical activity and dietary intake assessment methods. *International Journal of Industrial Ergonomics*, *32*(6), 389-404. https://doi.org/10.1016/S0169-8141(03)00098-2

Rachuy, C., Clemens, J., & Schill, K. (2013). Ubiquitous fall detection and activity recognition system for bathrooms. In P. Encarnacao, L. Azevedo, G. J. Gelderblom, A. Newell & N. E. Mathiassen (Eds.), *Assistive Technology: From Research to Practice* (pp. 95-100). IOS Press. https://doi.org/10.3233/978-1-61499-304-9-95

Rashid, S. A., Ghani, P. A., & Daud, N. (2014). Population trends in Malaysia: 1970-2010. *AIP Conference Proceedings*, *1635*(1), 875-882. https://doi.org/10.1063/1.4903686

Reinhardt, D., Khurana, M., & Acosta, L. H. (2021). "I still need my privacy": Exploring the level of comfort and privacy preferences of German-speaking older adults in the case of mobile assistant robots. *Pervasive and Mobile Computing*, *74*, Article 101397. https://doi.org/10.1016/j.pmcj.2021.101397

Romli, M. H., Tan, M. P., Mackenzie, L., Lovarini, M., Kamaruzzaman, S. B., & Clemson, L. (2018). Factors associated with home hazards: Findings from the Malaysian elders longitudinal research study. *Geriatrics Gerontology International*, *18*(3), 387-395. https://doi.org/10.1111/ggi.13189

Rose, G., Decalf, V., Everaert, K., & Bower, W. F. (2020). Toileting-related falls at night in hospitalised patients: The role of nocturia. *Australasian Journal on Ageing*, *39*(1), e70-e76. https://doi.org/10.1111/ajag.12696

Rosnah, M., Norazizan, S. S., Aizan, H. T., & Rizal, H. M. (2008). Home living environment design and perceptions of safety of older Malaysians. *Gerontechnology*, *168*(218), 43-45.

Rousseau, G. (2018). The impact of longevity on older consumer needs: Implications for business. *Journal of Family Ecology and Consumer Sciences=Tydskrif vir Gesinsekologie en Verbruikerswetenskappe*, *46*(1), 19-33. https://hdl.handle.net/10520/EJC-13b88a52e8

Salam, M. A. A., & Shams El-din, A. K. (2019). Developing smarter bathrooms for elderly and disabled people. *Journal of Al-Azhar University Engineering Sector*, *14*(52), 1024-1035.

Savchenko, O., Zhelykh, V., & Voll, H. (2017). Analysis of the systems of ventilation of residential houses of Ukraine and Estonia. *Selected Scientific Papers-Journal of Civil Engineering*, *12*(2), 23-30. https://doi.org/10.1515/sspjce-2017-0015

Sophonratanapokin, B., Sawangdee, Y., & Soonthorndhada, K. (2012). Effect of the living environment on falls among the elderly in Thailand. *Southeast Asian Journal of Tropical Medicineand Public Health*, *43*(6), Article 1537.

Stevens, J. A., Haas, E. N., & Haileyesus, T. (2011). Nonfatal bathroom injuries among persons aged≥ 15 years—United States, 2008. *Journal of Safety Research*, *42*(4), 311-315. https://doi.org/10.1016/j.jsr.2011.07.001

Sukadarin, E. H., Nawi, N. M., & Abd Ghani, A. A. (2021). Investigation on the ergonomics design of Wudhu'(ablution) station at a mosque in a higher learning institution. *Current Science and Technology*, *1*(1), 15-25. https://doi.org/10.15282/cst.v1i1.6442

Sveistrup, H., Lockett, D., Edwards, N., & Aminzadeh, F. (2006). Evaluation of bath grab bar placement for older adults. *Technology Disability*, *18*(2), 45-55. https://doi.org/10.3233/TAD-2006-18201

Swaminathan, V., & Audisio, R. (2012). Cancer in older patients: An analysis of elderly oncology. *Ecancermedicalscience*, *6*, Article 243. https://doi.org/10.3332/ecancer.2012.243

Terroso, M., Rosa, N., Torres Marques, A., & Simoes, R. (2014). Physical consequences of falls in the elderly: A literature review from 1995 to 2010. *European Review of Aging and Physical Activity*, *11*(1), 51-59. https://doi.org/10.1007/s11556-013-0134-8

Thapliyal, H., Nath, R. K., & Mohanty, S. P. (2017). Smart home environment for mild cognitive impairment population: Solutions to improve care and quality of life. *IEEE Consumer Electronics Magazine*, *7*(1), 68-76. https://doi.org/10.1109/MCE.2017.2755340

Tobi, S. M., Fathi, M., & Amaratunga, D. (2017). Ageing in place, an overview for the elderly in Malaysia. *AIP Conference Proceedings, 1891*(1), Article 020101. https://doi.org/10.1063/1.5005434.

Trappe, T. (2009). Influence of aging and long-term unloading on the structure and function of human skeletal muscle. *Applied Physiology, Nutrition, and Metabolism*, *34*(3), 459-464. https://doi.org/10.1139/H09-041

Tsuchiyama, K., & Kajiwara, A. (2019, January 20-23). *Accident detection and health-monitoring UWB sensor in toilet*. [Paper presentation]. IEEE Topical Conference on Wireless Sensors and Sensor Networks (WiSNet), Florida, USA. https://doi.org/10.1109/WISNET.2019.8711812

Tyng, C. S., & Hamid, T. A. (2015). Population ageing and the Malaysian Chinese: Issues and challenges. *Malaysian Journal of Chinese Studies*, *4*(1), 1-13.

United Nations. (2017). *World population prospects - 2017 revised: Ageing population*. United Nations. https://www.un.org/development/desa/publications/graphic/wpp2017-ageing-population

Vaccari, É., Lenardt, M. H., Willi, M. H., Betiolli, S. E., & de Oliveira, E. S. (2014). Safety of the hospital environment in terms of preventing falls on the part of the elderly: A descriptive study. *Online Brazilian Journal of Nursing*, *13*(3), 271-281.

Wang, D., Wu, J., & Lin, Q. (2018). A novel method for designing and optimizing the layout of facilities in bathroom for the elderly in home-based rehabilitation. *Disability Rehabilitation: Assistive Technology*, *13*(4), 333-341. https://doi.org/10.1080/17483107.2017.1319426

Yin-Fah, B. C., Masud, J., Hamid, T. A., & Paim, L. (2010). Financial wellbeing of older peninsular Malaysians: A gender comparison. *Asian Social Science*, *6*(3), 58-71.

Yu, J., Ma, G., & Jiang, X. (2017). Impact of the built environment and care services within rural nursing homes in China on quality of life for elderly residents. *Engineering, Construction Architectural Management*, *24*(6), 1170-1183. https://doi.org/10.1108/ECAM-08-2016-0187

Yuan, Y., Shu, H., Bowen, Z., & Haoyu, Z. (2021). 'Easyi'-A new toilet seat designed for senior adults to prevent them from falling when using the toilet. In J. Kalra, N. J. Lightner & R. Taiar (Eds.), *Advances in Human Factors and Ergonomics in Healthcare and Medical Device*s (pp. 493-498). Springer International Publishing.

Zacharia, B., Pai, P. K., & Paul, M. (2021). Focus group discussion as a tool to assess patient-based outcomes, practical tips for conducting focus group discussion for medical students - Learning with an example. *Journal of Patient Experience*, *8*. https://doi.org/10.1177/23743735211034276

Zaid, S. M., Yamin, A. A., & Yaacob, N. M. (2019). The environmental study on ageing in place: The design practice compliance to accessibility legislation and standards in Malaysia for elderly home environment. *Ekoloji*, *28*(107), 601-613.

Zuniga, G. C., Nelda, M., Seol, K. H., & Villarreal, E. (2011). Home hazards assessment among elderly in South Texas colonias. *Age*, *5*(54), 16-27.

Pertanika J. Sci. & Technol. 31 (4): 1881 - 1894 (2023)

PERTANIKA JOURNALS

SCIENCE & TECHNOLOGY

Journal homepage: http://www.pertanika.upm.edu.my/

Comparison of Count Data Generalised Linear Models: Application to Air-Pollution Related Disease in Johor Bahru, Malaysia

Zetty Izzati Zulki Alwani[1], Adriana Irawati Nur Ibrahim[1]*, Rossita Mohamad Yunus[1] and Fadhilah Yusof[2]

[1]Institute of Mathematical Sciences, Faculty of Science, Universiti Malaya, 50603 UM, Kuala Lumpur, Malaysia
[2]Department of Mathematical Sciences, Faculty of Science, Universiti Teknologi Malaysia, 81310 UTM, Johor Bahru, Malaysia

ABSTRACT

Poisson regression is a common approach for modelling discrete data. However, due to characteristics of Poisson distribution, Poisson regression might not be suitable since most data are over-dispersed or under-dispersed. This study compared four generalised linear models (GLMs): negative binomial, generalised Poisson, zero-truncated Poisson and zero-truncated negative binomial. An air-pollution-related disease, upper respiratory tract infection (URTI), and its relationship with various air pollution and climate factors were investigated. The data were obtained from Johor Bahru, Malaysia, from January 1, 2012, to December 31, 2013. Multicollinearity between the covariates and the independent variables was examined, and model selection was performed to find the significant variables for each model. This study showed that the negative binomial is the best model to determine the association between the number of URTI cases and air pollution and climate factors. Particulate Matter (PM_{10}), Sulphur Dioxide (SO_2) and Ground Level Ozone (GLO) are the air pollution factors that affect this disease significantly. However, climate factors do not significantly influence the number of URTI cases. The model constructed in this study can be utilised as an early warning system to prevent and mitigate URTI cases. The involved parties, such as the local authorities and hospitals, can also employ the model when facing the risk of URTI cases that may occur due to air pollution factors.

Keywords: Air pollution disease, count data, generalised linear model

ARTICLE INFO

Article history:
Received: 28 May 2022
Accepted: 02 November 2022
Published: 25 May 2023

DOI: https://doi.org/10.47836/pjst.31.4.16

E-mail addresses:
zettyziza@gmail.com (Zetty Izzati Zulki Alwani)
adrianaibrahim@um.edu.my (Adriana Irawati Nur Ibrahim)
rossita@um.edu.my (Rossita Mohamad Yunus)
fadhilahy@utm.my (Fadhilah Yusof)
*Corresponding author

ISSN: 0128-7680
e-ISSN: 2231-8526

INTRODUCTION

A generalised linear model (GLM) is commonly used to study the relationship between the response and the covariate(s). Generalised linear models are widely used in applying regression models for discrete data such as count data (Nelder & Wedderburn, 1972; Agresti, 2003; Cameron & Trivedi, 2013). Poisson regression is the most commonly used model to analyse count data. For example, Poisson regression was used to estimate the risk of hospitalisation for asthma in children after being exposed to air pollutants in a city in Southeast Brazil (Amâncio & Nascimento, 2012) and was used to study the relationship between air pollution concentration with upper respiratory tract infection (URTI) among children in Atlanta, Georgia (Darrow et al., 2014).

However, most real data are usually under-dispersed or over-dispersed. Therefore, real data may not fulfil the assumption of Poisson distribution which assumes equal dispersion. Negative binomial (NB) distribution is frequently used to handle over-dispersed data. Avcı (2018) used NB regression to study the effects of several people hospitalised with schizophrenia. Apart from that, several other count data models have been introduced to overcome both situations of under-dispersion and over-dispersion. The generalised Poisson (GP) distribution is one example of a distribution which can handle both cases. The GP regression model was applied in various areas to model over-dispersed data, such as household fertility data (Wang & Famoye, 1997) and accident data (Famoye et al., 2004).

Besides that, usually, the data is over-dispersed; thus, the response is usually truncated for some outliers or large values (Saffari et al., 2011). Using the usual regression for zero-truncated datasets may be difficult because it may try to predict zero counts despite the data, not including any zeros. Thus, zero-truncated models such as zero-truncated Poisson and NB may be more suitable. Zero-truncated Poisson was used to model the number of fishing trips taken during the fishing season in Alaska (Grogger & Carson, 1991), while zero-truncated NB was applied to estimate recreation demand in a national park in Canada (Martínez-Espiñeira & Amoako-Tuffour, 2008).

The study aims to investigate the link between air pollution and climate factors with the disease of upper respiratory tract infection (URTI). URTI is an upper respiratory tract infection that includes the throat, nose, pharynx, larynx, sinuses, and trachea (windpipe). URTI causes irritation and swelling of the upper airways (Thomas & Bomar, 2021). Several studies have shown that air pollution or/and climate can affect the number of URTI patients, using models such as Poisson GLM (Darrow et al., 2014; Çapraz & Deniz, 2021), Poisson generalised additive model (GAM) (Tam et al., 2014; Liu et al., 2015; Liu, Liu et al., 2015; Li et al., 2018; Zhang et al., 2019), GLM with quasi-Poisson (Liu et al., 2015) and case-crossover design with a fixed-effect model (Szyszkowicz et al., 2018). Since the Poisson distribution usually assumes equal dispersion, these models applied methods such as time series (Darrow et al., 2014) and GAM with quasi-likelihood (Tam et al., 2014; Liu, Guo

et al., 2015) to allow for over-dispersion. However, these studies did not consider models with specific distributions catering to under-dispersion and over-dispersion.

Therefore, this research aims to compare several count data GLMs with different distributions when investigating the relationship between the number of URTI cases with air pollution and climate variables in Johor Bahru, Malaysia. Previously, Jamaludin et al. (2017) had applied the NB GLM to investigate the relationship between URTI and several air pollution and climate variables in Johor Bahru, Malaysia, while Alwani et al. (2021) used the zero-truncated Poisson and zero-truncated NB GLMs to examine the association between the number of dengue cases with similar air pollution and climate factors for similar data.

Hence, this study shall also consider generalised Poisson (GP), zero-truncated Poisson and zero-truncated NB GLMs to examine the relationship between URTI cases and their significant factors, apart from the NB GLM. GP is chosen as it can handle over and under-dispersed data, while the two zero-truncated models may be good alternatives since the number of URTI cases in our data is strictly nonzero. Since the data are nonzero, this study does not consider models catering for many zeros, such as zero-inflated Poisson or NB and negative binomial-Lindley. Note that Conway-Maxwell Poisson has also been considered for this study, but the model application showed that it is unsuitable for the data.

Apart from that, this study shall also investigate multicollinearity between the covariates, i.e., the independent variables and perform model selection to find the final best model with the significant covariates for each model, both of which were not previously considered in previous studies.

MATERIALS AND METHODS

Description of Data

The study investigates the link between upper respiratory tract infection (URTI) with air pollution and climate variables. The data is obtained from Johor Bahru, the southernmost city in Peninsular Malaysia; the data is obtained weekly, which covers 105 weeks starting from January 2012 up to December 2013. The numbers of URTI cases were obtained from the Department of Information and Informatics, Johor Bahru District Health Office. The environmental pollution variables are Ground Level Ozone (GLO), Nitrogen Dioxide (NO_2), Particulate Matter (PM_{10}) and Sulphur Dioxide (SO_2), while the climate variables are rainfall, temperature and relative humidity. Data on air pollution levels were obtained from the Johor Department of Environment, rainfall data were acquired from the Department of Irrigation and Drainage Malaysia, and data on temperature and relative humidity were acquired from the Malaysian Meteorological Department.

Methodology

The study aims to model the relationship between the number of URTI cases and the pollution and climate factors using the data aggregated weekly. The lag effects are needed to study this relationship. It is because the number of cases of URTI may be not only influenced by the values of the factors in the same week but also by the values in earlier weeks, as the influences of these factors may not be immediate (delayed effect). The delayed effect can be a few days for the short term or weeks for the long term.

Jamaluddin et al. (2017) applied a long-term association between air pollution and URTI where the lag used was the same week (lag 0) up to the previous 20 weeks (lag 20). However, in most of the previous studies, the usual lags used were single-day lag and cumulative lag, where the lags can go from the same day up to 3 days (Zhang et al., 2021), 6 days (Tao et al., 2014; Li et al., 2018) or 20 days (Saldiva et al., 1994). Thus, this paper uses the weekly lag, which is similar to Jamaluddin et al. (2017) but for a shorter period where the lag is used in the same week (lag 0) up to the previous 4 weeks (lag 4).

Pearson's correlation is then used to examine the association between URTI and each of the factors at the different lags, and the most significant lag is chosen for each factor which is the time lag with the highest correlation value (Montgomery et al., 2021). To avoid or at least reduce multicollinearity between the explanatory variables at their significant lags, partial (Pearson's) correlation is used to find the collinearity between these variables while excluding the influence of the other variables; the explanatory variables are then reduced for pair(s) of variables which have a high partial correlation.

GLM using NB, COM-Poisson, GP, zero-truncated Poisson and zero-truncated NB are then fitted to the data using the reduced explanatory variables at their significant lags. In each of the models, the canonical link is the log link, such that $\log(\mu_i) = \boldsymbol{X}_i\boldsymbol{\beta}'$ where μ_i is the mean for observation y_i, $\boldsymbol{X}_i$ is the independent variables, and $\boldsymbol{\beta}$ is the regression parameters. The details for each model are given below:

1. Negative Binomial model

The NB model is usually used for over-dispersed count data, where the variance is assumed to be larger than the mean. The p.m.f. of NB distribution is expressed as Equation 1:

$$f(y_i;\mu_i,\theta) = \frac{\Gamma(y_i+\theta)}{\Gamma(\theta)\ y_i!} \cdot \frac{\mu_i^{y_i}\theta^{\theta}}{(\mu_i+\ \theta)^{y_i+\theta}}, \qquad y_i = 0,1,2,\dots, \tag{1}$$

where θ is the shape parameter and gamma function $\Gamma(.)$.

2) Generalised Poisson model

P.m.f. of GP can be expressed as Equation 2 (Consul & Jain, 1973; Consul & Famoye, 1992):

$$f(y_i;\mu_i,\kappa|y_i>0)=\frac{\left((1-\kappa)\mu_i+\kappa y_i\right)^{y_i-1}(1-\kappa)\mu_i\exp(-(1-\kappa)\mu_i-\kappa y_i)}{y_i!}, \quad [2]$$

where $0 < k < 1$.

3) Zero-truncated Poisson model

P.m.f. of zero-truncated Poisson is given as Equation 3 (Grogger & Carson, 1991; Zuur et al., 2009):

$$f(y_i;\mu_i|y_i>0)=\frac{\mu_i^{y_i}e^{-\mu_i}}{y_i!\,(1-e^{-\mu_i})}\,. \quad [3]$$

4) Zero-truncated negative Binomial model

Zero-truncated NB (Grogger & Carson, 1991; Zuur et al., 2009) has the p.m.f. as in Equation 4:

$$f(y_i;\alpha,\mu_i|y_i>0)=\frac{\Gamma(y_i+\alpha)}{\Gamma(\alpha)\,\Gamma(y_i+1)}\left(\frac{\alpha}{\mu_i+\alpha}\right)^{\alpha}\left(1-\frac{\alpha}{\mu_i+\alpha}\right)^{y_i}. \quad [4]$$

During the model fitting of each model, stepwise selection based on the Akaike information criterion (AIC) (Montgomery et al., 2021) is used to find the final model, which contains only the significant variables. Normal quantile-quantile (Q-Q) plot and several tests such as the Shapiro-Wilk (SW), Jarque-Berra (JB) and D' Agostino (DA) tests are then used to check for the normality assumption of the residuals of the final model for each model considered in this study. The normal Q-Q plot compares the quantiles of the data distribution with the quantile of the standardised normal distribution. The SW test uses the order and normalised order statistics for normality (Shapiro et al., 1968), while the DA test assesses symmetry and evaluates the distribution shape using normal approximation (D'Agostino & Pearson, 1973). The JB test, on the other hand, combines skewness and kurtosis in a single statistic (Wuertz & Katzgraber, 2005). The scatter plot of the residuals of the final model is also used to check for the assumptions that the residuals are mostly random, centred around zero and have constant variance.

Finally, to select the best final model among all the proposed GLMs, AIC and Bayesian information criterion (BIC) are used. The AIC is a penalised log-likelihood measure. Let L be the likelihood function for a specific model. The AIC is given by Equation 5:

$$\mathrm{AIC}=-2\ln L+2p, \quad [5]$$

where p is the number of parameters in the model. On the other hand, the Schwartz BIC is given by Equation 6:

$$\mathrm{BIC}=-2\ln L+p\ln n\,, \quad [6]$$

where n is the size of the data set. Generally, the smaller the values of AIC and BIC are,

the better the model. For more information on AIC and BIC, please refer to Montgomery et al. (2021).

To summarise the steps in modelling the relationship between the number of URTI cases and this study's pollution and climate factors, please refer to the flowchart in Figure 1. All analyses are applied using R and Excel. The R packages used for the GLMs are the *MASS* package for NB, and the *VGAM* package (Yee, 2021) for GP, zero-truncated Poisson and zero-truncated NB.

RESULTS

Descriptive Data

In this research, a weekly number of pollution-related disease cases, in particular URTI, and weekly level of environmental pollution (GLO, NO_2, SO_2 [all in ppm]; PM_{10} in $\mu g/m^3$ and climate [rainfall in mm), temperature in °C and relative humidity in %) throughout January 1, 2012, to December 31, 2013, were used. The total number of cases in these two years for URTI was 12244. The weekly time series plot of URTI is given in Figure 2, and the weekly number of cases for URTI fluctuated throughout the two years. Few cases occur between September to November of each year; September to November is one of the inter-monsoon periods, relatively calm with less rain and weaker winds (Jamaludin et al., 2017).

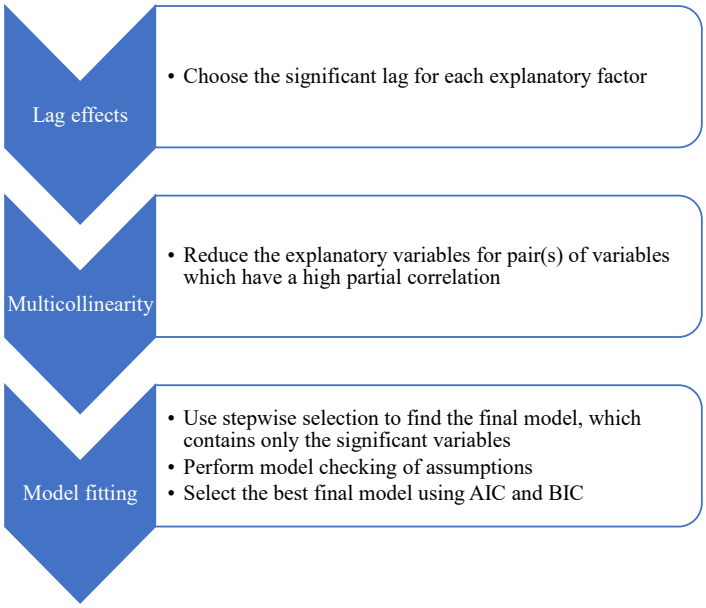

Figure 1. Flowchart of the methodology

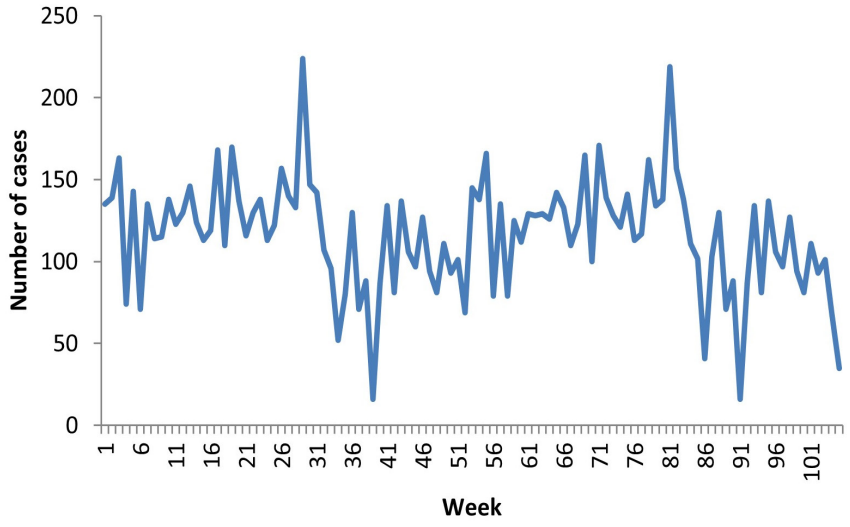

Figure 2. Weekly time series plot of URTI

Table 1 gives the descriptive statistics for several cases of URTI, environmental pollution and climate factors. From Table 1, the weekly numbers of cases recorded for URTI were all nonzero, and the variance for URTI is much larger than its mean. The table also shows that the levels of environmental pollution were very low, apart from PM_{10}, which had very high values. PM_{10} also had a large dispersion. For climate factors, rainfall had a very large dispersion due to Malaysia's wet and dry seasons.

Table 1

Descriptive statistics of the number of cases of URTI and level of environmental pollution and climate for 2012–2013

	Min	Max	Mean	Standard Deviation	Skewness	Variance
URTI	16	224	117	34.581	- 0.176	1195.86
GLO	0.017	0.073	0.043	0.012	0.557	0.0001
NO_2	0.005	0.023	0.014	0.004	- 0.491	0.00001
PM_{10}	22.30	225.49	42.70	20.728	6.880	429.67
SO_2	0.0002	0.0089	0.0031	0.0018	0.772	0.000003
Rainfall	0	194.50	53.43	51.006	0.989	2601.61
Temperature	25.24	29.00	26.78	0.704	0.354	0.496
Relative humidity	75.30	92.79	85.92	2.970	- 0.342	8.817

Relationship Between URTI And the Pollution and Climate Factors

Table 2 shows the result of Pearson's correlation between the URTI and the related factors; the values of each factor less influence the number of URTI cases in the same week but more influenced by values in the earlier weeks (lags). The factors affect the number of URTI cases at different lags. It may be due to different lagged/delayed effects of each pollution and climate factor on the patients, meaning that each factor's effects may differ based on the length of time (weeks) after exposure. Based on Table 2, NO_2 and SO_2 have a stronger relationship with the number of URTI cases in the same week (lag 0). However, some variables show stronger delayed effects on the number of URTI cases, such as GLO in the previous first week (lag 1), rainfall in the third week (lag 3) and PM_{10}, temperature and relative humidity in the fourth week (lag 4).

Pearson's partial correlation values between the air pollution and climate factors at their significant lags are shown in Table 3. SO_2 and NO_2, relative humidity and temperature are highly correlated (these correlations are also significant at a 1% level). Therefore, this study includes NO_2 instead of SO_2, as there is evidence from previous studies that NO_2 is more associated with URTI (Wong et al., 2006; Li et al., 2018). The relative humidity in the model is included instead of temperature, as a previous study found that absolute humidity was significantly associated with URTI (Mäkinen et al., 2009). Thus, the variables included in the models in the next discussion are NO_2, GLO and PM_{10} for the air pollution factors and rainfall and temperature for the climate factors, each at their significant lags.

Table 2

Pearson's correlation of URTI with air pollution and climate factors

Factor		Significant lag	Pearson correlation
Air pollution	GLO	1	- 0.169
	NO_2	0	0.195
	PM_{10}	4	0.325
	SO_2	0	0.142
Climate	Rainfall	3	- 0.219
	Relative humidity	4	- 0.100
	Temperature	4	0.4643

Table 3

Pearson's partial correlation between air pollution and climate factors at their significant lags

	GLO	NO_2	PM_{10}	SO_2	Rainfall	Relative humidity	Temperature
GLO	1.00						

Table 3 *(Continue)*

	GLO	NO_2	PM_{10}	SO_2	Rainfall	Relative humidity	Temperature
NO_2	0.44*	1.00					
PM_{10}	-0.08	0.11	1.00				
SO_2	-0.18	0.65**	-0.01	1.00			
Rainfall	0.19	-0.23*	-0.01	0.01	1.00		
Relative humidity	0.09	0.06	-0.22*	0.10	-0.03	1.00	
Temperature	0.03	0.21*	0.10	0.03	-0.14	-0.66**	1.00

* significant at 5% level; ** significant at 1% level

The Selection of Best Model

The over-dispersion test was conducted on the URTI data. From this test, the *p*-values for the test on URTI are less than 0.05. Thus, the number of URTI cases is over-dispersed, and the NB model is preferred over the Poisson model. It is why the Poisson GLM is not considered in this study.

GLM using NB, GP, zero-truncated Poisson, and zero-truncated NB are each applied to the URTI data. Some final models have different significant variables after applying the stepwise selection procedure. NB, zero-truncated NB, and GP models have the same significant variables, PM_{10}, NO_2 and GLO, while the zero-truncated Poisson final model has similar significant variables but with additional variables of rainfall and relative humidity.

Looking at Table 4, the final NB GLM has lower AIC and BIC values compared to the GP and zero-truncated Poisson models and has the same values as the zero-truncated NB model. Note that the NB and zero-truncated NB models have the same significant covariates in the final model, but the zero-truncated NB model has an extra parameter to be estimated compared to the NM model. Thus, the NB GLM is chosen as the best model to examine the effect of air pollution and climate factors on URTI cases for this data.

Table 4

Result of normality tests, AIC and BIC for URTI data

	NB	Generalised Poisson	Zero-truncated Poisson	Zero-truncated NB
Normality tests (*p*-value)	SW: 0.010 DA: 0.009 JB: 0.001	SW: 0.033 DA: 0.019 JB: 0.004	SW: 0.007 DA: 0.008 JB: 0.001	SW: 0.010 DA: 0.009 JB: 0.001
AIC	1013.072	1021.855	1647.067	1013.072
BIC	1026.098	1034.881	1662.698	1026.098

For the residuals of the fitted NB model, the *p*-values for the three normality tests are smaller than 0.05, as shown in Table 4, indicating strong evidence to reject the null hypothesis that residuals are normally distributed. However, from the Q-Q plot for the residuals of the fitted NB model given in Figure 3, this model mostly falls on a straight line except for the few points on the right tail. Therefore, this study concluded that the normality assumption when fitting the data using the NB model is not severely violated. The residuals of the fitted NB model are also mostly random, centred around zero and have approximately constant variance, as seen in Figure 4.

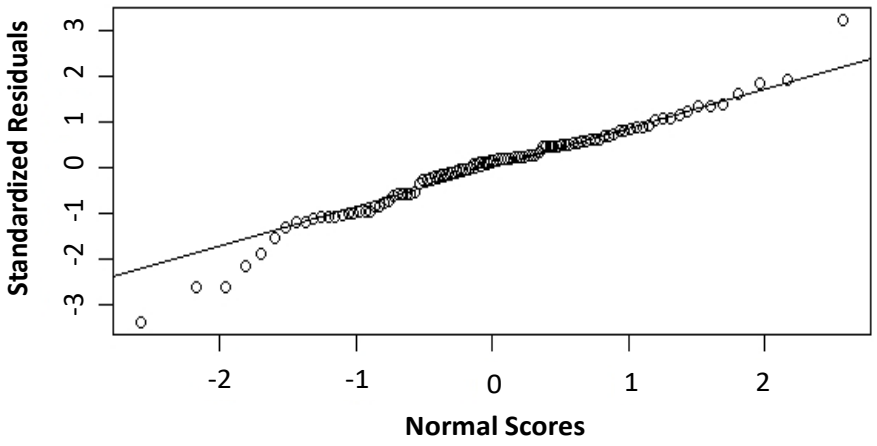

Figure 3. Q-Q plot for residuals of the fitted negative Binomial model for URTI data

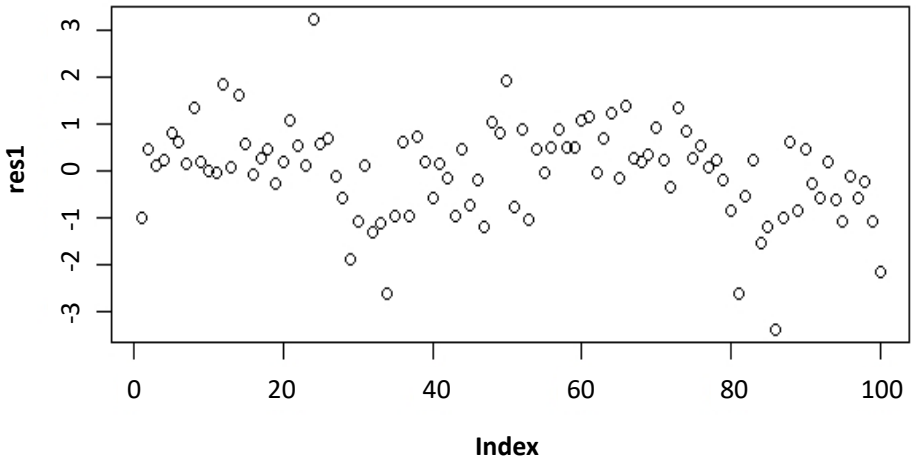

Figure 4. Scatter plot for residuals of the fitted negative Binomial model for URTI data

The parameter estimates for the fitted NB model are given in Table 5; the fitted model then gives the best final model as in Equation 7:

$$\hat{y} = \exp\left(4.621 + 2.346 \times 10^{-3}(\mathrm{PM}_{10}) + 18.236(\mathrm{NO}_2) - 5.700(\mathrm{GLO})\right) \quad [7]$$

where the fitted data follow the NB distribution (Equation 1) with an estimated shape parameter equal to 10.54. Note that although the parameter estimate for PM_{10} is small, the effect of this factor is still significant as the range of values for PM_{10} is quite large, as can be seen from Table 1; the minimum value for PM_{10} is around 22 μg/m^3, and the maximum value is around 225 μg/m^3.

Table 5

Summary of estimates for fitted negative Binomial model for URTI data

Parameter	Estimate	Std. error	*p*-value
Intercept	4.621	0.160	<0.001
PM_{10} (Lag 4)	2.346×10^{-3}	1.596×10^{-3}	0.142
NO_2 (Lag 0)	18.236	10.405	0.080
GLO (Lag 1)	-5.700	3.114	0.067

DISCUSSION

In this study, relative risk (RR) is used to estimate the impact of the significant factors on the number of URTI cases. The estimation of RR is $RR = \exp(\beta \times x_i)$, where β is the regression coefficient associated with a unit increment of the significant factors x_i (Çapraz & Deniz, 2021). A unit increment for each significant factor may differ according to the range of values for each factor. This study will present the result of excess relative risk (ERR), which is the percentage increase (%) in the number of URTI cases with a unit increment. ERR is derived from RR, calculated as $ERR = (RR\text{-}1) \times 100$. The values of RR and ERR for the final NB model are shown in Table 6. Note that the unit increment for each significant factor is chosen based on the range of values for each factor (Table 1). Hence, for the final NB model, an increment of 10 μg/m^3 in the concentration of PM_{10}, 0.005 ppm in the concentration of NO_2, and 0.01 ppm in the concentration of GLO correspond to an increase of URTI patients by 2.37% and 9.55% and a decrease of 5.54%, respectively.

Table 6

Relative risk (RR) and excess relative risk (ERR) for the final Negative Binomial model

Significant factor	Unit increment	RR	ERR (%)
PM_{10}	10	1.0237	2.37
NO_2	0.005	1.0955	9.55
GLO	0.01	0.9446	-5.54

CONCLUSION

In this paper, the weekly number of URTI cases in the city of Johor Bahru, Malaysia, from January 2012 to December 2013 have been studied. The explanatory factors have been reduced after checking for multicollinearity between the factors at their significant lags. The NB GLM is then found to be the best model to model the association

between URTI and the air pollution and climate factors at the corresponding significant lags. Air pollution factors that have significant effect on URTI are PM_{10}, NO_2 and GLO. However, climate factors do not significantly affect URTI. The model constructed in this study can be utilized as an early warning system to assist in the prevention and mitigation of URTI cases. The involved parties, such as the local authorities and hospitals can also employ the model as a precaution when facing the risk of URTI cases that may occur due to the air pollution factors. Note however that the results from this study are limited to the observed data for a particular period. Therefore, the effects of these air pollution and climate factors on URTI cases beyond the study period still remain unknown.

ACKNOWLEDGEMENTS

This work was financially supported by the Ministry of Higher Education, Malaysia, under the Fundamental Research Grant Scheme No: FRGS/1/2019/STG06/UM/02/2 (FP110-2019A).

REFERENCES

Agresti, A. (2003). *Categorical Data Analysis.* John Wiley & Sons.

Alwani, Z. Z., Ibrahim, A. I. N., Yunus, R. M., & Yusof, F. (2021). Application of zero-truncated count data regression models to air-pollution disease. *Journal of Physics: Conference Series*, *1988*(1), Article 012096. https://doi.org/10.1088/1742-6596/1988/1/012096

Amâncio, C. T., & Nascimento, L. F. (2012). Asthma and ambient pollutants: A time series study. *Revista da Associacao Medica Brasileira*, *58*(3), 302-307. https://doi.org/10.1590/S0104-42302012000300009

Avcı, E. (2018). Using count regression models to determine the factors which affects the hospitalization number of people with schizophrenia. *Journal of Data Science*, *16*(3), 511-530. https://doi.org/10.6339/JDS.201807_16(3).0004

Cameron, A. C., & Trivedi, P. K. (2013). *Regression Analysis of Count Data* (Vol. 53). Cambridge University Press.

Çapraz, Ö., & Deniz, A. (2021). Assessment of hospitalizations from asthma, chronic obstructive pulmonary disease and acute bronchitis in relation to air pollution in İstanbul, Turkey. *Sustainable Cities and Society*, *72*, Article 103040. https://doi.org/10.1016/j.scs.2021.103040

Consul, P. C., & Jain, G. C. (1973). A generalization of the Poisson distribution. *Technometrics*, *15*(4), 791-799. https://doi.org/10.1080/00401706.1973.10489112

Consul, P., & Famoye, F. (1992). Generalized Poisson regression model. *Communications in Statistics-Theory and Methods*, *21*(1), 89-109. https://doi.org/10.1080/03610929208830766

D'Agostino, R. B., & Pearson, E. S. (1973). Tests for Departure from Normality. *Biometrika*, *60*, 613-622. https://doi.org/10.2307/2335012

Darrow, L. A., Klein, M., Flanders, W. D., Mulholland, J. A., Tolbert, P. E., & Strickland, M. J. (2014). Air pollution and acute respiratory infections among children 0-4 years of age: An 18-year time-series study. *American Journal of Epidemiology*, *180*(10), 968-977. https://doi.org/10.1093/aje/kwu234

Famoye, F., Wulu, J. T., & Singh, K. P. (2004). On the generalized Poisson regression model with an application to accident data. *Journal of Data Science*, *2*(3), 287-295. https://doi.org/10.6339/JDS.2004.02(3).167

Grogger, J. T., & Carson, R. T. (1991). Models for truncated counts. *Journal of Applied Econometrics*, *6*(3), 225-238. https://doi.org/10.1002/jae.3950060302

Jamaludin, A. R. B., Yusof, F., Lokoman, R. M., Noor, Z. Z., Alias, N., & Aris, N. M. (2017). Correlational study of air pollution-related diseases (asthma, conjunctivitis, URTI and dengue) in Johor Bahru, Malaysia. *Malaysian Journal of Fundamental and Applied Sciences*, *13*, 354-361. https://doi.org/10.11113/mjfas.v13n4-1.897

Li, Y. R., Xiao, C. C., Li, J., Tang, J., Geng, X. Y., Cui, L. J., & Zhai, J. X. (2018). Association between air pollution and upper respiratory tract infection in hospital outpatients aged 0-14 years in Hefei, China: A time series study. *Public Health*, *156*, 92-100. https://doi.org/10.1016/j.puhe.2017.12.006

Liu, Y., Guo, Y., Wang, C., Li, W., Lu, J., & Shen, S. (2015). Association between temperature change and outpatient visits for respiratory tract infections among children in Guangzhou, China. *International Journal of Environmental Research and Public Health*, *12*, 439-454. https://doi.org/10.3390/ijerph120100439

Mäkinen, T. M., Juvonen, R., Jokelainen, J., Harju, T. H., Peitso, A., Bloigu, A., Silvennoinen-Kassinen, S., Leinonen, M., & Hassi, J. (2009). Cold temperature and low humidity are associated with increased occurrence of respiratory tract infections. *Respiratory Medicine*, *103*(3), 456-462. https://doi.org/10.1016/j.rmed.2008.09.011

Martínez-Espiñeira, R., & Amoako-Tuffour, J. (2008). Recreation demand analysis under truncation, overdispersion, and endogenous stratification: An application to Gros Morne National Park. *Journal of Environmental Management*, *88*(4), 1320-1332. https://doi.org/10.1016/j.jenvman.2007.07.006.

Montgomery, D. C., Peck, E. A., & Vining, G. G. (2021). *Introduction to Linear Regression Analysis*. John Wiley & Sons.

Nelder, J. A., & Wedderburn, R. W. (1972). Generalized linear models. *Journal of the Royal Statistical Society: Series A (General)*, *135*(3), 370-384. https://doi.org/10.2307/2344614

Saffari, S. E., Adnan, R., & Greene, W. (2011). Handling of over-dispersion of count data via truncation using poisson regression model. *Journal of Computer Science and Computational Mathematics*, *1*(1), 1-4. https://doi.org/10.20967/jcscm.2011.01.001

Saldiva, P. H., Lichtenfels, A. J. F. C., Paiva, P. S. O., Barone, I. A., Martins, M. A., Massad, E., Pereira, J. C. R., Xavier, V. P., Singer, J. M., & Bohm, G. M. (1994). Association between air pollution and mortality due to respiratory diseases in children in São Paulo, Brazil: A preliminary report. *Environmental Research*, *65*(2), 218-225. https://doi.org/10.1006/enrs.1994.1033

Shapiro S. S., Wilk M. B., & Chen V. (1968). A comparative study of various tests for normality. *Journal of American Statistical Association*, *63*, 1343-1372. https://doi.org/10.2307/2285889

Szyszkowicz, M., Kousha, T., Castner, J., & Dales, R. (2018). Air pollution and emergency department visits for respiratory diseases: A multi-city case crossover study. *Environmental Research*, *163*, 263-269. https://doi.org/10.1016/j.envres.2018.01.043

Tam, W. W., Wong, T. W., Ng, L., Wong, S. Y., Kung, K. K., & Wong, A. H. (2014). Association between air pollution and general outpatient clinic consultations for upper respiratory tract infections in Hong Kong. *PLoS One*, 9(1), Article e86913. https://doi.org/10.1371/journal.pone.0086913

Tao, Y., Mi, S., Zhou, S., Wang, S., & Xie, X. (2014). Air pollution and hospital admissions for respiratory diseases in Lanzhou, China. *Environmental Pollution*, *185*, 196-201. https://doi.org/10.1016/j.envpol.2013.10.035

Thomas, M., & Bomar, P. A. (2021). *Upper Respiratory Tract Infection.* StatPearls Publishing.

Wang, W., & Famoye, F. (1997). Modeling household fertility decisions with generalized Poisson regression. *Journal of Population Economics*, *10*(3), 273-283. https://doi.org/10.1007/s001480050043

Wong, T. W., Tam, W., Yu, I. T. S., Wun, Y. T., Wong, A. H., & Wong, C. M. (2006). Association between air pollution and general practitioner visits for respiratory diseases in Hong Kong. *Thorax*, *61*(7), 585-591. http://dx.doi.org/10.1136/thx.2005.051730

Wuertz, D., & Katzgraber, H. G. (2005). *Precise Finite-Sample Quantiles of the Jarque-Bera Adjusted Lagrange Multiplier Test.* ETHZ Preprint.

Yee T. W. (2021). *VGAM: Vector generalized linear and additive models R package version 1.1-5*. https://CRAN.R-project.org/package=VGAM

Zhang, D., Tian, Y., Zhang, Y., Cao, Y., Wang, Q., & Hu, Y. (2019). Fine particulate air pollution and hospital utilization for upper respiratory tract infections in Beijing, China. *International Journal of Environmental Research and Public Health*, *16*(4), Article 533. https://doi.org/10.3390/ijerph16040533

Zhang, F., Zhang, H., Wu, C., Zhang, M., Feng, H., Li, D., & Zhu, W. (2021). Acute effects of ambient air pollution on clinic visits of college students for upper respiratory tract infection in Wuhan, China. *Environmental Science and Pollution Research*, *28*(23), 29820-29830. https://doi.org/10.1007/s11356-021-12828-7

Zuur, A. F., Ieno, E. N., Walker, N. J., Saveliev, A. A., & Smith, G. M. (2009). GLM and GAM for count data. In *Mixed Effects Models and Extensions in Ecology with R* (pp. 209-243). Springer. https://doi.org/10.1007/978-0-387-87458-6_9

Pertanika J. Sci. & Technol. 31 (4): 1895 - 1910 (2023)

PERTANIKA JOURNALS

SCIENCE & TECHNOLOGY

Journal homepage: http://www.pertanika.upm.edu.my/

The Effect of Reinforcing Moringa Oleifera Bark Fibre on the Tensile and Deformation Behaviour of Epoxy and Silicone Rubber Composites

Nur Auni Izzati Jusoh[1], Nur Aini Sabrin Manssor[2], Praveena Nair Rajendra[3] and Jamaluddin Mahmud[1]*

[1]College of Engineering, Universiti Teknologi MARA, 40450 UiTM, Shah Alam, Selangor, Malaysia
[2]College of Engineering, Universiti Teknologi MARA, Cawangan Johor, Pasir Gudang, 81750 UiTM, Kampus Pasir Gudang, Johor, Malaysia
[3]GV Medhini Consultancy & Resources Sdn Bhd, Periwinkle, 42500 Bandar Rimbayu, Selangor, Malaysia

ABSTRACT

The moringa oleifera bark (MOB) is well-known for its medicinal properties and various benefits, where combining it with polymers could produce a new superior composite material for medicinal applications. Because this is a novel composite material, even basic information on how the MOB fibres altered the tensile properties of epoxy and silicone rubber is still lacking. Therefore, this study investigated the tensile and deformation behaviour of two newly introduced composite materials, MOB fibre reinforced into epoxy and silicone rubber. ASTM D3039 and ASTM D412 were adapted to prepare the hard and soft composite specimens (0, 4, 8, 12 and 16wt%.), respectively. T-test was conducted to determine the significant difference. The results show that the tensile modulus of MOB-epoxy biocomposite improved from 1240 MPa to 1668 MPa (35% increment) when the fibre content was increased to 16wt%. For MOB–silicone biocomposite, a similar trend was observed where the tensile modulus also increased from 0.076 MPa to 0.12 MPa (64% increment) as the fibre concentration increased from 0 to 16wt%. In conclusion, reinforcing MOB fibre affected the stiffness of silicone rubber more than epoxy; but affected the elongation of epoxy more than silicone rubber. Based on a t-score of 17.5, a significant difference is observed in how reinforcing MOB at various wt% affected the increment of tensile modulus for both hard and soft composites. Finally, the determined tensile modulus compared to other materials could be useful for benchmarking and exploring potential applications.

Keywords: Biocomposite material, epoxy and silicone rubber, moringa oleifera barks, tensile properties

ARTICLE INFO

Article history:
Received: 31 May 2022
Accepted: 07 September 2022
Published: 25 May 2023

DOI: https://doi.org/10.47836/pjst.31.4.17

E-mail addresses:
nuraunijusoh@gmail.com (NurAuni Izzati Jusoh)
nuraini0175@uitm.edu.my (Nur Aini Sabrin Manssor)
veena@gvmedhini.com (Praveena Nair Rajendra)
jm@uitm.edu.my (Jamaluddin Mahmud)
*Corresponding author

ISSN: 0128-7680
e-ISSN: 2231-8526

INTRODUCTION

Different composites have been produced and utilised for various purposes for decades. In 1500 B. C., the Egyptians and Mesopotamians manufactured bricks out of mud reinforced with straw to build strong, durable buildings (Keya et al., 2019). Another ancient composite which had been developed was concrete, a mix of small stones or gravel with cement. It gave a good compressive strength to the materials, which was suitable for the building sector. The revolution of composites manufacturing has developed over decades to meet specific requirements in different fields of applications. Composite materials have been widely used in many engineering applications such as in the domestic sector, automotive sector, aircraft industry and building industry (Bharath & Basavarajappa, 2016; Ahmed et al., 2021; Tataru et al., 2020). Many composite materials have considerably higher strength qualities than traditional metallic materials, allowing them to be lighter and stronger than individual materials. Because of these significant characteristics, many sectors have begun to rely on composite materials, and the development of composite materials has begun to accelerate. The research was done to improve materials by reinforcing the material with fibre, with either synthetic or natural components.

Over the past few years, the demand for synthetic fibres has risen in composite manufacturing, which has resulted in environmental sustainability issues such as climate change and pollution. Therefore, numerous studies have focused on converting synthetic to natural fibres as reinforcing materials to alleviate this problem. Natural fibres composite materials are lightweight, abundant, biodegradable and cost-effective (Maria, 2013). They may be used to replace synthetic fibres with bio-based materials that are both safer and more ecologically friendly. Among the known natural fibres are jute, hemp, flax, sisal and kenaf (Jusoh et al., 2016).

A composite material signifies combining two or more materials at a macroscopic scale to form a third useful material (Jones, 1999). A biocomposite is a material composed of two or more distinct constituent materials (one being naturally derived) combined to yield a new material with improved performance over individual constituent materials (Rudin & Choi, 2013). Since this study combines moringa oleifera bark (MOB), a natural resource, with the polymer matrix material, these new materials are introduced as biocomposites. The main idea of green materials is to address environmental concerns, which has led to the rigorous development of green composite materials among researchers. Surprisingly, green material has gained attention and is widely researched for various applications such as in technical applications, including automotive, home, building, aviation, structural and circuit boards (Bharath & Basavarajappa, 2016; Ahmed et al., 2021; Tataru et al., 2020). Within the last few decades, biocomposite materials have offered more significant sustainability, industrial ecology, eco-efficiency and green chemistry than conventional applications (Bharath & Basavarajappa, 2016). These fibres are renewable resources that can absorb

CO_2 and restore oxygen to the atmosphere with little or no energy usage (Pickering et al., 2016). It is a safe material selection for composite products in the long term.

Earlier studies have documented on investigations of various barks, such as poplar bark, Dirca L. bark and black spruce bark (Safdari et al., 2011; Hudson et al., 2021; Yemele et al., 2010). This study has focused on combining MOB into the polymer. The moringa oleifera tree is well-known for its medicinal properties. It is a cultivated member of the Moringaceae monogen family, also known as the miracle tree (Rockwood et al., 2013). Its bark has been scientifically proven to have certain significant virtues, including the potential to act as a bioremediation agent, removing heavy metals from polluted water (George et al., 2016). It also has antibacterial properties that can help break down bacterial infections such as Staphylococcus aureus, Citrobacter freundii, Bacillus megaterium and Pseudomonas fluorescens (Zaffer et al., 2014). Additionally, the bark possesses anti-inflammatory properties and can treat fever, dyspepsia (discomfort digestive system) and splenomegaly (infection in the lymphatic system) (Padayachee & Baijnath, 2020). Therefore, these remarkable features have encouraged the idea of creating novel material composites by reinforcing the MOB into epoxy and silicone rubber matrices.

In composite materials, the reinforcement acts as a load bearing and contributes critically to stress transfer and strengthening the composites while the matrix material binds and protects the reinforcing material when an external load is exerted on the composite (Manu et al., 2022). The mechanical characteristics of composites are influenced by various factors, including the properties of the matrix, the properties of the fibers, and the adhesion between the fibers and the matrix. In general, achieving excellent mechanical properties in composites relies heavily on the crucial aspect of fiber-matrix adhesion (Arbelaiz et al., 2020). Matrix materials in composites are divided into two categories: thermoset polymers and thermoplastic polymers. The research of thermoset polymers as matrix materials such as silicone and epoxies has been growing due to their wide range of applications in various sectors (Bahrain et al., 2022; Alshahrani & Arun Prakash, 2022). Ali Raza et al. (2012) studied the properties of two composites; carbon black reinforced with rubbery epoxy (CB/ RE) and carbon black reinforced with silicone (CB/ silicone). The results showed that the compressive strength of CB/silicone is 1.68 times lower than that of CB/silicone , thus suggesting that CB/silicone composites is more compliant than the CB/RE composites. However the author recommended that the CB/RE composites is a promising adhesive for electronic packaging applications. In a study by Atmakuri et al. (2022), the author reported that hemp and flax fiber reinforced with epoxy composites has two times greater mechanical properties compared to the fiber reinforced with ecopoxy composites. With the improved mechanical properties of the composites, the hemp and flax fiber reinforced with epoxy matrix composites are potential to replace the synthetic fiber composites in automobile, construction, micrfluidics and biomedical industries.

This research introduces two newly developed biocomposite materials, MOB-Epoxy and MOB-silicone biocomposites, which makes it novel since there has been no reported studies on the reinforcement of Moringa Oleifera bark fibers into silicone rubber. The tensile and deformation behaviour of these two recently developed composite materials was mainly examined in this work, including addressing research questions on how MOB fibres affect the tensile properties of polymers and the potential applications for such biocomposites. The tensile properties of both biocomposites were quantified, analysed, and compared in this work to show how MOB fibre content impacts the stiffness and deformation of the biocomposites.

MATERIAL AND METHODS

Raw Material and Matrix

The stem of Moringa Oleifera was supplied by GV Medhini Consultancy & Resources Sdn. Bhd. was harvested in Kota Kemuning, Selangor, Malaysia. The epoxy resin (Mirapox MH956) and silicon matrix (Ecoflex 00-30 Platinum Cure Silicone) were purchased from Miracon Sdn. Bhd. and Castmech, respectively.

Specimen Preparation

Moringa Oleifera (MO) stems were cut into 10 cm lengths, and the bark was peeled off. The bark was rinsed with tap water to eliminate impure particles before being dried in a 100°C oven for 24 hrs. It was crushed into small chip particles using a crusher machine and milled at 270 rpm for 30 seconds 4 times using a planetary mono mill to transform it into powdery form. Lastly, it was sieved at 150 μm in size to produce a uniform fine powder.

The specimens were produced at five different fibre compositions, 0wt%, 4wt%, 8wt%, 10wt%, 12wt% and 16wt%. Each fibre composition was fabricated with five specimens. The powder weight was measured to fabricate the exact fibre-matrix content solution. The solution was mixed under continuous stirring and performed in a specified lab environment. The mixture solution was moulded into respective moulds and hardened at room temperature for 24 hrs for MOB-Epoxy and 4 hrs for MOB-Silicone (MOBSil).

Mechanical Testing: Uniaxial Tensile Test

Tensile tests followed the American Society for Testing and Materials (ASTM), D3039 for MOB-Epoxy (Batu & Lemu, 2020) and D412 for MOB-Silicone (Bahrain & Mahmud, 2019), respectively. The specimen dimensions for both materials were as shown in Figure 1. Each specimen was evaluated using a 3383 Universal Testing Machine 100kN (Instron, United States of America, 2008) at a 500 mm/min speed. Tensile modulus referred to the stiffness of the materials, and the values were generated from the machine for each specimen once it reached the failure point. Therefore, these values were recorded for analysis.

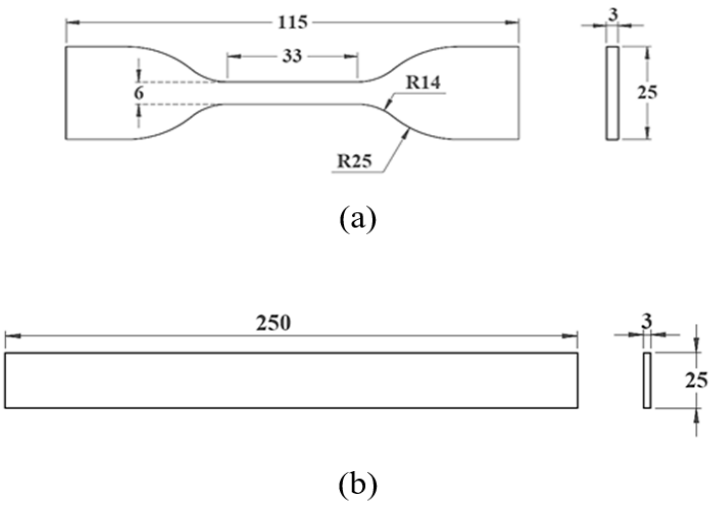

Figure 1. Specimen dimensions in millimetres (mm) for (a) MOB-Silicone (ASTM D412) and (b) MOB-Epoxy (ASTM D3039)

Statistical Analysis: Mean, SD, Var, Pair t-Test

Statistical analysis was also executed in this study to determine the mean, standard deviation and variance values. This analysis was also conducted to assess the reliability and accuracy of the data gained from the experiment. In order to compare the tensile properties of both materials (MOB-Epoxy and MOB-Silicone), a statistical analysis named t-test analysis was conducted. A t-test analysis aims to describe the significant difference between the means of the two groups concerning the tensile modulus of both materials. It required three key data values: mean values, variance, and the number of data values of each group. Equation 1 was used to calculate the t-score to define the differences between both materials.

$$t = \frac{|\bar{x}_1 - \bar{x}_2|}{\sqrt{\frac{S_1^2}{n_1} + \frac{S_2^2}{n_2}}} \quad [1]$$

Where, $\bar{x}_1$ and $\bar{x}_2$ are the mean value of the tensile modulus of MOB-Epoxy and MOB-Silicone, $S_1$and S_2 are the variance value of the tensile modulus of MOB-Epoxy and MOB-Silicone, respectively, and n_1 and n_2, are the number of observations for each material.

The study used the Data Analysis feature in Excel software to obtain the t-score value. It was noted that the higher values of the t-score indicated that a large difference existed between the two sample sets. The smaller t-score indicated that more similarity existed between the two samples. Therefore, this test was conducted to identify and observe the tensile properties of Moringa oleifera bark-epoxy biocomposite and Moringa oleifera bark-silicone biocomposite specimens.

RESULTS AND DISCUSSION

Moringa Oleifera Bark – Epoxy (MOB-Epoxy) Biocomposite

Figure 2 highlights the tensile behaviour of pure epoxy and MOB-Epoxy biocomposite specimens under uniaxial tension.

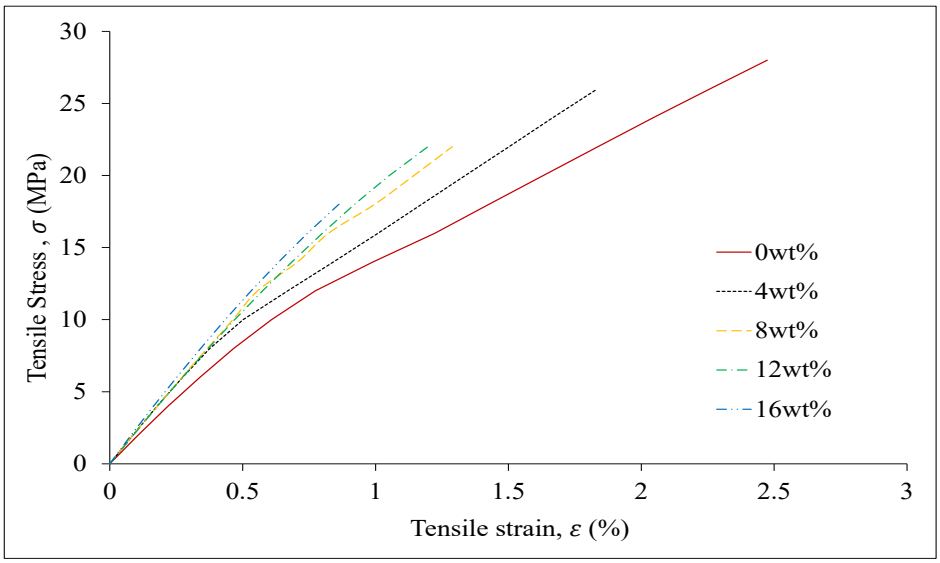

Figure 2. Average tensile stress-strain curves of MOB-Epoxy biocomposite

As illustrated in Figure 2, the trend observed showed that the pure epoxy specimen occupied the lowest curve (red line), thus indicating that the pure epoxy specimen was the least stiff compared to specimens with MOB fibre. By observing the curves, the slopes showed a gradually increasing trend, and the curves became more linear as the MOB fibre content increased. This finding is supported by the tensile modulus value summarised in Figure 3. The tensile modulus of the specimen gradually increased along with the further inclusion of fibre content from 1240.5 MPa to 1668.5 MPa. This increment indicated the enhancement of the properties of pure epoxy when adding the Moringa oleifera bark fibre as the reinforcement material. The low MOB content in the epoxy matrix made it strain more to reach the fracture point, where the 0wt% specimens had the highest maximum strain values followed by 4, 8, 12 and 16 of weightage (Table 1). In general, the material's properties were proven to have improved its tensile modulus. The maximum strain value was found to be 2.47 for pure epoxy, and this was reduced to 0.86 at 16wt% fibre content, in agreement with the finding in Kumar et al.'s study (Kumar et al., 2021). Both soft and hard composites became stiffer due to the reinforcement. It is due to the inclusion of filler in the composite to fill up the spaces between the chains, resulting in lower polymeric

chains mobility of the composite. Therefore, filler inclusion in the composite makes it stiffer and more resistant to deformation as it resists the movement of the polymer chain within the composite, as in agreement with previous studies (Benevides & Nunes, 2015; Ismail et al., 2015).

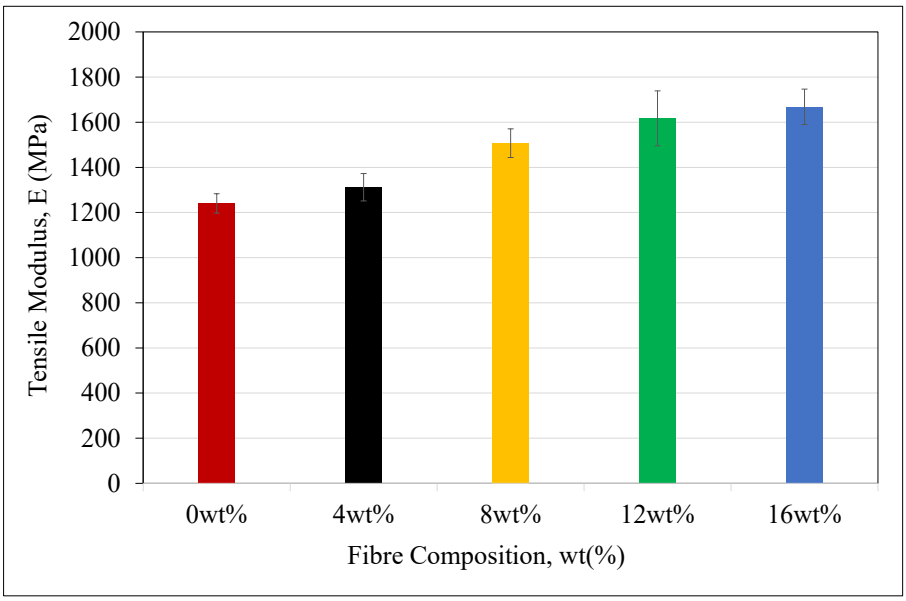

Figure 3. The average tensile modulus of MOB-Epoxy biocomposite

Table 1

Tensile properties (average value) of MOB-epoxy specimens

Weightage (%)	Tensile Modulus, E (MPa)	Maximum strain, ε (%)
0	1240.5	2.473
4	1312.1	1.834
8	1507.5	1.288
12	1617.3	1.197
16	1668.5	0.862

Table 2 compares the results obtained from this study with other studies. Similar to MOB-silicone biocomposite, Table 2 showed that the tensile stiffness of the current material, MOB-Epoxy biocomposite was comparable to Graphene nanoplatelets/epoxy composites and, thus, may open up ideas for new applications (Kilic et al., 2019).

Table 2

Comparison of tensile modulus, E Value between previous studies and the current study based on tensile tests

Tensile Modulus, E	Material Type	Reference
13.1 GPa	Micro-Bismuth (III) oxide (Bi2O3) epoxy composite	Muthamma et al. (2021)
3.6 GPa	Kevlar/Date palm epoxy hybrid composite	Muthalagu et al. (2020)
1.9 - 2 GPa	Kenaf epoxy biocomposite	Fauzi et al. (2016)
1.89 - 1.45 GPa	Para-aramid fibres (Kolon) epoxy composite	Obradović et al. (2021)
1.7 GPa	Graphene nanoplatelets/epoxy composites	Kilic et al. (2019)
1312 - 1668 MPa	Moringa Oleifera bark—epoxy biocomposite	Current study
577–645 MPa	Phoenix sp. fibre-reinforced epoxy composites	Rajeshkumar et al. (2017)
124 - 223 MPa	Alkali-treated bamboo fibre/epoxy	Huang and Young (2019)
113 -163 MPa	Untreated bamboo fibre epoxy composite	Huang and Young (2019)

Moringa Oleifera Bark – Silicone (MOBSil) Biocomposite

Figure 4 illustrates the average tensile stress-strain curve of MOB-Silicone specimens for every composition of fibre content (0wt%, 4wt%, 8wt%, 10wt%, 12wt% and 16wt%).

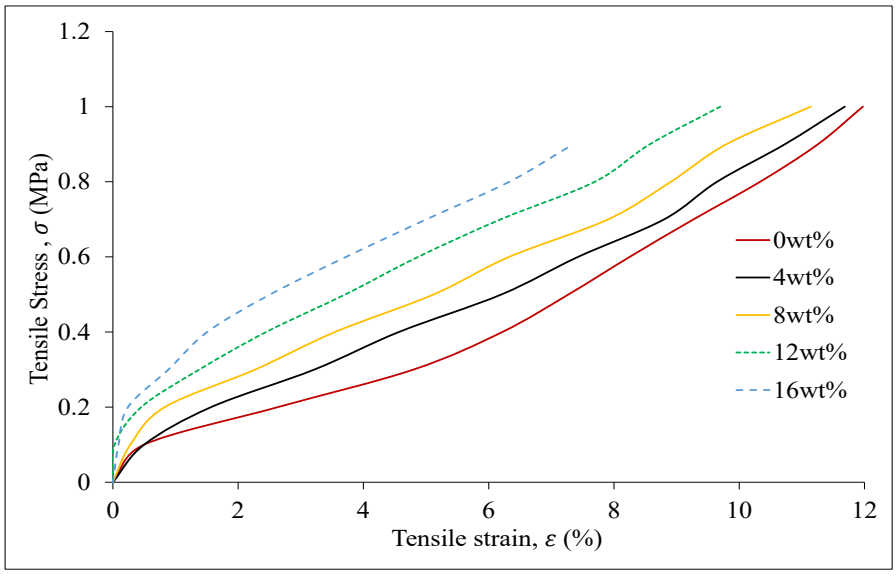

Figure 4. Tensile stress – Strain curves of MOB-silicone biocomposite

From the stress-strain curve, pure silicone rubber (0wt%) had the highest strain as it strained more than other specimens (reinforced with MOB fibre at 4, 8, 12, and 16wt%). Additionally, the uniaxial tensile load caused the pure silicone specimen to exhibit a highly nonlinear elastic behaviour (the red line in Figure 4). It occurred due to the weak bonding of the polymer chain with silicone rubber (Sarath et al., 2020). However, when the fibre content climbed from 0 to 16wt%, the curve trend began to lessen its nonlinear behaviour, resulting in a more linear curve at 16wt%. Due to the presence of Moringa oleifera bark fibre as a filler, the curve gradually became more linear as it enhanced the tensile properties of silicone rubber, as supported by the tensile modulus value illustrated in Figure 5. In terms of strain, it could be observed that adding fibre into the silicone rubber had affected the strain behaviour as it started to decrease in elongation to the failure point from the specimen of 0 until 16wt%, as summarised in Table 3.

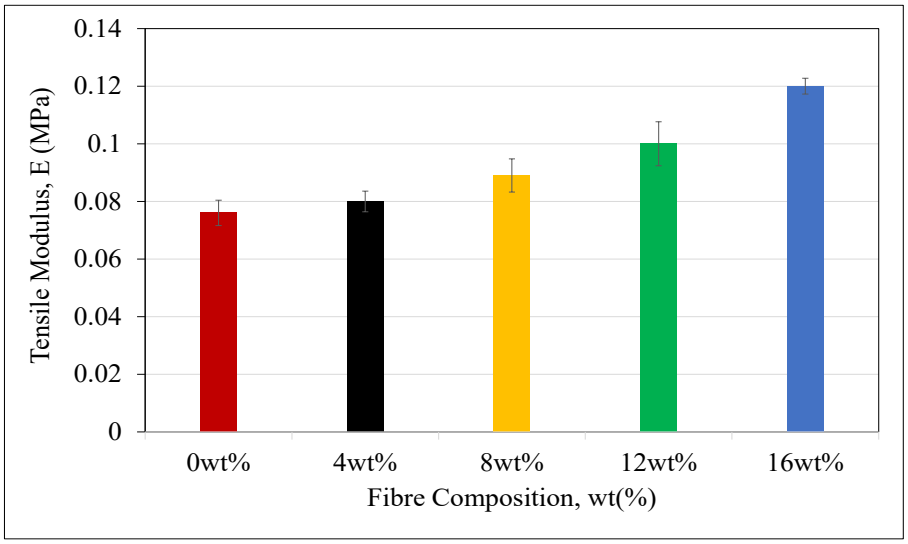

Figure 5. The average tensile modulus of MOB-silicone biocomposite

Table 3

Tensile properties (average value) of MOB-silicone specimens

Weightage (%)	Tensile Modulus, E (MPa)	Maximum Strain, ε (%)
0	0.076	0.1007
4	0.080	0.1099
8	0.089	0.0993
12	0.100	0.0914
16	0.120	0.0801

From Table 3, the tensile modulus of the specimen increased as the fibre content increased. The lowest tensile modulus could be seen at 0wt% with a value of 0.076 MPa, and the specimen of 16wt% recorded the highest with a value of 0.12 MPa. Therefore, this study proved that adding MOB fibre caused silicone rubber to have better resistance to deformation.

Halim et al. (2022) also reported a similar trend in which adding the Silica Aerogel (SA) into the room temperature vulcanised silicone rubber (RTV-SiR) reduced the tensile strain of the biocomposite (this addition, thereby forming SA/RTV-SiR) compared to pure RTV silicone rubber. The result also showed increasing tensile modulus values from 0.74 MPa for the RTV-SiR sample to 1.34 MPa for the SA/RTV-SiR sample. The presence of fibre was found to increase the stiffness of the silicone rubber. Similar behaviour had also been reported by Koushki et al. (2020), who reinforced hemp fibre into silicone rubber with a different fibre content of hemp fibre. The tensile modulus of the composite was increased with further addition of fibre content, and its elongation at break was gradually decreased.

However, a study by Kumar et al. (2022) reported that the increased filler content in RTV silicone rubber had caused increased tensile strain but with an increased tensile modulus value. The pure RTV silicone rubber only strained up to 50% compared to a 15 phr nanographite/ RTV silicone rubber composite specimen which was strained up to 120%. Another study was the work of Hu et al. (2022), who investigated a composite material made of silicone rubber reinforced with boron nitride (BN). The results showed a similar pattern where the tensile modulus value increased along with the increment of fibre content. It could be concluded that adding MOB fibre has improved the tensile behaviour of silicone rubber and epoxy compared to other researched materials such as Kenaf-Silicone biocomposite (Azmi et al., 2017), Arenga Pinnata-silicone biocomposite (Bahrain & Mahmud, 2019), phoenix-epoxy biocomposite (Rajeshkumar et al., 2017) and bamboo epoxy biocomposite (Huang & Young, 2019). Table 4 shows the measured tensile modulus of MOB-Silicone biocomposite (current study) compared to other materials which other researchers had developed. It could be highlighted that pure silicone is very weak (low tensile stiffness) and, thus, not suitable for many applications. MOB-Silicone Biocomposite is a newly introduced material with the potential for an organ substitute. Therefore, this study has reinforced various weight-percentage of MOB fibre into silicone rubber to increase the tensile stiffness. As shown in Table 4, this newly introduced tensile stiffness, E, is within the range for a few potential applications, such as connective tissue.

MOB-Silicone (Soft composite) Versus MOB-Epoxy (Hard Composite) Biocomposites

For the first time, this study introduces two types of biocomposite materials, MOB-Silicone biocomposites and MOB-Epoxy biocomposites, intended for soft and hard composite

Table 4

Tensile modulus, E of current study compared to other studies

Tensile Modulus, E	Material Type	Reference
0.4 to 8.2 MPa	RTV-Silicone Rubber/ graphene composites	Kumar et al. (2022)
0.4 to 0.7 MPa	RTV-Silicone Rubber/ graphite composites	Kumar et al. (2022)
3 to 8 MPa	Silicone/Hemp fibre biocomposite	Koushki et al. (2020)
0.3 to 0.85 MPa	Silicone-Organically modified montmorillonite composite	Bae and Chang (2013)
76 to 120 kPa	Moringa Oleifera bark-silicone (MOBSil) biocomposite	Current study
41 to 44.4 kPa	Porcine Orbital Fat & Connective Tissue in eye (OFCT)	Chen and Weiland (2011)
16.5 to 16.6 kPa	Human Orbital Fat & Connective Tissue in the Eye (OFCT)	Chen and Weiland (2011)
8.2 kPa	Hydrogel Matrix	Castilho et al. (2018)

applications, respectively. Comparing the MOB-Epoxy (hard composite) and MOB-Silicone (soft composite) biocomposite, MOB fibre interestingly affected silicone rubber and epoxy. Both the soft and hard composites became stiffer due to the reinforcement. By computation at 16wt% fibre content, the stiffness for silicone biocomposite had increased by 64%, while the increase was only 35% for epoxy biocomposite. In contrast, the stretch ratio had reduced by 27% for silicone, and the strain had reduced by 65% for epoxy biocomposite. By comparison, it can be concluded that reinforcing MOB fibre affected the stiffness of silicone rubber more than epoxy; but affected the elongation of epoxy more than silicone rubber. Table 5 shows the t-test results to highlight which Tensile Modulus of both matrix materials were affected more by the reinforcement of the MOB filler. Observing a significant difference in how the MOB filler affected the tensile modulus of silicone rubber and epoxy is interesting.

The t-score in Table 5 indicated that a large difference existed between the MOB-Epoxy and MOB-Silicone samples, where a high value of t-score was recorded at 17.55. It is well known that if the value of the t-score is small, a similarity between two samples exists. However, a large t-score indicates a difference between the groups. In this case, the characteristics of the two materials were demonstrated to be distinct, as shown by a

Table 5

Comparison test between MOB-Epoxy and MOB-Silicone via t-test

Weightage (wt%)	Average Tensile Modulus, E (MPa)	
	MOB-Epoxy	MOB-Silicone
0	1240.5	0.076
4	1312.1	0.080
8	1507.5	0.089
12	1617.3	0.100
16	1668.5	0.120
Mean	1469.18	0.091
Variance	35026.272	0.000398
Observations	5	5
t-score	17.5523855	

significant t-score in Table 5. Their behaviour under tensile stress also behaved differently under uniaxial tensile load. The MOB-Epoxy was seen to absorb a small load to reach the breaking point. However, this was in contrast to the MOB-Silicone sample. The MOB-Silicone sample was seen to require a high amount of load as it elongated to the breaking point. It was also seen to take longer elongation as it absorbed the load to elongate compared to the MOB-Epoxy sample. Finally, it could be observed that these two materials were very distinct in terms of their behaviour toward the tensile load, properties and elongation rates.

CONCLUSION

Based on supporting the idea of promoting green materials and addressing environmental issues, this research has successfully introduced two new types of biocomposites made of silicone and epoxy matrix reinforced with natural fibre: Moringa Oleifera bark (MOB). This study has successfully reported the effect of reinforcing MOB fibre on silicone and epoxy biocomposites' tensile and deformation behaviour. In general, soft and hard composites became stiffer due to the reinforcement. Nevertheless, interestingly, the main finding deduced that the reinforced MOB fibre had affected the stiffness of silicone rubber more than epoxy; but affected the elongation of epoxy more than silicone rubber. Finally, the quantified properties were compared to other materials for benchmarking and exploring potential applications. MOB-Silicone biocomposites were found to have higher stiffness than Kenaf- and Arenga Pinnata-Silicone biocomposites but were still in the range of Elastin and connective tissues, thus opening the possibility of producing synthetic tissues made of MOB-silicone biocomposites, or at least to bio-mimic the deformation of synthetic tissues.

ACKNOWLEDGEMENT

This study was supported by the Ministry of Higher Education and Universiti Teknologi MARA, Malaysia with grant no. FRGS/1/2019/TK03/UITM/03/7 (UiTM File. No. 600-IRMI/FRGS 5/3 (220/2019)).

REFERENCES

Ahmed, M. M., Dhakal, H. N., Zhang, Z. Y., Barouni, A., & Zahari, R. (2021). Enhancement of impact toughness and damage behaviour of natural fibre reinforced composites and their hybrids through novel improvement techniques: A critical review. *Composite Structures*, *259*, Article 113496. https://doi.org/10.1016/j.compstruct.2020.113496

Ali Raza, M., Westwood, A., Stirling, C., Brydson, R., & Hondow, N. (2012). Effect of nanosized carbon black on the morphology, transport, and mechanical properties of rubbery epoxy and silicone composites. *Journal of Applied Polymer Science*, *126*(2), 641–652. https://doi.org/10.1002/app.36655

Alshahrani, H., & Arun Prakash, V. R. (2022). Mechanical, fatigue and DMA behaviour of high content cellulosic corn husk fibre and orange peel biochar epoxy biocomposite: A greener material for cleaner production. *Journal of Cleaner Production, 374*, 133931. https://doi.org/10.1016/j.jclepro.2022.133931

Arbelaiz, A., Txueka, U., Mezo, I., & Orue, A. (2020). Biocomposites based on poly(lactic acid) matrix and reinforced with lignocellulosic fibers: The effect of fiber type and matrix modification. *Journal of Natural Fibers, 19*(1), 1–14. https://doi.org/10.1080/15440478.2020.1726247

Atmakuri, A., Palevicius, A., Vilkauskas, A., & Janusas, G. (2022). Numerical and experimental analysis of mechanical properties of natural-fiber-reinforced hybrid polymer composites and the effect on matrix material. *Polymers, 14*(13), 2612. https://doi.org/10.3390/polym14132612

Azmi, N. N., Hussain, A. K., & Mahmud, J. (2017). Kenaf silicone biocomposites: Synthesis and its hyperelastic behaviour. *Materials Science Forum*, *900*, 12-16. https://doi.org/10.4028/www.scientific.net/MSF.900.12

Bae, J. H., & Chang, S. H. (2013). A study on the mechanical behavior of silicone-organically modified montmorillonite composite under human body simulated environment. *Composites Science and Technology*, *85*, 90-97. https://doi.org/10.1016/j.compscitech.2013.06.008

Bahrain, S. H. K., & Mahmud, J. (2019). *Arenga pinnata* - Silicone biocomposite: Quantifying its tensile properties using neo-hookean model. *International Journal of Recent Technology and Engineering*, *8*(1), 3186-3190.

Bahrain, S. H.K, Masdek, N. R., Mahmud, J., Mohammed, M. N., Sapuan, S. M., Ilyas, R. A., Mohamed, A., Shamseldin, M. A., Abdelrahman, A., & Asyraf, M. R. (2022). Morphological, physical, and mechanical properties of sugar-palm (*Arenga pinnata* (Wurmb) merr.)-reinforced silicone rubber biocomposites. *Materials, 15*(12), 4062. https://doi.org/10.3390/ma15124062

Batu, T., & Lemu, H. G. (2020). Investigation of mechanical properties of false banana/glass fiber reinforced hybrid composite materials. *Results in Materials, 8*, 100152. https://doi.org/10.1016/j.rinma.2020.100152

Benevides, R. O., & Nunes, L. C. S. (2015). Mechanical behavior of the alumina-filled silicone rubber under pure shear at finite strain. *Mechanics of Materials*, *85*, 57-65. https://doi.org/10.1016/j.mechmat.2015.02.011

Bharath, K. N., & Basavarajappa, S. (2016). Applications of biocomposite materials based on natural fibers from renewable resources: A review. *Science and Engineering of Composite Materials*, *23*(2), 123-133. https://doi.org/10.1515/secm-2014-0088

Castilho, M., Hochleitner, G., Wilson, W., Van Rietbergen, B., Dalton, P. D., Groll, J., Malda, J., & Ito, K. (2018). Mechanical behavior of a soft hydrogel reinforced with three-dimensional printed microfibre scaffolds. *Scientific Reports*, *8*(1), 1-10. https://doi.org/10.1038/s41598-018-19502-y

Chen, K., & Weiland, J. D. (2011). Mechanical properties of orbital fat and its encapsulating connective tissue. *Journal of Biomechanical Engineering*, *133*(6), Article 064505. https://doi.org/10.1115/1.4004289

Fauzi, F. A., Ghazalli, Z., & Siregar, J. P. (2016). Effect of various kenaf fiber content on the mechanical properties of composites. *Journal of Mechanical Engineering and Sciences*, *10*(3), 2226-2233. https://doi.org/10.15282/jmes.10.3.2016.2.0208

George, K. S., Revathi, K. B., Deepa, N., Sheregar, C. P., Ashwini, T. S., & Das, S. (2016). A study on the potential of moringa leaf and bark extract in bioremediation of heavy metals from water collected from various lakes in Bangalore. *Procedia Environmental Sciences*, *35*, 869-880. https://doi.org/10.1016/j.proenv.2016.07.104

Halim, Z. A. A., Ahmad, N., Yajid, M. A. M., & Hamdan, H. (2022). Thermal insulation performance of silicone rubber / silica aerogel composite. *Materials Chemistry and Physics*, *276*, Article 125359. https://doi.org/10.1016/j.matchemphys.2021.125359

Hu, Q., Bai, X., Zhang, C., Zeng, X., Huang, Z., Li, J., Li, J., & Zhang, Y. (2022). Oriented BN/Silicone rubber composite thermal interface materials with high out-of-plane thermal conductivity and flexibility. *Composites Part A: Applied Science and Manufacturing*, *152*, Article 106681. https://doi.org/10.1016/j.compositesa.2021.106681

Huang, J. K., & Young, W. B. (2019). The mechanical, hygral, and interfacial strength of continuous bamboo fiber reinforced epoxy composites. *Composites Part B: Engineering*, *166*, 272-283. https://doi.org/10.1016/j.compositesb.2018.12.013

Hudson, Z. J., & Graves, W. R. (2021). Tensile strength of the bark of Dirca L. and other genera of the Thymelaeaceae1. *The Journal of the Torrey Botanical Society*, *149*(1), 1-7. https://doi.org/10.3159/torrey-d-21-00004.1

Ismail, A. M., Mahmoud, K. R., & Abd-El Salam, M. H. (2015). Electrical conductivity and positron annihilation characteristics of ternary silicone rubber/carbon black/TiB_2 nanocomposites. *Polymer Testing*, *48*, 37-43. https://doi.org/10.1016/j.polymertesting.2015.09.006

Jones, R. M. (1999). *Mechanics of Composite Materials* (2nd ed.). CRC Press.

Jusoh, A. F., Rejab, M. R. M., Siregar, J. P., & Bachtiar, D. (2016). Natural fiber reinforced composites: A review on potential for corrugated core of sandwich structures. *MATEC Web of Conferences*, *74*, 7-11. https://doi.org/10.1051/matecconf/20167400033

Keya, K. N., Kona, N. A., Koly, F. A., Maraz, K. M., Islam, M. N., & Khan, R. A. (2019). Natural fiber reinforced polymer composites: History, types, advantages, and applications. *Materials Engineering Research*, *1*(2), 69-87. https://doi.org/10.25082/mer.2019.02.006

Kilic, U., Sherif, M. M., & Ozbulut, O. E. (2019). Tensile properties of graphene nanoplatelets/epoxy composites fabricated by various dispersion techniques. *Polymer Testing*, *76*, 181-191. https://doi.org/10.1016/j.polymertesting.2019.03.028

Koushki, P., Kwok, T. H., Hof, L., & Wuthrich, R. (2020). Reinforcing silicone with hemp fiber for additive manufacturing. *Composites Science and Technology*, *194*, Article 108139. https://doi.org/10.1016/j.compscitech.2020.108139

Kumar, A., Verma, R. P., Avikal, S., & Singh, K. (2021). Mechanical characterization of epoxy composite reinforced with alkali treated walnut shell powder. *Materials Today: Proceedings*, *46*(20), 10642-10646. https://doi.org/10.1016/j.matpr.2021.01.383

Kumar, V., Alam, M. N., Manikkavel, A., & Park, S. S. (2022). Efficacy of graphitic allotrope's surface area in silicone rubber-based composites for reverse piezo-electric actution: Nano effect. *Sensors and Actuators, A: Physical*, *336*, Article 113411.

Manu, T., Nazmi, A., Shahri, B., Emerson, N., & Huber, T. (2022). Biocomposites: A review of materials and perception. *Materials Today Communications, 31*, 103308. https://doi.org/10.1016/j.mtcomm.2022.103308

Maria, M. (2013). Advanced composite materials of the future in aerospace industry. *Incas Bulletin*, *5*(3), 139-150. https://doi.org/10.13111/2066-8201.2013.5.3.14

Muthalagu, R., Murugesan, J., Kumar, S. S., & Babu, B. S. (2020). Tensile attributes and material analysis of Kevlar and date palm fibers reinforced epoxy composites for automotive bumper applications. *Materials Today: Proceedings*, *46*, 433-438. https://doi.org/10.1016/j.matpr.2020.09.777

Muthamma, M. V., Prabhu, S., Bubbly, S. G., & Gudennavar, S. B. (2021). Micro and nano Bi_2O_3 filled epoxy composites: Thermal, mechanical and γ-ray attenuation properties. In *Applied Radiation and Isotopes* (Vol. 174, p. 109780). Elsevier. https://doi.org/10.1016/j.apradiso.2021.109780

Obradović, V., Simić, D., Sejkot, P., Machalická, K. V., & Vokáč, M. (2021). Moisture absorption characteristics and effects on mechanical properties of Kolon/epoxy composites. *Current Applied Physics*, *26*, 16-23. https://doi.org/10.1016/j.cap.2021.03.015

Padayachee, B., & Baijnath, H. (2020). An updated comprehensive review of the medicinal, phytochemical and pharmacological properties of *Moringa oleifera*. *South African Journal of Botany*, *129*, 304-316. https://doi.org/10.1016/j.sajb.2019.08.021

Pickering, K. L., Efendy, M. G. A., & Le, T. M. (2016). A review of recent developments in natural fibre composites and their mechanical performance. *Composites Part A: Applied Science and Manufacturing*, *83*, 98-112. https://doi.org/10.1016/j.compositesa.2015.08.038

Rajeshkumar, G., Hariharan, V., Sathishkumar, T. P., Fiore, V., & Scalici, T. (2017). Synergistic effect of fiber content and length on mechanical and water absorption behaviors of Phoenix sp. fiber-reinforced epoxy composites. *Journal of Industrial Textiles*, *47*(2), 211-232. https://doi.org/10.1177/1528083716639063

Rockwood, J. L., Anderson, B. G., & Casamatta, D. A. (2013). Potential uses of Moringa oleifera and an examination of antibiotic efficacy conferred by M. oleifera seed and leaf extracts using crude extraction techniques available to underserved indigenous populations. *International Journal of Phytotherapy Research*, *3*(2), 61-71.

Rudin, A., & Choi, P. (2013). *The Elements of Polymer Science and Engineering* (3rd ed.). Academic Press.

Safdari, V., Khodadadi, H., Hosseinihashemi, S. K., & Ganjian, E. (2011). The effects of poplar bark and wood content on the mechanical properties of wood-polypropylene composites. *BioResources*, *6*(4), 5180-5192. https://doi.org/10.15376/biores.6.4.5180-5192

Sarath, P. S., Samson, S. V., Reghunath, R., Pandey, M. K., Haponiuk, J. T., Thomas, S., & George, S. C. (2020). Fabrication of exfoliated graphite reinforced silicone rubber composites-Mechanical, tribological and dielectric properties. *Polymer Testing*, *89*, Article 106601. https://doi.org/10.1016/j.polymertesting.2020.106601

Tataru, G., Guibert, K., Labbé, M., Léger, R., Rouif, S., & Coqueret, X. (2020). Modification of flax fiber fabrics by radiation grafting: Application to epoxy thermosets and potentialities for silicone-natural fibers composites. *Radiation Physics and Chemistry*, *170*, Article 108663. https://doi.org/10.1016/j.radphyschem.2019.108663

Yemele, M. C. N., Koubaa, A., Cloutier, A., Soulounganga, P., & Wolcott, M. (2010). Effect of bark fiber content and size on the mechanical properties of bark/HDPE composites. *Composites Part A: Applied Science and Manufacturing*, *41*(1), 131-137. https://doi.org/10.1016/j.compositesa.2009.06.005

Zaffer, M., Ahmad, S., Sharma, R., Mahajan, S., Gupta, A., & Agnihotri, R. K. (2014). Antibacterial activity of bark extracts of *Moringa oleifera* Lam. against some selected bacteria. *Pakistan Journal of Pharmaceutical Sciences*, *27*(6), 1857-1862.

Pertanika J. Sci. & Technol. 31 (4): 1911 - 1920 (2023)

PERTANIKA JOURNALS

SCIENCE & TECHNOLOGY

Journal homepage: http://www.pertanika.upm.edu.my/

Short Communication

Genetic Diversity of Asian Seabass (*Lates calcarifer*) in Captive Populations

Athirah Mohd Bakri[1] and Yuzine Esa[2]*

[1]*Department of Aquaculture, Faculty of Agriculture, Universiti Putra Malaysia, 43400, Selangor, Malaysia*
[2]*International Institute of Aquaculture and Aquatic Sciences, Universiti Putra Malaysia, Lot 960 Jalan Kemang 6, 71050 Port Dickson, Negeri Sembilan, Malaysia*

ABSTRACT

This study examined the genetic diversity of Asian seabass (*Lates calcarifer*) captive populations using sequencing of the mitochondrial DNA cytochrome c oxidase I (COI) fragment. The phylogenetic analyses of the 609 base pair regions of the COI fragment from 146 samples identified 15 haplotypes and divided them into two clades with a genetic divergence of 10%. Thus, phylogenetic results supported two genetic groups (the Australia/Southeast Asia group and the India/Myanmar group) within the captive populations under study. Mixed levels of genetic diversity were observed among captive populations, which indicated a certain degree of inbreeding depression. The findings would be useful for future aquaculture management of captive Asian seabass in Malaysia.

Keywords: captive, CO1 mtDNA, genetic distance, *L. calcarifer*

INTRODUCTION

Asian seabass or scientifically known as *Lates calcarifer,* is a marine teleost fish belonging to the order of Carangiformes. This prominent species had a widegeographical range across northern Australia and southward to southern Papua New Guinea, southern Japan, and Taiwan, including the Indo-West Pacific and the eastern edge of the Persian Gulf to China (Froese & Pauly, 2022). It is a remarkable aquaculture species worldwide, including Malaysia (Zhu et al., 2006). COI is the best marker compared to other mitochondrial genes as it retains more phylogenetic signal (Hebert et al., 2003). Genetic studies of Asian seabass in Malaysia's farm population are still lacking. Nevertheless, there are several studies on wildpopulations of Asian seabass using mitochondrial DNA markers (e.g.,

ARTICLE INFO

Article history:
Received: 01 June 2022
Accepted: 16 August 2022
Published: 25 May 2023

DOI: https://doi.org/10.47836/pjst.31.4.18

E-mail addresses:
athirahbakri17@gmail.com (Athirah Mohd Bakri)
yuzine@upm.edu.my (Yuzine Esa)
*Corresponding author

ISSN: 0128-7680
e-ISSN: 2231-8526

COI or cytochrome b), including Norfatimah et al. (2009). This study's mitochondrial DNA (mtDNA) analysis clarifies the genetic diversity of captive *L. calcarifer* in Peninsular Malaysia.

METHODOLOGY

Lates calcarifer juveniles (n = 146) from five commercial hatcheries were collected throughout Peninsular Malaysia, including the West coast (Selangor, n = 30), East coast (Terengganu, n = 30; Kelantan, n = 27), Southern territory (Johor, n = 30) and Northern Territory (Perak, n = 29) (Table 1). Alcohol of 95% concentration (ethanol) was used to preserve muscle tissues of the abdominal part. The ReliaPrep gDNA Tissue Miniprep System (Promega Corp, Madison, USA) standard extraction protocol was referred for DNA genomic extraction. Universal primers FishF1 (5'-TCAACCAACCA CAAAGACATTGGCAC-3'), and FishR1 (5'-TAGACTTCTGGGTGGCCAAAGAATCA-3') were used following Ward et al. (2005). The 25 µl total PCR mix's reaction contains 14.3 µl sterile distilled water, 5 µl Taq buffer 5×, 2.0 µl of 25 Mm MgCl, 0.5 µl of 10Mm dNTP, 0.5 µl of 10 µM of each primer, 0.2 µl of 5 µ μ^{-1} of Taq DNA polymerase and 2 µl of DNA template using Mastercycler Gradient PCR system (Eppendorf, Hamburg, Germany). PCR protocol was conducted according to the following profile: 2 min at 94°C, 30 cycles of 2 min at 94°C for denaturation, 1 min at 53°C (*COI*) for annealing, and 1 min and 30 s at 72°C for extension followed by a final step of 2 min at 72°C for the complete fragment extension. The PCR result was electrophoresed using a 1% agarose gel matrix from Fisher Scientific in New Jersey, USA. The GelRed (Thermo Fisher Scientific, USA) of 1 µl was used to stain the gel. Under UV light, the stained gel was visualized using AlphaImager HP (Biotechne, USA). The molecular weight (MV) standard used in this study was BenchTop 1kb DNA Ladder (Promega Corp, Madison, USA). The PCR products were sent for sequencing in only forward direction on an ABI 377 automated sequencer (Applied Biosystems) to the service supplier, First BASE Laboratories Sdn. Bhd. The phylogenetic analysis also included five COI sequences of *L. calcarifer* from GenBank. Three sequences originated from Southeast Asian waters (KU496228, DQ108026, and FJ237999), while another two were from Indian waters (EF60937 and JF919828). Kimura 2-parameter evolution model was used to calculate sequence divergence, grouped by the Neighbor-Joiningmethod (Figure 1), and bootstrapped with 1000 replications using MEGA7 (Kumar et al., 2016).

RESULTS AND DISCUSSION

The 609 bp of the COI sequences were retrieved after alignment and were characterized by 64 (10.5%) variable sites, including 63 parsimoniously informative sites and 545 (89.5%) conserved sites. The haplotypes contained 230 substitutions (190 transitions and 41 transversions). The mean total nucleotide composition was 21.9, 29.1, 30.7, and 18.3% for A, T, C, and G, respectively. In total, 15 haplotypes were identified from the 146

Table 1

Distribution of 15 observed haplotypes, nucleotide diversity, number of haplotypes, haplotype diversity, and number of polymorphic sites among populations of Lates calcarifer

		Populations				
Haplotypes	GenBank Accession Numbers	Kelantan (n = 27)	Terengganu (n = 30)	Perak (n = 29)	Selangor (n = 30)	Johor (n = 30)
LC1	MZ540093	0.4814	0.9666	0.4827	0.8333	0.5000
LC2	MZ540094	0.3703	-	0.2413	0.0666	0.1000
LC3	MZ540095	0.0370	-	-	-	-
LC4	MZ540096	0.0370	-	-	-	-
LC5	MZ540097	0.0370	-	-	-	-
LC6	MZ540098	0.0370	-	-	-	-
LC7	MZ540099	-	0.0333	-	-	0.0666
LC8	MZ540100	-	-	0.1379	-	0.2333
LC9	MZ540101	-	-	0.0344	-	-
LC10	MZ540102			0.0344	-	-
LC11	OK184465	-	-	0.0344	-	-
LC12	MZ540103	-	-	0.0344	-	-
LC13	MZ540104	-	-	-	0.1000	-
LC14	MZ540105	-		-	-	0.0666
LC15	MZ540106	-	-	-	-	0.0333
Nucleotide diversity (PiJC)		0.0475	0.0001	0.0389	0.0125	0.0237
Number of haplotypes		6	2	7	3	6
Haplotype diversity (Hd)		0.06496	0.0667	0.7094	0.3012	0.6989
Number of polymorphic sites		57	1	60	55	57

samples and were deposited to GenBank under accession numbers ranging from MZ540093 - MZ540106, OK184465, and ON920310 - ON920440 (Appendix).

Phylogenetic analysis using ML showed that the Asian seabass sampled could be divided into two clades in the tree. The first clade (L1) contains 10 haplotypes (120 samples) together with GenBank sequences from Australia and Southeast Asia, while the second clade (L2) contains 5 haplotypes (26 samples) together with GenBank sequences from India and Myanmar (Figure 1). Thus, based on phylogenetic analyses, the Asian seabass samples could be recognized into two genetic groups: the Australia/Southeast Asia (group 1) and the India/Myanmar region (group 2), with a genetic divergence value of 10% between them (Table 2).

Ward et al. (2008) claimed that Asian seabass originated from two different geographical regions: Australia and Myanmar. Rather than conspecific, it was identified

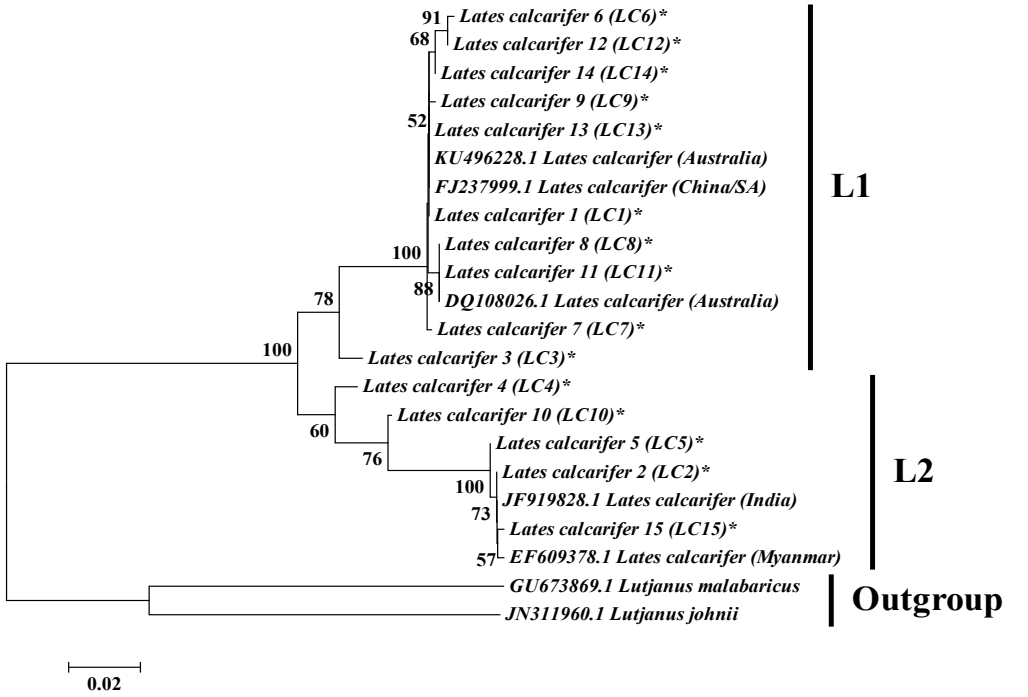

Figure 1. Neighbor-joining (nj) tree showing relationships among the seabasses. Samples were marked with an asterisk (*) at the end of the names. The number at each node represents the bootstrap value (%) based on the 1000 pseudoreplication of the dataset.

Note. SA = Southeast Asia

as congeneric. The proposition was further supported and confirmed by Vij et al. (2014) using comprehensive molecular and morphological analyses; plus, the Australian and Southeast Asia sequences were genetically close to each other (0.9% divergence); thus, they were not considered separate species. The current study also found similar results using captive or farm samples from different locations throughout Peninsular Malaysia. Thus, two different lineages in captive populations of Asian seabass might happen due to anthropogenic activities (Zhang et al., 2020) by exchanging fish stocks or seedlings between hatcheries or translocation across the country to obtain better breeds through importation. For example, fish farmers from Kelantan and even the Fisheries Research Institute (FRI), Department of Fisheries Malaysia (DOF), bought parental stocks of Asian seabass from neighboring farms located in Thailand (Idris et al., 2022).

The basic requirement of a successful selective breeding program is an appropriate base population. Starting from the production traits, an artificial population should harbor sufficient genetic diversity with selectable and desirable characteristics (Senanan et al., 2015). Two key indicators of genetic variation are haplotype (h) and nucleotide (π) diversity. A group with bigger h and π will have higher genetic variation and diversity (Falush et

Table 2

Pairwise Tamura-Nei genetic distance among 15 haplotypes of Lates calcarifer from five different farms in Malaysia

Haplotype	1	2	3	4	5	6	7	8	9	10	11	12	13	14	15	16	17	18	19	20	21	22
LC1	-																					
LC2	0.097	-																				
LC3	0.031	0.062	-																			
LC4	0.053	0.040	0.021	-																		
LC5	0.095	0.002	0.060	0.038	-																	
LC6	0.007	0.105	0.038	0.060	0.103	-																
LC7	0.002	0.099	0.033	0.055	0.097	0.008	-															
LC8	0.003	0.097	0.035	0.057	0.095	0.010	0.005	-														
LC9	0.002	0.099	0.033	0.055	0.097	0.008	0.003	0.005	-													
LC10	0.062	0.031	0.033	0.033	0.029	0.070	0.064	0.066	0.064	-												
LC11	0.003	0.097	0.035	0.057	0.095	0.010	0.005	0.000	0.005	0.066	-											
LC12	0.005	0.103	0.036	0.058	0.101	0.002	0.007	0.008	0.007	0.068	0.008	-										
LC13	0.000	0.097	0.031	0.053	0.095	0.007	0.002	0.003	0.002	0.062	0.003	0.005	-									
LC14	0.002	0.099	0.033	0.055	0.097	0.005	0.003	0.005	0.003	0.064	0.005	0.003	0.002	-								
LC15	0.099	0.002	0.064	0.042	0.003	0.107	0.101	0.099	0.101	0.033	0.099	0.105	0.099	0.101	-							
KU496228 LCAustralia	0.000	0.097	0.031	0.053	0.095	0.007	0.002	0.003	0.002	0.062	0.003	0.005	0.000	0.002	0.099	-						
DQ108026 LCAustralia	0.003	0.097	0.035	0.057	0.095	0.010	0.005	0.000	0.005	0.066	0.000	0.008	0.003	0.005	0.099	0.003	-					
FJ237999 LCChina/SA	0.000	0.097	0.031	0.053	0.095	0.007	0.002	0.003	0.002	0.062	0.003	0.005	0.000	0.002	0.099	0.000	0.003	-				
EF609378 LCMyanmar	0.099	0.002	0.064	0.042	0.003	0.107	0.101	0.099	0.101	0.033	0.099	0.105	0.099	0.101	0.003	0.099	0.099	0.099	-			
JF919828 LCIndia	0.097	0.000	0.062	0.040	0.002	0.105	0.099	0.097	0.099	0.031	0.097	0.103	0.097	0.099	0.002	0.097	0.097	0.097	0.002	-		
GU673869 *Lutjanusmalabaricus*	0.262	0.230	0.249	0.244	0.232	0.271	0.259	0.262	0.264	0.245	0.262	0.269	0.262	0.264	0.232	0.262	0.262	0.262	0.232	0.230	-	
JN311960 *Lutjanusjohnii*	0.249	0.254	0.251	0.256	0.252	0.258	0.246	0.249	0.251	0.251	0.249	0.256	0.249	0.251	0.257	0.249	0.249	0.249	0.257	0.254	0.196	-

Note. SA = Southeast Asia

al., 2003). Overall, *L. calcarifer* samples from Perak exhibited high haplotype diversity with low nucleotide diversity (h = 0.7094; π = 0.0389), while *L. calcarifer* samples from Terengganu displayed low haplotype and nucleotide diversity (h = 0.0667; π = 0.0001). According to Grant and Bowen (1998), *L. calcarifer* samples from Terengganu and Perak fall into the first and second categories. The first category (i.e., Terengganu) had a founder event by a single or a few mtDNA lineages or a recent population bottleneck. In contrast, the second category (i.e., Perak) indicates rapid population development and increased mutations after a population bottleneck. In addition, Perak haplotypes are mixed lineages of L1 and L2, while Terengganu is only from L1, which may cause the following result.

LC1 was shared among all Asian seabass populations signifying it as the ancestral haplotype. As the seed for Asian seabass came from either hatcheries or natural resources, the same origin of ancestral and the succeeding gene flow may be the main reason for the occurrence of sharing haplotypes among populations (Das et al., 2018). With only two haplotypes, the population in Terengganu possibly came from a small enclosed aquatic environment, resulting in inbreeding or collected samples from the same family (Zhang et al., 2020). High numbers (9 out of 15) of unique or private haplotypes were obtained across populations. Through mutation, the independent origin of haplotypes may produce a high percentage of unique haplotypes (Das et al., 2018). These population-specific haplotypes could also be used as an indicator for stock documentation.

CONCLUSION

The information on the genetic diversity of aquatic organisms is essential for the sustainable management of genetic resources, achieving productive aquaculture, and sustaining harvesting farm populations. In conclusion, this study has sorted out the species identification and genetic diversity of the important Asian seabass *L. calcarifer.* Two genetic groups (L1 and L2) were detected from 146 samples across five captive populations. Group L1 samples clustered with GenBank sequences from the South China Sea and Australia regions, whereas L2 clustered remaining samples with the GenBank sequences from India and Myanmar. The existence of two different mtDNA lineages in captive or farm populations in Peninsular Malaysia was possibly caused by translocation activities between hatcheries beyond countries rather than historical events. Identifying mixed genetic stocks or groups (South China Sea/Australia vs. India/Myanmar) in the captive populations highlighted the utility of the mitochondrial DNA COI marker for accurate genetic identification and selection of individual fish breeds for the breeding program. A mixed level of genetic diversity was observed across populations, with the Terengganu population harboring the lowest diversity level (h = 0.0667; π = 0.0001).

High numbers (9 out of 15) of unique or private haplotypes were also obtained across populations. The mixed levels of genetic diversity among the captive populations

indicated that evolutionary factors such as inbreeding might happen in populations with low genetic diversity due to the poor selection of stocks or breeds and poor maintenance of the population gene pool, which resulted in various growth development problems such as deformed opercula, slow growth, high vulnerability to diseases and many others. Upcoming research should concentrate on the complete phylogeographic and population structure of *L. calcarifer* across Malaysia's farm populations. Applying more sensitive markers, such as microsatellites, should be more informative in explaining the species' population structure. The findings of this pioneering study on captive *L. calcarifer* in Malaysia should be helpful for the selective breeding program of the species.

ACKNOWLEDGMENTS

We thank the Ministry of Higher Education, Malaysia for funding this project under the FRGS research grant (FRGS/1/2019/WAB01/UPM/02/26)—Genetic diversity and relatedness estimates for selective breeding. We also thank the Fish Genetic and Breeding Laboratory, Faculty of Agriculture, University Putra Malaysia, for laboratory facilities and everyone involved in sampling collection. The UPM-Kyutech International Symposium on Applied Engineering and Sciences 2021 (SAES2021) and Universiti Putra Malaysia were the main sponsor for the publication fee.

REFERENCES

Das, S. P., Swain, S., Jena, J., & Das, P. (2018). Genetic diversity and population structure of *Cirrhinus mrigala* revealed by mitochondrial ATPase 6 gene. *Mitochondrial DNA Part A: DNA Mapping, Sequencing, and Analysis*, *29*(4), 495-500. https://doi.org/10.1080/24701394.2017.1310852

Falush, D., Stephens, M., & Pritchard, J. K. (2003). Inference of population structure using multilocus genotype data: Linked loci and correlated allele frequencies. *Genetics*, *164*(4), 1567-1587. https://doi.org/10.1093/genetics/164.4.1567

Froese, R., & Pauly, D. (Eds.). (2022). *FishBase*. World Wide Web electronic publication. http://www.fishbase.org

Grant, W. S., & Bowen, B. W. (1998). Obituary: Professor Michael Laskowski Sr. *Acta Biochimica Polonica*, *30*(2), 113-114.

Hebert, P. D. N., Cywinska, A., Ball, S. L., & DeWaard, J. R. (2003). Biological identifications through DNA barcodes. *Proceedings of the Royal Society B: Biological Sciences*, *270*(1512), 313-321. https://doi.org/10.1098/rspb.2002.2218

Idris, S. M., Noordin, W. N. M., Manah, F. O., & Hamzah, A. (2022). Toward systematic breeding of asian sea bass, *Lates calcarifer* (Bloch, 1790), in Malaysia: status, challenges and prospects for future development. *Asian Fisheries Science*, *35*(1), 1-12. https://doi.org/10.33997/j.afs.2022.35.1.001

Kumar, S., Stecher, G., & Tamura, K. (2016). MEGA7: Molecular evolutionary genetics analysis version 7.0 for bigger datasets. *Molecular Biology and Evolution*, *33*(7), 1870-1874. https://doi.org/10.1093/molbev/msw054

Norfatimah, M. Y., Azizah, M. N. S., Othman, A. S., Patimah, I., & Jamsari, A. F. J. (2009). Genetic variation of *Lates calcarifer* in Peninsular Malaysia based on the cytochrome b gene. *Aquaculture Research*, *40*(15), 1742-1749. https://doi.org/10.1111/j.1365-2109.2009.02279.x

Senanan, W., Pechsiri, J., Sonkaew, S., Na-Nakorn, U., Sean-In, N., & Yashiro, R. (2014). Genetic relatedness and differentiation of hatchery populations of Asian seabass (*Lates calcarifer*) (Bloch, 1790) broodstock in Thailand inferred from microsatellite genetic markers. *Aquaculture Research*, *46*(12), 2897-2912. https://doi.org/10.1111/are.12442

Vij, S., Purushothaman, K., Gopikrishna, G., Lau, D., Saju, J. M., Shamsudheen, K. V., Vinaya Kumar, K., Basheer, V. S., Gopalakrishnan, A., Hossain, M. S., Sivasubbu, S., Scaria, V., Jena, J. K., Ponniah, A. G., & Orbán, L. (2014). Barcoding of Asian seabass across its geographic range provides evidence for its bifurcation into two distinct species. *Frontiers in Marine Science*, *1*, Article 30. https://doi.org/10.3389/fmars.2014.00030

Ward, R. D., Holmes, B. H., & Yearsley, G. K. (2008). DNA barcoding reveals a likely second species of Asian sea bass (barramundi) (*Lates calcarifer*). *Journal of Fish Biology*, *72*(2), 458-463. https://doi.org/10.1111/j.1095-8649.2007.01703.x

Ward, R. D, Zemlak, T. S., Innes, B. H., Last, P. R., & Hebert, P. D. N. (2005). DNA barcoding Australia's fish species. *Philosophical Transactions of the Royal Society B: Biological Sciences*, *360*(1462), 1847-1857. https://doi.org/10.1098/rstb.2005.1716

Zhang, Q., Sun, C., Zhu, Y., Xu, N., & Liu, H. (2020). Genetic diversity and structure of the round-tailed paradise fish (*Macropodus ocellatus*): Implications for population management. *Global Ecology and Conservation*, *21*(159), Article e00876. https://doi.org/10.1016/j.gecco.2019.e00876

Zhu, Z. Y., Lin, G., Lo, L. C., Xu, Y. X., Feng, F., Chou, R., & Yue, G. H. (2006). Genetic analyses of Asian seabass stocks using novel polymorphic microsatellites. *Aquaculture*, *256*(1-4), 167-173. https://doi.org/10.1016/j.aquaculture.2006.02.033

APPENDIX

Accession No.	Kelantan	Accession No.	Terengganu	Accession No.	Perak	Acccession No.	Selangor	Accesion No.	Johor
MZ540093	K1	ON920331	B1	ON920360	SE1	ON920384	S1	ON920413	J1
MZ540094	K2	ON920332	B2	ON920361	SE2	ON920385	S2	ON920414	J2
ON920310	K3	ON920333	B3	ON920362	SE3	ON920386	S3	ON920415	J3
ON920311	K4	ON920334	B4	MZ540100	SE4	ON920387	S4	ON920416	J4
ON920312	K5	ON920335	B5	ON920363	SE6	ON920388	S5	ON920417	J5
MZ540095	K6	ON920336	B6	ON920364	SE7	ON920389	S6	ON920418	J6
ON920313	K7	ON920337	B7	ON920365	SE8	ON920390	S7	ON920419	J7
ON920314	K8	ON920338	B8	ON920366	SE9	ON920391	S8	ON920420	J8
ON920315	K9	ON920339	B9	ON920367	SE10	ON920392	S9	ON920421	J9
MZ540096	K11	ON920340	B10	ON920368	SE11	ON920393	S10	ON920422	J10
ON920316	K12	ON920341	B11	ON920369	SE12	ON920394	S11	ON920423	J11
ON920317	K13	ON920342	B12	MZ540101	SE13	ON920395	S12	ON920424	J12
ON920318	K14	ON920343	B13	ON920370	SE14	ON920396	S13	ON920425	J13
ON920319	K15	ON920344	B14	ON920371	SE15	ON920397	S14	ON920426	J14
ON920320	K16	ON920345	B15	MZ540102	SE16	MZ540104	S15	ON920427	J15
ON920321	K17	ON920346	B16	ON920372	SE17	ON920398	S16	ON920428	J16
MZ540097	K18	MZ540099	B17	ON920373	SE18	ON920399	S17	ON920429	J17
ON920322	K20	ON920347	B18	ON920374	SE19	ON920400	S18	ON920430	J18
ON920323	K21	ON920348	B19	ON920375	SE20	ON920401	S19	MZ540105	J19
ON920324	K22	ON920349	B20	OK184465	SE21	ON920402	S20	ON920431	J20
ON920325	K23	ON920350	B21	MZ540103	SE23	ON920403	S21	ON920432	J21
ON920326	K25	ON920351	B22	ON920376	SE22	ON920404	S22	ON920433	J22
ON920327	K26	ON920352	B23	ON920377	SE24	ON920405	S23	MZ540106	J23
ON920328	K27	ON920353	B24	ON920378	SE25	ON920406	S24	ON920434	J24

APPENDIX (Continue)

Accession No.	Kelantan	Accession No.	Terengganu	Accession No.	Perak	Accession No.	Selangor	Accession No.	Johor
ON920329	K28	ON920354	B25	ON920379	SE26	ON920407	S25	ON920435	J25
MZ540098	K29	ON920355	B26	ON920380	SE27	ON920408	S26	ON920436	J26
ON920330	K30	ON920356	B27	ON920381	SE28	ON920409	S27	ON920437	J27
		ON920357		ON920382	SE29	ON920410	S28	ON920438	J28
		ON920358		ON920383	SE30	ON920411	S29	ON920439	J29
		ON920359		B30		ON920412	S30	ON920440	J30

Pertanika J. Sci. & Technol. 31 (4): 1921 - 1936 (2023)

PERTANIKA JOURNALS

SCIENCE & TECHNOLOGY

Journal homepage: http://www.pertanika.upm.edu.my/

Probability Formulation of Soft Error in Memory Circuit

Norhuzaimin Julai*, Farhana Mohamad, Rohana Sapawi and Shamsiah Suhaili

Department of Electrical and Electronics Engineering, Faculty of Engineering, Universiti Malaysia Sarawak, 94300 UNIMAS, Kota Samarahan, Sarawak, Malaysia

ABSTRACT

Downscaling threatens the designers invested in integrity and error mitigation against soft errors. This study formulated the probability of soft error changing the logic state of a Differential Logic with an Inverter Latch (DIL). Using Cadence Virtuoso, current pulses were injected into various nodes in stages until a logic flip was instigated. The voltage and temperature parameters were increased to observe the current level changes over time. The critical charge from each stage was obtained, and a method to formulate the probability of each instance was developed. The voltage produced a higher effect of the change to the critical charge of any instance as compared to temperature. The findings revealed that the N-channel metal-oxide semiconductor (NMOS) drain is more vulnerable to temperature and voltage variation than P-channel metal-oxide semiconductor (PMOS).

Keywords: Complementary metal-oxide semiconductor (CMOS), differential logic with inverter latch, probability, soft error

INTRODUCTION

Soft errors loom large as a threat to the integrity of electronics as the downscaling of technology challenges designers to maintain the robustness and reliability of modern electronic systems. Smaller transistor sizes bring lower operating voltages and node capacitances (Mamaluy & Gao, 2015), necessitating protection against soft errors caused by particle strikes from cosmic rays due to their increased vulnerability. At terrestrial levels, cosmic rays produce neutrons that can produce a nuclear reaction when interacting with particles in circuitry (Sawamura et al., 2003). These occurrences become more frequent with the downscaling

ARTICLE INFO

Article history:
Received: 08 June 2022
Accepted: 04 November 2022
Published: 13 June 2023

DOI: https://doi.org/10.47836/pjst.31.4.19

E-mail addresses:
jnorhuza@unimas.my (Norhuzaimin Julai)
farhanakuching@gmail.com (Farhana Mohamad)
srohana@unimas.my (Rohana Sapawi)
sushamsiah@unimas.my (Shamsiah Suhaili)
* Corresponding author

ISSN: 0128-7680
e-ISSN: 2231-8526

of process nodes in contemporary CMOS technology (Hubert et al., 2015). The generation of soft error effects can be categorised into three phases, namely, the charge injected through particle collision in the active circuit location, the transmission of the injected charge into the system, and the collection of the charge into the vulnerable area of the device (Autran & Munteanu, 2015; Hashimoto et al., 2019).

Related Works

In the event of a collision between an energised particle and a semiconductor device, one of two mechanisms will deposit an electrical charge along the collision path of the particle, that being the material of the device being ionised from the particle strike or nuclear response of the atoms of the material releasing resultant particles leading to ionisation (Hashimoto & Liao, 2020). The electrons formed from these interactions will generate electron-hole pairs corresponding to the path of the striking particle. The transmission of the carriers is facilitated via charge drift or charge diffusion.

The transmission of charges produces a parasitic current transient, which is more likely to affect systems with reverse-biased p-n junctions due to the depletion region's electric field. The intensity of the current transient and the number of compromised nodes may result in varying effects of ionising radiation, generally resulting in the flip of logical state in circuits operating on low power (Ke et al., 2018).

Irradiated environments also present a risk of transient faults to the operation of electronics due to the collision of ionised particles with the materials of the circuit components (Kastensmidt & Rech, 2015). Ionised particles can change transistor states and cause a failure in the logic operation. Collisions by neutrons, for example, produce ions which instigate transients by transferring charge in the transistor. These events are referred to as soft errors, as the behaviour is transient and does not cause lasting damage to the device. However, these events are not confined by industries in aerospace or radiation-heavy environments alone, as neutrons at ground level can also obstruct normal circuit operations. Single-effect transients predominantly occur as a consequence of radiation from cosmic rays, though other origins, such as package radiation, nuclear reactors, x-ray installation and research sites, also play a part (Andjelkovic et al., 2017). Boron-10 is yet another source of thermal neutrons that can affect the rate of soft errors (Weulersse et al., 2018). Boron-10 is a p-type dopant with a relatively high capture rate of thermal neutrons, exacerbating the frequency of soft error occurrences. When a Boron-10 particle interacts with a thermal neutron, alpha particles are released as a reaction. These particles can cause soft errors via indirect ionisation (Gadlage et al., 2017).

Soft error mitigation has now solidified itself as a necessity for crucial applications in the industries of aviation, military, and medical fields to maintain the reliability of electronic systems. Previous literature has researched and reported multiple avenues of

protection against soft errors. These include Hamming code (Yan et al., 2020) and the revised version, single-error correction and double-error detection (Hillier & Balyan, 2019). The Hamming code may even be modified to produce a detection and correction system capable of mitigating against multiple bit upsets at low complexity and high speed.

Alternatively, electronics can be hardened against the soft error effect at different levels of design architecture to withstand the transients caused by single event upsets (SEU). These levels are divided into system, device and circuit-level hardening techniques (Sayil, 2016). Triple modular redundancy is a popular technique wherein the circuit is triplicated and its results fed to a majority voter, disqualifying corrupted data (Wirthlin et al., 2016). While largely successful, the circuit must be duplicated, which leads to a large overhead. In the case of memory circuits, however, parity bit and checking are employed. This hardening technique involves the generation of a parity value which is then attached to the data (Lwin et al., 2019). When the data is retrieved, a checker will compare the stored parity bit to the one attached to the retrieved data and indicate whether an error has occurred. Unfortunately, this detection technique fails to detect multiple errors due to the double errors causing the parity to match.

Hardening techniques at the device level involve manipulating the material at the fabrication process to diminish charge collection at the site of the particle strike. One process implemented is the silicon-on-insulator complementary metal oxide semiconductor CMOS method which provides radiation hardening by surrounding the active device in a silicon layer that separates it from the substrate (Hara et al., 2019). This method lessens the source and drain capacitance, reducing the device's sensitivity to single-event effects.

Filters for single-event transients have also been proposed to block the signals from affecting memory in storage nodes through transmission gates (Sayil et al., 2017). The method employs a range of voltages for the body and gate to produce a design that can filter single-event transients. The transmission gate method was compared against conventional transmission gates and tuneable transient filters. Testing was found to produce significant results with a relatively low area overhead.

On the other hand, circuit-level hardening reduces single-event effects by altering the circuit design. Triple modular redundancy (TMR) can also be applied at this stage (Sielewicz et al., 2017). In order to offset the high area overhead incurred by the triple modular redundancy method, an alternative method referred to as approximate triple modular redundancy has been proposed, which produces the logic equivalent of TMR while using fewer logic gates (Arifeen et al., 2020). Alternatively, a buffer gate or C-element can be deployed, only producing a valid output when the inputs are the same (Jiang et al., 2018). A single event upset would result in differing inputs, which would cause the buffer gate to assume a high impedance state, obstructing the incorrect signal.

METHODOLOGY

The particle strike MOS device that causes soft error can be modelled as doubled exponential current pulse, as shown by Equation 1.

$$I(t) = \frac{Q_{total}}{\tau_f - \tau_r}(e^{-t/\tau_f} - e^{-t/\tau_r}) \quad [1]$$

The model is to have fast rising time τ_r and slow falling time τ_f with a shape resembling a trapezoidal. The Q_{total} denotes the total charge produced from the single event upset. The paper (Cha & Patel, 1993) proposed the rising and falling times for the soft error as 50 ps and 164 ps, respectively.

C-element is widely used in asynchronous systems. It has two inputs and one output. If both inputs are high, the output is high vice versa; if both are low, the output is low. If inputs are unequal, the output remains in the previous state. The C-element has seen use as a memory element in such systems as memory storage. In this study, we used one of the C-element circuits, Differential Logic with Inverter Latch (DIL), as shown in Figure 1, to observe and formulate the effect of soft error. When the inputs are unequal, the DIL configuration stores the previous value and will acts as memory storage. As DIL is an implementation of C-element, the memory storage of the circuit design is vulnerable to the effects of soft error, which may cause the bit in the inverter latch to flip, therefore storing an erroneous result.

The DIL inverter, which in this instance is used in 180nm technology, consists of weak inverters P5, P6, N5, N6 and two pull-down networks which consist of four transistors N1, N2, N3, and N4, as shown in Figure 1. The functionality of DIL can be explained as follows. Suppose both logic inputs A and B are low and A' and B' are high; under this condition, the output *Out'* is high.

The transistors N1 and N2 will be turned off, and N3 and N4 will be turned on. The transistor P5 will be turned off, and N5 will be turned on, discharging *Out* and pulling the signal down to low. If inputs A' and B' are low, with A and B being high, N1 and N2 will be turned on while N3 and N4 will be turned off. It will activate N6 and turn off P6, thus causing the output *Out'* to become low and *Out* to be high. If either A or B is not equal, the output value *Out'* is maintained by a weak transistor PMOS, which allows it to act as a memory circuit.

N1, N2, N3, N4 are set at 1.44μm, while N5 and N6 have a width of 440nm, with P5 and P6 set at

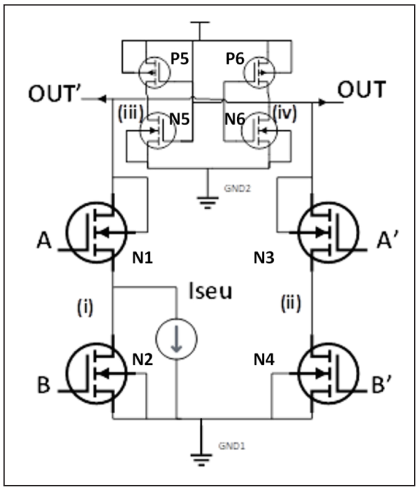

Figure 1. Differential logic with inverter latch

900nm. Vulnerable nodes are identified, and current is injected into the nodes of different configurations of C-element, labelled as (i), (ii), (iii) and (iv), as shown in Figure 1. The amplitude of the current is increased until the state flip. Three possible scenarios on the soft error can cause the present state to flip, as shown in Figures 2 and 3, depending on the amplitude of the current.

Two assumptions were made to compare the vulnerability of the nodes with soft error.

(i) As discussed earlier, the current pulse that caused the soft error is assumed to be trapezoidal, with fast rising and slow falling time.

(ii) The current pulse is assumed to hit the mid-point of the drain of PMOS and NMOS.

There are four nodes in DIL, and each is injected with the current pulse as described before. Three parameters are changed to observe the amount of critical charge needed to flip the state are as follows:

(a) Voltages are changed from 0.7 V to 1.5 V with a 0.1 V step interval. The temperature is set to room temperature (27 ºC)

(b) The temperature changes from -50 ºC to 200 ºC by taking only 5 points, -50 ºC, 0 ºC, 27 ºC, 125 ºC and 200 ºC. Voltage is set to 1 V.

(c) The dimensions of the circuit elements are set at 1x and 2x the original size, with the technology maintained at 180nm.

(d) The amplitude of the current pulse is increased until the state change is observed.

Three possible scenarios on the soft error can cause the present state to flip, as shown by Figures 2 and 3, depending on the amplitude of the current.

(i) As shown by (a) in Figures 2 and 3, the soft error did not cause any significant pulse and did not cause any state change. The study (Fuchs et al., 2009) stated that if the generated pulse is less than 20% of the original value, the pulse will be propagated in the system without causing the state to flip.

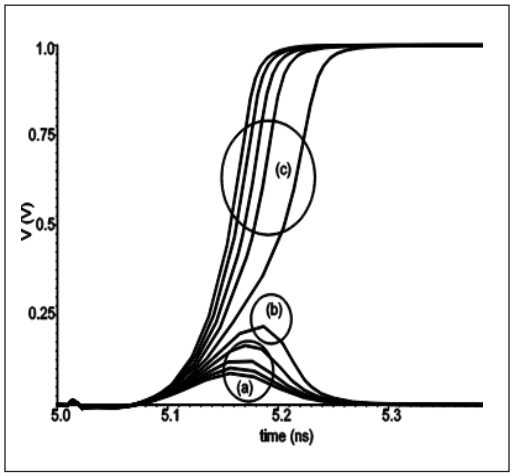

Figure 2. Varying current amplitude for 0–1 logic state

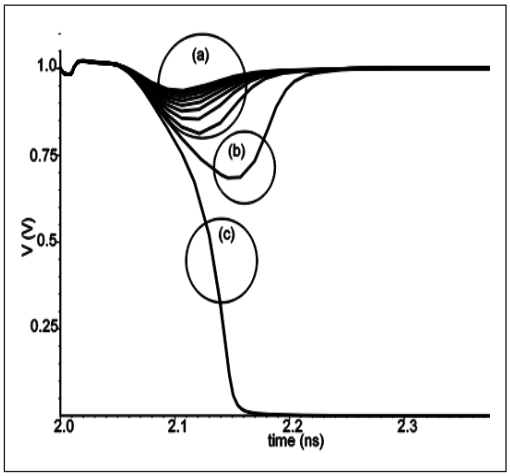

Figure 3. Varying current amplitude for 1–0 logic state

(ii) Figures 2 and 3 show that in (b), if the soft error causes a pulse that is more than 20% of the original value, the pulse propagates in the system and may cause a problem.

(iii) For (c) in Figures 2 and 3, the soft error causes the state to change. The corrupted value propagates in the system and causes other problems in another system.

RESULTS AND DISCUSSION

There are four vulnerable nodes identified in the DIL configuration, and current is injected in nodes (i), (ii), (iii) and (iv). Due to the symmetry construction of the circuit, the critical charge for nodes (i) and (iii) is equal to nodes (ii) and (iv). Figure 4 shows the critical charges needed to flip the state from 0–1 and 1–0 as the voltages changed from 0.7 to 1.5 V. Generally, as voltage increases, the current driving increases, and therefore the threshold will increase. For 0–1, the critical charge is increased by 124% in nodes (i) and (ii) and increased by 207% in nodes (iii) and (iv). For 1–0, the critical charge is increased by 130% in nodes (ii) and (iv) for the same increment of the supply voltage.

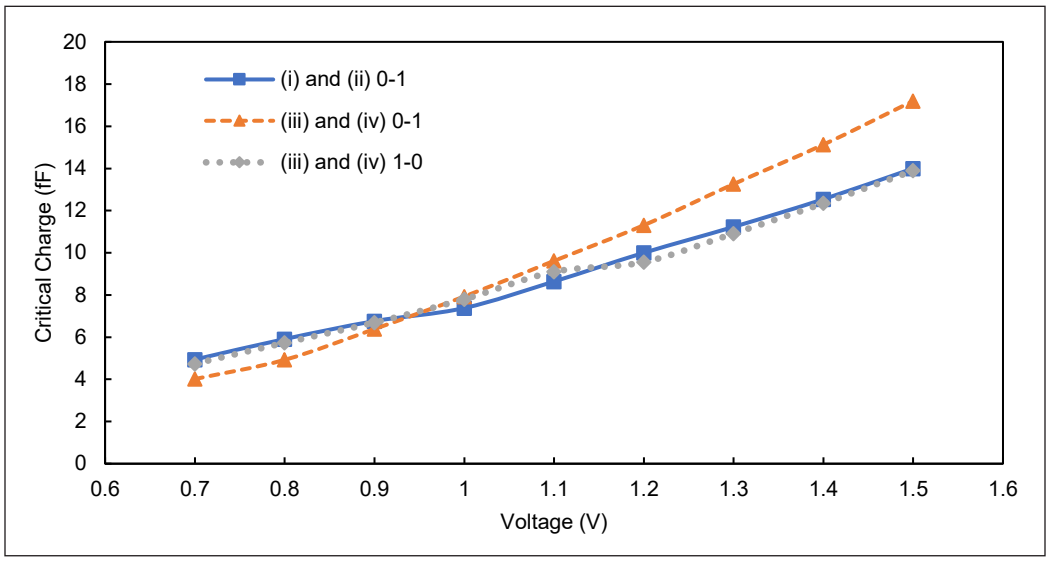

Figure 4. Critical charge (fF) vs voltage (V)

Figure 5 shows the critical charges needed to flip the state from 0-1 and 1-0 as the temperature changed from -50 ºC to 200 ºC. The maximum temperature of 200 ºC is selected to represent the temperature for automobiles utilising turbochargers and other boosting technologies. Generally, as temperature increases, the mobility of the carrier is reduced, causing the voltage threshold to be reduced. For 0-1, the critical charge is reduced by 3.7% in nodes (i) and (ii) and reduced by 16.8% in nodes (iii) and (iv). For 1–0, the critical charge is reduced by 3.8% in nodes (ii) and (iv) for the same increment of the supply voltage.

The temperature changes have a smaller effect compared with the voltage changes. As temperature increases, three factors have been degraded, contributing to lower critical charge. Lower critical charge results in the nodes becoming more vulnerable to soft error. The three factors are carrier mobility, threshold voltage and saturation velocity.

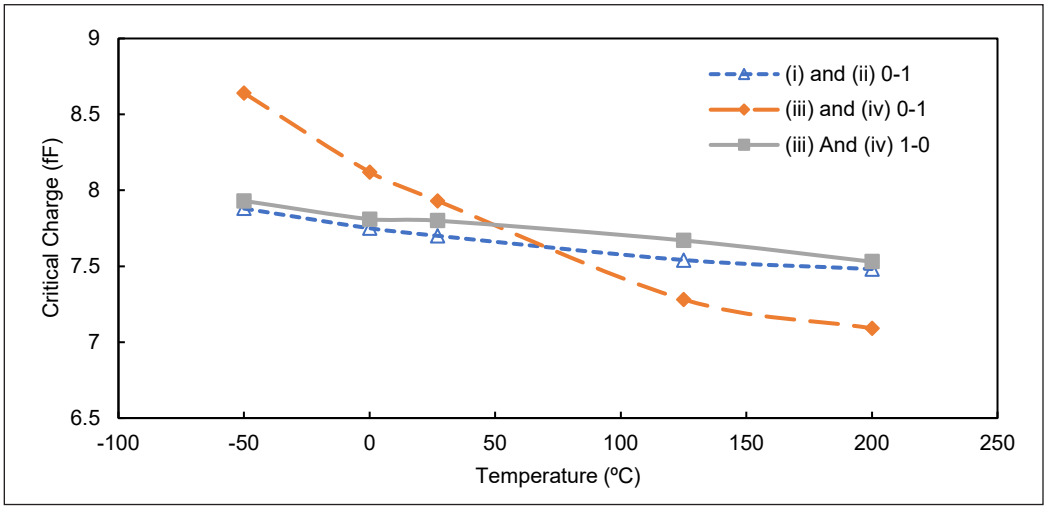

Figure 5. Critical charge (fF) vs temperature (ºC)

Figure 6 shows the threshold charge required to flip the logic state as the voltage increases for a circuit with doubled dimensions. For the logic transition of 0–1, nodes (i) and (ii), as well as nodes (iii) and (iv), see a rise in critical charge of 187% and 300%, respectively. Meanwhile, the 1–0 logic change at nodes (iii) and (iv) shows an increase of 180% with voltage. The critical charge follows a similar trend in the increase in voltage as it did at its original 1x dimensions.

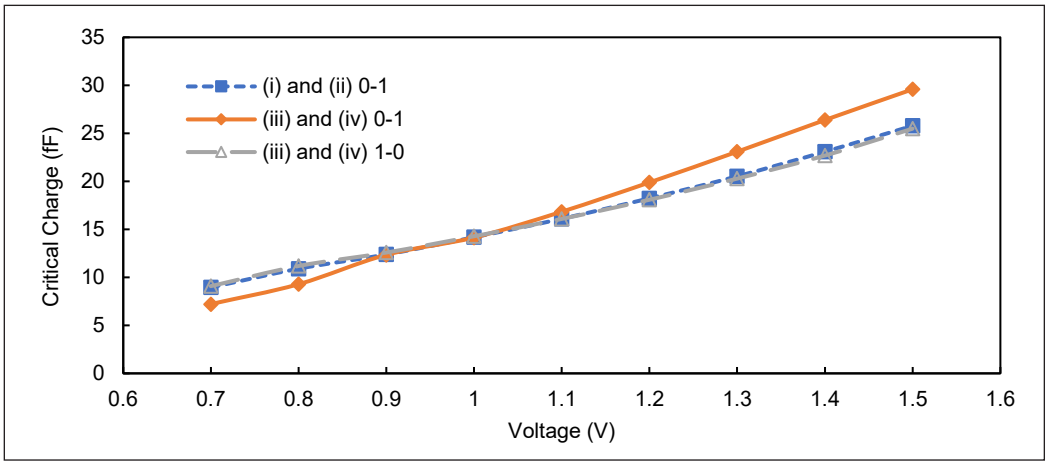

Figure 6. Critical charge (fF) vs voltage (V) transistor width doubled

The critical charge is also generally higher than that of the circuit at 1x due to the reduction of critical charge that comes with downscaling in CMOS technologies. As the charge depends on the circuit capacitance and supply voltage, the abovementioned parameters would also follow downscaling of circuit size, reducing the critical charge.

Figure 7 represents the critical charge of sensitive nodes (i), (ii), (iii) and (iv) as the temperature ranged from -50 ºC to 200 ºC with doubled dimensions. Node pairs (i), (ii), as well as (iii) and (iv), see critical charge at values much higher with doubled dimensions than with the original dimension size. The critical charge at nodes (i) and (ii) reduce by as much as 8% as the temperature increases. On the other hand, nodes (iii) and (iv) see a decrease in the critical charge of 20% at the transition point from 0–1 and 7% at 1–0. The effect of temperature on critical charge has a lesser degree compared to voltage.

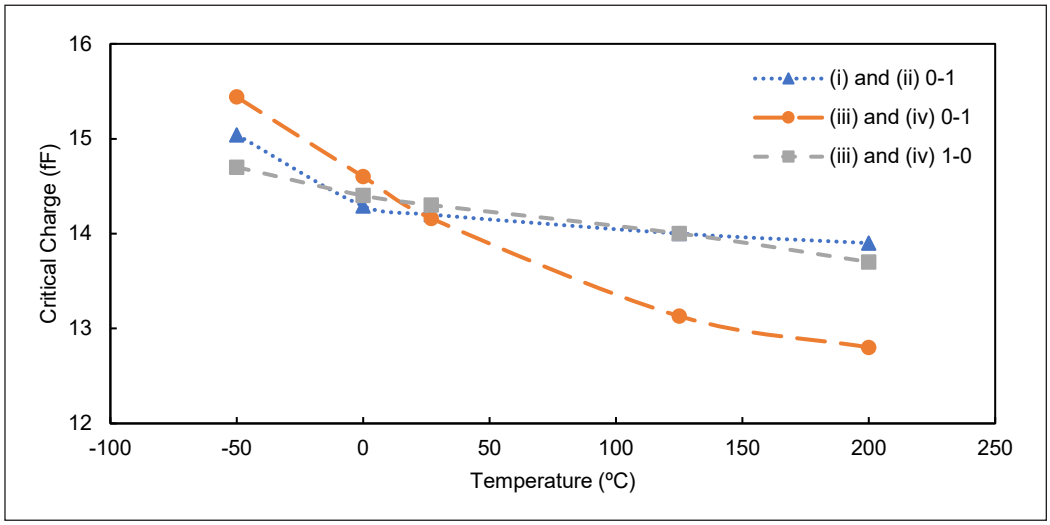

Figure 7. Critical charge (fF) vs temperature (ºC) 2x

In order to compare the effects of the voltage and the temperature towards soft error, the standard deviation of the critical charge was obtained. Figure 8 compares the standard deviation of the critical charges concerning the different nodes with different parameters. Generally, the standard deviation of the nodes with voltage changes is higher than with temperature changes. For nodes (iii) and (iv), the state change from 0–1 is higher than for nodes with a state change of 1-0. The NMOS transistor is more sensitive to variations than the PMOS transistor. By increasing supply voltage, as shown by the standard deviation values, the DIL configuration has better protection against soft error.

At 2x dimensions, the voltage variations maintain a higher standard deviation than temperature, as shown in Figure 9. The critical charge is more prone to a higher degree of change in voltage response than temperature. The standard deviations for all transition points are lower for 2x dimensions than at 1x dimensions, showing that the changes

caused by voltage and temperature have less of an effect on the probability of soft error. The NMOS transistor at nodes (iii) and (iv) still see a higher standard deviation due to its higher vulnerability to voltage and temperature changes.

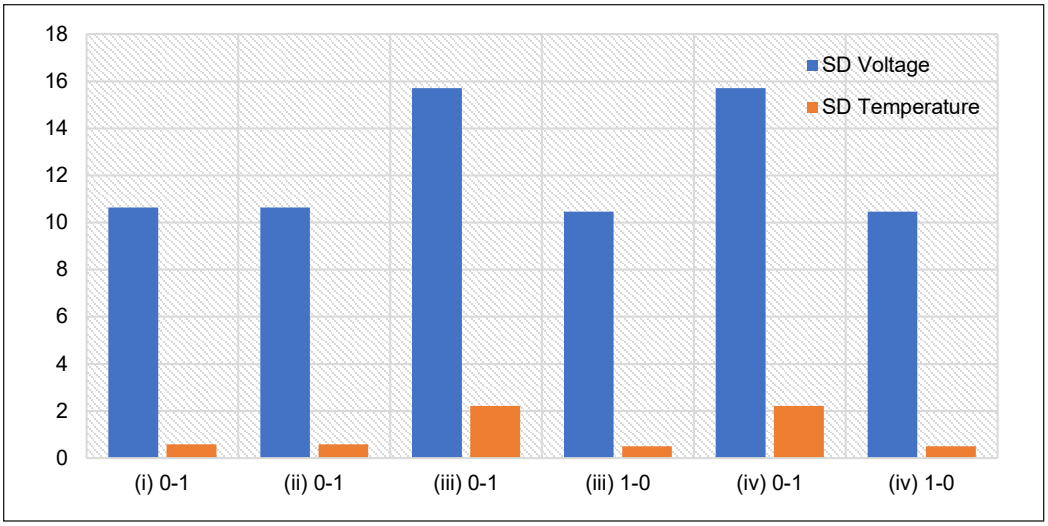

Figure 8. Standard deviation (SD) voltage and temperature 1x

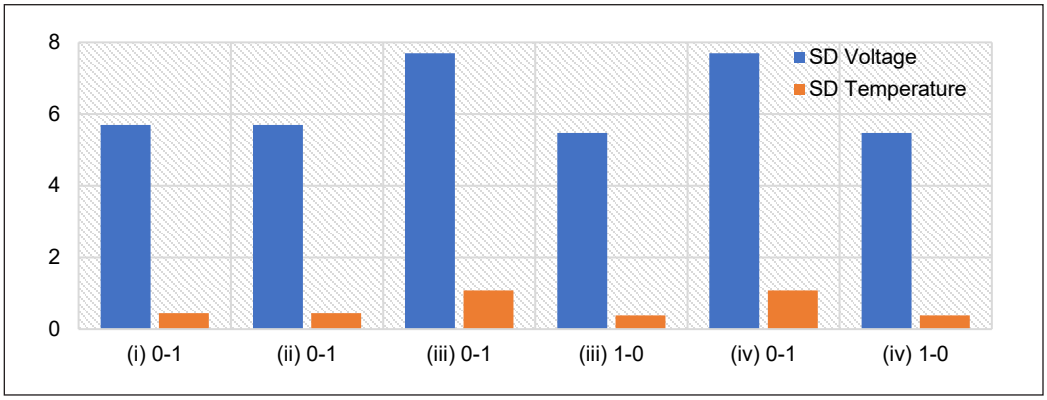

Figure 9. Standard deviation (SD) voltage and temperature 2x

The Q_s defines the scaling of the collection charge. At the same time, Q_{s2} and Q_{s1} define different collection charges based on their respective technologies. Hazucha & Svensson (2000) suggested the transformation shown in Equations 2 and 3 to find the collection charge for NMOS, $Q_{s2,N}$ and PMOS, $Q_{s2,P}$. fD_2/ fD_1 refer to the doping effects. fV_2/ fV_1 refers to the effect of V_{cc} scaling.

$$Q_{s2,N} = \frac{fV_{2,N}}{fV_{1.N}} * \frac{fD_{2,N}}{fD_{1,N}} * Q_{s1,N} \quad [2]$$

$$Q_{s2,P} = \frac{fV_{2,P}}{fV_{1,P}} * \frac{fD_{2,P}}{fD_{1,P}} * Q_{s1,P} \quad [3]$$

The values of fV_1 and fD_1 for gate length, L_G equal to 0.8 μm.,0.6 μm., 0.35 μm. and 0.1 μm were obtained from Hazucha & Svensson (2000). In this paper, the L_G was equated to 0.18 μm. A graph was plotted for fV_1 and fD_1 for N and P, and the equation was obtained as shown in Equations 4 to 7.

$$fV_N = 0.16L_G + 1.01 \quad [4]$$

$$fV_P = \begin{bmatrix} 0.32L_G + 0.79 \; L_G \leq 0.35 \\ 0.0065L_G + 0.9 \; L_G > 0.35 \end{bmatrix} \quad [5]$$

$$fD_N = 1.4L_G + 0.14 \quad [6]$$

$$fD_p = 1.85L_G + 0.005 \quad [7]$$

The collection charge, Q_{s2} for L_G, equal to 0.18, can be obtained using Equations 8 and 9 for P and N.

$$Q_{s2,N} = \frac{0.16L_G + 1.01}{fv_{1,N}} * \frac{1.4L_G + 0.14}{fD_{1,N}} * Q_{s1,N}$$
$$Q_{s2,N} = \frac{0.22{L_G}^2 + 1.44L_G + 0.14}{fv_{1,N}fD_{1,N}} \; Q_{s1,N} \quad [8]$$

$$Q_{s2,P} = \begin{bmatrix} \frac{0.32L_G + 0.79}{fv_{1,N}} * \frac{1.85L_G + 0.005}{fD_{1,N}} * Q_{s1,N} \; L_G \leq 0.35 \\ \frac{0.0065L_G + 0.9}{fv_{1,N}} * \frac{1.85L_G + 0.005}{fD_{1n}} * Q_{s1,N} \; L_G > 0.35 \end{bmatrix}$$
$$Q_{s2,P} = \begin{bmatrix} \frac{0.59{L_G}^2 + 1.46L_G + 0.004}{fv_{1,P}fD_{1,P}} \; Q_{s1,P} \; L_G \leq 0.35 \\ \frac{0.0129{L_G}^2 + 1.67L_G + 0.0045}{fv_{1,P}fD_{1,P}} \; Q_{s1,P} \; L_G > 0.35 \end{bmatrix} \quad [9]$$

The atmospheric neutron cross section per unit area ρ_{ENV} for N and P type drain are given below, which can be expanded from Equation 10, as shown in Equations 11 and 12. K is Coulomb's constant.

$$\rho_{ENV} = Kexp(^{-Q_{CRIT}}/_{Q_s}) \quad [10]$$

$$\rho_{N,ENV} = K * exp\left(\frac{-Q_{CRIT}}{\frac{0.22{L_G}^2 + 1.44L_G + 0.14}{fv_{1,N}fD_{1,N}}\ Q_{s1,N}}\right) \quad [11]$$

$$\rho_{P,ENV} = K * exp\left(\begin{matrix}\frac{-Q_{CRIT}}{\frac{0.59{L_G}^2 + 1.46L_G + 0.004}{fv_{1,P}fD_{1,P}}\ Q_{s1,P}} L_G \le 0.35 \\ \frac{-Q_{CRIT}}{\frac{0.0129x{L_G}^2 + 1.67L_G + 0.0045}{fv_{1,P}fD_{1,P}}\ Q_{s1,P}} L_G \le 0.35\end{matrix}\right) \quad [12]$$

We defined the sensitive area of N and P type of DIL implementation as below:

$A_{N,DIL}^{(i)}$ Sensitive drain area of N-type at node (i)
$A_{N,DIL}^{(ii)}$ Sensitive drain area of N-type at node (ii)
$A_{N,DIL}^{(iii)}$ Sensitive drain area of N-type at node (iii)
$A_{N,DIL}^{(iv)}$ Sensitive drain area of N-type at node (iv)
$A_{P,DIL}^{(iii)}$ Sensitive drain area of P-type at node (iii)
$A_{P,DIL}^{(iv)}$ Sensitive drain area of P-type at node (iv)

The total area of vulnerable for DIL is defined by Equation 13.

$$A_{vulnerable\ (DIL)} = A_{N,DIL}^{(i)} + A_{N,DIL}^{(ii)} + A_{N,DIL}^{(iii)} + A_{N,DIL}^{(iv)} + A_{P,DIL}^{(iii)} + A_{P,DIL}^{(iv)} \quad [13]$$

The probability of current that caused a soft error at the specific node after the current hit the drain is given as Equations 14 and 15 for N, $Prob_N$ and P, $Prob_p$.

$$Prob_N = Kexp\left(\frac{-Q_{CRIT}}{\frac{0.22{L_G}^2 + 1.44L_G + 0.14}{fv_{1,N}fD_{1,N}}\ Q_{s1,N}}\right)\frac{A_{N,DIL}^{(i)}}{A_{N,DIL}^{(i)} + A_{N,DIL}^{(ii)} + A_{N,DIL}^{(iii)} + A_{N,DIL}^{(iv)} + A_{P,DIL}^{(iii)} + A_{P,DIL}^{(iv)}} \quad [14]$$

$$Prob_P = Kexp\left(\begin{matrix}\frac{-Q_{CRIT}}{\frac{0.59{L_G}2 + 1.46L_G + 0.004}{fv_{1,P}fD_{1,P}}\ Q_{s1,P}} L_G \le 0.35 \\ \frac{-Q_{CRIT}}{\frac{0.0129{L_G}^2 + 1.67L_G + 0.0045}{fv_{1,P}fD_{1,P}}\ Q_{s1,P}} L_G \le 0.35\end{matrix}\right)\frac{A_{P,DIL}^{(i)}}{A_{N,DIL}^{(i)} + A_{N,DIL}^{(ii)} + A_{N,DIL}^{(iii)} + A_{N,DIL}^{(iv)} + A_{P,DIL}^{(iii)} + A_{P,DIL}^{(iv)}} \quad [15]$$

Figure 10 shows the probability of the node getting a soft error as the voltages changed from 0.7 to 1.5 V for 1x and 2x dimensions. The drain of PMOS is more vulnerable towards

soft error compared with NMOS. For nodes (i) and (ii) at 1x, the probability is reduced by 64% as the voltage increased due to the critical charge needed to flip the output increase by 183%, as discussed before. For the feedback inverter, the probability of NMOS drain (Node (iii) and Node (iv)) is reduced by 106% due to the critical charge increased by 327% for the same voltage increment. Similarly, for the feedback inverter, the probability of PMOS drain (Node (iii) and Node (iv)) is reduced by 124% due to the critical charge increasing by 193% for the same voltage increment.

The probabilities of soft error striking nodes with an increase in voltage with transistor widths doubled are shown in Figure 10, as the voltage ranges from 0.7 to 1.5V. Compared to the original dimensions, the probability of soft error affecting the nodes is generally lower with the doubled transistor dimensions than at the original dimensions. The variation in voltage was repeated in the simulations with the new dimensions. At nodes (i) and (ii), with dimensions at 2x, the probability of soft error sees a 151% decrease as the voltage was increased compared to the probability decrease of 64% at dimensions of 1x. For nodes (iii) and (iv) at the feedback inverter point at the NMOS drain, the decrease in probability was seen to be at 241% at doubled dimensions, with critical charge increasing by 309%. On the other hand, for the PMOS drain node at the feedback inverter, the soft error probability goes down by 323%.

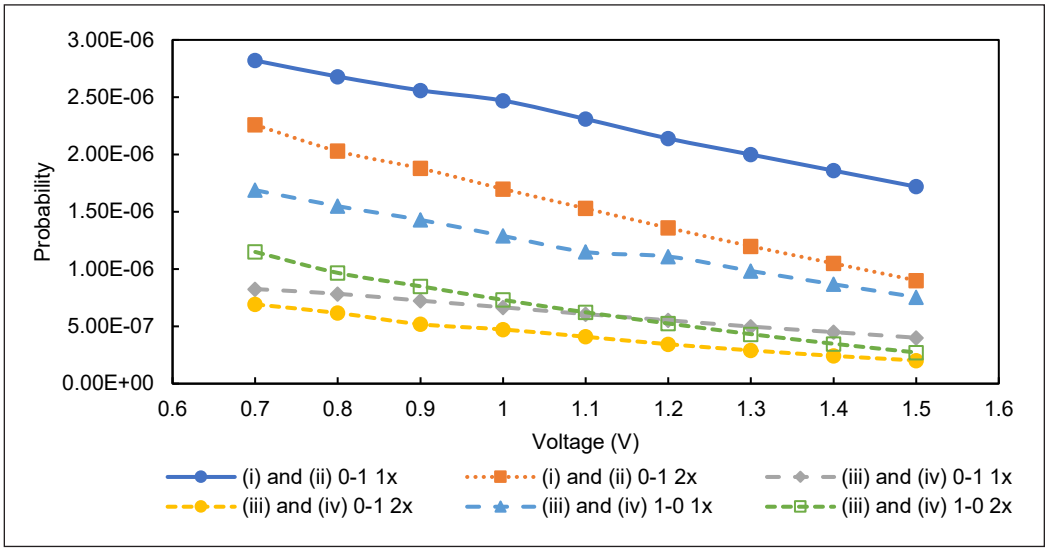

Figure 10. Probability vs Voltage (V) 1x and 2x

Figure 11 shows the probability of the node getting a soft error as the temperature changed from -50 ºC to 200 ºC for 1x and 2x dimensions. Compared with the probability due to the voltage changes, the probability of change due to temperature is insignificant. For nodes (i) and (ii), the probability is only increased by 2.5% as temperature increased due to

the critical charge needed to flip the output reduced by 5.1%, as discussed before. For the feedback inverter, the probability of NMOS drain (Node (iii) and Node (iv)) is increased by 9.1% due to the critical charge being reduced by 21.9% for the same temperature increment. Similarly, for the feedback inverter, the probability of PMOS drain (Node (iii) and Node (iv)) is increased by 3.9% due to the critical charge being reduced by 5.3% for the same temperature increment.

The probability of nodes being affected by soft error at a range of temperatures of -50ºC to 200ºC with doubled dimensions is shown in Figure 11. Nodes (i) and (ii) see an increase in the probability of about 6.79% at 2x dimensions as the temperature increases as opposed to the increase of 2.5% at 1x dimensions. For the transition from 0-1, nodes (iii) and (iv) see an increase of 15.4% in the probability of soft error. Meanwhile, 1-0 has a probability increase of 9.07% as the temperature increases. The probability at 2x dimensions is lower at all points than at 1x.

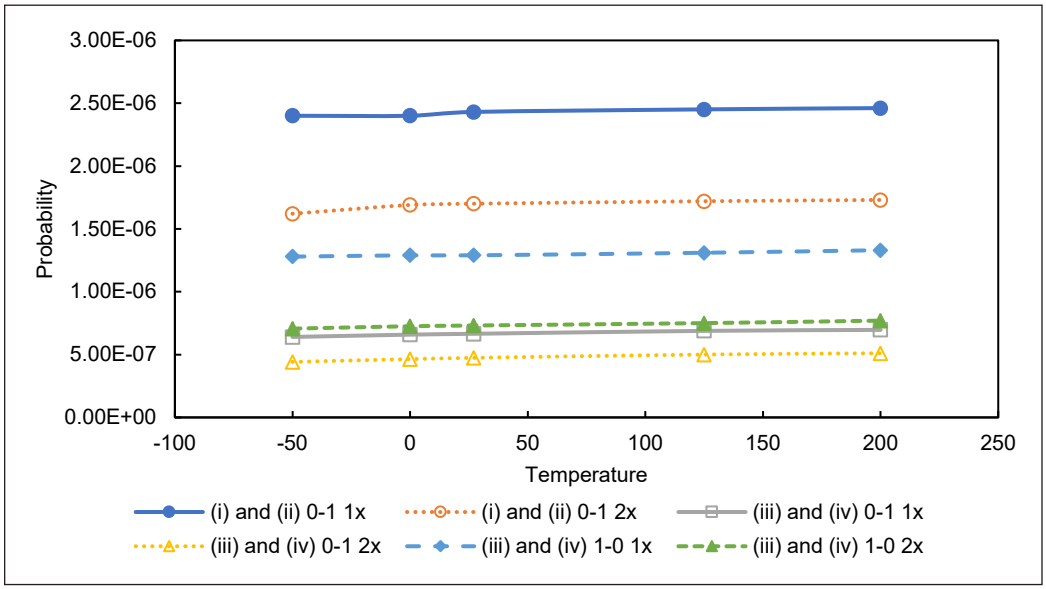

Figure 11. Probability vs temperature (ºC) 1x and 2x

CONCLUSION

In this paper, Cadence was used to simulate soft error in DIL. The vulnerable nodes were identified and injected with the current pulse, which has the characteristics of a single event upset (SEU) current. The critical charge was obtained to flip the output from 1-0 and 0-1. Two parameters as control were used in the simulation: voltage and temperature. The method of calculating the probability of SEU was developed. The critical voltage increases as voltage increases, reducing the probability of getting SEU. However, the opposite effect was observed as the increased temperature reduced the critical voltage . Hence, the

probability of getting SEU increases as temperature increases. From our simulation, the drain of NMOS is very sensitive to voltage and temperature changes compared with to drain of PMOS.

ACKNOWLEDGEMENT

The author thanks the Ministry of Higher Education, Malaysia, Fundamental Research Grant Scheme (FRGS/1/2020/TK0/UNIMAS/02/11) and Universiti Malaysia Sarawak (F02/FRGS/2035/2020) for supporting this work.

REFERENCES

Andjelkovic, M., Ilic, A., Stamenkovic, Z., Krstic, M., & Kraemer, R. (2017). An overview of the modeling and simulation of the single event transients at the circuit level. In *2017 IEEE 30th International Conference on Microelectronics (MIEL)* (pp 35-44). IEEE Publishing. https://doi.org/10.1109/MIEL.2017.8190065

Arifeen, T., Hassan, A. S., & Lee, J. A. (2020). Approximate triple modular redundancy: A survey. *IEEE Access*, *8*, 139851-139867. https://doi.org/10.1109/ACCESS.2020.3012673

Autran, J. L., & Munteanu, D. (2015). *Soft Errors from Particles to Circuits*. CRC Press. https://doi.org/10.1201/b18132

Cha, H., & Patel, J. H. (1993). A logic-level model for/spl alpha/-particle hits in CMOS circuits. In *Proceedings of 1993 IEEE International Conference on Computer Design (ICCD)* (pp. 538-542). IEEE Publishing. https://doi.org/10.1109/ICCD.1993.393319

Fuchs, G., Ffugger, M., & Steininger, A. (2009). On the threat of metastability in an asynchronous fault-tolerant clock generation scheme. In *2009 15th IEEE Symposium on Asynchronous Circuits and Systems* (pp. 127-136). IEEE Publishing. https://doi.org/10.1109/ASYNC.2009.15

Gadlage, M. J., Roach, A. H., Duncan, A. R., Williams, A. M., Bossev, D. P., & Kay, M. J. (2017). Soft errors induced by high-energy electrons. *IEEE Transactions on Device and Materials Reliability*, *17*(1), 157-162. https://doi.org/10.1109/TDMR.2016.2634626

Hara, K., Aoyagi, W., Sekigawa, D., Iwanami, S., Honda, S., Tsuboyama, T., Arai, Y., Kurachi, I., Miyoshi, T., Yamada, M., & Ikegami, Y. (2019). Radiation hardness of silicon-on-insulator pixel devices. *Nuclear Instruments and Methods in Physics Research, Section A: Accelerators, Spectrometers, Detectors and Associated Equipment*, *924*, 426-430. https://doi.org/10.1016/j.nima.2018.05.077

Hashimoto, M., Kobayashi, K., Furuta, J., Abe, S. I., & Watanabe, Y. (2019). Characterizing SRAM and FF soft error rates with measurement and simulation. *Integration*, *69*, 161-179. https://doi.org/10.1016/j.vlsi.2019.03.005

Hashimoto, M., & Liao, W. (2020). Soft error and its countermeasures in terrestrial environment. In *2020 25th Asia and South Pacific Design Automation Conference, (ASP-DAC*) (pp. 617-622). IEEE Publishing. https://doi.org/10.1109/ASP-DAC47756.2020.9045161

Hazucha, P., & Svensson, C. (2000). Impact of CMOS technology scaling on the atmospheric neutron soft error rate. *IEEE Transactions on Nuclear Science*, *47*(6), 2586-2594. https://doi.org/10.1109/23.903813

Hillier, C., & Balyan, V. (2019). Error detection and correction on-board nanosatellites using hamming codes. *Journal of Electrical and Computer Engineering*, *2019*, Article 3905094. https://doi.org/10.1155/2019/3905094

Hubert, G., Artola, L., & Regis, D. (2015). Impact of scaling on the soft error sensitivity of bulk, FDSOI and FinFET technologies due to atmospheric radiation. *Integration*, *50*, 39-47. https://doi.org/10.1016/j.vlsi.2015.01.003

Jiang, J., Xu, Y., Ren, J., Zhu, W., Lin, D., Xiao, J., Kong, W., & Zou, S. (2018). Low-cost single event double-upset tolerant latch design. *Electronics Letters*, *54*(9), 554-556. https://doi.org/10.1049/el.2018.0558

Kastensmidt, F., & Rech, P. (Eds). (2015). *FPGAs and Parallel Architectures for Aerospace Applications: Soft Errors and Fault-Tolerant Design*. Springer. https://doi.org/10.1007/978-3-319-14352-1

Ke, J., Huang, H., Sun, P., Abuogo, J., Zhao, Z., & Cui, X. (2018). Influence of parasitic capacitances on transient current distribution of paralleled SiC MOSFETs. In *2018 1st Workshop on Wide Bandgap Power Devices and Applications in Asia (WiPDA Asia)* (pp. 88-93). IEEE Publishing. https://doi.org/10.1109/WiPDAAsia.2018.8734667

Lwin, N. K. Z., Sivaramakrishnan, H., Chong, K. S., Lin, T., Shu, W., & Chang, J. S. (2019). Single-event-transient resilient memory for DSP in space applications. In *2018 IEEE 23rd International Conference on Digital Signal Processing(DSP)* (pp. 1-5). IEEE Publishing. https://doi.org/10.1109/ICDSP.2018.8631639

Mamaluy, D., & Gao, X. (2015). The fundamental downscaling limit of field effect transistors. *Applied Physics Letters*, *106*(19), 1-6. https://doi.org/10.1063/1.4919871

Sawamura, H., Iguchi, T., & Handa, T. (2003). Soft errors of semiconductors caused by secondary cosmic-ray neutrons. In O. Takaaki & F. Tokio (Eds.), *Proceedings of the 2002 Symposium on Nuclear Data* (pp. 271-276). Japan Atomic Energy Research Institute. http://dx.doi.org/10.11484/JAERI-Conf-2003-006

Sayil, S. (2016). *Soft Error Mechanisms, Modeling and Mitigation*. Springer. https://doi.org/10.1007/978-3-319-30607-0

Sayil, S., Shah, A. H., Zaman, M. A., & Islam, M. A. (2017). Soft error mitigation using transmission gate with varying gate and body bias. *IEEE Design & Test*, *34*(1), 47-56. https://doi.org/10.1109/MDAT.2015.2499272

Sielewicz, K. M., Rinella, G. A., Bonora, M., Giubilato, P., Lupi, M., Rossewij, M. J., Schambach, J., & Vanat, T. (2017). Experimental methods and results for the evaluation of triple modular redundancy SEU mitigation techniques with the Xilinx Kintex-7 FPGA. In *2017 IEEE Radiation Effects Data Workshop (REDW)* (pp. 1-7). IEEE Publishing. https://doi.org/10.1109/NSREC.2017.8115451

Weulersse, C., Houssany, S., Guibbaud, N., Segura-Ruiz, J., Beaucour, J., Miller, F., & Mazurek, M. (2018). Contribution of thermal neutrons to soft error rate. *IEEE Transactions on Nuclear Science*, *65*(8), 1851-1857. https://doi.org/10.1109/TNS.2018.2813367

Wirthlin, M., Keller, A., McCloskey, C., Ridd, P., Lee, D. S., & Draper, J. (2016). SEU mitigation and validation of the LEON3 soft processor using triple modular redundancy for space processing. In *Proceedings of the 2016 ACM/SIGDA International Symposium on Field-Programmable Gate Arrays* (pp. 205-214). ACM Publishing. https://doi.org/10.1145/2847263.2847278

Yan, Z., Shi, Y., Liao, W., Hashimoto, M., Zhou, X., & Zhuo, C. (2020). When single event upset meets deep neural networks: observations, explorations, and remedies. In *2020 25th Asia and South Pacific Design Automation Conference (ASP-DAC*) (pp.163-168). IEEE Publishing. https://doi.org/10.1109/ASP-DAC47756.2020.9045134

Pertanika J. Sci. & Technol. 31 (4): 1937 - 1955 (2023)

PERTANIKA JOURNALS

SCIENCE & TECHNOLOGY

Journal homepage: http://www.pertanika.upm.edu.my/

Nutrient Leaching Losses from Continuous Application of Washed Rice Water on Three Contrasting Soil Textures

Abba Nabayi[1,2], Christopher Boon Sung Teh[1]*, Ngai Paing Tan[1] and Ali Kee Zuan Tan[1]

[1]Department of Land Management, Faculty of Agriculture, Universiti Putra Malaysia, 43400 UPM, Serdang, Selangor, Malaysia

[2]Department of Soil Science, Faculty of Agriculture, Federal University Dutse, PMB 7156, Ibrahim Aliyu bye-pass Jigawa state, Nigeria

ABSTRACT

Washed rice water (WRW) is often used as liquid plant fertilizer. However, there is no study on nutrient leaching of soils due to frequent WRW application. Therefore, a column study was undertaken to evaluate the rate of nutrient leaching losses, nutrient retention, and recovery of elements in leachates of three different soil textures irrigated with WRW. The treatments were 3 soil textures and 2 water types. The treatments were evaluated for 8 weeks, and the soils and leachates were measured biweekly. Factorial and repeated measurements in a completely randomized design were therefore employed. Higher cumulative leaching of the elements was found in sandy clay loam soil with 666.29, 378.13, 138.51, 50.82, 44.61, and 27.30 mg L^{-1} of K, P, Mg, Ca, NH_4^+-N, and NO_3^--N, respectively. Higher percentages of elements recovery in leachate were found in the sandy clay loam soil with a range of increase by 37.8–283.1% than the other two soil textures. In contrast, after 8 weeks of WRW application, the clay and silt loam soils had a range of increase in nutrient retention by 0.43–1358.5% than the sandy clay loam, with P and NO_3^--N being the highest and the lowest elements retained, respectively, for all soil textures. This study showed that frequent WRW disposal on sandy textured soils risks higher environmental contamination, mainly due to the soil's lower water retention and nutrients, leading to nutrient leaching. Therefore, organic amendments should be added to sandy textured soils.

Keywords: Contamination, environment, leaching, nutrients, nutrient retention, soil texture

ARTICLE INFO

Article history:
Received: 29 June 2022
Accepted: 11 October 2022
Published: 13 June 2023

DOI: https://doi.org/10.47836/pjst.31.4.20

E-mail addresses:
abba.nabayi@fud.edu.ng (Abba Nabayi)
chris@upm.edu.my (Christopher Boon Sung Teh)
ngaipaing@upm.edu.my (Ngai Paing Tan)
tkz@upm.edu.my (Ali Kee Zuan Tan)
* Corresponding author

ISSN: 0128-7680
e-ISSN: 2231-8526

INTRODUCTION

Milled rice is washed prior to cooking to remove the bran, dust, and dirt from the rice (Juliano, 1993). However, rice washing removed a significant amount of water-soluble nutrients from the rice into the washed rice water (WRW), and these leached nutrients could be used as a liquid plant nutrient source and soil amendment (Nabayi, Teh, et al., 2021). The WRW nutrient contents depend on the rice washing rates: the volume of water used, how long and how aggressively the rice is washed, as well as the time the WRW was kept before use. These factors have all been found to affect the concentration of the elements in WRW (Nabayi, Sung, Zuan & Paing, 2021; Nabayi, Sung, Zuan, Paing & Akhir, 2021). Several studies (Juliano, 1993; Wulandari et al., 2012) have reported the N, P, K, Ca, Mg, and S contents of WRW to range from 40 to 16,306 mg L^{-1}. Furthermore, He, Feng, Hu et al. (2016) reported that WRW has concentrations of NO_3^-,NO_2^-, NH_4^+, total N, and total P in the range of 4.19–10.14, 0–0.08, 2.57–39.72, 51.26–84.79, and 23.41–58.12 mg L^{-1}, respectively. Therefore, Siagian (2018) stated that the indiscriminate disposal of WRW is harmful to the environment (e.g., via N and P pollution).

Nutrient leaching varies with soil properties and rainfall amount. This problem is problematic for highly weathered tropical soils, e.g., Oxisols and Ultisols, characterized by low nutrient retention capacity and rapid organic residue decomposition (Ishak & Jusop, 2010). The leaching of nutrients is mainly controlled by the soil type and the soil's sand and clay contents (Tahir & Marschner, 2017). Malaysian soils range widely in texture, from having as low as 3% (sandy soils) to over 90% (clayey soils) of clay content. The average amount of sand in Malaysian soils is 41%, nearly the same as that of the clay content, 43% (Teh et al., 2017). Malaysian soils have bulk density values ranging from 0.8 to 1.9 Mg m^{-3} (Teh et al., 2017), depending on the soil management practices. Differences in the soil bulk directly affect soil porosity, determining soil water retention. Sandy soils usually have higher void ratios, leading to a higher leaching rate than clayey textured soils (Tahir & Marschner, 2017). Depending on the soil compaction, organic matter content, and soil texture, different soils have different saturation, field capacity, and permanent wilting points. For Malaysian soils, the volumetric soil water content at saturation, field capacity, and permanent wilting point can range between 36–89%, 10–67%, and 3–49%, respectively, giving the available volumetric soil water content between 1% and 13% (Teh et al., 2017). Therefore, in contrast to its clayey soils, sandy soils would experience larger nutrient leaching due to the former soils' higher porosity and hydraulic conductivity. Nutrient retention is typically low in sandy soils, and therefore, 20–80% of applied nutrients would be leached or runoff into ground and surface waters (Manevski et al., 2015; Yaghi & Hartikainen, 2013). Waste nutrients flow easily into the estuary because of the inherent properties of hydrological connectivity (Yin et al., 2020). If wastewater's soluble reactive P concentration exceeds 0.04 mg L^{-1}, eutrophication may develop (Zeng et al., 2016).

Similarly, because conventional K fertilizers are very soluble, a large amount of K might be lost through leaching (Alfaro et al., 2004).

WRW contains nutrients in appreciable quantities, including N and P, which found their way to the water bodies and environments; N and P are the two main sinks of all domestic and industrial waste. The improper disposal of the WRW could accumulate these elements in water bodies and the groundwater, resulting in eutrophication that threatens humans and marine life (He, Feng, Peng, et al., 2016). Many studies have reported using WRW as liquid fertilizer to increase plant growth, and they attributed the plant increased growth to the nutrients contained in the WRW (Bahar, 2016; Sairi et al., 2018; Wardiah et al., 2014). However, these WRW nutrients are in soluble forms, which makes them prone to leaching. Different soil textures exhibit different water and nutrient retention characteristics, with sandy soils having lower nutrient retention capabilities (Matichenkov et al., 2020). WRW is beneficial in what is probably the first and most in-depth study on WRW (Nabayi, Sung, Zuan, Paing & Akhir 2021), but what is still lacking is the information on nutrient losses when WRW have to be applied frequently (such as daily). Therefore, there is a need to assess the nutrient leaching rate of different soil textures for a short-term period to guide how different soil textures behave when subjected to a continuous WRW application. Hence, the objectives of the study were: (1) to determine the nutrients: NH_4^+–N, NO_3^-–N, P, K, Ca, and Mg leaching losses from different soil textures under continuous WRW application, and (2) to determine the soil nutrient retention and element percent recovery from the leachate of these soils due to the continuous WRW application.

MATERIALS AND METHODS

Soil Collection

Three soils with contrasting textures (i.e., sandy clay loam, silt loamy, and clay) were collected from various locations in Universiti Putra Malaysia (UPM), Faculty of Agriculture complex (2.984761° N, 101.7336° E). All soils were taken from a depth of 0-0.3 m. A preliminary survey was carried out to assess the soil textures before the soil collection. The soils (separately) were collected using a shovel and auger, mixed thoroughly, and air-dried in the laboratory (Department of land management, UPM). In addition, disturbed and undisturbed (using core samplers) soil samples were also collected to determine other physical and chemical properties.

Soil and WRW Preparation and Analysis

Washed rice water was prepared in the laboratory using commercially available medium-grained rice (Rambutan brand) (Padiberas Nasional Berhad, Malaysia). Fresh WRW was prepared in the volumetric water-to-rice ratio of 3:1, the recommended water-to-

rice washing ratio by Nabayi, Sung, Zuan, and Paing (2021) and Nabayi, Sung, Zuan, Paing, and Akhir (2021). The mixture was obtained using a mixing machine (Bossman Kaden Matte BK-100S, Japan) at 80 rpm (0.357g) for 90 seconds. The mixture was then separated using sieves (<0.5 mm sizes). The WRW was only prepared during application time to preserve its freshness. Atomic absorption spectrophotometer (AAS) (Perkin Elmer, PinAAcle, 900T, Waltham, MI, USA) was used to determine K, Ca, and Mg elements, while P was determined by Auto Analyzer (AA) (Leachat QuikChem FIA+ 8000 series, Ontario, Canada). NH_4^+–N and NO_3^-–N were determined by the Kjeldahl procedure (Stevenson, 1996).

Soil pH was measured in a soil-water suspension with a soil: water ratio of 1:2.5 (McLean, 1983) using the 827pH lab meter (Metrohm AG, Zurich, Switzerland). The combustion method measured soil total C and N (Skjemstad & Baldock, 2007) using the Leco CR-412 Carbon Determinator (LECO Corp., St. Joseph, MI, USA). The contents of exchangeable soil bases (K, Ca, and Mg) and cation exchange capacity (CEC) were assessed by AAS and AA, respectively, after being extracted by the leaching method using neutral 1 M ammonium acetate (NH_4OAc) solution (Thomas, 1982). Soil available P was extracted using the Bray II method (Bray & Kurtz, 1945) and determined using AA (Leachat QuikChem FIA+ 8000 series, Ontario, Canada).

The pipette method determined soil particle size analysis (Gee & Bauder, 1986). The pressure plate method measured the soil water retention curve for matric potentials 0.0 to -1.5 MPa (Richards, 1947). Soil water content at saturation (SAT), field capacity, and the permanent wilting point is the amount of water held in the soil at 0.0, -0.33, and -1.5 MPa, respectively. Volumetric soil moisture contents were determined following Gardner (1986).

Preparation of Soil Columns

Each soil texture was air-dried and sieved through a 4-mm sieve, removing the stones and soil clods. Soil columns were constructed and fitted using PVC tubing and end caps on the bottom. Drainage holes of about 0.3 cm were made through the caps' end and attached to each column's end. Each column measured 78 mm in diameter, and 300 mm in length, giving a volume of 1433.7 cm^3. A plastic net was cut and placed at the bottom of each tube, followed by 100 g of coarse sand to prevent waterlogging. The concave part of the end cap that extended below the base of the PVC column was filled with sand (Figure 1). Each soil column was packed with air dry weight equivalent of about 2.15

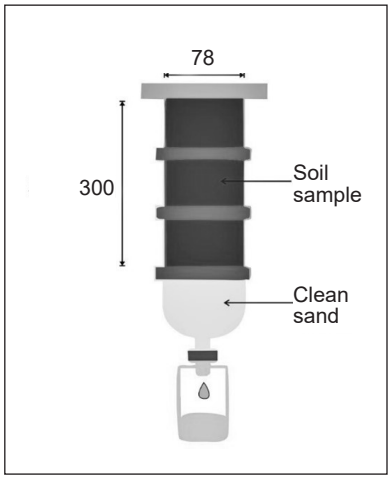

Figure 1. Lysimeter column set-up
Note. Dimension in mm

kg soil via packing down the columns with concurrent soil addition. All the columns, irrespective of their soil texture content, were finally packed to have a bulk density of 1.5 Mg m^{-3}.

Soil Column Incubation and Leaching

For 8 weeks, the columns were incubated at a constant temperature and relative humidity of 28 ^{o}C and 65%, respectively. A total of 18 columns were used, with 9 (3 soil textures replicated 3 times) receiving WRW treatments, while the remaining 9 (3 soil textures replicated 3 times) receiving tap water treatment. Before the application of either WRW or tap water, the dry soils, after packing, were wet to their initial saturation level (SAT) moisture content. The amount of water added was computed by multiplying the SAT moisture content of each soil texture by the volume of the PVC tube. The water was added slowly with glass to prevent water ponding and pores clogging and help diffuse water drops. After 12 hrs of the initial wetting, the application of the treatment (WRW or tap water) started. About 5 mm equivalent of either water type was applied once daily. Leachate was collected using a plastic bottle attached to the leaching tube to minimize evaporation from each column for about 24 hrs after the start of the leaching event. The leachate collected was measured daily before a subsequent watering event and transferred into a plastic vial. The leachates collected were pooled biweekly and measured for NH_4^+–N and NO_3^-–N using the Kjeldahl digestion and distillation procedure (Stevenson, 1996). About 100 mL of leachates samples were filtered (Whatman No. 2, 11µm size) and analyzed for P, K, Ca, and Mg after acidifying (using 0.1N HCl) biweekly using AAS (Perkin Elmer, PinAAcle, 900T, Waltham, MI, USA). The different soils under WRW treatment were also sampled biweekly for volumetric moisture content determination.

Data Analysis

The overall experimental design used was completely randomized in factorial arrangement, which comprised 3 soil textures and 2 water types with 3 replications (18 columns). Leachate samples were collected from each leaching column daily for 8 weeks, while the nutrient analysis was carried out biweekly. Nutrient retention of the elements in the soils was determined using Equation 1, and the mass balance analysis was used to estimate the percentage of element recovery in the leachate using Equation 2, as given by Laird et al. (2010):

$$Nxi = Nwrx - NLi \quad [1]$$

$$R_{xi} = \frac{(X_{li} - X_c)*100}{X_{mwi}} \quad [2]$$

where *Nxi* is the mass retained for *X* element for column i, *Nwrx* is the mass of *X* element present in the WRW, *NLi* is the mass of the element leached *L* from column *i*, R_{xi} is the percent nutrient recovery of *X* element for column *i,* X_{Li} is the mass of *X* element that leached from column *i*, X_c is the average mass of *X* element that leached from control columns for the different soil texture, and X_{mw} is the mass of *X* element in the WRW that was added to column *i*. The nutrient retention was only analyzed for WRW treatment based on the different soil textures. Statistical analysis was conducted using Minitab for Windows, *version* 20 (Pennsylvania State University, USA). Percent element recovery and soil nutrient retention were analyzed using one-way ANOVA, while nutrient leaching was analyzed factorially with the soil texture and sampling weeks as factors. Significant means were separated using Tukey's Studentized Range test at a threshold probability level of 5%.

RESULTS AND DISCUSSION

Effect of WRW Application on Nutrient Leaching

The highest leaching of all elements was consistently observed in sandy clay loam soil, which differed significantly ($p<0.01$) from the other two soil types that mostly have similar losses with each other irrespective of the sampling week. The leaching of the elements increased in the order of sandy clay loam> silt loam> clay for NH_4^+–N, NO_3^-–N, P, K, Ca, and Mg. In the last week of the experiment (8 weeks), the sandy clay loam soil had a range increase in NH_4^+–N, NO_3^-–N, P, K, Ca, and Mg leaching by 29.6–33.6, 21.3–25.9, 34.5–36.8%, 31.9–40.9%, 26.9–39.9%, and 30.3–46.5%, respectively, then the silt loam and clay soils (Figure 2). The leaching losses for other elements in clay and silt loam soils are constant over time. Significantly higher leaching of the elements in sandy clay loam soil could be attributed to its lower water and nutrient retention relative to the other two soils. Sandy soils usually have low nutrient retention capabilities (Matichenkov et al., 2020). The lower retention of nutrients in the sandy clay loam could also be seen in its comparatively lower water-holding capacity than the other two soil textures (Table 1). The leaching of the elements from these soils due to the continuous WRW application indicates the nutrient leaching potentials of WRW to the groundwater, particularly in sandy soils, because of its lower water retention that led to the higher leaching volume, as shown in Figure 3a. Sandy soils have a higher leaching rate than clayey textured soils due to the higher void ratios of the former (Tahir & Marschner, 2017).

The physical structure and water-holding capacity have been suggested as the main factors that affect the soil retention capacities of NO_3^- and P (Pratiwi et al., 2016). The addition of WRW over time has slightly raised the volumetric moisture contents of the soils used in this study (Figure 3b). Sandy clay loam soil had the least response to WRW amendment application, with only a 4.8% increase in volumetric moisture content at week

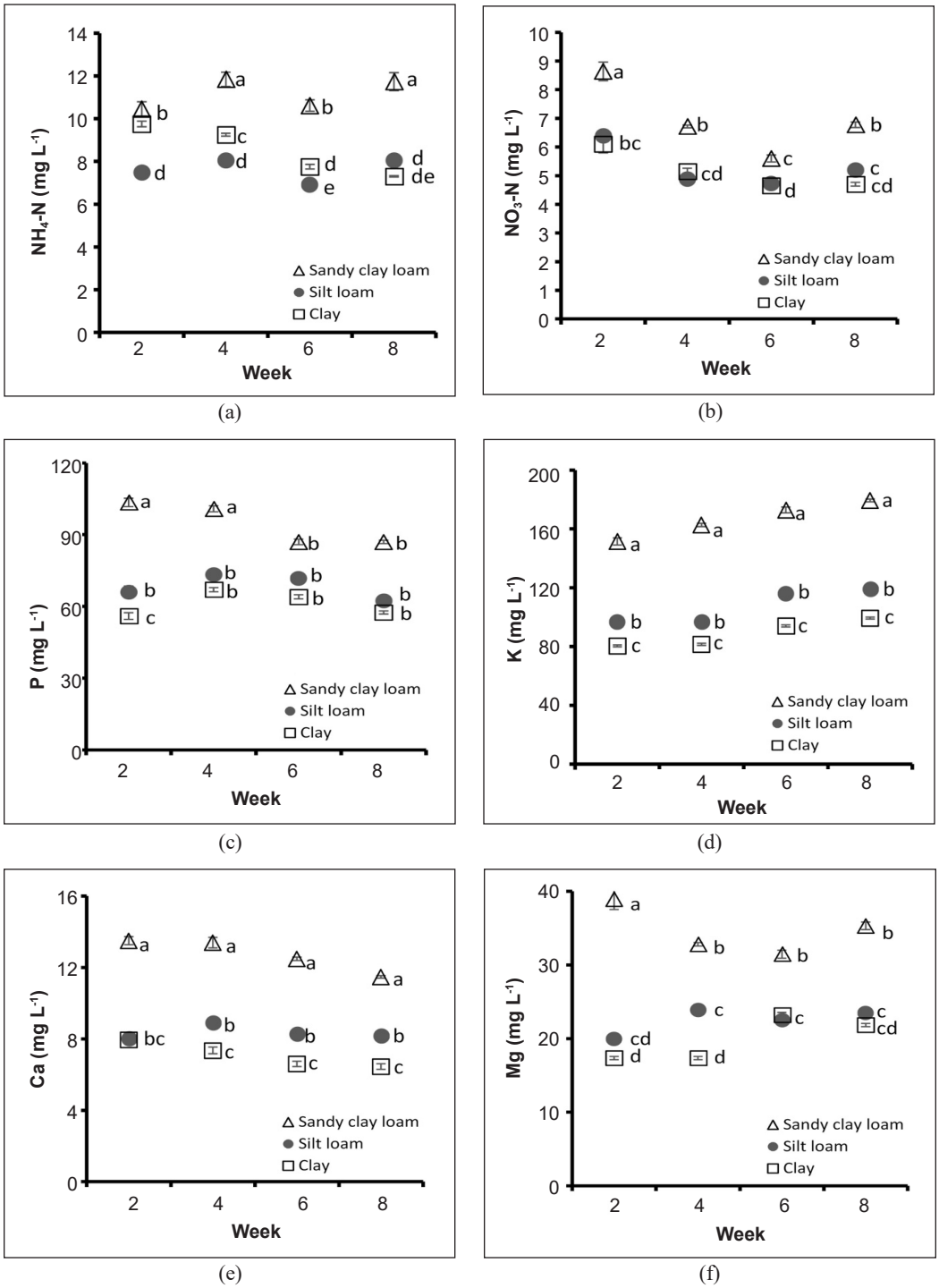

Figure 2. Means (± SE) of the interaction effect between sampling week and soil texture on the leaching of (a) NH_4^+–N, (b) NO_3^-–N, (c) P, (d) K, (e) Ca, and (f) Mg. Within the same chart, means with different letters are significantly different ($p<0.05$) based on the Tukey test

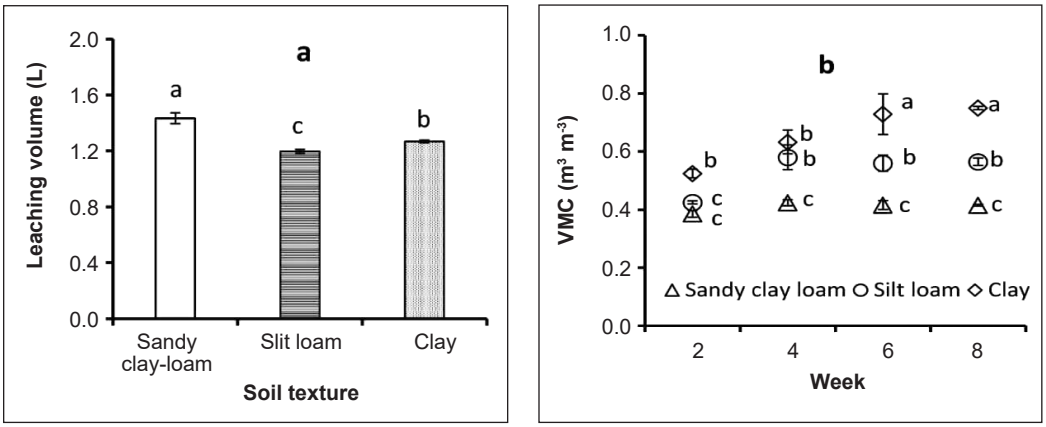

(a) (b)

Figure 3. Means (± SE) of (a) leaching volume under continuous WRW application and (b) interaction effect between the soil texture and sampling week on volumetric moisture content. Within the same chart, means with different letters are significantly different ($p<0.05$) based on the Tukey test

Table 1
Physicochemical properties of the different soils used in the study

Parameters	Sandy clay loam	Silt loam	Clay
pH	5.32±0.21	6.3±0.11	6.8±0.26
EC (dS m^{-1})	0.72±0.05	1.03±0.10	0.62±0.04
Particle size distribution (%)			
Clay (<2 µm)	21.59±1.21	17.8±1.01	65.19±2.76
Silt (2-50 µm)	6.63±0.67	54.69±1.37	9.28±0.07
Sand (> 50 µm)	71.78±3.41	27.51±1.62	25.53±1.60
Texture class (USDA)	Sandy clay loam	Silt loam	Clay
Total C (%)	1.01±0.05	1.47±0.10	1.75±0.03
Total N (%)	0.08±0.01	0.12±0.01	0.15±0.01
NH_4^+–N (mg kg^{-1})	38.8±0.24	31.9±1.26	34.54±1.75
NO_3^-–N (mg kg^{-1})	3.70±0.12	5.96±0.42	4.85±0.32
P (mg kg^{-1})	12.4±0.41	23.6±1.02	19.2±0.81
K (cmol kg^{-1})	2.70±0.08	0.98±0.05	1.51±0.03
Ca (cmol kg^{-1})	7.89±0.52	5.41±0.11	7.79±0.22
Mg (cmol kg^{-1})	2.81±0.11	1.72±0.03	0.95±0.05
Bulk density (Mg m^{-3})	1.50±0.04	1.60±0.04	1.55±0.02
CEC (cmol kg^{-1})	7.24±0.13	6.33±0.14	11.24±0.30
Volumetric soil water content (m^3 m^{-3})			
Saturation	0.62±0.03	0.73±0.02	0.78±0.03
Field capacity	0.31±0.01	0.37±0.01	0.45±0.01
Permanent wilting point	0.13±0.01	0.21±0.01	0.26±0.01

8 relative to the second week of sampling. The addition of amendments found improved soil aggregate and pore structure and subsequent increase in water holding capacity of soils (Liu et al., 2020; Villagra-Mendoza & Horn, 2018). In this study, the improvement in volumetric moisture content could be due to WRW elements, particularly the C content that is transferred altogether during the watering. Continuous rice washing will increase the nutrients leaching from the rice into the WRW. The WRW contains a greater amount of carbon (3.63 g L^{-1}) (Table 2), which could help bind the soil particles together, thereby improving the water and nutrient-holding capacity of the soil. Nabayi, Sung, Zuan, Paing, and Akhir (2021) reported C among the greater elements leached from washing rice, which could help improve the soil's retention capacity. The significantly lower retention of the NO_3^-–N in the soils, especially the sandy clay loam, could be attributed to the lower retention and higher leaching of NO_3^-–N in the soil relative to the other soil textures. Leaching results by Cui et al. (2021) infer that NO_3^-–N is more susceptible to leaching than the P, corroborating our results. The decrease in the concentration of P leaching of the soils relative to what was added from the WRW could be due to the increase in soil P retention or precipitation of P by Ca and or Mg ions, as stated by other studies (Fang et al., 2020; Mitrogiannis et al., 2017). Similarly, Tahir and Marschner (2017) reported lower leaching of inorganic N in clay-amended soil than in sandy soil.

The cumulative leaching of the elements from the different textured soils at the end of the 8-week study was in the order K > P > Mg > NH_4^+–N > Ca > NO_3^-–N. The higher cumulative leaching of K and P could be due to their greater content in the WRW relative to other elements (Table 2). The least Ca leachate recorded in the soils relative to other elements could be attributed to its precipitation by P and other micronutrients such as Zn.

Table 2
Means (± SE) element analyses of washed rice water (WRW) and tap water

Parameters	WRW *	Tap Water
pH	6.53 ± 0.02	6.58 ± 0.02
EC (µS cm^{-1})	372.83 ± 34.53	125.36 ± 28.21
Total C (g L^{-1})	3.63±0.12	0.03 ± 0.002
S (g L^{-1})	0.60±0.04	100 ± 9.64
Total N (mg L^{-1})	80.50 ± 5.20	30.20 ± 4.12
NH_4^+–N (mg L^{-1})	18.88 ± 1.68	1.44 ± 0.04
NO_3^-–N (mg L^{-1})	16.02 ± 1.41	1.45 ± 0.03
P (mg L^{-1})	57.74±3.76	0.05 ± 0.02
K (mg L^{-1})	123.84±14.21	5.74 ± 0.15
Ca (mg L^{-1})	18.68±2.10	10.95 ± 0.06
Mg (mg L^{-1})	19.37±1.76	0.97 ± 0.06

Note. * the WRW was obtained at 3:1 volumetric water-to-rice ratio washed at 80 rpm

Kleinman et al. (2002) and Nabayi, Sung, Zuan, Paing, and Akhir (2021) found a positive relationship between Ca and P which indicates that the availability of one would affect the other. The higher cumulative leaching of K, irrespective of the soil texture, could be due to its monovalent nature, which makes it more easily leachable than other elements. Monovalent elements such as K, NH_4^+–N, and NO_3^-–N, among others, have higher solubility relative to their divalent counterparts (i.e., Ca and Mg) (Petrucci et al., 2011) and, therefore, leached easily (Nabayi, Sung, Zuan, Paing & Akhir, 2021). For soil texture, the sandy clay loam had higher cumulative leaching of the elements with 666.29, 378.13, 138.51, 50.82, 44.61, and 27.30 mg L^{-1} of K, P, Mg, Ca, NH_4^+–N, and NO_3^-–N, respectively, while the least were mostly obtained in the textured clay soil (Figure 4). After 8 weeks of WRW application, the clay and silt loam soils were shown to retain the WRW nutrients more than the sandy clay loam soil. The higher retention in clay and silt loam soils could be due to their greater proportions of smaller particle sizes with higher surface area to attract the elements rather than being allowed to leach, as was the case in the sandy clay loam soil. Clay soil is dominated by micropores which can retain higher water and nutrients than sandy soil (Bollyn et al., 2017). Tahir and Marschner (2017) reported that amending sandy soil with clay soil decreased N and P nutrient leaching and increased their retention in the sandy amended soil.

The summary of ANOVA for the leachate analyzed parameters under different soil textures, water types, and weeks is presented in Table 3. The interaction between soil texture, water type, and week on NH_4^+–N and NO_3^-–N, P and K, and Ca and Mg, respectively, showed that significantly higher elements were observed in the WRW-treated soils while the least was obtained in the tap water treated soils (Figures 5 to 7). Under all the tap water treatments, the leaching of the nutrients was in the order Ca > K > Mg > P > NH_4^+–N > NO_3^-–N. The tap water treatments, irrespective of the soil texture, leached lower NH_4^+–N (152.6-206.6%), NO_3^-–N (37.1–170%), P (1509.8–1815.9%), K (896.4–1080.0%), and Mg (329.1–431.1%) than the WRW treated soils. On the other hand, the tap water-treated soils had higher leaching of Ca (25.5–47.7%) than the WRW-treated soils.

Table 3
Summary of analysis of variance (ANOVA) showing Pr > F for leachate analyzed parameters under different soil texture (ST), water type (WT), and week (W)

Parameters	ST	WT	W	STxWT	STxW	WTxW	STxWTxW
NH_4^+–N	**	**	**	**	**	ns	*
NO_3^-–N	**	**	**	**	**	ns	*
P	**	**	**	**	**	**	**
K	**	**	**	**	ns	**	ns
Ca	**	**	ns	ns	**	**	**
Mg	**	**	ns	***	**	*	**

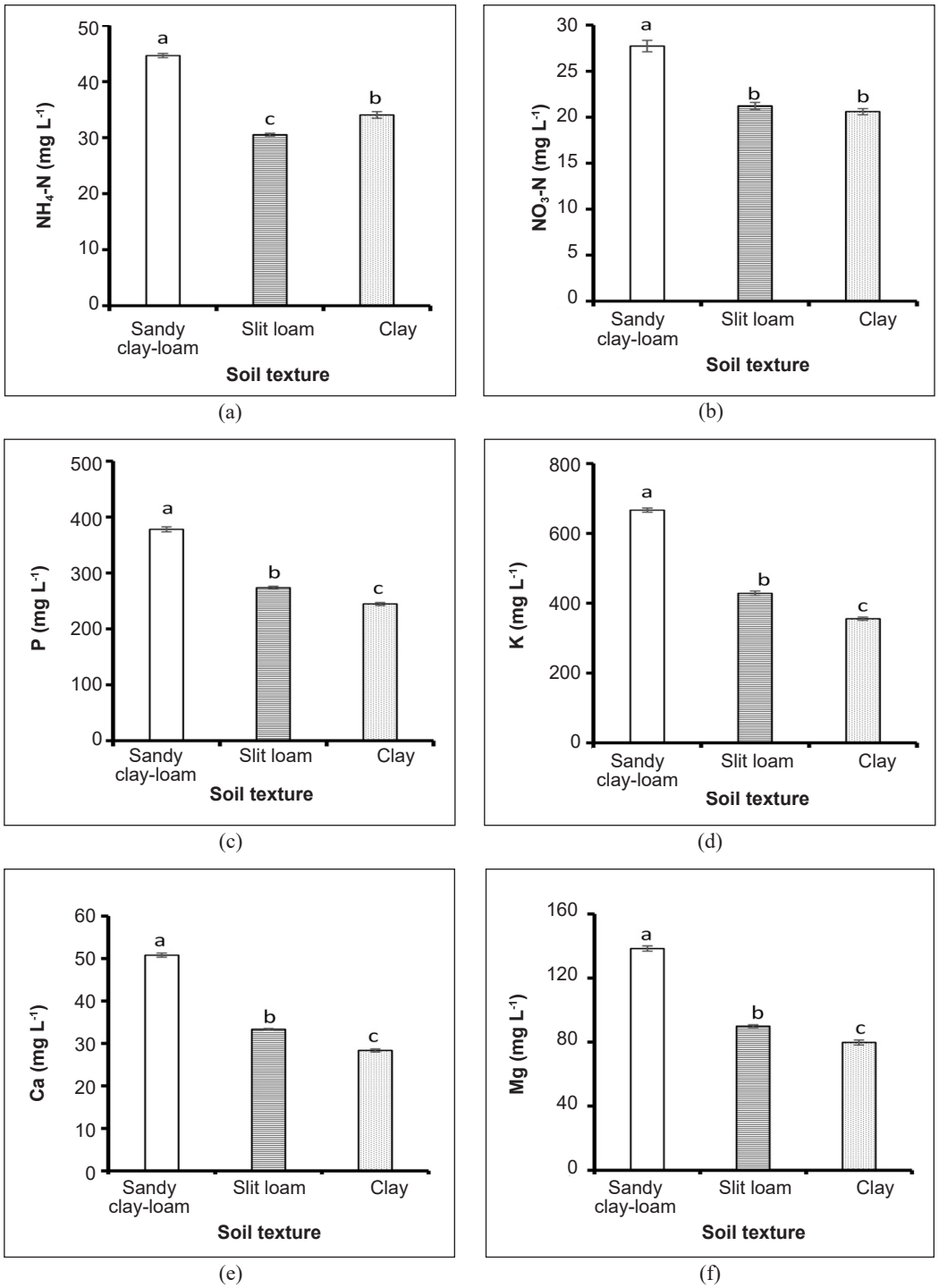

Figure 4. Cumulative leaching (±SE) after 8 weeks for (a) NH_4^+–N, (b) NO_3^-–N, (c) P, (d) K, (e) Ca, and (f) Mg under different soil textures. Within the same chart, means with different letters are significantly different ($p<0.05$) based on the Tukey test

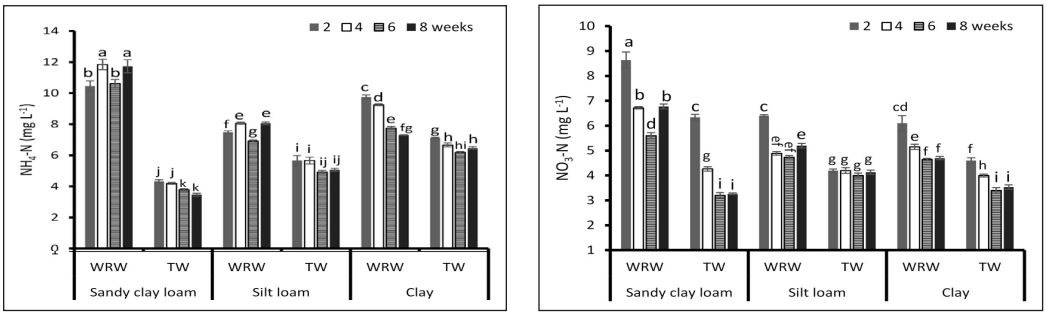

(a) (b)

Figure 5. Means (± SE) of an interaction effect between ST, WT, and W on (a) NH_4^+–N and (b) NO_3^-–N leaching. Within the same chart, means with different letters are significantly different ($p<0.05$) based on the Tukey test (means separations based on all treatment combinations). WRW washed rice water, TW tap water, ST soil texture, WT water type, W sampling week

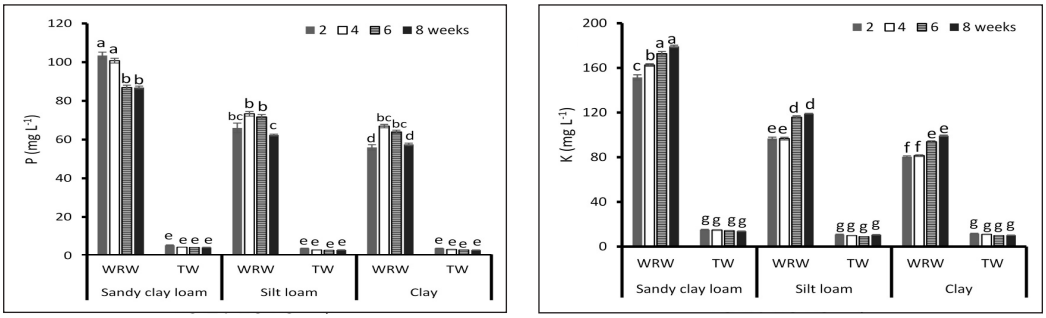

(a) (b)

Figure 6. Means (± SE) of an interaction effect between ST, WT, and W on (a) P and (b) K leaching. Within the same chart, means with different letters are significantly different ($p<0.05$) based on the Tukey test (means separations based on all treatment combinations). WRW washed rice water, TW tap water, ST soil texture, WT water type, W sampling week

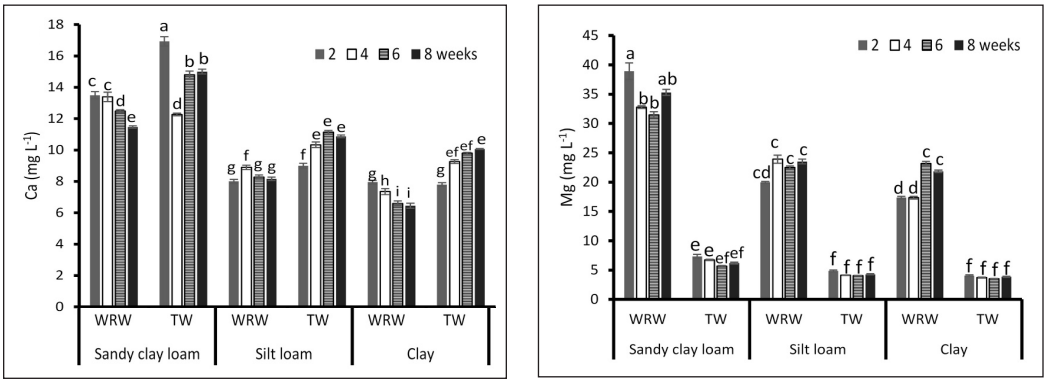

(a) (b)

Figure 7. Means (± SE) of an interaction effect between ST, WT, and W on (a) Ca and (b) Mg leaching. Within the same chart, means with different letters are significantly different ($p<0.05$) based on the Tukey test (means separations based on all treatment combinations). WRW washed rice water, TW tap water, ST soil texture, WT water type, W sampling week

Soil Nutrient Retention and Percentages of Elements Recovery in Leachate

The mass of the elements added with the WRW, nutrient retention in the soil after WRW application for 8 weeks, and percentage mass of element recovery in leachate is shown in Table 4. In contrast to the cumulative nutrients leached from different soil textures, there was higher retention of the nutrients due to the WRW application observed in clay soil, followed by silt loam, while the sandy clay loam soil had the least. The clay and silt loam textured soils had a range increase of 3.9–18.2% NH_4^+–N, 0.43–8.4% NO_3^-–N, 25.4–1358.5% P, 18.1–187.5% K, 5.3–30.1% Ca, and 25.2–705% Mg than the sandy clay loam textured soil. The K was the highest element leached and retained regardless of soil texture. Despite its solubility, the higher retention of the K could be associated with its greater amount (relative to other elements) in the WRW (Table 2). Despite K being easily leached due to its higher solubility (Nabayi, Sung, Zuan, Paing & Akhir, 2021; Petrucci et al., 2011), it also can replace elements in the soil surface via adsorption. The higher retention of other elements in the clay compared to the silt loam and sandy clay loam soils could be attributed to the soil's higher nutrient and water retention capacity, indicated in its higher CEC (Table 1).

The availability of nutrients in soils and streams is mainly affected by the soil colloids, and the smaller the colloids, the higher the retention sites of the soils (Bollyn et al., 2017). The soil colloids may bind large portions of readily available plant nutrients and organic matter (Carstens et al., 2018). Clay soil is dominated by micropores that retain higher water and nutrients than sandy soil. Tahir and Marschner (2017) reported that amending sandy soil with clay soil decreased N and P nutrient leaching and increased their retention in the sandy amended soil. However, the least retained element was Mg, irrespective of the soil texture, which was negative in sandy clay loam (Table 4). The negative retention in sandy clay loam indicated the leaching of Mg greater than the amount added through WRW application, and this surplus came from the inherent soil Mg content. The lower retention of Mg in all soil textures could be associated with the lower Mg content of the WRW. The significantly ($p<0.01$) higher percentage recovery of the elements in the leachate was recorded in the sandy clay loam, which differed from the other soil textures.

The increase in the recovery of the elements was higher in the sandy clay loam leachate by 212.5–283.1% NH_4^+–N, 106.5–128.8% NO_3^-–N, 37.8–55.5% P, 58.6–97.1% K, and 58.6–76.5% Mg. Irrespective of the soil texture, the Ca recovered in the leachate was higher than the Ca content of the WRW, which led to a negative percent recovery (Table 4). The percentage recovery result agrees with the cumulative leachate results (Figure 2), which still highlights the sandy textured soils' inefficiency in retaining nutrients compared to other soil textures. The results ranging from the nutrient leaching of the elements to the percentage of elements recovered in the leachates by the different soil textures, suggested

Table 4
Mass of the elements added with the WRW (mg per column), Nutrient retention in the soil after WRW application for 8 weeks, and percentage mass of element recovery in leachate due to WRW application. The percentage of elements added with the WRW was computed based on mass balance calculations (mass: mass). The percent recovery for each element was calculated by subtracting the average mass of each element recovered in the leachate for columns that did not receive WRW from the mass recovery for columns that did receive WRW, dividing by the mass of the element in the WRW added to the column, and then multiplying by 100

Mass of elements added to the columns with the WRW (mg element per column)						
Soil texture	NH_4^+–N	NO_3^-–N	P	K	Ca	Mg
All soils	30.6	28.22	97	208.06	31.38	32.54
Nutrient retention per column (mg element per column)						
Soil texture	NH_4^+–N	NO_3^-–N	P	K	Ca	Mg
Sandy clay loam	19.42 ± 0.59b	21.28 ± 0.39b	2.46 ± 0.21c	41.46 ± 4.10c	18.66 ± 1.63b	-2.08 ± 0.11c
Silt loam	22.96 ± 0.72a	22.92 ± 0.51a	28.62 ± 2.20b	100.92 ± 6.4b	23.06 ± 2.14ab	10.06 ± 0.57b
Clay	22.08 ± 0.84a	23.08 ± 0.43a	35.88 ± 1.87a	119.22 ± 3.98a	24.28 ± 0.81a	12.60 ± 0.35a
Percentage of elements added with the WRW recovered in the leachate (mg added: mg recovered)						
Soil texture	NH_4^+–N	NO_3^-–N	P	K	Ca	Mg
Sandy clay loam	23.56 ± 4.22a	9.44 ± 2.03a	92.71 ± 4.83a	74.02 ± 11.06a	-6.27 ± 0.76a	86.79 ± 12.94a
Silt loam	7.54 ± 1.31b	4.14 ± 0.32b	67.27 ± 3.82b	46.66 ± 5.84b	-6.37 ± 0.61a	54.70 ± 4.20b
Clay	6.15 ± 0.91b	4.57 ± 0.74b	59.61 ± 3.29c	37.55 ± 4.98c	-6.89 ± 0.69a	49.17 ± 3.12b

Note. Numbers followed by a different letter(s) within the same column differ significantly from one another at a 5% level of significance based on the Tukey test

an improvement in the soil's water and nutrient retention so that these elements can be retained and used by plants.

Though greater improvement is needed in the sandy clay loam, it would also be equally influential in the silt loam and clay soils. In addition, despite the higher recovery of K in the silt loam and clay, the K could create an imbalance in plant nutrient uptake. Adding lower-density organic materials such as biochar and compost could improve the soil's retention of water and nutrients from the WRW. Furthermore, adding the organic amendment would also improve the CEC of the soils, thereby raising their fertility levels. Recent research has demonstrated that using biochar improves soils' ability to retain NO_3^-–N and phosphate-P, hence lowering leaching (Chandra et al., 2020; Matichenkov et al., 2020; Riddle et al., 2018; Wu et al., 2019), which could also reduce the leaching of K, Ca, and Mg due to the improved CEC that will result from the use of the amendment. In addition, applying natural minerals such as zeolite reduced K leaching (Macolino & Zanin, 2014). Soil optimization of mycorrhizal biomass can also decrease element losses

of K, NO_3^-, NH_4^+, and other elements (Cavagnaro et al., 2015). The increase in the soil microbial population can also promote nutrient retention and improve a plant's ability to sequester nutrients, thereby reducing their leaching (Drinkwater et al., 2017). The 38-day leaching study on two contrasting soils by Cui et al. (2021) suggested the addition of mineral-loaded biochar to potentially lower the soil P and NO_3^-–N leaching risk. Similarly, using clay soil to amend sandy soil was also found to increase the retention of N and P by more than 2-fold in the amended soil (Tahir & Marschner, 2017).

The findings of this study show that WRW addition to the contrasting soil textures improves the nutrient contents of the soils. The results agree with Laird et al. (2010), who reported that improved retention of these nutrients in the soil profile should increase the possibility for plants to uptake these nutrients, thus minimizing the risk of environmental pollution and contamination that the accumulation of the leached nutrients would have caused. This study's overall impact will enhance the efficiency of nutrient and water use, reducing the chemical fertilizer need. A long-term field experiment aimed at testing this hypothesis is underway.

The present study is limited to using only a fresh form of WRW for 8 weeks. Washed rice water fermented at different periods exhibits chemical and biological behaviors (Nabayi, Teh et al., 2021) and physically, which could affect the leaching pattern of the different soil textures. On the other hand, though the results reported in this study are tentative, as *a priori* subjecting the soils to WRW application for a longer period will show the soils' water and nutrient retention at full capacity.

CONCLUSION

This study's 8-week leaching experiment demonstrated that continuous application of WRW could potentially lead to surface and groundwater contamination, particularly due to the relatively higher P and K contents of the WRW. Different soil textures responded differently to the WRW application, where the sandy clay loam soil had more leaching losses in terms of nutrient concentrations (37.8–238.1%), and leaching volume (13.1–19.8%), but the other two soil textures (silt loam and clay) had comparable results with each other. The least nutrient and water retention were observed in the sandy clay loam soil, with 26–44% lower than the other two soil textures. This study highlighted the need for amendment strategies to retain these elements in the soils for plant use. Therefore, it is suggested that the WRW should be used as a plant nutrient source rather than discarded for agricultural purposes. It is also recommended that organic material should be added to the soil prior to the WRW application to improve the water and nutrient retention of the soils, particularly for soils high in sand content, and that WRW should be added in small amounts but frequently to minimize the risk of nutrient leaching losses.

ACKNOWLEDGMENTS

The authors acknowledged TETFund Nigeria for providing a Ph.D. scholarship to the first author. The authors also acknowledged colleagues and staff at Universiti Putra Malaysia Selangor Campus for their support and cooperation. This research was funded by the Universiti Putra Malaysia Grant 2022, Geran Inisiatif Putra Siswazah (GP-IPS) (No. GP-IPS/2022/9709600).

REFERENCES

Alfaro, M. A., Jarvis, S. C., & Gregory, P. J. (2004). Factors affecting potassium leaching in different soils. *Soil Use and Management*, *20*(2), 182-189. https://doi.org/10.1111/j.1475-2743.2004.tb00355.x

Bahar, A. E. (2016). Pengaruh pemberian limbah air cucian beras terhadap pertumbuhan tanaman kangkung darat (*Ipomoea reptans* Poir) [Effect of applying washed rice wastewater on the growth of land spinach (*Ipomoea reptans* Poir)]. *Jurnal Ilmiah Mahasiswa Fakultas Pertanian*, *3*(2), 1-9.

Bollyn, J., Faes, J., Fritzsche, A., & Smolders, E. (2017). Colloidal-bound polyphosphates and organic phosphates are bioavailable: a nutrient solution study. *Journal of Agricultural and Food Chemistry*, *65*(32), 6762-6770. https://doi.org/10.1021/acs.jafc.7b01483

Bray, R. H., & Kurtz, L. T. (1945). Determination of total, organic, and available forms of phosphorus in soils. *Soil Science*, *59*(1), 39-46.

Carstens, J. F., Bachmann, J., & Neuweiler, I. (2018). Effects of organic matter coatings on the mobility of goethite colloids in model sand and undisturbed soil. *European Journal of Soil Science*, *69*(2), 360-369. https://doi.org/10.1111/ejss.12510

Cavagnaro, T. R., Bender, S. F., Asghari, H. R., & van der Heijden, M. G. A. (2015). The role of arbuscular mycorrhizas in reducing soil nutrient loss. *Trends in Plant Science*, *20*(5), 283-290. https://doi.org/10.1016/j.tplants.2015.03.004

Chandra, S., Medha, I., & Bhattacharya, J. (2020). Potassium-iron rice straw biochar composite for sorption of nitrate, phosphate, and ammonium ions in soil for timely and controlled release. *Science of the Total Environment*, *712*, Article 136337. https://doi.org/10.1016/j.scitotenv.2019.136337

Cui, S., Kong, F., Li, Y., Jiang, Z., & Xi, M. (2021). Effect of mineral loaded biochar on the leaching performances of nitrate and phosphate in two contrasting soils from the coastal estuary area. *Science of the Total Environment*, *779*, Article 146346. https://doi.org/10.1016/j.scitotenv.2021.146346

Drinkwater, L. E., Schipanski, M., Snapp, S., Jackson, L. E. (2017). Ecologically based nutrient management, In S. Snapp & B. Pound (Eds.), *Chapter 7: Agroecology and Rural Innovation for Development Agricultural Systems (2nd ed.)* (pp. 203-257). Academic Press. https://doi.org/10.1016/B978-0-12-802070-8.00007-4

Fang, L., Li, J. S., Donatello, S., Cheeseman, C. R., Poon, C. S., & Tsang, D. C. W. (2020). Use of Mg/Ca modified biochars to take up phosphorus from acid-extract of incinerated sewage sludge ash (ISSA) for fertilizer application. *Journal of Cleaner Production*, *244*, Article 118853. https://doi.org/10.1016/j.jclepro.2019.118853

Gardner, W. H. (1986). Water content. In A. Klute (Ed.), *Methods of Soil Analysis: Part 1 Physical and Mineralogical Properties* (pp. 493-544) American Society of Agronomy-Soil Science Society of America. https://doi.org/10.2136/sssabookser5.1.2ed.c21

Gee, G. W., & Bauder, J. W. (1986). Particle size analysis. In A. Klute (Ed.), *Methods of Soil Analysis: Part 1 Physical and Mineralogical Properties* (pp. 383-411). American Society of Agronomy-Soil Science Society of America. https://doi.org/10.2136/sssabookser5.1.2ed.c15

He, Q., Feng, C., Hu, Q., Li, R., & Chen, N. (2016). Biological denitrification using rice washing drainage (RWD) as carbon source for removing nitrate from groundwater. *Desalination and Water Treatment*, *57*(46), 21990-21999. https://doi.org/10.1080/19443994.2015.1127780

He, Q., Feng, C., Peng, T., Chen, N., Hu, Q., & Hao, C. (2016). Denitrification of synthetic nitrate-contaminated groundwater combined with rice washing drainage treatment. *Ecological Engineering*, *95*, 152-159. https://doi.org/10.1016/j.ecoleng.2016.06.043

Ishak, C. F., & Jusop, S. (2010). *Weathered Tropical Soils: The Ultisols and Oxisols*. UPM Press.

Juliano, B. O. (1993). *Rice in Human Nutrition.* International Rice Research Institute.

Kleinman, P. J. A., Sharpley, A. N., Wolf, A. M., Beegle, D. B., & Moore Jr, P. A. (2002). Measuring water-extractable phosphorus in manure as an indicator of phosphorus in runoff. *Soil Science Society of America Journal*, *66*(6), 2009-2015. https://doi.org/10.2136/sssaj2002.2009

Laird, D., Fleming, P., Wang, B., Horton, R., & Karlen, D. (2010). Biochar impact on nutrient leaching from a Midwestern agricultural soil. *Geoderma*, *158*(3-4), 436-442. https://doi.org/10.1016/j.geoderma.2010.05.012

Liu, S., Kong, F., Li, Y., Jiang, Z., Xi, M., & Wu, J. (2020). Mineral-ions modified biochars enhance the stability of soil aggregate and soil carbon sequestration in a coastal wetland soil. *Catena*, *193*, Article 104618. https://doi.org/10.1016/j.catena.2020.104618

Macolino, S., & Zanin, G. (2014). Effectiveness of a zeolite-based fertilizer in reducing nutrient leaching in a recently sodded turfgrass. In *XXIX International Horticultural Congress on Horticulture: Sustaining Lives, Livelihoods and Landscapes (IHC2014)* (pp. 73-82). Acta Horticulturae. https://doi.org/10.17660/ActaHortic.2016.1122.10

Manevski, K., Børgesen, C. D., Andersen, M. N., & Kristensen, I. S. (2015). Reduced nitrogen leaching by intercropping maize with red fescue on sandy soils in North Europe: A combined field and modeling study. *Plant and Soil*, *388*, 67-85. https://doi.org/10.1007/s11104-014-2311-6

McLean, E. O. (1983). Soil pH and lime requirement. In A. L. Page, R. H. Miller & D. R. Keeney (Eds.), *Methods of Soil Analysis: Part 2 Chemical and Microbiological Properties* (pp.199-224). American Society of Agronomy-Soil Science Society of America. https://doi.org/10.2134/agronmonogr9.2.2ed.c12

Matichenkov, V., Bocharnikova, E., & Campbell, J. (2020). Reduction in nutrient leaching from sandy soils by Si-rich materials: Laboratory, greenhouse and filed studies. *Soil and Tillage Research*, *196*, Article 104450. https://doi.org/10.1016/j.still.2019.104450

Mitrogiannis, D., Psychoyou, M., Baziotis, I., Inglezakis, V. J., Koukouzas, N., Tsoukalas, N., Palles, D., Kamitsos, E., Oikonomou, G., & Markou, G. (2017). Removal of phosphate from aqueous solutions by

adsorption onto $Ca(OH)_2$ treated natural clinoptilolite. *Chemical Engineering Journal*, *320*, 510-522. https://doi.org/10.1016/j.cej.2017.03.063

Nabayi, A., Sung, C. T. B., Zuan, A. T. K., & Paing, T. N. (2021). Fermentation of washed rice water increases beneficial plant bacterial population and nutrient concentrations. *Sustainability*, *13*(23), Article 13437. https://doi.org/10.3390/su132313437

Nabayi, A., Sung, C. T. B., Zuan, A. T. K., Paing, T. N., & Akhir, N. I. M. (2021). Chemical and microbial characterization of washed rice water waste to assess its potential as plant fertilizer and for increasing soil health. *Agronomy*, *11*(12), Article 2391. https://doi.org/10.3390/agronomy11122391

Nabayi, A., Teh, C. B. S., Ngai, T. P., & Tan, A. K. Z. (2021). Wastewater from washed rice water as plant nutrient source: Current understanding and knowledge gaps. *Pertanika Journal of Science and Technology*, *29*(3), 1347-1369. https://doi.org/10.47836/pjst.29.3.11

Petrucci, R. H., Herring, F. G., Madura, J. D., & Bissonnette, C. (2011). *General Chemistry: Principles and Modern Applications.* Pearson Prentice Hall.

Pratiwi, E. P. A., Hillary, A. K., Fukuda, T., & Shinogi, Y. (2016). The effects of rice husk char on ammonium, nitrate and phosphate retention and leaching in loamy soil. *Geoderma*, *277*, 61-68. https://doi.org/10.1016/j.geoderma.2016.05.006

Richards, L. A. (1947). Pressure-membrane apparatus, construction and use. *Agricultural Engineering*, *28*(10), 451-454.

Riddle, M., Cederlund, H., Schmieder, F., & Bergström, L. (2018). Magnetite-coated biochar as a soil phosphate filter: From laboratory to field lysimeter. *Geoderma*, *327*, 45-54. https://doi.org/10.1016/j.geoderma.2018.04.025

Sairi, F., Ismail, N., & Ibrahim, N. (2018). The effect of FRAW towards the growth of chilli seedlings and its associated microorganisms. *Malaysian Journal of Microbiology*, *14*(6), 606-610.

Siagian, A. S. (2018). *Respon pemberian pupuk organik cair air cucian beras terhadap pertumbuhan dan produksi tanaman selada hijau* (*Lactuca Satvia L.*) [Response of organic fertilizer to liquid water wash on growth and production of lettuce (*Lactuca sativa L)*]. (Unpublished diploma thesis). University of Medan Area Faculty of Agricultural, Indonesia. http://repository.uma.ac.id/handle/123456789/10578

Skjemstad, J. O., & Baldock, J. A. (2007). Total and organic carbon. In M. R. Carter & E. G. Gregorich (Eds.), *Soil Sampling and Methods of Analysis* (2nd ed.) (pp. 225-239). CRC Press. https://doi.org/10.1201/9781420005271

Stevenson, F. J. (1996). Nitrogen-organic forms. In D. L. Sparks, A. L. Page, P. A. Helmke, R. H. Loeppert, P. N. Soltanpour, M. A. Tabatabai, C. T. Johnston & M. E. Sumner (Eds.), *Methods of Soil Analysis: Part 3 Chemical Methods* (pp. 1185-1200). Wiley. https://doi.org/https://doi.org/10.2136/sssabookser5.3.c39

Tahir, S., & Marschner, P. (2017). Clay addition to sandy soil reduces nutrient leaching-effect of clay concentration and ped size. *Communications in Soil Science and Plant Analysis*, *48*(15), 1813-1821. https://doi.org/10.1080/00103624.2017.1395454

Teh, C. B. S., Ishak, C. F., Rosazlin, A., Othman, R., Panhwar, Q. A., & Aziz, M. M. A. (2017). Soil properties (physical, chemical, biological, mechanical) In M. A. Ashraf, R. Othman & C. F. Ishak (Eds.), *Soils of Malaysia*, (pp. 103-154). CRC Press. https://doi.org/10.1201/b21934

Thomas, G. W. (1982). Exchangeable cations. In A. L. Page, R. H. Miller & D. R. Keeney (Eds.), *Methods of Soil Analysis: Part 2 Chemical and Microbiological Properties* (pp. 159-165). American Society of Agronomy-Soil Science Society of America.

Villagra-Mendoza, K., & Horn, R. (2018). Effect of biochar addition on hydraulic functions of two textural soils. *Geoderma*, *326*, 88-95. https://doi.org/10.1016/j.geoderma.2018.03.021

Wardiah, W., Linda, L., & Rahmatan, H. (2014). Potensi limbah air cucian beras sebagai pupuk organik cair pada pertumbuhan pakchoy (*Brassica rapa* L.) [Potential of washed rice water as a liquid organic fertilizer on the growth of pakchoy (*Brassica rapa* L.)]. *Jurnal Biologi Edukasi*, *6*(1), 34-38.

Wu, L., Wei, C., Zhang, S., Wang, Y., Kuzyakov, Y., & Ding, X. (2019). MgO-modified biochar increases phosphate retention and rice yields in saline-alkaline soil. *Journal of Cleaner Production*, *235*, 901-909. https://doi.org/10.1016/j.jclepro.2019.07.043

Wulandari, C. G. M., Muhartini, S., & Trisnowati, S. (2012). Pengaruh air cucian beras merah dan beras putih terhadap pertumbuhan dan hasil selada (*Lactuca sativa* L.) [Effect of washed brown and white rice water on the growth and yield of lettuce (*Lactuca sativa* L.)]. *Vegetalika*, *1*(2), 24-35.

Yaghi, N., & Hartikainen, H. (2013). Enhancement of phosphorus sorption onto light expanded clay aggregates by means of aluminum and iron oxide coatings. *Chemosphere*, *93*(9), 1879-1886. https://doi.org/10.1016/j.chemosphere.2013.06.059

Yin, S., Bai, J., Wang, X., Wang, X., Zhang, G., Jia, J., Li, X., & Liu, X. (2020). Hydrological connectivity and herbivores control the autochthonous producers of coastal salt marshes. *Marine Pollution Bulletin*, *160*, Article 111638. https://doi.org/10.1016/j.marpolbul.2020.111638

Zeng, Q., Qin, L., Bao, L., Li, Y., & Li, X. (2016). Critical nutrient thresholds needed to control eutrophication and synergistic interactions between phosphorus and different nitrogen sources. *Environmental Science and Pollution Research*, *23*, 21008-21019. https://doi.org/10.1007/s11356-016-7321-x

Pertanika J. Sci. & Technol. 31 (4): 1957 - 1970 (2023)

PERTANIKA JOURNALS

SCIENCE & TECHNOLOGY

Journal homepage: http://www.pertanika.upm.edu.my/

Experimental Study on Spring Constants of Structural Glass Panel Joints Under In-Plane Loading

Saddam Hussain*, Pei Shan Chen, Nagisa Koizumi, Baoxin Liu and Xiangdong Yan

Department of Civil Engineering and Architecture, Kyushu Institute of Technology, Kitakyushu 804-0015, Japan

ABSTRACT

Commonly, the columns and beams of glass panels are frequently subjected to in-plane loading, in which their joints will transfer the in-plane forces. Therefore, it is necessary to investigate the spring constants of the joints of these glass panels for the mechanical analysis of the structures. However, few issues were published on this subject, so estimating the spring constants of glass structure joints is important. Devote themselves to proposing methods to evaluate the spring constants of the joints of structural glass panels. This study tests two types of glass panels with thicknesses of 12 mm and 19 mm based on static and cycling loading. In addition, two types of Cushions: (1) aluminum and (2) rubber with a hardness of 65 and 90 degrees, are set between steel bolt(s) and glass panel(s) for the experiments. The spring constants are determined by the ratios of measured loads and the displacements between the glass panels and bolts. In addition, the authors proposed an equation to evaluate the bending spring constant from its axial spring constant determined by the loading tests. The experimental results showed that the joints with the aluminum cushion appear exactly non-linear elasticity while loading and unloading. Also, the pin junction within the central region (no Curve) is 0.6 mm. It is also determined that aluminum (cushion) slides of approximately ±0.3 mm under compression and tension. While loading (Tension/compression) is incremental, rubber acts nonlinearly but linear as unloaded.

Keywords: Frameless glass structure, in-plan loading, joint of glass panels, spring constant, tempered glass

ARTICLE INFO

Article history:
Received: 02 July 2022
Accepted: 05 October 2022
Published: 13 June 2023

DOI: https://doi.org/10.47836/pjst.31.4.21

E-mail addresses:
saddam.hussain372@mail.kyutech.jp (Saddam Hussain)
chen.pei-shan156@mail.kyutech.jp (Pei Shan Chen)
koizumi.nagisa830@mail.kyutech.jp (Nagisa Koizumi)
Liu.baoxin510@mail.kyutech.jp (Baoxin Liu)
yan.xiangdong760@mail.kyutech.jp (Xiangdong Yan)
* Corresponding author

INTRODUCTION

The authors are researching to realize frameless glass structures as new structural art. The frameless glass structure is close to pure glass, composed of tempered glass panels and minimal metal joints, expanding

ISSN: 0128-7680
e-ISSN: 2231-8526

the possibilities of unique architectural designs with excellent lighting (Santarieso et al., 2019; Centelles et al., 2019). However, the mechanical analysis and/or structural calculation for the frameless glass structures need the spring constants of its joints subjective to in-plane forces, as mentioned below. However, evaluating the spring constants of structural glass joints remains an unsolved issue. Therefore, the paper reports some important experimental results and methodology to evaluate the spring constant.

Researchers proposed some new structural systems to realize frameless glass structures as a kind of new structural system (Hussain et al., 2021; Bedon et al., 2019; Bedon et al., 2018a; 2019b). The frameless glass structure system comprises tempered glass panels and small metal joints, expanding the possibilities for unique architectural designs (Dispersyn et al., 2016; Chen, 2008). Inspired by the configuration of 1.5-Layer Space Frames, several assembling patterns for frameless glass are proposed by Chen (2011), and Figure 1 shows two examples of the proposals.

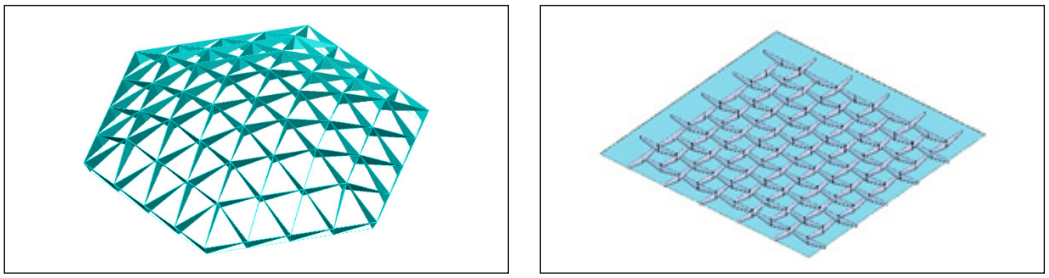

(a) (b)

Figure 1. Examples of frameless glass structures: (a) Reciprocal Triple-Connecting glass structure; and (b) Lap panel frameless glass structure

For a frameless glass structure, the joints are important key parts. In earlier research by Chen (2010), some examples of three-dimensional connections are proposed. Figure 2(a) shows a common example of connecting two glass panels with aluminum sheets and bolts. Another example of the Lap assembling method is shown in Figure 2(b), in which the joints are designed to transfer the forces.

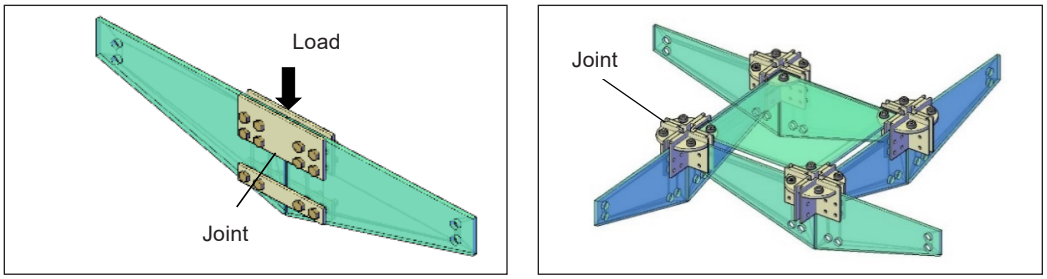

(a) (b)

Figure 2. The analytical models of joints: (a) One-piece glass panel; and (b) Lap-unit

In common, the Finite element method (FEM) can analyze a glass panel by meshing it into many elements, as in the meshed glass panel shown in Figure 3. However, it is difficult to analyze the whole structure with FEM because all the glass panels consisting in the structure have to mesh and analyzed (Hadimam et al., 2008; Overed et al., 2007; Hussain et al., 2022; Honfi et al., 2014), which may cost more Central Processing Unit (CPU) time. Accordingly, a methodology for structural design and mechanical analysis for the whole structure is proposed, which transforms the glass panels into equivalent beams of the same bending stiffness and axial stiffness (Chen & Tsai, 2019; Giaralis & Spanos, 2010). As shown in Figure 3, the glass panels are replaced by beams, and joints are transformed into springs in axial and rotating directions for mechanical analyses of the whole structure. Therefore, the investigation of the spring constant for joints is required.

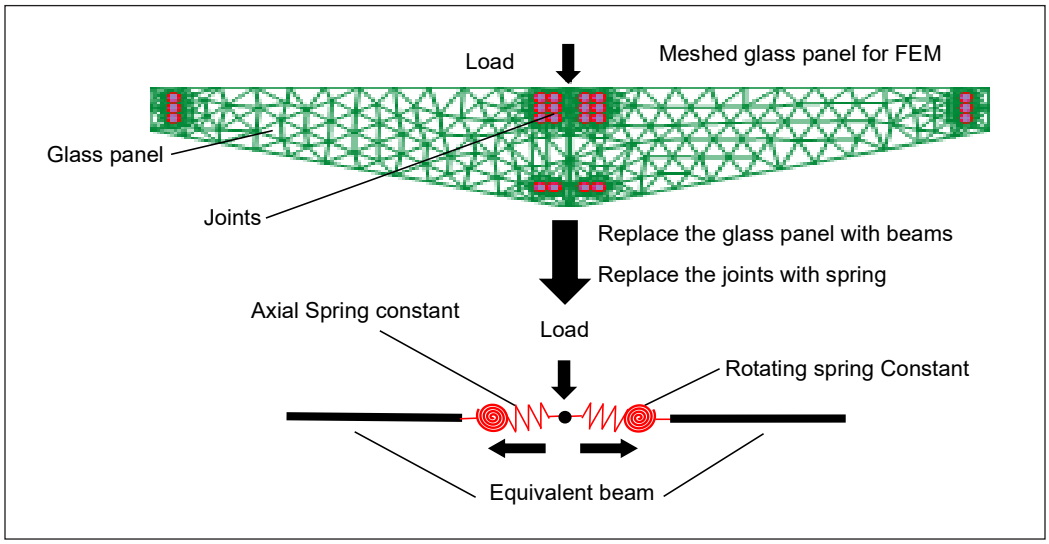

Figure 3. Replacing a glass panel with an equivalent beam method

However, few or no previous issues focused on the spring constants of the joints connecting glass panels. Accordingly, due to the lack of experimental research on such a topic, it appears vital to investigate the mechanical properties and develop a methodology to calculate the spring constants of joints of the structural glass panels. The design method of the three-dimensional combined glass panel structure proposed in the previous research, structural analysis, was proposed by the substitution method, as shown in Figure 3. When replacing the glass panel with an equivalent beam, the structure with a cylindrical curved surface cannot generate axial force in the glass surface. Therefore, here authors propose a structural design method in which a glass panel is used as an equivalent beam, and the joint portion is replaced with a spring. Therefore, a spring constant for the junction portion is required, and it is necessary to obtain this by experiment.

The final objective of this research is to complete the structural design theory of frameless glass structures and to put it into practical use. This paper evaluates the mechanical properties of glass joints, which are essential for structural analysis and calculation, especially their spring constants. The spring constants of tempered glass plate joints are experimental. The purpose of this research is to propose methods for calculating the spring constants of the joints for the structural glass panel. Based on the experimental results, the authors propose an equation to evaluate the bending spring constant for the mechanical analysis of the frameless glass structures.

MATERIALS AND METHODS

Mechanical Principle

In common, the seismic and/or wind loads could be considered recycling loading acting on the members and the joints connecting the structural members. Therefore, the authors experiment with recycling loading (compression/tension) to investigate the spring constant of the joints. This study uses an experimental setup to measure the displacements between the joint bolts and the glass panels with the recycling load. In subsequence, the spring constant can be calculated as the load-displacement ratio.

Experimental Setup

The experimental setup frame shown in Figure 4 is used for compression-tension tests to measure the displacements between the glass panels and the bolts. Notably, the load is applied with a double-action jack, and the load cell connected to the jack is used to measure the compression and tension load.

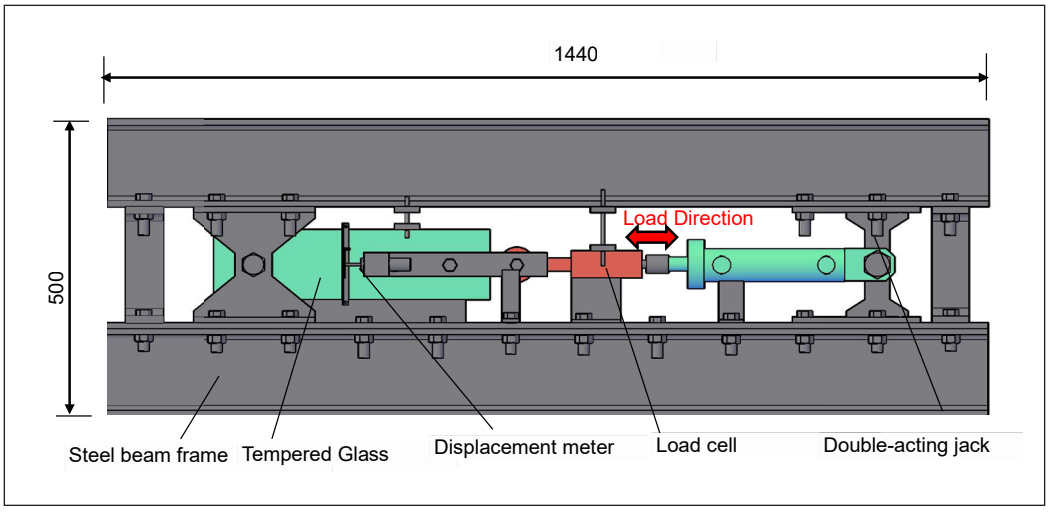

Figure 4. Assembly of the experimental setup (dimensions in mm)

Figure 5 exhibits that between the bolts and holes, there is a cushion. The bolt (a) is used to fix the glass panel to the experimental setup frame. The load is transferred through bolt (d) from the load cell connecting to the jack. The displacement meters are connected to the aluminum bars on both sides, which are used to measure the displacement between the stoppers and bolts (b)-(c); the stoppers are connected to the glass panel surface.

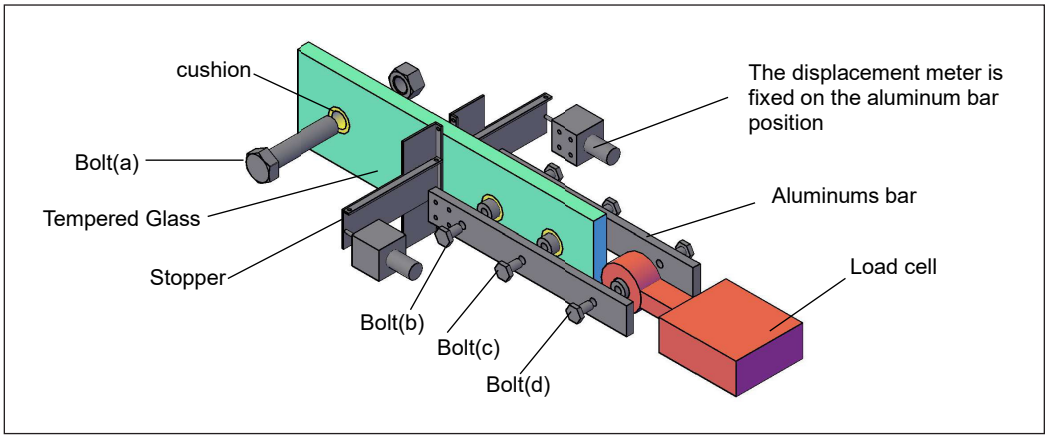

Figure 5. Details of specimen position during loading

As illustrated in Figure 6, two cushion materials are used,1) chloroprene rubber (CR), a couple of hardness (Hs) types (90, 65), labeled as CR Hs90 and CR Hs65, respectively, and 2) aluminum A5052 Japanese Industrial Standards (JIS) labeled as A5052.

Consequently, these cushion materials prevent direct contact between the bolt and the glass. The bolt-hole diameter is 32 mm, and the thickness of the cushion material is 5 mm. Bolts of M22 (S45C material, JIS) are utilized.

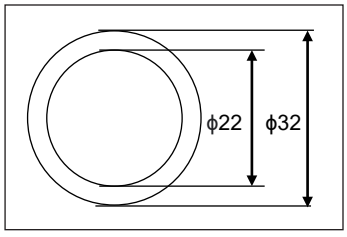

(a)

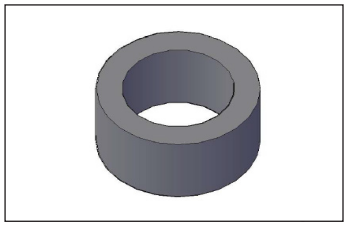

(b)

Figure 6. Cushion material and dimensions: (a) Diameter of cushioning; and (b) Cushion material (dimensions in mm)

The Specimens

The specimens are two types of tempered glass panels with 19 mm and 12 mm thicknesses, respectively. Moreover, two types of joints with two holes and one hole are used, as shown in Figure 7. The panels are 450 mm and 120 mm long and wide, respectively. In addition, spacing of 90 mm bolt-to-bolt and 65 mm between the edges of the glass panel and bolt hole is provided. Further details of the specimens are presented in Table 1.

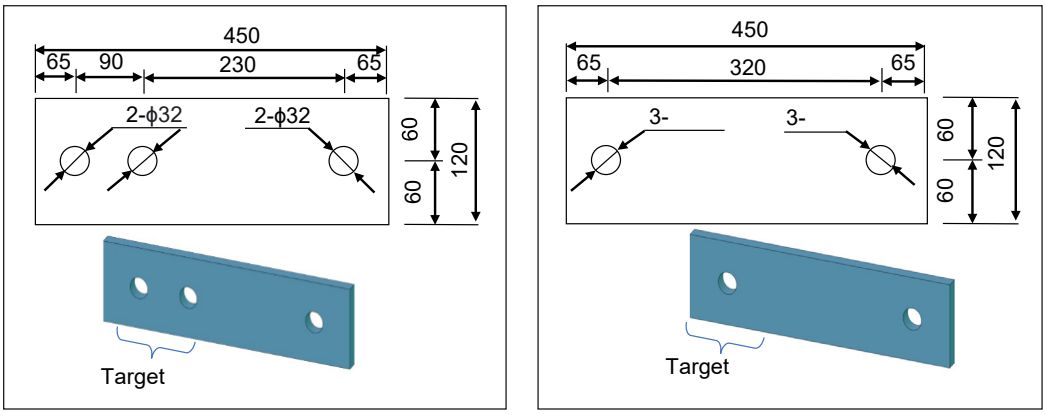

Figure 7. Specimen type and dimension: (a) Specimen with two holes; and (b) Specimen with one hole (dimensions in mm)

Table 1
Details of experimental specimens

Specimen type	Symbols		
	Cushion CR Hs90	Cushion CR Hs65	Cushion A5052
19mm-2	19-2-CR Hs90,	19-2-CR Hs65	19-2-A5052
19mm-1	19-1-CR Hs90	19-1-CR Hs65	19-1-A5052
12mm-2	12-2-CR Hs90	12-2-CR Hs65	12-2-A5052
12mm-1	12-1-CR Hs90	12-1-CR Hs65	12-1-A5052

The Recycle Loading

For the joints with rubber Cushions (90,65) degrees, the peak load is ±3600N, and ten times recycling loading is performed for the experiments. At the same time, each time incremental of repeating load is set as a ±400N. For the joints with aluminum cushion, ten times of recycling loading are performed for tests, and the peak load for each repeating is set as ±5000N, ±7000N, ±10000N, and ±15000N.

RESULTS AND DISCUSSION

Summary of the Experimental Results

Experimental testing of glass panels is illustrated in Figure 8. The load-displacement curves are shown in Figures 9 to 12. The displacement measured in the experiments is the average of the two displacement meters set on both sites of the glass panel.

Figure 9(a) shows the results of specimens 19-2-CR Hs90, and the maximum applied load is ±3600N. The maximum and minimum displacements are 2.409 mm and -3.149 mm, respectively. Figure 9(b) shows the outcomes of 19-2-CR Hs65. It is indicated that the maximum and minimum displacements are 3.487mm and -3.806 mm, respectively.

The average displacement is 0.159 mm. In Figure 9(c), the outcome of 19-2-A5052, the maximum applied load is ±15000N; consequently, the maximum displacement is 0.456 mm, and the minimum displacement is -0.576 mm. Moreover, the load does not enhance up to a displacement of ±0.3 mm, and bolts and glass panels slide with each other.

Figure 10(a) presents the result of 19-1-CR Hs90, in which the maximum load implicates to ±3600N. As a result, the maximum and minimum displacement is found to be 3.804 mm and - 4.149 mm, respectively. The average of the peak displacements is 3.999 mm. Figure 10(b) expresses the load-displacement curves for 19-1-CR Hs65, where the maximum load is ±3600N. The maximum and minimum displacements were 3.958 mm and -3.918 mm, respectively. It is illustrated in Figure 10(c) for 19-1-A5052, and it is observed that the maximum load is ±7000N, and the maximum displacement was 0.975

Figure 8. Experimental setup and specimens during the performing test

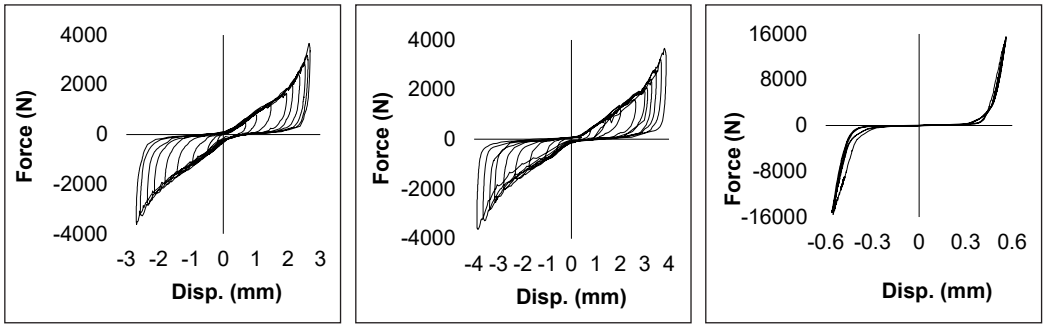

(a) (b) (c)

Figure 9. Recycling loading of test of 19mm thickness glass panel with 2 bolt holes: (a) 19-2-CR Hs90; (b) 19-2-CR Hs65; and (c) 19-20A5052

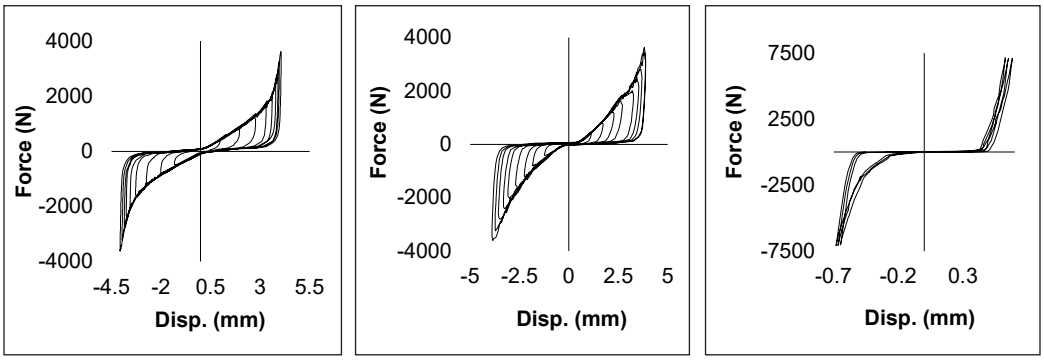

(a) (b) (c)

Figure 10. Recycling loading of test of 19mm thickness glass panel with 1 bolt hole: (a) 19-1-CR Hs90: (b) 19-1-CR Hs65; and (c) 19-1-A5052

mm; the minimum displacement was -0.388 mm. Furthermore, the average displacement is ±0.2935 mm.

Figure 11(a) indicates the result of 12-2-CR Hs90 with a maximum load of ±3600N, 3.884 mm is the maximum displacement, and minimum displacement is determined as -3.662 mm, which the average displacement is ±0.111 mm. Figure 11(b) presents the displacement results for 12-2-CR-Hs65. The maximum and minimum displacements were 3.395mm and -3.707 mm, respectively. The maximum load is 3600 N, and the average displacement is ±0.156 mm. Figure 11(c) indicates the outcome of 12-2-A5052; the max load is ±10000N. As a result, the maximum displacement is 0.495 mm, the minimum displacement is -0.746 mm and the average displacement is ±0.6205 mm.

Figure 12(a) depicts the result of 12-1-CR Hs90 on a maximum load of ±3600N, and the average displacement is 4.093 mm. Figure 12(b) shows the outcomes of 12-1-CR Hs65 with the maximum load of ±3600N. The maximum displacement is 4.560 mm, the minimum is 3.315 mm, and the average is 3.938 mm. Figure 12(c) shows the result of 12-1-A5052 with a maximum load of 5000N. The maximum and minimum displacements are 0.785 mm and 0.283 mm, respectively. Moreover, the average displacement is ±0.251 mm.

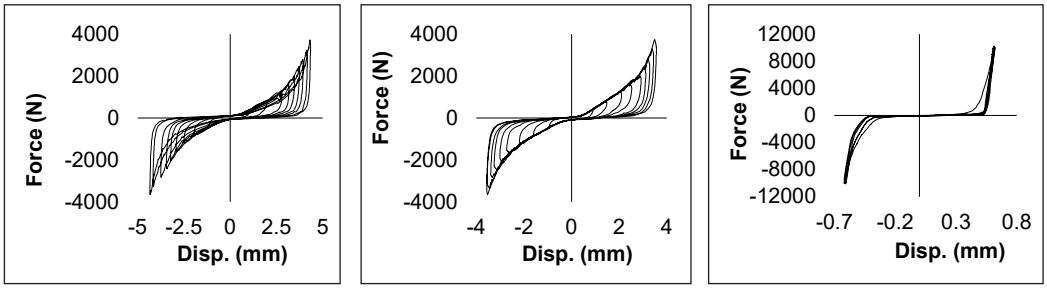

(a) (b) (c)

Figure 11. Recycling loading of 12mm thickness glass panel test with 2 bolt holes: (a) 12-2-CR Hs90: (b) 12-2-CR Hs65; and (c) 12-2-A5052

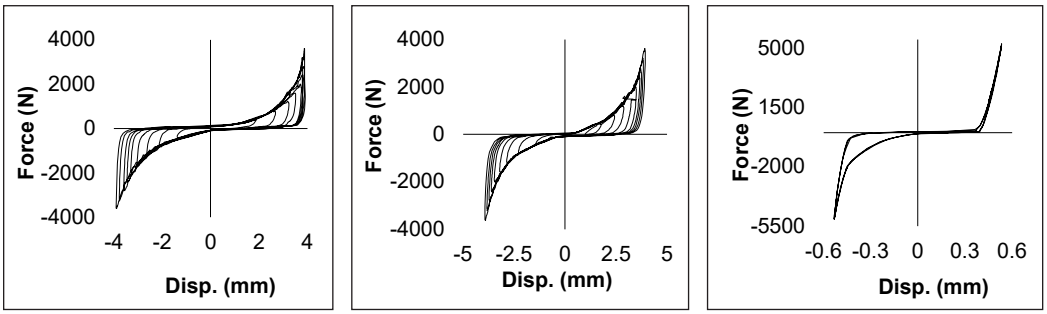

(a) (b) (c)

Figure 12. Recycling loading of test of 12mm thickness glass panel and 1 bolt hole: (a) 12-1-CR Hs90: (b) 12-1-CR Hs65; and (c) 12-1-A5052

Estimation of the Spring Constants

In the frameless glass structure, axial forces are applied in the tempered glass panels. As mentioned, the authors proposed replacing the tempered glass panels with equivalent beams and the joints with springs for the mechanical analysis with a model consisting of all structural members. The spring constants can be obtained from the load-displacement ratio, in which the displacement is measured between the glass panel and bolts under in-plane loading.

Figure 13(a) presents the recycling curve of the specimens with a rubber cushion, which is close to a straight line during increasing loading and shows a non-linear curve during unloading. Figure 13(b) shows the load and displacement curve of the specimens with the aluminum cushion, which shows non-linear elasticity while loading and unloading. Furthermore, the curve appears as a pin junction within the central region, as shown in the diagram. It is also determined that aluminum (cushion) slides of approximately ±0.3 mm under compression and tension.

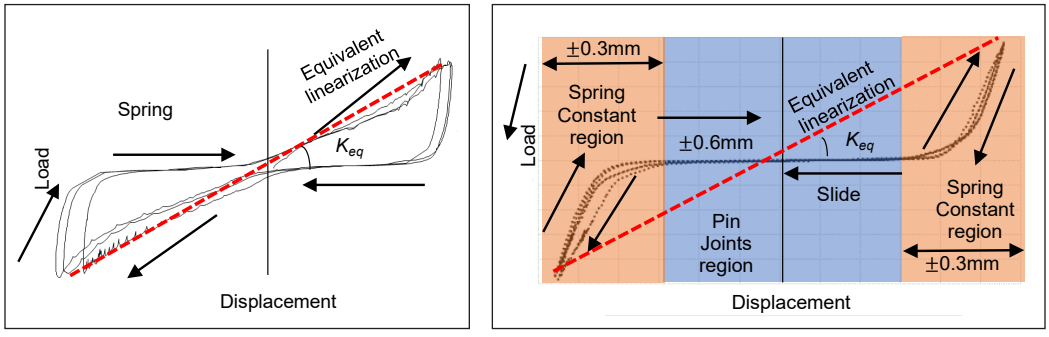

(a) (b)

Figure 13. Mechanical behavior of the spring constants joint: (a) Chloroprene rubber cushioning material; and (b) Aluminum cushioning material

The proposed mechanical analysis methodology, especially for dynamic mechanical analysis during seismic design, is based on equivalent linearization. The equivalent linearization replaces each non-linear stiffness with a quasilinear stiffness (Koliopulos et al., 1994; Overend, 2007). It inspires authors to find the spring constant for the mechanical analysis with equivalent linearization. The spring constant of equivalent linearization is directly proportional to the average forces (P_{max} and P_{min}) and the associated values of the average displacements (δ_{max} and δ_{min}). Figure 13 shows the image of spring constants of equivalent linearization with the slope of red lines, which connects the peak points of forces and displacements. The spring constant of equivalent linearization K_{eq} is calculated in Table 2.

Table 2
Spring constants for equivalent linearization (unit: N/mm)

Spring constants, K_{eq}	CR Hs90	CR Hs65	A5052
19mm-2	1248.60	942.65	27363.73
19mm-1	863.72	863.56	1040.5
12mm-2	911.37	955.33	16120.06
12mm-1	829.02	850.44	9641.47

Calculation Formula of Spring Constant for Bending

This discussion elaborates an equation to calculate the bending spring constant K_R from its axial spring constant K_A determined by the loading tests. Figure 14 exhibits the calculation model; a and l indicate the distances between the bolts, C_1, C_2 and T describe the forces acting on the bolts, and δ_1, δ_2, and δ_3 in Equation 1 represent the displacements between the bolts and glass panel.

In this calculation and derivation model shown in Appendix A, the distance from the top bolt center to the neutral axis is x_n, which the following calculation can derive. $x_n = \frac{a+l}{3}$,

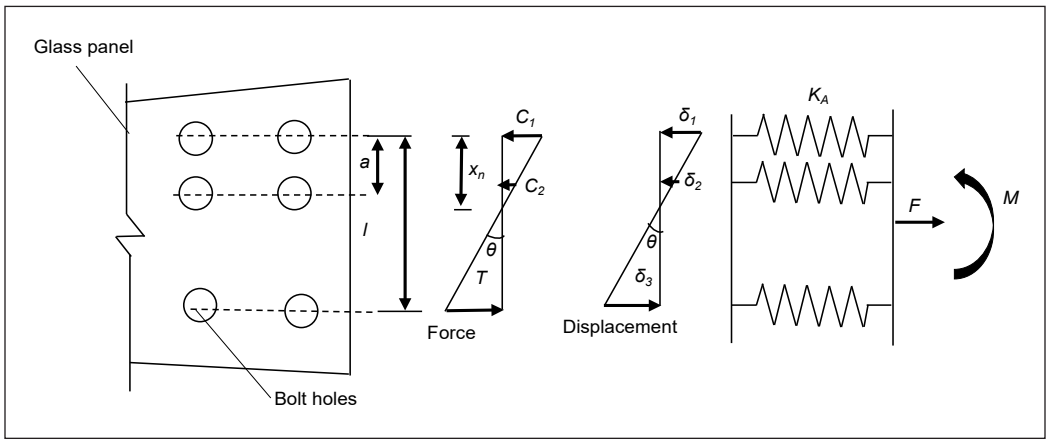

Figure 14. Calculation model for constant spring calculation

Consequently, the moment can be expressed by the distance between the neutral axis and bolts, which can be modified using Equation 2 in Appendix A.

$$M=\frac{x_n{}^2+(x_n\text{-}a)^2+(l\text{-}x_n)^2}{x_n}\cdot\delta_1\cdot K_A \tag{1}$$

The bending spring constant(K_R)is defined as $K_R=\frac{M}{\theta}$, where the bending angle θ can be calculated by Equation 3.

$$\theta=\frac{\delta_1+\delta_3}{l}=\left(\delta_1+\frac{l\text{-}x_n}{x_n}\cdot\delta_1\right)\cdot\frac{1}{l}=\frac{\delta_1}{x_n} \tag{2}$$

$$K_R=\frac{2}{3}\cdot\left(a^2+l^2\text{- }a\cdot l\right)\cdot K_A \tag{3}$$

CONCLUSION

In this study, the authors conducted experiments and theoretical research to evaluate the spring constants of structural glass panel joints. Moreover, the spring constant for equivalent linearization K_{eq} was summarized in 800-1000N/mm. It was found that the specimen with rubber cushion exhibited non-linear behavior. Specimens with aluminum cushions exhibit a slip of approximately ±0.3 mm and behavior elastic non-linear during compression and tension. It can be set as a pin joint in this region. The spring constant for equivalent linearization of specimens with aluminum cushions is summarized as 10000-27000N/mm. Future issues include a problem with the mechanism of this test specimen, which caused errors and a large amount of residual strain and slippage. The rubber may behave similarly and plasticize when the load is increased. It is considered feasible to propose a joint using aluminum or other materials. It is also necessary to study the spring constant by changing the approximation method based on the results of this experiment. Glass panel bolts from the market were investigated to limit the scope of the research. The bolts and their designs, including the, serve as the in-plane testing. The thickness of the glass is chosen based on experience, consultation, and avoiding too many sets of testing.

The future purpose of this study is to propose the structural design theory of the frameless glass structures, a three-dimensional combination glass panel structure. In addition, it determines the non-linear behavior elastic region behavior of spring constants in material joints and glass panels.

ACKNOWLEDGEMENTS

In this research, the authors thank the Building Structure Laboratory of Kyushu Institute of Technology, Japan, for its support of experiments.

REFERENCES

Bedon, C., Amadio, C., & Noé, S. (2019). Safety issues in the seismic design of secondary frameless glass structures. *Safety*, *5*(4), Article 80. https://doi.org/10.3390/safety5040080

Bedon, C., & Santarsiero, M. (2018b). Transparency in structural glass systems via mechanical, adhesive, and laminated connections-existing research and developments. *Advanced Engineering Materials*, *20*(5), Article 1700815.

Bedon, C., & Santarsiero, M. (2018a). Laminated glass beams with thick embedded connections–Numerical analysis of full-scale specimens during cracking regime. *Composite Structures*, *195*, 308-324. https://doi.org/10.1016/j.compstruct.2018.04.083

Bedon, C., Zhang, X., Santos, F., Honfi, D., Kozłowski, M., Arrigoni, M., & Lange, D. (2018). Performance of structural glass facades under extreme loads - Design methods, existing research, current issues, and trends. *Construction and Building Materials*, *163*, 921-937.

Chen, P. S. (2008). A study report on an ancient chinese wooden bridge hongqiao, *Structural Engineering International, 18*(1), 84-87. https://doi.org/10.2749/1016866 08783726614

Chen, P. S. (2010, November 8-12). A study on the geometrical configuration of an ancient wooden bridge in *Qingming Shanghe Tu.* In *Proceeding of IASS2010.* Shanghai, China.

Chen, P. S. (2011, September 20-23). A report on the innovation of 1.5-layer space frames. In *Proceeding of IABSE IASS.* London, UK.

Chen, P. S., & Tsai, M. T. (2019). On configuration and structural design of frameless glass structures. In J. S. C. Paulo (Ed.), *Structures and Architecture: Bridging the Gap and Crossing Borders* (pp. 628-637). CRC Press. https://doi.org/10.1201/9781315229126

Centelles, X., Castro, J. R., & Cabeza, L. F. (2019): Experimental results of mechanical, adhesive, and laminated connections for laminated glass elements - A review. *Engineering Structures, 180*, 192-204. https://doi.org/10.1016/j.engstruct.2018.11.029

Dispersyn, J., & Belis, J (2016). Numerical research on stiff adhesive point-fixings between glass and metal under uniaxial load. *Glass Structures & Engineering, 1,* 115-130. https://doi.org/10.1007/s40940-016-0009-2

Giaralis, A., & Spanos, P. D. (2010). Effective linear damping and stiffness coefficients of nonlinear systems for design spectrum-based analysis. *Soil Dynamics and Earthquake Engineering*, *30*(9), 798-810. https://doi.org/10.1016/j.soildyn.2010.01.012

Hussain, S., & Chen, P. S. (2021). Future importance and demand of frameless glass structure. *World Journal of Advanced Scientific Research*, *4*(2), 1-19.

Honfi, D., Reith, A., Vigh, L. G., & Stocker, G. (2014). Why glass structures fail? Learning from failures of glass structures. In L. Christian, B. Freek, B. Jan & L. Jean-Paul (Eds.), *Challenging Glass 4 & Cost Action TU0905 Final Conference* (pp. 791-800). CRC Press. https://doi.org/10.1201/b16499

Hussain, S., Chen, P. S., Koizumi, N., Rufai, I., Rotimi, A., Malami, S. I., & Abba, S. I. (2022). Feasibility of computational intelligent techniques for the estimation of spring constant at joint of structural glass plates: a dome-shaped glass panel structure. *Glass Structures & Engineering, 8*, 141-157. https://doi.org/10.1007/s40940-022-00209-6

Koliopulos, P. K., Nichol, E. A., & Stefanou, G. D. (1994). Comparative performance of equivalent linearization techniques for inelastic seismic design. *Engineering Structures 16*(1), 5-10. https://doi.org/10.1016/0141-0296(94)90099-X

Santarsiero, M., Bedon, C., & Moupagitsoglou, K. (2019). Energy-based considerations for the seismic design of ductile and dissipative glass frames. *Soil Dynamics and Earthquake Engineering*, *125*, Article 105710. https://doi.org/10.1016/j.soildyn.2019.105710

Overend, M., De Gaetano, S., & Haldimann, M. 2007. Diagnostic Interpretation of Glass Failure. *Structural Engineering International*, *17*(2), 151-158. https://doi.org/10.2749/101686607780680790

APPENDIX A

In the session of results and discussions, Figure 14 demonstrates the calculation formula of spring constant for the bending model; a and l indicate the distances between the bolts, C_1, C_2, and T describe the forces acting on the bolts, and δ_1, δ_2, and δ_3 represents the displacements between the bolts and glass panel. The following Equation 4 indicates the basic conditions of force equilibrium.

$$T = C_1+C_2 \quad ; \quad \delta_3 K_A = \delta_1 K_A+\delta_2 K_A \tag{4}$$

In this calculation model, the distance from the top bolt center to the neutral axis is x_n, Equation 5, which the following calculation can derive.

$$\frac{\delta_1}{x_n} = \frac{\delta_2}{x_n - a} = \frac{\delta_3}{l - x_n} \; ; \quad \frac{l - x_n}{x_n} \cdot \delta_1 = \delta_1 + \frac{x_n - a}{x_n} \cdot \delta_1 \; ; \tag{5}$$

Consequently, the moment can be expressed by the distance between the neutral axis and the bolts as in Equation 6, which can be modified as Equation 7 using Equation 2.

$$M= x_n \cdot C_1+(x_n\text{-}a)\cdot C_2+(l\text{-}x_n)\cdot T \tag{6}$$

$$M=\frac{x_n{}^2+(x_n\text{-}a)^2+(l\text{-}x_n)^2}{x_n} \cdot \delta_1 K_A \tag{7}$$

The bending spring constant K_R is defined as Equation 8, where the bending angle θ can be calculated by Equation 7. Therefore, the bending rigidity spring constant K_R can be obtained by substituting Equations 8 and 9 into Equation 10.

$$\mathrm{K_R}=\frac{\mathrm{M}}{\theta} \tag{8}$$

$$\theta=\frac{\delta_1+\delta_3}{l} = \left(\delta_1+\frac{l\text{-}x_n}{x_n}\cdot\delta_1\right)\cdot\frac{1}{l} = \frac{\delta_1}{x_n} \tag{9}$$

$$K_R=\frac{2}{3}\cdot\left(a^2+l^2\text{-}\; a\cdot l\right) \tag{10}$$

Pertanika J. Sci. & Technol. 31 (4): 1971 - 1990 (2023)

PERTANIKA JOURNALS

SCIENCE & TECHNOLOGY

Journal homepage: http://www.pertanika.upm.edu.my/

Extraction of Metalloporphyrins Using Subcritical Toluene-Assisted Thermally Stable Ionic Liquid

Nor Faizatulfitri Salleh[1,2], Suzana Yusup[3], Pradip Chandra Mandal[4] and Muhammad Syafiq Hazwan Ruslan[5,6]*

[1]Department of Chemical Engineering, Universiti Teknologi PETRONAS, 32610 UTP, Seri Iskandar, Perak, Malaysia
[2]Centre of Research in Ionic Liquids, Institute of Contaminant Management, Universiti Teknologi PETRONAS, 32610 UTP, Seri Iskandar, Perak, Malaysia
[3]Fuel & Combustion Section, Generation Unit, Generation & Environment Department, TNBResearch, 43000 Kajang, Selangor, Malaysia
[4]Titas Gas Transmission and Distribution Co. Ltd., 105 Kuzi Nazrul Islam Avenue, Kawran Bazar, Dhaka, 1215, Bangladesh
[5]School of Chemical Engineering, College of Engineering, Universiti Teknologi MARA, 40450 UiTM, Shah Alam, Selangor, Malaysia
[6]Centre of Lipids Engineering and Applied Research, Ibnu Sina Institute of Scientific and Industrial Research, Universiti Teknologi Malaysia, 81310 UTM, Johor Bahru, Johor, Malaysia

ABSTRACT

Due to the depleting production of conventional petroleum, heavy oil is turned to as an alternative. However, the presence of trace nickel and vanadium in heavy oil poses problems for the refining process in producing lighter-end products. Such problems are its tendency to poison the catalyst, accumulate during distillation, and corrode the equipment. The objective of this work is to remove the metal porphyrins from model oil using the thermally stable ionic liquid 1-butyl-3-methylimidazolium octylsulfate, [BMIM][OS] assisted by subcritical toluene (above boiling point, 110.6°C and below a critical point, 318.6°C at 41.264 bar) in a novel attempt. The experiments were conducted at 150ºC to 210ºC under a mixing time of 30 to 90 minutes while the pressure was monitored. Four metal porphyrins are used: nickel etioporphyrin, nickel tetraphenylporphyrin, vanadium oxide etioporphyrin, and vanadium oxide tetraphenylporphyrin. The results show that more than 40% of removal is achieved for all metal porphyrins, which shows great potential for further technological improvement. The Nuclear Magnetic

ARTICLE INFO

Article history:
Received: 11 June 2022
Accepted: 11 October 2022
Published: 13 June 2023

DOI: https://doi.org/10.47836/pjst.31.4.22

E-mail addresses:
faizatulfitri23@gmail.com (Nor Faizatulfitri Salleh)
suzana.yusup@tnb.com.my (Suzana Yusup)
pradipbd2002@yahoo.com (Pradip Chandra Mandal)
syafiqhazwan@uitm.edu.my (Muhammad Syafiq Hazwan Ruslan)
* Corresponding author

ISSN: 0128-7680
e-ISSN: 2231-8526

Resonance (NMR) shows that the ionic liquid did not decompose at the process temperature, which proves great stability. The extraction of metal porphyrins follows the second-order extraction model with an R2 of more than 0.98.

Keywords: 1-butyl-3-methylimidazolium octylsulfate, heavy metals, heavy oil upgrading, metalloporphyrins, subcritical toluene

INTRODUCTION

The growth of population, transportation, and industry growth are the major drivers in increasing the demand for petroleum resources (Ali et al., 2018). The International Energy Agency reported that heavy oil production from Canada and Venezuela might reach 6 million barrels daily by 2030. Heavy oil can be defined as crude oil with the American Petroleum Institute (API) gravity of 10 to 20º, with high density and viscosity. Heavy oil fields are mostly in the United States, Russia, Canada, Venezuela, and the Middle East (Santos et al., 2014).

However, heavy oils contain a trace number of heavy metals, the most abundant being nickel and vanadium, which are highly troublesome heavy metals (Mandal et al., 2014). The content of vanadium can go up to 1200 ppm, while the content of nickel is up to 150 ppm (Agrawal & Wei, 1984). The presence of heavy metals can significantly impact the oil upgrading processes (Castañeda et al., 2014; Mandal & Alias, 2017; Mandal et al., 2011, 2012a, 2012b). It can cause the catalysts to be deactivated and poisoned, corrosion to the equipment, and raise concerns regarding toxic contents that may lead to environmental pollution.

Several porphyrin series are found in crude oil, with the most common type of porphyrin being etioporphyrin (ETIO) and deoxophylloerythroetio porphyrin (DPEP) (Zhao et al., 2015). Heavy metals in heavy oil are agglomerated in the asphaltene portion as porphyrin compounds referred to as metalloporphyrin (Rana et al., 2007). Treibs is reported to be the first to demonstrate the presence of metalloporphyrin in petroleum (Mandal et al., 2014). The general structure of porphyrins is shown in Figure 1.

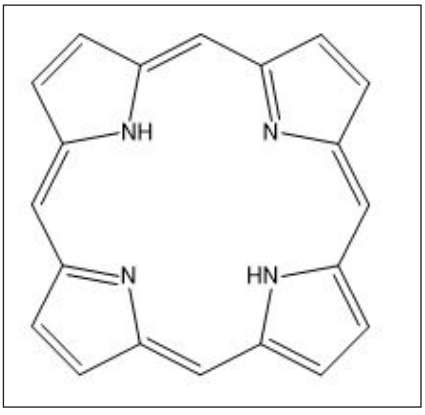

Figure 1. The general structure of porphyrin

Due to the drawbacks of conventional technologies, interest has grown in exploring unconventional methods to remove heavy metals from heavy oil. Examples of such methods are salting-out separation (Ameur & Husein, 2012), the use of zeolites as ion exchangers (Ikyereve et

al., 2014), electrochemical (Welter et al., 2009), microbial demetallization (Salehizadeh et al., 2007), microwave radiation (Wang et al., 2011), supercritical fluid application (Mandal et al., 2011, 2012a, 2012b; Manjare & Dhingra, 2019; Trucillo et al., 2019) and biosorption (Beni & Esmaeili, 2020). Furthermore, there are a few methods explored to remove heavy metals from various environments, such as using ion exchange textiles (Elektorowicz & Muslat, 2008), via hydrochloric with alcohol extraction (Yuan et al., 2019) and integrated remediation processes (Selvi et al., 2019). However, these methods have their limitations.

Toluene is a good solvent for asphaltene (Painter et al., 2015), making it easier for metalloporphyrin extraction as it agglomerates in the asphaltene portion. Subcritical toluene is when toluene is above its boiling point (110.6ºC) and below its critical point (318.6ºC at 41.264 bar). The subcritical condition of toluene can generate a good environment for metal transfer during extraction. Furthermore, maintaining a subcritical condition is much easier than a supercritical condition due to the lower temperature and pressure requirement (Tavakoli & Yoshida, 2005).

Ionic liquids are salts that appear liquid at temperatures below 100°C and consist of cations and anions. Ionic liquids have seen applications for various purposes, such as CO_2 capture (Bara et al., 2010; Bates et al., 2002; Karadas et al., 2010; Ramdin et al., 2012), lubricants (Jiménez & Bermúdez, 2007; Qu et al., 2009), drug delivery agents (Dobler et al., 2013; Moniruzzaman et al., 2010; Monti et al., 2017), in biofuels (Fadeev & Meagher, 2001; Liu et al., 2012; Fauzi & Amin, 2012; Muhammad et al., 2015; Vancov et al., 2012), in the food industry (Hijo et al., 2016) and liquid-liquid extraction (Huddleston et al., 1998; Sun et al., 2012; Visser et al., 2001; Khaidzir et al., 2021). Researchers recognize Ionic liquids as a green solvent due to their unique properties, including their thermal stability, nonflammability, negligible vapor pressure, wide tunability for anions and cations, low volatility, and recyclability (Kumano et al., 2006; Sowmiah et al., 2009). In addition, ionic liquids have recently seen wide industrial use for applications in the separations, electroplating, reactions, and gas processing industry (Siriwardana, 2015).

Therefore, this study aims to extract the metalloporphyrin component in the heavy oil sample using ionic liquids under subcritical toluene solution as an alternative to heavy oil upgrading technology. Four metalloporphyrin components were selected: nickel etioporphyrin (NiEP), nickel tetraphenylporphyrin (NiTPP), vanadium oxide etioporphyrin (VOEP), vanadium oxide tetraphenylporphyrin (VOTPP), were selected for this study as the composition of these metals is significant in the heavy oil sample. A kinetic study on the extraction mechanism was also conducted to explain the fundamental behavior of the extraction process.

MATERIALS AND METHODS

Material and Apparatus

Nickel etioporphyrin (NiEP), nickel tetraphenylporphyrin (NiTPP), vanadium oxide etioporphyrin (VOEP), vanadium oxide tetraphenylporphyrin (VOTPP), 1-butyl-3-methylimidazolium octylsulfate, [BMIM][OS], and toluene were purchased from Avantis Laboratory Supply, Malaysia and were used without further treatment. The selection process was made using Conductor-like Screening Model for Realistic Solvents (COSMO-RS) software, where the prediction of the selectivity, capacity, and performance index toward the 4 metalloporphyrin metals.

All metalloporphyrin structures were drawn and optimized in the TURBOMOLE program using its quantum chemical calculation. Functional BP86 with triple-ζ valence polarized (TZVP) basis set, a function in density functional theory (DFT), was used to optimize the metalloporphyrin structure. The optimized structures were then imported to the COSMO-RS software for activity coefficient estimation. Cations and anions for the ionic liquids were called from the existing COSMO-RS library. The activity coefficient in infinite dilution was used to estimate the selectivity and capacity of ionic liquid towards metalloporphyrin. Equations 1 to 3 shows the equation used to calculate the tested ionic liquid's capacity, selectivity, and performance index

$$C^{\infty} = \left(\frac{1}{\gamma_1^{\infty}}\right)^{IL\ phase} \quad [1]$$

$$S_{12}^{\infty} = \frac{\gamma_2^{\infty}}{\gamma_1^{\infty}} \quad [2]$$

$$PI = C^{\infty} \times S^{\infty} = \left(\frac{\gamma_2^{\infty}}{(\gamma_1^{\infty})^2}\right)^{IL\ phase} \quad [3]$$

Whereby C^{∞} is the capacity at infinite dilution, $\gamma_1{}^{\infty}$ is the activity coefficient of metalloporphyrin at infinite dilution in ionic liquid, $\gamma_2{}^{\infty}$ is the activity of toluene at infinite dilution in ionic liquid, $S_{12}{}^{\infty}$ is the selectivity of metalloporphyrin and toluene towards the ionic liquid in infinite dilution, and *PI* is the performance indicator.

The 12 shortlisted ionic liquids are 1-ethyl-3-methylimidazolium octylsulfate [EMIM][OS], 1-ethyl-3-methylimidazolium bis((trifluoromethyl)sulfonyl)imide [EMIM][NTf2], 1-ethyl-3-methylimidazolium hydrogensulfate [EMIM][HS], 1-ethyl-3-methylimidazolium methanesulfonate [EMIM][MS], 1-butyl-3-methylimidazolium octylsulfate [BMIM][OS], 1-butyl-3-methylimidazolium bis((trifluoromethyl)sulfonyl)imide [BMIM][NTf2], 1-butyl-3-methylimidazolium hydrogensulfate [BMIM][HS], 1-butyl-3-methylimidazolium methansulfonate [BMIM][MS], tetrabutylphosphonium octylsulfate

[TBP][OS], tetrabutylphosphonium bis((trifluoromethyl)sulfonyl)imide [TBP][NTf2], tetrabutylphosphonium hydrogensulfate [TBP][HS], and tetrabutylphosnium methanesulfonate [TBP][MS].

Based on the screening process, $[TBP]^+$ cation shows the best performance index, followed by $[BMIM]^+$ and $[EMIM]^+$. However, $[TBP]^+$ has low selectivity towards the metalloporphyrin complex. Moreover, it is unstable due to the formation of an unwanted by-product, phosphine oxide, in the presence of oxygen.

Meanwhile, for the anion screening, $[OS]^-$ and $[NTf_2]^-$ show potential since both anions show good performance index compared to $[HS]^-$ and $[MS]^-$. However, a study has shown that [OS] was reasonably non-toxic, has an acceptable biodegradability, and is a cheaper option compared to $[NTf_2]$- (Dávila et al., 2007; Davis & Fox, 2003). Therefore, [BMIM][OS] was selected as the extractant.

The experiments were conducted in a 100 mL autoclave-stirred reactor from Amar Equipment Pvt. Ltd., India. The reactor was manufactured from stainless steel, with a stirrer and pressure gauge attached, and was designed for temperatures of up to 500ºC and pressures up to 20 MPa.

Generating Calibration Curve

Five standard solutions of model oil ranging from 20 to 100 ppm were prepared. The samples were analyzed using UV-Visible Spectrophotometer 1800 model from Shimadzu Scientific Instrument, US, and were scanned at 200 to 700 nm wavelengths. The analysis used 12.5 × 12.5 × 45 mm quartz cuvettes, and toluene was used as a reference. The concentration of porphyrin was computed by applying the Lambert-Beer Law.

Experiment Procedure

A stock solution of model oil was first prepared. Then, 0.015 g of metal porphyrin was dissolved in 50 mL of toluene at 30ºC with continuous stirring at 150 rpm. Next, 150 mL of toluene was added thrice over a certain period. After the metal porphyrin had completely dissolved, the mixture was transferred into a 250 mL volumetric flask, and toluene was added till the calibration mark.

Metal porphyrins were extracted by loading 20 mL of model oil and 2 mL of [BMIM][OS] into the autoclave reactor. Then, the mixture was heated up at temperatures of 150 to 210ºC under mixing times of 30 to 90 minutes, with intervals of 30ºC and 30 minutes, respectively. Meanwhile, the pressure throughout the extraction process was monitored. Next, the mixture was cooled down at room temperature and transferred into a separating funnel. In the 2 layers observed to form, the bottom layer was the extract, and the upper layer was the raffinate. After that, the two layers were separated and sent for analysis for further examination.

The percentage of metal porphyrin extraction was calculated using the following Equation 4:

$$\text{Removal (\%)} = [(C_i - C_f)/C_i] \times 100 \qquad [4]$$

where C_i is the initial concentration of model oil, and C_f is the final concentration of the model oil.

Analysis

UV-Visible (UV-Vis spectrophotometer 1800 model, Thermo Fisher Scientifc Inc., US) and Fourier Transform Infrared Spectroscopy (FTIR) coupled with diamond Attenuated Total Reflectance (Nicolet iS5, Thermo Fisher Scientifc Inc., US) were used for the upper layer which contains model oil. The wavelength of FTIR used ranges from 4000 to 400 cm^{-1} with 16 cycles of scanning. Meanwhile, FTIR and Nuclear Magnetic Resonance (NMR) (Bruker Advance III 500 MHz, Bruker Corporation, US) was used to analyze the bottom layer, which contains [BMIM][OS] and the metal porphyrin. The NMR analysis was done at ambient temperature, and dimethyl sulfoxide (DMSO) was used as a solvent.

Kinetic Study

A second-order extraction model was used to determine the mechanism of the metal porphyrins extraction. The model was calculated using the following linear Equation 5:

$$t/C_t = [1/(k_2 C_s^2)] + (t/C_s) \qquad [5]$$

where C_s and C_t are concentrations of metal porphyrin at saturation (mg/L) and metal porphyrin at any extraction time (mg/L), respectively, k_2 was the rate coefficient of second-order extraction (min^{-1}), and t was the extraction time (min). C_s and k_2 were obtained from the slope and intercept of the t/C_t vs. t graph.

RESULTS AND DISCUSSION

Effect of Temperature

Subcritical Condition. The experiment was carried out to study the effect of temperature on metalloporphyrin extraction using subcritical toluene-assisted ionic liquid. The experiment was done at 150°C (9 bar), 180°C (10 bar), and 210°C (11 bar). The ionic liquid used in this work is [BMIM][OS]. Four types of metalloporphyrin are studied in this work: NiEP, NiTPP, VOEP, and VOTPP. The results obtained are shown in Figures 2 to 4.

Figure 2 demonstrates the extraction results for NiEP. It was observed that the temperature and mixing time affected the extraction of NiEP differently. The removal (%) indicates the efficiency of metalloporphyrin extraction using subcritical toluene-assisted

thermally stable ionic liquid. As the mixing time increased, the extraction of NiEP increased. It is due to the longer contact time between [BMIM][OS] and the metal complexes, resulting in more metal complexes being extracted. However, the removal of NiEP increased from 30% ± 0.9 to 60% ± 1.1 when the temperature was raised from 150ºC to 180ºC. As rising temperatures could reduce the viscosity of the extractant, this also leads to a higher solubility of the metal complexes. The solubility increased from 265 µg NiEP/g [BMIM][OS] at 150ºC to 399 µg NiEP/g [BMIM][OS] at 180ºC. Then, the extraction of NiEP decreased by 13% ± 0.75 when the temperature reached 210ºC. The maximum extraction of NiEP is achieved at 60%, under a temperature of 180ºC and mixing time of 90 minutes. The most significant parameter is temperature. However, the deep knowledge of the fate of metal in this reaction remains unclear. Mandal et al. (2012b) stated that the fate of the central metal group in the reaction was not explained.

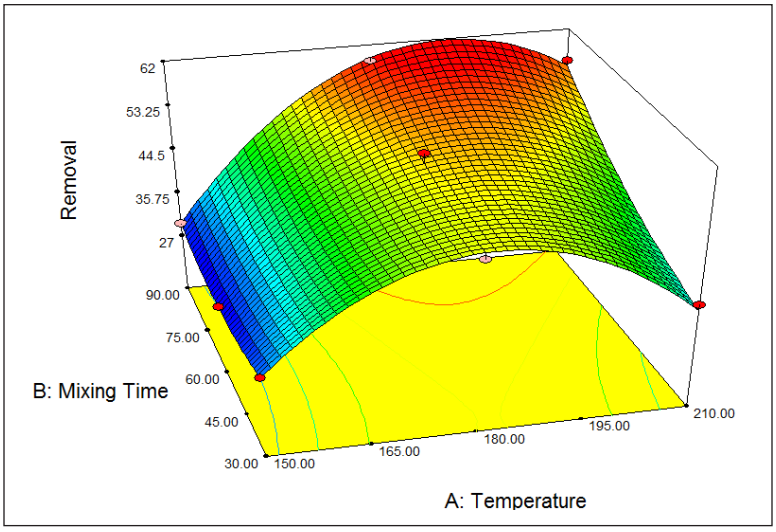

Figure 2. Effect of mixing time and temperature on the removal percentage of NiEP (%)

Meanwhile, Figure 3 illustrates the extraction results for NiTPP. The surface plot shows that the removal decreased by 10% (from 50% ± 0.4 to 40% ± 0.9) when the temperature increased from 150ºC to 180ºC. Then, it increased up to 60% ± 0.9 of extraction when the temperature reached 210ºC, except for the case of 90 minutes of mixing time where the extraction was reduced by as much as 20% ± 0.6 as the temperature increased. The highest extraction of NiTPP was accomplished at a temperature of 150ºC and a mixing time of 90 minutes, where [BMIM][OS] could extract approximately 70% of NITPP. Mandal et al. (2011) reported that the fate of a central metal group of NiTPP under supercritical conditions remains uncertain. This sentiment was supported by the work of Bonné et al. (2001), which also stated that the fate of the central metal group under non-catalytic demetallization remained obscure.

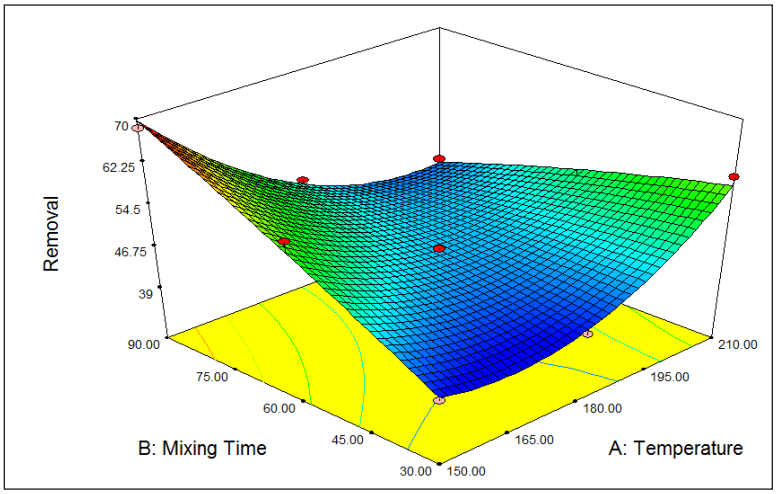

Figure 3. Effect of mixing time and temperature on the removal percentage of NiTPP (%)

Similarly, the extraction of NiEP was slightly increased when extraction time increased from 30 minutes to 60 minutes. Then, it increased by 10% when the extraction time increased to 90 minutes. These results indicate that the longer the extraction time, the longer the extractant contacted NiEP, thus increasing the NiEP extraction. On the other hand, the NiTPP extraction was increased as extraction time increased except for a temperature of 210ºC, where the NiTPP was slightly decreased.

Figure 4 shows the effect of temperature on VOEP extraction. As the temperature increased from 150ºC to 180ºC, the extraction drastically increased by almost 20% (from 30% ± 0.5 to 50% ± 0.9). It then increased slightly further by 7% (57% ± 0.8) when the

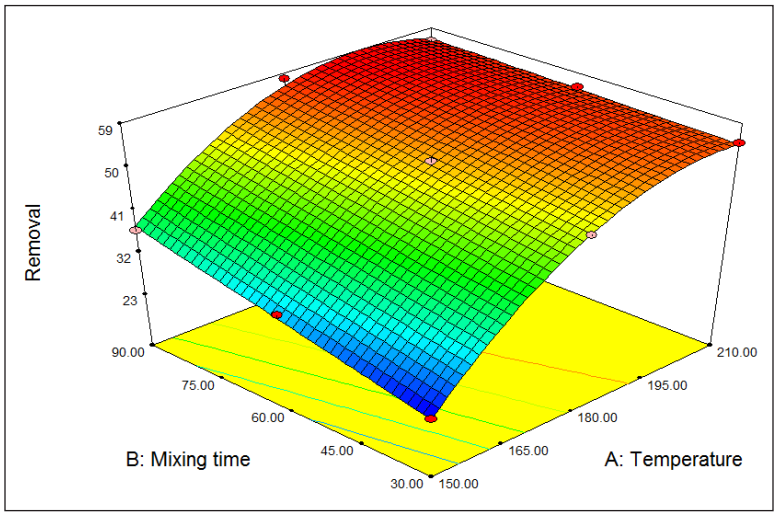

Figure 4. Effect of mixing time and temperature on the removal percentage of VOEP (%)

temperature was extended to 210ºC. It is due to the reduction of the viscosity of [BMIM][OS], which increases the contact surface, thus leading to higher extraction of VOEP. Besides, the reduction in viscosity of [BMIM][OS] also leads to an increase in metal transfer in ionic liquid (Germani et al., 2007). Consequently, VOEP extraction was increased as temperature increased. However, when the mixing time is increased from 30 minutes to 90 minutes, the removal of VOEP increases slightly. Mandal et al. (2012a) studied the removal of VOEP using supercritical water. The results showed that the conversion rate of VOEP showed a significant increase, followed by a slight increase when the temperature was raised to 490ºC. It is stated that the reversible reaction took place and reached equilibrium within a reaction time of 90 minutes.

Figure 5 reveals the extraction of VOTPP using subcritical toluene assisted [BMIM][OS]. Based on the surface plot, the VOTPP extraction was reduced by 10 to 13% extraction (from 30% ± 0.5 to approximately 20% ± 0.5) when the temperature was increased from 150ºC to 180ºC. Then, the extraction was increased by 5 to 10% (approximately 30% ± 0.8) when the temperature extended to 210ºC. However, the prediction of the structure of porphyrin conformation under several environments was challenging because only low amounts of energy were used to change the conformation of porphyrin structure. A deep understanding of detailed porphyrin conformation in solution remained obscure due to inadequate knowledge of solvent-porphyrin interactions (Fleischer, 1970).

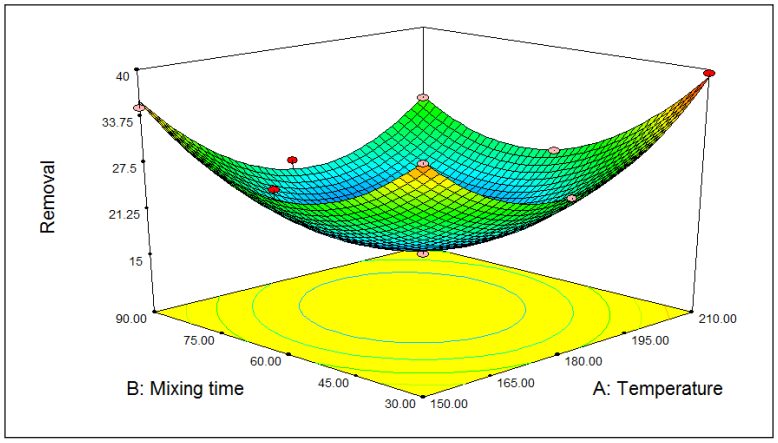

Figure 5. Effect of mixing time and temperature on the removal percentage of VOTPP (%)

Likewise, the VOEP extraction was significantly increased when extraction time increased from 30 minutes to 90 minutes. However, VOEP extraction slightly inclined when it operated at 210ºC. On the other hand, the VOTPP extraction declined when the extraction time increased from 30 minutes to 60 minutes, then increased when the extraction time was extended to 90 minutes.

Comparison of Metalloporphyrin Removal at Normal Condition and Subcritical Condition. Experiments were done to compare the performance of toluene-assisted [BMIM][OS] on metalloporphyhrin extraction at normal conditions (below boiling point, 90ºC) and subcritical condition (210ºC). The results obtained with the error bar are shown in Figure 6. It was observed that subcritical toluene had improved in assisting [BMIM][OS] to extract the metalloporphyrin. Nickel porphyrin extraction was higher than vanadium porphyrin extraction. It is because nickel porphyrin is more stable with regard to demetallization due to the shorter distance of the Ni-Nitrogen bond (Fleischer, 1970). The extraction of nickel porphyrin increased from 23% to 36% and from 39% to 60% for NiEP and NiTPP, respectively. Meanwhile, the extraction of vanadium porphyrin increased from 40% to 55% and from 23% to 40% for VOEP and VOTPP, correspondingly.

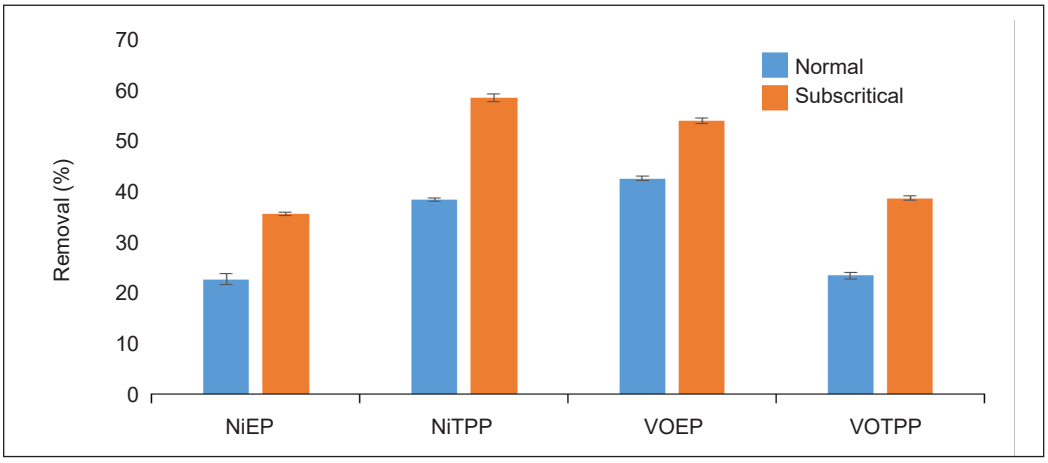

Figure 6. Comparison of metalloporphyrin extraction at normal conditions and subcritical condition

Analysis

Fourier Transform Infrared Spectroscopy (FTIR). The functional groups of [BMIM][OS] were studied regarding their structural changes before and after extraction. Therefore, FTIR analysis was carried out. Figures 7 to 10 illustrate the spectra of pure [BMIM][OS], pure toluene, [BMIM][OS] after extraction, and pure metal porphyrins (NiEP, NiTPP, VOEP, and VOTPP). It was observed that spectra bands above 3000 cm^{-1} represented the C-H at imidazolium rings of [BMIM][OS], while bands of 2927 to 2853 cm^{-1} represented CH_2 of alkyl chains. Wavelengths between 1466.05 to 1457 cm^{-1} show the symmetry and asymmetry stretching of C-H scissoring vibrations of CH_3-moiety. C-C stretching vibrations were observed at a wavelength of 1572 cm^{-1}.

In addition, the spectra bands at 1379 cm^{-1} refer to the C=C stretching vibrations. The spectra peaks of C-N stretching shifted from the wavelength of 1217 cm^{-1} to 1219-1210 cm^{-1}. On the other hand, spectra bands at 1057 cm^{-1} and 982 cm^{-1} correspond to C-O and

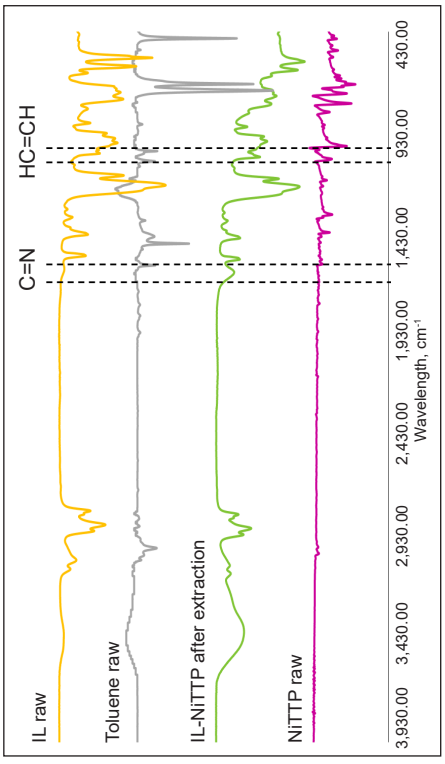

Figure 7. IR spectra of pure [BMIM][OS], pure toluene, [BMIM][OS] after extraction and pure NiEP

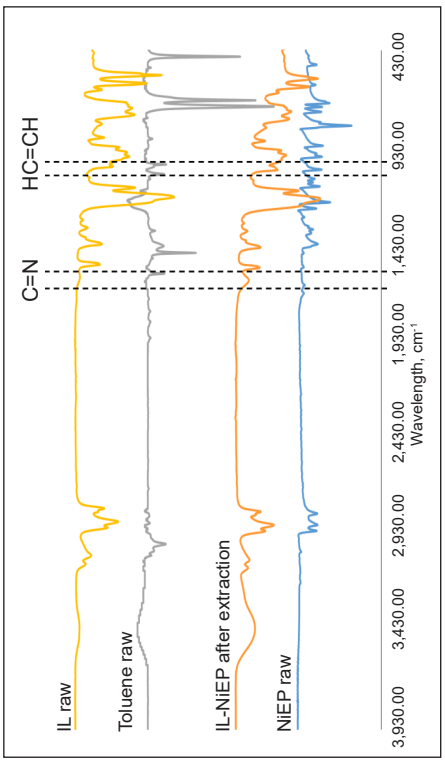

Figure 9. IR spectra of pure [BMIM][OS], pure toluene, [BMIM][OS] after extraction and pure VOEP

Figure 8. IR spectra of [BMIM][OS], pure toluene, [BMIM][OS] after extraction and pure NiTPP

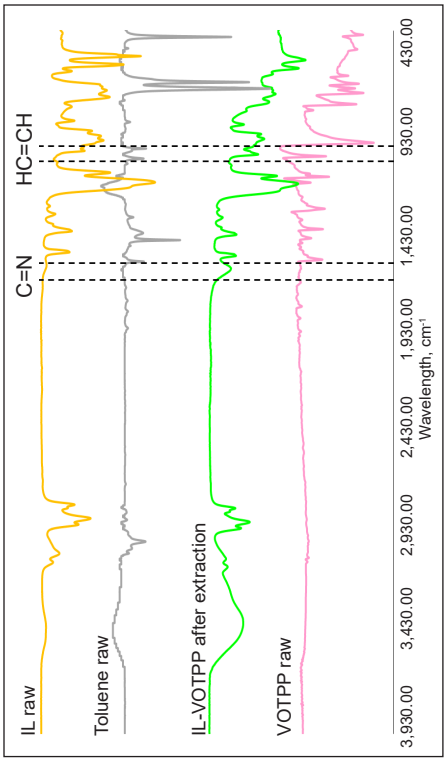

Figure 10. IR spectra of pure [BMIM][OS], pure toluene, [BMIM][OS] after extraction and pure VOTPP

S-O stretching vibrations, respectively, while the spectra at 905 cm^{-1} represent aromatic C-H bending vibrations. However, new peaks were detected at wavelengths of 1637 and 1060 cm^{-1}. These peaks represent C=N and HC=CH of metal porphyrins in [BMIM][OS] after the extraction, respectively, indicating that the [BMIM][OS] was able to extract metal porphyrins successfully.

Figure 11 compares IR spectra of pure [BMIM][OS], pure toluene, and NiEP solution after extraction. It is noted that no new peaks were found in the NiEP solution after the extraction, indicating that the [BMIM][OS] does not dissolve into the model oil solution while extracting the metalloporphyrins. The same result was obtained for NiTPP, VOEP, and VOTPP solutions. It shows that the ionic liquid is suitable for extraction, as the extracting agent is immiscible to the solution containing the solute to be extracted.

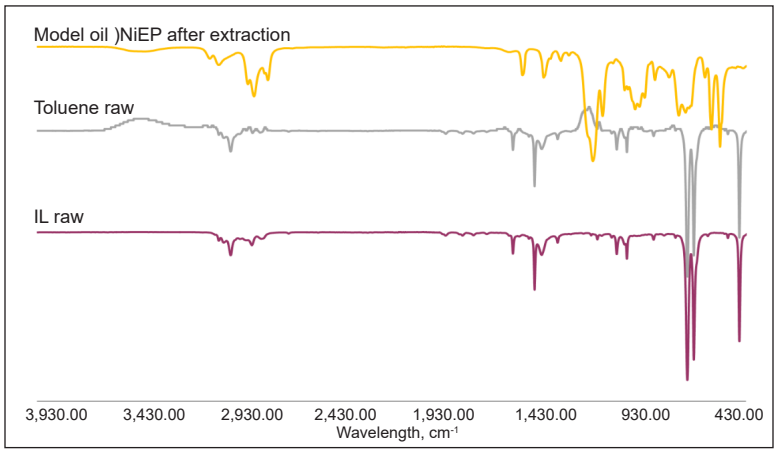

Figure 11. IR spectra of pure [BMIM][OS], pure toluene, and NiEP solution after extraction

Nuclear Magnetic Resonance (NMR). Initially, [BMIM][OS] was thermally stable at the operating temperature used in this work. A study of the structural decomposition of [BMIM][OS] was carried out using NMR analysis to confirm this. [BMIM[OS] has the molecular formula of $C_{16}H_{32}N_2O_4S$. Figure 12 demonstrates the NMR spectrum of [BMIM][OS] before and after the extraction of metalloporphyrin, where dimethyl sulfoxide (DMSO) was used as a solvent.

The ^{1}H NMR peaks of DMSO were 2.5 and 3.5 ppm. Meanwhile, for [BMIM][OS], ^{1}H NMR (δ/ppm): 9.157 (s, 1H), 7.79 and 7.72 (two s, 2 × 1H), 4.19 to 4.16 (t, 2H), 3.867 (s, 3H), 3.717 and 3.69 (t, 2H), 1.802 to 1.749 (m, 2H), 1.5 to 1.459 (m, 2H), 1.287 to 1.249 (m, 12H), 0.91 (t, 3H) and 0.9 (t, 3H). The comparison of peaks found in Figure 12 indicates that the structure of [BMIM][OS] does not decompose during the metalloporphyrin extraction process, therefore confirming the thermal stability of [BMIM][OS] for the application within this work. Hence, [BMIM][OS] can be recovered for further experiments, though the actual recoverable amount of [BMIM][OS] is not further studied

in this work. However, ^{1}H NMR cannot detect the extracted metalloporphyrin in [BMIM][OS] due to the limitations of the equipment.

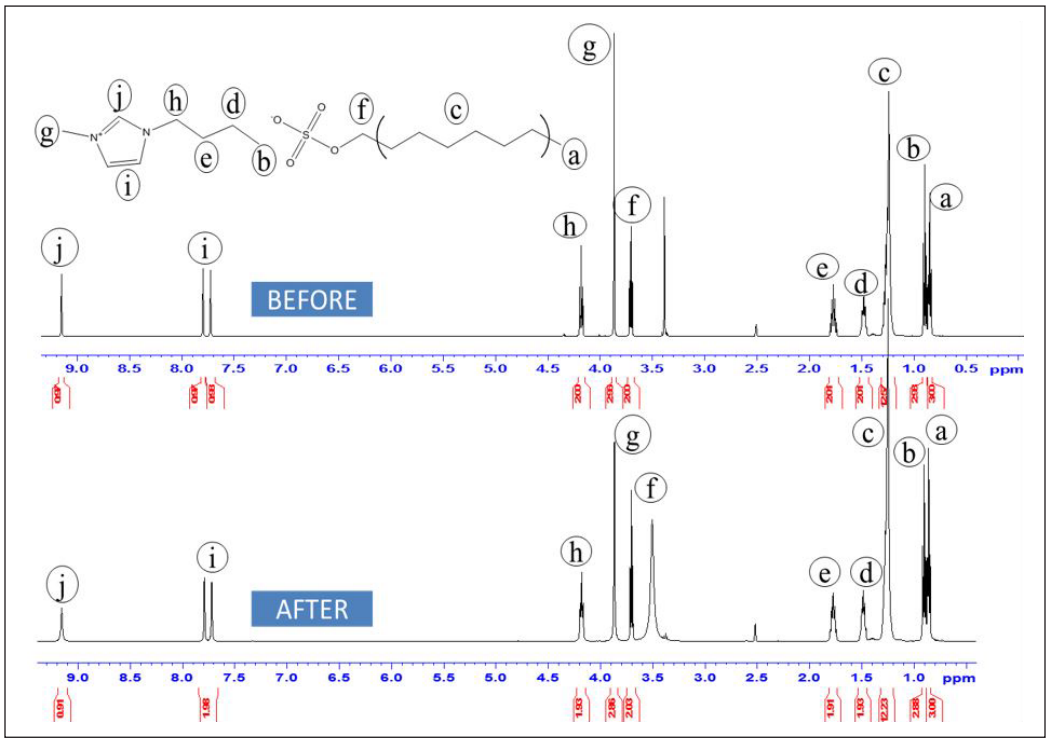

Figure 12. ^{1}H NMR of [BMIM][OS] before and after the extraction

Kinetic Study

The mechanism of metalloporphyrin extraction using subcritical toluene-assisted thermally stable [BMIM][OS] was studied by applying a second-order extraction model. Several graphs were plotted using Equation 5 for all the different cases of metalloporphyrin extraction (Figures 13 to 16). Based on the linear graph, it was concluded that the second-order model accurately described the experimental data of metalloporphyrin extraction, as the data fitted closely in a straight line.

The value of C_s and k were obtained from the slope and intercept of the linear graphs in Figures 13 to 16, and all values found in the kinetic study are tabulated in Table 1. The R^2 of the second-order models was higher than 0.98, further supporting that the model fitted the experimental data very well. The C_s calculated using the second-order model are close to those obtained from the experiment. The value of k increases as the temperature is raised from 150ºC to 180ºC, and it decreases when the temperature rise is prolonged until it reaches 210ºC, except for NiEP. The main finding here is that the extraction of metalloporphyrin is faster at temperatures between 150ºC to 180ºC.

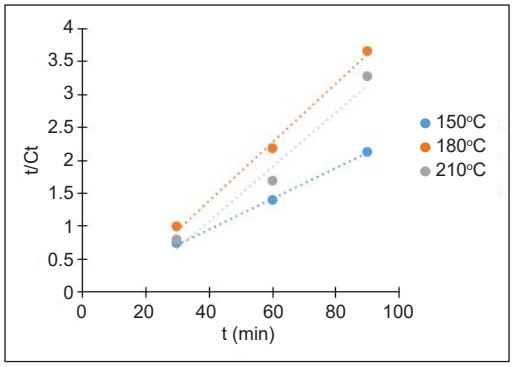

Figure 13. Linear graph of extraction second-order model for NiEP

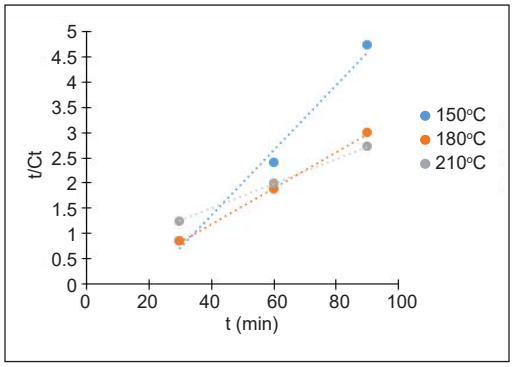

Figure 14. Linear graph of extraction second-order model for NiTPP

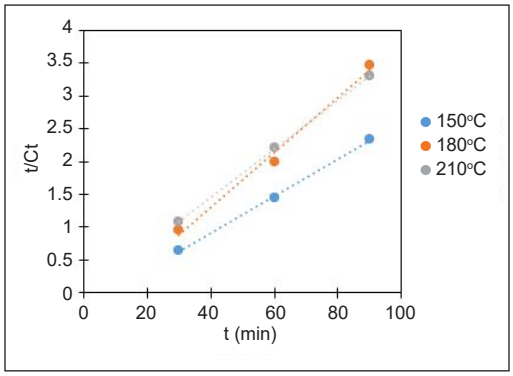

Figure 15. Linear graph of extraction second-order model for VOEP

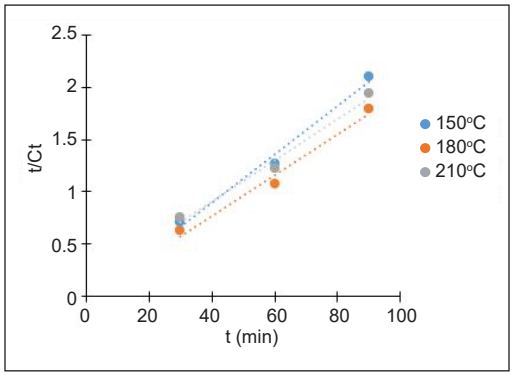

Figure 16. Linear graph of extraction second-order model for VOTPP

The extraction is kinetic and was compared with the pseudo-first-order kinetic model ($\ln (C_s/(C_s\text{-}C_t) = k_1 t$). Based on the tabulated data in Table 1, the pseudo-first-order model is not in good agreement with an average R^2 value of 0.69. Compared with the second-order kinetic model R^2 value of 0.99, the second-order model shows a better fit. The high R^2 obtained indicates that the sorption process of extraction of metalloporphyrin is based on chemisorption. The results demonstrate good agreement with the FTIR spectra gained, where new peaks were found in [BMIM][OS] spectra after the extraction, showing that the extraction occurred through chemical interactions. Besides, subcritical conditions' pressure resulted in chemisorption as this sorption required high pressure. However, a deep understanding of the underlying mechanism of metalloporphyrins removal using subcritical toluene-assisted thermally stable [BMIM][OS] is still obscure.

Previous work done by Mandal et al. (2012a, 2012b) reported that the disappearance of NiEP and VOEP under supercritical water followed a first-order model. Similar results were also reported by Chen and Massoth, where the disappearance rate of nickel porphyrins

Table 1
Data comparison of the pseudo-first-order and second-order kinetic model

Metal Porphyrin	T (°C)	Pseudo First-order model				Second order model				
		Cs_{exp} (mg/L)	Cs_{cal} (mg/L)	z (min^{-1})	R^2	Cs_{exp} (mg/L)	Cs_{cal} (mg/L)	k (L/ (mg/ min)	h (mg/L. min)	R^2
NiEP	150	42.31	41.002	0.000461	0.3274	42.31	42.92	0.030499	56.18	0.9989
	180	24.65	33.81	0.003455	0.9993	24.65	22.52	0.005038	2.56	0.9964
	210	27.59	46.47	0.005527	0.8928	27.59	24.21	0.002995	1.76	0.9744
NiTPP	150	19.04	47.6	0.010364	0.996	19.04	15.48	0.003416	0.82	0.9864
	180	30.11	37.95	0.002533	0.9832	30.11	28.09	0.005421	4.28	0.9994
	210	33.15	21.03	0.005297	0.9519	33.15	40.82	0.001173	1.96	0.9864
VOEP	150	38.46	50.71	0.003224	0.9942	38.46	35.46	0.00365	4.59	0.9986
	180	25.9	35.56	0.003455	0.9271	25.9	27.03	0.051082	37.31	0.9999
	210	27.29	27.98	0.00023	0.6931	27.29	23.75	0.004575	2.58	0.9904
VOTPP	150	42.92	43.9	0.000138	0.0042	42.92	43.1	0.014626	27.17	0.9876
	180	50.12	49.25	0.000691	0.0672	50.12	51.28	0.04321	113.64	0.9814
	210	46.44	38.72	0.002533	0.4919	46.44	50.51	0.003374	8.61	0.9855

*Cs_{exp} and Cs_{cal} represent the concentration of metalloporphyrin extracted from experimental work and calculation, respectively.

using $CoMo/Al_2O_3$ catalyst followed a first-order kinetic model behavior (Chen & Massoth, 1988). Tangentially, the disappearance rate of nickel porphyrins using a $CoO\text{-}MoO_3/Al_2O_3$ catalyst was reported to follow a half-order kinetic model (Hung & Wei, 1980).

CONCLUSION

The presence of heavy metals in heavy oils presents significant challenges to current upgrading technologies, necessitating the development of pretreatment methods to remove these heavy metals. Using subcritical toluene-assisted thermally stable ionic liquid, [BMIM][OS] shows remarkable results on metalloporphyrin extraction where approximately 60%, 68%, 58%, and 40% removal is achieved for NiEP, NiTPP, VOEP, and VOTPP respectively. The FTIR spectra supported the results, where new peaks were found in [BMIM][OS], representing the metalloporphyrins' structure. Besides, the NMR spectrum shows [BMIM][OS] does not decompose during the extraction process, indicating this IL is thermally stable at the operational condition. Furthermore, the extraction has proven to follow a second-order model, which reveals that the process involves chemisorption. Therefore, the extraction efficiency obtained in this work indicates that subcritical toluene-assisted thermally stable ionic liquid had the potential for metalloporphyrin removal. For a future perspective, it is suggested that a continuous process is required to study the extraction of metalloporphyrin, as this work was done by processing per batch. Furthermore, it is proposed to investigate the recovery of ionic liquid with the highest extraction of metalloporphyrin. Besides, it is recommended to examine techno-economic analysis to study the feasibility of implementing this technology on a larger scale.

ACKNOWLEDGMENTS

The authors thank the Centre of Research in Ionic Liquids (CORIL), Universiti Teknologi PETRONAS (UTP), Perak, Malaysia, for providing a conducive environment and necessary facilities for this research work. This research was funded by Yayasan Universiti Teknologi PETRONAS (YUTP) (Cost center: 0153AA-E33) and (Cost center: 015LC0-257).

REFERENCES

Agrawal, R., & Wei, J. (1984). Hydrodemetalation of nickel and vanadium porphyrins. 1. Intrinsic kinetics. *Industrial & Engineering Chemistry Process Design and Development*, *23*(3), 505-514. https://doi.org/10.1021/i200026a017

Ali, S. A., Suboyin, A., & Haj, H. B. (2018). Unconventional and conventional oil production impacts on oil price - Lessons learnt with glance to the future. *Journal of Global Economics*, *06*(1), Article 1000286. https://doi.org/10.4172/2375-4389.1000286

Ameur, Z. O., & Husein, M. M. (2012). Salting-out induced aggregation for selective separation of vanadyl-oxide tetraphenyl-porphyrin from heavy oil. *Energy & Fuels*, *26*(7), 4420-4425. https://doi.org/10.1021/ef300482h

Bara, J. E., Camper, D. E., Gin, D. L., & Noble, R. D. (2010). Room-temperature ionic liquids and composite materials: Platform technologies for CO $_2$ capture. *Accounts of Chemical Research*, *43*(1), 152-159. https://doi.org/10.1021/ar9001747

Bates, E. D., Mayton, R. D., Ntai, I., & Davis, J. H. (2002). CO_2 capture by a task-specific ionic liquid. *Journal of the American Chemical Society*, *124*(6), 926-927. https://doi.org/10.1021/ja017593d

Beni, A. A., & Esmaeili, A. (2020). Biosorption, an efficient method for removing heavy metals from industrial effluents: A review. *Environmental Technology & Innovation, 17*, Article 100503. https://doi.org/10.1016/j.eti.2019.100503

Bonné, R. L. C., van Steenderen, P., & Moulijn, J. A. (2001). Hydrogenation of nickel and vanadyl tetraphenylporphyrin in absence of a catalyst: A kinetic study. *Applied Catalysis A: General, 206*(2), 171-181. https://doi.org/10.1016/S0926-860X(00)00587-1

Castañeda, L. C., Muñoz, J. A. D., & Ancheyta, J. (2014). Current situation of emerging technologies for upgrading of heavy oils. *Catalysis Today*, *220-222*, 248-273. https://doi.org/10.1016/j.cattod.2013.05.016

Chen, H. J., & Massoth, F. E. (1988). Hydrodemetalation of vanadium and nickel porphyrins over sulfided cobalt-molybdenum/alumina catalyst. *Industrial & Engineering Chemistry Research*, *27*(9), 1629-1639. https://doi.org/10.1021/ie00081a012

Dávila, M. J., Aparicio, S., Alcalde, R., García, B., and Leal, J. M. (2007). On the properties of 1-butyl-3-methylimidazolium octylsulfate ionic liquid. *Green Chemistry*, *9*(3), 221-232. https://doi.org/10.1039/B612177B.

Davis, Jr., J. H. & Fox, P. A. (2003). From curiosities to commodities: Ionic liquids begin the transition. *Chemical Communications, 11*, 1209-1212, https://doi.org/10.1039/b212788a.

Dobler, D., Schmidts, T., Klingenhöfer, I., & Runkel, F. (2013). Ionic liquids as ingredients in topical drug delivery systems. *International Journal of Pharmaceutics*, *441*(1-2), 620-627. https://doi.org/10.1016/j.ijpharm.2012.10.035

Elektorowicz, M., & Muslat, Z. (2008). Removal of heavy metals from oil sludge using ion exchange textiles. *Environmental Technology*, *29*(4), 393-399. https://doi.org/10.1080/09593330801984290

Fadeev, A. G., & Meagher, M. M. (2001). Opportunities for ionic liquids in recovery of biofuels. *Chemical Communications*, *3*, 295-296. https://doi.org/10.1039/b006102f

Fauzi, A. H. M., & Amin, N. A. S. (2012). An overview of ionic liquids as solvents in biodiesel synthesis. *Renewable and Sustainable Energy Reviews*, *16*(8), 5770-5786. https://doi.org/10.1016/j.rser.2012.06.022

Fleischer, E. B. (1970). Structure of porphyrins and metalloporphyrins. *Accounts of Chemical Research*, *3*(3), 105-112. https://doi.org/10.1021/ar50027a004

Germani, R., Mancini, M., Savelli, G., & Spreti, N. (2007). Mercury extraction by ionic liquids: Temperature and alkyl chain length effect. *Tetrahedron Lette*rs, *48*(10), 1767-1769. https://doi.org/10.1016/j.tetlet.2007.01.038

Hijo, A. A. C. T., Maximo, G. J., Costa, M. C., Batista, E. A. C., & Meirelles, A. J. A. (2016). Applications of ionic liquids in the food and bioproducts industries. *ACS Sustainable Chemistry & Engineering*, *4*(10), 5347-5369. https://doi.org/10.1021/acssuschemeng.6b00560

Huddleston, J. G., Willauer, H. D., Swatloski, R. P., Visser, A. E., & Rogers, R. D. (1998). Room temperature ionic liquids as novel media for 'clean' liquid-liquid extraction. *Chemical Communications. 16*, 1765-1766. https://doi.org/10.1039/A803999B

Hung, C. W., & Wei, J. (1980). The kinetics of porphyrin hydrodemetallation. 1. Nickel compounds. *Industrial & Engineering Chemistry Process Design and Development*, *19*(2), 250-257. https://doi.org/10.1021/i260074a009

Ikyereve, R. E., Nwankwo, C., & Mohammed, A. (2014). Selective removal of metal ions from crude oil using synthetic zeolites. *International Journal of Scientific and Research Publications*, *4*(5), 411-413.

Jiménez, A. E., & Bermúdez, M. D. (2007). Ionic liquids as lubricants for steel-aluminum contacts at low and elevated temperatures. *Tribology Letters*, *26*(1), 53-60. https://doi.org/10.1007/s11249-006-9182-9

Karadas, F., Atilhan, M., & Aparicio, S. (2010). Review on the use of ionic liquids (ILs) as alternative fluids for CO_2 capture and natural gas sweetening. *Energy & Fuels*, *24*(11), 5817-5828. https://doi.org/10.1021/ef1011337

Khaidzir, S., Masri A. N., Ruslan, M. S. H., & Mutalib, M. I. A. (2021). Ultrasonic-assisted technique as a novel method for removal of naphthenic acid from model oil using piperidinium-based ionic liquids. *ACS Omega*, *6*(14), 9629-9637.

Kumano, M., Yabutani, T., Motonaka, J., & Mishima, Y. (2006). Recovery and extraction of heavy metal ions using ionic liquid as green solvent. *International Journal of Modern Physics B*, *20*(25n27), 4051-4056. https://doi.org/10.1142/S0217979206040842

Liu, C. Z., Wang, F., Stiles, A. R., & Guo, C. (2012). Ionic liquids for biofuel production: Opportunities and challenges. *Applied Energy*, *92*, 406-414. https://doi.org/10.1016/j.apenergy.2011.11.031

Mandal, P., & Alias, M. A. (2017). Investigation of asphaltene under subcritical water treatment. *International Journal of Materials, Mechanics and Manufacturing*, *5*(1), 11-15. https://doi.org/10.18178/ijmmm.2017.5.1.279

Mandal, P. C., Goto, M., & Sasaki, M. (2014). Removal of nickel and vanadium from heavy oils using supercritical water. *Journal of the Japan Petroleum Institute*, *57*(1), 18-28. https://doi.org/10.1627/jpi.57.18

Mandal, P. C., Wahyudiono, Sasaki, M., & Goto, M. (2011). Nickel removal from nickel-5,10,15,20-tetraphenylporphine using supercritical water in absence of catalyst: A basic study. *Journal of Hazardous Materials*, *187*(1-3), 600-603. https://doi.org/10.1016/j.jhazmat.2011.01.059

Mandal, P. C., Wahyudiono, Sasaki, M., & Goto, M. (2012a). Non-catalytic vanadium removal from vanadyl etioporphyrin (VO-EP) using a mixed solvent of supercritical water and toluene: A kinetic study. *Fuel*, *92*(1), 288-294. https://doi.org/10.1016/j.fuel.2011.07.002

Mandal, P. C., Wahyudiono, Sasaki, M., & Goto, M. (2012b). Nickel removal from nickel etioporphyrin (Ni-EP) using supercritical water in the absence of catalyst. *Fuel Processing Technology*, *104*, 67-72. https://doi.org/10.1016/j.fuproc.2011.07.004

Manjare, S., & Dhingra, K. (2019). Supercritical fluids in separation and purification: A review. *Materials Science for Energy Technologies*, *2*(3), 463-484. https://doi.org/10.1016/j.mset.2019.04.005

Moniruzzaman, M., Tahara, Y., Tamura, M., Kamiya, N., & Goto, M. (2010). Ionic liquid-assisted transdermal delivery of sparingly soluble drugs. *Chemical Communications*, *46*(9), Article 1452. https://doi.org/10.1039/b907462g

Monti, D., Egiziano, E., Burgalassi, S., Chetoni, P., Chiappe, C., Sanzone, A., & Tampucci, S. (2017). Ionic liquids as potential enhancers for transdermal drug delivery. *International Journal of Pharmaceutics*, *516*(1-2), 45-51. https://doi.org/10.1016/j.ijpharm.2016.11.020

Muhammad, N., Elsheikh, Y. A., Mutalib, M. I. A., Bazmi, A. A., Khan, R. A., Khan, H., Rafiq, S., Man, Z., & khan, I. (2015). An overview of the role of ionic liquids in biodiesel reactions. *Journal of Industrial and Engineering Chemistry*, *21*, 1-10. https://doi.org/10.1016/j.jiec.2014.01.046

Painter, P., Veytsman, B., & Youtcheff, J. (2015). Guide to asphaltene solubility. *Energy & Fuels*, *29*(5), 2951-2961. https://doi.org/10.1021/ef502918t

Qu, J., Blau, P. J., Dai, S., Luo, H., & Meyer, H. M. (2009). Ionic liquids as novel lubricants and additives for diesel engine applications. *Tribology Letters*, *35*(3), 181-189. https://doi.org/10.1007/s11249-009-9447-1

Ramdin, M., de Loos, T. W., & Vlugt, T. J. H. (2012). State-of-the-art of CO_2 capture with ionic liquids. *Industrial & Engineering Chemistry Research*, *51*(24), 8149-8177. https://doi.org/10.1021/ie3003705

Rana, M. S., Sámano, V., Ancheyta, J., & Diaz, J. A. I. (2007). A review of recent advances on process technologies for upgrading of heavy oils and residua. *Fuel*, *86*(9), 1216-1231. https://doi.org/10.1016/j.fuel.2006.08.004

Salehizadeh, H., Mousavi, M., Hatamipour, S., & Kermanshahi, K. (2007). Microbial demetallization of crude oil using *Aspergillus* sp.: Vanadium oxide octaethyl porphyrin (VOOEP) as a model of metallic petroporphyrins. *Iranian Journal of Biotechnology*, *5*(4), 226-231.

Santos, R. G., Loh, W., Bannwart, A. C., & Trevisan, O. V. (2014). An overview of heavy oil properties and its recovery and transportation methods. *Brazilian Journal of Chemical Engineering*, *31*(3), 571-590. https://doi.org/10.1590/0104-6632.20140313s00001853

Selvi, A., Rajasekar, A., Theerthagiri, J., Ananthaselvam, A., Sathishkumar, K., Madhavan, J., & Rahman, P. K. S. M. (2019). Integrated remediation processes toward heavy metal removal/recovery from various environments - A review. *Frontiers in Environmental Science*, *7*, 1-15. https://doi.org/10.3389/fenvs.2019.00066

Siriwardana, A. I. (2015). Industrial applications of ionic liquids. In A. A. J. Torriero (Ed.), *Electrochemistry in Ionic Liquids* (pp. 563-603). Springer International Publishing. https://doi.org/10.1007/978-3-319-15132-8_20

Sowmiah, S., Srinivasadesikan, V., Tseng, M. C., & Chu, Y. H. (2009). On the chemical stabilities of ionic liquids. *Molecules*, *14*(9), 3780-3813. https://doi.org/10.3390/molecules14093780

Sun, X., Luo, H., & Dai, S. (2012). Ionic liquids-based extraction: A promising strategy for the advanced nuclear fuel cycle. *Chemical Reviews*, *112*(4), 2100-2128. https://doi.org/10.1021/cr200193x

Tavakoli, O., & Yoshida, H. (2005). Effective recovery of harmful metal ions from squid wastes using subcritical and supercritical water treatments. *Environmental Science & Technology*, *39*(7), 2357-2363. https://doi.org/10.1021/es030713s

Trucillo, P., Campardelli, R., Scognamiglio, M., & Reverchon, E. (2019). Control of liposomes diameter at micrometric and nanometric level using a supercritical assisted technique. *Journal of CO_2 Utilization*, *32*, 119-127. https://doi.org/10.1016/j.jcou.2019.04.014

Vancov, T., Alston, A. S., Brown, T., & McIntosh, S. (2012). Use of ionic liquids in converting lignocellulosic material to biofuels. *Renewable Energy*, *45*, 1-6. https://doi.org/10.1016/j.renene.2012.02.033

Visser, A. E., Swatloski, R. P., Reichert, W. M., Davis Jr., J. H., Rogers, R. D., Mayton, R., Sheff, S., & Wierzbicki, A. (2001). Task-specific ionic liquids for the extraction of metal ions from aqueous solutions. *Chemical Communications*, *1*, 135-136. https://doi.org/10.1039/b0080411

Wang, S., Xu, X., Yang, J., & Gao, J. (2011). Effect of the carboxymethyl chitosan on removal of nickel and vanadium from crude oil in the presence of microwave irradiation. *Fuel Processing Technology*, *92*(3), 486-492. https://doi.org/10.1016/j.fuproc.2010.11.001

Welter, K., Salazar, E., Balladores, Y., Márquez, O. P., Márquez, J., & Martínez, Y. (2009). Electrochemical removal of metals from crude oil samples. *Fuel Processing Technology*, *90*(2), 212-221. https://doi.org/10.1016/j.fuproc.2008.09.004

Yuan, J., Yang, Y., Zhou, X., Ge, Y., & Zeng, Q. (2019). A new method for simultaneous removal of heavy metals and harmful organics from rape seed meal from metal-contaminated farmland. *Separation and Purification Technology*, *210*, 1001-1007. https://doi.org/10.1016/j.seppur.2018.09.056

Zhao, X., Xu, C., & Shi, Q. (2015). Porphyrins in heavy petroleums: A review. In C. Xu & Q. Shi (Eds.), *Structure and Modeling of Complex Petroleum Mixtures* (Vol. 168: pp. 39-70). Springer International Publishing. https://doi.org/10.1007/430_2015_189

Pertanika J. Sci. & Technol. 31 (4): 1991 - 2011 (2023)

PERTANIKA JOURNALS

SCIENCE & TECHNOLOGY

Journal homepage: http://www.pertanika.upm.edu.my/

Forecasting Geo Location of COVID-19 Herd

Divyansh Agarwal[1], Nishita Patnaik[1], Aravind Harinarayanan[1], Sudha Senthilkumar[1]*, Brindha Krishnamurthy[2] and Kathiravan Srinivasan[1]

[1]School of Computer Science and Engineering, Vellore Institute of Technology, Vellore 632014, Tamil Nadu, India
[2]School of Information Technology and Engineering, Vellore Institute of Technology, Vellore 632014, Tamil Nadu, India

ABSTRACT

Thanks to the growth in data storage capacity, nowadays, researchers can use years' worth of mathematical models and depend on past datasets. A pattern of all pandemics can be identified through the assistance of Machine Learning. The movement of the COVID-19 herd and any future pandemic can be predicted. These predictions will vary based on the dataset, but it will allow the preparation beforehand and stop the spreading of COVID-19. This study focuses on developing Spatio-temporal models using Machine Learning to produce a predictive visualized heat regional map of COVID-19 worldwide. Different models of Machine Learning are compared using John Hopkins University dataset. This study has compared well-known basic models like Support Vector Machine (SVM), Prophet, Bayesian Ridge Regression, and Polynomial Regression. Based on the comparison of various metrics of the Support Vector Machine, Polynomial Regression Model was found to be better and hence can be assumed to give good results for long-term prediction. On the other hand, ARIMA, Prophet Model, and Bayesian Ridge Reduction models are good for short-term predictions. The metrics such as Mean Absolute Error (MAE), Mean Squared Error (MSE), and Root Mean Square Error (RMSE) are better for Support Vector Machines compared to other models. The metrics such as R^2 Score and Adjusted R-Square are better for the polynomial Regression model.

Keywords: ARIMA, Bayesian ridge regression, COVID-19, polynomial regression, predictions, prophet, support vector machine (SVM)

ARTICLE INFO

Article history:
Received: 16 July 2022
Accepted: 02 November 2022
Published: 13 June 2023

DOI: https://doi.org/10.47836/pjst.31.4.23

E-mail addresses:
divyansh.agarwal2019@vitstudent.ac.in (Divyansh Agarwal)
nishita.patnaik2019@vitstudent.ac.in (Nishita Patnaik)
inaravind.harinarayanan2019@vitstudent.ac.in (Aravind Harinarayanan)
sudha.s@vit.ac.in (Sudha Senthilkumar)
brindha.k@vit.ac.in (Brindha Krishnamurthy)
kathiravan.srinivasan@vit.ac.in (Kathiravan Srinivasan)
* Corresponding author

ISSN: 0128-7680
e-ISSN: 2231-8526

INTRODUCTION

Over the last decade, Machine Learning (ML) has emerged as a major field of study as it has solved many complex real-world problems. The forecasting areas are the main important areas of ML. Various ML algorithms forecast future events for applications like weather, disease, and stock market prediction. ML techniques have been used to forecast diseases such as breast cancer, coronary artery, and cardiovascular disease. Specifically, this article aims to provide real forecasting of COVID-19 cases.

Five types of pandemics have been seen in recent decades: H1N1 (2009–2014), Polio (2014–r2016), Zika (2016–2019), and Ebola (Democratic Republic of Congo). On January 30, 2020, the World Health Organization registered COVID-19 as the sixth worldwide pandemic. Deaths and morbidities cause a high and huge amount of economic loss worldwide. Almost every country infected with a pandemic experienced serious health-related concerns, and pandemics negatively impact the socioeconomic situation. The COVID-19 pandemic is the greatest threat to public health. WHO has received 608,328,548 reported cases worldwide, with 6,501,469 deaths (Li et al., 2020). As of September 16, 2022, Table 1 shows the COVID-19-affected countries worldwide.

Currently, computerized data are collected in a way that makes it difficult to analyze and predict disease growth locally and globally. The disease and its progression can be successfully mapped using ML algorithms. In order to train an ML model to predict the number of global confirmed cases prone to the disease in the coming days, supervised models with associated algorithms (like LR, SVR, and time series algorithms) are used to analyze data for regression and classification. This proposal collects and pre-processes the global dataset and extracts the number of confirmed cases up to a particular date, serving as the model's training set. In order to predict the growth of cases in the upcoming days, the model is being trained by supervised ML algorithms.

Table 1
COVID-19 affected countries worldwide as of September 16, 2022 ("World Health Organization," 2020)

Country name	Total cases	Total deaths	Active cases reported in last 7 days
USA	94,237,260	1,041,323	414,468
India	44,522,777	528,273	38,048
France	33,796,693	151,089	161,584
Australia	10,153,910	50,077	14,682
South Africa	4,015,347	102,146	1,626
UK	23,585,309	189,484	26,045
Brazil	**34,558,902**	**685,121**	**59,079**

Based on massive datasets, we aim to produce an ML model that aims at high-precision prediction of the movement of COVID-19 cases (He et al., 2021). This study will help

prepare before the peak/waves of COVID-19 strikes. This model's data collection can be used for other (Liu et al., 2018) pandemics over future centuries and allows for stopping/predicting/simulating viruses and their effect. With the help of various parameters, features of regional heat maps changing with time can be added (Shilo et al., 2020), which gives any person easy understandability (Looi, 2020). With the rising number of vaccinations for COVID-19, the number of cases and deaths might change unpredictably.

The data was taken for one year only as there were chances of oversampling of data (Pullano et al., 2020). This study seeks to exhibit future forecasting on the overall count of total cases in India in the next 30 days to contribute to controlling the spread and growing count of current cases in India. Models were tested with the last month of data. For every date, the global map prediction was analyzed and presented as a map, with the impact factor of each country (Allwood et al., 2022; Garrido et al., 2022; Mogensen et al., 2022).

The model is assessed for performance measures like accuracy during this procedure. Accuracy calculates the model's performance over unknown data by splitting the number of adequately predicted features by the number of accessible features to be forecasted. Many ML methods are applied to anticipate and forecast future appearances. SVM classifier, Prophet, Bayesian Networks, Polynomial Ridge Regression, and ARIMA are the ML methods used for prediction and analysis. According to the information conducted for this study, Support Vector Machine and Polynomial regression models were found to be better and hence can be assumed to give good results for long-term prediction. They had the highest accuracy of all classifiers, and we tested prediction methods when evaluating model efficiency (Bird et al., 2020).

Particularly, our research focused on the following objectives.

- The various models are chosen to compare the results (Lu et al., 2020). The three models: SVM, Polynomial Regression, and Bayesian Ridge Model, use over one year of data to get trained and produce the result for COVID-19 cases (Aarthi et al., 2018; Klyushin, 2020).
- We have added a visualization map of the data collected for over two years, showcasing the (Mudenda et al., 2021) region-wise cases, deaths, and recoveries with increasing dates. We have used choropleth maps to implement this visualization feature to understand the disease with increasing time better. It showcases the impact factor for each country with the help of a color bar which helps to analyze which country is impacted severely by COVID-19 immediately.
- The ML models were trained using the COVID-19 Johns Hopkins dataset. This dataset is pre-processed and segregated into three subsets: training dataset (70%) and, validation dataset (15%), testing dataset (15%). The model performance is

evaluated using key metrics such as R^2 score, Adjusted R^2 score, mean squared error (MSE), mean absolute error (MAE), and root mean square error (RMSE). We presented the comparison of performance metrics with various models.

RELATED WORKS

Bae et al. (2021) proposed that SEIR and Regression models are used to anticipate disease infection worldwide. The number of reported cases over the following 21 days was anticipated based on 62 days of training and 5 days of testing. The statistics were not steady and exhibited an exponential rise after 40 days, starting on January 22, 2020. Overfitting is still a serious issue in disease transmission (Bae et al., 2021).

Rustam et al. (2020) suggested that the model uses four standard forecasting models: SVM, LASSO, LR, and ES. Each model estimates three data types for the next 10 days, along with the number of freshly infected persons, fatalities, and recoveries. The findings demonstrate that the ES beats all other models closely by the LR and LASSO (Rustam et al., 2020).

Liu et al. (2020) discussed that the clustering strategy, and even a data augmentation technique, is used in machine learning methodology to leverage the geographic synchronicity of COVID-19 movement across Chinese regions. Their model can produce steady forecasts two days before the actual event. The limitation of this model is that there was a constant drop in COVID-19 cases reported over the testing period of our strategies; therefore, this approach could not be tested for its ability to recognize pandemic spikes across regions (Liu et al.,2020).

Wynants et al. (2020) suggested that SEIR and Regression models are used to anticipate disease infection worldwide. The number of reported cases over the following 21 days was anticipated based on 62 days of training and 5 days of testing. The statistics were not steady and exhibited an exponential rise after 40 days, starting on January 22, 2020. Overfitting is still a serious issue in disease transmission time series data (Wynants et al., 2020).

Mahdavi et al. (2021) presented that the model uses four standard forecasting models: SVM, LASSO, LR, and ES. Each model estimates three data types for the next 10 days, along with the number of freshly infected persons, fatalities, and recoveries. The findings demonstrate that the ES beats all other models, closely by the LR and LASSO, while the SVM performs poorly in all prediction situations given the available data (Mahdavi et al., 2021; Quah et al., 2020).

Pan et al. (2021) developed the spatial-temporal-susceptible-infected-removed model (STSIR). To make SIR a dynamic system, they combine both intra-city and inter-city mobility indices. This model can accurately predict the total pandemic scale using the observable index. In terms of predicting the final scale of the pandemic, this model achieves an MAE of 7.76 (Pan et al., 2021).

With Olszewski et al. (2012) model, it is possible to analyze changes in the number of cases over time and in space. In addition to considering spatial conditions in terms of population distributions, such as places of work, rest, and residence, the methodology also uses multi-agent modeling to examine spatial interactions. The model was further enhanced by introducing a multi-variant vaccination policy (Olszewski et al., 2021).

SVR and ARIMA models were compared to predict daily imported new COVID-19 cases in Shanghai, China, by Zhao and Zhang (2022). Their epidemic trend was predicted using ARIMA models. The SVR model outperformed the ARIMA model in the study. An early warning of the COVID-19 outbreak can help prevent and control the outbreak in Shanghai, China.

PRELIMINARIES

Machine Learning Models

SVM Model. A Supervised Learning model is used for solving classification and regression problems. Using SVM, n-dimensional space can be easily categorized into classes so that future data points can be easily assigned to the right category. (Shaukat et al., 2015)

The Support Vector Machine (SVM) is a powerful learning method for binary classification. Its main purpose isto find the best hyperplane for correctly dividing data into two groups. Aside from that, it excels at dealing with high-dimensional and nonlinear data. As a result, we used the SVM model to anticipate confirmed instances, as shown in Equation 1.

$$\boldsymbol{f(x) = w^T x + b = \sum_{j=1}^{M} w_j x_j + b = 0} \quad (1)$$

Polynomial Regression Model. Polynomial Regression is a method that handles an nth-degree polynomial to characterize the link be- tween a dependent variable (y) and an independent variable (x). Equation 2 is as follows:

$$\boldsymbol{y = b_0 + b_1 x_1 + b_2 x_1^2 + b_3 x_1^3 + \cdots b_n x_1^n} \quad (2)$$

It is also known as the special case of Multiple Linear Regression in machine learning because we modify the Multiple Linear Regression equation with some polynomial terms to make it polynomial regression.

Prophet Model. The Prophet library is a free, open-source library for forecasting univariate time series datasets. It is easy to use and designed to automatically find a good set of hyperparametersfor the model to generate reliable data forecasts. The prophet

forecasting model employs a perishable model comprising three primary factors:trends, holidays, and seasonality. They are shown in the following Equation 3.

$$\boldsymbol{y(t) = g(t) + s(t) + h(t)} + \in \tag{3}$$

g(t) is a section-wise logistical or linear growth curve used in statistics to describe non-periodic variations,
s(t) is seasonal fluctuations that can occur weekly oryearly,
h(t) is the effects of user-provided holidays with varying schedules,
ε estimates of error terms used in any major changes not included in the model.

Exponential smoothing and a prophet use the same method to simulate periodicity as a supplement component. Because exponentially declining weights areallocated owing to the appearance of the data, the dominant facts are given equal importance in predicting than the earlier observations in exponential smoothing.

ARIMA. ARIMA (Auto Regressive Integrated Moving Average) is a type of model that describes a time series based on its prior values, i.e., lags and delayed prediction errors, so that it can be used to forecast future values. ARIMA models can model any non-seasonal time series with patterns, not random white noise.

An ARIMA model is defined by three terms: p, d, and q, where p is the ARIMA order and q is the order of the Moving Average (MA). The term d denotes the number of differencing necessary to make the time series steady. As a result, the generic ARIMA Equation 4 is shown below:

$$\boldsymbol{Y_t = \alpha + \beta_1 Y_{t-1} + \beta_2 Y_{t-2} + \cdots + \beta_p Y_{t-p} \; + \; \varepsilon_t} \tag{4}$$

where Y_t is the anticipated target is a constant value plus a linear combination of Y delays taken till p lags andthe mixture of delayed prediction error taken till q lags.

Similarly, a pure Moving Average (MA alone) model is one in which Y_t is determined only by the delayed forecast errors, as shown in Equation 5:

$$\boldsymbol{Y_t = \alpha + \varepsilon_t + \phi_1 \varepsilon_{t-1} + \phi_2 \varepsilon_{t-2} \ldots + \phi_q \varepsilon_{t-q}} \tag{5}$$

where the variance of the error term is the auto-regressive model errors for the relevant delays, the errors t and t-1 represent the results of Equations 6 and 7.

$$\boldsymbol{Y_t = Y_{t-1} + \beta_2 Y_{t-2} + \cdots + \beta_0 Y_0 \; + \; \varepsilon_t} \tag{6}$$

$$\boldsymbol{Y_{t-1} = \beta_1 Y_{t-2} + \beta_2 Y_{t-3} \ldots + \beta_0 Y_0 \; + \; \varepsilon_{t-1}} \tag{7}$$

In an ARIMA model, the time series is divided into two classes at most once to keep it stationary, and the AR and MA conditions are mingled. As a result, Equation 8 is shown below:

$$Y_t = \alpha + \beta_1 Y_{t-1} + \beta_2 Y_{t-2} + \cdots + \beta_p Y_{t-p}\ \varepsilon_t + \phi_1 \varepsilon_{t-1} + \phi_2 \varepsilon_{t-2} \ldots + \phi_q \varepsilon_{t-q} \quad (8)$$

Bayesian Ridge Polynomial Regression Model. Bayesian regression defends poorly distributed data using natural processes. Instead of being estimated as a single number, the outputor answer 'y' is designed to select from the probability distribution.
The answer y is assumed to be a Gaussian distribution with X_w to design a fully probabilistic model, as shown below in Equation 9.

$$p(y|X, w, \propto) = N(y|X_w, \propto) \quad (9)$$

Bayesian Ridge regression, which computes a probabilistic model of regression issues, is one of the most useful variants of Bayesian regression. Spherical Gaussian provides the following antecedent for the coefficient w shown in Equation 10.

$$p\ (w\ |\lambda\ ) = N\ (w\ |0, \lambda^{-1} I_p) \quad (10)$$

Gamma distributions, the corresponding prior for Gaussian accuracy, are chosen as throughout the model fit, the regularization parameters, and the parameters w, alpha, and gamma, are computed simultaneously, with the log residual likelihood being maximized. Hyper-parameters such as lambda and alpha were tweaked to generate considerably better outcomes.

DATASET DETAILS

The Johns Hopkins University COVID-19 Data Repository is referred for this study and used by the Center for Systems Science and Engineering (CSSE). The JHU CSSE's GitHub public repository can be used for educational and academic research. It is publicly available at the URL https://github.com/CSSEGISandData/COVID-19. csse_covid_19_time_series data consists of two cumulative datasets that Johns Hopkins produces, with the latest files updated daily at 23:59 UTC. The attributes such as Country, State/City, Confirmed cases, Recovered cases, and Death counts were considered for evaluation. The dataset contains 192445 records with 10 attributes, 134711 records for training, 28867 records for testing, and 28867 records are used for validation.

EVALUATION PARAMETERS

The parameters Root Mean Squared Error (RMSE), R^2 Score, Mean square Error (MSE), Mean absolute error (MAE), and Adjusted R-Square (R^2adjusted) are considered in the evaluation and comparison of Models.

Mean Square Error (MSE)

The square error suggests a different technique for evaluating the existence of reviewing models. MSE takes the information distance, concentrates on the return line, and squares it. Coupling is essential because it removes the minus number and adds weight to the primary differentiation. A little square error indicates how near you are to obtaining the optimal condition line.

It is calculated by finding the variance among the original and predicted values of the data, then calculating the square of this result, and then taking the average as shown in Equation 11.

$$\boldsymbol{MSE = \frac{1}{N}(\sum_{J=1}^{n}(act_{value} - pred_{value})} \quad (11)$$

N is the total number of observations, act_value indicates the actual value, and pred_value indicates the predicted value.

Root Mean Squared Error (RMSE)

When a prediction is made on a dataset, the RMSE is defined as the standard deviation of errors. It is similar to MSE; however, the root of its value is considered, as shown in Equation 12.

$$\boldsymbol{RMSE = \sqrt{MSE}} \quad (12)$$

R^2 Score

The R-squared (R^2) scale is a calculating scale used to evaluate review models' presentation. The degree of the relationship between adaptation and inversion models is determined by a positive size ranging from 0 to 100 percent (Equation 13).

$$\boldsymbol{R^2 = 1 - \frac{RSS}{TSS}} \quad (13)$$

RSS denotes squares of residuals sum, and TSS denotes the total sum of squares.

Adjusted R^2 Score

It is a variant of the R^2 score. The adjusted R^2 score automatically adjusts according to various features considered for the prediction model. This metric value increases in case new features lead to improvement and decreases in case the new features do not lead to much improvement. Equation 14 denotes the formula for Adjusted R^2 score calculation.

$$\boldsymbol{Adjusted\ R^2 = 1 - \frac{(1 - R^2)(N - 1)}{(N - p - 1)}} \tag{14}$$

R^2 denotes sample R-square, N is the total sample size, and p is the predicators count.

Mean Absolute Error (MAE)

The average of all individual differences between the model predictions and actual data is computed by averaging test data (Equation 15).

$$\boldsymbol{MAE = \frac{\sum_{j=1}^{m} |y_j - x_j|}{m}} \tag{15}$$

Y_j indicates the prediction value, x_j indicates the true value, and m indicates the total number of data samples.

METHODOLOGY

Many ML methods are applied in this study to anticipate and forecast future appearances of COVID-19 cases, such as SVM classifier, Prophet, Bayesian Networks, Polynomial Ridge Regression, and ARIMA. The model having the highest accuracy is picked for forecasting or prediction during the model evaluation. This proposed work aims to achieve future forecasting for the next 10 days to identify the total number of recovery cases, daily confirmed cases and death rate.

The dataset is divided into 70% for training, 15% for testing, and 15% for validation. The six models, SVM, Polynomial Regression, Bayesian Ridge Model, ARIMA, and Prophet, use data over a range of 1-year data to get trained, validated, and tested to produce results with better precision and accuracy.

First, the data set is retrieved from a webpage. Web scraping makes the extraction feasible (Rustam et al., 2020). Following the conclusion of web scraping, the data set is related to data wrangle and pre-processing before being saved to the local storage. The pre-processed data is now shown for a flawless result, a high-level data set summary. The dataset is divided into 70% for training, 15% for testing, and 15% for validation. The 15% of test data collected from the same dataset is kept hidden from the model during one of the training periods; hiding a portion of the dataset aids in discovery. Determine

if the model has under-fit or over-fit and some of the most significant challenges while developing any model. The ARIMA Model is trained by supplying a training dataset. The model is ready for testing once it has been trained. One of the most difficult aspects of training any model is over-fitting. Before the model is tested, the Facebook Prophet (Arabi et al., 2020) provides the dates for the next 30 days as well as the timestamp to forecast. Finally, the time and date stamp provided by Facebook Prophet is applied to the test data set. The model is currently being trained on the entire number of active case patterns. The ARIMA model has been analyzed and reported on key metrics such as R-Squared Score, MAE, MSE, and RMSE (Grasselli et al., 2020)

The Prophet and ARIMA are specifically designed mostly for prediction. Hence, we have trained these models with data over 2 years. Bayesian Ridge polynomial reduction, Prophet, SVM, and Polynomial regression give almost similar results. These various models are trained on the confirmed, recovered, and death cases. Further, ML models have been evaluated using various key metrics such as MSE, RMSE, R 2 -score, R 2 adjusted score, and MAE, and results are produced.

The system architecture diagram for data processing, model development, and deployment, followed by the monitoring, is shown in Figure 1.

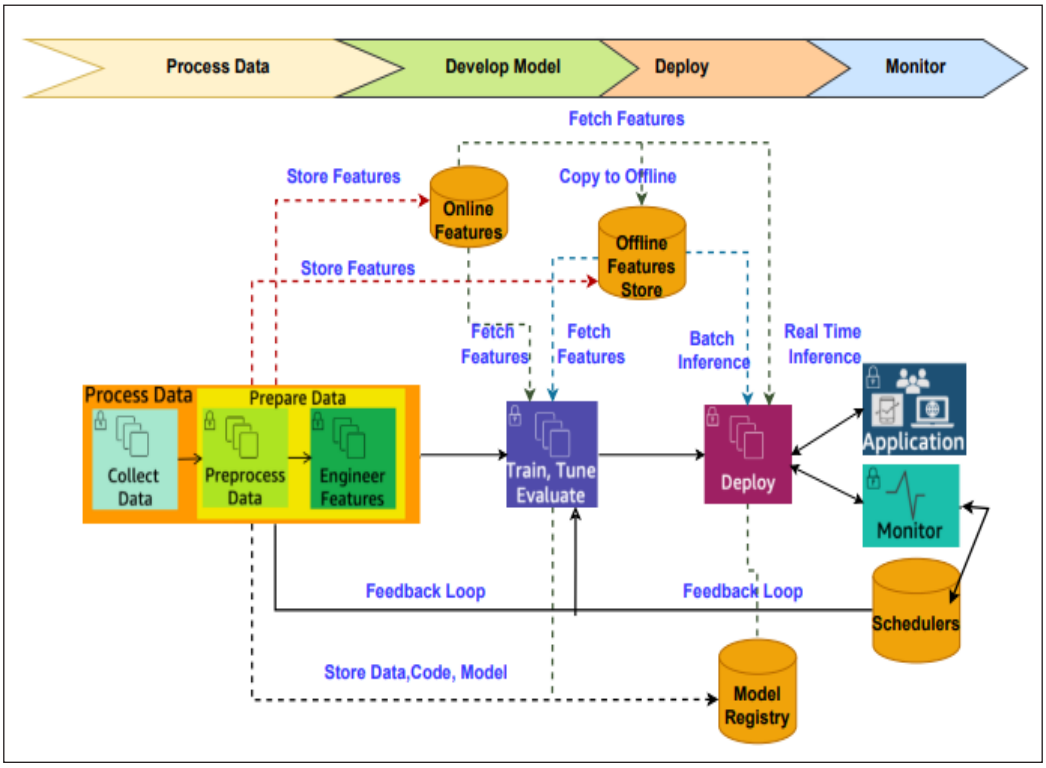

Figure 1. Proposed system architecture

RESULT

To analyze the result performance of all the models tested with three different sizes of testing, training, and validation datasets. Initially, the dataset is divided into 70% for training, 15% for testing, and 15% for validation. This result performance is shown in Table 2, with various metrics evaluated in Test 1. Again, the same dataset is split into 80% for training, 10% for testing, and 10% for validation. This result is indicated in Table 3, with various metrics evaluated in Test 2. Finally, the same dataset is divided into 76% for training, 12% for testing, and 12% for validation. This experimental result is indicated in Table 4, with various metrics evaluated in Test 3. Among all the tests Support Vector Machine and Polynomial regression models were found to be better and hence can be assumed to give good results for long-term prediction.

SVM Model

The SVM Prediction and Test Data are very close, showing good results with large datasets (Abedini et al., 2017). It takes past data and does the analysis based on that. A higher percentage of training will produce more accurate results. There are chances of overfitting with large amounts of data, which is avoided by doing the pre-processing. Figure 2 shows the SVM model predictions. Big-O notation is used to calculate the complexity of an algorithm. An algorithm will process amounts of data, where N is a symbol for amounts of data. The lower bound, upper bound and total number of loop iterations determine the complexity. The computational complexity of SVM is $O(n^3)$.

Polynomial Regression

The Polynomial Regression model (Bae et al., 2021) is much closer to the test data compared to the SVM Model, so it shows that we can use this model for prediction. This model also provides good results when trained with a large dataset. Polynomial Regression also takes the past trend and forecasts the COVID-19 cases. In this model, factors affect it largely. So,

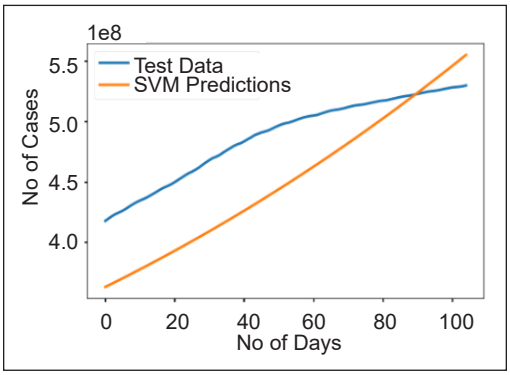

Figure 2. SVM model predictions

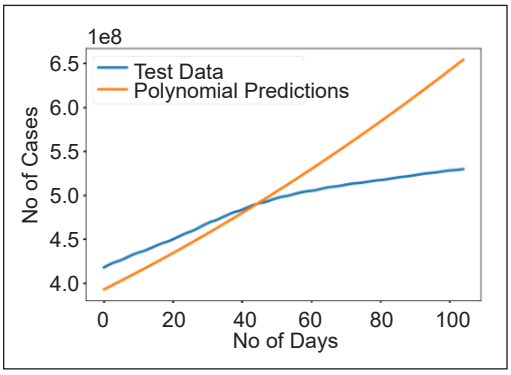

Figure 3. Polynomial regression predictions

it becomes necessary to take appropriate parameters for better prediction. Figure 3 denotes the polynomial regression predictions. It uses a linear regression model to fit complex, nonlinear functions and datasets. In the m degree polynomial regression with n measured values ($n \geq m + 1$), the computational complexity is $O(n^2m)$.

Prophet

The Prophet also gives a good result but not as good as polynomial regression. It is better than the SVM model to be used for prediction. The prophet prediction is slightly lower than the test data. Figure 4 shows the Prophet Facebook time series model. It takes all the past trends and forecasts the trend. It is good for a large dataset but cannot be forecast longer. It gives good results when it is forecast within 25 days.

ARIMA

ARIMA is giving a good result with almost overlapping the test data, but later as the COVID-19 cases dip, it cannot continue. This model is specifically built for time series models. It gives good results for small values but also needs to be checked with large ones. Figure 5 shows that ARIMA gives a good result when the forecast time is within 25 days. The model does not face any over-fitting problems, or it can neglect some noise in the data. The computational complexity of the ARIMA model is $O(n^2T)$, where n is the number of parameters (n =p+q+P+Q) where p, q & P, and Q are non-seasonal and seasonal orders and T is the length of the time series.

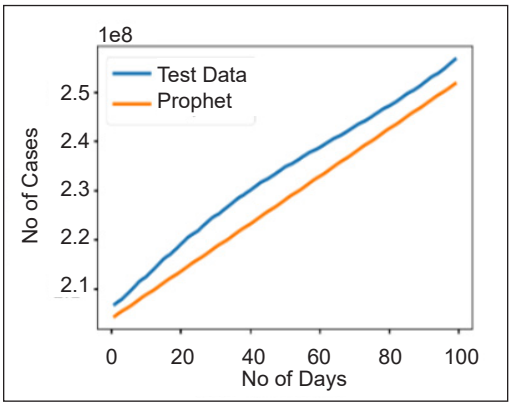

Figure 4. Prophet Facebook time series model

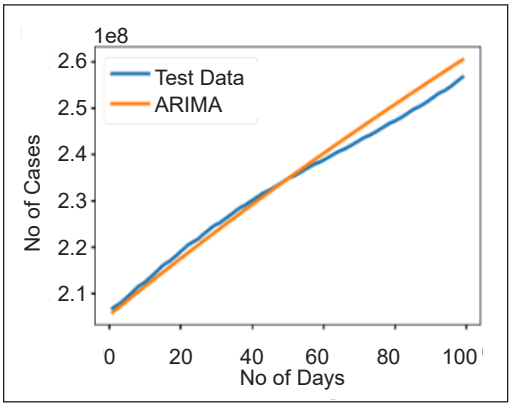

Figure 5. ARIMA model predictions

Bayesian Ridge Polynomial Reduction

Bayesian Ridge is almost giving the same result as SVM. It is not giving good results with test data. Figure 6 shows the Bayesian Ridge Polynomial Reduction Model. The model ispurely based on the number of days; hence noise should be avoided, or it can lead

to over-fitting. The trained models can be tested with all the data and also predict for the forecast 10 days. This model was tested with the real-time dataset from March 2020 to now and forecasted for the next 10 days. The over-fitting problem can be solved by removing noise during a pre-processing phase. Linear Regression has a runtime complexity of O(k). Linear regression has a long training time but is very efficient during testing. Tests/predictions are performed in O(k) time, where k is the data's number of features/dimensions.

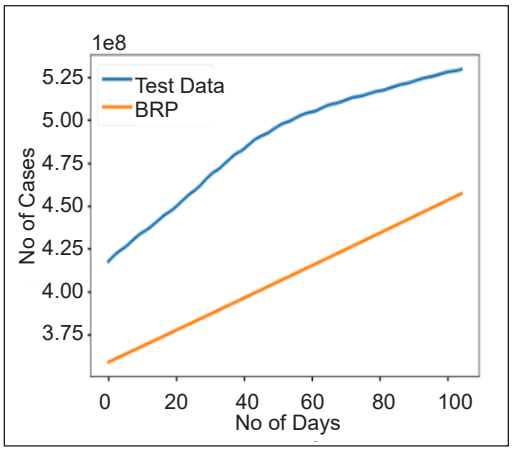

Figure 6. Bayesian Ridge Polynomial Reduction Prediction Model

Growth Factor

It is not possible to determine the growth factor from the data since we only have access to the number of cases per day. An experimental daily observation can be used to determine the growth factor with various statistical models. The average growth factor is calculated based on the 500 days of data observations. The performance was tested with large datasets. It is the simplest method for forecasting trends. It calculates the average growth of COVID-19 cases daily based on the prediction. Figure 7 denotes the prediction growth factor.

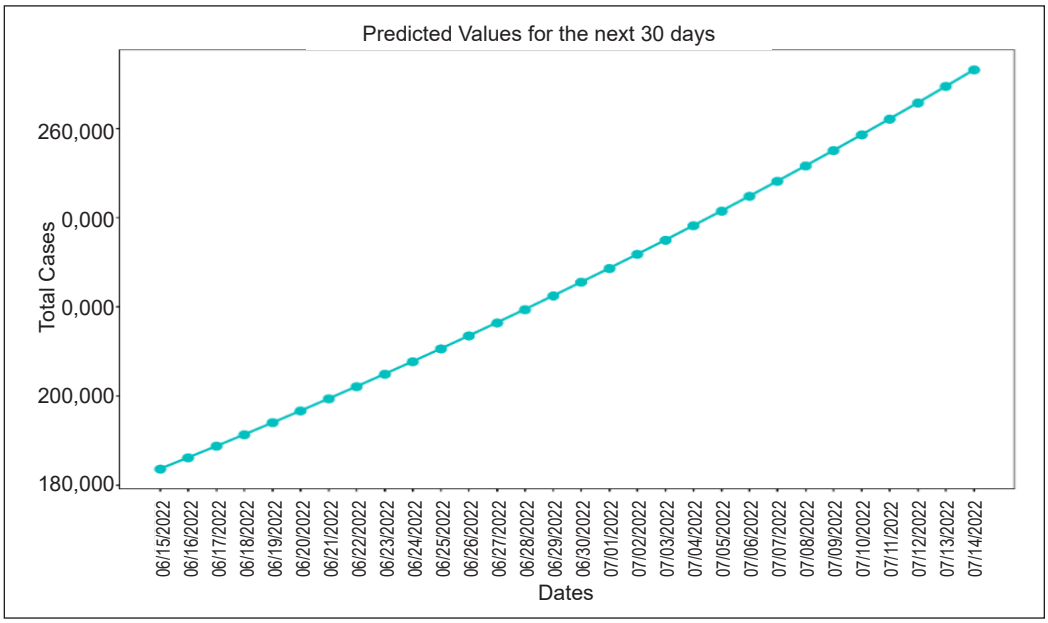

Figure 7. Prediction growth factor

SVM Prediction

Figure 8 shows the SVM Model predicts that for the next 500 days from January 2022. The SVM Model produces an accurate result for past trends.

Polynomial Regression

This model predicts good results for large datasets. The growth factor is considered for monthly or yearly COVID-19 cases. Figure 9 shows Polynomial Regression based on growth factor with minimum deviation. This model produces a better result for the present trend.

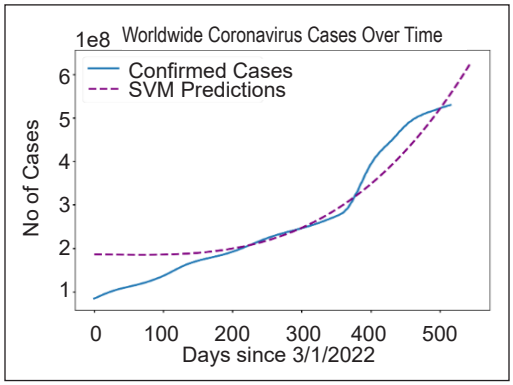

Figure 8. SVM Prediction based on growth factor

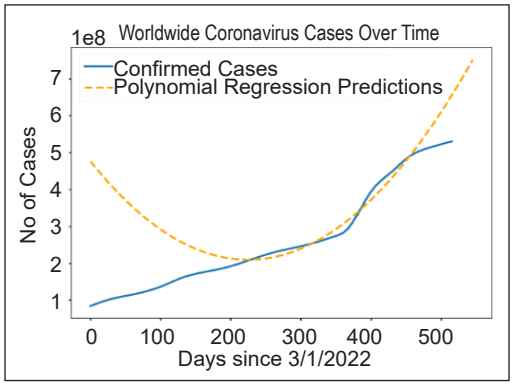

Figure 9. Polynomial Regression based on growth factor

Bayesian Ridge Regression

This model predicts better results for large datasets. The growth factor is considered for monthly or yearly COVID-19 cases. Figure 10 shows Bayesian Ridge Regression based on growth factor with minimum deviation.

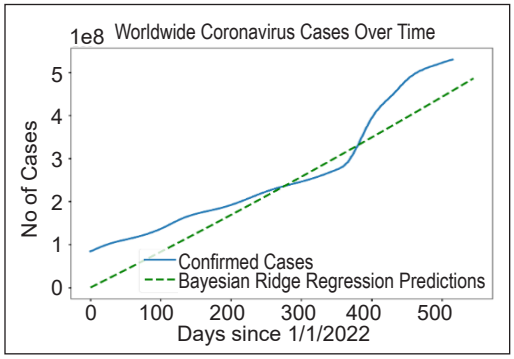

Figure 10. Bayesian Ridge Regression based on growth factor

ARIMA Prediction

It predicts and forecasts the trends based on the input data. It gives the best result for past and future trends. Figure 11 denotes that the dotted yellow line predicts the COVID-19 cases compared with actual data. This model produces the best results for a small period of forecast days.

Prophet Prediction

The Prophet Model is the open-source time series forecasting algorithm developed by Facebook. The black dots that form a line in the figure represent historical training data in

the model. The blue line represents the forecast or fitted curve generated for the past and the future. The light blue shaded region represents the brands of uncertainty. In COVID-19, the growth factor considered for the number of days was 19 cases. Based on the forecasting days, it gives peak results for 10-15 days. Figure 12 depicts the Facebook Prophet model based on the growth factor (Estenssoro et al., 2022). The graph shows the predicted number of cases as well as the uncertainty band that it provides based on seasonality.

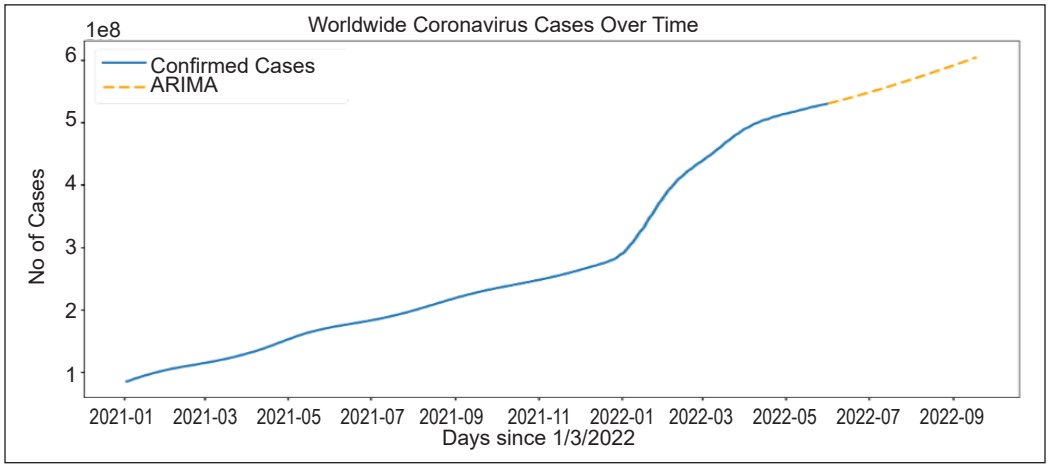

Figure 11. ARIMA prediction based on growth factor

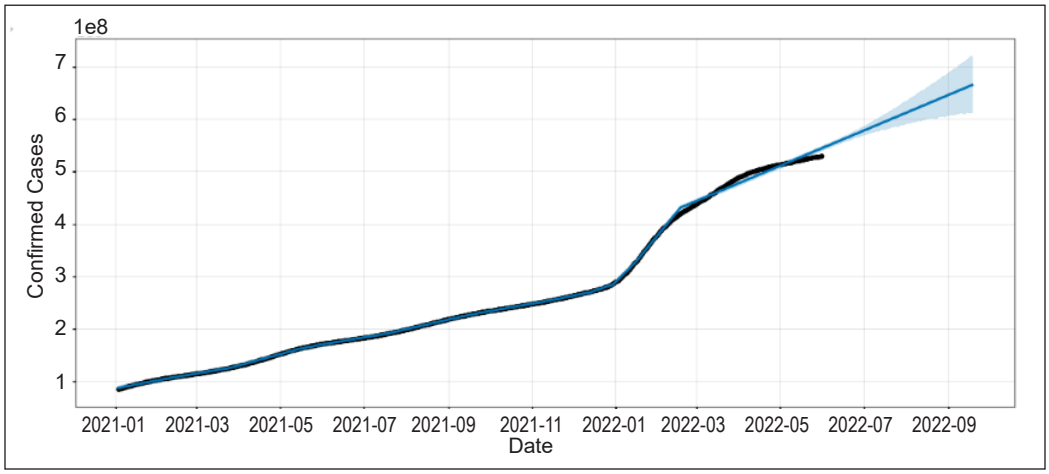

Figure 12. Facebook Prophet model based on growth factor

DISCUSSION

The Polynomial Regression and Prophet model produces good results with the number of cases it has predicted compared to other models we considered for the COVID-19 prediction. The model has predicted the cases from June 15, to June 24, 2022, in which

prophet and polynomial produce good results. The result in Figure 13 denotes that the SVM model is good for a stable increase in COVID-19 cases for long-term prediction. However, given different scenarios, ARIMA and Prophet are good for predicting the next 5–10 days. Figure 13 shows the Heat Maps prediction with various models used in this proposed work (Dong et al., 2020).

	Date	SVM Predicted	Polynomial Predicted	Prophet Predicted	Bayesian Ridge Predicted	ARIMA Predicted
625	06/15/2022	647426725.000000	734134235.000000	638283359.000000	505338012.000000	599097843.000000
626	06/16/2022	650345177.000000	737643759.000000	639154022.000000	506506416.000000	599830334.000000
627	06/17/2022	653275799.000000	741164990.000000	640294788.000000	507675630.000000	600564196.000000
628	06/18/2022	656218615.000000	744697929.000000	641329917.000000	508845655.000000	601299412.000000
629	06/19/2022	659173650.000000	748242574.000000	642352812.000000	510016490.000000	602035967.000000
630	06/20/2022	662140929.000000	751798927.000000	643335671.000000	511188135.000000	602773847.000000
631	06/21/2022	665120477.000000	755366987.000000	644127269.000000	512360590.000000	603513037.000000
632	06/22/2022	668112319.000000	758946754.000000	644794321.000000	513533855.000000	604253521.000000
633	06/23/2022	671116480.000000	762538229.000000	645664983.000000	514707930.000000	604995287.000000
634	06/24/2022	674132985.000000	766141411.000000	646805749.000000	515882816.000000	605738318.000000

Figure 13. Heat Maps prediction with various models

Global Visualization

Figure 14 showcases the data visualization, the trends of COVID-19 for each country, and the number of cases, deaths, and recovery for each day (27–29). It provides the best and easiest manner to understandand analyze the pandemic (Franch-Pardo et al., 2020). The ranges are denoted in different shades, starting from 0 cases to 1–5,000, 5,001–50,000, 50,001–5,000,000, and > 5,000,000.

Tables 2, 3 and 4 compare performance metrics with machine learning models for different test data sets. The dataset is divided into 70% for training, 15% for testing, and 15% for validation in Test 1, and the performance of various evaluation metrics are shown in Table 2. Further, the same dataset is split into 80% for training, 10% for testing, and 10% for validation in Test 2, and the performance result for various metrics is indicated in Table 3. Finally, the same dataset is divided into 76% for training, 12% for testing, and 12% for validation in Test 3, and its experimental result is indicated in Table 4 with various evaluation metrics. Among all the tests Support Vector Machine and Polynomial regression models were found to be better and hence can be assumed to give good results

for long-term prediction in terms of producing small errors such as in Mean Absolute Error and Mean Squared Error in a different set of tests.

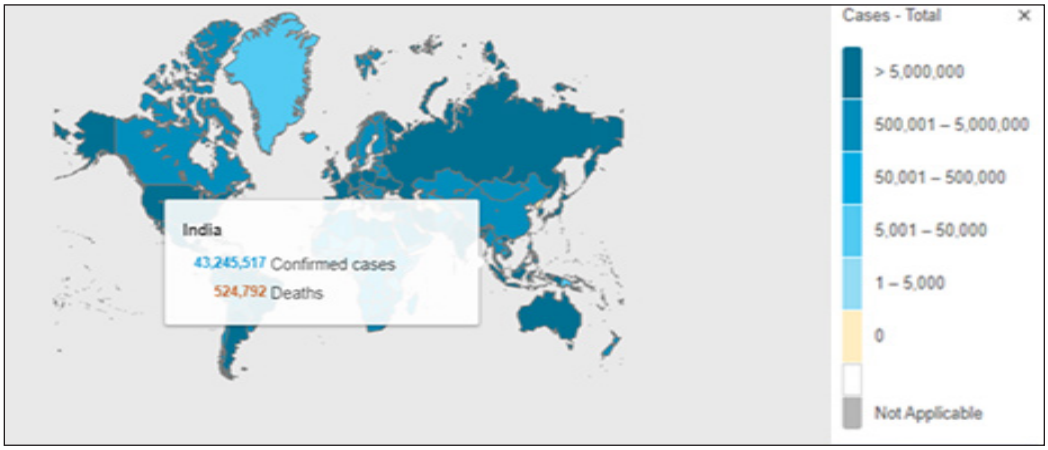

Figure 14. Global visualization

Table 2
Comparison of performance metrics with various models for Test 1

Model	Mean Absolute Error	Mean Squared Error	Root Mean Squared Error	R^2 Score	Adjusted R^2 score
Support Vector Regression (Woolf et al., 2021)	3.430898e+07	1.419470e+15	3.767585e+07	0.647203	0.64718
Polynomial Regression (Woolf et al., 2021)	4.988888e+07	4.703992e+15	6.858565e+07	0.312027	0.311991
Bayesian Ridge Polynomial Reduction (Muhammad et al., 2021)	7.051741e+07	5.038594e+15	7.098306e+07	-4.075667	-4.075931
Prophet Prediction	1.081270e+08	1.175406e+16	1.084161e+08	-10.750889	-10.751499
ARIMA	6.914564e+07	5.011705e+15	7.079340e+07	13.341083	-13.341828

Table 3
Comparison of performance metrics with various models for Test 2

Model	Mean Absolute Error	Mean Squared Error	Root Mean Squared Error	R^2 Score	Adjusted R^2 score
Support Vector Regression (Woolf et al., 2021)	3.772292e+07	1.774247e+15	4.212181e+07	0.648596	0.648578
Polynomial Regression (Woolf et al., 2021)	6.025114e+07	6.806394e+15	8.250088e+07	0.201452	0.201411
Bayesian Ridge Polynomial Reduction (Muhammad et al., 2021)	6.893719e+07	4.836871e+15	6.954762e+07	-3.054984	-3.055195
Prophet Prediction	1.068353e+08	1.148542e+16	1.071701e+08	-10.629112	-10.629716
ARIMA	7.480714e+07	5.781636e+15	7.603707e+07	-10.997513	-10.998137

Table 4
Comparison of performance metrics with various models for Test 3

Model	Mean Absolute Error	Mean Squared Error	Root Mean Squared Error	R^2 Score	Adjusted R^2 score
Support Vector Regression (Woolf et al., 2021)	5.410193e+07	5.258222e+15	7.251360e+07	0.148236	0.148192
Polynomial Regression (Woolf et al., 2021)	8.040728e+07	1.071893e+16	1.035323e+08	-0.355910	-0.355981
Bayesian Ridge Polynomial Reduction (Muhammad et al., 2021)	4.119488e+07	1.903292e+15	4.362673e+07	-0.399827	-0.399900
Prophet Prediction	9.205843e+07	8.527751e+15	9.234582e+07	-10.125871	-10.126450
ARIMA	6.239042e+07	3.971764e+15	6.302193e+07	-9.794867	-9.795428

CONCLUSION

The proposed system compared with Support Vector Regression, Polynomial Regression, ARIMA, Poly Prophet, and Bayesian Ridge Polynomial Reduction. Based on the comparison of the R^2 Score, the R^2 score of the Support Vector Machine and Polynomial regression models was found to be better and hence can be assumed to give good results for the long-term prediction. On the other hand, ARIMA, Prophet Models, and Bayesian Ridge Reduction models are good for short-term predictions (Muhammad & Al-Turjman, 2021). Here, the ARIMA modeling concerning the changing seasonality of the data is used to create a Machine Learning model in comparison to support vector regressions. The results also showcased the accuracy of SVM along with ARIMA techniques and also helped to understand the latest trends in the pattern of the disease, thus enabling further preventive measures. We can also improve the accuracy and precision of the predictions through these techniques. Additionally, we can add features to implement the predictions on the choropleth global map, providing a better understanding of the disease. In the future, we can have more precise datasets having details about various strains of the virus, and we can implement a strain-specific prediction model for COVID-19 as well in the future.

ACKNOWLEDGEMENT

The authors thank all the colleagues who helped to complete this project successfully at Vellore Institute of Technology, Vellore, India.

REFERENCES

Aarthi, A. D., & Gnanappazham, L. (2018). Urban growth prediction using neural network coupled agents-based cellular automata model for Sriperumbudur taluk, Tamil Nadu, India. *The Egyptian Journal of Remote Sensing and Space Science, 21*(3), 353-362. https://doi.org/10.1016/j.ejrs.2017.12.004

Abedini, M., Ghasemyan, B., & Rezaei Mogaddam, M. H. (2017). Landslide susceptibility mapping in Bijar city, Kurdistan province, Iran: A comparative study by logistic regression and AHP models. *Environmental Earth Sciences, 76*(8), Article 308. https://doi.org/10.1007/s12665-017-6502-3

Allwood, B. W., Koegelenberg, C. F., Ngah, V. D., Sigwadhi, L. N., Irusen, E. M., Lalla, U., Yalew, A., Tamuzi, J. L., McAllister, M., Zemlin, A. E., Jalavu, T. P., Erasmus, R., Chapanduka, Z. C., Matsha, T. E., Fwemba, I., Zumla, A., & Nyasulu, P. S. (2022). Predicting COVID-19 outcomes from clinical and laboratory parameters in an intensive care facility during the second wave of the pandemic in South Africa. *IJID Regions, 3*, 242-247. https://doi.org/10.1016/j.ijregi.2022.03.024

Arabi, Y. M., Murthy, S., & Webb, S. (2020). COVID-19: A novel coronavirus and a novel challenge for critical care. *Intensive Care Medicine, 46*(5), 833-836. https://doi.org/10.1007/s00134-020-05955-1

Bae, S., Sung, E., & Kwon, O. (2021). Accounting for social media effects to improve the accuracy of infection models: Combatting the COVID-19 pandemic and infodemic. *European Journal of Information Systems, 30*(3), 342-355. https://doi.org/10.1080/0960085x.2021.1890530

Bird, J. J., Barnes, C. M., Premebida, C., Ekárt, A., & Faria, D. R. (2020). Country-level pandemic risk and preparedness classification based on COVID-19 data: A machine learning approach. *PLoS ONE, 15*(10), Article e0241332. https://doi.org/10.1371/journal.pone.0241332

Dong, E., Du, H., & Gardner, L. (2020). An interactive web-based dashboard to track COVID-19 in real-time. *The Lancet Infectious Diseases, 20*(5), 533-534. https://doi.org/10.1016/s1473-3099(20)30120-1

Estenssoro, E., Loudet, C. I., Dubin, A., Kanoore Edul, V. S., Plotnikow, G., Andrian, M., Romero, I., Sagardía, J., Bezzi, M., Mandich, V., Groer, C., Torres, S., Orlandi, C., Rubatto Birri, P. N., Valenti, M. F., Cunto, E., Sáenz, M. G., Tiribelli, N., Aphalo, V., Bettini, L., Rios, F. G., & Reina, R. (2022). Clinical characteristics, respiratory management, and determinants of oxygenation in COVID-19 ards: A prospective cohort study. *Journal of Critical Care, 71*, Article 154021. https://doi.org/10.1016/j.jcrc.2022.154021

Franch-Pardo, I., Napoletano, B. M., Rosete-Verges, F., & Billa, L. (2020). Spatial analysis and GIS in the study of COVID-19. A review. *Science of the Total Environment, 739*, Article 140033. https://doi.org/10.1016/j.scitotenv.2020.140033

Garrido, J., Martínez-Rodríguez, D., Rodríguez-Serrano, F., Pérez-Villares, J., Ferreiro-Marzal, A., Jiménez-Quintana, M., & Villanueva, R. (2022). Mathematical model optimized for prediction and health care planning for COVID-19. *Medicina Intensiva (English Edition), 46*(5), 248-258. https://doi.org/10.1016/j.medine.2022.02.020

Grasselli, G., Pesenti, A., & Cecconi, M. (2020). Critical care utilization for the COVID-19 outbreak in Lombardy, Italy. *JAMA, 323*(16), Article 1545. https://doi.org/10.1001/jama.2020.4031

He, X., Zhou, C., Wang, Y., & Yuan, X. (2021). Risk assessment and prediction of COVID-19 based on epidemiological data from spatiotemporal geography. *Frontiers in Environmental Science, 9*, Article 634156. https://doi.org/10.3389/fenvs.2021.634156

Klyushin, D. A. (2020). Nonparametric analysis of tracking data in the context of COVID-19 pandemic. In A. E. Hassanien, N. Dey & S. Elghamrawy (Eds.), *Big Data Analytics and Artificial Intelligence Against COVID-19: Innovation Vision and Approach* (pp. 35-50). Springer. https://doi.org/10.1007/978-3-030-55258-9_3

Li, J., Li, S., Cai, Y., Liu, Q., Li, X., Zeng, Z., Chu, Y., Zhu, F., & Zeng, F. (2020). *Epidemiological and clinical characteristics of 17 hospitalized patients with 2019 novel coronavirus infections outside Wuhan, China*. MedRxiv. https://doi.org/10.1101/2020.02.11.20022053

Liu, D., Clemente, L., Poirier, C., Ding, X., Chinazzi, M., Davis, J., Vespignani, A., & Santillana, M. (2020). Real-time forecasting of the COVID-19 outbreak in Chinese provinces: Machine learning approach using novel digital data and estimates from mechanistic models. *Journal of Medical Internet Research, 22*(8), Article e20285. https://doi.org/10.2196/20285

Liu, Q. Y., Kwong, C. F., Zhang, S., & Li, L. (2018, November 4). *A hybrid fuzzy-MADM based decision-making scheme for QoS aware handover*. [Paper presentation]. IET Doctoral Forum on Biomedical Engineering, Healthcare, Robotics and Artificial Intelligence 2018 (BRAIN 2018), Ningbo, China. https://doi.org/10.1049/cp.2018.1728

Looi, M. (2020). COVID-19: Is a second wave hitting Europe? *BMJ, 371,* Article 4113. https://doi.org/10.1136/bmj.m4113

Lu, R., Zhao, X., Li, J., Niu, P., Yang, B., Wu, H., Wang, W., Song, H., Huang, B., Zhu, N., Bi, Y., Ma, X., Zhan, F., Wang, L., Hu, T., Zhou, H., Hu, Z., Zhou, W., Zhao, L., ... & Tan, W. (2020). Genomic characterisation and epidemiology of 2019 novel coronavirus: Implications for virus origins and receptor binding. *The Lancet, 395*(10224), 565-574. https://doi.org/10.1016/s0140-6736(20)30251-8

Mahdavi, M., Choubdar, H., Zabeh, E., Rieder, M., Safavi-Naeini, S., Jobbagy, Z., Ghorbani, A., Abedini, A., Kiani, A., Khanlarzadeh, V., Lashgari, R., & Kamrani, E. (2021). A machine learning based exploration of COVID-19 mortality risk. *PLoS ONE, 16*(7), Article e0252384. https://doi.org/10.1371/journal.pone.0252384

Mogensen, I., Hallberg, J., Björkander, S., Du, L., Zuo, F., Hammarström, L., Pan-Hammarström, Q., Ekström, S., Georgelis, A., Palmberg, L., Janson, C., Bergström, A., Melén, E., Kull, I., Almqvist, C., Andersson, N., Ballardini, N., Bergström, A., Björkander, S., ... & Schwenk, J. M. (2022). Lung function before and after COVID-19 in young adults: A population-based study. *Journal of Allergy and Clinical Immunology: Global, 1*(2), 37-42. https://doi.org/10.1016/j.jacig.2022.03.001

Mudenda, S., Mukosha, M., Mwila, C., Saleem, Z., Kalungia, A. C., Munkombwe, D., Daka, V., Witika, B. A., Kampamba, M., Chileshe, M., Hikaambo, C., Kasanga, M., Mufwambi, W., Mfune, R. L., Matafwali, S. K., Bwalya, A. G., Banda, D. C., Gupta, A., Phiri, M. N., ... & Kazonga, E. (2021). *Impact of the coronavirus disease (COVID-19) on the mental health and physical activity of pharmacy students at the University of Zambia: A cross-sectional study*. MedRxiv. https://doi.org/10.1101/2021.01.11.21249547

Muhammad, M. A., & Al-Turjman, F. (2021). Application of IoT, AI, and 5G in the fight against the COVID-19 pandemic. In F. Al-Turhman (Ed.), *Artificial Intelligence and Machine Learning for COVID-19* (pp. 213-234). Springer. https://doi.org/10.1007/978-3-030-60188-1_10

Olszewski, R., Pałka, P., & Wendland, A. (2021, December 13-16). *Agent-based modeling as a tool for predicting the spatial-temporal diffusion of the COVID-19 pandemic*. [Paper presentation]. 2021 IEEE International Conference on Industrial Engineering and Engineering Management (IEEM), Singapore. https://doi.org/10.1109/IEEM50564.2021.9672878

Pan, W., Deng, Q., Li, J., Wang, Z., & Zhu, W. (2021, July 18-22). *STSIR: A spatial temporal pandemic model with mobility data-A COVID-19 study*. [Paper presentation]. 2021 International Joint Conference on Neural Networks (IJCNN), Shenzhen, China. https://doi.org/10.1109/IJCNN52387.2021.9533596

Pullano, G., Pinotti, F., Valdano, E., Boëlle, P., Poletto, C., & Colizza, V. (2020). Novel coronavirus (2019-nCoV) early-stage importation risk to Europe, January 2020. *Eurosurveillance, 25*(4), Article 2000057. https://doi.org/10.2807/1560-7917.es.2020.25.4.2000057

Quah, P., Li, A., & Phua, J. (2020). Mortality rates of patients with COVID-19 in the intensive care unit: A systematic review of the emerging literature. *Critical Care, 24*, Article 285. https://doi.org/10.1186/s13054-020-03006-1

Rustam, F., Reshi, A. A., Mehmood, A., Ullah, S., On, B., Aslam, W., & Choi, G. S. (2020). COVID-19 future forecasting using supervised machine learning models. *IEEE Access, 8*, 101489-101499. https://doi.org/10.1109/access.2020.2997311

Shaukat, K., Masood, N., Shafaat, A., Jabbar, K., Shabbir, H., & Shabbir, S. (2015). Dengue fever in perspective of clustering algorithms. *Journal of Data Mining in Genomics & Proteomics, 6*(3), Article 1000176. https://doi.org/10.4172/2153-0602.1000176

Shilo, S., Rossman, H., & Segal, E. (2020). Axes of a revolution: Challenges and promises of big data in healthcare. *Nature Medicine, 26*(1), 29-38. https://doi.org/10.1038/s41591-019-0727-5

Woolf, S. H., Chapman, D. A., & Lee, J. H. (2021). COVID-19 as the leading cause of death in the United States. *Jama, 325*(2), 123-124. https://doi.org/10.1001/jama.2020.24865

World Health Organization. (2020). *Dashboard of the Coronavirus Disease (COVID-19) Outbreak Situation*. World Health Organization. https://covid19/who.int/

Wynants, L., Van Calster, B., Collins, G. S., Riley, R. D., Heinze, G., Schuit, E., Bonten, M. M., Dahly, D. L., Damen, J. A., Debray, T. P., de Jong, V. M., De Vos, M., Dhiman, P., Haller, M. C., Harhay, M. O., Henckaerts, L., Heus, P., Kammer, M., Kreuzberger, N., ... & van Smeden, M. (2020). Prediction models for diagnosis and prognosis of COVID-19: Systematic review and critical appraisal. *BMJ, 369*, Article 1328. https://doi.org/10.1136/bmj.m1328

Zhao, D., & Zhang, H. (2022, March 25-27). *Comparison of the SVR and ARIMA models for prediction of daily imported new cases of COVID-19 in Shanghai, China*. [Paper presentation]. 2022 Asia Conference on Algorithms, Computing and Machine Learning (CACML), Hangzhou, China. https://doi.org/10.1109/CACML55074.2022.00048

Pertanika J. Sci. & Technol. 31 (4): 2013 - 2029 (2023)

PERTANIKA JOURNALS

SCIENCE & TECHNOLOGY

Journal homepage: http://www.pertanika.upm.edu.my/

Evaluation of the Interface of Green Bilayer Powder Compact (BPC) of Iron (Fe) Under Different Die Wall Conditions

Syamimi Mohd Yusoff[1]*, Suraya Mohd Tahir[1], Azmah Hanim Mohamed Ariff[1], Eris Elliandy Supeni[1] and Mohd Shamsul Anuar[2]

[1]*Department of Mechanical and Manufacturing Engineering, Universiti Putra Malaysia, 43400 UPM, Serdang, Selangor, Malaysia*

[2]*Department of Process and Food Engineering, Universiti Putra Malaysia, 43400 UPM, Serdang, Selangor, Malaysia*

ABSTRACT

The current work evaluates cross-sectioned green bilayer powder compact (green BPC) of iron (Fe) under different die conditions. At first, finite element-based (FE) simultaneous compaction modelling is used to model the uniaxial, one-sided compaction of the green BPC of Fe and its interface. A Tri-mesh of 0.03 mm and mesh refinement along the interfacial boundary is set up with the condition of each node from both sides of layers (namely lower layer, L and upper layer, U) is mapped precisely to ensure its mutual interconnection along the horizontal edges of interface. Additionally, the modelling part utilised and validated our recently proposed image analysis under the metallographic technique's standard framework. Our approach to model the interface to gain the same effect as from the experimental result of green BPC of Fe is in good agreement. It is significantly found that the use of the lubricated die condition contributed to increasing the local RD distribution along the interface of the green BPC of Fe. In contrast, the distribution is gradually dissuaded from the interface for the unlubricated die condition as the applied height: diameter (H:D) ratio increases.

Keywords: Fe, Finite element, green BPC, H:D ratio, interface, local RD

ARTICLE INFO

Article history:
Received: 16 July 2022
Accepted: 11 October 2022
Published: 13 June 2023

DOI: https://doi.org/10.47836/pjst.31.4.24

E-mail addresses:
cikmimi88@gmail.com (Syamimi Mohd Yusoff)
su_mtahir@upm.edu.my (Suraya Mohd Tahir)
azmah@upm.edu.my (Azmah Hanim Mohamad Ariff)
eris@upm.edu.my (Eris Elliandy Supeni)
mshamsul@upm.edu.my (Mohd Shamsul Anuar)
* Corresponding author

INTRODUCTION

Powder Metallurgy (PM) compaction is a metal-forming technique to fabricate a metal-based powder compact from loose powder. This PM workpiece is frequently produced at once with one layer and is simply known as a green single powder

ISSN: 0128-7680
e-ISSN: 2231-8526

compact (or green SPC). PM compaction is well-known for its effectiveness in delivering the near-net shape of green SPC. Thus, any additional machining works are not necessary. Enhancement of the strength of green SPC was proposed by notable investigations and practically implemented by industries such as green machining technique (Kulkarni & Dabhade, 2019) and high-velocity compaction (HVC) (Yuan et al., 2021). Instantly, the use of the PM compaction route is widely contributing to various circles of industries, for instance, automobile (Masooth et al., 2022), composites (Arifin et al., 2022), military products (Santos et al., 2018) and healthcare (Elsayed et al., 2022) industries.

Nevertheless, the friction condition of a die wall is a major cause that deteriorates the homogeneity of produced green SPC under PM compaction, as overviewed by Edosa et al. (2022). Past discoveries on techniques in minimising the effect of friction were elaborated that included the designed compaction technique (Canta & Frunza, 2003; Grigoriev et al., 2019; Wang et al., 2009), the initial determination of powder relative bulk density (RBD) (Radchenko, 2004), critical consideration of determined H:D ratio and geometrical powder compact shape (Cristofolini et al., 2018), the mixing method (Chen et al., 2020) and the layering strategy of green SPC to form green BPC in which pioneered by Sopchak and Misiolek (2000). This layering foundation had launched for up-to-date manufacturing of green BPCs that have been thoroughly designed across different fields specifically to formulate drugs (Bellini et al., 2019), Ti6Al4V/20CoCrMo-highly porous Ti6Al4V biomedical bilayer (Mihalcea et al., 2021), Ti6al4V-Ti6Al4V/30Ta bilayer for orthopaedic application (Chávez et al., 2020), ceramics (Hasan et al., 2019), composites (Wang et al., 2019), machining, cutting and drilling tools (Ojo-kupoluyi et al., 2019). It is also a valuable pattern for generating functionally graded materials (FGMs) (Masooth et al., 2022).

Compared to growing numbers of modelling for other techniques to further predict the density quality of green SPC, progression in green BPC has surprisingly outnumbered since then, in particular, for metals (Rowe & Nikfar, 2017). It is due to difficulty in classical assessment on the percentage of internal porosities that limit the basis in bilayer formulation as a modelling start-up wherever concerning its interface. Therefore, each researcher had to create a physical test on BPCs to truly assess the structural type of interface and its mechanism framework along with doubled compaction steps. They made attempts to discover the calibration of BPC parameters through compaction forces (Abebe et al.,2014), three-point bending (Favrot et al., 1999), four-point bending (Boonyongmaneerat & Schuh, 2006) and flexure (Castrati et al., 2016) experiments are commonly utilised, and certain possible datasets had been presented for each test. Henceforth, the identified type of interfacial structures was released, such as interlocking (or dry binding) for green BPC of Fe (Abebe et al.,2014; Sopchak & Misiolek, 2000), cohesive for pharmaceutical BPC of Microcrystalline Cellulose (MCC) and Sodium Dilactose (SDLac) (Castrati et al., 2016) as well as pharmaceutical BPC of MCC and lactose anhydrate (Chang & Sun, 2019) and adhesive for bilayers of Aluminum Oxide (Al_2O_3) and Tungsten (W) powder compact

(Boonyongmaneerat & Schuh, 2006). Recently, El-Nasr and his team have inspired the design of an imaging technique known as a Computer Vision System (CVS) to easy-in-access the computation of internal porosities of BPC of Fe without being in contact with the powder surface (El-Nasr et al., 2020).

Sinka (2007) modelled the interfacial BPC of MCC layers under a tangential surface model for modelling. Accordingly, an assumption of a friction coefficient of 0.5 between the layers was stated without experimental validation (Sinka, 2007). Meanwhile, Castrati et al. (2016) modelled the diametrical breaking test with the tested interfacial BPC of MCC and SDLac assigned as the cohesive model. On the other hand, Yohannes et al. (2017) suggested discretising the contact model between individual particles on both sides of layers, whereby the contact force model was integrated as elastic and plastic deformation-dependent of deformed particles. Apart from their experiment, Boonyongmaneerat and Schuh (2006) introduced the use of FE-based modelling to handle the discretisation of fractural constitutive equations under the fracture mechanism between composite BPC of Al_2O_3 and W. Since the formed interface between the layers is utilised from different materials and had undergone the sintered process via firing cycles; therefore, the type of interaction is regarded as an adhesive (Boonyongmaneerat & Schuh, 2006). Concerned about the development behaviour of BPC of Tungsten Carbide–Cobalt (WC-Co) -based cermets under high temperatures, Favrot et al. (1999) included an assessment of the interfacial response by implementing factors such as different sizes and percentages of WC and Co, respectively on each layer using FE-based modelling. According to them, the curvature of the mesh rightfully indicated the interface condition of the compressed bilayer. Thus, no assigned model had been addressed for their findings. It was proven through a sectioned image from their conducted experiment through cold compaction. In addition, as mentioned in a previous report by Thomazic and his team, the assigned two layers of WC and Fe were arranged under an axial column shape to each other. Finally, they obtained a homogeneous BPC structure whenever Fe is located as a lower (*L*) layer. The effect of the interface is not significant in their cases, but the density gradient was successfully reduced (Thomazic et al.,2010). Above all, for all types of bilayer powder investigations and evaluation on different mechanical effects, in particular, friction coefficient and other interactions between particles that exist along the horizontal layers of BPC are simply precluded as caused by the ongoing development of advanced characterisation to gain rightful datasets of adhesive-cohesive inter-relation and invalidate the assumption of interfacial friction coefficient. Therefore, the constitutive model and its calibrations become a hotspot for incoming investigations. This situation rather prolonged the progressive modelling of the interface of BPC.

The present research work presents the formation of green BPC of ASC 100.29 Fe powder to visualise the evolution of local RD gradient that focuses on the interface to strengthen the Fe- based workpieces in metal forming industries. It became the metal of

choice, did not require alloying to be useful, and was used to manufacture nails, tools, utensils, agricultural equipment, and weapons. Experimentally, adding a layer of green SPC to make green BPC of Fe is well known to reduce the local RD gradient. However, quantitative-based assessment for local RD distribution and modelling evaluations on the interface of green BPC of Fe is not considered for documentation. Plus, a comparative study on changes under different die wall conditions and height-to-diameter (H:D) ratio of green BPC with constantly applied load compaction of 30 kN and 95 kN for lower, *L* and upper *U* layers, respectively, were important to be a highlight, therefore, resulted from variation in local RD distribution can be analysed. As an output, a significant way to strengthen the interface to deliver a robust green BPC of Fe can be emphasised. It can potentially contribute to producing defect-free green BPC of Fe.

MATERIAL AND METHODS

Experimental Methods for Validation

Double Steps of Uniaxial One-Sided Compaction. PM compaction was conducted using a universal testing machine (model 3382, Instron, UK) with a load cell with a 100 kN maximum capacity, as depicted in Figure 1. A lower speed of 2 mm min-1 crosshead was used in this work. To produce the green BPC under lubricated die condition (labelled as sample B), magnesium stearate, MgSn, was used to lubricate the die cavity before starting the compaction test. Otherwise, the green BPC without lubricated die condition will be released (labelled as sample A). Next, 11 g of loose Fe powder for the first layer was prepared and manually filled into the rigid die cavity of 20 mm diameter, D, as seen in Figure 1(a). The initial height of the lower layer, HL, was approximately 10 mm. Consequently, as depicted in Figure 1(b), the minimum load compaction, Fu of 30 kN, was then applied via an upper punch to compact the lower L layer of Fe powder, with the bottom punch in a stationary condition. As a result, the height, HL, is reduced to nearly 5 mm. Prior to the compaction of the upper U layer, as seen in Figure 1(c), another layer of Fe powder is compacted under the maximum load compaction, Fu of 95 kN. As a result, the upper layer of Fe powder will have the same final height, HU of 5 mm, as shown in Figure 1(d). Before the ejection process, the base of the die set tool had been replaced by the ejection container, as seen in Figure 1(e), to extrude the green BPC from the die cavity. Another sample is repeated using the same procedures. Table 1 lists the two types of green BPC produced using the steps of PM compaction.

The Use of Low Speed on Compaction and Ejection Force in the Downward Direction. Since a very small mass of loose Fe powder of 11 g is used, a crosshead speed of 2 mm min^{-1} is then employed on each green BPC to reduce the possibility of capping at the bottom of the green BPC and ensure the bonding of the compressed upper, *U* layer of Fe powder

Table 1
Samples produced under PM compaction on lower, L and upper U layers of the green BPCs of Fe

Samples	H:D ratio	MgSn lubricant applied	F_u on *L* (kN)	F_u on *U* (kN)
A	**1.0**	**No**	**30**	95
B	**1.0**	**Yes**	**30**	95

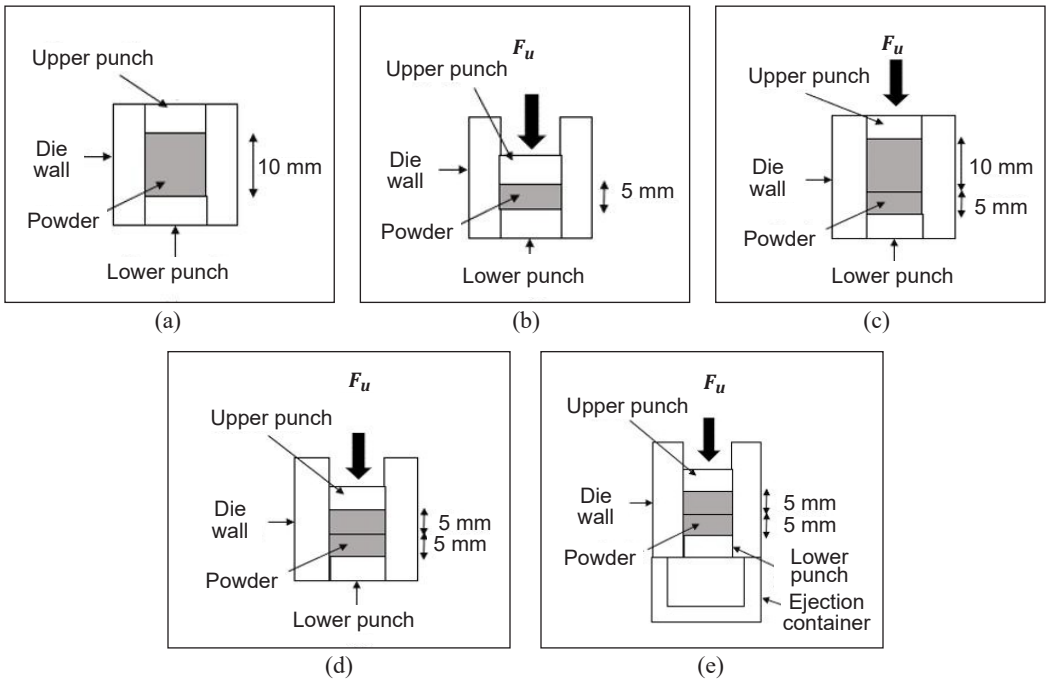

Figure 1. PM compaction steps for producing the green BPC of Fe

to the lower, *L* one. Delamination issues can be avoided with the same speed applied for ejection force, thus reducing the impact from the container on its bottom part, as shown in Figure 1(e). Theoretically, the low speed of both compaction and ejection forces hinders the rise of the springback phenomenon. Then, the obtained cylindrical-shaped green BPC with a thickness of 10 mm for sample A and 10 mm for sample B were cross-sectioned following the arranged procedures under a metallographic technique as the authors did (Yusoff et al., 2021). The cross-sectioned were conveniently displayed in Figures 8(a) and 8(b).

Image Analysis Procedures for the Green BPCs. A systematic preparation according to the sequence steps of image analysis procedures from phase to phase 4 in Table 2 was used for validation with the FE-based model to obtain the final local RD distribution across the section of the green BPCs, as in Figure 5. Phase 1 can be represented as per Figures 1(a), 1(b), 1(c), 1(d), and 1(e). The details of phases (2) and (3) were referred to in the previous work of authors (Syamimi et al., 2021).

Table 2
The workflow process to calculate local RD distribution of the cross-sectioned green BPCs of Fe

Phase	Descriptions
(1)	Uniaxial one-sided compaction
(2)	Metallographic methods, including grinding and polishing
(3)	(a) The cross-section of the green BPC with a final thickness of 10 mm (5 mm for both upper, *U* and lower, *L* layers) is indicated in Figure 1(e). Next, under a magnification of 100X, a total of 525 TIF-based pictures were snapped by the camera through the Olympus BX51 software. (b) TIF-based pictures were converted into binary images separately via MATLAB software, as shown in Figure 2. (c) A Fortran code was developed to create a uniform rectangular grid representing a magnification size of 100X. In addition, a centre-point coordinate (marked as a small red dot colour on each centre of the element) was located within the element size of 0.68 mm and 0.40 mm in the x-direction and y-direction, respectively. Tecplot software has been used to visualise the data retrieved from Fortran in the form of.DAT file. The result of visualisation is indicated in Figure 3. The dimensions are given in this rectangular grid's x- and y- directions were based on the final thickness of the compressed green BPC of sample B in millimetres (mm).
(4)	Under this phase, a one-to-one mapping procedure was performed whereby a binary image of sample B was located backwards of the transparent visualised grid, as displayed in Figure 4. The Origin Lab software was employed to map the part from a result of RD calculation obtained in the previous phase into the specified colourised contour. Specific areas with labelled RD distribution are shown in Figure 5 to indicate the selected areas as major distribution levels.

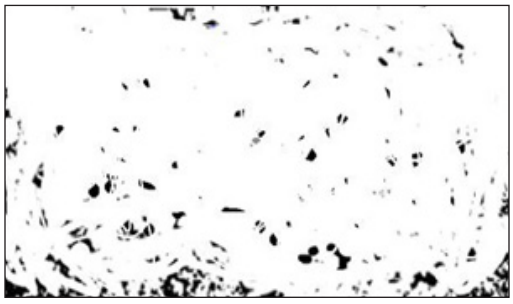

Figure 2. A resulting binary image from TIF-based pictures after conversion with MATLAB software

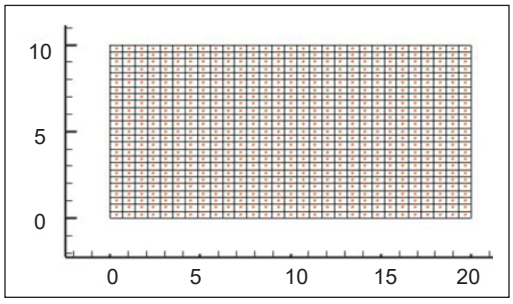

Figure 3. The visualisation of the regular grid arrangement in Tecplot as a result of the performed algorithm in Fortran software

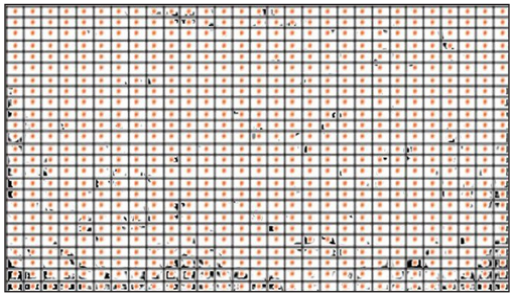

Figure 4. A one-to-one mapping procedure was performed manually in each region of elements that covered the bilayer sample

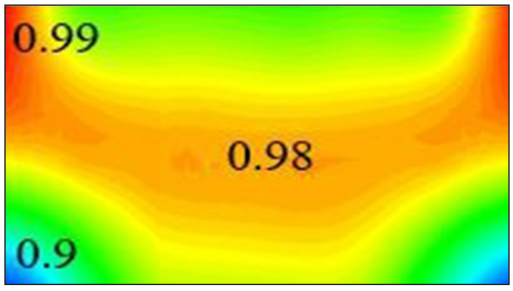

Figure 5. The Origin Lab displayed the resulting contour of RD values

Development of Simultaneous Compaction Model Using FE-Based Modelling

Geometrical Model for Green BPC Compaction. An axisymmetric geometrical model was set up similarly in the experiment to compact the loose Fe powder of ASC 100.29 simultaneously in Abaqus 6.20. Initially, the height H of undeformed Fe powder is 10 mm. In addition, the pair of punches is always set as same as the die mould's radius of 10 mm. Therefore, the length, l, for each punch's length is 10 mm. Finally, the height, H_d, of the die wall is set to follow the height, H, of undeformed Fe powder

FE Parameters for Variation in H:D Ratios. To further analyse the changes in interfacial local RD distribution concerning the changes in height, H (mm) of the powder layer, an implementation of measurement through the H:D ratio is conducted. As indicated in Table 3, H:D ratios of 1.0, 1.3, and 1.6 are selected, whereby each height of lower, H_L and upper H_U layers of green BPC are set. A load of compaction, F_u (kN) applied is 30 kN for the lower layer, L and 95 kN upper layer, U. For all H:D ratios, modelling procedures are applied in each module starting from part and assembly, followed by the property, mesh, step module and finally the job modules in Abaqus 6.20. All the modules were done in similar ways with the same data. An exception had been granted only for the changes in heights of lower, H_L and upper H_U layers of Fe powder parts.

Table 3
List of H:D ratios under a load of compaction, F_u for green BPCs of Fe of samples A, B, C and D

Samples of green BPC	H:D ratio	H_L (mm)	H_U (mm)	F_u on L (kN)	F_u on U (kN)
A	**1.0**	**10**	**10**	**30**	95
B	**1.0**	**10**	**10**	**30**	95
C	**1.3**	**13**	**13**	**30**	95
D	**1.6**	**16**	**16**	**30**	95

Mesh. Despite using Quad dominated-based mesh on the Fe powder layer, a Tri-based mesh is important to utilise both layers of the modelled green BPC with the main element under the size of 0.03 mm. With a correct mapping towards the boundary interface, approximately 100 seedings were used to refine the Tri-based mesh from both sides of the layer. This description can be visualised in Figure 6.

The Properties of Green BPCs of Fe. Ranging from Modulus, E to Yield Stress, p_s, the properties of ASC 100.29 Fe powder as the material of formed green BPC serve as input parameters of built-in Drucker-Prager Cap (DPC) model with an initial local RD of 35 gmm^{-3} or 0.5 and final local RD of 70 gmm^{-3} or 1.0. Table 4 contained the properties in which processing under the property module in Abaqus 6.20 for PM compaction. The Brewin equations calculate the data (Brewin et al., 2007).

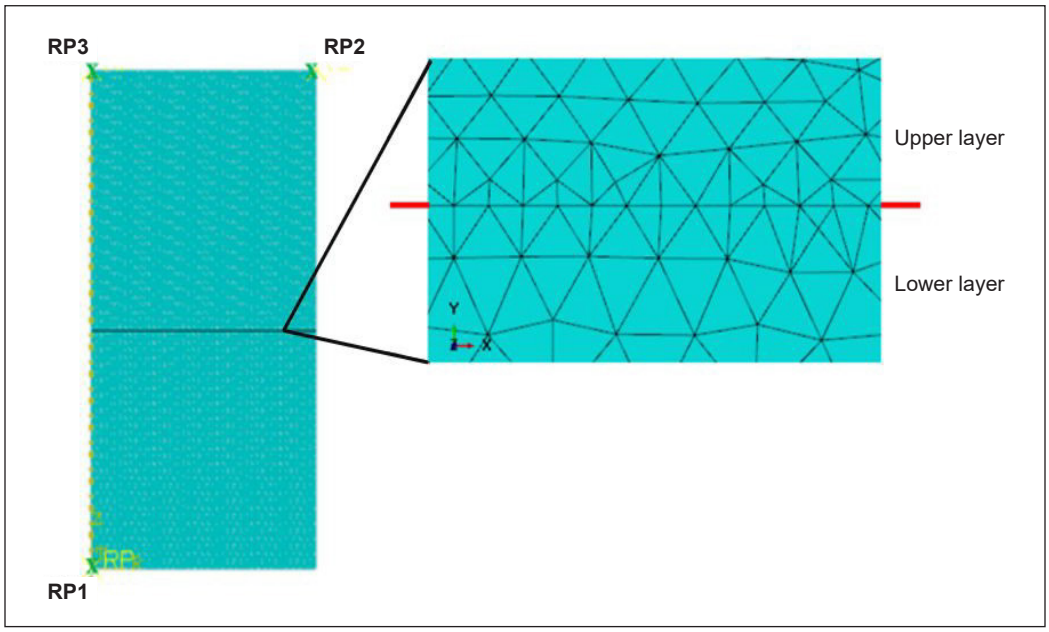

Figure 6. An arrangement of an FE-based model for undeformed green BPC modelling with a close-up of precisely connected nodes between both sides of layers. The red side lines indicate an actual boundary of an interface between two compressed layers of Fe

Table 4
List of input parameters for modelled green BPCs of Fe using the built-in Drucker-Prager Cap (DPC) model

Local RD	Modulus $\boldsymbol{E}$ (MPa)	Poisson Ratio v	Cohesiveness c (MPa)	Angle of Repose tan f	Cap eccentricity C	Yield stress $\boldsymbol{ps}$ (MPa)	Plastic Strain $\boldsymbol{\varepsilon pl}$
0.5	5644.12	0.0556	0.001	72.48784	0.56465685	12.89	0
0.55	7752.25	0.0607	0.2485472	72.05262	0.57774487	24.78	0.3738570
0.7	16317.06	0.0909	3.0391120	70.85212	0.66822970	110.1	0.6150191
0.75	21301.68	0.1059	6.1909922	70.47973	0.72582784	165.8	0.6840119
0.8	29109.18	0.1234	12.040375	70.11856	0.80407416	242.6	0.7485505
0.85	42633.40	0.1433	22.486328	69.76742	0.90835824	346.2	0.8091751
0.9	68727.35	0.1658	40.517986	69.42531	1.04501934	483.6	0.8663335
0.95	125703.4	0.1907	70.717656	69.09136	1.22144311	662.9	0.9204007
1.0	270046.3	0.2182	119.94670	68.76484	1.44616171	893.7	0.9716940
0.7	16317.06	0.0909	3.0391120	70.85212	0.66822970	110.1	0.6150191
0.75	21301.68	0.1059	6.1909922	70.47973	0.72582784	165.8	0.6840119
0.8	29109.18	0.1234	12.040375	70.11856	0.80407416	242.6	0.7485505
0.85	42633.40	0.1433	22.486328	69.76742	0.90835824	346.2	0.8091751
0.9	68727.35	0.1658	40.517986	69.42531	1.04501934	483.6	0.8663335
0.95	125703.4	0.1907	70.717656	69.09136	1.22144311	662.9	0.9204007
1.0	270046.3	0.2182	119.94670	68.76484	1.44616171	893.7	0.9716940

FEM Parameters for Variation in Die Wall Condition in Terms of Friction Coefficient, μ. In Abaqus 6.20, the selected interactions are manually done under the interaction module. It includes the first interaction, assigned between the lower punch and the bottom side of the Fe powder lower layer. It is followed by the second interaction, which consists of the die surface and the side of the Fe powder lower layer and the third interaction, between the die surface and the side of the Fe powder upper layer. In addition, the fourth interaction consists of the upper side of the Fe powder upper layer and the lower side of the upper punch. Lastly, the fifth interaction is between the upper side and the lower side of the lower and upper layers of Fe powder, respectively. The location of each interaction is seen in Figure 7.

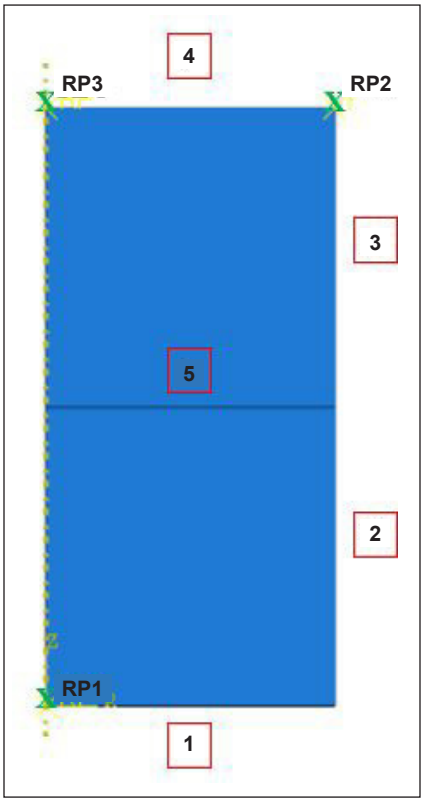

Figure 7. Each side is numbered to indicate the area used to define the interactions involved in the modelling of the green BPCs of Fe

Consequently, in Tables 5 and 6, each interaction was assigned with friction coefficient values, μ, by applying one of the available mechanical constraint formulations in Abaqus 6.20, namely the penalty contact method. The penalty contact method is a type of contact property that falls under tangential contact surfaces. To model the interface of undeformed green BPC under the lubricated die condition, a value of friction coefficient, μ of 0.08, is used. Whereas for the modelling under the unlubricated die condition, a value of friction coefficient, μ of 0.18, is used. For unlubricated surfaces, such as indicated under interactions of 1 and 4 for the green BPC of the Fe model, a selected value of friction coefficient, μ of 0.5, is used.

Table 5
List of employed values for friction coefficient, μ for the green BPC of Fe (sample A) under unlubricated die condition

Number of interactions	μ
1	0.5
2	0.18
3	0.18
4	0.5
5	0.08

Table 6
List of employed values for friction coefficient, μ for the green BPC of Fe (sample B) under lubricated die condition

Number of interactions	μ
1	0.5
2	0.08
3	0.08
4	0.5
5	0.08

RESULTS AND DISCUSSION

Few dissimilarities of local RD distribution are found between the sectioned of the green BPCs of sample A (unlubricated) and B (lubricated with MgSn). As referred to the left of Figures 8(a) and 8(b), both samples mutually appeared smooth around their mid-region and the uppermost corner of green BPCs of Fe regions. In contrast, the lowermost corner regions were visibly gloomy in colour. These results are fundamentally consistent with the works of Rajab and Coleman (1985), Sopchak and Misiolek (2000) and Zadeh (2010) for ASC 100.29 Fe powder. Theoretically, the Fe powder particles positioned nearer to the die wall and upper punch tend to densify and re-arrange as the compaction force is further applied in the gravitational direction. Meanwhile, the darkening regions were deteriorated by randomly distributed porosities and less received the effect of densification from the upper punch.

However, sample A's mid-region is devoted to having few scattered porosities. At the same time, sample B's mid-region is almost impossible to have any physically observed porosities. Therefore, it is essential to use a high magnification of 100X under the optical microscope to gain details measurements regarding local RD distribution across the section of green BPCs. As an outcome, the experimental contour for local RD distribution is displayed on the right of Figures 8(a) and 8(b). A large range between 0.82 and 0.99 is displayed by sample A under unlubricated die condition, whereas a short range between 0.9 and 0.99 is displayed by sample B.

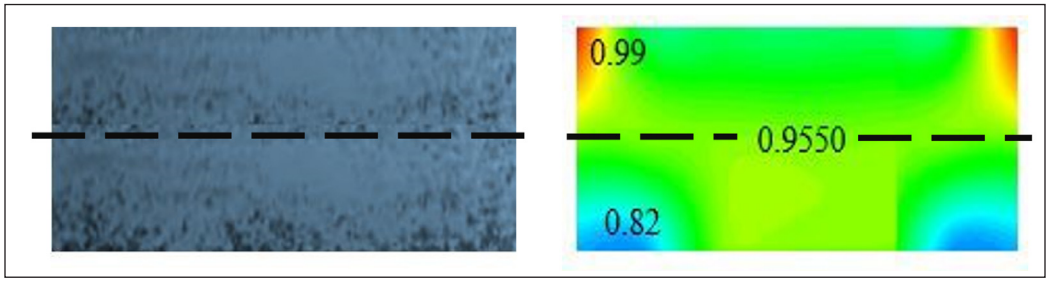

(a)

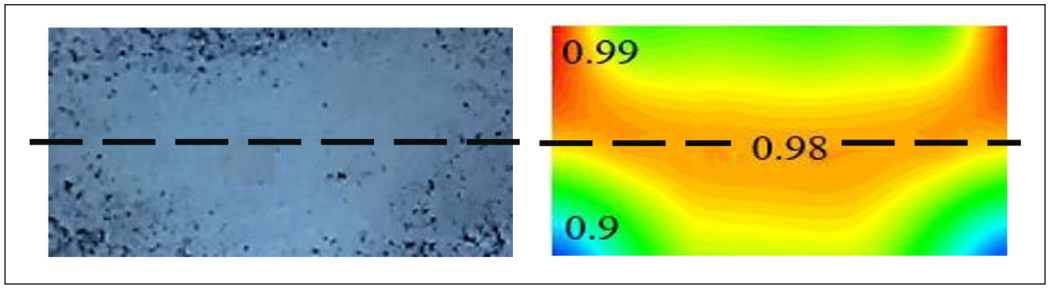

(b)

Figure 8. Experimental local RD distributions obtained for a whole geometrical shape of green BPCs of Fe: (a) Sample A; and (b) Sample B

Validation of the Axisymmetric FE-Based Modelling

The modelling of PM compaction for green BPC of samples A and B is validated with the experimental results (Figure 9). It is found that, under the modelling part, the unlubricated die condition delivered a large gradient of local RD distribution within sample A, indicated by the solution-dependent variable (SDV1) contour. Compared to the experimental result, each value under the three main regions of the uppermost and lowermost corners and the mid-region are nearer to the modelling results by only differences of 0.79%, 2.27% and 0.79%, correspondingly. Differing to sample B, a small gradient of local RD distribution is captured under lubricated die condition. Indeed, the only differences between the experiment and modelling were only 0.21%, 1.5% and 0.52% for regions of the uppermost and lowermost corner and mid-region, respectively. The validation is conveniently achieved by satisfying the basic work on evaluation under PM compaction, whereby the difference in percentages with less than 5.0% is allowable (Tweed et al., 2008).

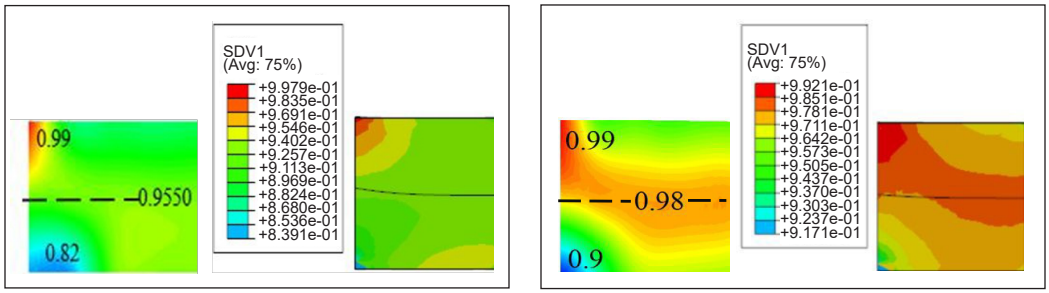

(a) (b)

Figure 9. Comparison of RD distributions obtained from experimental work (left) and FE (right) for (a) sample A and (b) sample B of green BPCs of Fe

Mesh Convergence and Sensitivity Analysis

A mesh convergence study was performed to determine the optimal element size. The relative density convergence plot of eight different element sizes is displayed in Figure 10. It was found that an element size of 0.03 mm was able to produce a converged solution within a reasonable period. Previous agreements and their convergence have given confidence in the predictive capabilities of the proposed model (for compaction).

In Equation 1, 0.98 is an obtained value of local RD from the experiment. Using the largest tri-element size of 0.5 mm on the upper and lower layers recorded large errors between FEM and the experimental values with errors of 0.035. Finally, using the smallest size of 0.1 mm with 110 total seedings, a nearer value of interfacial local RD is obtained, as indicated in Figure 11. A good prediction of local RD values in other region parts was also obtained, similar to the good prediction at the interface.

$$Error(\Delta) = Value\ of\ local\ RD\ at\ the\ interface\ (FE) - 0.98 \quad (1)$$

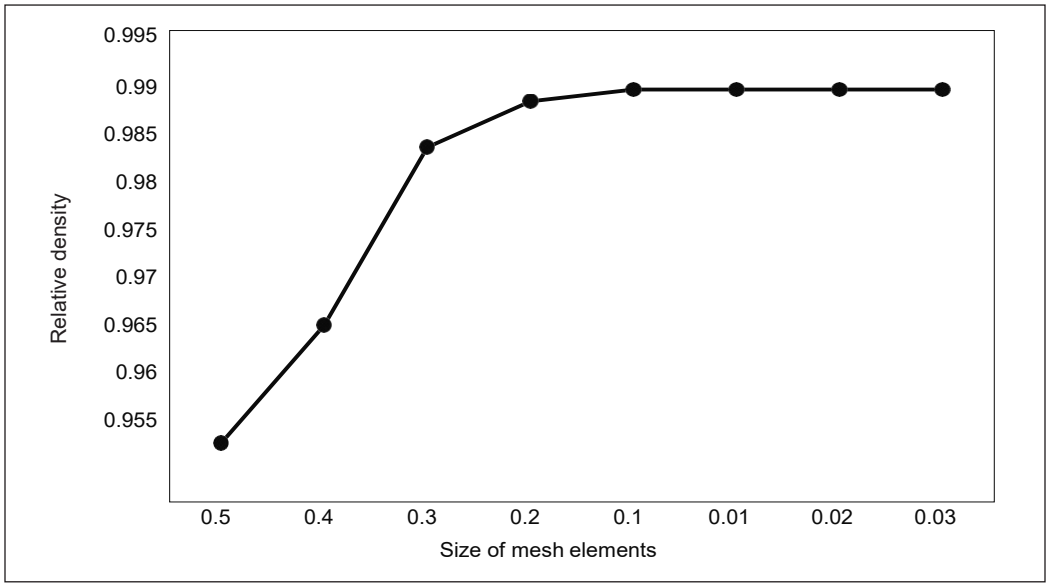

Figure 10. Mesh convergence analysis

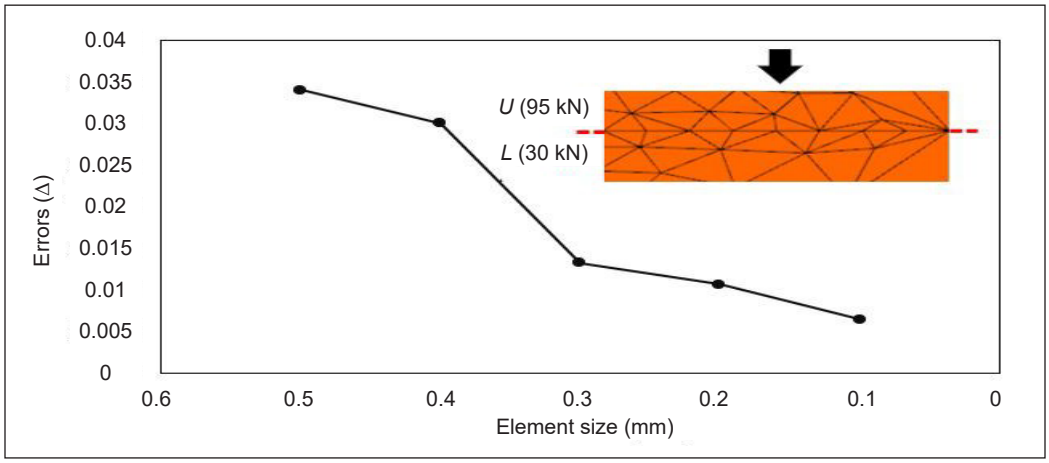

Figure 11. A graph of errors against element sizes (in mm). A picture inside indicated a close-up of the interface of the green BPC of Fe at the final compaction stage with a precise connection between its nodes

Local RD Distributions for Variation in H/D Ratios of the Green BPC of Fe Under Different Applied Friction Coefficients

In Figures 12(a), 12(b) and 12(c), two modelled green BPC of Fe with their corresponding H:D ratios of 1.0, 1.3 and 1.6 were compared under different die conditions. The left and right of Figure 12 show the unlubricated and lubricated die results with applied friction coefficient values, μ equal to 0.18 and 0.08, respectively. In Figure 12(a), the green BPC under lubricated die condition had enhanced its local RD distribution within the average of 0.9816 along the interface with the range of local RD distribution between 0.9781 and

0.9851. It is noticed that the interfacial densification within the green BPC that was compressed under the unlubricated die condition had not emerged with a recorded higher range between 0.9402 and 0.9546.

Same in Figure 12(b), the compressed green BPC of Fe with an H:D ratio of 1.3 did not receive the densification support along its interfacial region under the unlubricated die condition with local RD distribution slightly reducing within the range between 0.9323 and 0.9456. Compared to the green BPC of Fe that was compressed under the lubricated die condition, significant horizontal densification is discovered between the two layers within an increased average of 0.98. In addition, it resulted in the local RD distribution within the range between 0.9817 and 0.9882.

As Figure 12(c) observed, the unlubricated die condition had delivered unfamiliar distribution of local RD right below its interface with captured average values of 0.9686. For the green BPC of Fe under the lubricated die condition, an increase of its local RD distribution is seen along its horizontal interface but less covered on its lower layer. With the increase of powder thickness with an H:D ratio of 1.6 under the unlubricated die condition, higher local RD distribution formed along the side of the die wall. Consequently, extended densification of powder particles is seen localised at the middle region of the lower layer and thus creates discontinuity of distributed local RD values between two compressed layers. Current findings are consistent with the results reported by previous literature whereby the mid-region of formed green BPC under unlubricated die condition is lower compared to the regions nearer to the side of the die wall.

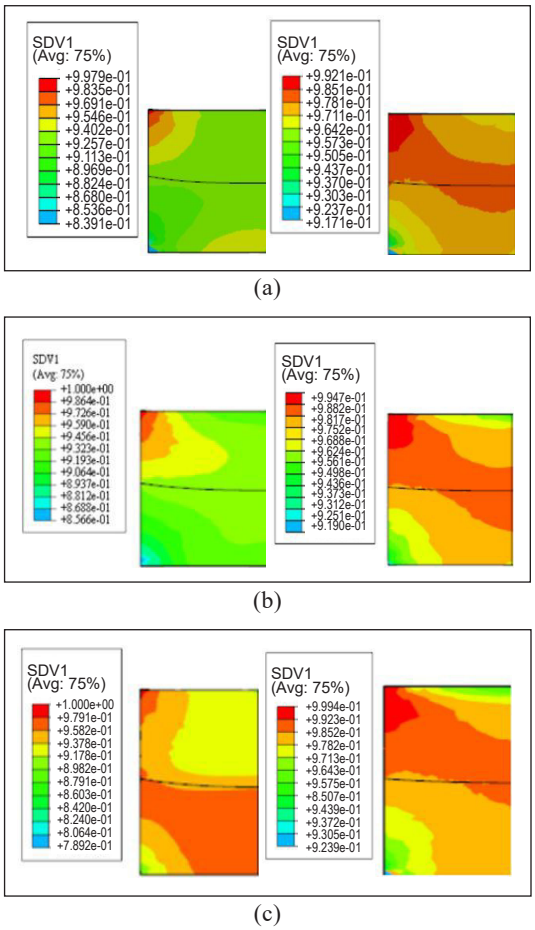

Figure 12. Contour results of local RD distribution for H:D ratios of (a) 1.0, (b) 1.3, and (c) 1.6

CONCLUSION

This evaluation on the interface of green bilayer powder compact (BPC) of iron (Fe) under two different die wall conditions provides both qualitative and quantitative insights

into distributions of the local relative density (or local RD). The study revealed that axial friction from the die wall under unlubricated die conditions had disrupted the flowability of the compressed upper *U* layer onto the lower *L* layer of Fe to form an interlocking type of densification. Whereas lubricated die condition supported the interface of BPC whereby less friction from the die wall had allowed for the flowability and promoted an interlocking between compressed upper, *U* layer onto lower, *L* layer of Fe during the second time of PM compaction. This condition would strengthen the bilayer system and reduce the local RD gradient across its internal cross-sectioned. The FE-based simultaneous compaction modelling results suggest that the nodes along the interfacial boundary between upper, *U*- and lower, *L*- surface layers of BPC of Fe must be in mutual interconnection to gain the interlocking (or dry binding) effect in which similarly obtained in experimental results. Also, the modelling study showed that the increment of height to diameter (H:D) ratio with constantly applied load magnitude had released less interlocking effect from the upper to lower part of the BPC structure. It is estimated that the increase in load magnitude must be done proportionally for both layers, i.e., 60 kN and 190 kN for upper, *U*- and lower, *L*- surface layers, respectively, to get the mid-interlocking effect which will help minimise the local gradient as H:D ratio is increased. In addition, it is evidenced that using input parameters from Brewin equations with the medium of built-in DPC in Abaqus 6.20 agrees well with the experimental results of local RD with the condition that the tri-based mesh elements with refinement along the interface must be provided. Also, the selection of friction coefficient, μ of 0.08 and 0.18 to denote the lubricated and unlubricated die wall conditions, respectively, is proved suitable, therefore, benefited the establishment of green BPC of the Fe model. It can potentially contribute to producing defect-free green layered Fe powder compacts.

ACKNOWLEDGEMENT

The authors thank IPS Putra Grant (GP-IPS/2019/9654100), Universiti Putra Malaysia, Malaysia, for allowing them to deliver the research outputs.

REFERENCES

Abebe, A., Akseli, I., Sprockel, O., Kottala, N., & Cuitiño, A. M. (2014). Review of bilayer tablet technology. *International Journal of Pharmaceutics*, *461*(1-2), 549-558. https://doi.org/10.1016/j.ijpharm.2013.12.028

Arifin, A., Gunawan, G., & Yani, I. (2022). *Plagiarism and similarity checker of porous titanium alloy/hydroxyapatite composite using powder compaction route*. Turnitin Universitas Sriwiajaya. https://repository.unsri.ac.id/66950/

Bellini, M., Walther, M., & Bodmeier, R. (2019). Evaluation of manufacturing process parameters causing multilayer tablets delamination. *International Journal of Pharmaceutics*, *570*, Article 118607. https://doi.org/10.1016/j.ijpharm.2019.118607

Boonyongmaneerat, Y., & Schuh, C. A. (2006). Contributions to the interfacial adhesion in co- sintered bilayers. *Metallurgical and Materials Transactions A*, *37*(5), 1435-1442. https://doi.org/10.1007/s11661-006-0088-9

Brewin, P. R., Coube, O., Doremus, P., & Tweed, J. H. (2008). *Modelling of Powder Die Compaction* (Vol. 329). Springer.

Canta, T., & Frunza, D. (2003). Friction-assisted pressing of PM components. *Journal of Materials Processing Technology*, *143-144*, 645-650. https://doi.org/10.1016/S0924-0136(03)00475-8

Castrati, L., Mazel, V., Busignies, V., Diarra, H., Rossi, A., Colombo, P., & Tchoreloff, P. (2016). Comparison of breaking tests for the characterization of the interfacial strength of bilayer tablets. *International Journal of Pharmaceutics*, *513*(1-2), 709-716. https://doi.org/10.1016/j.ijpharm.2016.10.005

Chang, S. Y., & Sun, C. C. (2019). Effect of particle size on interfacial bonding strength of bilayer tablets. *Powder Technology*, *356*, 97-101. https://doi.org/10.1016/j.powtec.2019.07.100

Chávez, J., Jiménez Alemán, O., Flores Martínez, M., Vergara-Hernández, H. J., Olmos, L., Garnica-González, P., & Bouvard, D. (2020). Characterization of Ti_6Al_4V–Ti_6Al_4V/30Ta bilayer components processed by powder metallurgy for biomedical applications. *Metals and Materials International*, *26*(2), 205-220. https://doi.org/10.1007/s12540-019-00326-y

Chen, W., Wang, J., Wang, S., Chen, P., & Cheng, J. (2020). On the processing properties and friction behaviours during compaction of powder mixtures. *Materials Science and Technology (United Kingdom)*, *36*(10), 1057-1064. https://doi.org/10.1080/02670836.2020.1747779

Cristofolini, I., Molinari, A., Pederzini, G., & Rambelli, A. (2018). From experimental data, the mechanics relationships describing the behaviour of four different low alloyed steel powders during uniaxial cold compaction. *Powder Metallurgy*, *61*(1), 10-20. https://doi.org/10.1080/00325899.2017.1361507

Edosa, O. O., Tekweme, F. K., & Gupta, K. (2022). A review on the influence of process parameters on powder metallurgy parts. *Engineering and Applied Science Research*, *49*(3), 433- 443.

El-Nasr, A. A., Saleh, A., & Alshennawy, A. A. (2020). Porosity measurement of iron oxide by using computer vision system. *International Journal of Engineering Research and Technology, 13*(4), 653-659.

Elsayed, M. M., Aboelez, M. O., Mohamed, M. S., Mahmoud, R. A., El-Shenawy, A. A., Mahmoud, E. A., Al-Karmalawy, A. A., Santali, E. Y., Alshehri, S., Elsadek, M. E. M., El Hamd, M. S., & Ramadan, A. E. H. (2022). Tailoring of rosuvastatin calcium and atenolol bilayer tablets for the management of hyperlipidemia associated with hypertension: a preclinical study. *Pharmaceutics*, *14*(8), Article 1629.

Favrot, N., Besson, J., Colin, C., & Delannay, F. (1999). Cold Compaction and Solid-State Sintering of WC-Co-Based Structures: Experiments and Modeling. *Journal of the American Ceramic Society*, *82*(5), 1153-1161. https://doi.org/10.3390/pharmaceutics14081629

Grigoriev, S. N., Dmitriev, A. M., Korobova, N. V., & Fedorov, S. V. (2019). A cold-pressing method combining axial and shear flow of powder compaction to produce high-density iron parts. *Technologies*, *7*(4), 2-17. https://doi.org/10.3390/technologies7040070

Hasan, M., Zhao, J., Huang, Z., Wei, D., & Jiang, Z. (2019). Analysis and characterization of WC- 10Co and AISI 4340 steel bimetal composite produced by powder-solid diffusion bonding. *The International Journal of Advanced Manufacturing Technology*, *103*(9), 3247-3263. https://doi.org/10.1007/s00170-019-03709-y

Kulkarni, H., & Dabhade, V. V. (2019). Green machining of powder-metallurgy-steels (PMS): An overview. *Journal of Manufacturing Processes*, *44*, 1-18. https://doi.org/10.1016/j.jmapro.2019.05.009

Masooth, P. H. S., Bharathiraja, G., Jayakumar, V., & Palani, K. (2022). Microstructure and mechanical characterisation of ZrO_2 reinforced Ti_6Al_4V metal matrix composites by powder metallurgy method. *Materials Research Express*, *9*(2), Article 020003. https://doi.org/10.1088/2053-1591/ac5352

Mihalcea, E., Vergara-Hernández, H. J., Jimenez, O., Olmos, L., Chávez, J., & Arteaga, D. (2021). Design and characterization of Ti_6Al_4V/20CoCrMo− highly porous Ti_6Al_4V biomedical bilayer processed by powder metallurgy. *Transactions of Nonferrous Metals Society of China*, *31*(1), 178- 192. https://doi.org/10.1016/S1003-6326(20)65486-3

Ojo-kupoluyi, O. J., Tahir, S. M., Hanim, M. A., Anuar, M. S., & Dele-Afolabi, T. T. (2019). Investigating the effect of sintering temperature on the microstructure and hardness of cemented tungsten carbide/steel bilayer. *IOP Conference Series: Materials Science and Engineering, 469*(1), Article 012020. https://doi.org/10.1088/1757-899X/469/1/012020

Radchenko, A. K. (2004). Mechanical properties of unsintered pressings. I. phenomenological relations for unsintered pressing strength. *Powder Metallurgy and Metal Ceramics, 43*(9), 447-460. https://doi.org/10.1007/s11106-004-0003-0

Rajab, M., & Coleman, D. S. (1985). Density distributions in complex shaped parts made from iron Powders. *Powder Metallurgy, 28*(4), 207-216.

Rowe, J. M., & Nikfar, F. (2017). Modeling approaches to multilayer tableting. In P. Pandey & R. Bharadwaj (Eds.), *Predictive Modeling of Pharmaceutical Unit Operations* (pp. 229-251). Woodhead Publishing. https://doi.org/10.1016/B978-0-08-100154-7.00009-0

Santos, T. D. E. D. S., Regiani, I., Rocha, R. J., & Rocco, J. A. F. F. (2018). Copper/iron brake friction for military aircraft application. *Journal of Aerospace Technology and Management*, *10*, Article e2018. https://doi.org/10.5028/jatm.v10.834

Sinka, C. (2007). Modelling powder compaction. *KONA Powder and Particle Journal*, *25*, 4-22. https://doi.org/10.14356/kona.2007005

Sopchak, N. D., & Misiolek, W. Z. (2000). Density gradients in multilayer compacted iron powder parts. *Materials and Manufacturing Processes*, *15*(1), 65-79. https://doi.org/10.1080/10426910008912973

Thomazic, A., Guennec, Y. L., Kamdem, Y., Pascal, C., Chaix, J. M., Doremus, P., Imbault, D., Bouvard, D., & Doré, F. (2010, October 10-14). *Fabrication of bimaterial components by conventional powder metallurgy*. [Paper presentation]. In Proceedings of the International Powder Metallurgy World Congress & Exhibition, Florence, Italy.

Wang, J. Z., Qu, X. H., Yin, H. Q., Yi, M. J., & Yuan, X. J. (2009). High velocity compaction of ferrous powder. *Powder Technology*, *192*(1), 131-136. https://doi.org/10.1016/j.powtec.2008.12.007

Wang, L., Wang, D., Huang, S., Guo, X., Wan, G., Fan, J., & Chen, Z. (2019). Controllable shape changing and tristability of bilayer composite. *ACS Applied Materials & Interfaces*, *11*(18), 16881-16887. https://doi.org/10.1021/acsami.8b21214

Yohannes, B., Gonzalez, M., Abebe, A., Sprockel, O., Nikfar, F., Kiang, S., & Cuitiño, A. M. (2017). Discrete particle modeling and micromechanical characterization of bilayer tablet compaction. *International Journal of Pharmaceutics*, *529*(1-2), 597-607. https://doi.org/10.1016/j.ijpharm.2017.07.032

Yuan, X., Qu, X., Yin, H., Feng, Z., Tang, M., Yan, Z., & Tan, Z. (2021). Effects of sintering temperature on densification, microstructure and mechanical properties of al-based alloy by high-velocity compaction. *Metals*, *11*(2), Article 218. https://doi.org/10.3390/met11020218

Yusoff, S. M., Tahir, S. M., Hanim, M. A. A., Supeni, E. E., & Anuar, M. S. (2021). Fabrication and evaluation of density distribution in green bilayer iron powder compact. *Materials and Manufacturing Processes*, *36*(6), 660-667. https://doi.org/10.1080/10426914.2020.1854474

Zadeh, H. K. (2010). *Finite Element Analysis and Experimental Study of Metal Powder Compaction*. Queen's University.

Pertanika J. Sci. & Technol. 31 (4): 2031 - 2045 (2023)

PERTANIKA JOURNALS

SCIENCE & TECHNOLOGY

Journal homepage: http://www.pertanika.upm.edu.my/

Algorithm for the Joint Flight of Two Uncrewed Aerial Vehicles Constituting a Bistatic Radar System for the Soil Remote Sensing

Gennady Linets, Anatoliy Bazhenov, Sergey Malygin, Natalia Grivennaya*, Tatiana Chernysheva and Sergey Melnikov

Department of Infocommunications, North Caucasus Federal University, Pushkin str., 1, Stavropol, 355000, Russia

ABSTRACT

The study of soil agrophysical and agrochemical properties is based on ground-based point measurements and measurements conducted using radiometric remote sensing systems (satellite or airborne). A disadvantage of the existing remote sensing systems using normal surface irradiation is the insignificant depth of penetration of the probing radiation into the soil layer. It is proposed to use a radar system for remote sensing agricultural lands to eliminate this drawback. The system uses a method for assessing the soil's physical and chemical properties based on the interference measurements of direct and reflected electromagnetic waves at incidence angles that provide a total refraction effect, i.e., close to Brewster's angle. The possibility of using this method for remote assessment of soil's physical and chemical properties, including the subsurface layer moisture, was established. A feature of the bistatic system is that it is necessary to coordinate the mutual arrangement of the transmitting and receiving positions, which imposes special requirements on the UAVs' flight algorithm. The UAVs' relative position makes it possible to form the conditions for the manifestation of the total refraction effect, to determine the current value of Brewster's angle, and to fix these conditions for the subsequent flight, making it possible to measure the soil's physical and chemical parameters. The research results can be used to implement precision farming technology in hard-to-reach places, large agricultural areas, and digital agriculture.

Keywords: Brewster's angle, flight algorithm, radar system, remote sensing, soil moisture, total refraction, UAV

ARTICLE INFO

Article history:
Received: 18 July 2022
Accepted: 02 November 2022
Published: 13 June 2023

DOI: https://doi.org/10.47836/pjst.31.4.25

E-mail addresses:
kbytw@mail.ru (Gennady Linets)
a_bazenov61@rambler.ru (Anatoliy Bazhenov)
malygin.sergei1959@yandex.ru (Sergey Malygin)
katrinastenton@yandex.ru (Natalia Grivennaya)
chta1987@mail.ru (Tatiana Chernysheva)
territoreer@yandex.ru (Sergey Melnikov)
* Corresponding author

ISSN: 0128-7680
e-ISSN: 2231-8526

INTRODUCTION

Soil moisture (SM) is one of the most important parameters in agricultural applications such as agricultural land mapping (Dari et al., 2021), irrigation planning, flood monitoring (S. Wang et al., 2021), draft monitoring (Filion et al., 2016), and yield forecasting (Brook et al., 2020). They can promote water-saving agriculture (Tran et al., 2015) and provide food security, especially in arid and semi-arid regions (Gago et al., 2015; Martins et al., 2021; Fugazza et al., 2022). Traditionally, SM is studied using ground-based point measurements based on interpolated lines or grids using geophysical methods (Tavakol et al., 2021) (tensiometers, neutron moisture meters, capacitive sensors, thermal impulse sensors, underground radars) (Mallet et al., 2021; Xie et al., 2022), which, despite their relatively high accuracy, have limited spatial representativeness (several square meters maximum) (Brook et al., 2020; Babaeian et al., 2021; Rohil & Mathur, 2022; Rouf et al., 2021). Over the past 50 years, active satellite observations in electromagnetic spectra (L (0.39–1.55 GHz), C (3.9–5.75 GHz) and X (5.75–5.75 GHz) and X (5.75–0.9 GHz), rarely P-band) have been used to study SM and multispectral characteristics of vegetation cover (Bargiel et al., 2013; Su et al., 2014; Ludeno et al., 2018; Li et al., 2021; H. Wang et al., 2021). There are also several algorithms (Nguyen et al., 2022), models (Pandey & Jain, 2022; Yang et al., 2021), and software products (Salam et al., 2019; Kim, 2021; Barca et al., 2021) available for real use (Saddik et al., 2021). However, most of the information about SM obtained using radiometric remote (satellite) sensing systems (ASCAT, AMSR-E, AMSR2, SMAP, SMOS) (Amazirh et al., 2018; Faye et al.,2018; Mandal et al.,2020) are usually surface SM (a few millimeters deep for optical and thermal range) (Barca et al., 2021; Elkharrouba et al., 2022) or near surface SM (a few centimeters deep for X-, C-, or L-frequency microwave sensors) (Bandini et al., 2020; Ivushkin et al., 2021). It is not possible to estimate the moisture content of the root zone.

The use of a bistatic (or multistatic) satellite radar system (GNSS-R) (Rohil & Mathur, 2022) makes it possible to partially solve the sounding depth problem by expanding the observation limits (both in angle and operating frequencies) and introducing new parameters due to signal scattering (Kaasiku et al., 2021). Despite the prospects for reflectometry of global navigation satellite signals (Bhogapurapu et al., 2022), cloud cover, vegetation cover, topography, soil structure, climate, and other factors remain significant limitations of the applicability of all remote (satellite) soil sensing methods with relatively high measurement accuracy (Zhu et al., 2019; Babaeian et al., 2021).

Using crewless aircraft makes it possible to remove significant limitations for remote (satellite) sensing (Tran et al., 2015; Gopaiah et al., 2021). The problem of the limited depth of studies of the soil root zone (Sahaar et al., 2022) can be solved by using a radar-sounding system in the ultrashort wave range (up to 860 MHz). The system registers a signal reflected from soil inhomogeneities and carries information about the physical and

chemical properties of the soil (Babaeian et al., 2021). The joint use of the multispectral cameras installed on the UAV and the radar-sounding system will ensure the necessary spatial and temporal consistency of observations of the soil's physical and chemical properties and the state of the surveyed area vegetation cover.

Thus, the relevance of research is determined by the need to expand information sources used in making management decisions in precision farming through radar sounding of subsurface soil layers.

In radar soil sounding, the reflected signal can be represented as the sum of several constituents: the signal falling directly on the receiving antenna, the reflected signal from the air-surface boundary (air-surface interface), and the reflected signal from the inner ground layers located at the entire penetration depth. Given the problem to be solved, the reflection from the air-surface boundary is not informative and, conversely, worsens the conditions for determining the physico-chemical composition of the subsurface soil layers.

As is known, when a plane electromagnetic wave is incident on the interface between two dielectric media, the fraction of reflected energy is determined by the reflection coefficient R. Thus, the purpose of the research is to create conditions under which the reflection coefficient from the air-surface interface will tend to zero ($R \rightarrow 0$), and the energy of the incident wave will penetrate the soil to form a reflected signal from the inner layers. To satisfy this condition, Bazhenov et al. (2021) propose to use the effect of total refraction, i.e., carry out surface irradiation at Brewster's angle, while the remote radar sensing system should be placed on two crewless aerial vehicles (UAVs) and implemented as bistatic. Chandra & Tanzi (2018) performed mathematical modeling of subsurface layers' radar sounding to search for and rescue people during earthquakes and other global disasters using "oblique" surface irradiation at angles close to Brewster's angles. They determined the key requirements for GPR and research conditions and also confirmed the sufficient energy level of the reflected signal to search for objects with an effective scattering surface of about 1 m^2 to a depth of 10 meters.

The disadvantage of existing approaches is that their implementation requires a priori information about the physical and chemical parameters of the soil, namely its dielectric constant and specific conductivity. In this case, Brewster's angle can be calculated from the known expressions. At the same time, the dielectric constant and specific conductivity of the earth's surface layer is not constant value and depends on the soil composition and structure, the presence of salts, and its moisture content. Therefore, before conducting the soil remote sensing with an emphasis on its inner layers, it is necessary to determine the value of Brewster's angle for the specific conditions of radar sounding.

Thus, the scientific task of the study is to develop an algorithm for the flight of two UAVs that make up a bistatic radar system for soil sounding, which allows, under conditions of a priori uncertainty about the physicochemical parameters of the soil surface, provide

the condition (R → 0), determine the current value of Brewster's angle and subsequently maintain flight parameters that make it possible to irradiate the earth's surface at an angle close to Brewster's angle.

MATERIALS AND METHODS

Determination of the main ways of solving the problem and existing restrictions.

The Brewster's angle is determined from the expression for the reflection coefficient for a vertically polarized electromagnetic wave (Bazhenov et al., 2021) (Equation 1):

$$\dot{R}_V = \frac{\dot{Z}_{C2} \cdot cos\ \varphi - \dot{Z}_{C1} \cdot cos\ \phi}{\dot{Z}_{C2} \cdot cos\ \varphi + \dot{Z}_{C1} \cdot cos\ \phi}, \quad [1]$$

with the reflection coefficient equal to zero.

Here, Z_{C1} is the characteristic resistance of the first medium (air); Z_{C2} is the characteristic resistance of the soil surface layer (in the general case, a complex value); φ is the incidence angle of a plane electromagnetic wave on the interface between two media; φ is the angle of refraction.

It follows from Equation 1 that to ensure a zero-reflection coefficient R_v, the following condition must be met (Equation 2):

$$\varphi_B = acos \frac{Z_{C1} \cdot cos\ \phi}{Z_{C2}}, \quad [2]$$

where φ_B is Brewster's angle.

The angle of refraction in Equation 2 is determined under Snell's second law in Equation 3,

$$\frac{n_2}{n_1} = \frac{sin\ \varphi}{sin\ \phi}, \quad [3]$$

where n_1, n_2 is the refractive indices of the first and second medium.

Figures 1(a) and 1(b) show the reflection coefficient's dependence on the incidence angle for radio waves with vertical and horizontal polarizations. In Figure 1(a), the specific conductivity of soil is 0.017 S/m, corresponding to dry soil. Figure 1b shows the soil-specific conductivity of 0.7 S/m, i.e., highly moistened soil.

As follows from Figures 1(a) and 1(b), an increase in specific conductivity leads to a shift in Brewster's angle towards larger values, and in this case, the minimum value of the reflection coefficient is increasingly different from zero.

In the absence of a priori data on the specific conductivity and permittivity, it is not possible to determine the value of Brewster's angle only from the amplitude of the radar signal reflected from the earth's surface since the total received signal may not have a pronounced minimum at this angle of incidence.

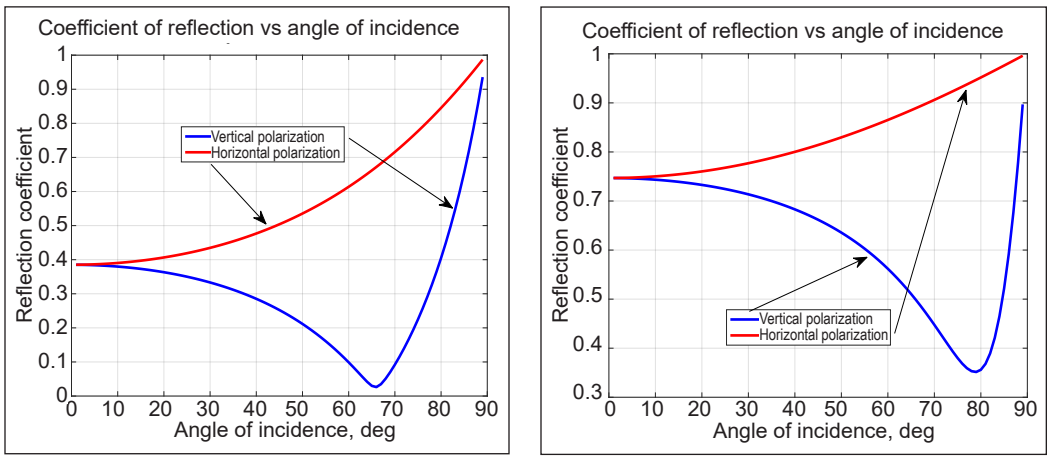

Figure 1. The dependence of the reflection coefficient on the angle of incidence: (a) specific conductivity of soil is 0.017 S/m; (b) specific conductivity of soil is 0.7 S/m

It is proposed to use the interference of direct and reflected waves with the successive application of vertical and horizontal polarization to substantiate the algorithm for the joint flight of two crewless aerial vehicles that make up a bistatic radar system for remote soil sensing, which provides the detection of the total refraction effect. Figure 2 shows the conditions for the formation of the interference wave.

In Figure 2, the following designations are accepted: h_1 and h_2 are the heights of the transmitting and receiving antennas, respectively; φ is the angle of incidence; $L_1 = h_1 \cdot tg\varphi$ is the projection on the Earth's surface of the distance D_1 between the transmitting position and the place where the reflected signal is formed; $L_2 = h_2 \cdot tg\varphi$ is the projection onto the Earth's surface of the distance D_2 between the receiving position and the place where the reflected signal is formed; $L = (h_1 + h_2) \cdot tg\varphi$ is the sum of distances L_1 и L_2; $D_0 = \sqrt{(h_1 - h_2)^2 + L^2}$ is the path that the direct wave travels. In sum, $D_1 = \sqrt{h_1^2 + L_1^2}$ and $D_2 = \sqrt{h_2^2 + L_2^2}$ are the path traveled by the reflected wave.

The instantaneous value of the direct wave amplitude at the moment t has the form presented in Equation 4,

$$U_0 = A \cdot e^{-j\omega t} \cdot e^{-j\frac{2\pi}{\lambda}D_0} \qquad [4]$$

Here, A is the electric field strength; $\omega = 2\pi f$ is the cyclic signal frequency and λ wavelength.

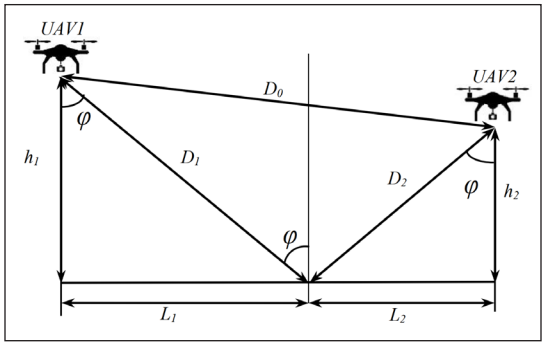

Figure 2. Conditions for the formation of the interference wave

The instantaneous value of the reflected wave amplitude at the moment t is determined by Equation 5:

$$U_1 = A \cdot \dot{R} \cdot e^{-j\omega t} \cdot e^{-j\frac{2\pi}{\lambda}\left(\sqrt{h_1^2+L_1^2}+\sqrt{h_2^2+L_2^2}\right)}. \quad [5]$$

Considering Equations 4 and 5, the total signal $U_\Sigma = U_0 + U_1$ will be as stated in Equation 6:

$$U_\Sigma = A \cdot e^{-j\omega t}\left(e^{-j\frac{2\pi}{\lambda}D_0} + \dot{R} \cdot e^{-j\frac{2\pi}{\lambda}(D_1+D_2)}\right). \quad [6]$$

Considering the substitution $\dot{K} = A \cdot e^{-j\omega t}$, Equation 6 can be written as Equation 7:

$$\dot{U}_Z = \dot{K} \cdot \left(e^{-j\frac{2\pi}{\lambda}D_0} + \dot{R} \cdot e^{-j\frac{2\pi}{\lambda}(D_1+D_2)}\right). \quad [7]$$

The reflection coefficient R˙ for a lossy dielectric such as wet soil will have a complex character and different formulas for calculating vertical and horizontal polarization. Substituting the formula for calculating the reflection coefficient for horizontal polarization into Equation 7, we obtain the expression for the total wave presented in Equation 8:

$$\dot{U}_{ZH} = \dot{K} \cdot \left[\left\{cos\left(\frac{2\pi}{\lambda} \cdot D_0\right) - j \cdot sin\left(\frac{2\pi}{\lambda} \cdot D_0\right)\right\} + \frac{\dot{Z}_{C2} \cdot cos\,\phi - \dot{Z}_{C1} \cdot cos\,\varphi}{\dot{Z}_{C2} \cdot cos\,\phi + \dot{Z}_{C1} \cdot cos\,\varphi} \cdot \left\{cos\left(\frac{2\pi}{\lambda} \cdot (D_1 + D_2)\right) - j \cdot sin\left(\frac{2\pi}{\lambda} \cdot (D_1 + D_2)\right)\right\}\right]. \quad [8]$$

For vertical polarization, Equation 7 will be as follows, presented as Equation 9:

$$\dot{U}_{ZV} = \dot{K} \cdot \left[\left\{cos\left(\frac{2\pi}{\lambda} \cdot D_0\right) - j \cdot sin\left(\frac{2\pi}{\lambda} \cdot D_0\right)\right\} + \frac{\dot{Z}_{C2} \cdot cos\,\varphi - \dot{Z}_{C1} \cdot cos\,\phi}{\dot{Z}_{C2} \cdot cos\,\varphi + \dot{Z}_{C1} \cdot cos\,\phi} \cdot \left\{cos\left(\frac{2\pi}{\lambda} \cdot (D_1 + D_2)\right) - j \cdot sin\left(\frac{2\pi}{\lambda} \cdot (D_1 + D_2)\right)\right\}\right]. \quad [9]$$

Dependence of the electric field strength at a distance r [km] from the transmitter, taking into account the transmitting antenna gain G_1 and the transmitter power P_1 [kW] (Equation 10).

$$A = \frac{173 \cdot \sqrt{P_1 \cdot G_1}}{r}, \text{ [mV/m]}. \quad [10]$$

The results of modeling Equations 8 to 10 in the MathLab environment are shown in Figures 3(a) and 3(b). The reflection coefficient's dependences on the incidence angle for vertical and horizontal polarization used in the simulation correspond to Figure 1(a).

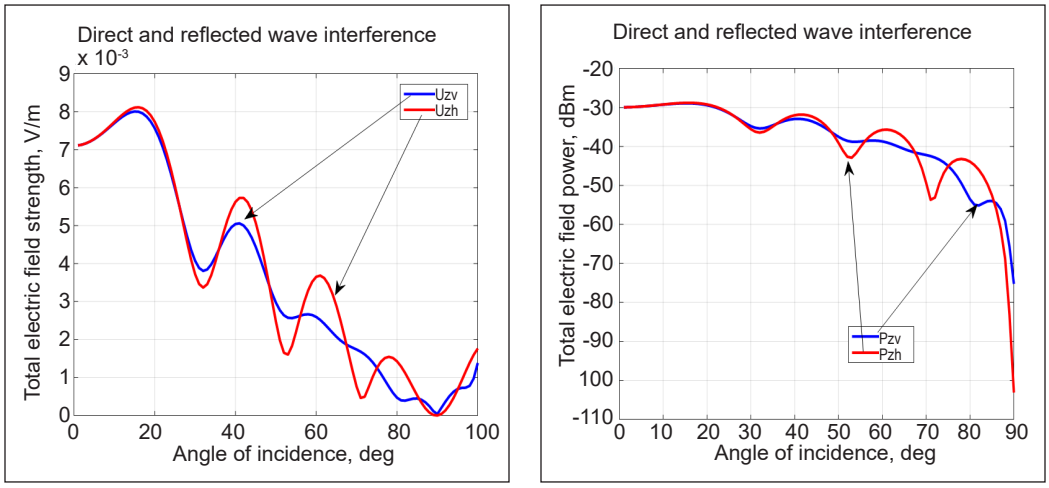

(a) (b)

Figure 3. The results of modeling the interference of the incident and reflected waves: (a) field strength, V/m; (b) total electric field power, dBm

Analysis of the simulation results presented in Figure 3 allows drawing the following conclusions:

- The condition of total refraction (Brewster's effect) is accompanied by a change in the nature of the oscillations: at an angle of the incident (and reflected) signal smaller than Brewster's angle, the horizontally and vertically polarized waves arriving at the receiver are in-phase, and at a larger angle, a phase shift is observed between them;
- the level of the signal that enters the receiver at an angle of the incident (and reflected) signal greater than Brewster's angle, and represents the result of the passage of an electromagnetic wave below the air-surface interface, is sufficient for subsequent processing and analysis of the soil physical and chemical parameters;
- comparison of the oscillations of the total signal on vertical and horizontal polarization can serve as the basis for the algorithm of the joint flight of two UAVs that make up a bistatic radar system for remote soil sensing, which ensures the manifestation of the total refraction effect.

Figure 4 shows the conditions for implementing the flight algorithm (Figure 5) in determining Brewster's angle. Initial position: UAVs are at the same height at a distance of d_0, which ensures safe piloting

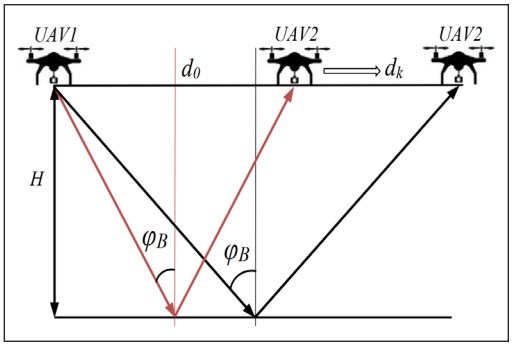

Figure 4. The UAVs' position while determining Brewster's angle

and the lowest possible value of Brewster's angle. The radio transmitter on the UAV1 irradiates the earth's surface with a radar signal with alternating horizontal and vertical polarization. The radio receiver located on the UAV2 receives the signal reflected from the earth's surface and fixes the level of the total reflected signal, changing the type of polarization of the received signal synchronously with the transmitting position.

UAV2 starts horizontal movement in the selected direction with zero roll and pitch angles. As UAV2 moves away from UAV1, the angle of incidence increases. The change in the level of the reflected signal is recorded in the radio receiver, and sequences of measured values of interference wave oscillations are formed in each polarization variant. The angle at which the oscillations of a vertically polarized wave shift in phase relative to the oscillations of a horizontally polarized wave is fixed as the required Brewster's angle. All algorithm steps (Figure 5) can be repeated to increase the reliability of the result.

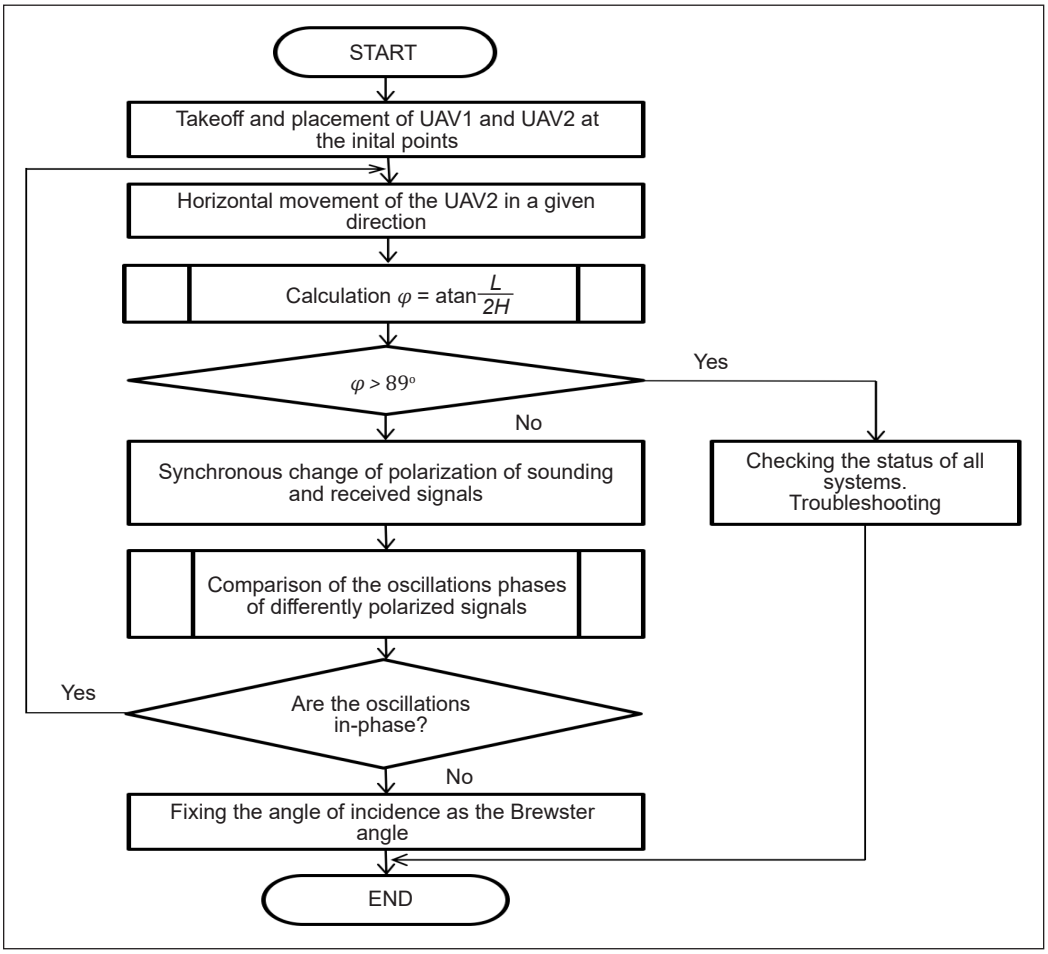

Figure 5. Algorithm for the joint flight of the two UAVs' bistatic radar system for remote soil sensing, which ensures the detection of the effect of total refraction

The termination condition of the algorithm is the opposite of the condition for the applicability of the Vvedensky formula presented in Equation 11 when the effect of interference of the direct and reflected waves can be neglected:

$$L < \frac{18 \cdot h_1 \cdot h_2}{\lambda}. \quad [11]$$

The implementation of the proposed algorithm puts forward requirements for the implementational accuracy of the following tasks:

- the implementation of a horizontal flight of a UAV with a receiver in a given direction;
- stationary hovering of a UAV with a transmitter at the same height as the moving UAV;
- determining the distance between UAVs;
- determination of the distance from each UAV to the place of radio signal reflection from the earth's surface;
- determination of the flight altitude of each UAV.

Both UAVs have GPS/GLONASS navigation systems to solve the navigation task. Typically, the GPS signal accuracy of satellite navigation systems in horizontal dimensions is approximately 1–2 meters (assuming good sky visibility). Altitude accuracy (over the sea) is usually 2–5 times less than positioning accuracy under the same conditions (i.e., from 2 to 10 meters under perfect conditions). Since the distance between UAVs is less than 100 meters, the reason for positioning errors for both UAVs will be the same, and errors will be compensated while determining their relative position.

The required accuracy of calculating the angular values is 1 degree, which is ensured even with positioning errors of 2–3 meters.

Analysis of the mathematical equations required for algorithm implementation showed that the computational complexity for these algorithms is low and can be implemented by an on-board RISC microcontroller with a clock frequency of 120 Mhz and a memory capacity of 128 KB, in addition to the execution of existing flight control algorithms.

RESULTS AND DISCUSSION

Experimental studies were conducted to validate the efficiency of the proposed algorithm.

Experimental design includes:

- a transmitting Yagi antenna, permanently located at the height of 5.6 m, designed for the decimeter range of the television signal;
- a spike antenna placed on a freely movable base at the height of 1.2 m;
- a Kenwood TK-450S transmitter tuned to a 469 MHz frequency, free from other radio transmitting devices operating in the experiment area;

- the analyzer of radio engineering paths and signals, portable S362E from Anritsu Company;
- TDR 150 moisture meter to measure humidity and conductivity at the radio signal reflection spot;
- a transmitting antenna turntable that allows setting the incidence angle in increments of 5 degrees.

The vegetation and surface relief at the test site ensured the Raleigh requirement to implement specular reflection. The soil dispersion under the entire experiment conditions remained unchanged. The general scheme of the experiment was similar to the scheme shown in Figure 2. Equation 11 was provided for the range of spatial relationships of the UAVs.

A series of two experiments were conducted. During the first experiment, the measured specific conductivity was σ=0.017 S/m, soil moisture vwc= 19.9%, Brewster's angle calculated value φ_B =66°C, and the reflection coefficient R_V=0.023. The results of the experiment are presented in Figure 6(a).

During the second experiment, the specific conductivity was σ=0.06 S/m, soil moisture vwc=34%, the calculated value of Brewster's angle φ_B= 67°C, and the reflection coefficient value R_V=0.089. The results of the experiment are shown in Figure 6(b).

The results of experimental studies show that at an angle of incidence greater than the value of Brewster's angle, a phase shift is formed between the oscillations of interference waves with vertical and horizontal polarizations. At higher humidity, an increase in the reflection coefficient is observed, resulting in a significant increase in the amplitude of the interference waves. An increase in soil conductivity by a factor of 3.5 (from 0.017 to 0.06 cm/m) provided an increase in Brewster's angle by only one degree, but at the same time, the minimum value of the reflection coefficient increased from 0.023 to 0.089. The

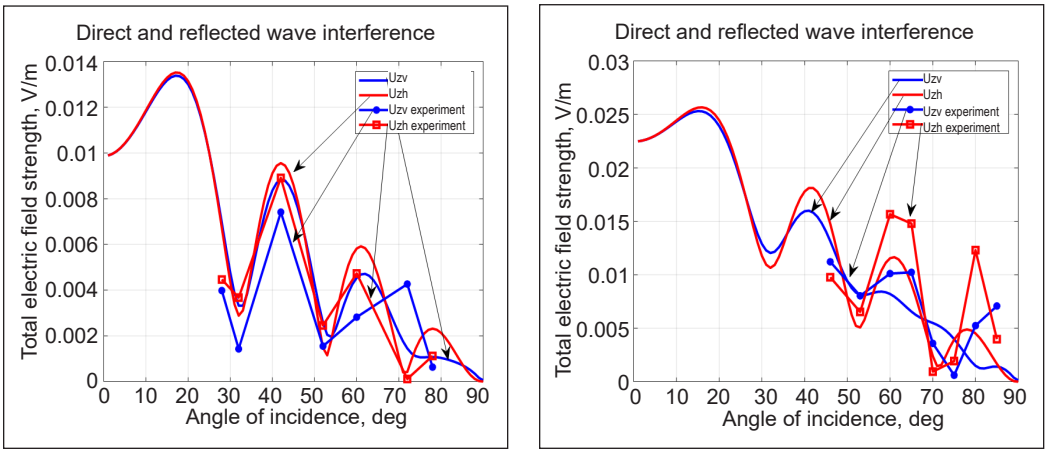

(a) (b)

Figure 6. Results of the experiment: (a) soil specific conductivity 0.017 S/m, soil moisture 19.9%; (b) soil specific conductivity 0.06 S/m, soil moisture 34%

experimental data are in good agreement with the simulation results. At the extremum points, the relative arrangement of the amplitudes of the interference waves of horizontal and vertical polarization obtained experimentally and by the method of mathematical modeling coincides. Some deviations of the experimental data from the calculated ones may be due to the representation of the relief when modeling a smooth surface, and in the experiment, there was vegetation and minor irregularities (with the Rayleigh constraints for specular reflection). Mathematical modeling and experimental studies confirmed the possibility of using the emerging phase shift in the oscillations of interference waves with horizontal and vertical polarization as a sign of transition through the incidence angle with the effect of total refraction. The level of the reflected signal at vertical polarization is formed considering the physicochemical parameters of the soil subsurface layers. A proportional increase in the signal level is observed with an increase in soil conductivity due to an increase in its moisture.

The obtained experimentally confirmed method of measuring Brewster's angle by comparing the oscillations of horizontally and vertically polarized interference waves makes it possible, under conditions of a priori uncertainty in the soil physical and chemical parameters, to create conditions for subsurface radar sounding.

Determination of Brewster's angle allows calculating the dielectric constant of topsoil and estimating the moisture percentage by its change over a certain observation period.

Using "skew" irradiation of soil at an incidence angle close to Brewster's angle creates conditions for spreading the refracted radio signal in a depth of several meters and can be used for determining the groundwater level and estimating the moisture percentage accumulated during the autumn-winter period. Based on this information, reasonable agricultural decisions can be made for efficient crop production.

The next steps in creating a georadar based on a bistatic system of two UAVs are the justification of the receiving and transmitting antennas' designs, the choice of the probing signal's modulation type, and the formation of requirements for the controller of the receiving equipment. The authors associate the most likely direction in receiving equipment with SDR technology.

CONCLUSION

An algorithm for the joint flight of two crewless aerial vehicles that make up a bistatic radar system for remote sensing of the soil is proposed. Under conditions of absence regarding the soil's physical and chemical parameters, this algorithm makes it possible to determine Brewster's angle at which the subsurface soil layers contribute to the reflected signal.

The proposed algorithm provides conditions under which the reflection from the air-soil interface is minimized and allows for solving various problems: to assess soil moisture in the root zone, determine the groundwater level and find extensive inhomogeneities.

The level of oscillations of interferential waves and their mutual phase shift can serve as information markers for assessing the soil's physical and chemical parameters below the air-soil boundary, including moisture.

ACKNOWLEDGMENT

The study was conducted as part of implementing the "Priority 2030" strategic program of academic leadership with the financial support of the Ministry of Education and Science of Russia (Agreement No. 075-15-2021-1319).

REFERENCES

Amazirh, A., Merlin, O., Er-Raki, S., Gao, Q., Rivalland, V., Malbeteau, Y., Khabba, S., & Escorihuela, M. J. (2018). Retrieving surface soil moisture at high spatio-temporal resolution from a synergy between Sentinel-1 radar and Landsat thermal data: A study case over bare soil. *Remote Sensing of Environment*, *211*, 321-337. https://doi.org/10.1016/j.rse.2018.04.013

Babaeian, E., Paheding, S., Siddique, N., Devabhaktuni, V. K., & Tuller, M. (2021). Estimation of root zone soil moisture from ground and remotely sensed soil information with multisensor data fusion and automated machine learning. *Remote Sensing of Environment*, *260*, Article 112434. https://doi.org/10.1016/j.rse.2021.112434

Bandini, F., Sunding, T. P., Linde, J., Smith, O., Jensen, I. K., Köppl, C. J., Butts, M., & Bauer-Gottwein, P. (2020). Unmanned Aerial System (UAS) observations of water surface elevation in a small stream: Comparison of radar altimetry, LIDAR and photogrammetry techniques. *Remote Sensing of Environment*, *237*, Article 111487. https://doi.org/10.1016/j.rse.2019.111487

Barca, E., De Benedetto, D., & Stellacci, A. M. (2019). Contribution of EMI and GPR proximal sensing data in soil water content assessment by using linear mixed effects models and geostatistical approaches. *Geoderma*, *343*, 280-293. https://doi.org/10.1016/j.geoderma.2019.01.030

Bargiel, D., Herrmann, S., & Jadczyszyn, J. (2013). Using high-resolution radar images to determine vegetation cover for soil erosion assessments. *Journal of Environmental Management*, *124,* 82-90. https://doi.org/10.1016/j.jenvman.2013.03.049

Bazhenov, A., Sagdeev, K., Goncharov, D., & Grivennaya, N. (2021). Bistatic system for radar sensing of soil moisture. *International Scientific Conference Engineering for Rural Development (ERDev)*, *Jelgava, Latvia, 2021*, 919-925. https://doi.org/10.22616/ERDev.2021.20.TF207

Bhogapurapu, N., Dey, S., Homayouni, S., Bhattacharya, A., & Rao, Y.S. (2022). Field-scale soil moisture estimation using sentinel-1 GRD SAR data. *Advances in Space Research*, *70*(12), 3845-3858. https://doi.org/10.1016/j.asr.2022.03.019

Brook, A., De Micco, V., Battipaglia, G., Erbaggio, A., Ludeno, G., Catapano, I., & Bonfante, A. (2020). A smart multiple spatial and temporal resolution system to support precision agriculture from satellite images: Proof of concept on Aglianico vineyard. *Remote Sensing of Environment*, *240*, Article 111679, https://doi.org/10.1016/j.rse.2020.111679

Chandra, M., & Tanzi, T. J. (2018). Drone-borne GPR design: Propagation issues. *Comptes Rendus Physique*, *19*(1-2), 72-84. https://doi.org/10.1016/j.crhy.2018.01.002

Dari, J., Quintana-Seguí, P., Escorihuela, M. J., Stefan, V., Brocca, L., & Morbidelli, R., (2021). Detecting and mapping irrigated areas in a Mediterranean environment by using remote sensing soil moisture and a land surface model. *Journal of Hydrology*, *596*, Article 126129. https://doi.org/10.1016/j.jhydrol.2021.126129

Elkharrouba, E., Sekertekin, A., Fathi, J., Tounsi, Y., Bioud, H., & Nassim, A. (2022). Surface soil moisture estimation using dual-Polarimetric Stokes parameters and backscattering coefficient. *Remote Sensing Applications: Society and Environment*, *26*, Article 100737. https://doi.org/10.1016/j.rsase.2022.100737

Faye, G., Frison, P. L., Diouf, A. A., Wade, S., Kane, C. A., Fussi, F., Jarlan, L., Niang, M. F. K., Ndione, J. A., Rudant, J. P., & Mougin, E. (2018). Soil moisture estimation in Ferlo region (Senegal) using radar (ENVISAT/ASAR) and optical (SPOT/VEGETATION) data. *The Egyptian Journal of Remote Sensing and Space Science*, *21*(Supplement 1), 13-22. https://doi.org/10.1016/j.ejrs.2017.11.005

Filion, R., Bernier, M., Paniconi, C., Chokmani, K., Melis, M., Soddu, A., Talazac, M., & Lafortune, F.-X. (2016). Remote sensing for mapping soil moisture and drainage potential in semi-arid regions: Applications to the Campidano plain of Sardinia, Italy. *Science of the Total Environment, 543*(Part B), 862-876. https://doi.org/10.1016/j.scitotenv.2015.07.068

Fugazza, D. G., Aletti, Bertoni, D., & Cavicchioli, D. (2022). Farmland use data and remote sensing for ex-post assessment of CAP environmental performances: An application to soil quality dynamics in Lombardy, *Remote Sensing Applications: Society and Environment*, *26*, Article 100723. https://doi.org/10.1016/j.rsase.2022.100723

Gago, J., Douthe, C., Coopman, R.E., Gallego, P.P., Ribas-Carbo, M., Flexas, J., Escalona, J., & Medrano, H. (2015). UAVs challenge to assess water stress for sustainable agriculture. *Agricultural Water Management*, *153*, 9-19. https://doi.org/10.1016/j.agwat.2015.01.020

Gopaiah, M., Saha, R., Das, I. C., Sankar, G. J., & Kumar, K. V. (2021). Quantitative assessment of aquifer potential in near shore coastal region using geospatial techniques and ground penetrating radar, *Estuarine, Coastal and Shelf Science*, *262*, Article 107590. https://doi.org/10.1016/j.ecss.2021.107590

Ivushkin, K., Bartholomeus, H., Bregt, A. K., Pulatov, A., Franceschini, M. H. D., Kramer, H., van Loo, E. N., Jaramillo Roman, V. J., & Finkers, R. (2019). UAV based soil salinity assessment of cropland. *Geoderma, 338*, 502-512. https://doi.org/10.1016/j.geoderma.2018.09.046

Kaasiku, T., Praks, J., Jakobson, K., & Rannap, R. (2021). Radar remote sensing as a novel tool to assess the performance of an agri-environment scheme in coastal grasslands. *Basic and Applied Ecology*, *56*, 464-475. https://doi.org/10.1016/j.baae.2021.07.002

Kim, J. Y. (2021). Software design for image mapping and analytics for high throughput phenotyping. *Computers and Electronics in Agriculture*, *191*, Article 106550. https://doi.org/10.1016/j.compag.2021.106550

Li, Z. L., Leng, P., Zhou, C., Chen, K. S., Zhou, F. C. & Shang, G. F. (2021). Soil moisture retrieval from remote sensing measurements: Current knowledge and directions for the future. *Earth-Science Reviews*, *218*, Article 103673. https://doi.org/10.1016/j.earscirev.2021.103673

Ludeno, G., Catapano, I., Renga, A., Vetrella, A.R., Fasano, G., & Soldovieri, F. (2018). Assessment of a micro-UAV system for microwave tomography radar imaging. *Remote Sensing of Environment*, *212*, 90-102. https://doi.org/10.1016/j.rse.2018.04.040

Mallet, F., Marc, V., Douvinet, J., Rossello, P., Joly, D., & Ruy, S. (2020). Assessing soil water content variation in a small mountainous catchment over different time scales and land covers using geographical variables. *Journal of Hydrology*, *591*, Article 125593. https://doi.org/10.1016/j.jhydrol.2020.125593

Mandal, D., Kumar, V., Ratha, D., Dey, S., Bhattacharya, A., Lopez-Sanchez, J. M., McNairn, H., & Rao, Y. S. (2020). Dual polarimetric radar vegetation index for crop growth monitoring using sentinel-1 SAR data. *Remote Sensing of Environment*, *247*, Article 111954. https://doi.org/10.1016/j.rse.2020.111954

Martins, R. N., Portes, M. F., Fialho e Moraes, H. M., F. Junior, M. R., Fim Rosas, J. T., & Orlando Junior, W. A. (2021). Influence of tillage systems on soil physical properties, spectral response and yield of the bean crop. *Remote Sensing Applications: Society and Environment*, *22*, Article 100517, https://doi.org/10.1016/j.rsase.2021.100517

Nguyen, T. T., Ngo, H. H., Guo, W., Chang, S. W., Nguyen, D. D., Nguyen, C. T., Zhang, J., Liang, S., Bui, X. T., & Hoang, N. B. (2022). A low-cost approach for soil moisture prediction using multi-sensor data and machine learning algorithm. *Science of the Total Environment*, *833*, Article 155066. https://doi.org/10.1016/j.scitotenv.2022.155066

Pandey, A., & Jain, K. (2022) An intelligent system for crop identification and classification from UAV images using conjugated dense convolutional neural network. *Computers and Electronics in Agriculture*, *192*, Article 106543.https://doi.org/10.1016/j.compag.2021.106543

Rohil, M. K., & Mathur, S. (2022). CYGNSS-derived soil moisture: Status, challenges and future. *Ecological Informatics*, *69*, Article 101621. https://doi.org/10.1016/j.ecoinf.2022.101621

Rouf, T., Girotto, M., Houser, P., & Maggioni, V. (2021) Assimilating satellite-based soil moisture observations in a land surface model: The effect of spatial resolution. *Journal of Hydrology*, *13*, Article 100105. https://doi.org/10.1016/j.hydroa.2021.100105

Saddik, A., Latif, R., Elhoseny, M., & El Ouardi, A. (2021). Real-time evaluation of different indexes in precision agriculture using a heterogeneous embedded system. *Sustainable Computing: Informatics and Systems*, *30*, Article 100506. https://doi.org/10.1016/j.suscom.2020.100506

Sahaar, S. A., Niemann, J. D., & Elhaddad, A. (2022). Using regional characteristics to improve uncalibrated estimation of rootzone soil moisture from optical/thermal remote-sensing. *Remote Sensing of Environment*, *273*, Article 112982. https://doi.org/10.1016/j.rse.2022.112982

Salam, A., Vuran, M.C., & Irmak, S. (2019). Di-Sense: In situ real-time permittivity estimation and soil moisture sensing using wireless underground communications. *Computer Networks*, *151*, 31-41. https://doi.org/10.1016/j.comnet.2019.01.001

Su, C. H., Ryu, D., Crow, W. T., & Western, A. W. (2014). Stand-alone error characterisation of microwave satellite soil moisture using a Fourier method. *Remote Sensing of Environment*, *154*, 115-126. https://doi.org/10.1016/j.rse.2014.08.014

Tavakol, A., McDonough, K. R., Rahmani, V., Hutchinson, S. L., & Hutchinson, J. M. S. (2021). The soil moisture data bank: The ground-based, model-based, and satellite-based soil moisture data.

Remote Sensing Applications: Society and Environment, *24*, Article 100649. https://doi.org/10.1016/j.rsase.2021.100649

Tran, A. P., Bogaert, P., Wiaux, F., Vanclooster, M., & Lambot, S. (2015). High-resolution space–time quantification of soil moisture along a hillslope using joint analysis of ground penetrating radar and frequency domain reflectometry data. *Journal of Hydrology*, *523*, 252-261. https://doi.org/10.1016/j.jhydrol.2015.01.065

Wang, H., Magagi, R., Goïta, K., Colliander, A., Jackson, T., McNairn, H., & Powers, J. (2021). Soil moisture retrieval over a site of intensive agricultural production using airborne radiometer data. *International Journal of Applied Earth Observation and Geoinformation*, *97*, Article 102287. https://doi.org/10.1016/j.jag.2020.102287

Wang, S., Zhang, K., Chao, L., Li, D., Tian, X., Bao, H., Chen, G., & Xia, Y. (2021). Exploring the utility of radar and satellite-sensed precipitation and their dynamic bias correction for integrated prediction of flood and landslide hazards. *Journal of Hydrology*, *603*, Article 126964, https://doi.org/10.1016/j.jhydrol.2021.126964

Xie, F., Lai, W.W. L., & Dérobert, X. (2022). Building simplified uncertainty models of object depth measurement by ground penetrating radar. *Tunnelling and Underground Space Technology*, *123*, Article 104402. https://doi.org/10.1016/j.tust.2022.104402

Yang, H., Xiong, L., Liu, D., Cheng, L., & Chen, J. (2021). High spatial resolution simulation of profile soil moisture by assimilating multi-source remote-sensed information into a distributed hydrological model. *Journal of Hydrology*, *597*, Article 126311. https://doi.org/10.1016/j.jhydrol.2021.126311

Zhu, L., Walker, J. P., Tsang, L., Huang, H., Ye, N., & Rüdiger, C. (2019). Soil moisture retrieval from time series multi-angular radar data using a dry down constraint. *Remote Sensing of Environment*, *231*, Article 111237. https://doi.org/10.1016/j.rse.2019.111237

Pertanika J. Sci. & Technol. 31 (4): 2047 - 2066 (2023)

PERTANIKA JOURNALS

SCIENCE & TECHNOLOGY

Journal homepage: http://www.pertanika.upm.edu.my/

The Effect of Different Precursor Solutions on the Structural, Morphological, and Optical Properties of Nickel Oxide as an Efficient Hole Transport Layer for Perovskite Solar Cells

Subathra Muniandy[1]*, Muhammad Idzdihar Idris[1], Zul Atfyi Fauzan Mohammed Napiah[1], Nurbahirah Norddin[1], Marzaini Rashid[2], Ahmad Wafi Mahmood Zuhdi[3] and Luke Bradley[4]

[1]Faculty of Electronics and Computer Engineering, University Technical Malaysia Melaka, 75450 UTeM, Melaka, Malaysia
[2]School of Physics, University Science Malaysia, 11800 USM, Penang, Malaysia
[3]Department of Electrical & Electronic Engineering, Universiti Tenaga Nasional, 43000 UNITEN, Selangor, Malaysia
[4]School of Engineering, Newcastle University, England

ABSTRACT

Perovskite solar cell (PSC) technologies have recently become a popular research topic. The hole transport layers (HTL) are important in establishing stable and efficient PSC by regulating charge absorption, interlayer recombination losses, and band alignment. Spiro-OMeTAD was extensively used as the HTL to fabricate highly efficient PSCs. Despite Spiro-OMeTAD having the benefit of providing high PCEs, it is costly, hazardous to the ecology, and cannot provide high efficiencies in the lack of additional additives that can reduce their stabilities. Inorganic HTL, specifically nickel oxide (NiO), has garnered much interest due to its low-cost, enhanced mobility, and strong stability to attain high efficiency. This study investigated different precursor solutions of NiO synthesis (Method I, II, and III) and deposited using the spin coating approach. The films were annealed at different annealing temperatures (400°C, 550°C, and 700°C) and evaluated by X-ray powder diffraction (XRD), UV-Vis spectroscopy, and Scanning electron microscopy (SEM) to test their structural, morphological, and optical characteristics, respectively. The findings of XRD revealed that a higher annealing temperature increases

ARTICLE INFO

Article history:
Received: 22 July 2022
Accepted: 02 November 2022
Published: 13 June 2023

DOI: https://doi.org/10.47836/pjst.31.4.26

E-mail addresses:
m022020016@student.utem.edu.my (Subathra Muniandy)
idzdihar@utem.edu.my (Muhammad Idzdihar Bin Idris)
zulatfyi@utem.edu.my (Zul Atfyi Fauzan Bin Mohammed Napiah)
nurbahirah@utem.edu.my (Nurbahirah Binti Norddin)
marzaini@usm.my (Marzaini Rashid)
wafi@uniten.edu.my (Ahmad Wafi Bin Mahmood Zuhdi)
luke.bradley@newcastle.ac.uk (Luke Bradley)
* Corresponding author

ISSN: 0128-7680
e-ISSN: 2231-8526

the crystallite size and decreases the microstrain through the study from Scherrer's and Williamson-Hall's (WH) equations. From the SEM analysis, the films show uniformity, large crystals, and agglomeration of particles. The annealing temperature from 400°C to 700°C reduced bandgap energy from 3.6 eV to 2.1 eV. According to the result, NiO produced at an annealing temperature of 700°C (Method I) exhibited the best characteristics and might be a viable option for HTL in PSCs.

Keywords: Hole transport material, nickel oxide, perovskite solar cells, spin coating

INTRODUCTION

Solar energy is one of the renewable sources that can support the world's increasing energy demand and address the emerging energy crisis caused by the depletion of fossil fuels. In comparison with nuclear technology, the worldwide spreading of sunshine (unlike the wind, geothermal, or hydropower sources in particular regions) and the lack of dangerous waste creation, and the decentralization of energy generation are the major advantages over many other renewable energy sources (Mohammadian-Sarcheshmeh et al., 2020), (Du John H et al., 2020). Photovoltaic solar cells function by transforming energy into electrical energy from incoming photons. Numerous photovoltaic approaches have been developed in three generations (Younas et al., 2019). Regarding the various 3G solar cell technologies research, perovskite solar cells (PSCs) are now the technology that develops most fast (Abbas et al., 2020; Gil et al., 2019; Ibn-Mohammed et al., 2017; Nkele et al., 2020). Recently, PSCs have globally pushed conventional solar cell methods for resolving global energy production, safety, and environmental issues as a cost-effective (Haider et al., 2019) and environmentally feasible renewable technology choice (Ebhota & Jen, 2020; Mariotti et al., 2020; Roy et al., 2020; Wilson et al., 2020). Ever since this finding, PSCs have been researched intensively for the last five years with their distinctive features like large absorption coefficients, open-circuit voltage (V_{OC}) (Wang et al., 2017), and long load carrier (electron-hole) diffusion length (Wang et al., 2019). Perovskite absorbers are also desirable because they are simple to solution-process at low temperatures with low-cost chemicals and do not rely on components in limited supplies, unbalanced solvents like hydrazine, or high-temperature processing (Pitaro et al., 2022; Yang et al., 2020)

PSCs are typically made up of charge transport layers called electron transport layers (ETL) and hole transporting layers (HTL) that interface with the perovskite material for efficient and selective charge absorption(Łuszczek et al., 2021) (Yin et al., 2019). Detailed attention was paid to the HTL layer concerning the PSC design. The materials used for HTL have a major influence on the performance of PSCs. One of the most popular HTLs in PSCs was Spiro-OMeTAD. As a result, the impedance and the interfacial recombine loss in PSCs are minimized, enabling to improve of PSCs' fill factor (FF) and open-circuit

voltage (V_{OC}), apart from efficiency in the transmission of holes to the counter electrode (Gil et al., 2019). Even though PSCs based on Spiro-OMeTAD have better power conversion efficiencies (PCEs), high costs for Spiro-OMeTAD remain important barriers in marketing PSCs owing to the extensive and poor productivity synthetic methodology (Shariatinia, 2020). To enhance the innate conductibility and hole mobility of Spiro-OMeTAD (Wang et al., 2017), which also raises the manufacturing cost of PSCs containing Spiro-OMeTAD, ionic addition products like bis(trifluoromethane) sulfonamide lithium salt (Li-TFSI) and 4-tert-butyl pyridine (TBP) and co-doping are also to be added. Due to their inherently high selectivity, high ion charge mobility, and cheap overall cost, some inorganic substances are investigated as HTLs (Hajakbari et al., 2017). In addition, several inorganic hole transport materials (HTM) such as copper thiocyanate (CuSCN), copper iodide (CuI), copper oxide (CuO), cuprous oxide (Cu2O), and nickel oxide (NiO) are studied for PSCs. Inorganic materials, which can be acquired at a considerably lower cost than organic materials, are considered to have a better possibility of becoming a major role in solar cell technology due to the stability of their structures in the face of environmental factors, including humidity, light, and temperature stress.

Although organic HTL materials provide great potential, it can be argued that inorganic materials, with the refinement of their manufacturing methods, have more potential to overcome present impediments in commercialization. Copper-based inorganic semiconducting HTM has demonstrated potential for use in dye- and quantum dot-sensitized solar cells. The solution technique to deposit these materials ensures that the pores are filled, and the resulting broadband gap semiconductors exhibit excellent conductivity, an appropriate energy level, and great transparency (Li et al., 2016). However, structures containing copper-based inorganic materials have demonstrated poor efficiency and stability problems (Nkele et al., 2020). Experts explored how inorganic materials, especially NiO, a p-type HTL, are used in organic solar and dye-sensitized solar cells (DSSC) to overcome this problem. Numerous research institutions have actively studied DSSCs due to their cheap manufacturing cost, non-toxicity, and potential for strong energy conversion efficiencies (Atli et al., 2019; Atli et al., 2018).

For the development of DSSCs, it is important to develop a counter electrode (CE) material with outstanding catalytic activity, inherent stability, and cheap cost (Yildiz et al., 2021). It is because sensitizing a p-type material with broadband content, such as NiO, could help the interfacial charge-carrying behavior of perovskites and is thus vital to forming wide-range device topologies that were noticed since closer exploring into NiO HTL. NiO is recognized as a p-type semiconductor with a broad energy bandgap (3.2 to 4.0 eV) and has considerable promise as a catalyst for replacing Spiro-OMeTAD owing to its outstanding features including cheap cost materials, nontoxicity, physical-chemical stability, and strong iodine-based catalyst function (Gil et al., 2019), [17]. NiO is a substance

that is extremely resistant to thermal and chemical processing and improves the strength of PSCs, among several other inorganic hole transporters. In this study, the influence of NiO was explored in three different methods by synthesizing with varying precursor solutions. The NiO was deposited using a spin-coating procedure and annealed at different annealing temperatures (400°C, 550°C, and 700°C). The resultant films were then examined to study the morphological, structural, and optical characteristics of NiO using Scanning Electron Microscopy (SEM), X-ray diffraction (XRD), and UV–vis spectroscopy, respectively.

HTM is important in collecting holes (positive charges) from the absorber material following excitation and directing such charges toward the active electrode. Since HTMs are anticipated to enhance the functionality of devices, they were developed to substitute the dye in a DSSC and create a solid solar cell (Nkele et al., 2020). In conjunction with better performance and durability, a low-cost manufacturing method with strong heat and humidity resistance is crucial for achieving a marketable dimension. An ideal HTM candidate features inherently high hole mobility, an appropriate energy level, long-term stability in the air, and excellent photochemical and thermal durability. Additionally, it must be solution-processed to create HTL, particularly when used in typical (n-i-p) PSCs. Consideration must also be given to the low cost and simplicity of HTM preparation for manufacture on a large scale and additional commercial applications (Li et al., 2021; Park, 2021).

METHODOLOGY

Material and Preparation

Nickel acetate tetrahydrate (purity, 98%) and diethanolamine (DEA) were bought from the Sigma Aldrich website. Besides that, nickel oxide powder, ethanol (purity, 95%), potassium hydroxide, and isopropyl alcohol (IPA) were purchased from Chemiz (M) Sdn Bhd. Deionized water was used to prepare all aqueous solutions. The substrates of ITO glass and beakers were washed with a detergent one by one and dried in the ultrasound bath with IPA, ethanol, and deionized water to eliminate pollution and strain on the surface. This study synthesized and coated three different precursor solutions (Methods I, II, and III) by spin coating techniques on the ITO glass substrate. The sample of NiO films was then annealed at various temperatures (400°C, 550°C, and 700°C).

Syntheses of NiO (Method I)

0.622 g nickel acetate tetrahydrate was dissolved in ethanol (15 ml) and IPA (10 ml). Afterward, potassium hydroxide (0.56 g), mixed with distilled water (100 mL), was dropped into the solution till the pH of the mixture was attained at level 10, as seen in Figure 1. The solution was then mixed on the hot plate. The resulting solution in greenish color is

refined by rinsing the unreacted chemicals over five times using ethanol. The concentrated solution was then dried and placed in the oven for 1 hr. The resulting powder of NiO was then acquired to continue the coating procedure and characterization.

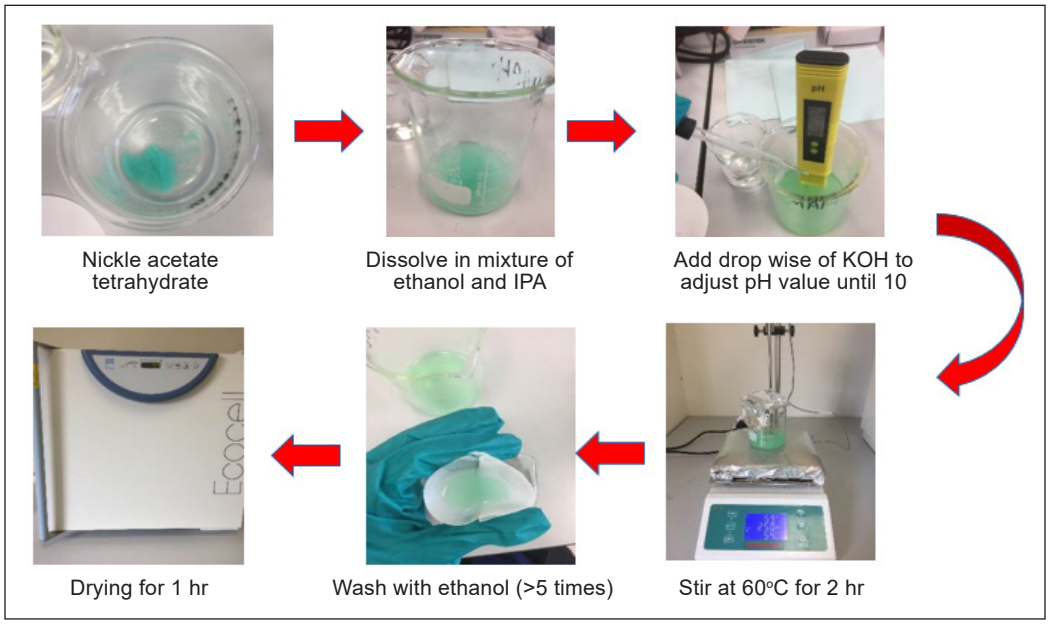

Figure 1. Schematic representation of Method I for synthesizing NiO using nickel acetate tetrahydrate, ethanol, and potassium hydroxide

Synthesis of NiO (Method II)

Nickel acetate tetrahydrate, ethanol, and DEA were employed as solutes, solvents, and stabilizers. First, 0.1 M nickel acetate was mixed in ethanol and agitated for 2 hr to a pure and uniform mixture at 60°C on a hot plate (Figure 2). In the agitation, DEA dropwise was added to the mixture. To avoid aggregation or agglomerations, the function of DEA

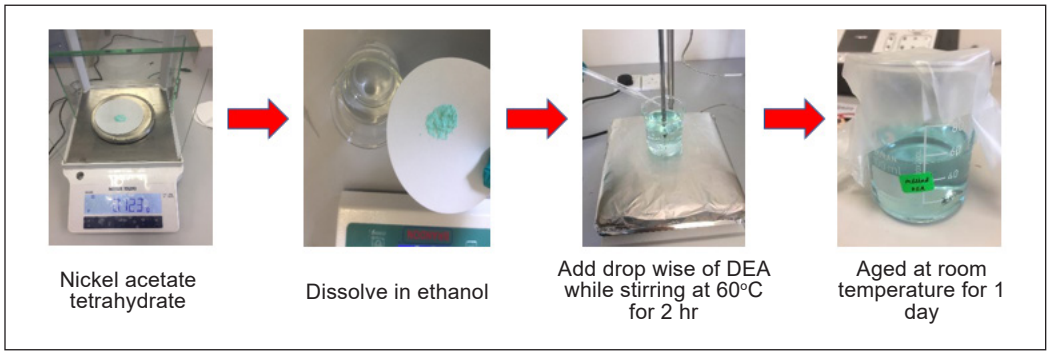

Figure 2. Schematic representation of Method II for the synthesizing NiO nickel acetate tetrahydrate, ethanol, and DEA

works as a stabilizing agent and increases hydrolysis stability. The nickel acetate molar ratio to DEA was maintained at 1:1. The mixture was then stored for a whole day at room temperature to enhance its consistency and transform it into a concentrated solution.

Synthesis of NiO (Method III)

NiO powder purchased from Chemiz was just 40 ml ethanol diluted and sonicated for 15 minutes (min) to maintain that the NiO powder in ethanol was dissolved thoroughly. The NiO was then utilized with the spin coater for the additional coating procedure. The three different synthesis methods of NiO are summarized in Table 1.

Table 1
A comparison between three different methods (I, II, and III)

Method	Precursor
I	Nickel acetate tetrahydrate, ethanol, isopropyl alcohol, potassium hydroxide, and distilled water
II	Nickel acetate tetrahydrate, ethanol, and DEA
III	NiO powder, ethanol

Deposition of Nio Thin Film

Disposing of NiO covered by spin-coating techniques on ITO glass substrates. At 3000 rpm/s acceleration, the NiO produced was treated by a spin-coater for 30 sec. After spins,

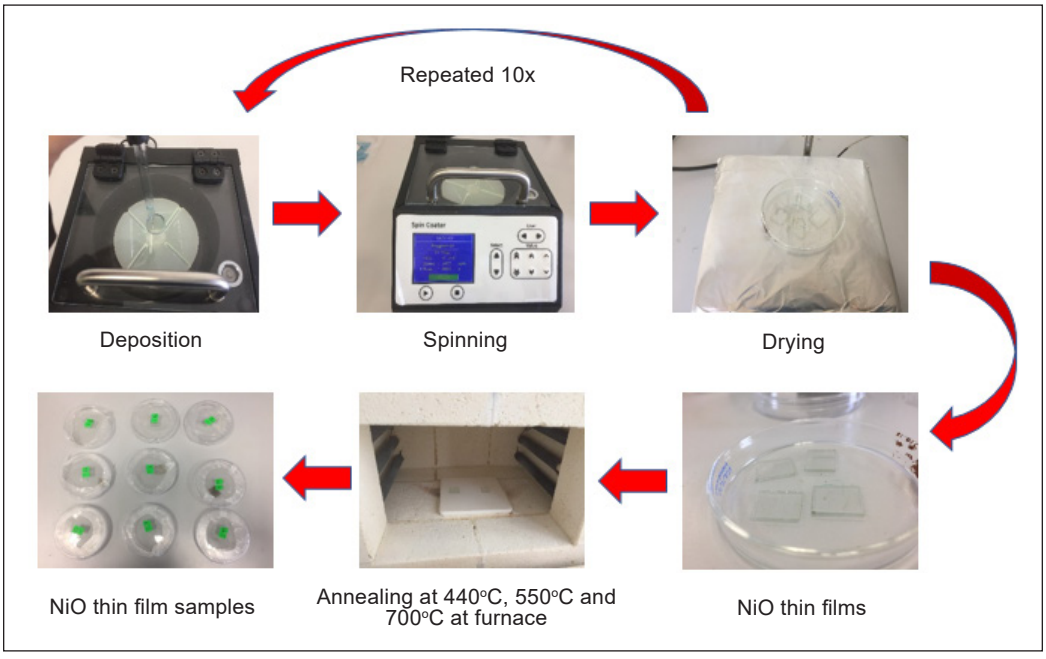

Figure 3. Illustration for deposition of NiO using spin coating technique for every specimen in all the methods (Methods I, II, and III)

organic residues were evaporated on a thermal plate for 15 minutes (min). The coating and drying processes were performed for 10 cycles for every specimen to boost the thickness of the NiO layer. The samples were progressively rinsed in ambient conditions for 400°C, 550°C, and 700°C for 1 h. The thin NiO films were finally obtained, as illustrated in Figure 3. The structural characteristics were defined by X-rays Powder Diffraction (PANalytical system) fitted with Cu Kα (0.154056 nm) scanning, which was supplied by a (θ-2θ) scan of each NiO thin film. A scanning electron microscope (SEM) performed surface morphology. To analyze the morphology of the film, a gold coating was applied to produce a uniform surface for SEM investigation analysis and imaging. The absorbance of the films was measured using a Shimadzu UV-1800 spectrophotometer within the wavelength range of 200 to 900 nm.

RESULT AND DISCUSSION

Structural Analysis

Figure 4(a) shows the XRD pattern of NiO thin films from Method I at three different temperatures. The XRD pattern of the NiO film at 400°C and 550°C only showed two prominent peaks at 37.2° and 79.3°, that is, (1 1 1) and (2 2 2) diffraction of the cubic NiO diffraction planes (ICDD 00-044-1159). The NiO film at 700˚C shows well-defined spread peaks at 37.2°, 43.3°, 68.2°, 75.2° and 79.4° which correspond to (1 1 1), (2 0 0), (2 2 0), (3 1 1), and (2 2 2). No secondary peaks indicated that the Ni was fully oxidized, and no NiO formation by-products were detected (Desissa, 2021; Muniandy et al., 2021). Based on the XRD, the intensity of every diffraction peak increased as the temperature increased, and therefore the peak went sharper from 400°C to 700°C, which is also an equivalent statement made (Guo et al., 2017). It was also in conjunction with the studies of Temesgen D. Desissa (Desissa, 2021), who discovered that temperatures exceeding 700°C (about 900°C) lead to an XRD pattern, which suggested that the interface remains stable with no more phases. Evidently, with the increase in temperature, the strength of all spikes was enhanced. It indicates that NiO films can enhance their crystalline quality by increasing temperature. All NiO films showed the highest intensive diffraction peak and were orientated at (111). Scherrer's equation (Equation 1) was applied to measure the average crystallite size:

$$D = 0.9\lambda / \beta \cos \theta \qquad [1]$$

where D is the crystallite size (nm), λ is the incident wavelength, β is the half-width of the diffraction peak quantified in radians, and θ is the peak location. Increasing the annealing temperature increases the crystallite size value, leading to larger grain morphology. Table 2 summarizes the characteristics, including crystallite size, full width at half maximum

(FWHM), and position angle examines the influence of different annealing temperatures on the structural features of NiO films. The FWHM decreased from 0.3607° to 0.2509°, indicating that the crystal formation of the NiO film is enhanced at rising temperatures, resulting in a crystallite size increase from 23 to 33 nm. It also explains the high degree of ordering and structural improvement of crystallization—in other words, when the intensity is increased, the FWHM is minimal and vice versa (Takko et al., 2021). Throughout this investigation, it is considered that the crystallite size increases as the annealed temperature increases. In order to gain a deeper knowledge of the structural characteristics of the materials, we utilized Williamson-Hall (W-H) analysis. The Williamson-Hall (W-H) equation (Equation 2) was used to figure out the size of the crystallites and the microstrain from the width of the principal XRD peak intensity (Serin et al., 2017; Yildiz et al., 2015):

$$\beta hkl = \left({}^{0.9\lambda}/_{D} \right) + 4\varepsilon \sin\theta \qquad [2]$$

in which D is the crystallite size (nm), λ is the radiation wavelengths (here, CuKα), β_{hkl} is the FWHM of the principal peak intensity, ε refers to the microstrain that is caused to flaws inside the crystalline lattice, and θ is the diffraction angle. Plots of the β cos θ versus 4 sin θ for the preferred orientation peaks of the samples are depicted in Figure 5. The graph displayed a positive strain for the samples as the annealing temperature increased. The findings of the crystallite size derived by the W-H equation are lower than Scherrer's due to peak narrowing induced by micro strain acquired by W-H analysis (Table 2). The findings show that as the annealing temperature rises from 400°C to 700°C, the crystallite size grows, and the microstrain decreases gradually. The smaller value of the microstrain implies that the thin films are more crystalline and have a low number of flaws. It means that annealing the film changes the way the atoms are arranged in the crystal lattice, which minimizes the lattice imperfections and enhances the overall quality of the crystals (Aswathy et al., 2020). The larger crystallite size and reduced microstrain in NiO for the sample annealed at 700°C thin film confirm the enhancement of crystalline quality. A similar observation also made by, Aswathy et al. (2020) obtained an average crystallite size of 19.68 nm with a microstrain of 1.03×10^{-3} at an annealing temperature of 600°C for NiO thin films produced by spin coating deposition techniques. Furthermore, as the temperature rises, the drop in the FWHM of the diffraction peaks leads to a reduction of the slope (c), showing that the strain in the NiO lattice declines progressively (Pagar & Shinde, 2021). The tensile stress in the films at high annealing temperatures tends to cause the microstrain to change with increasing temperature (Jamal et al., 2019).

The XRD results of NiO films using Method II indicated only hollow peaks, as shown in Figure 4(b). No diffraction peaks occurred even after increasing the annealing temperature to 700°C. It indicates that the layer is in an amorphous phase containing a

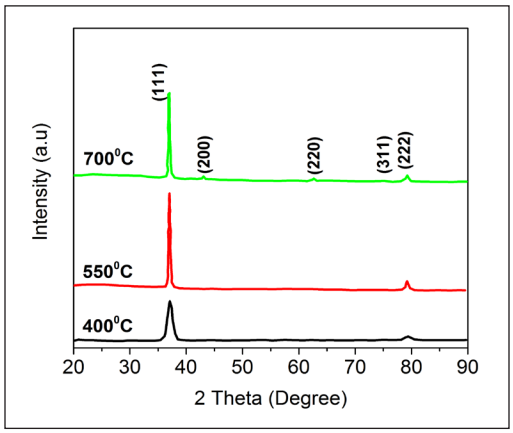

(a)

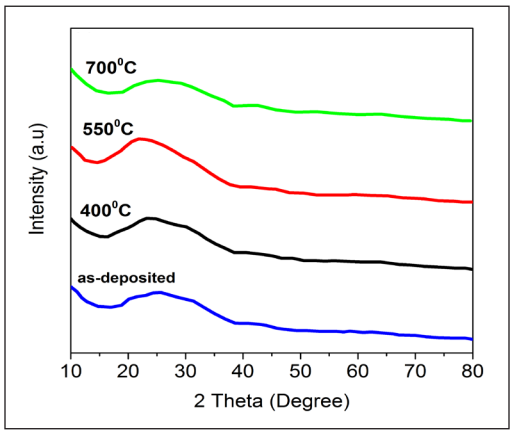

(b)

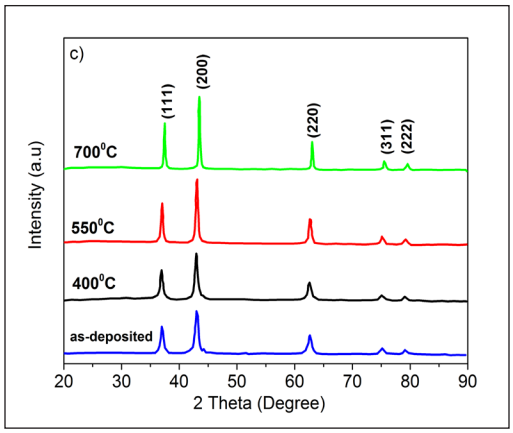

(c)

Figure 4. XRD pattern of NiO thin film by (a) Method I, (b) Method II, and (c) Method III at different annealing temperatures (400°C, 550°C, and 700°C)

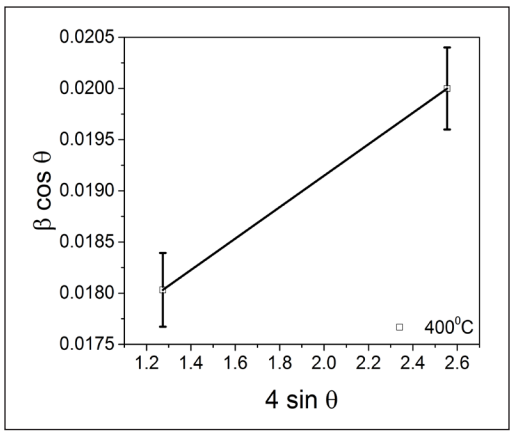

(a)

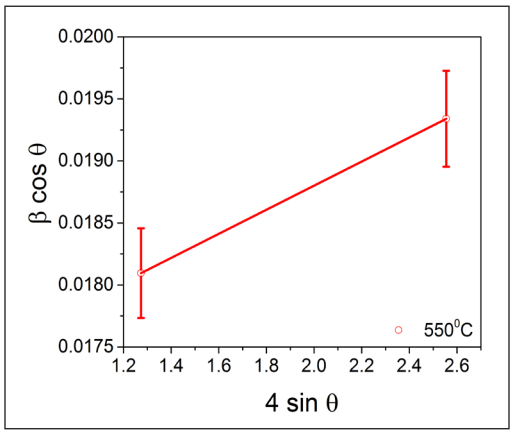

(b)

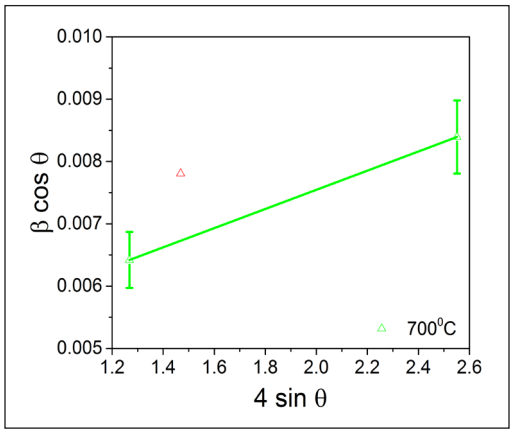

(c)

Figure 5. The WH analysis for the NiO thin film by Method I (a) 400°C, (b) 550°C, and (c) 700°C. Solid lines represent best-fitting lines, while error bars represent standard deviations

Table 2
Structural parameter for (111) plane of the NiO thin film properties by Method I, Method II, and Method III

Annealing Temperature	hkl plane	2 Theta (degree)	FWHM	c × 10 $^{-2}$ (nm)	[a]Crystallite size (nm)	[b]Crystallite size (nm)	Ɛ × 10 $^{-3}$
Method I							
400°C	(111)	37.28	0.3607	1.80	23.24	7.67	0.74
550°C	(111)	37.05	0.2844	0.52	29.46	26.56	1.05
700°C	(111)	37.05	0.2509	0.55	33.40	33.25	1.00
Method II							
400°C	-	-	-	-	-	-	-
550°C	-	-	-	-	-	-	-
700°C	-	-	-	-	-	-	-
Method III							
As-deposited	(111)	37.0	0.2175	0.93	38.52	15.00	1.03
400°C	(111)	37.0	0.2175	0.61	38.52	22.77	1.02
550°C	(111)	37.2	0.1388	0.43	60.39	32.02	2.21
700°C	(111)	37.5	0.1171	0.32	71.64	43.06	1.19

[a]From Scherrer's equation
[b]From Williamson-Hall (WH) analysis

solvent agent or nickel salt. A lack of ordered internal structure in the amorphous phase in which the atoms and molecules are not arranged in a specific lattice pattern results in broader diffraction peaks instead of high-intensity narrower peaks. It may attribute to the modification of solvent material which used ethanol instead of 2-methoxyethnaol. Furthermore, as described in (Hajakbari, 2020), the XRD patterns show that the NiO thin films contain a single cubic crystal arrangement. Nevertheless, a wide peak at 2θ = 24° may be seen, corresponding to the quartz substrate. Similar patterns demonstrating the impact of annealing were achieved for silver, molybdenum oxide, and zirconium oxide thin films (Lupo et al., 2020). The XRD peaks were broad when the annealing temperature was raised, which was attributable to an improvement in particle size and crystallinity. The FWHM was seen to drop with annealing temperature, which might be attributed to a change in the concentration of lattice defects.

In the process of Method III, NiO films had five main prominent peaks of 37.2°, 43.2°, 62.8°, 75.4°, and 79° of 2 theta angle corresponding to the crystal plane of NiO (1 1 1), (2 0 0), (2 2 0), (3 1 1) and (2 2 2). The values "d" produced are equivalent to the NiO cubic phase with a=b=c=4.170 A°. The diffracted intensity for the planes of (1 1 1), (2 0 0), and (2 2 0) keep increasing sharply with an increasing annealing temperature, as observed in Figure 4(c). As in Method I, the high diffraction peak was observed at (111) for all the samples and obtained the average crystallite size. The crystallite size increased from 38 to 71 nm using Scherrer's equation and 15 to 43 nm using the W-H equation—the nickel

oxidation bond deficiencies on the bounds of grain with enhanced annealing temperature from 400°C to 700°C. Compared with the findings given in the journals, Ramesh et al. (Mulik, 2019), the findings available in different crystallite sizes were determined to be between 40 to 52 nm. The increasing annealed temperature provides crystallites with more energy that transfers them into permanent balance sites, resulting in the improvement of the crystallinity of NiO (Yang et al., 2019). Similar to Method I, a positive strain is obtained as the annealing temperature increases from 400°C to 700°C, illustrated in Figure 6. The strain of the sample decreases slowly as the as-deposited sample is annealed to 400°C. Subsequently, a quick rise in the strain value was observed at 550°C temperature and decreased as it reached 700°C, indicating a lower number of lattice imperfections. It could be due to the increasing temperature; the film becomes thick and lacks cracks and voids, allowing for faster crystal development (Jamal et al., 2019; Kumar et al., 2017).

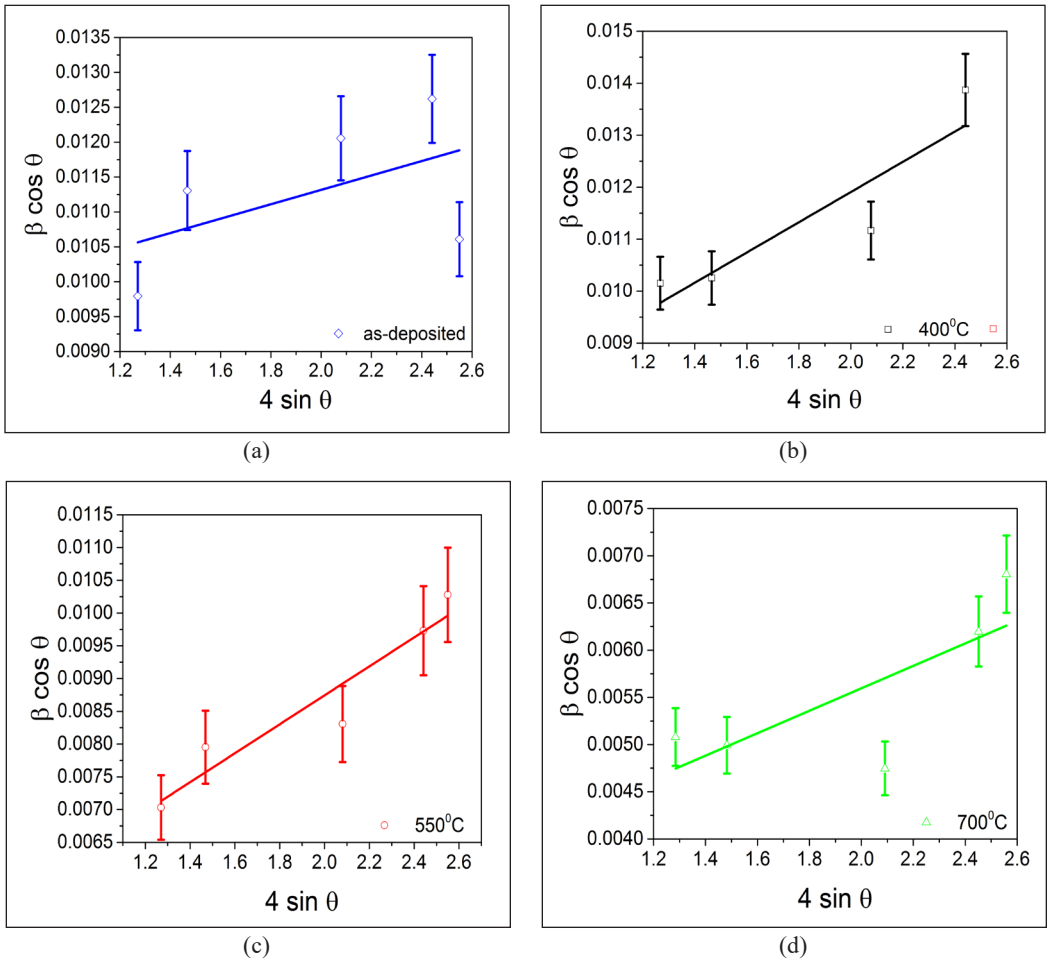

Figure 6. The WH analysis for the NiO thin film by Method III (a) as-deposited, (b) 400°C, (c) 550°C, and (d) 700°C. Solid lines represent best-fitting lines, while error bars represent standard deviations

Morphological Analysis

As illustrated in Figure 7, nanoparticles of green color NiO become black during the annealing process, which can be related to the previous results (Renaud et al., 2013), leading to a shortage or existence of nickel vacancy. The black-colored NiO films were subsequently transformed to bleach, with the rise in the annealing temperatures. The NiO thin films using Method I are thermally treated at various temperatures to study the surface morphology using SEM, as seen in Figure 8(a), with a magnification of 10,000. The NiO films comprise nanocrystalline grain, including a flat homogeneous substrate surface covered with top viewpoint for the films by the micrographs. The higher the temperature of the films, the more grains grew, and the condition of the films improved. It might be attributed to an enhancement in adatoms' thermal energy, which speeds up the migration of

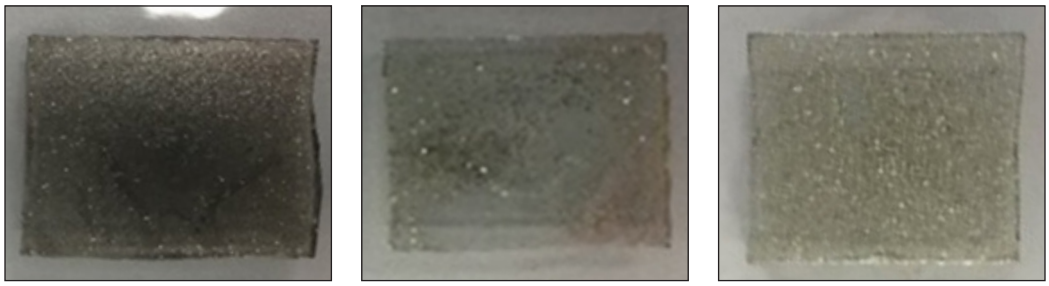

(a) (b) (c)

Figure 7. NiO films after annealed at (a) 400°C (b) 550°C (c) 700°C

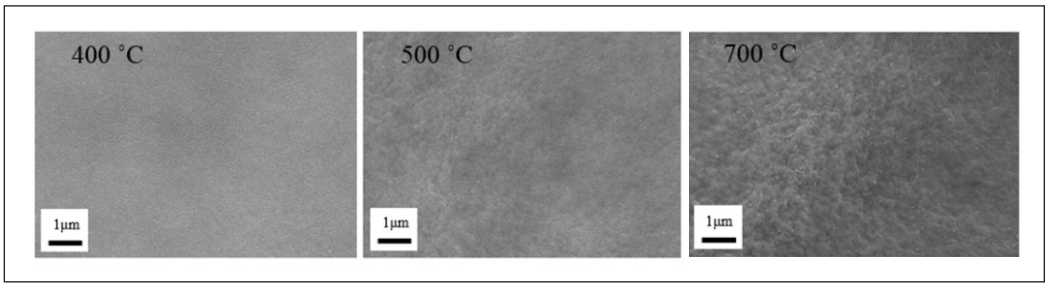

(a)

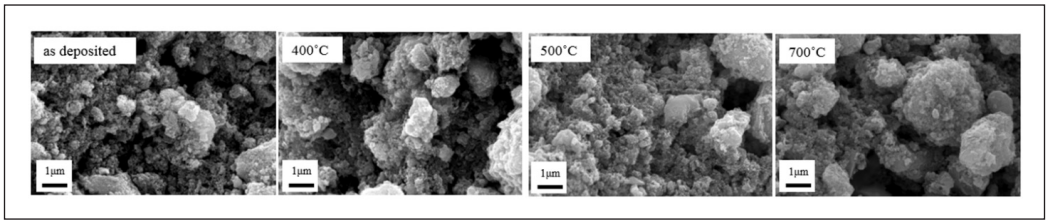

(b)

Figure 8. Surface morphologies performed at a magnification of 10.00kX annealed at different temperatures (400°C, 550°C, and 700°C) obtained from (a) Method I and (b) Method II

adatoms to favorable nucleation and growth sites, resulting in larger grain sizes. Christian et al. (Lupo et al., 2020) observed comparable SEM results for NiO films. However, there are a few small fractures discovered throughout the layer. It might be owing to the higher annealing temperatures utilized. The annealed temperature is considered to affect the interface structure of NiO films. The increased annealing temperature has a significant effect on the crystallite size of NiO (Haider et al., 2019; Yazdani et al., 2018).

SEM analysis was also conducted for the NiO films from Method III at various annealing temperatures [Figure 8 (b)]. The nanoparticles of NiO used in Method III were cubical and spherical. It can be seen that atoms are linked to one another from agglomerated particles. As the annealing temperature rose from 400°C to 550°C, the grains grew, indicating that the NiO films' structure had improved, as validated by the XRD results. It is clearly shown in Figure 8(b)) that certain bigger nanoparticles and strongly gathered when the annealing temperature is set to 700°C. A parallel finding was revealed in research (Wu et al., 2017), which suggested that this might be attributable to the large surface energy and the pressure of nanoparticles. The rise in grain size with raising the annealing temperature to 700°C indicates that the crystalline condition of the NiO film has improved. This increment is due to an expansion in the thermal energy of atoms, which promotes the movement of the atoms to appropriate nucleation and growing positions, leading to the formation of larger grains and an improvement in crystallinity. Bigger grain size results in transparent surfaces due to the decrease of grain borders and, as a result, fewer scatterings at the grain boundary (Sahoo & Thangavel, 2018).

Optical Properties

UV-Vis Spectroscopy was used to evaluate the produced NiO's optical characteristics, shown in Figure 9. The highest absorption peak of the NiO films in Method I was determined at a wavelength of about 336 nm. The absorption was greater than in the report presented by Ashique Kota and Hyung-Kee Seo (Kotta & Seo, 2019), who found absorption peaks at a wavelength of 321 nm. It might be owing to the various techniques and precursors employed. The optical energy band gaps of NiO were calculated by Tauc's equation (Equation 3) (Atak & Coşkun, 2017; Muniandy et al., 2021) based on the results from UV-Vis absorption spectra:

$$(\alpha h\nu)^{n} = A(h\nu - E_g) \qquad [3]$$

where *hv* is photo energy, α is absorption coefficient, and n is 2 for direct bandgap material. Based on the equation, it is possible to extrapolate the linear part of $(\alpha h\nu)^{n}$ to *hv*, i.e., to zero, to the optical band space for the absorption pitch. The band gap energy decreased at the higher annealing temperature from 3.6 to 3.1 eV. According to Patil et al. (2011), the

bandgap of the NiO materials annealed at 400°C to 700°C is decreased by 3.86 to 3.47 eV. The fall in deficient dimensions and the increase in particle size caused the decrease of E_g with a rising annealing temperature (Agbogu et al., 2018; Kayani et al., 2018; Muhammad et al., 2022). It is consistent with the results obtained from XRD analysis. According to XRD results, the crystallite size has increased as the annealing temperature increases. The increase in crystallite size indicated a decrease in the semiconductor's energy bandgap, similar to the findings reported by (Dwivedi et al. 2022; Muniandy et al., 2021; Kumar et al., 2017). Compared to bulk NiO (4.0eV), the produced samples exhibit lower Eg values. Consequently, the annealing temperature is inversely proportional to the energy band gap. The change in bandgap value may also be affected by several other variables, such as carrier concentrations, crystallite size, structural characteristics, impurity presence, and lattice strain (Dwivedi et al., 2022).

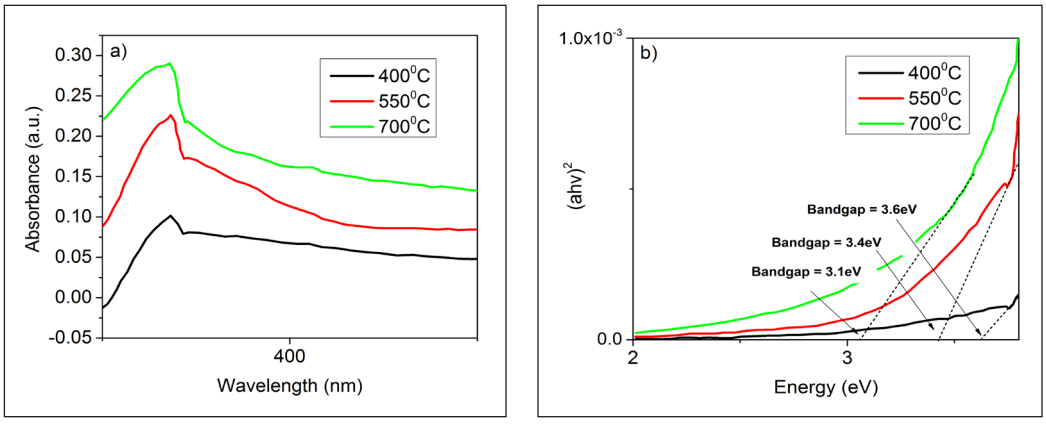

(a) (b)

Figure 9. The method I result shows (a) the NiO spectrum of absorption from UV-Vis at various annealing temperatures (400°C, 550°C, and 700°C); (b) NiO thin sheet Tauc plot to measure the optical absorption.

The UV region of NiO film using Method II exhibited the highest absorption at about 339nm, although the XRD results did not prevail at any peaks. In addition, with the increasing annealing temperature from 400°C to 700°C, as indicated in Figure 10, the absorption factor of films increased. It might be due to an improvement in hole density with increasing annealing temperature. The higher the annealing temperature, the band gaps were observed to drop from 3.5 to 2.7eV. The decrease in the bandgap with an increased temperature may be due to crystalline growth and even to a decrease in the interface zone. According to the XRD findings, the grain size increased as the temperature increased. As grain size expanded, the density of the grain limit of the film decreased, and carriers at grain boundaries became less dispersed (Aftab et al., 2021).

Figure 11 shows the highest absorption peaks of NiO thin films using Method III in the UV region at about 339 nm wavelength. The absorbance coefficient of annealed

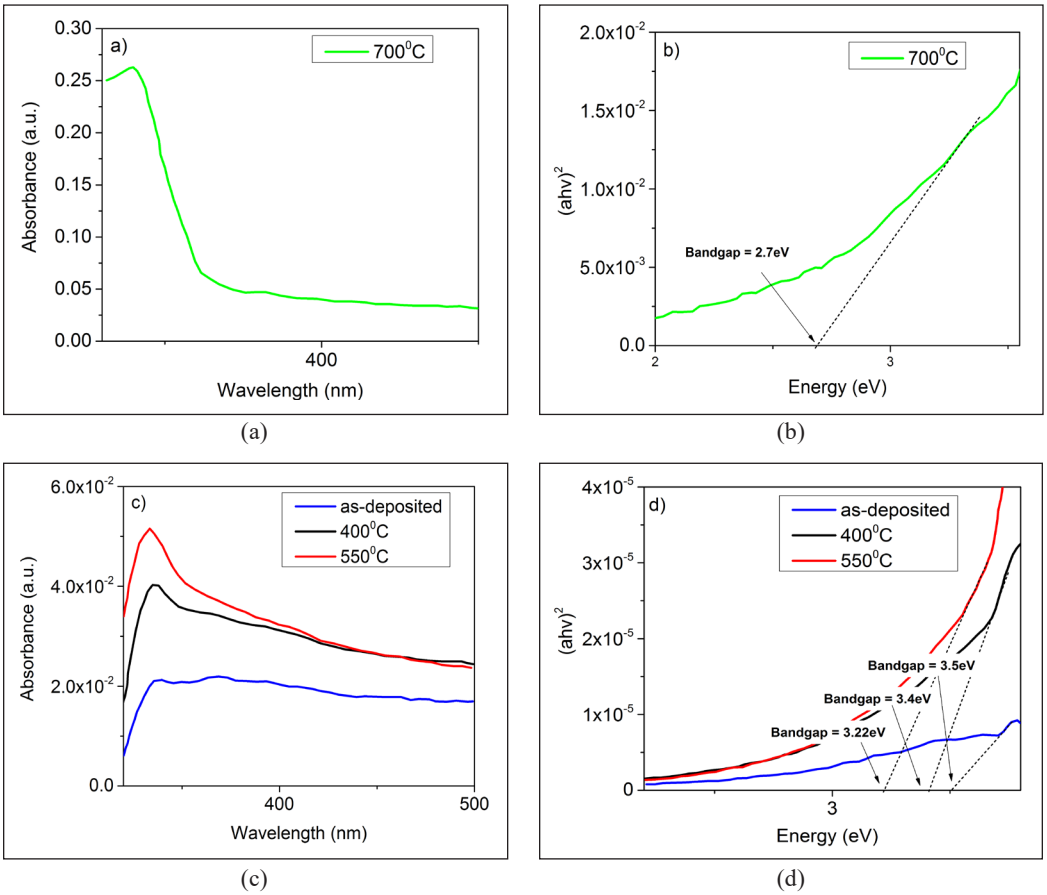

(a) (b) (c) (d)

Figure 10. Method II outcome of NiO film (a) UV-Vis absorption spectrum at a temperature of 700°C, (b) Tauc plot for the evaluation of the optical bandgap at 700°C, (c) UV-Vis absorption spectrum at a different annealing temperature of the films (as-deposited, 400°C, and 550°C), and (d) Tauc plot of thin films at various temperatures for the optical bandgap (as-deposited, 400°C, and 550°C)

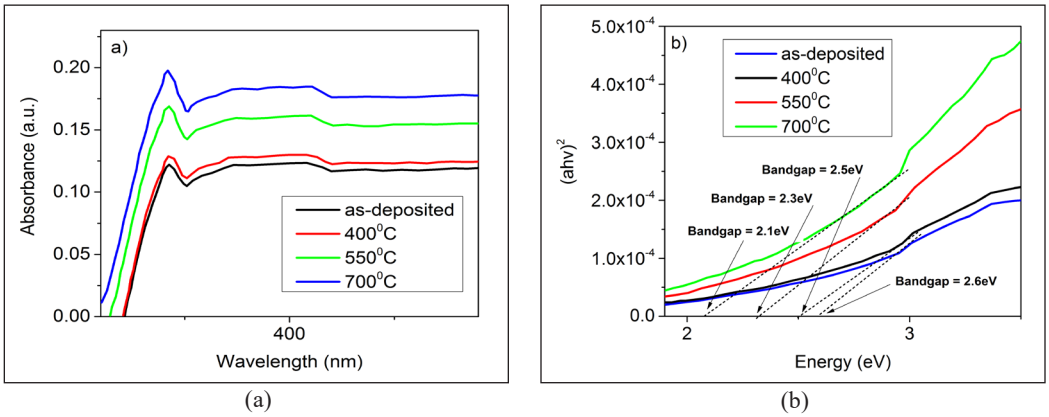

(a) (b)

Figure 11. Method III outcome indicates (a) the NiO spectrum of absorptions at various temperatures (400°C, 550°C, and 700°C), and (b) a Tauc plot to evaluate the optical band gap

films increases as the annealing temperature rises, comparable to Method I and II. The absorbance coefficient of films annealed at a lower temperature (400°C) is less than that of films annealed at a higher temperature. The NiO films at 700°C efficiently absorbed photon energy and displayed greater absorption in the UV band when contrasted to the as-deposited and lower temperatures. According to the Tauc displayed graph, the bandgap decreases from 2.38 to 2.15eV when the annealing temperature increases from 400°C to 700°C. It resists chemical flaws or vacancies in the crystal structure, reducing bandgap energy. The fall in energy from the bandgap can be associated with increasing grain size and decreasing concentration of defect sites that lead to reduced defeat. The bandgap may therefore be determined directly by the size of the grain.

CONCLUSION

The NiO nanoparticles were synthesized with three different precursors and deposited using the spin coating. Method I, II, and III samples were annealed at different temperatures (400°C, 550°C, and 700°C). The NiO thin films were studied in detail according to the results obtained from XRD, SEM, and UV-Vis spectroscopy. Comparing these three methods, Method I have shown more potential to be an HTL layer resulting in increasing crystallite size, reducing microstrain, uniform surface of the film with the absence of agglomerated particles and pin-hole free, and decreasing bandgap energies. The thermal treatment considerably impacts the structures' forms, sizes, and energy band gap. The XRD result revealed that when the annealing temperature increased, the crystallite size of the NiO thin film also increased from 23 to 71 nm obtained from Scherrer's equation and 7.6 to 43 nm attained from Williamson-Hall's (WH) equation. An excellent diffract intensity of NiO was demonstrated using Methods I and III. Nevertheless, only hollow peaks were found from Method II, even annealed after increasing the annealing temperature to 700°C. The surface morphology of Method I NiO thin film exhibited a denser and uniform surface in contrast to Method III demonstrated agglomerated particles. Furthermore, the band gap energies were decreased from 3.60 to 2.10 eV with an increase in annealing temperature. Henceforth, the synthesis of NiO thin film performed well at the annealing temperature of 700°C, the crystallinity of NiO has enhanced owing to its greater absorption coefficient, uniform, and pinhole-free surface area, fast deposition crystallization, and a lower number of lattice imperfections occur due to the size and microstrain which aspects that proposed NiO as a good candidate for HTM.

ACKNOWLEDGEMENT

This work was supported by the Ministry of Higher Education Malaysia and Universiti Teknikal Malaysia Melaka through the Fundamental Research Grant Scheme with Project No PJP/2021/FTKEE/S01822 and FRGS/1/2020/FKEKK-CETRI/F00423.

REFERENCES

Abbas, M., Zeng, L., Guo, F., Rauf, M., Yuan, X. C., & Cai, B. (2020). A critical review on crystal growth techniques for scalable deposition of photovoltaic perovskite thin films. *Materials*, *13*(21), Article 4851. https://doi.org/10.3390/ma13214851

Aftab, M., Butt, M. Z., Ali, D., Bashir, F., & Khan, T. M. (2021). Optical and electrical properties of NiO and Cu-doped NiO thin films synthesized by spray pyrolysis. *Optical Materials*, *119*, Article 111369. https://doi.org/10.1016/j.optmat.2021.111369

Agbogu, A. N. C., Orji, M. P., & Ekwealor, A. B. C. (2018). Investigations into the influence of temperature on the optical properties of NiO thin films. *Indian Journal of Pure and Applied Physics*, *56*(2), 136-141.

Aswathy, N. R., Varghese, J., & Vinodkumar, R. (2020). Effect of annealing temperature on the structural, optical, magnetic and electrochemical properties of NiO thin films prepared by sol-gel spin coating. *Journal of Materials Science: Materials in Electronics*, *31*, 16634-16648. https://doi.org/10.1007/s10854-020-04218-5

Atak, G., & Coşkun, Ö. D. (2017). Annealing effects of NiO thin films for all-solid-state electrochromic devices. *Solid State Ionics*, *305*, 43-51. https://doi.org/10.1016/j.ssi.2017.05.002

Atli, A., Atilgan, A., Altinkaya, C., Ozel, K., & Yildiz, A. (2019). St. Lucie cherry, yellow jasmine, and madder berries as novel natural sensitizers for dye-sensitized solar cells. *International Journal of Energy Research*, *43*(8), 3914-3922. https://doi.org/10.1002/er.4538

Atli, A., Atilgan, A., & Yildiz, A. (2018). Multi-layered TiO_2 photoanodes from different precursors of nanocrystals for dye-sensitized solar cells. *Solar Energy*, *173*, 752-758. https://doi.org/10.1016/j.solener.2018.08.027

Desissa, T. D. (2021). NiO-ZnO based junction interface as high-temperature contact materials. *Ceramics International*, *47*(6), 8053-8059. https://doi.org/10.1016/j.ceramint.2020.11.159

Du John H, V., Moni D, J., & Gracia, D. (2020). A detailed review on Si, GaAs, and CIGS/CdTe based solar cells and efficiency comparison. *Przegląd Elektrotechniczny*, *96*(12), 9-18. http://dx.doi.org/10.15199/48.2020.12.02

Dwivedi, S., Nayak, H. C., Parmar, S. S., Kumhar, R. P., & Rajput, S. (2022). Calcination temperature reflected structural, optical and magnetic properties of nickel oxide. *Magnetism*, *2*(1), 45-55. https://doi.org/10.3390/magnetism2010004

Ebhota, W. S., & Jen, T. C. (2020). Fossil fuels environmental challenges and the role of solar photovoltaic technology advances in fast tracking hybrid renewable energy system. *International Journal of Precision Engineering and Manufacturing-Green Technology*, *7*, 97-117. https://doi.org/10.1007/s40684-019-00101-9

Gil, B., Yun, A. J., Lee, Y., Kim, J., Lee, B., & Park, B. (2019). Recent progress in inorganic hole transport materials for efficient and stable perovskite solar cells. *Electronic Materials Letters*, *15*, 505-524. https://doi.org/10.1007/s13391-019-00163-6

Guo, Y., Yin, X., & Que, W. (2017). NiOx mesoporous films derived from Ni $(OH)_2$ nanosheets for perovskite solar cells. *Journal of Alloys and Compounds*, *722*, 839-845. https://doi.org/10.1016/j.jallcom.2017.06.185

Haider, A. J., Al-Anbari, R., Sami, H. M., & Haider, M. J. (2019). Photocatalytic activity of nickel oxide. *Journal of Materials Research and Technology*, *8*(3), 2802-2808. https://doi.org/10.1016/j.jmrt.2019.02.018

Hajakbari, F, Afzali, M. T., & Hojabri, A. (2017). Nanocrystalline nickel oxide (NiO) thin films grown on quartz substrates: Influence of annealing temperatures. *Acta Physica Polonica A*, *131*(3), 417-419. https://doi.org/10.12693/APhysPolA.131.417

Hajakbari, F. (2020). Characterization of nanocrystalline nickel oxide thin films prepared at different thermal oxidation temperatures. *Journal of Nanostructure in Chemistry*, *10*(1), 97-103. https://doi.org/10.1007/s40097-020-00332-2

Ibn-Mohammed, T., Koh, S. C. L., Reaney, I. M., Acquaye, A., Schileo, G., Mustapha, K. B., & Greenough, R. (2017). Perovskite solar cells: An integrated hybrid lifecycle assessment and review in comparison with other photovoltaic technologies. *Renewable and Sustainable Energy Reviews*, *80*, 1321-1344. https://doi.org/10.1016/j.rser.2017.05.095

Jamal, M. S., Shahahmadi, S. A., Chelvanathan, P., Alharbi, H. F., Karim, M. R., Dar, M. A., Luqman, M., Alharthi, N. H., Al-Harthi, Y. S., Aminuzzaman, M., Asim, N., Sopian, K., Tiong, S. K., Amin, N., & Akhtaruzzaman, M. (2019). Effects of growth temperature on the photovoltaic properties of RF sputtered undoped NiO thin films. *Results in Physics*, *14*, Articles 102360. https://doi.org/10.1016/j.rinp.2019.102360

Kayani, Z. N., Butt, M. Z., Riaz, S., & Naseem, S. (2018). Synthesis of NiO nanoparticles by sol-gel technique. *Materials Science-Poland*, *36*(4), 547-552. https://doi.org/10.2478/msp-2018-0088

Kotta, A., & Seo, H.-K. (2019). Nickel Oxide Monodispersed Quantum Dots as Hole Transport Layer in *n-i-p* Hybrid Perovskite Solar Cells . *Journal of Nanoelectronics and Optoelectronics*, *14*(7), 895-899. https://doi.org/10.1166/jno.2019.2660

Li, M. H., Yum, J. H., Moon, S. J., & Chen, P. (2016). Inorganic p-type semiconductors: Their applications and progress in dye-sensitized solar cells and perovskite solar cells. *Energies*, *9*(5), Article 331. https://doi.org/10.3390/en9050331

Li, S., Cao, Y. L., Li, W. H., & Bo, Z. S. (2021). A brief review of hole transporting materials commonly used in perovskite solar cells. *Rare Metals*, *40*, 2712-2729. https://doi.org/10.1007/s12598-020-01691-z

Lupo, C., Eberheim, F., & Schlettwein, D. (2020). Facile low-temperature synthesis of nickel oxide by an internal combustion reaction for applications in electrochromic devices. *Journal of Materials Science*, *55*, 14401-14414. https://doi.org/10.1007/s10853-020-04995-8

Łuszczek, M., Łuszczek, G., & Świsulski, D. (2021). Simulation investigation of perovskite-based solar cells. *Przegląd Elektrotechniczny*, *2021*(5), 99-102. https://doi.org/10.1109/ECACE.2019.8679283

Mariotti, N., Bonomo, M., Fagiolari, L., Barbero, N., Gerbaldi, C., Bella, F., & Barolo, C. (2020). Recent advances in eco-friendly and cost-effective materials towards sustainable dye-sensitized solar cells. *Green Chemistry*, *22*, 7168-7218. https://doi.org/10.1039/D0GC01148G

Mohammadian-Sarcheshmeh, H., Arazi, R., & Mazloum-Ardakani, M. (2020). Application of bifunctional photoanode materials in DSSCs: A review. *Renewable and Sustainable Energy Reviews*, *134*, Article 110249. https://doi.org/10.1016/j.rser.2020.110249

Muhammad, S., Nomaan, A. T., Idris, M. I., & Rashid, M. (2022). Structural, optical and electrical investigation of low-temperature processed zinc oxide quantum dots based thin films using precipitation-spin coating on flexible substrates. *Physica B: Condensed Matter*, *635*, Article 413806. https://doi.org/10.1016/j.physb.2022.413806

Mulik, R. N. (2019). Microstructural studies of nanocrystalline nickel oxide. *International Journal Of Research And Analytical Reviews*, *6*(2), 973-981. https://doi.org/10.1063/1.4802404

Muniandy, S., Idris, M. I. B., Napiah, Z. A. F. B. M., Yusof, H. H. M., Chachuli, S. A. M., & Rashid, M. (2021). An investigation on NiO for hole transport material in perovskite solar cells. In *2021 IEEE Regional Symposium on Micro and Nanoelectronics (RSM)* (pp. 112-115). IEEE Publishing. https://doi.org/10.1109/RSM52397.2021.9511573

Nkele, A. C, Nwanya, A. C, Shinde, N. M., Ezugwu, S., Maaza, M., Shaikh, J. S., & Ezema, F. I. (2020). The use of nickel oxide as a hole transport material in perovskite solar cell configuration: Achieving a high performance and stable device. *International Journal of Energy Research*, *44*(13), 9839-9863. https://doi.org/10.1002/er.5563

Pagar, U., & Shinde, U. P. (2021). Annealing effect on structural, morphological and electrical properties by screen printed bunsenite NiO thick films. *International Journal of Innovative Technology and Exploring Engineering*, *10*(6), 80-85. https://doi.org/10.35940/ijitee.F8826.0410621

Park, H. H. (2021). Efficient and stable perovskite solar cells based on inorganic hole transport materials. *Nanomaterials*, *12*(1), Article 112. https://doi.org/10.3390/nano12010112

Patil, V. P., Pawar, S., Chougule, M., Godse, P., Sakhare, R., Sen, S., & Joshi, P. (2011). Effect of annealing on structural, morphological, electrical and optical studies of nickel oxide thin films. *Journal of Surface Engineered Materials and Advanced Technology*, *1*(2), 35-41. https://doi.org/10.4236/jsemat.2011.12006

Pitaro, M., Tekelenburg, E. K., Shao, S., & Loi, M. A. (2022). Tin halide perovskites: From fundamental properties to solar cells. *Advanced Materials*, *34*(1), Article 2105844. https://doi.org/10.1002/adma.202105844

Renaud, A., Chavillon, B., Cario, L., Pleux, L. Le, Szuwarski, N., Pellegrin, Y., Blart, E., Gautron, E., Odobel, F., & Jobic, S. (2013). Origin of the black color of NiO used as photocathode in p-type dye-sensitized solar cells. *Journal of Physical Chemistry C*, *117*(44), 22478-22483. https://doi.org/10.1021/jp4055457

Roy, A., Ghosh, A., Bhandari, S., Sundaram, S., & Mallick, T. K. (2020). Perovskite solar cells for BIPV application: A review. *Buildings*, *10*(7), Article 129. https://doi.org/10.3390/buildings10070129

Sahoo, P., & Thangavel, R. (2018). Effect of annealing temperature on physical properties of solution processed nickel oxide thin films. In *AIP Conference Proceedings* (Vol. 1961, p. 30041). AIP Publishing LLC. https://doi.org/10.1063/1.5035243

Kumar, R. S., Johnson Jeyakumar, S., Jothibas, M., Kartharinal Punithavathy, I., & Prince Richard, J. (2017). Influence of molar concentration on structural, optical and magnetic properties of NiO nanoparticles. *Journal of Materials Science: Materials in Electronics*, *28*(20), 15668-15675.

Serin, T., Atilgan, A., Kara, I., & Yildiz, A. (2017). Electron transport in Al-Cu co-doped ZnO thin films. *Journal of Applied Physics* (Vol. 121, No. 9, p. 95303). AIP Publishing LLC. https://doi.org/10.1063/1.4977470

Shariatinia, Z. (2020). Recent progress in development of diverse kinds of hole transport materials for the perovskite solar cells: A review. *Renewable and Sustainable Energy Reviews*, *119*, Article 109608. https://doi.org/10.1016/j.rser.2019.109608

Takko, S. Y., Amin, B. D. E., Y, C. I., & Shekarau, J. I. (2021). Crystallinity, amorphousity and characterization of synthesized Sb_2O_3, BaO and NiO nanoparticles and nanocomposites. *International Journal of Innovative Science and Research Technology*, *6*(11), 822-831.

Wang, H., Yu, Z., Jiang, X., Li, J., Cai, B., Yang, X., & Sun, L. (2017). Efficient and stable inverted planar perovskite solar cells employing CuI as hole-transporting layer prepared by solid-gas transformation. *Energy Technology*, *5*(10), 1836-1843. https://doi.org/10.1002/ente.201700422

Wang, K., Tian, Y., Jiang, H., Chen, M., & Xu, S. (2019). Surface treatment on nickel oxide to enhance the efficiency of inverted perovskite solar cells. *International Journal of Photoenergy*, *2019*, Article 4360816. https://doi.org/10.1155/2019/4360816

Wilson, G. M., Al-Jassim, M., Metzger, W. K., Glunz, S. W., Verlinden, P., Xiong, G., Mansfield, L. M., Stanbery, B. J., Zhu, K., Yan, Y., Berry, J. J., Ptak, A. J., Dimroth, F., Kayes, B. M., Tamboli, A. C., Peibst, R., Catchpole, K., Reese, M. O., Klinga, C. S., … & Sulas-Kern, D. B. (2020). The 2020 photovoltaic technologies roadmap. *Journal of Physics D: Applied Physics*, *53*(49), Article 493001. https://doi.org/10.1088/1361-6463/ab9c6a

Wu, J., Lan, Z., Lin, J., Huang, M., Huang, Y., Fan, L., Luo, G., Lin, Y., Xie, Y., & Wei, Y. (2017). Counter electrodes in dye-sensitized solar cells. *Chemical Society Reviews*, *46*(19), 5975-6023. https://doi.org/10.1039/C6CS00752J

Yang, P., Li, L., Yu, S., Zheng, H., & Peng, W. (2019). The annealing temperature and films thickness effect on the surface morphology, preferential orientation and dielectric property of NiO films. *Applied Surface Science*, *493*, 396-403. https://doi.org/10.1016/j.apsusc.2019.06.223

Yang, W. F., Igbari, F., Lou, Y. H., Wang, Z. K., & Liao, L. S. (2020). Tin halide perovskites: Progress and challenges. *Advanced Energy Materials*, *10*(13), Article 1902584. https://doi.org/10.1002/aenm.201902584

Yazdani, A., Zafarkish, H., & Rahimi, K. (2018). The variation of Eg-shape dependence of NiO nanoparticles by the variation of annealing temperature. *Materials Science in Semiconductor Processing*, *74*, 225-231. https://doi.org/10.1016/j.mssp.2017.10.048

Yildiz, A, Cansizoglu, H., Abdulrahman, R., & Karabacak, T. (2015). Effect of grain size and strain on the bandgap of glancing angle deposited AZO nanostructures. *Journal of Materials Science: Materials in Electronics*, *26*, 5952-5957. https://doi.org/10.1007/s10854-015-3167-0

Yildiz, Abdullah, Chouki, T., Atli, A., Harb, M., Verbruggen, S. W., Ninakanti, R., & Emin, S. (2021). Efficient iron phosphide catalyst as a counter electrode in dye-sensitized solar cells. *ACS Applied Energy Materials*, *4*(10), 10618-10626. https://doi.org/10.1021/acsaem.1c01628

Yin, X., Guo, Y., Xie, H., Que, W., & Kong, L. B. (2019). Nickel oxide as efficient hole transport materials for perovskite solar cells. *Solar RRL*, *3*(5), Article 1900001. https://doi.org/10.1002/solr.201900001

Younas, M., Gondal, M. A., Dastageer, M. A., & Baig, U. (2019). Fabrication of cost effective and efficient dye sensitized solar cells with WO_3-TiO_2 nanocomposites as photoanode and MWCNT as Pt-free counter electrode. *Ceramics International*, *45*(1), 936-947. https://doi.org/10.1016/j.ceramint.2018.09.269

Pertanika J. Sci. & Technol. 31 (4): 2067 - 2087 (2023)

PERTANIKA JOURNALS

SCIENCE & TECHNOLOGY

Journal homepage: http://www.pertanika.upm.edu.my/

Correlation of Stromelysin-1 and Tissue Inhibitor of Metalloproteinase-1 with Lipid Profile and Atherogenic Indices in End-Stage Renal Disease Patients: A Neural Network Study

Habiba Khdair Abdalsada[1], Hadi Hassan Hadi[2], Abbas F. Almulla[3]*, Asawer Hassan Najm[4], Ameer Al-Isa[2] and Hussein Kadhem Al-Hakeim[2]

[1]Al-Muthanna University, College of Pharmacy, Al-Muthanna, Iraq
[2] Department of Chemistry, College of Science, University of Kufa, Najaf, Iraq
[3]Medical Laboratory Technology Department, College of Medical Technology, The Islamic University, Najaf, Iraq
[4]College of Pharmacy, Jabir Ibn Hayyan University for Medical and Pharmaceutical Sciences. Najaf, Iraq

ABSTRACT

End-stage renal disease (ESRD) patients are prone to cardiovascular disease (CVD). The search for a biomarker that determines patients at great risk of CVD is still a hot topic of study. In the present study, stromelysin-1 and its inhibitor (TIMP1), in addition to atherogenic indices, were studied in ESRD patients. We assessed stromelysin-1, TIMP1, and lipid profile parameters in the serum of 60 ESRD patients and 30 healthy controls. A neural network study was conducted to determine the best factors for predicting ESRD patients more susceptible to developing CVD using the cut-off value of the atherogenic index of plasma (AIP) >0.24. ESRD patients have dyslipidemia, high atherogenic indices, and elevated levels of stromelysin-1 and TIMP1. There is a correlation between the rise in stromelysin-1 and its inhibitor and several atherogenic indices and lipids in those patients. The neural network results indicated that the area under the curve predicting CVD, using the measured eight parameters, was 0.833, with 80 % sensitivity and 100% specificity. The relative importance of the top four most effective input variables that represent the most important determinants for the prediction of high risk of CVD stromelysin-1 (100%), followed by eGFR (77.9%), TIMP1 (66.0%), and TIMP1/stromelysin-1 (30.7%). ESRD

ARTICLE INFO

Article history:
Received: 03 August 2022
Accepted: 30 November 2022
Published: 13 June 2023

DOI: https://doi.org/10.47836/pjst.31.4.27

E-mail addresses:
habiba.khdair@mu.edu.iq (Habiba Khdair Abdalsada)
hhadi0615@gmail.com (Hadi Hassan Hadi)
abbass.chem.almulla1991@gmail.com (Abbas F. Almulla)
asawer_h2010@yahoo.com (Asawer Hassan Najm)
molaryameer1986@yahoo.com (Ameer Al-Isa)
headm2010@yahoo.com (Hussein Kadhem Al-Hakeim)
* Corresponding author

ISSN: 0128-7680
e-ISSN: 2231-8526

patients have dyslipidemia and are prone to CVD, and stromelysin-1 is the best parameter for predicting CVD in ESRD patients.

Keywords: Cardiovascular disease, ESRD, lipid profile, Stromelysin-.1TIMP1

INTRODUCTION

End-stage renal disease (ESRD) is the final and fifth chronic kidney disease (CKD) stage. ESRD is defined by a glomerular filtration rate (GFR) of less than 15 mL/min/1.73 m^2 for a minimum of 90 days (Benjamin & Lappin, 2021). During this stage, patients must receive renal replacement (hemodialysis, peritoneal dialysis, or kidney transplantation) therapy to stay alive (Benjamin & Lappin, 2021). Approximately 10–15% of the world's population suffers from chronic kidney disease, linked to a lower standard of living and a shorter lifespan (Levin et al., 2017). When CKD advances to ESRD, the most common therapy is hemodialysis (Gillespie et al., 2015).

In ESRD patients, cardiovascular comorbidities are common (overall prevalence of 70.6%), even in young patients (Saran et al., 2017). In ESRD patients, cardiovascular disease (CVD)-related mortality varied between 27% and 69% (Neovius, Jacobson, Eriksson, Elinder, & Hylander, 2014; Steenkamp et al., 2015). About 1.4 million CVD-related fatalities and 25.3 million CVD disability-adjusted life years were attributed to impaired kidney function (Bikbov et al., 2020). CVD has traditionally been the primary cause of death and morbidity among ESRD patients (Cozzolino et al., 2018). CVD is 20 times more common in those with ESRD than in the general population (Stenvinkel et al., 2008). Patients with ESRD continue to have a 20-fold greater frequency of CVD than the general population (Cozzolino et al., 2018).

Abnormalities in lipoprotein metabolism and particle size, as well as in lipid metabolism and transport, all contribute to CVD. Patients with all phases of CKD have recognized risk factors for CVD, including dyslipidemia and lipoprotein abnormalities (Visconti et al., 2016). In previous studies, lipid-lowering medication has delayed the course of CKD (Kochan et al., 2021; Theofilis et al., 2021). These studies found a direct link between blood lipids and the beginning of CKD (Zhang et al., 2014). Serum lipids are linked to CKD, although results are mixed (Rahman et al., 2014; Rosenstein & Tannock, 2022); this might be because the samples investigated were diverse in composition. Chronic venous thromboembolism (VTE) is a leading cause of mortality and disability in CKD patients (Thompson et al., 2015). Chronic VTE may be caused by various mechanisms in patients with CKD (Gregg & Hedayati, 2018). Dyslipidemia is prevalent in non-dialyze-dependent renal patients, patients with nephrotic range proteinuria, patients with ESRD, and renal transplant recipients, causing an increased risk of CVD in those patients (Mikolasevic et al., 2017).

The lipid profile, a common blood test used to monitor and screen for risk of CVD, is related to the kidney function level and proteinuria degree (Liang et al., 2020; Vaziri et al., 2022). The abnormality in lipoprotein degradation is due to inappropriate activity of the lipid metabolic pathways and enzymes, which leads to early-stage kidney failure and dyslipidemia, which is also a risk factor for the development of atherosclerosis (Tunbridge & Jardine, 2021). These metabolic abnormalities contribute to CKD progression and adversely affect renal function (Vaziri et al., 2022).

A set of zinc-dependent endopeptidases known as the matrix metalloproteases (MMPs) are secreted by several cells, including macrophages (Hibbs, Hoidal, & Kang, 1987; Iyer, Patterson, Fields, & Lindsey, 2012) and endothelial cells (Haas, Davis, & Madri, 1998). It is also known that MMPs contribute to the breakdown and hydrolysis of extracellular matrix (ECM) elements (Altemtam, El Nahas, & Johnson, 2012), triggering of chemokines, cells functions, and host defense (Marchant et al., 2014; Rydlova et al., 2008). Various MMPs are found in nephron compartments, vasculature, and connective tissue (Parrish, 2017). Therefore, MMPs exert substantial effects on the physiological functions of the body. When their expression is disturbed or their function is dysregulated, it can result in the emergence of certain illnesses, such as cancer, diabetes, chronic inflammatory diseases, cardiovascular and renal diseases, and neurological disorders (Zakiyanov et al., 2019).

The MMP-3 (stromelysin-1) is a crucial type of MMP that has recently been linked to the pathophysiology of chronic kidney disease (CKD) (Andreucci et al., 2021). Additionally, abnormal soluble stromelysin-1 serum levels are a risk factor for renal disease and CVD (Wang et al., 2021). The stromelysin-1 genetic polymorphisms and changes in its expression level are risk factors for cardiovascular disease, atherosclerosis, and renal disease (Cheng et al., 2017; Nolan et al., 2013). Mesangial expansion and glomerular damage enhanced in tubular atrophy and interstitial lesions were adversely associated with stromelysin-1 (Suzuki et al., 1997). Hemodialysis patients had higher serum levels of stromelysin-1 activity (Naganuma et al., 2008b).

One of the MMP inhibitors is the tissue inhibitor of metalloproteinase 1 (TIMP-1), a glycoprotein that binds directly to the MMP catalytic site, keeping substrates away from the MMPs (Murphy & Nagase, 2008). TIMP-1 is a potent inhibitor of stromelysin-1 (Hamze et al., 2007). All experiments *in vivo* and *in vitro* have displayed the antiangiogenic action of TIMP1 (Martin et al., 1999). TIMP1 regulates MMP proteolytic activity at the transcriptional and posttranslational levels and in tissues (Tan & Liu, 2012). The integrity of connective tissue, particularly cartilage, is thought to be affected by the activity of MMPs and TIMPs (Kageyama et al., 2000). In one research, there was an increase in the expression of stromelysin-1 and TIMP1 in atrophied tubules that were negatively linked with established glomerular mesangial expansion (Suzuki et al., 1997). We speculate that

stromelysin-1 and TIMP-1 are essential in ESRD and are probably associated with disease complications.

Thus, we aim to investigate the correlation between the lipid profile and atherogenic indices with the stromelysin-1 and its inhibitor (TIMP-1) to determine the possible interaction between these parameters in ESRD patients. Also, we used the levels of these biomarkers to predict the risks of developing CVD in ESRD patients.

METHODOLOGY

Subjects

We recruited 60 patients with ESRD (32/28 male/female) with an average age of 46.45±10.29 years who participated in this case-control study. Each patient had a history of acute kidney injury (AKI) that developed into renal failure and was treated by dialysis. The patients were gathered in the Al-Hakeem General Hospital and Al-Sadr Medical City dialysis units between December 2021 and February 2022 in the AL-Najaf governorate of Iraq. A thorough medical history that considered the existence of any systemic diseases was used to examine patients. The research excluded patients with diabetes, hepatic conditions, and CVD. A senior physician diagnosed the patients using the tenth version of the International Statistical Classification of Diseases and Related Health Problems (2021 ICD-10-CM Diagnosis Code N18.6). The included patients were diagnosed with chronic renal failure in the end stage and on hemodialysis as a treatment regimen in addition to the routine drug regimen.

All patients received calcium carbonate, epoetin alpha (Eprex®), heparin, and continuous folic acid or iron and folate formula (Fefol®). Thirty healthy people (19 men and 11 women) were recruited as a control group without observable physical diseases. Their ages are 47.09±6.83 years old, which matches the patients' ages. The study complied with international and Iraqi rules governing ethics and privacy. All participants, or first-degree relatives of patients, provided written informed consent before participating in this study. The study received approval from the Institutional Review Board (IRB) of the Faculty of Science at the University of Kufa in Iraq (Document number 622/2021), which adheres to the International Guideline for the Protection of Human Subjects of the Declaration of Helsinki.

Measurements

After a 12-hour fast, participants' venous blood samples were taken between 8 and 9 in the morning. The venous blood samples were collected in serum gel tubes. Before the test, samples were aliquoted among three fresh Eppendorf® tubes and kept at -80 °C for further analysis. Prior to the hemodialysis session, serum was taken to evaluate all parameters.

ELISA kits provided by Melsin Medical Co., Ltd., Jilin, China, were used to determine the amounts of serum stromelysin-1 and TIMP1. The kits' inter-assay CV percent was less than 10%, and their sensitivities were under 0.1 ng/ml. Spectrophotometric measurements of glucose, albumin, urea, uric acid, inorganic phosphate, and creatinine were made using ready-to-use kits from Biolabo® (Maizy, France). According to the Modification of Diet in Renal Disease (MDRD) study equation (Levey et al., 2007), Equation 1 was used to determine the estimated glomerular filtration rate (eGFR):

$$eGFR = 175 \times (S_{\cdot}Cr)^{-1.154} \times (Age)^{-0.203} \times 0.742 \text{ [if female]} \times 1.212 \text{ [if Black]} \quad (1)$$

The Friedewald formula (low-density lipoprotein cholesterol, LDLc = Total cholesterol, TC [Triglyceride (TG)]/2.19 + High-density lipoprotein cholesterol, HDLc) was used to calculate LDLc. The formula can be used when cholesterol and TG concentrations exceed 400mg/dl (Friedewald, Levy, & Fredrickson, 1972). Castelli's Risk Indices (CRI) are based on TC, LDLc, and HDLc, and they are categorized into two indices; CRI-I and CRI-II (Castelli, Abbott, & McNamara, 1983). Mathematically, it is calculated as CRI-I = TC/HDLc and CRI-II = LDLc/HDLc. Atherogenic Index of Plasma (AIP) is a logarithmically transformed molar ratio of TG to HDLc (AIP= Log10 [TG/HDLc] ratio) (Dobiásová, Frohlich, Sedová, Cheung, & Brown, 2011). We utilized the atherogenic coefficient (AC), an indirect assessment of cholesterol found in lipoproteins: very low-density lipoprotein cholesterol (VLDLc), intermediate-density lipoprotein cholesterol (IDLc), and LDLc to the HDLc fraction. It is expressed mathematically as AC = (TC – HDLc)/HDLc or AC = (Non-HDLc)/HDLc (Bhardwaj et al., 2013).

The patients were also classified according to the values of AIP obtained into two groups: ESRD with a high risk of CVD (AIP>0.24) and low or medium risk of CVD (AIP<0.24) (Dobiasova, 2006).

Statistics

We employed the χ^2-test to examine the relationships among the nominal variables and the analysis of variance (ANOVA) to study group differences in continuous variables. In addition, we utilized Pearson's product-moment and Spearman's rank-order correlation coefficients to investigate the correlations between stromelysin-1 and TIMP1 and their ratio to all other biomarkers. Depending on the preceding study, we used neural network analysis to examine the relationship between the diagnosis (ESRD with a high risk of CVD (AIP>0.24)) and biomarkers as input variables (Moustafa & El-Seddek, 2020). In the current study, the neural network (NN) analysis of SPSS was used according to the manual of the software (https://www.ibm.com/products/spss-neural-networks). NN involves the nodes that are known as neurons. The neurons are structured into layers and connected using

variable connection weights. Each layer can have several different neurons with various transfer functions. While no one definition adequately describes the complete model family, the neural network is a massively parallel distributed processor with a natural predisposition for storing and making accessible experience knowledge (Gurney, 2018).

It mimics the brain in two ways: the network acquires information via a learning process, and the knowledge is stored using interneuron connection strengths known as synaptic weights (Ripley, 2007). The automated feedforward architecture, or multilayer perceptron neural network model, explored the link between biomarkers (input variables) and the diagnosis of high CVD risk (output variables). We used two hidden layers, each with up to four nodes, 20-50 epochs, and minibatch training using gradient descent to train the model's hidden layers. The halting condition was satisfied by a single, consecutive step with no further reduction in the error term. It was necessary to take three samples to ensure the final network was accurate: a holdout sample (6.8%), a training sample (71.2%); and a testing sample (22.0%); all of which were used to prevent overtraining. We calculated the error, the relative error, and the relevance and importance of each input variable. A priori power analysis conducted to compute the required sample size for a bivariate correlation, using a 2-tailed test at $\alpha=0.05$ and assuming an effect size of 0.26 with a power of 0.80, shows that the sample size should be 90. Power analysis for unequal sample sizes (ratio 2/1) shows that the analysis of parameter differences between 60 patients and 30 controls is > 0.8. We employed the IBM SPSS Windows version 27, 2017, to perform all statistics.

RESULTS

Demographic and Clinical Data

Table 1 displays the demographic and clinical information for the ESRD and healthy control groups**.** The results showed no significant difference in the demographic characteristics (age, sex ratio, tobacco use disorder (TUD), height, weight, body mass index (BMI), and family history) between ESRD patients and the healthy control group. The routinely measured parameters showed that ESRD is accompanied by high serum urea, creatinine, uric acid, phosphate, and a decrease in the eGFR in ESRD. The results of the lipid profile showed a state of dyslipidemia. There is an increase in TG ($p<0.001$), total cholesterol ($p=0.002$), HDLc ($p<0.001$), VLDLc ($p<0.001$), and LDLc ($p=0.001$), in addition to a significant increase in the atherogenic indices CRI-I, CRI-II, AC, and AIP (all $p<0.001$). Stromelysin-1 and TIMP1 in ESRD patients were also significantly elevated ($p=0.007$ and $p=0.005$, respectively) compared with the control group. In addition, the TIMP1/Stromelysin-1 ratio showed no significant difference among patients and healthy control.

Table 1
Demographic and clinical data of end-stage renal disease (ESRD) patients and healthy controls group

Parameter	Control	ESRD patients	F/χ^2	df	p
Age (year)	47.09±6.831	46.46±10.285	0.096	1/88	0.758
Sex F/M	11/19	28/32	2.015	1	0.156
Height cm	162.22±11.152	165.3±12.146	1.392	1/88	0.241
Weight kg	74.38±13.072	66.48±10.25	9.851	1/88	0.002
BMI kg/m^2	28.646±6.396	24.363±3.110	17.85	1/88	<0.001
TUD No/Yes	29/1	55/5	0.012	1	0.998
Duration of Disease Years	-	4.896±2.575	-	-	-
Family history No/Yes	30/0	54/6	3.679	1	0.055
Creatinine mg/dl	1.441±2.005	8.782±3.803	102.564	1/88	<0.001
Urea mg/dl	28.31±7.507	157.16±53.383	183.453	1/88	<0.001
Pi mg/dl	5.013±0.661	7.298±0.870	165.551	1/88	<0.001
Uric acid mg/dl	4.722±0.845	6.050±1.566	19.69	1/88	<0.001
TG mM	1.268±0.449	1.636±0.370	17.305	1/88	<0.001
Total cholesterol mM	5.142±0.602	5.606±0.688	10.094	1/88	0.002
HDLc mM	1.193±0.228	1.006±0.205	15.515	1/88	<0.001
VLDLc mM	0.577±0.205	0.747±0.169	17.599	1/88	<0.001
LDLc mM	3.373±0.508	3.852±0.660	12.572	1/88	0.001
CRI-I	4.532±1.287	5.782±1.305	18.829	1/88	<0.001
CRI-II	3.020±1.120	4.013±1.200	14.599	1/88	<0.001
AC	3.532±1.287	4.780±1.305	18.829	1/88	<0.001
AIP	0.016 ± 0.165	0.209±0.118	40.663	1/88	<0.001
eGFR mL/min /1.73 m^2	99.070(74.842-124.407)	6.396(4.673-10.141)	0.105	1/88	<0.001
Stromelysin-1 ng/ml	49.005(28.830-97.540)	73.804(50.596-115.046)	MWUT	1/88	0.007
TIMP1 ng/ml	530.360(215.970-862.799)	725.953(526.173-1056.849)	MWUT	1/88	0.005
TIMP1/Stromelysin-1	9.600(5.010-17.953)	8.955(5.014-16.324)	MWUT	1/88	0.742

Note. [A, B, C]: Pairwise comparison, BMI: Body mass index, TUD: Tobacco use disorder, eGFR: estimated glomerular filtration rate, Pi: inorganic phosphate, TIMP1: tissue inhibitors of metalloproteinase-1, TC: Total cholesterol, TG: triglycerides, HDLc: high-density lipoprotein cholesterol, LDLc: low-density lipoprotein cholesterol, VLDLc: very-low-density lipoprotein cholesterol, CRI-I and CRI-II: Castelli's Risk index I & 2, respectively, AC: Atherogenic coefficient, AIP: atherogenic index of plasma.

Correlation Between Stromelysin-1, TIMP1, and TIMP1/stromelysin-1 with All Parameters

Stromelysin-1 significantly correlates with creatinine (ρ=0.257, $p<0.05$), urea (ρ=0.269, $p<0.05$), inorganic phosphate (Pi) (ρ=0.241, $p<0.05$), TIMP1 (ρ=347, $p<0.01$), TG (ρ=0.367, $p<0.01$), total cholesterol (ρ=0.252, $p<0.05$), VLDLc (ρ=0.366, $p<0.01$), LDLc

(ρ=0.226, p<0.05), CRI-I (ρ=0.291, p<0.01), CRI-II (ρ=0.250, p<0.05), AC (ρ=0.291, p<0.01), and AIP (ρ=0.397, p<0.01) (Table 2). In contrast, an inverse correlation was found between stromelysin-1 with TIMP1/stromelysin-1 ratio (ρ=-0.348, p<0.01), and eGFR (ρ=-0.224, p<0.05). Serum TIMP1 level significantly correlates with height (ρ=0.267, p<0.05), weight (ρ=0.224, p<0.05), TIMP1/Stromelysin-1 ratio (ρ=0.605, p<0.001), TG (ρ=0.435, p<0.01), total cholesterol (ρ=0.211, p<0.05), VLDLc (ρ=0.435, p<0.01), CRI-I (ρ=0.240, p<0.05), AC (ρ=0.240, p<0.05),, and AIP (ρ=0.427, p<0.01).

Table 2
Correlation of Stromelysin-1, : tissue inhibitors of metalloproteinase-1 (TIMP1), and their ratio with all other parameters

Parameters	Stromelysin-1	TIMP1	TIMP1/Stromelysin-1
Sex	0.059	0.15	0.037
Age	-0.127	0.095	0.081
TUD	0.087	0.182	0.033
Family history	0.045	0.099	-0.025
Duration of Dis	0.132	0.121	0.019
Height	0.017	0.267*	0.111
Weight	-0.024	0.224*	0.167
BMI	-0.018	0.113	0.072
Creatinine	0.257*	-0.015	-0.026
Urea	0.269*	0.067	0.093
Pi	0.241*	0.068	0.028
Uric acid	0.009	0.111	0.010
Stromelysin-1	1.000	0.347**	-0.348**
TIMP1	0.347**	1.000	0.605**
TIMP1/Stromelysin	-0.348-**	0.605**	1.000
TG	0.367**	0.435**	0.183
Total cholesterol	0.252*	0.211*	0.032
HDLc	-0.186	-0.153	-0.041
VLDLc	0.366**	0.438**	0.186
LDLc	0.226*	0.164	0.018
CRI-I	0.291**	0.240*	0.071
CRI-II	0.250*	0.186	0.044
AC	0.291**	0.240*	0.071
AIP=Log(TG/HDL)	0.397**	0.427**	0.205
eGFR	-0.224*	-0.180	0.024

Note. BMI: Body mass index, TUD: Tobacco use disorder, eGFR: estimated glomerular filtration rate, Pi: inorganic phosphate, TIMP1: tissue inhibitors of metalloproteinase-1, TC: Total cholesterol, TG: triglycerides, HDLc: high-density lipoprotein cholesterol, LDLc: low-density lipoprotein cholesterol, VLDLc: very-low-density lipoprotein cholesterol, CRI-I, and CRI-II: Castelli's Risk index I & 2, respectively, AC: Atherogenic coefficient, AIP: atherogenic index of plasma.

Neural Network Study

The results of neural network information of the model on ESRD patients for predicting ESRD patients with a high risk of CVD (AIP>0.24) versus ESRD patients with low or medium risk of CVD (AIP<0.24) are presented in Table 3. The NN analysis used feedforward architecture because the network connections flow from the input layer to the output layer without any feedback loops. In this analysis, the input layer contains the predictors. The hidden layer contains unobservable nodes or units. The value of each hidden unit is some function of the predictors; the exact form of the function depends in part upon the network type and part upon user-controllable specifications. The last layer is the output layer contains the responses. Since the history of default is a categorical variable with two categories, it is recorded as two indicator variables. Each output unit is some function of the hidden units.

Again, the exact form of the function depends partly on the network type and controllable specifications. There are 8 units (measured parameters) in the input layer (layer containing factors for predicting the CVD risk). The hyperbolic tangent and identity were used as activation functions in the hidden layers, and identity was used in the output

Table 3
The results of neural networks with ESRD with a high risk of CVD (AIP>0.24) and low or medium risk of CVD high disease activity (AIP<0.24) as the reference group

	Models	**AIP>0.24 *vs.* AIP<0.24**
Input Layer	Number of units	8
	Rescaling method	Normalized
Hidden layers	Number of hidden layers	2
	Number of units in hidden layer 1	3
	Number of units in hidden layer 2	2
	Activation Function	Hyperbolic tangent
Output layer	Dependent variables	AIP>0.24 ***vs.*** AIP<0.24
	Number of units	2
	Activation function	Identity
	Error function	Sum of squares
Training	The sum of the squares error term	7.594
	% Incorrect or relative error	31.7%
	Prediction (sensitivity, specificity)	58%, 75.6%
Testing	The sum of Squares error	1.826
	% Incorrect or relative error	7.7%
	Prediction (sensitivity, specificity)	80.0%, 100%
	AUC ROC	0.833
Holdout	% Incorrect or relative error	40.0%
	Prediction (sensitivity, specificity)	33.3%, 100%

Note. AUC ROC: area under the curve of receiver operating curve

layer to train this model, which has two hidden layers with three units in layer 1 and two units in layer 2. The area under the curve (AUC) of the receiver operating characteristic (ROC) was 0.833, with a sensitivity of 80 % and a specificity of 100 %, in each of the three data sets. It is shown in Figure 1 how significant each of the model's input variables is in terms of the model's predictive ability. In terms of predictive capability, stromelysin-1 is the best model (100%) for the prediction of high-risk CVD, followed by eGFR (77.9%), TIMP1 (66.0%), TIMP1/Stromelysin-1 (30.7%), creatinine (29.7%), urea (21.1%), Uric acid (6.6%), and Pi 1.1%.

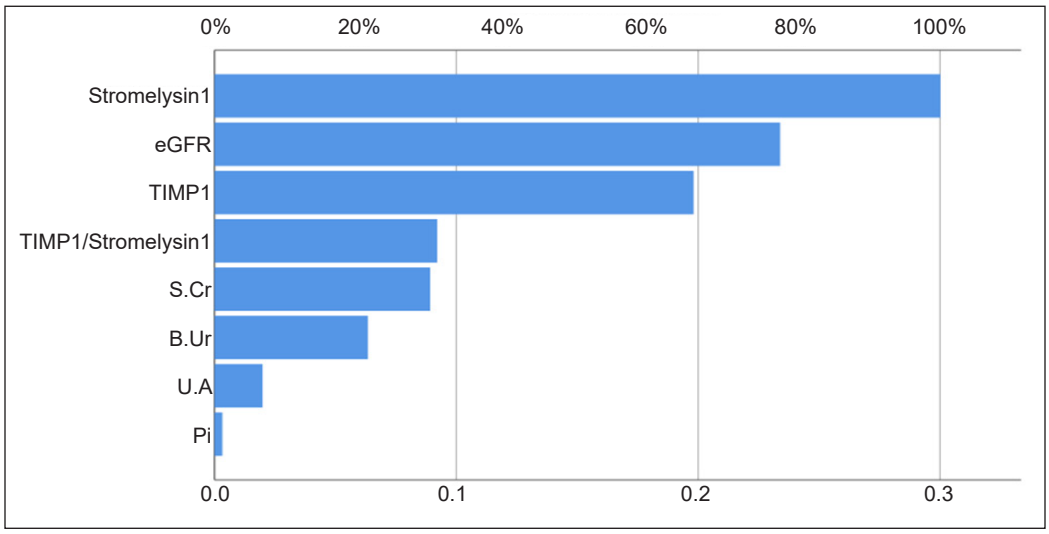

Figure 1. The importance of the biomarkers for predicting end-stage renal disease (ESRD) patients with a high risk of cardiovascular diseases by neural network analysis.
Note. Pi: inorganic phosphate; S.Cr: serum creatinine; B.Ur: blood urea; UA: uric acid; eGFR: estimated GFR; TIMP1: tissue inhibitors of metalloproteinase-1

DISCUSSION

The state of dyslipidemia in ESRD patients represents the first key finding of the current study, as seen in Table 1. Dyslipidemia is expressed as hypercholesterolemia, hypertriglyceridemia, and hypoalphalipoproteinemia (low HDLc), reflecting the increased incidence of dyslipidemia consequences, especially CVD and renal disease progression (Mesquita et al., 2010). The increase in the atherogenic indices CRI-I, CRI-II, AC, and AIP confirms our patients' CVD risk. Chronic inflammation and atherogenic dyslipidemia have long been implicated as key risk factors for CVD mortality and morbidity in individuals with ESRD (Shifris, 2020). Once hemodialysis commences in ESRD patients, they develop an atherogenic serum lipid profile. Total cholesterol, LDLc, TG, and VLDLc levels were elevated in regular hemodialysis patients compared to irregular hemodialysis patients (Maurya et al., 2018).

The increasing number of dialysis sessions is associated increase in the level of TC and LDLc, TG, and VLDLc levels in regular chronic renal failure (CRF) patients indicating the bad prognosis of hemodialysis on the levels of lipid profile parameters. HDLc level decreases as compared to irregular hemodialysis patients. Patients on hemodialysis must be treated for dyslipidemia to avoid CVD (Maurya et al., 2018). Dyslipidemias are present in male and female CRF patients regardless of sex, and the hemodialysis procedure does not affect this (Sharma, Shah, Gorasia, & Baria, 2012). There are a variety of mechanisms through which circulating fatty acids or saturated fats, which may accumulate in the kidneys, might cause renal lipotoxicity (Lin & Duann, 2020). When there is inflammation and fibrosis in the kidney, renal lipotoxicity may lead to oxidative stress and albuminuria and control the intracellular signaling pathways in renal lipid metabolism (Nishi et al., 2019). Renal tubular epithelial cells are critical to developing renal fibrosis due to incomplete fatty acid oxidation (Kang et al., 2015).

Another major finding in the current research is that stromelysin-1 and TIMP1 were significantly increased in ESRD patients compared to healthy control, as seen in Table 1. The current findings are consistent with a prior study indicating that ESRD patients (before and after hemodialysis) showed an increase in several MMPs, including stromelysin-1, and two TMP inhibitors of MMPs, including TIMP1 (Velasquez-Mao et al., 2021). After dialysis, stromelysin-1 decreased on average in those patients (Velasquez-Mao et al., 2021). Serum stromelysin-1 is probably a substantial predictor of chronic inflammation (Ishizaki, Matsunaga, Adachi, & Miyashita, 2004). All dialyzed patients had considerably higher median TIMP1 values than controls (Musiał & Zwolińska, 2011). Stromelysin-1 is suggested to be involved in the pathophysiology of CKD (Andreucci et al., 2021) because it is increased in hemodialysis patients (Preston et al., 2002). Since recent studies have shown a tight relationship between the MMP/TIMP system and oxidative stress and inflammation in hemodialysis patients, several putative dialysis-related trigger factors may be responsible for ESRD (Pawlak et al., 2005). The proteolytic activity of MMPs, including stromelysin-1, is controlled by endogenous inhibitors, especially TIMP1 (Tan & Liu, 2012). TIMP1 has an erythroid potentiating activity, B cell apoptosis suppression activity, and its inhibitory effect on MMPs (Stetler-Stevenson, 2008). Therefore, the elevation of MMP3 and TIMP1 results from increasing inflammation and blood homeostasis, which are important factors in CVD development (Cui, Hu, & Khalil, 2017; Sarnak et al., 2003).

Table 2 showed several important correlations between stromelysin-1, TIMP1, and their ratio with other measured parameters in ESRD patients. The link between stromelysin-1 and its inhibitor TIMP1 and lipid-associated oxidative stress indicators can be used to extract the relationship between lipid profile parameters and the abovementioned parameters. It is found that oxidative stress activates MMPs (Jacob-Ferreira et al., 2013; Martínez & Andriantsitohaina, 2009) and increases MMP-3 protein levels in human cell lines (Alge-

Priglinger et al., 2009) and disease (Chung et al., 2013). Also, increased stromelysin-1 levels are found in inflammatory diseases (Geneva-Popova, Popova-Belova, Popova, Chompalov, & Batalov, 2022; Marônek et al., 2021). It is found that oxidative stress activates latent resident myocardial MMPs (Hunt et al., 2002). Nitric oxide and oxidative stress can disturb the cysteine switch leading to converting proMMPs to activate MMPs (Gaffney, Solomonov, Zehorai, & Sagi, 2015). TIMP-1, which resides in the catalytic site of MMP, thus, regulates activity (Zakiyanov et al., 2019). Protein degradation by TIMPs can be influenced by the relative amounts of enzymes in action and their inhibitors in the body (Arpino, Brock, & Gill, 2015).

Stromelysin-1 was more highly linked with tubular atrophy and interstitial lesions than mesangial expansion and glomerular damage (Suzuki et al., 1997). Serum stromelysin-1 levels correlate significantly with disease duration (NAGANUMA et al., 2008a). High BMI and central obesity are linked to an increased risk of CKD. A higher waist-to-hip ratio was linked to lower GFR, lower effective renal plasma flow, and a higher filtration percent, which was revealed by multivariate analysis. The same results were obtained after adjusting for sex, age, mean arterial pressure, and BMI (Kwakernaak et al., 2013). The pathogenesis of kidney injury may be influenced by inflammation, oxidative stress, endothelial dysfunction, prothrombotic state, hypervolemia, adipokine derangements, and obesity (Kazancioğlu, 2013; Mirrakhimov, 2012).

The neural network results in Table 3 indicated good predictability of the measured parameters (lipid profile parameter excluded) in discriminating between ESRD patients with high risk for CVD and lower-risk patients. Stromelysin-1, followed by eGFR, TIMP1, and the TIMP-1/stromelysin-1 ratio, are the top four parameters validated for predicting ESRD patients with a high risk of CVD seen in Figure 1. In previous work, significantly higher plasma levels of TIMP1 were observed in individuals with CVD (Peeters et al., 2015). Before starting dialysis, individuals with ESRD have a higher risk of CVD, but after starting dialysis, their dyslipidemia becomes better. Additionally, to improve the quality of life of CKD patients in terms of the non-development of risk factors for cardiovascular diseases, adequate dialysis treatment and timely monitoring of lipid profile should be done in conjunction with other modes of therapy such as a properly advised diet, modifications to lifestyle, and treatment that lowers lipid levels (Saini et al., 2021).

A new biomarker of atherosclerosis and CVD is AIP, and the relevant studies revealed that AIP accurately predicts CVD more than routine lipid profile (Essiarab, Taki, Lebrazi, Sabri, & Saile, 2014). Patients on peritoneal dialysis had significantly greater AIPs, which were found to be related to peritoneal dialysis (Lee et al., 2017). AIP was significantly increased in ESRD patients (Erdur et al., 2013). In males, higher serum TG and AIP levels were shown to be related to a substantial deterioration in renal function. In women, neither

serum lipids nor AIP was associated with significant kidney function declines (Huang et al., 2021). Serum lipid profile components (TC, TG, HDLc, and LDLc) are a less reliable predictor of CVD risk than CRI-I and CRI-II, which have similar risk evaluations (Bhardwaj et al., 2013). Higher serum TG/HDLc ratio was associated with an increased risk of all-cause and CVD mortality in ESRD patients undergoing peritoneal dialysis. A simple criterion based on these findings could be used to identify people with a higher-than-average risk of cardiovascular mortality (Wu et al., 2015). ESRD patients' pericarditis and pericardial effusion are often caused by toxic metabolites building up, increased albuminuria, decreased creatinine clearance, and difficulties maintaining normal blood pressure during dialysis (Rehman et al., 2017).

Another cause of the increased risk of CVD in ESRD patients is the elevation in serum urea. CKD patients with elevated serum urea levels had a higher risk of CVD outcomes and death (Laville et al., 2022). Various metabolites may generate or be absorbed due to elevated serum urea levels, leading to malnutrition, inflammation, and uremic toxicity (Crespo-Salgado et al., 2016). TIMP1 is expressed in human glomeruli and is upregulated in glomerulosclerosis (Carome et al., 1993). Even though TIMP1 overexpression is present in fibrosis and may contribute to it in the absence of MMP inhibition, TIMP1 deletion cannot stop it since other TIMPs are likely compensating by upregulating. Thus, it cannot be prevented (Kim et al., 2001). Patients with diabetic kidney disease (DKD) have MMP/TIMP modulation abnormalities in clinical studies. The dysregulation of MMP/TIMP is documented in clinical research conducted on DKD patients. In patients with DKD, increasing glomerular lesions are associated with reductions in serum TIMP1 and TIMP-2 levels and increases in serum and urine TIMP1 levels (Mora-Gutiérrez et al., 2020; Rysz et al., 2007).

CONCLUSION

There is a state of dyslipidemia with high atherogenic indices and increased stromelysin-1 and TIMP1 in ESRD patients. The increase in stromelysin-1 and its inhibitor are correlated with some atherogenic indices and lipids. The neural network results indicated good predictability of the top four parameters (stromelysin-1, followed by eGFR, TIMP1, and the TIMP-1/stromelysin-1 ratio) in discriminating between ESRD patients with high risk for CVD from the lower-risk patients.

ACKNOWLEDGMENTS

We thank the personnel of Al-Sadr Teaching Hospital in Najaf governorate, Iraq, for their assistance in collecting samples. We also appreciate the hospital's highly trained internal lab personnel for their assistance in determining biomarker levels.

REFERENCES

Alge-Priglinger, C. S., Kreutzer, T., Obholzer, K., Wolf, A., Mempel, M., Kernt, M., Kampik, A., & Priglinger, S. G. (2009). Oxidative Stress-Mediated Induction of MMP-1 and MMP-3 in Human RPE Cells. *Investigative Ophthalmology & Visual Science, 50*(11), 5495-5503. https://doi.org/10.1167/iovs.08-3193

Altemtam, N., El Nahas, M., & Johnson, T. (2012). Urinary matrix metalloproteinase activity in diabetic kidney disease: A potential marker of disease progression. *Nephron Extra, 2*(1), 219-232. https://doi.org/10.1159/000339645

Andreucci, M., Provenzano, M., Faga, T., Michael, A., Patella, G., Mastroroberto, P., Serraino, G. F., Bracale, U. M., lelapi, N., & Serra, R. (2021). Aortic Aneurysms, Chronic Kidney Disease and Metalloproteinases. *Biomolecules, 11*(2), Article 194. https://doi.org/10.3390%2Fbiom11020194

Arpino, V., Brock, M., & Gill, S. E. (2015). The role of TIMPs in regulation of extracellular matrix proteolysis. *Matrix Biology, 44-46*, 247-254. https://doi.org/10.1016/j.matbio.2015.03.005

Benjamin, O., & Lappin, S. L. (2021). *End-Stage Renal Disease*. StatPearls Publishing.

Bhardwaj, S., Bhattacharjee, J., Bhatnagar, M. K., & M., Tyagi, S. (2013). Atherogenic index of plasma, castelli risk index and atherogenic coefficient-new parameters in assessing cardiovascular risk. *International Journal of Pharmacy and Biological Science, 3*(3), 359-364.

Bikbov, B., Purcell, C. A., Levey, A. S., Smith, M., Abdoli, A., Abebe, M., Adebayo, O. M., Afarideh, A., Agarwal, S. K., Agudelo-Botero, M., Ahmadian, E., Al-Aly, Z., Alipour, V., Almasi-Hashiani, A., Al-Raddadi, R. M., Alvis-Guzman, N., Amini, S., Andrei, T., Andrei, C. L., … & Murray, C. J. L. (2020). Global, regional, and national burden of chronic kidney disease, 1990–2017: A systematic analysis for the Global Burden of Disease Study 2017. *The Lancet, 395*(10225), 709-733. https://doi.org/10.1016/S0140-6736(20)30045-3

Carome, M. A., Striker, L. J., Peten, E. P., Moore, J., Yang, C. W., Stetler-Stevenson, W. G., & Striker, G. E. (1993). Human glomeruli express TIMP-1 mRNA and TIMP-2 protein and mRNA. *American Journal of Physiology-Renal Physiology, 264*(6), F923-F929. https://doi.org/10.1152/ajprenal.1993.264.6.F923

Castelli, W. P., Abbott, R. D., & McNamara, P. M. (1983). Summary estimates of cholesterol used to predict coronary heart disease. *Circulation, 67*(4), 730-734. https://doi.org/10.1161/01.CIR.67.4.730

Cheng, Z., Limbu, M. H., Wang, Z., Liu, J., Liu, L., Zhang, X., Chen, P., & Liu, B. (2017). MMP-2 and 9 in Chronic Kidney Disease. *International Journal of Molecular Sciences, 18*(4), Article 776. doi:10.3390/ijms18040776

Chung, Y. C., Kim, Y. S., Bok, E., Yune, T. Y., Maeng, S., & Jin, B. K. (2013). MMP-3 contributes to nigrostriatal dopaminergic neuronal loss, BBB damage, and neuroinflammation in an MPTP mouse model of Parkinson's disease. *Mediators of Inflammation, 13,* Article 370526. https://doi.org/10.1155/2013/370526

Cozzolino, M., Mangano, M., Stucchi, A., Ciceri, P., Conte, F., & Galassi, A. (2018). Cardiovascular disease in dialysis patients. *Nephrology Dialysis Transplantation, 33*(suppl_3), iii28-iii34. https://doi.org/10.1093/ndt/gfy174

Crespo-Salgado, J., Vehaskari, V. M., Stewart, T., Ferris, M., Zhang, Q., Wang, G., Blanchard, E. E., Taylor, C. M., Kallash, M., Greenbaum, L. A., & Aviles, D. H. (2016). Intestinal microbiota in pediatric patients

with end stage renal disease: A midwest pediatric nephrology consortium study. *Microbiome, 4*, Article 50. https://doi.org/10.1186/s40168-016-0195-9

Cui, N., Hu, M., & Khalil, R. A. (2017). Biochemical and biological attributes of matrix metalloproteinases. *Progress in Molecular Biology and Translational Science, 147*, 1-73. https://doi.org/10.1016/bs.pmbts.2017.02.005

Dobiasova, M. (2006). AIP-Atherogenic index of plasma as a significant predictor of cardiovascular risk: From research to practice. *Vnitrni lekarstvi, 52*(1), 64-71.

Dobiásová, M., Frohlich, J., Sedová, M., Cheung, M. C., & Brown, B. G. (2011). Cholesterol esterification and atherogenic index of plasma correlate with lipoprotein size and findings on coronary angiography. *Journal of Lipid Research, 52*(3), 566-571. https://doi.org/10.1194/jlr.P011668

Erdur, M. F., Tonbul, H. Z., Ozbiner, H., Ozcicek, A., Ozcicek, F., Akbas, E. M., Ozbek, O., Hamur, H., & Turkmen, K. (2013). The relationship between atherogenic index of plasma and epicardial adipose tissue in hemodialysis and peritoneal dialysis patients. *Renal Failure, 35*(9), 1193-1198. https://doi.org/10.3109/0886022X.2013.823826

Essiarab, F., Taki, H., Lebrazi, H., Sabri, M., & Saile, R. (2014). Usefulness of lipid ratios and atherogenic index of plasma in obese Moroccan women with or without metabolic syndrome. *Ethnicity & Disease, 24*(2), 207-212.

Friedewald, W. T., Levy, R. I., & Fredrickson, D. S. (1972). Estimation of the concentration of low-density lipoprotein cholesterol in plasma, without use of the preparative ultracentrifuge. *Clinical Chemistry, 18*(6), 499-502. https://doi.org/10.1093/clinchem/18.6.499

Gaffney, J., Solomonov, I., Zehorai, E., & Sagi, I. (2015). Multilevel regulation of matrix metalloproteinases in tissue homeostasis indicates their molecular specificity *in vivo*. *Matrix Biology, 44-46*, 191-199.

Geneva-Popova, M., Popova-Belova, S., Popova, V., Chompalov, K., & Batalov, A. (2022). Assessment of serum and synovial fluid MMP-3 and MPO as biomarkers for psoriatic arthritis and their relation to disease activity indices. *Rheumatology International*, *42*, 1605-1615. https://doi.org/10.1007/s00296-022-05159-4

Gillespie, F., Amicosante, A., Lo Scalzo, A., Chiarolla, E., Ondei, P., Paone, S., & Cerbo, M. (2015). *Adapted HTA report: Valutazione HTA delle ModalitÀ di dialisi in Italia*. [Report adaptation: Health technology assessment of the different dialysis modalities in Italy]. National Agency for Regional Health Services Rome, Italy.

Gregg, L. P., & Hedayati, S. S. (2018). Management of traditional cardiovascular risk factors in CKD: What are the data? *American Journal of Kidney Diseases, 72*(5), 728-744. https://doi.org/10.1053/j.ajkd.2017.12.007

Gurney, K. (2018). *An Introduction to Neural Networks*. CRC press. https://doi.org/10.1201/9781315273570

Haas, T. L., Davis, S. J., & Madri, J. A. (1998). Three-dimensional type I collagen lattices induce coordinate expression of matrix metalloproteinases MT1-MMP and MMP-2 in microvascular endothelial cells. *Journal of Biological Chemistry, 273*(6), 3604-3610. https://doi.org/10.1074/jbc.273.6.3604

Hamze, A. B., Wei, S., Bahudhanapati, H., Kota, S., Acharya, K. R., & Brew, K. (2007). Constraining specificity in the N-domain of tissue inhibitor of metalloproteinases-1; gelatinase-selective inhibitors. *Protein Science, 16*(9), 1905-1913. https://doi.org/10.1110/ps.072978507

Hibbs, M. S., Hoidal, J. R., & Kang, A. H. (1987). Expression of a metalloproteinase that degrades native type V collagen and denatured collagens by cultured human alveolar macrophages. *The Journal of Clinical Investigation, 80*(6), 1644-1650. https://doi.org/10.1172/JCI113253

Huang, F., Wang, L., Zhang, Q., Wan, Z., Hu, L., Xu, R., Cheng, A., Lv, Y., & Liu, Q. (2021). Elevated atherogenic index and higher triglyceride increase risk of kidney function decline: A 7-year cohort study in Chinese adults. *Renal Failure, 43*(1), 32-39. https://doi.org/10.1080/0886022X.2020.1853569

Hunt, M. J., Aru, G. M., Hayden, M. R., Moore, C. K., Hoit, B. D., & Tyagi, S. C. (2002). Induction of oxidative stress and disintegrin metalloproteinase in human heart end-stage failure. *American Journal of Physiology-Lung Cellular and Molecular Physiology, 283*(2), L239-L245. https://doi.org/10.1152/ajplung.00001.2002

Ishizaki, M., Matsunaga, T., Adachi, K., & Miyashita, E. (2004). Serum matrix metalloproteinase-3 in hemodialysis patients with dialysis-related amyloidosis. *Hemodialysis International, 8*(3), 219-225. doi:https://doi.org/10.1111/j.1492-7535.2004.01099.x

Iyer, R. P., Patterson, N. L., Fields, G. B., & Lindsey, M. L. (2012). The history of matrix metalloproteinases: milestones, myths, and misperceptions. *American Journal of Physiology-Heart and Circulatory Physiology, 303*(8), H919-H930. https://doi.org/10.1152/ajpheart.00577.2012

Jacob-Ferreira, A. L., Kondo, M. Y., Baral, P. K., James, M. N. G., Holt, A., Fan, X., & Schulz, R. (2013). Phosphorylation status of 72 kDa MMP-2 determines its structure and activity in response to peroxynitrite. *PLoS One, 8*(8), Article e71794. https://doi.org/10.1371/journal.pone.0071794

Kageyama, Y., Miyamoto, S., Ozeki, T., Hiyoshi, M., Suzuki, M., & Nagano, A. (2000). Levels of rheumatoid factor isotypes, metalloproteinase-3 and tissue inhibitor of metalloproteinase-1 in synovial fluid from various arthritides. *Clinical Rheumatology, 19*, 14-20. https://doi.org/10.1007/s100670050004

Kang, H. M., Ahn, S. H., Choi, P., Ko, Y.-A., Han, S. H., Chinga, F., Park, A. S. D., Tao, J., Sharma, K., Pullman, J., Bottinger, E. P., Goldberg, I. J., & Susztak, K. (2015). Defective fatty acid oxidation in renal tubular epithelial cells has a key role in kidney fibrosis development. *Nature Medicine, 21*(1), 37-46. https://doi.org/10.1038/nm.3762

Kazancioğlu, R. (2013). Risk factors for chronic kidney disease: An update. *Kidney International Supplements, 3*(4), 368-371. https://doi.org/10.1038%2Fkisup.2013.79

Kim, H., Oda, T., Lopez-Guisa, J., Wing, D., Edwards, D. R., Soloway, P. D., & Eddy, A. A. (2001). TIMP-1 deficiency does not attenuate interstitial fibrosis in obstructive nephropathy. *Journal of the American Society of Nephrology, 12*(4), 736-748.

Kochan, Z., Szupryczynska, N., Malgorzewicz, S., & Karbowska, J. (2021). Dietary lipids and dyslipidemia in chronic kidney disease. *Nutrients, 13*(9), Article 3138. https://doi.org/10.3390/nu13093138

Kwakernaak, A. J., Zelle, D. M., Bakker, S. J. L., & Navis, G. (2013). Central body fat distribution associates with unfavorable renal hemodynamics independent of body mass index. *Journal of the American Society of Nephrology, 24*(6), 987-994. https://doi.org/10.1681/asn.2012050460

Laville, S. M., Couturier, A., Lambert, O., Metzger, M., Mansencal, N., Jacquelinet, C., Laville, M., Frimat, L., Fouque, D., Combe, C., Robinson, B. M., Stengel, B., Liabeuf, S., Massy, Z. A. (2022). Urea levels and cardiovascular disease in patients with chronic kidney disease. *Nephrology Dialysis Transplantation*, *38*(1), 184-192. https://doi.org/10.1093/ndt/gfac045

Lee, M. J., Park, J. T., Han, S. H., Kim, Y. L., Kim, Y. S., Yang, C. W., Kim, N. H., Kang, S. W., Kim, H. J., & Yoo, T. H. (2017). The atherogenic index of plasma and the risk of mortality in incident dialysis patients: Results from a nationwide prospective cohort in Korea. *PloS One, 12*(5), Article e0177499. https://doi.org/10.1371/journal.pone.0177499

Levey, A. S., Coresh, J., Greene, T., Marsh, J., Stevens, L. A., Kusek, J. W., & Lente, F. V. (2007) Expressing the modification of diet in renal disease study equation for estimating glomerular filtration rate with standardized serum creatinine values. *Clinical Chemistry, 53*(4), 766-772. https://doi.org/10.1373/clinchem.2006.077180

Levin, A., Tonelli, M., Bonventre, J., Coresh, J., Donner, J.-A., Fogo, A. B., Fox, C. S., Gansevoort, R. T., Heerspink, H. J. L., Jardine, M., Kasiske, B., Köttgen, A., Kretzler, M., Levey, A. S., Luyckx, V. A., Mehta, R., Moe, O., Obrador, G., Pannu, N., … & Eckardt, K. U. (2017). Global kidney health 2017 and beyond: a roadmap for closing gaps in care, research, and policy. *The Lancet, 390*(10105), 1888-1917. https://doi.org/10.1016/S0140-6736(17)30788-2

Liang, X., Ye, M., Tao, M., Zheng, D., Cai, R., Zhu, Y., Jin, J., & He, Q. (2020). The association between dyslipidemia and the incidence of chronic kidney disease in the general Zhejiang population: a retrospective study. *BMC Nephrology, 21*, Article 252. https://doi.org/10.1186/s12882-020-01907-5

Lin, P. H., & Duann, P. (2020). Dyslipidemia in kidney disorders: perspectives on mitochondria homeostasis and therapeutic opportunities. *Frontiers in Physiology*, *11,* Article 1050. https://doi.org/10.3389/fphys.2020.01050

Marchant, D. J., Bellac, C. L., Moraes, T. J., Wadsworth, S. J., Dufour, A., Butler, G. S., Bilawchuk, L. M., Hendry, R. G., Robertson, A.G., Cheung, C. T., Ng, J., Ang, L., Luo, Z., Heilbron., K., Norris, M. J., Duan, W., Bucyk, T., Karpov, A., Devel, L., ... & Overall, C. M. (2014). A new transcriptional role for matrix metalloproteinase-12 in antiviral immunity. *Nature Medicine, 20*(5), 493-502. https://doi.org/10.1038/nm.3508

Marônek, M., Marafini, I., Gardlík, R., Link, R., Troncone, E., & Monteleone, G. (2021). Metalloproteinases in inflammatory bowel diseases. *Journal of Inflammation Research, 14*, 1029-1041.

Martin, D. C., Sanchez-Sweatman, O. H., Ho, A., Inderdeo, D. S., Tsao, M.-S., & Khokha, R. (1999). Transgenic TIMP-1 inhibits simian virus 40 T antigen-induced hepatocarcinogenesis by impairment of hepatocellular proliferation and tumor angiogenesis. *Laboratory Investigation; a Journal of Technical Methods and Pathology, 79*(2), 225-234.

Martínez, M. C., & Andriantsitohaina, R. (2009). Reactive nitrogen species: molecular mechanisms and potential significance in health and disease. *Antioxidants & Redox Signaling, 11*(3), 669-702.

Maurya, N. K., Sengar, N., & Arya, P. (2018). Impact of hemodialysis on lipid profile among chronic renal failure patients (Regular and Non Regular Haemodialysis). *The Pharma Innovation, 7*(4), 363-365.

Mesquita, J., Varela, A., & Medina, J. L. (2010). Dyslipidemia in renal disease: Causes, consequences and treatment. *Endocrinología y Nutrición, 57*(9), 440-448. https://doi.org/10.1016/j.endonu.2010.06.003

Mikolasevic, I., Žutelija, M., Mavrinac, V., & Orlic, L. (2017). Dyslipidemia in patients with chronic kidney disease: Etiology and management. *International Journal of Nephrology and Renovascular Disease, 10*, 35-45. https://doi.org/10.2147/ijnrd.s101808

Mirrakhimov, A. E. (2012). Obstructive sleep apnea and kidney disease: Is there any direct link? *Sleep and Breathing, 16*, 1009-1016.

Mora-Gutiérrez, J. M., Rodríguez, J. A., Fernández-Seara, M. A., Orbe, J., Escalada, F. J., Soler, M. J., Roblero, M. F. S., Riera, M., Páramo, J. A., & Garcia-Fernandez, N. (2020). MMP-10 is increased in early stage diabetic kidney disease and can be reduced by renin-angiotensin system blockade. *Scientific Reports, 10*, Article 26. https://doi.org/10.1038/s41598-019-56856-3

Moustafa, H. E. D. S., & El-Seddek, M. (2020). Accurate diagnosis of covid-19 based on deep neural networks and chest x-ray images. *Mansoura Engineering Journal, 45*(3), 11-15. https://doi.org/10.21608/bfemu.2020.30471.1001

Murphy, G., & Nagase, H. (2008). Progress in matrix metalloproteinase research. *Molecular Aspects of Medicine, 29*(5), 290-308. https://doi.org/10.1016/j.mam.2008.05.002

Musiał, K., & Zwolińska, D. (2011). Neutrophil gelatinase-associated lipocalin (NGAL) and matrix metalloproteinases as novel stress markers in children and young adults on chronic dialysis. *Cell Stress and Chaperones, 16*, 163-171. https://doi.org/10.1007/s12192-010-0228-4

Naganuma, T., Sugimura, K., Uchida, J., Taishiro, K., Yoshimura, R., Takemoto, Y., & Nakatani, T. (2008a). Increased levels of serum matrix metalloproteinase-3 in haemodialysis patients with dialysis-related amyloidosis. *Nephrology, 13*(2), 104-108. https://doi.org/10.1111/j.1440-1797.2007.00845.x

Naganuma, T., Sugimura, K., Uchida, J., Tashiro, K., Yoshimura, R., Takemoto, Y., & Nakatani, T. (2008b). Increased levels of serum matrix metalloproteinase-3 in haemodialysis patients with dialysis-related amyloidosis. *Nephrology, 13*(2), 104-108.

Neovius, M., Jacobson, S. H., Eriksson, J. K., Elinder, C.-G., & Hylander, B. (2014). Mortality in chronic kidney disease and renal replacement therapy: A population-based cohort study. *BMJ Open, 4*(2), Article e004251. https://doi.org/10.1136/bmjopen-2013-004251

Nishi, H., Higashihara, T., & Inagi, R. (2019). Lipotoxicity in kidney, heart, and skeletal muscle dysfunction. *Nutrients, 11*(7), Article 1664. https://doi.org/10.3390/nu11071664

Nolan, D., Kraus, W. E., Hauser, E., Li, Y.-J., Thompson, D. K., Johnson, J., Chen, H.-C., Nelson, S., Haynes, C., Gregory, S. G., Kraus, V. B., & Shah, S. H. (2013). Genome-wide linkage analysis of cardiovascular disease biomarkers in a large, multigenerational family. *PLoS One, 8*(8), Article e71779. https://doi.org/10.1371/journal.pone.0071779

Parrish, A. R. (2017). Matrix metalloproteinases in kidney disease: Role in pathogenesis and potential as a therapeutic target. *Progress In Molecular Biology And Translational Science, 148*, 31-65.

Pawlak, K., Pawlak, D., & Mysliwiec, M. (2005). Circulating β-chemokines and matrix metalloproteinase-9/tissue inhibitor of metalloproteinase-1 system in hemodialyzed patients–Role of oxidative stress. *Cytokine, 31*(1), 18-24. https://doi.org/10.1016/j.cyto.2004.12.020

Peeters, S. A., Engelen, L., Buijs, J., Chaturvedi, N., Fuller, J. H., Schalkwijk, C. G., & Stehouwer, C. D., & EURODIAB Prospective Complications Study Group (2015). Plasma levels of matrix metalloproteinase-2,-3,-10, and tissue inhibitor of metalloproteinase-1 are associated with vascular complications in patients with type 1 diabetes: the EURODIAB Prospective Complications Study. *Cardiovascular Diabetology, 14*(1), Article 31. https://doi.org/10.1186/s12933-015-0195-2

Preston, G. A., Barrett, C. V., Alcorta, D. A., Hogan, S. L., Dinwiddie, L., Jennette, J. C., & Falk, R. J. (2002). Serum Matrix Metalloproteinases MMP-2 and MMP-3 Levels in Dialysis Patients Vary Independently of CRP and IL-6 Levels. *Nephron, 92*(4), 817-823. https://doi.org/10.1159/000065464

Rahman, M., Yang, W., Akkina, S., Alper, A., Anderson, A. H., Appel, L. J., He, J., Raj, D. S., Schelling, J., Strauss, L., Teal, V., Rader, D. J., & CRIC Study Investigators. (2014). Relation of serum lipids and lipoproteins with progression of CKD: The CRIC study. *Clinical Journal of the American Society of Nephrology, 9*(7), 1190-1198. https://doi.org/10.2215/cjn.09320913

Rehman, K. A., Betancor, J., Xu, B., Kumar, A., Rivas, C. G., Sato, K., Wong, L. P., Asher, C. R., & Klein, A. L. (2017). Uremic pericarditis, pericardial effusion, and constrictive pericarditis in end-stage renal disease: Insights and pathophysiology. *Clinical Cardiology, 40*(10), 839-846. https://doi.org/10.1002/clc.22770

Ripley, B. D. (2007). *Pattern Recognition and Neural Networks*. Cambridge University Press. https://doi.org/10.1017/CBO9780511812651

Rosenstein, K., & Tannock, L. R. (2022). *Dyslipidemia in Chronic Kidney Disease*. In K. R. Feingold, B. Anawalt, M. R. Blackman, A. Boyce, G. Chrousos, E. Corpas, W. W. D. Herder, K. Dhatariya, K. Dungan, J. Hofland, S. Kalra, G. Kaltsas, N. Kapoor, C. Koch, P. Kopp, M. Korbonits, C. S. Kovacs, W. Kuohung, B. Laferrère & D. P. Wilson (Eds.), *Endotext [Internet]*. MDText.com, Inc.

Rydlova, M., Holubec, L., Ludvikova, M., Kalfert, D., Franekova, J., Povysil, C., & Ludvikova, M. (2008). Biological activity and clinical implications of the matrix metalloproteinases. *Anticancer Research, 28*(2B), 1389-1397.

Rysz, J., Banach, M., Stolarek, R. A., Pasnik, J., Cialkowska-Rysz, A., Koktysz, R., & Baj, Z. (2007). Serum matrix metalloproteinases MMP-2 and MMP-9 and metalloproteinase tissue inhibitors TIMP-1 and TIMP-2 in diabetic nephropathy. *Journal of Nephrology, 20*(4), 444-452.

Saini, M., Vamne, A., Kumar, V., & Chandel, M. (2021). Lipid Profile in Pre-dialysis and Post-dialysis End Stage Renal Disease Patients: A Cross-Sectional Comparative Study in Lucknow, India. *Cureus, 13*(9), 1-4.

Saran, R., Robinson, B., Abbott, K. C., Agodoa, L. Y., Albertus, P., Ayanian, J., Balkrishnan, R., Bragg-Gresham, J., Cao, J., Chen, J. L. T., Cope, E., Dharmarajan, S., Dietrich, X., Eckard, A., Eggers, P. W., Gaber, C., Gillen, D., Gipson, D., Gu, H., … & Shahinian, V. (2017). US renal data system 2016 annual data report: Epidemiology of kidney disease in the United States. *American Journal of Kidney Diseases, 69*(3), A7-A8. https://doi.org/10.1053/j.ajkd.2016.12.004

Sarnak, M. J., Levey, A. S., Schoolwerth, A. C., Coresh, J., Culleton, B., Hamm, L. L., McCullough, P. A., Kasiske, B. L., Kelepouris, E., Klag, M. J., Parfrey, P., Pfeffer, M., Raij, L., Spinosa, D. J., & Wilson, P. W. (2003). Kidney disease as a risk factor for development of cardiovascular disease: A statement from the American Heart Association Councils on Kidney in Cardiovascular Disease, High Blood Pressure Research, Clinical Cardiology, and Epidemiology and Prevention. *Hypertension, 42*(5), 1050-1065. https://doi.org/10.1161/01.HYP.0000102971.85504.7c

Sharma, H., Shah, T. J., Gorasia, J. H., & Baria, D. P. (2012). Lipid profile and lipoprotein (a) in chronic renal failure patients with and without hemodialysis. *International Journal of Medicine and Public Health, 2*(4), 28-31. https://dx.doi.org/10.5530/ijmedph.2.4.6

Shifris, I. (2020). Д²АБЕТИЧНИЙ СТАТУС, КОМОРБ²ДН²СТЬ ТА ВИЖИВАН²СТЬ ПАЦ²АНТ²В З ХРОН²ЧНОЮ ХВОРОБОЮ НИРОК VД СТАД²¯: КОГОРТНЕ ДОСЛ²ДЖЕННЯ [Diabetic status, comorbidity and survival in patients with chronic kidney disease stage 5: A cohort study]. *Problems of Endocrine Pathology, 72*(2), 95-103. https://doi.org/10.21856/j-PEP.2020.2.12

Steenkamp, R., Rao, A., & Roderick, P. (2015). UK renal registry 17th annual report: Chapter 5 survival and cause of death in UK adult patients on renal replacement therapy in 2013: National and centre-specific analyses. *Nephron, 129*(Suppl. 1), 99-129. https://doi.org/10.1159/000370275

Stenvinkel, P., Carrero, J. J., Axelsson, J., Lindholm, B., Heimbürger, O., & Massy, Z. (2008). Emerging biomarkers for evaluating cardiovascular risk in the chronic kidney disease patient: how do new pieces fit into the uremic puzzle? *Clinical Journal of the American Society of Nephrology, 3*(2), 505-521. https://doi.org/10.2215/cjn.03670807

Stetler-Stevenson, W. G. (2008). Tissue inhibitors of metalloproteinases in cell signaling: metalloproteinase-independent biological activities. *Science Signaling, 1*(27), Article re6. https://doi.org/10.1126/scisignal.127re6

Suzuki, D., Miyazaki, M., Jinde, K., Koji, T., Yagame, M., Endoh, M., Nomoto, K., & Sakai, H. (1997). In situ hybridization studies of matrix metalloproteinase-3, tissue inhibitor of metalloproteinase-1 and type IV collagen in diabetic nephropathy. *Kidney International, 52*(1), 111-119. https://doi.org/10.1038/ki.1997.310

Tan, R. J., & Liu, Y. (2012). Matrix metalloproteinases in kidney homeostasis and diseases. *American Journal of Physiology - Renal Physiology, 302*(11), F1351-1361. https://doi.org/10.1152/ajprenal.00037.2012

Theofilis, P., Vordoni, A., Koukoulaki, M., Vlachopanos, G., & Kalaitzidis, R. G. (2021). Dyslipidemia in chronic kidney disease: Contemporary concepts and future therapeutic perspectives. *American Journal of Nephrology*, *52*(9), 693-701. https://doi.org/10.1159/000518456

Thompson, S., James, M., Wiebe, N., Hemmelgarn, B., Manns, B., Klarenbach, S., & Tonelli, M. (2015). Cause of death in patients with reduced kidney function. *Journal of the American Society of Nephrology, 26*(10), 2504-2511. https://doi.org/10.1681/asn.2014070714

Tunbridge, M. J., & Jardine, A. G. (2021). Atherosclerotic vascular disease associated with chronic kidney disease. *Cardiology Clinics, 39*(3), 403-414. https://doi.org/10.1016/j.ccl.2021.04.011

Vaziri, N. D., Moradi, H., & Zhao, Y.-Y. (2022). Chapter 4 - Altered lipid metabolism and serum lipids in chronic kidney disease. In J. D. Kopple, S. G. Massry, K. Kalantar-Zadeh & D. Fouque (Eds.), *Nutritional Management of Renal Disease* (4th ed.) (pp. 43-60). Academic Press. https://doi.org/10.1016/B978-0-12-818540-7.00009-4

Velasquez-Mao, A. J., Velasquez, M. A., Hui, Z., Armas-Ayon, D., Wang, J., & Vandsburger, M. H. (2021). Hemodialysis exacerbates proteolytic imbalance and pro-fibrotic platelet dysfunction. *Scientific Reports, 11*, Article 11764. https://doi.org/10.1038/s41598-021-91416-8

Visconti, L., Benvenga, S., Lacquaniti, A., Cernaro, V., Bruzzese, A., Conti, G., Buemi, M., & Santoro, D. (2016). Lipid disorders in patients with renal failure: Role in cardiovascular events and progression of chronic kidney disease. *Journal of Clinical & Translational Endocrinology, 6*, 8-14. https://doi.org/10.1016%2Fj.jcte.2016.08.002

Wang, Y., Meagher, R. B., Ambati, S., Cheng, H., Ma, P., & Phillips, B. G. (2021). Patients with obstructive sleep apnea have altered levels of four cytokines associated with cardiovascular and kidney disease, but near normal levels with airways therapy. *Nature and Science Sleep, 13*, 457-466. https://doi.org/10.2147/NSS.S282869

Wu, H., Xiong, L., Xu, Q., Wu, J., Huang, R., Guo, Q., Mao, H., Yu, X., & Yang, X. (2015). Higher serum triglyceride to high-density lipoprotein cholesterol ratio was associated with increased cardiovascular mortality in female patients on peritoneal dialysis. *Nutrition, Metabolism and Cardiovascular Diseases, 25*(8), 749-755. https://doi.org/10.1016/j.numecd.2015.05.006

Zakiyanov, O., Kalousová, M., Zima, T., & Tesař, V. (2019). Matrix metalloproteinases in renal diseases: a critical appraisal. *Kidney and Blood Pressure Research, 44*(3), 298-330. https://doi.org/10.1159/000499876

Zhang, X., Xiang, C., Zhou, Y. H., Jiang, A., Qin, Y. Y., & He, J. (2014). Effect of statins on cardiovascular events in patients with mild to moderate chronic kidney disease: a systematic review and meta-analysis of randomized clinical trials. *BMC Cardiovascular Disorders, 14*, Article 19. https://doi.org/10.1186/1471-2261-14-19

Pertanika J. Sci. & Technol. 31 (4): 2089 - 2103 (2023)

PERTANIKA JOURNALS

SCIENCE & TECHNOLOGY

Journal homepage: http://www.pertanika.upm.edu.my/

An Instrument to Measure Perceived Cognitive, Affective, and Psychomotor (CAP) Learning for Online Laboratory in Technology and Engineering Courses

Sim Tze Ying[1], Ng Kok Mun[2]*, A'zraa Afhzan Ab Rahim[2], Mitra Mohd Addi[3] and Mashanum Osman[4]

[1]Centre for American Education, School of Interdisciplinary Studies, Sunway University, Bandar Sunway, 47500 Petaling Jaya, Selangor, Malaysia
[2]School of Electrical Engineering, College of Engineering, Universiti Teknologi MARA, UiTM, 40450 Shah Alam, Selangor, Malaysia
[3]School of Electrical Engineering, Faculty of Engineering, Universiti Teknologi Malaysia, 81310 UTM, Johor Bahru, Johor, Malaysia
[4]Faculty of Information Technology and Communication, Universiti Teknikal Malaysia Melaka, Hang Tuah Jaya, 76100 UTeM, Durian Tunggal, Melaka, Malaysia

ABSTRACT

The effectiveness of student learning in an online laboratory environment requires appropriate measurements from the cognitive, affective, and psychomotor (CAP) domains. However, current self-reporting perceived CAP instruments are general and focused on non-technical fields, hence unsuitable for comprehensively measuring and evaluating technology and engineering (TE) online laboratory courses. This work aims to develop and validate a new instrument to measure perceived CAP learning domains in technology and engineering (TE) online laboratory courses. An initial instrument with 22 questions to assess CAP attributes was developed based on adaptation and expert consultation. About 1414 questionnaires were deployed and obtained a response rate of 25%, which meets the requirement of a confidence level of 90% with a 5% error. Principal Component Analysis (PCA) and Exploratory Factor Analysis (EFA) were used to further reduce the items to 13. Items reliability was verified using Cronbach Alpha. The finalized items consist of 5 cognitive, 4 affective, and 4 psychomotor items. For cognitive, the five items relate to students' perception of self-directed learning, reproducing study guides

ARTICLE INFO

Article history:
Received: 09 August 2022
Accepted: 02 November 2022
Published: 13 June 2023

DOI: https://doi.org/10.47836/pjst.31.4.28

E-mail addresses:
tzeyings@sunway.edu.my (Sim Tze Ying)
ngkokmun@uitm.edu.my (Ng Kok Mun)
azraa@uitm.edu.my (A'zraa Afhzan Ab Rahim)
mitra@utm.my (Mitra MohdAddi)
mashanum@utem.edu.my (Mashanum Osman)
* Corresponding author

ISSN: 0128-7680
e-ISSN: 2231-8526

for future students, organizing their tasks and solving problems, relating lab works with fundamental concepts and theories, and completing all tasks. The four affective items are associated with students' perception of active involvement in learning, communication of findings, collaboration with team members, and awareness of safety and requirements. The four psychomotor items are linked to students' perceived attainment in performing the experiment, visualizing the procedure, demonstrating technical skills, and operating the equipment. The tool is verified to self-measure CAP attainment for online laboratories.

Keywords: Affective, bloom taxonomy, cognitive, instrument validation, learning domains, learning measurement, online laboratory, psychomotor

INTRODUCTION

A deadly virus (known as COVID-19), which started in Wuhan, China, has caused a worldwide pandemic (Nature News, 2020). The COVID-19 pandemic has led to the closure of many tertiary institutions to prevent the spread of the disease (Murphy, 2020). Many higher learning institutions in Malaysia quickly adopt e-learning under the online distance learning (ODL) mode (Tan, 2021). The ODL also includes laboratory courses using the traditional model of face-to-face instruction. In an online setting, some institutions have conducted laboratory courses via virtual labs, remote control labs, or video-based labs (Zhai et al., 2012). Virtual labs adopt the use of simulation tools and virtual reality. Remote laboratories enable students to access and perform experiments in the lab from remote areas. In contrast, video-based labs provide an overview of a physical lab for the students to visualize the whole experimental process and its outputs through a video demonstration. These methods were widely adopted during the pandemic period.

The emergence of any methods in teaching and learning, whether offline or online, places the need to evaluate student learning outcomes to evaluate the impact on learning. Hence, online laboratories may impact the learning outcomes and experiences that must be evaluated comprehensively. Chan and Fok (2009) measured students' perception of traditional and virtual laboratories on whether the laboratories are easy to understand, operate, flexible, stimulating, and satisfying. Kapilan et al. (2021) distributed a perception survey on mechanical engineering students' learning experiences in fluid mechanics virtual laboratories during the pandemic to gauge students' experience and cognitive learning, such as improvement in knowledge or skill set, the effectiveness of the virtual laboratories, the flow and usefulness of the course. Chowdury et al. (2019) developed nine questions to obtain students' feedback on the effectiveness of the delivery and students' learning experience for the online laboratory conducted via video demonstration and computer simulations.

One of the immediate challenges with online laboratories is the difficulty of achieving hands-on practical skills effectively (Gamage et al., 2020; Lewis, 2014). In addition, other

learning attributes need to be measured and evaluated, such as integrating theory with practice, experimental design and problem-solving skills, data recording and analysis; communication and interpersonal skills; technical judgment, and professional ethics (Davies, 2008). From a pedagogical perspective, these attributes can be categorized into cognitive, affective, and psychomotor (CAP) learning domains. These categories of learning in the cognitive, affective, and psychomotor domains were introduced by Bloom et al. (1956). A well-known definition of cognitive learning derived from Bloom et al. (1956) is "recall or recognition of knowledge and the development of intellectual abilities and skills." The cognitive domain includes knowledge, comprehension, application of knowledge to solve a problem, analysis; evaluation; and knowledge creation (Anderson et al., 2001). Affective learning is "an increasing internalization of positive attitudes toward the content or subject matter" (Kearney, 1994). The affective domain focuses on developing attitudes and behavior, consisting of five attributes: interests, opinions, emotions, attitudes, and values (Anderson et al., 2001; Krathwohl et al., 1964). Simpson (1974) defined the psychomotor domain as having five attributes: detecting cues to response (perception), performing a specific act under guidance (guided response); performing a learned task independently (a mechanism); performing a complex action; altering an act to respond to a new situation (adaptation), and the developing new acts (origination).

The immediate challenge is measuring CAP learning independent of the course content, instructor, student grades, institution, academic level, and other limiting factors. Rovai et al. (2009) developed a self-reporting instrument to measure perceived CAP learning that gathers student perception on these domains to address this. It is measured from the student's viewpoint, independent of course content and academic assessments. Perceived CAP was implemented to compare online and offline courses (Carpenter-Horning, 2018). Kawasaki et al. (2021) conducted perceived CAP learning on fifty-six third-year nursing students who took emergency remote teaching during the pandemic. Like Rovai et al. (2009), the authors developed a 9-item self-reporting instrument that explicitly measures CAP in nursing skills. In another work, Rachmawati et al. (2019) developed questionnaires to measure students' cognitive, affective, and psychomotor learning in the bakery industry. There was other research on evaluating the learning outcome, but questionnaires were not shared (Triyanti et al., 2021).

Based on the literature reviewed, a comprehensive instrument to measure perceived CAP learning for online laboratory courses in technology and engineering major (TE) has not yet been developed. Some instruments that measure the effectiveness of online laboratories have been developed (Chan & Fok, 2009; Chowdury et al., 2019; Kapilan et al., 2021) but mainly focus on the student learning experiences and feedback and do not assess the CAP achievements. Besides, the authors did not provide evidence that these instruments were validated. Although the instrument from Rovai et al. (2009) can be used to evaluate

any course, it could only provide a general achievement of CAP. The instrument cannot scrutinize some important attributes of learning related to online laboratories, whereas other CAP instruments focus on non-technical fields (Kawasaki et al., 2021; Rachmawati et al., 2019). Therefore, a comprehensive instrument may help practitioners evaluate CAP attributes of TE online labs, such as knowledge of the subject matter, experimental design, problem-solving skills, hands-on competencies, valuing of occupational safety and health, professional attitudes, and ethics. These are some detailed attributes not measured comprehensively by currently available instruments.

Given the need to comprehensively measure CAP's effectiveness in TE online laboratory courses, this work aims to develop and validate an instrument to collect perceived CAP domains of learning in TE online laboratory courses. Based on the existing self-reporting instrument for CAP and consultation with experts, this research developed and validated an extended self-reporting instrument suitable to measure CAP learning in TE online labs. The methodology implemented in this research includes cleaning the data, validating the questions' reliability, and finalizing the instrument (MacLeod et al., 2018; Martin et al., 2020). The results and discussions highlight findings from the data analysis and the instrument's limitations.

METHODS

Development of Self-Reporting Instrument to Measure Perceived CAP Domains

Table 1 lists the attributes of the abilities under each CAP area by referring to Davies (2008) and Rovai et al. (2009). New attributes were added based on consultation with experts. The items developed for the instrument are then compared against the list of abilities to determine the suitable CAP category.

Table 1
Attributes of cognitive, affective, and psychomotor (CAP) learning

Cognitive	Affective	Psychomotor
• Ability to relate theory and practice* • Ability to collect and analyze data* • Ability to analyze and solve problems* • Ability to understand and apply knowledge independently** • Ability to organize knowledge**	• Ability to regulate attitude of learning* • Ability to collaborate with others* • Ability to communicate results and findings* • Ability to communicate effectively with instructor/peers* • Ability to evaluate the learning experience* • Ability to value safety and ethic***	• Ability to demonstrate the practical skills learned** • Ability to perform laboratory work safely*** • Ability to handle actual equipment after learning stimulated/video-based experiments*** • Ability to conduct experiments via guided responses*

*(Davies, 2008), ** (Rovai et al., 2009), *** New attributes

Instrument Development

The items in the instrument for this research are selected and modified based on previous research (Chowdury et al., 2019; Chan & Fok, 2009; Kapilan et al., 2021; Rachmawati et al., 2019; Rovai et al., 2009). In addition, some items are developed based on consultations with subject matter experts. The newly developed instrument for verification has 22 items, as shown in Table 2. Each item was developed to measure targeted attributes in Table 1 and categorized into CAP domains. Some items may be interpreted for two different areas and later would be verified statistically on the more suitable category (refer to column 1 of Table 2). There were five cognitive items, eleven for affective, and six for psychomotor. The fourth column of Table 2 indicates that the item was developed based on adaptation and improvising (AI) from related sources. New items were developed based on consultation with experts. The previous research shows that most items measure cognitive and psychomotor perspectives. Therefore, more affective items were developed for this instrument.

Table 2
Twenty-two (22) cognitive, affective, and psychomotor (CAP) items to measure perceived student learning (original questionnaire)

CAP Area	Label	Items Description	Source
C	C1	I can organize course material into a logical structure	AI Rv
C	C2	I cannot produce a course study guide (compilation of topics, exercises, learning activities) for future students	AI Rv
C	C3	I can self-learn, understand and apply the lessons and concepts in this course	AI Rv
C	C4	I cannot organize my tasks, apply appropriate methods and solve related problems to achieve the desired outputs	AI Chdh
C	C5	I cannot relate the online lab experiments to fundamental concepts and theories	AI Chdh
A	A1	I changed my attitude about the course subject matter as a result of this course.	AI Rv
A, P	A2	I am actively involved in the learning process through the online lab.	AI Chdh
A	A3	I prefer hands-on experiments compared to online lab	AI Chan
A	A4	I can communicate my findings and results through reports and oral presentations	AI Rchw
A	A5	I can collaborate well with others in my group	AI Rchw
A	A6	I feel that tasks can be assigned effectively during an online lab	AI Rchw
C, A, P	A7	I cannot complete all the required group tasks effectively and timely	AI Rchw
A, P	A8	I am aware of the safety requirements when working in a physical lab compared to an online lab	New Items
A	A9	I cannot discuss and clarify issues effectively with my instructor via the available communication platform	New Items

Table 2 *(continue)*

CAP Area	Label	Items Description	Source
A	A10	I can discuss and clarify issues effectively with my peers via the available communication platform	New Items
A	A11	I believe computer simulation can replace actual experiments.	AI Chdh
A, P	P1	I can perform the online lab experiments multiple times, unrestricted by laboratory space, rules, and safety concerns	New Items
C, P	P2	I cannot complete the online lab independently	AI Rchw
P	P3	I cannot handle the lab's equipment without the lab supervisor's assistance through the online lab videos	AI Chdh
P	P4	I can visualize the procedure for using the lab's equipment through the online lab videos	AI Chdh
P	P5	I can demonstrate to others the physical/technical skills learned in this course	New Items
P	P6	I can operate actual equipment confidently after conducting online lab experiments using simulated/virtual equipment	AI Chdh

Notes. Rchw (Rachmawati et al., 2019), Chdh (Chowdhury et al., 2019), Rv (Rovai et al., 2009), and Chan (Chan & Fok, 2009)

The developed items are a combination of positive statements and negative statements. It is to ensure that the participants are paying attention and alert when doing the survey. The respondent then chooses the option of a 5-point Likert scale answer, with one representing strongly disagree and five representing strongly agree. Questions with inconsistent responses will be eliminated during the statistical validation process.

Data Collection

The survey instrument was deployed via Google Forms across four public/private higher learning institutions in Malaysia on multiple courses and cohorts of online laboratories. These courses include programming for Year 1 Computer Science students (to represent Technology fields) and engineering labs for Year 1 to Year 3 Electrical/Electronic Engineering students. Due to the pandemic, all these courses were delivered online. A total of 1414 surveys were sent, and 349 responded to the survey. The response rate of 25% is within the typical response rate of 5% and 30%. Participation is voluntary, and there is no reward for completing the survey. Using a sample size calculator (https://www.calculator.net/sample-size-calculator.html; https://www.surveysystem.com/sscalc.html; https://www.qualtrics.com/au/experience-management/research/determine-sample-size/; https://select-statistics.co.uk/calculators/sample-size-calculator-population-proportion/), it is safe to conclude that the sample size of 300 participants and above qualifies for the confidence level of 90%, with a 5% error margin.

Validation of the Instrument

The following steps were taken to analyze the data:

1. Cleaning the data,
2. Performing Exploratory Factor Analysis (EFA) to identify the groupings of the items and the possible elimination of unrequired items,
3. Performing Cronbach Alpha Analysis (CAA) to ascertain internal reliability and consistency of items within the same group, and
4. Performing Inter-Item Correlation to identify whether a group's items are repetitive or redundant.

Cleaning the Data

All 349 respondents should and had answered all the questions. Out of the 349 respondents, six (6) respondents disagreed with the data to be used in the research. Therefore, their responses were excluded for further analysis, resulting in the total number of respondents for statistical analysis being 343. As the questions were all set as compulsory, all respondents answered all the questions. There were no outliers in the responses, as the answers are in the Likert scale range (1–5). Therefore, it was not required to remove outliers' data before the analysis.

Next, the negatively stated items need to be reverse-coded. The negative statement items with the keyword "cannot" in Table 2, i.e., items labeled C2, C4, C5, A7, A9, P2, and P3, were reverse coded. It is done by reversing the value of the response for negative statement items. The value for one is reverse-coded to five; two is reverse-coded to four, and three remains, four is reverse-coded to two, and five is reverse-coded to one, using the SPSS software.

Performing Exploratory Factor Analysis (EFA). Exploratory factor analysis (EFA) is one of the factor reduction methods. Under SPSS, the Principal Component Analysis (PCA) is conducted as part of the EFA process. The PCA calculates the inter-correlation among the items, which will cause the items to be clustered into principal components. Hence, PCA can reduce items to category areas that account for the most variance. The PCA process identifies the number of relevant components. Each set of components is known as the principal component. It also means that each component is distinctively different from another. The initial number of principal components is identified using the Eigenvalues of the covariance matrix greater than one. For example, if three Eigenvalues of the covariance matrix are greater than one, then there are three principal components for the items. Assuming that the items in Table 2 are distinctively different for this research, the PCA will cluster the items into three components, each representing the cognitive, affective, and psychomotor domains, respectively. Hence, the items should converge to three components: cognitive, affective, and psychomotor, after the items are reduced using

PCA. The PCA results will also reveal whether it passes the Kaiser-Meyer-Oikin (KMO) sampling adequacy above 0.5 and the commonality of each item above 0.3.

Factor rotation is part of the step in EFA to arrive at the rotated component matrix. There are two ways to do the factor rotation, i.e., oblique or orthogonal. The orthogonal rotation requires the factors to be uncorrelated, while the oblique rotation allows the factors to correlate. It is necessary to explore the oblique rotations first to get a correct factor structure (Jolliffe, 2014). Therefore, the oblique rotation test, i.e., the Oblimin test in SPSS, was conducted. The choice between using the oblique or orthogonal depends on the values in the Principal Component Correlation Matrix (PCCM) produced by the oblique rotation. Absolute values in PCCM closer to one indicate that the factors are correlated; hence, the oblique rotation is suitable for implementation. Values closer to zero indicate that the factors are unrelated, so the orthogonal rotation is suitable. The threshold for this research is 0.5. The oblique rotation method will be used if any of the absolute PCCM values is 0.5 or greater. Otherwise, the orthogonal rotation should be used. An example of orthogonal rotation in SPSS is the Varimax rotation. The rotated component matrix will display the factor loading value for each item. If an item has values for two components, the higher factor loading above 0.5 will be considered.

Performing Cronbach Alpha (CA) Analysis and Inter-Item Correlation. Cronbach alpha (CA) analysis measures the consistency within a component or group. This step is done after all items are grouped into the same component in the EFA. Each item within each component is analyzed using CA. The reliability coefficient of 0.70 is considered reliable and will be used as the baseline for measurement. The CA value of 0.70 is reliable, and values lower will require justification (Waltner et al., 2019). Next, an inter-item correlation was conducted to evaluate the correlation across all items—the inter-item correlation matrix measures if the questions measure the same aspect. Acceptable inter-item is between 0.2 and 0.5, a value greater than 0.7 is very similar, and a value of 1.0 is the same question.

RESULTS AND DISCUSSION

Exploratory Factor Analysis (EFA)

Six of the 349 respondents disagreed with the data used in the analysis. Therefore, only 343 responses were analyzed. The PCA revealed that the KMO measurement of sampling adequacy is at 0.889. This sampling adequacy is good as it exceeds the required minimum of 0.50. According to Bartlett's test of sphericity, the significance is at 0.000. It means at least one correlation exists between the 22 items analyzed. The extraction of commonalities indicated that all 22 items have a value greater than 0.30. Therefore, we do not need special consideration to eliminate questions at this initial analysis stage.

Based on the PCA result, the number of components is indicated by eigenvalues greater than one. The rotation method was then applied to identify the items related to each component, using either the oblique or orthogonal method. As all the absolute values for the PCCM are less than 0.5, the orthogonal rotation method was applied to derive the rotated component matrix. The PCA and rotation method will be repeated after each round of item elimination to obtain the final validated instrument that converges into three CAP components.

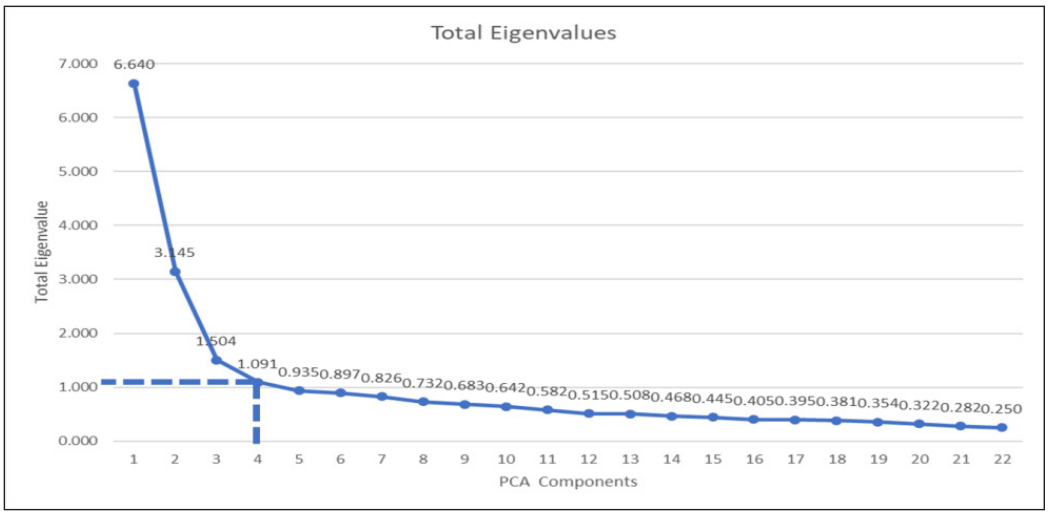

Figure 1. Scree plot from PCA

Based on Figure 1, there are four components with Eigenvalues greater than one. However, the fourth component just slightly exceeded one. Figure 2(a) shows that the fourth component has only two items. According to (Laerd Statistics, 2018), each component should not be fewer than three items. A component with fewer than three items is weak and unstable. Hence, the fourth component is insignificant. As the fourth component has less than three items, the two items (i.e., A1 and A3) were eliminated from the following rotation list. With the elimination of these two items, PCA and orthogonal rotation were conducted for the remaining 20 items.

Figure 2(b) shows the orthogonal rotated component matrix for 20 items. The results show that items C1, A10, A2, and A4 have factor loadings across two components. The four items can potentially be measured in two components. Higher factor loading signifies a stronger relationship between the items and the component. Therefore, factor loadings with a higher value will be considered. It means C1 and A10 will be considered under component 1, not component 3. A2 and A4 will be considered under component 3 and not component 1. Component 1 has more psychomotor items; component 2 has more cognitive items, whereas all affective items were successfully grouped in component 3.

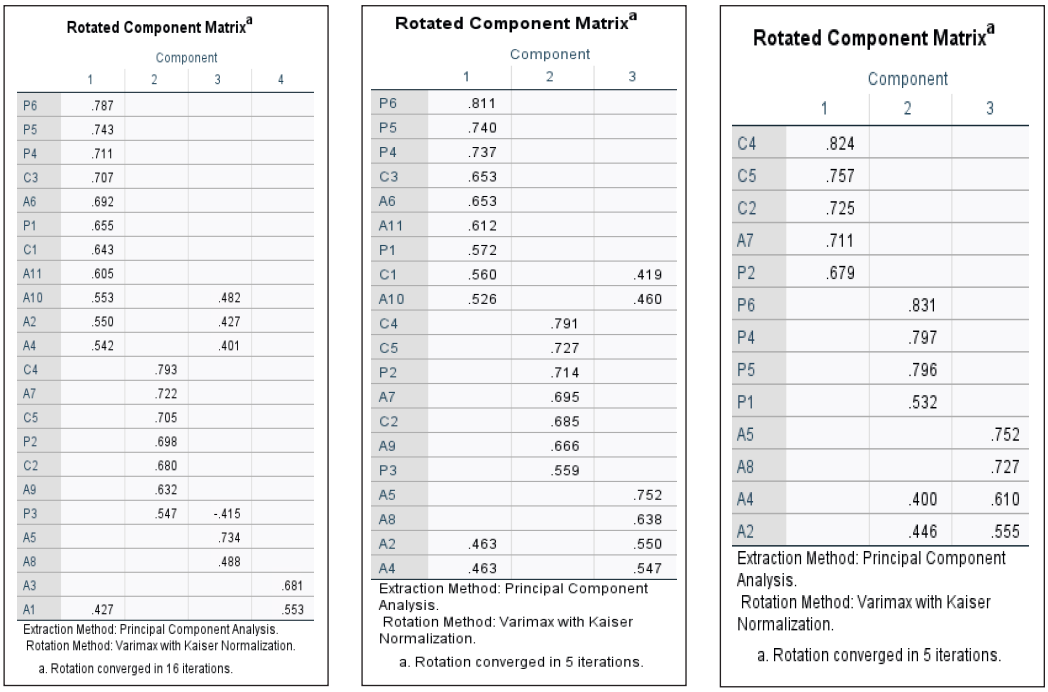

Rotated Component Matrix[a]

	Component			
	1	2	3	4
P6	.787			
P5	.743			
P4	.711			
C3	.707			
A6	.692			
P1	.655			
C1	.643			
A11	.605			
A10	.553		.482	
A2	.550		.427	
A4	.542		.401	
C4		.793		
A7		.722		
C5		.705		
P2		.698		
C2		.680		
A9		.632		
P3		.547	-.415	
A5			.734	
A8			.488	
A3				.681
A1	.427			.553

Extraction Method: Principal Component Analysis.
Rotation Method: Varimax with Kaiser Normalization.
a. Rotation converged in 16 iterations.

(a)

Rotated Component Matrix[a]

	Component		
	1	2	3
P6	.811		
P5	.740		
P4	.737		
C3	.653		
A6	.653		
A11	.612		
P1	.572		
C1	.560		.419
A10	.526		.460
C4		.791	
C5		.727	
P2		.714	
A7		.695	
C2		.685	
A9		.666	
P3		.559	
A5			.752
A8			.638
A2	.463		.550
A4	.463		.547

Extraction Method: Principal Component Analysis.
Rotation Method: Varimax with Kaiser Normalization.
a. Rotation converged in 5 iterations.

(b)

Rotated Component Matrix[a]

	Component		
	1	2	3
C4	.824		
C5	.757		
C2	.725		
A7	.711		
P2	.679		
P6		.831	
P4		.797	
P5		.796	
P1		.532	
A5			.752
A8			.727
A4		.400	.610
A2		.446	.555

Extraction Method: Principal Component Analysis.
Rotation Method: Varimax with Kaiser Normalization.
a. Rotation converged in 5 iterations.

(c)

Figure 2. Rotated component matrix for (a) 22 items, (b) 20 items, and (c) 13 items

The next step is excluding items in Figure 2(b) that do not belong to the same component. It is done by comparing with the items in Table 2. Component 1 is considered a psychomotor component as it contains more psychomotor items. Based on Table 2, items C1, C3, A6, A10, and A11 were removed from the list in component 1 as these items did not measure psychomotor attributes. Component 2 is considered a cognitive component as it has more cognitive items. Hence, items with labels from psychomotor and affective such as A7, A9, P2, and P3, are considered for removal. Based on Table 2 (refer to labels in column 1), the authors opined that "complete tasks" in A7 and P2 can be considered a problem-solving process involving psychomotor, affective, or cognitive processes in A7 cognitive or psychomotor process in P2. Hence, these two items can be considered in any one of these learning domains. Figure 2(b) results grouped A7 and P2 with cognitive items. Therefore, "completing the tasks" is categorized as a cognitive process. It is supported by literature gathered in Elif (2018), where scientists agreed that problem-solving is an activity that requires domain knowledge and appropriate cognitive strategies. By maintaining items A7 and P2, only A9 and P3 were eliminated from component 2.

After eliminating seven items in the previous step, the orthogonal rotation matrix for the new list is shown in Figure 2(c). Figure 2(c) shows the orthogonal rotated component matrix for 13 items. Only A2 and A4 have factor loading for two components. Both items

have higher factor loading values in component 3, so A2 and A4 will be categorized under component 3. Finally, after three iterations, the original list of 22 items was reduced to 13 and successfully grouped in the respective CAP components using the EFA.

Cronbach Alpha Analysis (CAA)

Cronbach Alpha Analysis was conducted on component 1 (cognitive) with C4, C5, C2, A7, and P2. The Cronbach Alpha Analysis generated a value of 0.803. Therefore, all five items are relevant to component 1. Figure 3 shows items-total statistics and inter-items correlation matrix for component 1. The inter-item correlation matrix shows that each question measures independent yet related aspects.

The second component (psychomotor) is P6, P4, P5, and P1. The Cronbach's Alpha (CA) value is 0.802. At this stage, the best practice is to delete items to obtain higher internal reliability (i.e., higher CA value). For example, Figure 4 item-total statistics indicated that deleting the item with the label P1 will increase the reliability value to 0.816. However, this deletion is unnecessary because the current reliability value exceeds 0.70. The inter-item correlation matrix indicates that all items tend to measure similar aspects.

The third component (affective) contains the items containing A2, A4, A5, and A8. The Cronbach Alpha's value for this component slightly exceeded the minimum value of 0.70

Item-Total Statistics

	Scale Mean if Item Deleted	Scale Variance if Item Deleted	Corrected Item-Total Correlation	Cronbach's Alpha if Item Deleted
C4	12.48	11.291	.693	.733
C5	12.68	11.616	.622	.754
C2	12.80	12.418	.527	.783
A7	12.41	11.769	.536	.781
P2	12.59	11.224	.568	.773

Inter-Item Correlation Matrix

	C2	C4	C5	A7	P2
C2	1.000	.532	.437	.339	.349
C4	.532	1.000	.610	.462	.475
C5	.437	.610	1.000	.395	.458
A7	.339	.462	.395	1.000	.466
P2	.349	.475	.458	.466	1.000

Figure 3. Cronbach alpha analysis for component 1 (cognitive)

Item-Total Statistics

	Scale Mean if Item Deleted	Scale Variance if Item Deleted	Corrected Item-Total Correlation	Cronbach's Alpha if Item Deleted
P1	9.77	6.735	.470	.816
P4	10.08	5.797	.650	.735
P5	10.13	5.861	.653	.734
P6	10.38	5.378	.696	.710

Inter-Item Correlation Matrix

	P1	P4	P5	P6
P1	1.000	.408	.388	.411
P4	.408	1.000	.547	.611
P5	.388	.547	1.000	.634
P6	.411	.611	.634	1.000

Figure 4. Cronbach alpha analysis for component 2 (psychomotor)

at 0.702. The item-total statistics in Figure 5 indicate that the reliability can be increased to 0.719 by deleting item A8. However, as the current reliability value is sufficient, the deletion of A8 is insignificant. Hence, A8 is a valid item in the third component. The inter-item correlation matrix in Figure 5 has values between 0.2 and 0.5, indicating that each item measures related yet independent aspects.

Item-Total Statistics

	Scale Mean if Item Deleted	Scale Variance if Item Deleted	Corrected Item-Total Correlation	Cronbach's Alpha if Item Deleted
A2	11.67	4.666	.515	.620
A4	11.74	4.953	.544	.606
A5	11.36	4.747	.548	.600
A8	11.39	5.302	.356	.719

Inter-Item Correlation Matrix

	A2	A4	A5	A8
A2	1.000	.482	.437	.259
A4	.482	1.000	.470	.271
A5	.437	.470	1.000	.326
A8	.259	.271	.326	1.000

Figure 5. Cronbach alpha analysis for component 3 (affective)

Finalized Questionnaire

Upon completing the Exploratory Factor Analysis (EFA) and Cronbach alpha analysis, the finalized questionnaire is shown in Table 3.

Table 3
Thirteen (13) cognitive, affective, and psychomotor (CAP) items to measure perceived student learning (finalized questionnaire)

Questions	Survey Items	Label
I1	I cannot produce a course study guide (compilation of topics, exercises, learning activities) for future students	C1r
I2	I cannot organize my tasks, apply appropriate methods and solve related problems to achieve the desired outputs	C2r
I3	I cannot relate the online lab experiments to fundamental concepts and theories	C3r
I4	I cannot complete the online lab independently	C4r
I5	I cannot complete all the required group tasks effectively and timely	C5r
I6	I am actively involved in the learning process through the online lab.	A1
I7	I can communicate my findings and results through reports and oral presentations	A2
I8	I can collaborate well with others in my group	A3
I9	I am aware of the safety requirements when working in a physical lab compared to an online lab	A4
I10	I can perform the online lab experiments multiple times, unrestricted by laboratory space, rules, and safety concerns	P1
I11	I can visualize the procedure for using the lab's equipment through the online lab demonstration	P2
I12	I can demonstrate to others the physical/technical skills learned in this course	P3
I13	I can operate actual equipment confidently after conducting online lab experiments using simulated/virtual equipment	P4

CONCLUSION

The research successfully developed and validated a 13-item self-reporting instrument of perceived learning according to the CAP domains for technology and engineering online laboratory courses. This instrument was validated and refined statistically using perceived CAP responses from computer science and engineering students. Compared to the previous research instruments, this newly developed instrument has more items covering CAP learning. The items for each area are well balanced, with cognitive having five items, affective having four items, and psychomotor having four items. This study only validates this instrument or questionnaire, which can be used to study the reality of online lab learning. It will be the basis for studying the reality of online labs upon implementation**.** Hence, this instrument can assist practitioners in measuring and analyzing the related attributes of CAP learning in engineering and technology online laboratories.

This pilot study was only conducted with computer science and engineering students. This research can be extended to make this tool suitable for science and mathematics. Hence, future works on the instrument will be conducted in the science and mathematics courses to fine-tune this instrument to be a suitable tool for all science, technology, engineering, and mathematics (STEM) courses. The instrument can be implemented for face-to-face lab sessions by modifying the psychomotor items, as the existing psychomotor items are designed to measure perceived CAP learning for online lab sessions during the COVID-19 pandemic.

ACKNOWLEDGEMENT

The authors thank the College of Engineering, Universiti Teknologi MARA, Shah Alam, Malaysia, for providing the funds to support this research.

REFERENCES

Anderson, L., Krathwohl, D. R., Airasian, P. W., Cruikshank, K. A., Richard, M., Pintrich, P. R., Raths, J. D., & Wittrock, M. C. (2001). *A taxonomy for Learning, Teaching and Assessing: A Revision of Bloom's Taxonomy of Educational Objectives*. Longman.

Bloom, B. S., Engelhart, M. D., Furst, E. J., Hill, W. H., & Krathwohl, D. R (1956). *Taxonomy of Educational Objectives; The Classification of Education Goals - Handbook 1 Cognitive Domain*. Longmans.

Carpenter-Horning, A. K. (2018). *The Effects of Perceived Learning on Open-Sourced Classrooms within the Community Colleges in the South-Eastern Region of the United States*. Liberty University.

Chan, C., & Fok, W. (2009). Evaluating learning experiences in virtual laboratory training through student perceptions: A case study in electrical and electronic engineering at the University of Hong Kong. *Journal of the Higher Education Academy*, *4*(2), 70-75. https://doi.org/10.11120/ened.2009.04020070

Chowdury, H., Alam, F., & Mustary, I. (2019). Development of an innovative technique for teaching and learning of laboratory experiments for engineering courses. *Energy Procedia, 160*, 806-811. https://doi.org/10.1016/j.egypro.2019.02.154

Davies, C. (2008). *Laboratory and Practical Work in the Engineering Curriculum: Learning and Teaching in Laboratories*. The Higher Educational Academy Engineering.

Elif, I. (2018). An overview of problem solving studies in physics education. *Journal of Education and Learning*, *7*(4), 191-200. https://doi.org/10.5539/jel.v7n4p191

Gamage, K. A. A., Wijesuriya, D. I., Ekanayake, S. Y., Rennie, A. E. W., Lambert, C. G., & Gunawardhana, N. (2020). Online delivery of teaching and laboratory practices: Continuity of university programmes during COVID-19 pandemic. *Education. Sciences*, *10*(10), Article 291. https://doi.org/10.3390/educsci10100291

Jolliffe, I. (2014). Principal component analysis. In N. Balakrishnan, T. Colton, B. Everitt, W. Piegorsch, F. Ruggeri, L. Jozef & Teugels (Eds.), *Wiley StatsRef: Statistics Reference Online* (pp. 2-29). John Wiley & Sons. https://doi.org/10.1002/0470013192.bsa501

Kapilan, N., Vidhya, P., & Gao, X. Z. (2021). Virtual laboratory: A boon to the mechanical engineering education during COVID-19 pandemic. *Higher Education for the Future*, *8*(1), 31-46. https://doi.org/10.1177/2347631120970757

Kawasaki, H., Yamasaki, S., Masuoka, Y., Iwasa, M., Fukita, S., & Matsuyama, R. (2021) Remote teaching due to COVID-19: An exploration of its effectiveness and issues. *International Journal of Environmental Research and Public Health, 18*(5), Article 2672. https://doi.org/10.3390/ijerph18052672

Kearney, P. (1994). Affective learning scale. In R. B. Rubin, P. Palmgreen, & H. E. Sypher (Eds.), *Communication Research Measures: A Sourcebook* (pp. 81-85 & pp. 238-241). The Guilford Press.

Krathwohl, D. R., Bloom, B. S., & Masia, B. B. (1964). *Taxonomy of Educational Objectives: The Classification of Educational Goals - Handbook II: Affective Domain*. David McKay.

Laerd Statistics. (2018). *Principal component analysis (PCA) using SPSS statistics*. Laerd Statistics. https://statistics.laerd.com/spss-tutorials/principal-components-analysis-pca-using-spss-statistics.php/Accessed

Lewis, L. D. (2014). *The Pedagogical Benefits and Pitfalls of Virtual Tools for Teaching and Learning Laboratory Practices in the Biological Sciences*. https://www.advance-he.ac.uk/knowledge-hub/pedagogical-benefits-and-pitfalls-virtual-tools-teaching-and-learning-laboratory

MacLeod, J., Yang, H. H., Zhu, S., & Li, Y. (2018). Understanding students' preferences toward the smart classroom learning environment: Development and validation of an instrument. *Computers & Education*, *122*, 80-91. https://doi.org/10.1016/j.compedu.2018.03.015

Martin, F., Stamper, B., & Flowers, C. (2020). Examining student perception of readiness for online learning: Importance and confidence. *Online Learning Journal, 24*(2), 38-58.

Murphy, M. P. (2020). COVID-19 and emergency e-learning: Consequences of the securitisation of higher education for post-pandemic pedagogy. *Contemporary Security Policy*, *41*(3), 492–505. https://doi.org/10.1080/13523260.2020.1761749

Nature News. (2020, April 22). Corononavirus: The first three months as it happened. *Nature News*. https://www.nature.com/articles/d41586-020-00154-w

Rachmawati, E., Mufidah, L., Sulistiyani, T., & Ab-Latif, Z. (2019). Examining the students' cognitive, affective and psychomotor abilities in the bakery industry. *Journal of Technology and Operations Management*, *14*(2), 1-9. https://doi.org/10.32890/jtom2019.14.2.1

Rovai, A. P., Wighting, M. J., Baker, J. D., & Grooms, L. D. (2009). Development of an instrument to measure perceived cognitive, affective, and psychomotor learning in traditional and virtual classroom higher education settings. *Internet and Higher Education*, *12*(1), 7-13. https://doi.org/10.1016/j.iheduc.2008.10.002

Simpson, E. J. (1974). The classification of educational objectives in the psychomotor domain. In R. J. Kibler, D. J. CegalaL, L. Barker & D. T. Miles (Eds.), *Objectives for Instruction and Evaluation* (pp. 107-112). Allyn and Bacon.

Tan, P. L. (2021, June 1). Online learning: Leave no student behind. *The Star*. https://www.thestar.com.my/opinion/letters/2021/06/01/online-learning-leave-no-student-behind

Triyanti, Murtono, & Sri, U. (2021). Problem-based technology and science development to improve science learning outcomes in elementary schools. *ANP Journal of Social Science and Humanities*, *2*(2), 151-156. https://doi.org/10.53797/anp.jssh.v2i2.21.2021

Waltner, E. M., Rieß, W., & Mischo, C. (2019). Development and validation of an instrument for measuring student sustainability competencies. *Sustainability*, *11*(6), Article 1717. https://doi.org/10.3390/su11061717

Zhai, G., Wang, Y., & Liu, L. (2012). Design of electrical online laboratory and e-learning. *IERI Procedia*, *2,* 325-330. https://doi.org/10.1016/j.ieri.2012.06.096

Pertanika J. Sci. & Technol. 31 (4): 2105 - 2121 (2023)

PERTANIKA JOURNALS

SCIENCE & TECHNOLOGY

Journal homepage: http://www.pertanika.upm.edu.my/

Sound-Based Health Monitoring of Induction Motor Considering Load and Measuring Distance Variations Using Frequency Calculation and Statistical Analysis

Iradiratu Diah Prahmana Karyatanti[1,2]*, Nuddin Harahab[2], Ratno Bagus Edy Wibowo[2], Agus Budiarto[2] and Ardik Wijayanto[3]

[1]*Department of Electrical Engineering, Faculty of Engineering and Marine Science, Hang Tuah University, Indonesia*
[2]*Environmental Science, Postgraduate, Brawijaya University, Malang, Indonesia*
[3]*Department of Electronic Engineering, Electronic Engineering Polytechnic Institute of Surabaya, Indonesia*

ABSTRACT

Bearing is an important part of the induction motor, whose function is to help the rotor spin. It contributes the highest percentage of damage compared to other parts. When operated in this condition, it causes overheating, imbalance in the rotation of the rotor shaft, sparks, and noise pollution to the environment. A bearing monitoring system must be implemented and developed to avoid further damage. Furthermore, a non-invasive technique through sound signals was developed in this study. A sound signal is easy to overlap with the noise from other sources. Environmental noise is unavoidable during data collection, affecting health monitoring accuracy (HM). Therefore, this study aims to develop an HM method for sound-based induction motors based on measurement differences, load variation, frequency calculations, and statistics. The distance measured was used as an independent variable of the non-machine noise. The load variations were also applied as required, and the operation of the motor varies according to users' needs. In an effort to prevent negative environmental impacts, noise monitoring was carried out from the motor operation, and the results showed an HM of accuracy of 83.09%. The best distance for performing HM conditions is 100 cm and 83.59 dB(A). The noise value does not exceed the industrial worker threshold. Therefore, close surveillance of the motor's condition tends to be conducted with or without a load. It is because the load variation does not affect the accuracy of health monitoring.

Keywords: Fault detection, health monitoring, machine condition diagnosis, sound

ARTICLE INFO

Article history:
Received: 14 August 2022
Accepted: 14 November 2022
Published: 13 June 2023

DOI: https://doi.org/10.47836/pjst.31.4.29

E-mail addresses:
iradiratu@hangtuah.ac.id (Iradiratu Diah Prahmana Karyatanti)
marmunnuddin@ub.ac.id (Nuddin Harahab)
rbagus@ub.ac.id (Ratno Bagus Edy Wibowo)
agusfpt@ub.ac.id (Agus Budiarto)
ardik@pens.ac.id (Ardik Wijayanto)
* Corresponding author

ISSN: 0128-7680
e-ISSN: 2231-8526

INTRODUCTION

The induction motor is called an 'asynchronous motor' because it operates at speed less than the synchronous and is one of the most important components of a spinning rotor. A survey by the Electric Power Research Institute (EPRI) shows that the percentage of damage to motor parts in bearings, stators, and rotors is 41%, 36%, and 9%, respectively (Barusu & Deivasigamani, 2020). Bearing is a motor component whose function is to help the rotor spin, and the relative motion between the outer and inner races makes it susceptible to damage. Small damage to the bearing causes more severe deterioration of other parts (Das & Ray, 2020). In addition to mechanical factors, bearing damage is caused by external factors such as contamination, corrosion, brinelling, installation, and lubrication errors. Brinelling is a phenomenon that gives rise to the formation of indentations in the race bearings due to excessive load, while Installation errors occur due to incorrect set-up of the bearing on the shaft. Furthermore, lubrication errors are caused by insufficient or excessive lubricant application, leading to overheating and accelerating the process of bearing damage (He et al., 2020).

The negative effect of damage to motor parts should be avoided as early as possible by providing proper maintenance. Therefore, Health Monitoring (HM) and Fault Diagnosis (FD) of industrial driving machines are important for maintenance actions and should be conducted regularly and routinely. Further action should be taken to effect restoration when the tool is operating abnormally. In addition, the advantages of the HM system include predicting early damage, more optimal maintenance actions, minimizing surveillance costs, and increasing industrial productivity and motor reliability (Amanuel et al., 2021).

The general stages in conducting HM include data acquisition, namely collecting information from the instrument used (current, vibration, thermal, and sound). The second stage is data processing, which includes several methods, such as time domain data analysis, Fast Fourier Transform (FFT), Wavelet Transform (WT), Hilbert-Huang Transform (HHT), and Soft Time Fourier Transform (STFT). The third stage is making decisions regarding the treatment based on diagnostic and prognostic methods (Goyal et al., 2021). HM has the advantage of a microphone as a low-cost sound sensor and does not require contact with the diagnosed engine part. However, the drawback is that the sound signal easily overlaps with other sources and sometimes does not change when there is a change in the rotation of the engine components (AlShorman et al., 2021).

Because it has the advantages of a low price and simple application, HM, through sound regulation, began to be developed further. Sound signals are superior to HM using vibrations, indicated by a significant spike in amplitude when the motor part is abnormal (Nirwan & Ramani, 2022). Accuracy is needed to follow up the maintenance phase. The effect of placing the microphone as sound data acquisition needs to be considered, hence, as not to cause the capture of noise signals originating from background sound as HM data

is susceptible to environmental noise. Consequently, placing the microphone 30 cm from the rotor avoids overlapping sound signals from other sources (Glowacz et al., 2018). With the same consideration, several studies placed the microphone 50 cm from the machine body (Zhong et al., 2018). The importance of sound signal distance on accuracy results promotes this research regarding HM bearing and induction motor noise calculation at various measuring distances and loads. Load variations are tested as an approach to be operated on, with different loads according to the user requirements. HM was developed by processing sound signals using the FFT algorithm. Band-pass filtering was used to determine the frequency of failure as a diagnosis of bearing conditions. The result of the test was presented in the form of a percentage of detection accuracy. The best measurement distance was determined by considering the highest HM accuracy and noise that does not exceed the threshold that harms the environment. Statistical analysis was used to analyze the proposed hypothesis. This study greatly contributes to the development of HM bearings with non-invasive techniques through sound signals, followed by an analysis of the effect of variations in distance and load on the accuracy of HM bearings. The proposed method offers solutions that are considered by comparing similar studies. Statistical analysis provides the benefit of avoiding excessive noise by not neglecting the main importance of HM accuracy. Therefore, the proposed method is an effective, simple, inexpensive alternative to HM and minimizes noise exposure for industrial workers, especially machine operators.

MATERIALS AND METHODS

The developed HM bearing considers noise, non-engine noise variables, and load variations. The conceptual framework of the study is shown in Figure 1. The induction motor tested has specifications of 1.5 kW, 380 V, 3.68 A, 3 phases, and 4 poles. The treatment to determine the effect of non-machine sound is carried out by recording and diagnosing bearing conditions from sound signals with distances of 0cm (S1), 50cm (S2), 100cm

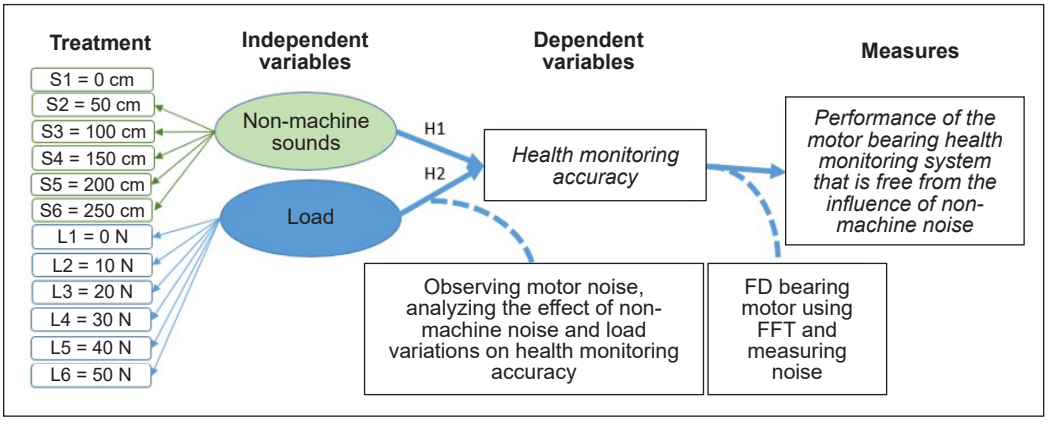

Figure 1. Study conceptual framework

(S3), 150cm (S4), 200cm (S5), and 250cm (S6). In addition, the effect of the load value variable is tested on the HM system with a value of 0 Newton (L1), 10 Newton (L2), 20 Newton (L3), 30 Newton (L4), 40 Newton (L5), and 50 Newton (L6). The noise in all tests is observed as information and warning of the sound level generated by the motor to avoid negative environmental impacts early. The hypotheses obtained include whether the non-machine noise and the load variation variable affect the accuracy of bearing health monitoring. From this, it is known that the performance of the induction motor health monitoring system is free from the influence of non-engine noise. The flowchart of this study is depicted in Figure 2.

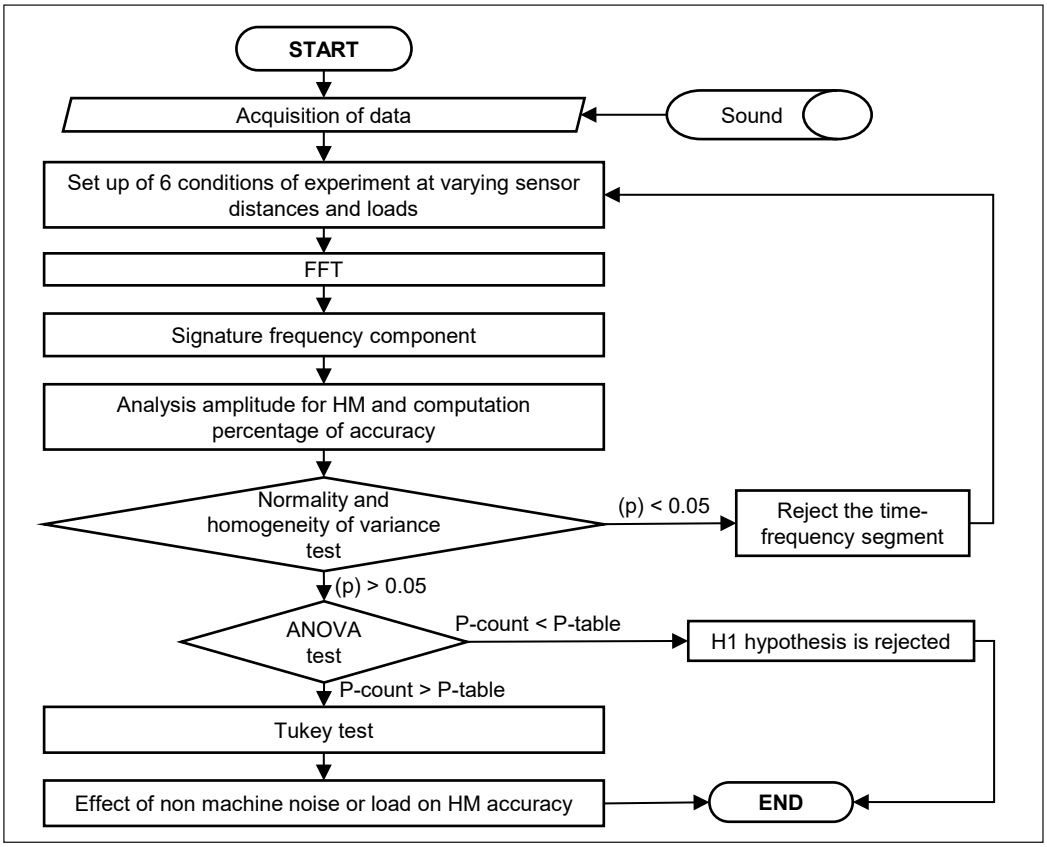

Figure 2. Flowchart of the study

Figure 3 shows the configuration of the HM being tested. The sound amplitude value in the frequency domain is used for the FD bearing. The time sound signal obtained from the microphone is transformed into the frequency domain. The sound signal transformation algorithm applied is Fast Fourier Transform (FFT). It is an algorithm derived from the Discrete Fourier Transform (DFT) calculation. Mathematically, the FFT of a discrete signal is X_n using N points (Karyatanti et al., 2019) (Equation 1).

$$X_n = \sum_{n=0}^{N-1} x_n e^{-i2\pi \frac{k}{N} n} \qquad k = 0,1,2,\ldots,(N\text{-}1) \qquad (1)$$

In one cycle, a signal is sampled several N and is grouped into 2, namely odd and even. Then, each group is divided into 2 continuously until 2 samples are left. Each group is subjected to DFT per 2 samples. In radix-2 FFT, the DFT process is conducted by dividing the sample N DFT by a number to the power of two, enabling many steps as p, which is determined by $2^p = N$.

Each sound source has its frequency, and to determine the specific sound produced by motor bearing, this study proposed using a band-pass filter. The frequency value is unique and used as the FD observation point. When the bearing is damaged, it causes the induction motor to produce different harmonic frequencies. It is because the flux density in the air gap becomes asymmetrical and affects the inductance in the stator. Signals carrying harmonic information describe defective or non-ideal conditions that occur in them (Nirwan & Ramani, 2022).

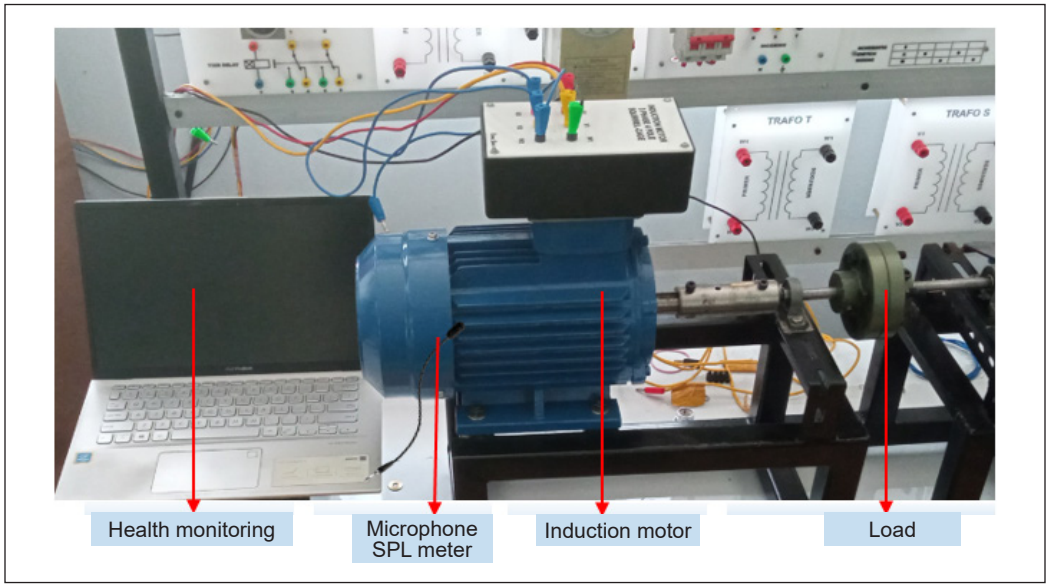

Figure 3. HM bearing configuration

Figure 4 shows the bearing section based on calculating frequency characteristics and tested bearing conditions. Where ω = angular velocity, N= number of ball bearings, d = diameter of ball bearings, D_p = diameter of pitch, and Θ= contact angle. A spike in amplitude occurs when the bearing rotates, and a ball defect occurs (Ewert et al., 2020). The frequency of the ball bearing is formulated as Ball Spin Frequency (BSF) as in Equation 2:

$$f_{BSF} = \frac{N}{2d}\omega\left[1-\left(\frac{d\cos\theta}{D_p}\right)^2\right] \quad (2)$$

The f_{BSF} harmonic frequency is obtained from Equation 3. Where f_p is the harmonic frequency, f_v s is the frequency of the bearing component of Equation 2, and k is the constant k=1,2,3,...

$$f_p = |k.f_v| \quad (3)$$

Statistical testing for the effect of distance and load variation on HM accuracy using a Completely Randomized Design (CRD) approach. The CRD Equation 4 is as below:

$$Y_{ij} = \pi + \tau_i + \varepsilon_{ij} \quad (4)$$

with

Y_{ij} = observations on treatment i and repetition j, π = general average, τ_i = effect of treatment i, ε_{ij} = random effect on treatment i, repetition j, i = 1,2, … , t and j = 1,2, …, r

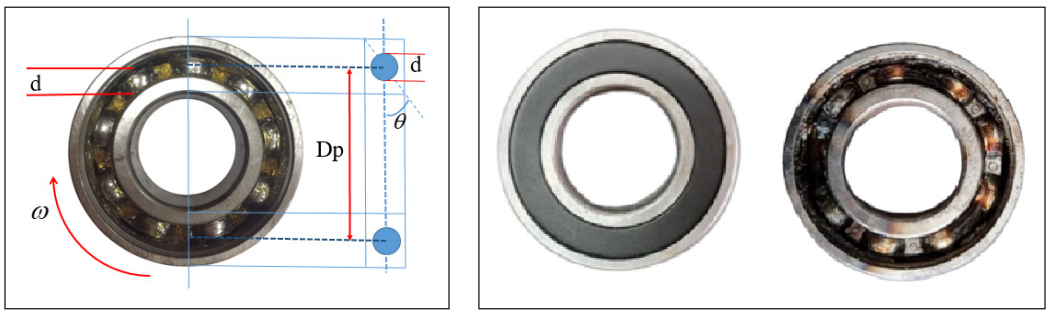

(a) (b)

Figure 4. Bearing (a) front view; and (b) healthy and damage bearing

RESULTS AND DISCUSSION

The sound characteristics tend to change when the motor is loaded. The value of the load greatly affects the rotational speed of the motor and gives the effect of changing the sound. Tests were conducted when the motor was not loaded and was measured in comparison with the initial conditions of the motor. The noise measurements in the healthy and the damaged motor at various distances and loads are shown in Table 1. The data retrieval was conducted for 30 seconds by recording. Table 1 shows that the farther the distance from the sound source, the lower the noise level. Various noise levels were produced both in healthy and damaged conditions. When the motor operates under damaged and loaded bearing

conditions, there is an increase in noise. The noise threshold value in the industrial environment is 85 dB(A) (Aminian et al., 2021). Motors as industrial propulsion tools operate mostly under high load conditions. Hence, the noise level does not get worse, and because of this, monitoring is needed. From this test, noise measurement is not recommendable as a parameter to determine motor conditions. Although the damage caused increased noise, the location of the faulty part is usually unknown. Therefore, the HM system is needed as a bearing monitoring system.

Table 1
Average motor operating noise under conditions of healthy and damaged bearings

Treatment	Noise healthy bearing db(A)	Noise Damaged bearing db(A)
S1	87.92	88.42
S2	80.97	85.24
S3	76.31	83.59
S4	72.31	82.03
S5	70.24	80.36
S6	72.50	79.85
L1	82.91	85.24
L2	87.81	89.03
L3	86.96	87.09
L4	85.86	89.00
L5	86.27	86.96
L6	85.96	89.50

Effect of Non-Machine Noise on HM Bearing Accuracy

The sound signal from the microphone is processed by FFT, band-pass filtering and the motor bearing condition is analyzed. By applying Equations 3 and 4, the amplitude of each frequency is observed to determine the bearing condition. It is declared defective when the test amplitude exceeds the healthy value. The HM results are accurate when each harmonic frequency states many damaged conditions because the bearing test reconstructed the defective condition. Figure 5 shows the HM results of the sound signal in the frequency domain by testing different sound measurement distances. The blue sound graph is the signal for the healthy motor condition, and the red color is the test signal.

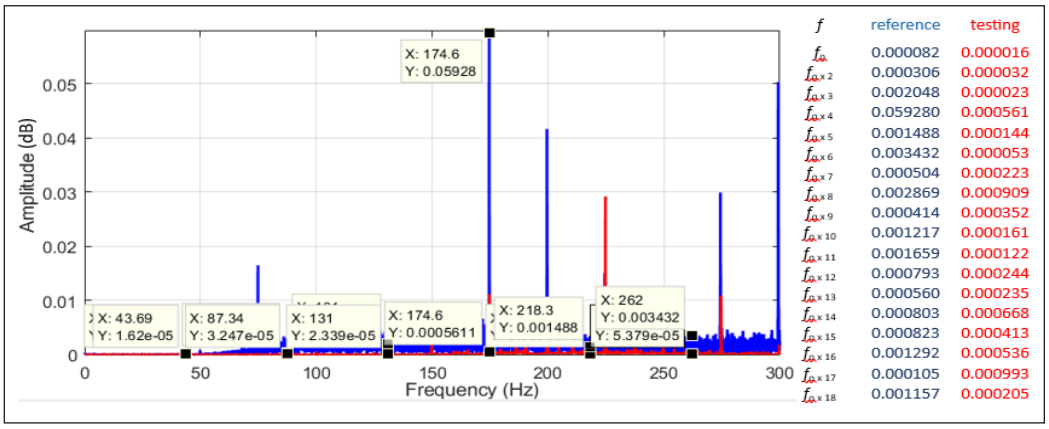

(a)

Figure 5. Sound signal in the frequency domain in bearing damage test with various measurement distances: (a) Treatment S1

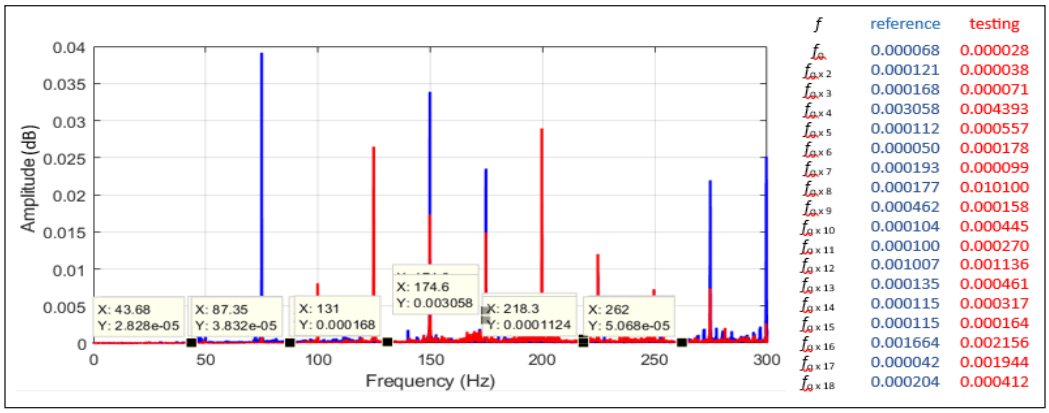

f	reference	testing
f_o	0.000068	0.000028
$f_{o\times 2}$	0.000121	0.000038
$f_{o\times 3}$	0.000168	0.000071
$f_{o\times 4}$	0.003058	0.004393
$f_{o\times 5}$	0.000112	0.000557
$f_{o\times 6}$	0.000050	0.000178
$f_{o\times 7}$	0.000193	0.000099
$f_{o\times 8}$	0.000177	0.010100
$f_{o\times 9}$	0.000462	0.000158
$f_{o\times 10}$	0.000104	0.000445
$f_{o\times 11}$	0.000100	0.000270
$f_{o\times 12}$	0.001007	0.001136
$f_{o\times 13}$	0.000135	0.000461
$f_{o\times 14}$	0.000115	0.000317
$f_{o\times 15}$	0.000115	0.000164
$f_{o\times 16}$	0.001664	0.002156
$f_{o\times 17}$	0.000042	0.001944
$f_{o\times 18}$	0.000204	0.000412

(b)

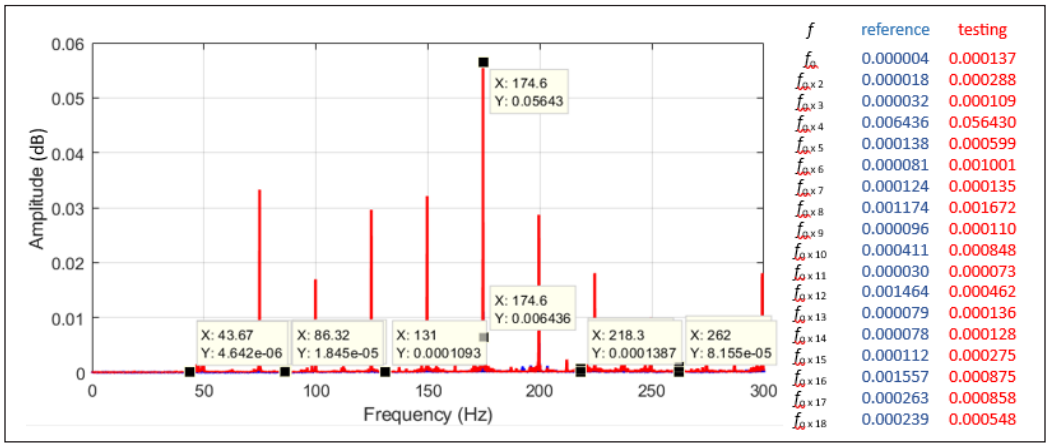

f	reference	testing
f_o	0.000004	0.000137
$f_{o\times 2}$	0.000018	0.000288
$f_{o\times 3}$	0.000032	0.000109
$f_{o\times 4}$	0.006436	0.056430
$f_{o\times 5}$	0.000138	0.000599
$f_{o\times 6}$	0.000081	0.001001
$f_{o\times 7}$	0.000124	0.000135
$f_{o\times 8}$	0.001174	0.001672
$f_{o\times 9}$	0.000096	0.000110
$f_{o\times 10}$	0.000411	0.000848
$f_{o\times 11}$	0.000030	0.000073
$f_{o\times 12}$	0.001464	0.000462
$f_{o\times 13}$	0.000079	0.000136
$f_{o\times 14}$	0.000078	0.000128
$f_{o\times 15}$	0.000112	0.000275
$f_{o\times 16}$	0.001557	0.000875
$f_{o\times 17}$	0.000263	0.000858
$f_{o\times 18}$	0.000239	0.000548

(c)

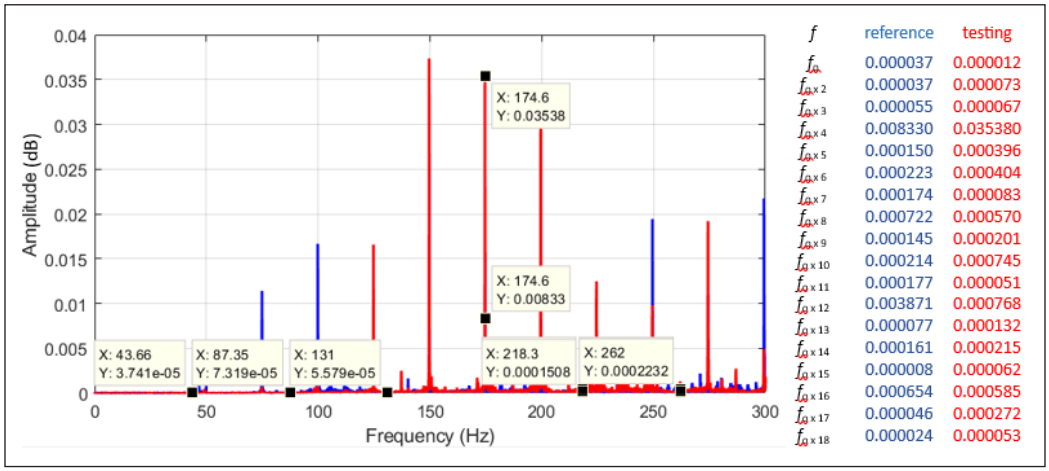

f	reference	testing
f_o	0.000037	0.000012
$f_{o\times 2}$	0.000037	0.000073
$f_{o\times 3}$	0.000055	0.000067
$f_{o\times 4}$	0.008330	0.035380
$f_{o\times 5}$	0.000150	0.000396
$f_{o\times 6}$	0.000223	0.000404
$f_{o\times 7}$	0.000174	0.000083
$f_{o\times 8}$	0.000722	0.000570
$f_{o\times 9}$	0.000145	0.000201
$f_{o\times 10}$	0.000214	0.000745
$f_{o\times 11}$	0.000177	0.000051
$f_{o\times 12}$	0.003871	0.000768
$f_{o\times 13}$	0.000077	0.000132
$f_{o\times 14}$	0.000161	0.000215
$f_{o\times 15}$	0.000008	0.000062
$f_{o\times 16}$	0.000654	0.000585
$f_{o\times 17}$	0.000046	0.000272
$f_{o\times 18}$	0.000024	0.000053

(d)

Figure 5 (continue). Sound signal in the frequency domain in bearing damage test with various measurement distances:(a) Treatment S1; (b) Treatment S2; (c) Treatment S3; and (d) Treatment S4

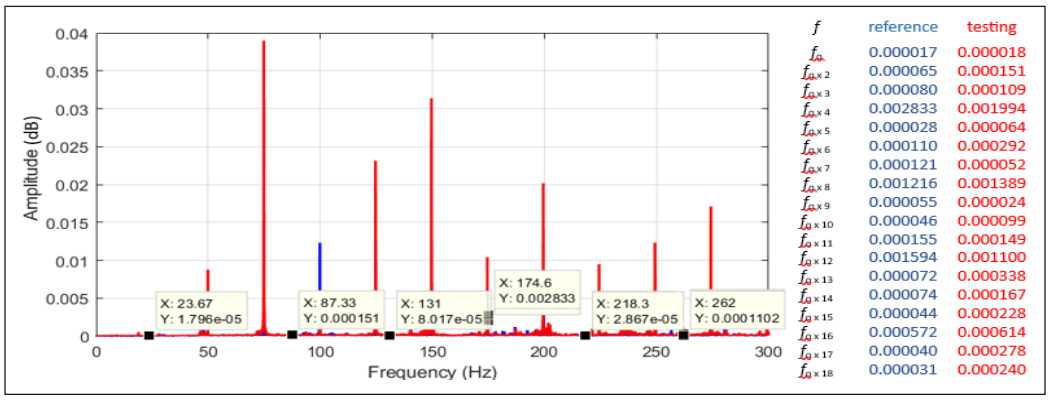

(e)

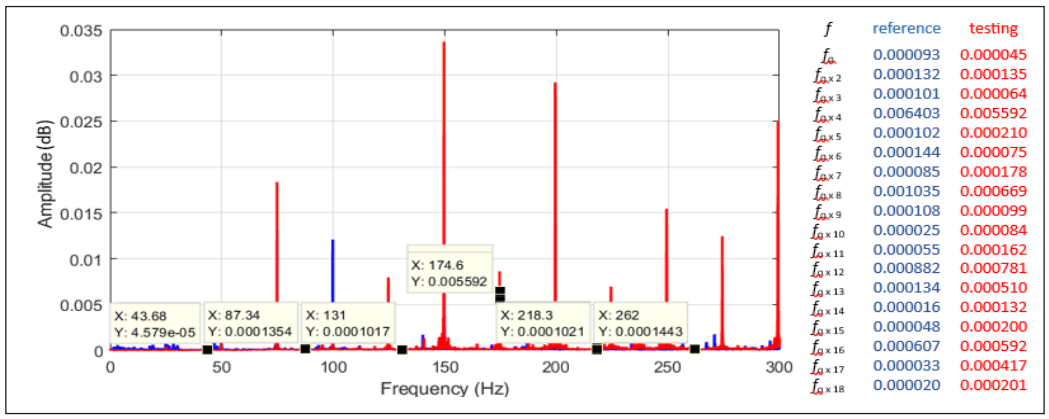

(f)

Figure 5 (continue). Sound signal in the frequency domain in bearing damage test with various measurement distances:(e) Treatment S5; and (f) Treatment S6

Each condition is tested four times; the results represent the actual situation. Figure 5 shows the sound signal from the first test data (r1). At the measurement distance of 0 cm, the first data found that all harmonic frequencies had a lower amplitude than the reference. Therefore, they did not detect damage. This result is a detection error because the bearing is damaged. When presented, the detection accuracy in testing data 1 is 0%.

At the measurement distance of 50 cm, it was found that in the r1 data, five harmonic frequencies did not detect the bearing damage. Hence the HM accuracy is 72.22%. The test is conducted on all conditions of the measurement distance variation with four repetitions. Table 2 shows the tabulation of the influence of non-machine noise on the accuracy of HM bearings.

The validity of the data for CRD analysis is tested for homogeneity and is carried out with Levene's test. The significance value (p) > 0.05 is said to be homogeneous, while if (p) < 0.05, hence the data is not homogeneous. HM data with the measurement

Table 2
Data tabulation of the effect of non-machine noise on the accuracy of HM bearing

Non-machine sound	Repetition (r)				Average
	1	2	3	4	
S1	0	5.55	0	0	1.3875
S2	72.22	66.66	61.11	66.66	66.6625
S3	83.33	83.33	88.88	88.88	86.105
S4	66.66	61.11	61.11	61.11	62.4975
S5	72.22	72.22	77.77	77.77	74.995
S6	55.55	55.55	61.11	61.11	85.33

distance variations get a calculated value of 0.831. When the value is greater than 0.05, homogeneity is achieved. Parametric statistical analysis requires data with a normal distribution; therefore, carrying out the Anderson-Darling normality test is necessary. The results showed that the P-value is 0.196, which means it is greater than the value of 0.05. Hence, it is stated that the HM data is normally distributed.

Hypothesis testing using CRD with the calculation of the analysis of variance is shown in Table 3. From the ANOVA, the effect of distance measurement as a treatment of non-machine noise factor on the accuracy of HM gets an F-count value greater than the F-table. Hence the hypothesis (H1) is accepted. It means that there is an effect of distance measurement, as a non-machine sound factor, on the accuracy of HM. When analyzed through the coefficient of determination (R Square), the influence of non-machine sound on the accuracy of HM contributes 98.87%. At the same time, other factors cause the remaining 1.13%. The R square value of 0.75, 0.50, and 0.25 belongs to the strong, moderate, and weak categories, respectively (Gouda et al., 2020). The results found that non-machine sound is a strong category.

Table 3
Analysis of variance on the effect of non-machine sound on the accuracy of HM

Source of Diversity	Free Degrees	Sum of squares	Middle square	F-count	F-table
Treatment	5	17513.7	3502.74	314.56	2.77
Galat	18	200.4	11.14		
Total	23	17714.1			

Further analyses use the Tukey test or Honest Significance Difference (HSD) to discover the best measurement distance. Tukey's test is used to compare all treatment pairs after the analysis of variance was performed. The principle is to compare the difference between each average with a critical value (w). When the absolute value of the average difference being compared is more than or equal to the critical value, it is stated that the two averages are significantly different (Priyastama, 2020). The follow-up tests showed that HM produces

the best accuracy with a measuring distance of 100 cm and the largest average of 86.10. The noise experienced by industrial machine maintenance operators when sound data is taken at 100 cm from the machine body is contaminated with the noise of 83.59dB(A). This value is still below the specified noise permit (85 db(A)).

Effect of Motor Load Variation on HM Bearing Accuracy

The operation of electric motors in the industry is always under load conditions. The load varies depending on the desired production capacity and is used as the basis for all tests on electrical machine systems. Figure 6 shows a sound signal in the frequency domain transformed by the FFT algorithm in testing the condition of the motor under load. The bearing conditions are known by comparing the amplitude values for each harmonic

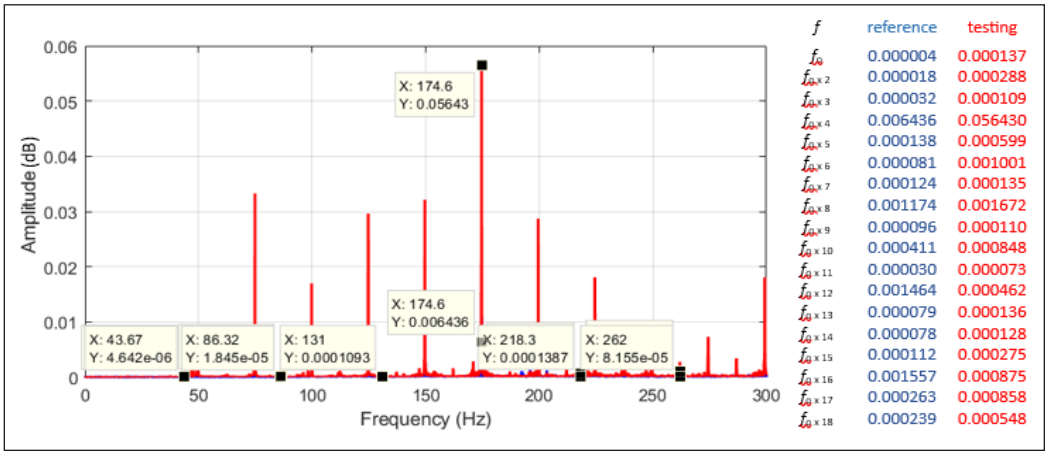

(a)

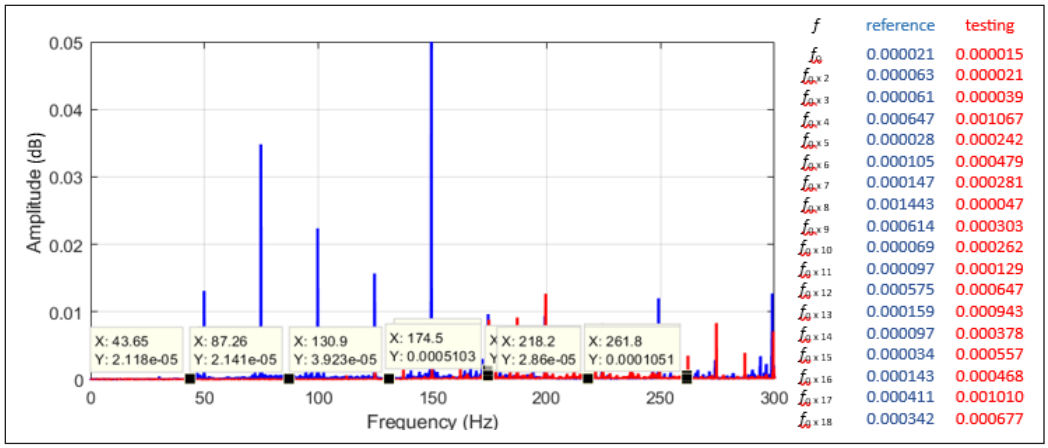

(b)

Figure 6. Frequency domain sound signal under: (a) Treatment L1 with 0N load; and (b) Treatment L2 with 10N load

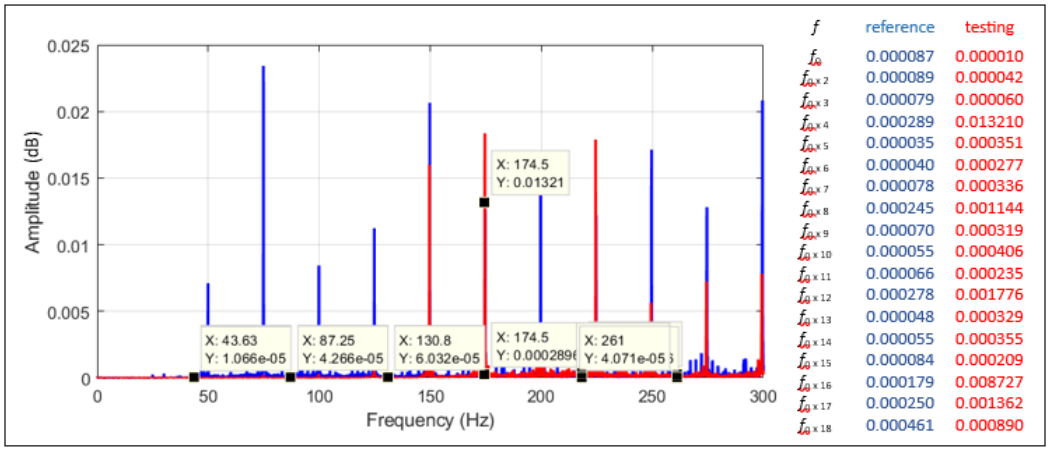

(c)

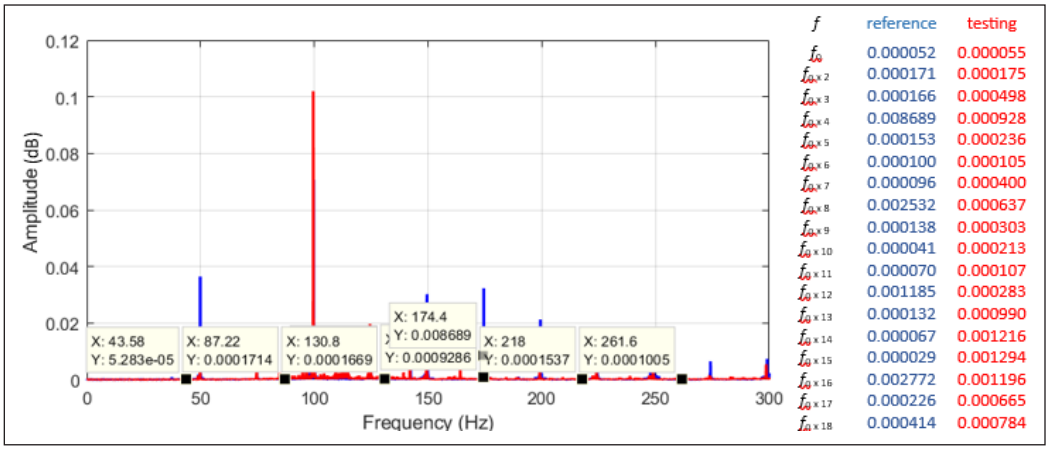

(d)

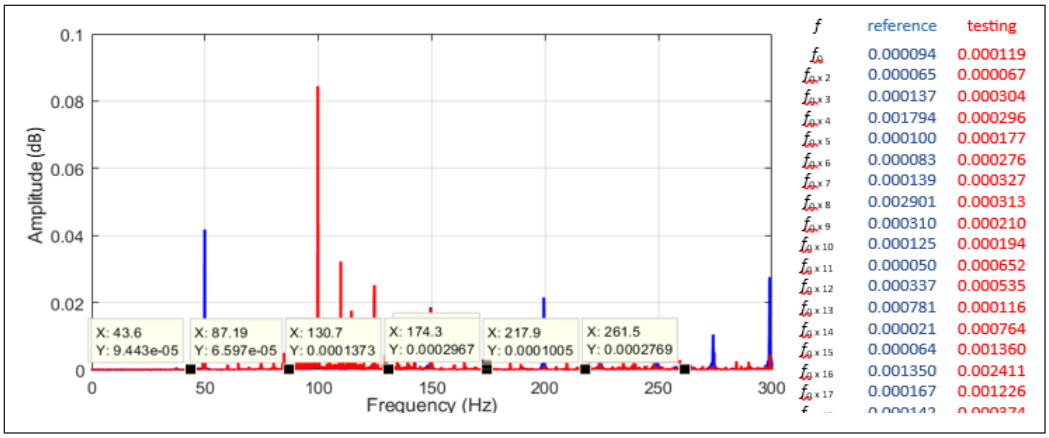

(e)

Figure 6 (continue). Frequency domain sound signal under: (c) Treatment L3 with 20N load; (d) Treatment L4 with 30N load; and (e) Treatment L5 with 40N load

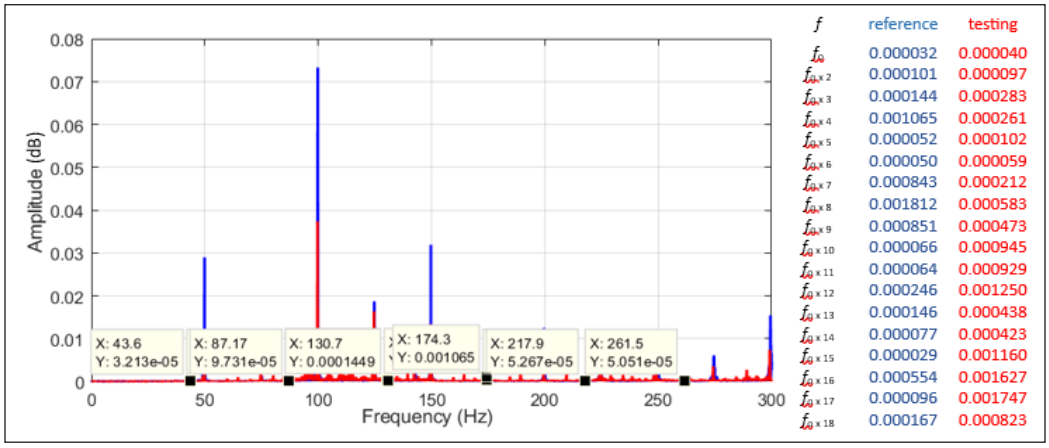

(f)

Figure 6 (continue). Frequency domain sound signal under: (f) Treatment L6 with 50N load

frequency. Each sound signal is observed up to the 18th harmonic frequency with the sound signal for 30 seconds. Table 4 shows the results of HM accuracy by conducting four tests repeatedly until it is observed that all HM results get a high percentage of accuracy.

The CRD variance analysis showed that the F-count (0.06) was smaller than the F-table (2.77). Hence, the H1 hypothesis is rejected. It means that loading does not affect the accuracy of HM. The analysis of R Square showed a value of 14.29%. Hence, the independent variable (load variation) is categorized as weakly affecting the accuracy of HM. Therefore, HM bearings are performed on the motor operating without or with different load values.

Table 4
Tabulation of the effect of load variations on the accuracy of HM

Load Variation	**Repetition (r)**				**Average**
	1	2	3	4	
L1	83.33	83.33	88.88	88.88	86.105
L2	72.22	88.88	88.88	77.77	81.9375
L3	77.77	83.33	83.33	77.77	80.55
L4	77.77	83.33	88.88	77.77	80.55
L5	83.33	83.33	88.88	77.77	82.3275
L6	88.88	83.33	88.88	77.77	84.715
General average					82.86417

Some previous research was discussed to develop the HM system further. Table 5 presents the differences between the previous research and the proposed development. It shows the differences in data input, signal processing techniques, noise measurement, the effect of non-machine variables on HM accuracy, and load variations. One of the health

monitoring systems that must be developed is to examine the effect of environmental noise on the accuracy of HM (AlShorman et al., 2020). The proposed method contributes to the development of bearings by considering noise, measuring distance, and load variations. Using non-invasive techniques, FFT signal processing, and band-pass filtering, the bearing approach provides promising diagnostic results. It is necessary to consider the backfill distance when performing motor monitoring actions to obtain low noise and good HM accuracy.

Table 5
Similar HM research

Works	HM Data	Signal processing technique	Noise Monitoring	Non-machine Sound Effect	Motor load variation
Elasha et al. (2017)	Vibration	FFT	No	No discussion on measuring distance	Yes
Daraz et al. (2018)	Sound signal, vibration	FFT	No	No discussion on measuring distance	No
Nirwan and Ramani (2022)	Sound signal, vibration	FFT	No	No discussion on measuring distance	Yes
Lucena-Junior et al. (2020)	Sound signal	signal analysis based on chaos using a density of maxima (SAC-DM)	No	No discussion on measuring distance	Yes
Glowacs et al. (2018)	Sound signal	MSAF-20-MULTIEXPANDED	No	Fixed measuring distance of 30 cm	Yes
Zhong et al. (2018)	Sound signal	Ensemble empirical mode decomposition	No	Fixed measuring distance of 50 cm	No
AlShorman et al. (2020)	Review	Artificial Intelligence Methods		provide future challenges and trends for the next researcher to discuss the effect of environmental noise	
AlShorman et al. (2021)	Sound signal	Review all technique		Review, challenges and future trends are also discussed	
Proposed method	Sound signal	FFT	Yes	Best measurement distance analysis on HM accuracy and noise	Yes

CONCLUSION

With non-invasive techniques through motor sound and signal processing using the FFT algorithm, the HM system produces an average accuracy of 83.09%. Therefore, this technique is recommendable as an alternative to HM in preventing negative environmental

impact. When the results of the HM state that the bearing is in a damaged condition, maintenance actions should be conducted to prevent damage to other motor parts. The operation of faulty motor parts increases the noise level. According to the analysis data, the noise of the damaged bearing conditions is above the threshold intensity of 85dB(A). Hence, it needs to be maintained for the safety of industrial workers. Sound data retrieval for HM is influenced by non-engine noise and variations in motor loading. The sound of the engine easily overlaps with that of the non-machine or the vibration from the engine body. The CRD statistical analysis showed that hypothesis (H1) was accepted. It means that the measurement distance, an independent variable of non-machine sound, affects the accuracy of the HM. The Tukey test indicated that the best HM accuracy was obtained at 100 cm with the noise level not exceeding the intensity value of 83.59 dB(A). The effect of loading on the motor does not affect the accuracy of the HM. Hence the condition of the motor part is diagnosed with or without load. Therefore, as negative environmental prevention, HM is conducted at any time and periodically when the motor operates with or without load.

The proposed HM provides the advantages of a simple and inexpensive technique. Hence it is recommendable as an alternative for monitoring the condition of other motor parts, for example, the rotor bar, stator, and shaft balance. Further research needs to be conducted on the severity of bearing damage. The reliability of the HM does not need to be doubted when tested with minor damage. The signal processing technique could be developed using deep learning methods and signal to filter for noise reduction, affecting HM accuracy. The weakness of the proposed method is that changes strongly influence the determination of the bearing frequency in motor speed. Therefore, speed measurement accuracy is needed to prevent errors in conducting FD bearings.

ACKNOWLEDGEMENTS

The authors are grateful to the team from the Electrical Machinery Laboratory of Hang Tuah University, Surabaya, Indonesia.

REFERENCES

AlShorman, O., Irfan, M., Saad, N., Zhen, D., Haider, N., Glowacz, A., & AlShorman, A. (2020). A review of artificial intelligence methods for condition monitoring and fault diagnosis of rolling element bearings for induction motor. *Shock and Vibration*, *2020,* Article 8843759. https://doi.org/10.1155/2020/8843759

AlShorman, O., Alkahatni, F., Masadeh, M., Irfan, M., Glowacz, A., Althobiani, F., Kozik, J., & Glowacz, W. (2021). Sounds and acoustic emission-based early fault diagnosis of induction motor: A review study. *Advances in Mechanical Engineering*, *13*(2), Article 1687814021996915. https://doi.org/10.1177/1687814021996915

Amanuel, T., Ghirmay, A., Ghebremeskel, H., Ghebrehiwet, R., & Bahlibi, W. (2021). Comparative analysis of signal processing techniques for fault detection in three phase induction motor. *Journal of Electronics*, *3*(01), 61-76. https://doi.org/10.36548/jei.2021.1.006

Aminian, O., Saraie, M., Ahadi, M., & Eftekhari, S. (2021). Association of the working environment noise with occupational stress in industrial workers. *Journal of Public Health, 2021*, Article 152. https://doi.org/10.1007/s10389-021-01605-y

Barusu, M. R., & Deivasigamani, M. (2020). Non-invasive vibration measurement for diagnosis of bearing faults in 3-phase squirrel cage induction motor using microwave sensor. *IEEE Sensors Journal*, *21*(2), 1026-1039. https://doi.org/10.1109/JSEN.2020.3004515

Daraz, A., Alabied, S., Smith, A., Gu, F., & Ball, A. D. (2018, September 6-7). *Detection and diagnosis of centrifugal pump bearing faults based on the envelope analysis of airborne sound signals.* [Paper presentation]. 24th International Conference on Automation and Computing (ICAC), Newcastle Upon Tyne, UK. https://doi.org/10.23919/IConAC.2018.8749053

Das, A., & Ray, S. (2020, February 28-29). *A review on diagnostic techniques of bearing fault and its modeling in induction motor*. [Paper presentation]. 2020 IEEE Calcutta Conference (CALCON), Kolkata, India. https://doi.org/10.1109/CALCON49167.2020.9106511

Elasha, F., Greaves, M., Mba, D., & Fang, D. (2017). A comparative study of the effectiveness of vibration and acoustic emission in diagnosing a defective bearing in a planetry gearbox. *Applied Acoustics*, *115*, 181-195. https://doi.org/10.1016/j.apacoust.2016.07.026

Ewert, P., Kowalski, C. T., & Orlowska-Kowalska, T. (2020). Low-cost monitoring and diagnosis system for rolling bearing faults of the induction motor based on neural network approach. *Electronics*, *9*(9), Article 1334. https://doi.org/10.3390/electronics9091334

Glowacz, A., Glowacz, W., Glowacz, Z., & Kozik, J. (2018). Early fault diagnosis of bearing and stator faults of the single-phase induction motor using acoustic signals. *Measurement*, *113*, 1-9. https://doi.org/10.1016/j.measurement.2017.08.036

Gouda, O. E., & El-Hoshy, S. H. (2020). Diagnostic technique for analysing the internal faults within power transformers based on sweep frequency response using adjusted R-square methodology. *IET Science, Measurement & Technology*, *14*(10), 1057-1068. https://doi.org/10.1049/iet-smt.2020.0048

Goyal, D., Mongia, C., & Sehgal, S. (2021). Applications of digital signal processing in monitoring machining processes and rotary components: a review. *IEEE Sensors Journal*, *21*(7), 8780-8804. https://doi.org/10.1109/JSEN.2021.3050718

He, F., Xie, G., & Luo, J. (2020). Electrical bearing failures in electric vehicles. *Friction*, *8*(1), 4-28. https://doi.org/10.1007/s40544-019-0356-5

Karyatanti, I. D. P., Dewantara, B. Y., & Utomo, W. M. (2019). Healthy monitoring and fault detection outer race bearing in induction motor using stator current. *International Journal of Integrated Engineering*, *11*(3), 181-193. https://doi.org/10.30880/ijie.2019.11.03.019

Lucena-Junior, J. A., de Vasconcelos Lima, T. L., Bruno, G. P., Brito, A. V., de Souza Ramos, J. G. G., Belo, F. A., & Lima-Filho, A. C. (2020). Chaos theory using density of maxima applied to the diagnosis of three-

phase induction motor bearings failure by sound analysis. *Computers in Industry*, *123*, Article 103304. https://doi.org/10.1016/j.compind.2020.103304

Priyastama, R., (2020). *The Book of SPSS: Pengolahan & Analisis Data*. Penerbit Anak Hebat Indonesia.

Nirwan, N. W., & Ramani, H. B. (2022). Condition monitoring and fault detection in roller bearing used in rolling mill by acoustic emission and vibration analysis. *Materials Today: Proceedings*, *51*, 344-354. https://doi.org/10.1016/j.matpr.2021.05.447

Zhong, J. H., Wong, P. K., & Yang, Z. X. (2018). Fault diagnosis of rotating machinery based on multiple probabilistic classifiers. *Mechanical Systems and Signal Processing*, *108*, 99-114. https://doi.org/10.1016/j.ymssp.2018.02.009

Pertanika J. Sci. & Technol. 31 (4): 2123 - 2143 (2023)

PERTANIKA JOURNALS

SCIENCE & TECHNOLOGY

Journal homepage: http://www.pertanika.upm.edu.my/

Self-Consistent Positive Streamer-Leader Propagation Model Based on Finite Element Method (FEM) and Voltage Distortion Method (VDM)

Ziwei Ma, Jasronita Jasni*, Mohd Zainal Abidin Ab Kadir and Norhafiz Azis

Department of Electrical and Electronic Engineering, Faculty of Engineering, Universiti Putra Malaysia, 43400 UPM, Serdang, Selangor, Malaysia

ABSTRACT

Researchers have worked on positive leader propagation models and proposed different theoretical and numerical approaches. The charge simulation method (CSM) has traditionally been chosen to model the quasi-static electric field of each stage of leader propagation. The biggest drawback of the CSM is that the calculation is complicated and time-consuming when dealing with asymmetric electric field structures. On the contrary, the finite element method (FEM) is more suitable and reliable for solving electrostatic field problems with asymmetric and complex boundary conditions, avoiding the difficulties of virtual charge configuration and electric field calculation under complex boundary conditions. This paper modeled a self-consistent streamer-leader propagation model in an inverted rod-plane air gap based on FEM and the voltage distortion method (VDM). The voltage distortion coefficient was analyzed to calculate the streamer length and space charge. The physical dynamic process of the discharge was simulated with the help of COMSOL Multiphysics and MATLAB co-simulation technology. The results show that the initial voltage of the first corona is -1036 kV, close to the experiment value of -1052 kV. The breakdown voltage of -1369 kV is highly consistent with the experimental value of -1365 kV. The largest streamer length is 2.72 m, slightly higher than the experimental value of 2.3 m. The leader velocity is 2.43×104 m/s, close to the experiment value of 2.2×104 m/s. This model has simple calculations and can be used in complex electrode configurations and arbitrary boundary conditions without simplifying the model structure, making the model more flexible.

Keywords: COMSOL, FEM, leader progression model, space charge, streamer, voltage distortion method

ARTICLE INFO

Article history:
Received: 22 August 2022
Accepted: 14 November 2022
Published: 13 June 2023

DOI: https://doi.org/10.47836/pjst.31.4.30

E-mail addresses:
GS59360@student.upm.edu.my (Ziwei Ma)
jas@upm.edu.my (Jasronita Jasni)
mzk@upm.edu.my (Mohd Zainal Abidin Ab Kadir)
norhafiz@upm.edu.my (Norhafiz bin Azis)
* Corresponding author

ISSN: 0128-7680
e-ISSN: 2231-8526

INTRODUCTION

Long-gap discharge experiments under various electrode structures carried out by Les Renardières Group (1972, 1974) have made people systematically recognize the phenomenon and characteristics of the leader discharge. Based on the understanding of the physics of leader inception and development, the leader propagation method (LPM) was introduced to simulate the process of leader discharge in the 1970s. In engineering applications, such as lightning protection design, LPM is recommended as a more physically reasonable method to evaluate the lightning protection performance of grounded structures under the influence of lightning downward leader (Cigre, 2021). Theoretical approaches and numerical models of positive leader discharge based on LPM have been developed in the past few decades.

Rizk (1989) developed a mathematical model for stable leader inception and breakdown of rod-plane gaps under positive switching impulse voltage based on the basic theory of the electrostatic field. This model was successfully extended to conductor-plane gaps and could predict the 50% breakdown voltage for a wide range of air spacing. However, this model cannot simulate the dynamic process of leader development.

Bondiou and Gallimberti (1994) proposed a self-consistent leader inception and propagation model (SLIM) based on the mass, momentum, and energy conservation equations. In this model, the output of each discharge stage is used as the next stage's input, and the input parameters are only the electrode geometry and the applied voltage waveform. However, the model involves many physical parameters, making the calculation process complex.

Based on the Bondiou & Gallimberti model, Goelian et al. (1997) introduced a numerical model to calculate the space charge and the streamer length using the voltage distortion method (VDM). However, the function used to calculate the streamer space charge is related to the electrode structure and to the streamers' length, number, and radius. So, the calculation process is much more complicated. At the same time, the model only considers the case where the electrode voltage is constant, while the electrode voltage is a constantly changing voltage in most actual situations.

Becerra and Cooray (2006a) proposed a simplified self-consistent upward leader model-based VDM. In this model, the calculation of streamer space charge is simplified by using the electrode geometry coefficient K_Q multiplied by the area difference between the background voltage U_1 and the streamer voltage U_2. However, the model chooses the geometric coefficient K_Q as a constant value and does not further analyze the factors affecting K_Q. In addition, to simplify the calculation, the model replaces the distribution of the background voltage U_1 with a straight-line segment, exaggerating the areas enclosed by U_1 and U_2 so that the calculated space charge of the streamer may be larger than the actual value. Simplified VDM proposed by Becerra and Cooray (2006a) is widely used in leader discharge simulation, such as the research done by Mohammadi et al. (2019) and Gu et al. (2020).

The models mentioned above use the charge-simulated method (CSM) to calculate the electric field distribution generated by the applied voltage and streamer space charge. The disadvantage of the CSM is that the calculation process will become so sophisticated when encountering asymmetric and complex electric field structures that the computation time and computational memory requirements become large. Because of this, it is often necessary to simplify the complex electric field structure into a simple structure, leading to a large error between the calculated and actual results. For the problem of the electrostatic field, the finite element method (FEM) is a more effective and reliable method for the electrostatic boundary value problems. Especially when dealing with asymmetric electrode structures and complex boundary conditions in practical engineering, FEM can take advantage of its faster calculation speed and higher calculation accuracy. The research done by Talaat et al. (2019), Becerra (2013), Zhou et al. (2018), and Diaz et al. (2018) has proved that.

Today's advancement of FEM commercial software, such as COMSOL, has multiphysics coupling functions and powerful computing capabilities and has been widely used in engineering applications and scientific research. For example, Gao et al. (2020), Hnatiuc et al. (2019), Brezmes and Breitkopf (2014), and Arevalo et al. (2012) used COMSOL Multiphysics to simulate the discharge process in air. Rodrigues et al. (2019), Yang et al. (2017), Chen et al. (2016), and Xu and Chen (2013) used COMSOL Multiphysics to research the characteristics of lightning strike protection in engineering.

The main goal of this paper is to develop a positive self-consistent leader Inception and propagation model of an inverted rod plane under the switching impulse voltage based on the latest physical knowledge obtained in DC discharge experiments. The calculation adopts the FEM and the VDM to calculate the streamer length and steamer space charge at every step of the discharge process. Based on the previous calculation, the velocity and the length of the leader, the length of the final jump, and the breakdown voltage can be calculated. The model can complete the self-iterative calculation through COMSOL and MATLAB co-simulation technology. The validity of this model can be verified by comparing it with experimental results in the literature. Ultimately, this numeric model will be extended to simulate the development process of the positive upward leader generated from EHV TLs under the impact of the lightning downward leader so that the lightning shielding performance of EHV TLs can be evaluated.

INPUT PARAMETERS AND METHODOLOGY

Design Parameters for Simulation Model

In order to verify the validity of the simulation, the size of the simulation model is the same as the actual experimental model (He et al., 2012). The electrode system of the model is an inverted rod-plane structure (Figure 1). The plane electrode is suspended in the air

at 5 m above the ground and is connected to the generator of switching impulse voltage. The rod electrode covered with a spherical head is placed on the grounded and directly grounded. A negative standard switching impulse voltage with an amplitude of 1500 kV is applied to the plane electrode. The geometric parameters and applied voltage of the experimental setup are shown in Table 1.

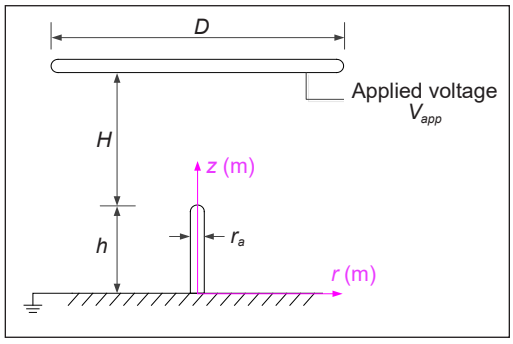

Figure 1. The inverted rod-plane electrode structure of the experiment

Table 1
Geometric parameters and applied voltage of the simulation model

Parameter item	Parameter value	Unit
The height of the rod h	2	m
The radius of the rod r_a	15	cm
The length of the air gap H	3	m
The side length of plane D	6	m
The amplitude of the applied voltage V_{app}	1500	kV
The wavefront/tail time of V_{app} T_f/T_t	250/2500	μs

Simulation Modeling

A 2D symmetrical model is built in COMSOL Multiphysics (Figure 2). The boundary conditions are constrained: 1 is a high voltage boundary, 2 and 3 are zero potential, and 4 is an infinite element domain. The infinite element domain replaces the infinitely extending space around the electrode system. The electric field does not change abruptly on the inner boundary of the infinite element domain, while on the outer boundary of the infinite domain, the electric potential is zero. The model is symmetric, so only half of the computational domain is shown in Figure 2.

Meshing is the key to FEM calculation. The index for judging the quality of meshing is the element quality. COMSOL provides seven element quality measurement tools: skewness, maximum angle, volume versus circumradius, volume versus length, condition number, growth rate, and bending skewness. Skewness is suitable for most mesh types and is adopted as the measurement tool of mesh quality for this

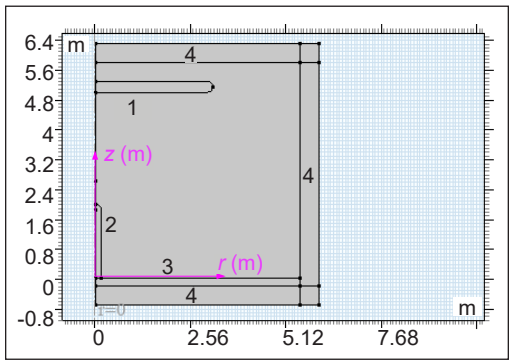

Figure 2. 2D axisymmetric simulation model

model. Skewness refers to the degree of closeness between the mesh element and the equal-angle ideal element. The calculation method is shown in Equation 1, where θ_e is the vertex angle of the ideal element, and θ is the vertex angle of the divided mesh element, as shown in Figure 3. Green represents the high-quality meshes, and red represents the low-quality meshes. The mesh element quality measure is between 0 and 1, with 1 being extremely high quality and 0 being extremely poor quality. The criteria for the mesh element quality are shown in Table 2.

$$Skewness = 1 - \max\left(\frac{\theta - \theta_e}{180 - \theta_e}, \frac{\theta_e - \theta}{\theta_e}\right) \quad [1]$$

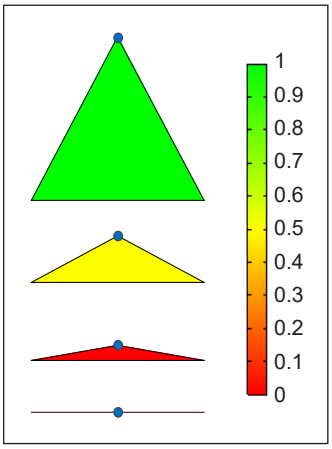

Figure 3. Schematic diagram of mesh skewness measurement

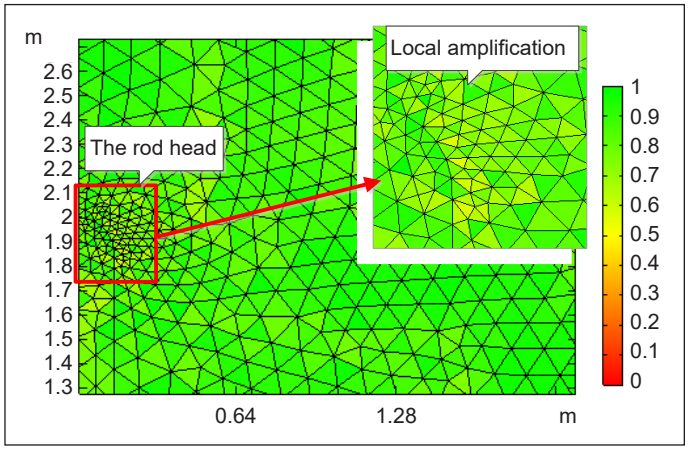

Figure 4. Mesh element quality in rod head region in a 2D axisymmetric model

Adaptive meshing is used in this model. Except for the infinite element domain, which uses a regular quadrilateral mesh, the rest of the domains are all triangular meshes. The mesh quality of the rod electrode head, which is of most concern, is shown in Figure 4. The curvature of the rod electrode head is large, so the quality of the mesh element is relatively poor, as shown in the yellow part in Figure 4.

Table 2
The criteria for the mesh element quality

Skewness	Mesh element quality
< 0.02	Extremely poor
0.02 ≤ Skewness < 0.2	Poor
0.2 ≤ Skewness < 0.35	Basic
0.35 ≤ Skewness < 0.75	Medium
0.75 ≤ Skewness < 1	High
1	Extremely high

After applying a locally refined mesh to the rod electrode head region, the number of low-quality elements is reduced (Figure 5). From the mesh statistics, after local refinement, the minimum and average element quality are improved (Table 3). The average element quality of this model is above 0.9, indicating that the mesh quality is high.

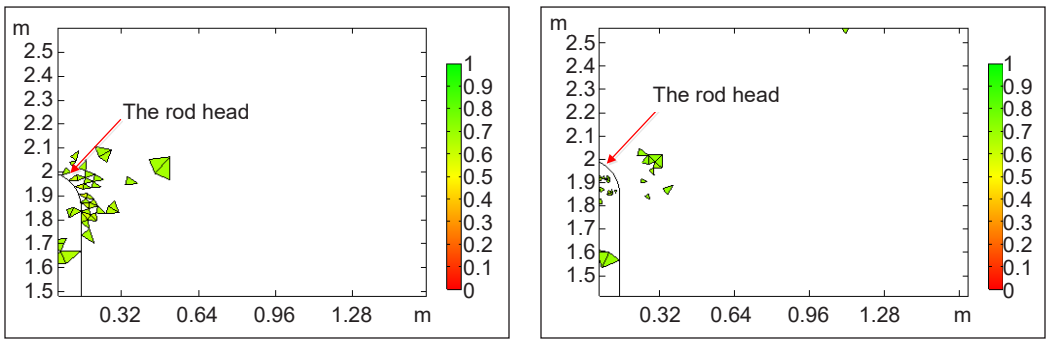

Figure 5. Comparison of mesh element quality before and after mesh refinement in the region of the rod head: (a) Before mesh refinement; and (b) After mesh refinement

Table 3
Meshing statistics of the 2D axisymmetric model

Mesh parameters	Before refinement	After refinement
Number of elements	6030	7117
Number of triangle elements	5365	6452
Number of quadrilateral elements	665	665
Minimal element quality	0.5503	0.5836
Average element quality	0.9102	0.9152

The Streamer-Leader Propagation Model

Many experimental studies have shown that the positive leader discharge process consists of five stages: initial streamer formation, streamer-leader transition, streamer-leader system development, final jump, and gap breakdown. If the radius of the positive electrode is larger than the critical radius, a stable streamer-leader discharge system can be generated after the initial corona (Les Renardières Group, 1972, 1974). This model does not cover the case where the radius of the positive electrode is smaller than the critical radius.

The theory of positive streamer discharge holds that the applied external electric field supplies the energy to generate the primary electron avalanche on the surface of the positive electrode (Nijdam et al., 2020). When the number of positive charges of the primary avalanche is greater than the critical value of 10^8 (Naidu & Kamaraju, 2013), the electric field generated by these charges is equivalent to the external applied electric field will induce secondary electron avalanches near the anode electrode. The secondary electron avalanches are attracted to the tail of the main avalanche, and the electrons are absorbed, leaving the newly generated positive charges in the tail of the main avalanche. This process continues to repeat, thus forming a streamer that develops from the anode to the cathode. It is generally considered that the critical field strength of the positive streamer inception is 2600 kV/m (Cooray, 2014; Gallimberti et al., 2002).

After the initial streamer is formed, multiple branched streamers in a dendritic shape are formed during its development. The free electrons generated by the branched streamers flow into the anode through the common streamer stem. As the streamers' current increases, the streamers' stem is heated. When the temperature exceeds 1500 K, thermal ionization greatly increases the electrical conductivity at the streamer stem, which turns the streamer stem into a high-temperature and high-conductivity leader channel (El-Zein et al., 2018; Gallimberti et al., 2002).

The field strength in the leader channel is relatively low, generally considered 30–50 kV/m (Becerra & Cooray, 2006a; Rizk, 2009). When the leader channel extends forward, most of the voltage of the anode is transmitted to the leader's head through the leader channel, which is equivalent to the forward extension of the anode. When the field strength of the leader's head reaches the critical intensity of air discharge, a new streamer is generated. This process is repeated to form a streamer-leader discharge development system (Figure 6). As the leader travels from the previous streamer zone, the streamer space charges form a corona sheath around the leader channel. Whether the leader can continue to develop depends on whether the streamer discharge at the leader's head can continuously provide energy to maintain the thermal ionization of the leader channel.

When the streamer at the head of the leader reaches the cathode, the final jump occurs. As a result, the leader channel quickly bridges the remaining gap, and a strong short-circuit current flows through the leader channel to break down the entire gap.

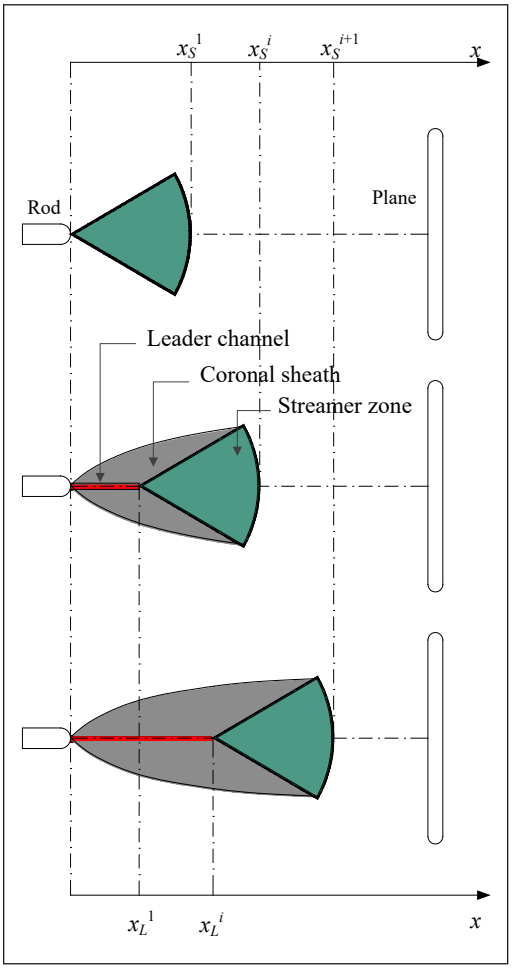

Figure 6. Schematic diagram of the streamer-leader system development

The Calculation of the Initial Streamer Length and Streamer Space Charge

The potential distribution generated by the applied voltage in the rod-plate gap is an exponential distribution curve, referred to as the potential background V_1 for short. During the streamer development, the streamer space charge will cause electric field distortion

in the gap between the electrodes. It is generally considered that the electric field inside the streamer zone is constant, and the value is about 450 kV/m–500 kV/m (Ding et al., 2016; Rizk, 2020; Petrov & Waters, 2021). Therefore, the voltage distribution in the streamer region is a linear curve, referred to as the streamer potential V_2 for short. The difference between these two voltage curves can calculate the degree of voltage distortion. In this way, the voltage distortion method (VDM) can be used to calculate the streamer length and space charge (Figure 7).

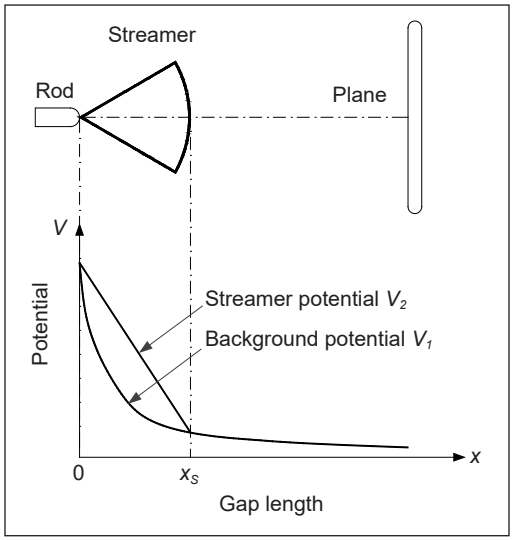

Figure 7. Calculation of streamer length and streamer space charge by VDM

The horizontal axis x in Figure 7 is the gap length, and the vertical axis V is the potential in the gap. The abscissa length x_s corresponding to the intersection of V_1 and V_2 is the length of the initial streamer. The streamer space charge can be calculated by multiplying the area A enclosed by the two curves by the voltage distortion coefficient K_Q (Equation 2).

$$Q = K_Q A = K_Q \int_0^{x_s} (V_2 - V_1) dx \qquad [2]$$

The Calculation of the Subsequent Streamer-Leader System

For this simulation model, the rod electrode radius is 15 cm, greater than the critical radius of 12.5 cm (He et al., 2012). Therefore, a stable development leader can be formed once the initial streamer is generated, which is also confirmed by the experiments (He et al., 2012). The discharge develops in a stepwise fashion. As mentioned earlier, continuous leader development depends on the charge provided by the streamer discharge at the head of the leader. The step length of the leader can be calculated by Equation 3 (Becerra & Cooray, 2006b), where Q_i is the space charge generated at ith step discharge in μC, τ is the charge density of the leader channel in μC/m.

$$l_L{}^i = \frac{Q_i}{\tau} \qquad [3]$$

Regarding the charge density of the positive leader channel, Gallimberti et al. (2002) considered it to be 20–50 μC/m. Petrov and Waters (2021) considered it to be 20 μC/m. Rizk (1989) and Becerra and Cooray (2006b) considered it 45–50 μC/m. Experiments by Wang et al. (2016) also indicated that the positive leader channel's charge density is 40–50

μC/m. Li et al. (2013) experiments confirmed the charge densities in the 30–50 μC/m. The experiments of Zeng et al. (2013) showed that the charge density is 30–70 μC/m. By artificially triggered lightning experiments, Lalande et al. (2002) observed a positive leader charge density of 65 μC/m. In this paper, the charge density of the positive leader channel is 25 μC/m.

The diameter of the leader channel is generally considered to be several millimeters, and this model takes 2 mm. The leader channel's voltage drop is calculated using Equation 4, where E_L is the average field strength of the leader channel in kV/m, and $l_L{}^i$ is the step length of the leader development to the ith step. The leader channel E_L's average field strength is 50 kV/m.

$$V_L{}^i = E_L l_L{}^i \qquad [4]$$

The velocity of the positive streamer development is on the order of 10^5 m/s. The experiments of Ding et al. (2016) and He et al. (2012) show that the average development speed of the positive streamer is 1×10^5 m/s. Cooray (2014) considered it to be 2×10^5 m/s. However, Nijdam et al. (2020) considered the velocity of the streamer to be on the order of 10^5–10^6 m/s. In this paper, the positive streamer's average velocity is assumed to be 1×10^5 m/s.

The potential distribution in the gap during the streamer-leader propagation is shown in Figure 8. $V_L{}^{i-1}$ is the voltage drop of the leader channel at step i-1. $V_2{}^{i-1}$ is the streamer voltage at step i-1. Once a new streamer is generated at the head of the leader channel, the streamer voltage decreases to $V_2{}^i$ due to the voltage clamping of the leader channel. The shaded area in Figure 8 is the area of voltage distortion caused by the newly generated streamer space charge. The newly generated streamer space charge can be calculated by multiplying this part of the area by the voltage distortion coefficient K_Q. The abscissa intersection $x_S{}^i$ of the two curves $V_1{}^i$ and $V_2{}^i$ is the position of the new streamer head, and the length of the new streamer can

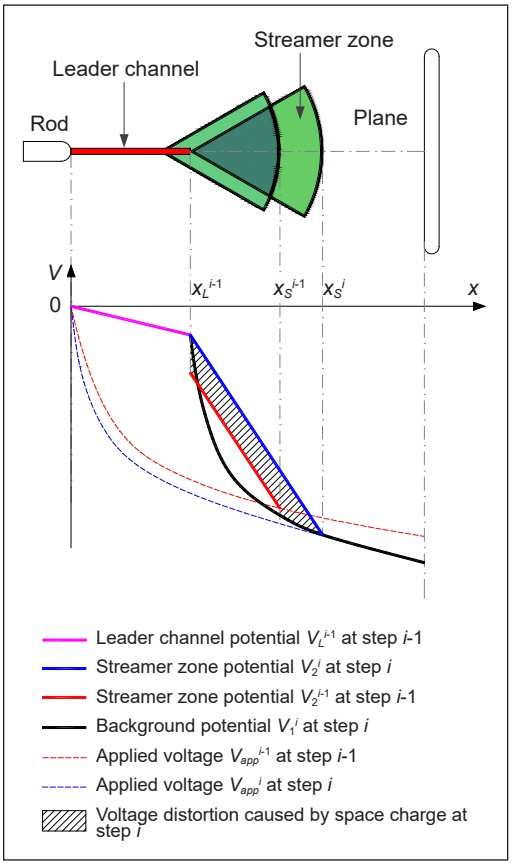

Figure 8. The streamer-leader system propagation and the potential gap distribution at step i

be obtained by subtracting the length of the leader channel V_L^{i-1} from x_S^i. V_{app}^{i-1} and V_{app}^{i} are the applied voltage on the plane at step i-1 and step I, respectively.

The streamer space charge at step i can be calculated by using Equation 5. x_L^{i-1} represents the leader channel length at step i-1. x_S^{i-1} and x_S^{i} represent the position of the streamer head at steps i-1 and i, respectively.

$$Q_i = K_Q \int_{x_L{}^{i-1}}^{x_S{}^{i-1}} \left(V_2{}^{i} - V_2{}^{i-1}\right) \mathrm{d}x + K_Q \int_{x_S{}^{i-1}}^{x_S{}^{i}} \left(V_2{}^{i} - V_1{}^{i}\right) \mathrm{d}x \quad [5]$$

This model only needs to input the electrode parameters and apply voltage waveform to simulate the dynamic process of streamer-leader propagation. Using the co-simulation technology of COMSOL Multiphysics and MATLAB, the streamer-leader size and applied voltage amplitude of each step of the discharge process can be calculated in MATLAB according to the voltage distribution of V_1 and V_2 output by the COMSOL model. The output of the previous step of the simulation is used as the input of the next step, and the model can realize self-iterative calculation. The simulation flowchart is shown in Figure 9.

RESULTS

The Critical Inception Voltage of the Streamer

Before the initial streamer is generated, there is no free-charge distribution in the plane-rod gap. The voltage distribution in the air gap is a Laplace function (Equation 6), where V is a scalar potential distribution function.

$$-\nabla^2 V(x, y, z) = 0 \quad [6]$$

At the boundary, the potential is constant. For the high-voltage electrode, the potential is the applied voltage (Equation 7), and for the ground electrode, the potential is 0 (Equation 8).

$$V(x, y, z) = V_0 \quad [7]$$

$$V(x, y, z) = 0 \quad [8]$$

Given the boundary potential, the problem of finding the spatial electric field distribution is the Dirichlet boundary problem. Due to the uniqueness of the electric field distribution, the unique function of the spatial potential distribution can be obtained by solving the Laplace Equation 6. The electric field strength vector is the negative value of the gradient of the scalar potential function; that is, the relationship of Equation 9 is satisfied. Based on these basic equations, the electric field distribution in the inverted rod-plane gap is calculated.

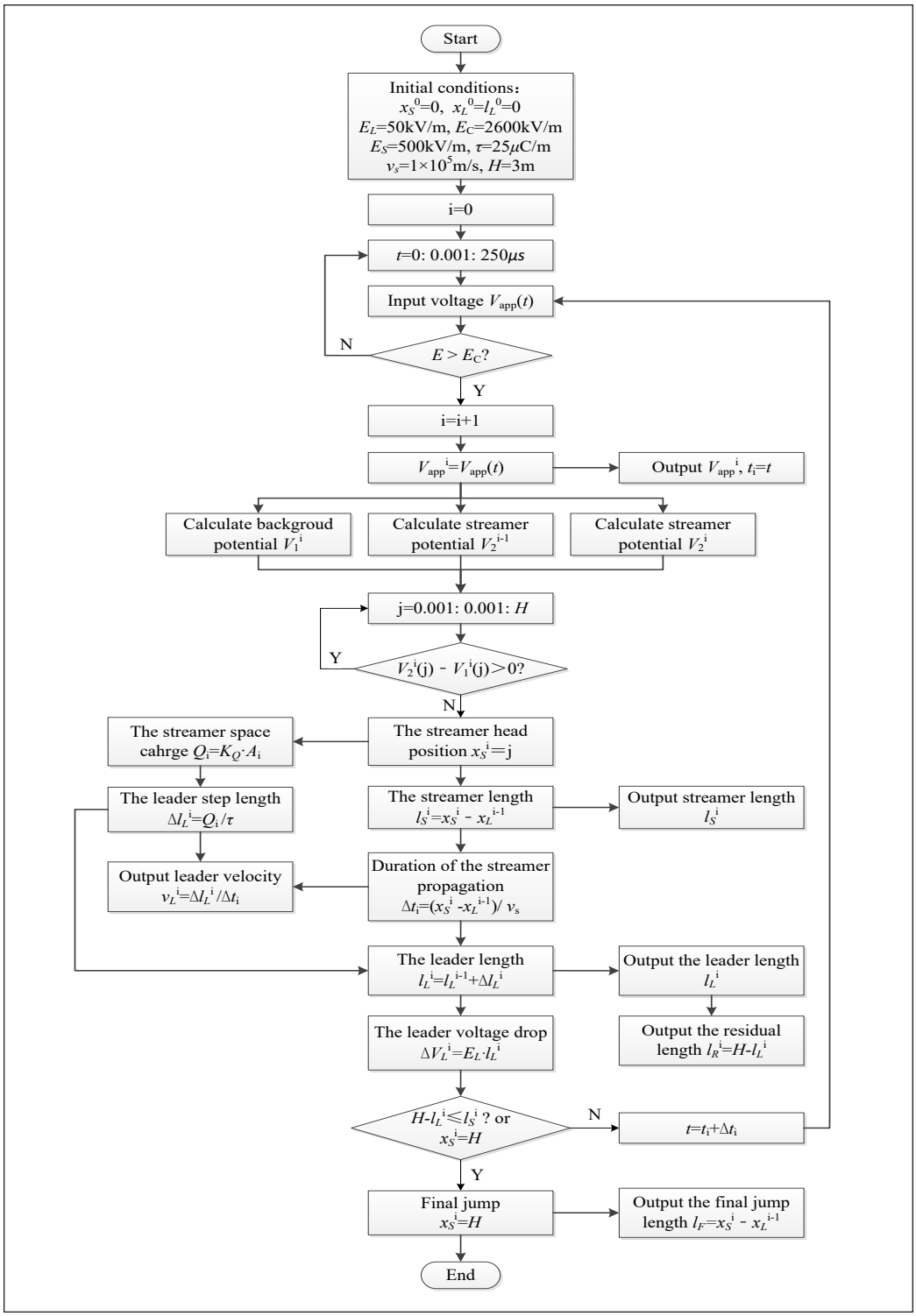

Figure 9. The simulation flowchart of the streamer-leader propagation model

$$\vec{E}(x,y,z) = -\nabla V(x,y,z) \quad [9]$$

The input voltage is a 250/2500 μs switching impulse voltage formed by a double exponential function with an amplitude of 1500 kV (Figure 10). With the gradual increase of the applied voltage, the electric field strength on the surface of the rod electrode increases gradually. When the electric field intensity reaches the critical electric discharge intensity of 2600 kV/m, the initial streamer is generated, and this moment is taken as the first step of the simulation process.

The simulation result shows that when the applied voltage of the plane electrode is increased to -1036 kV, the electric field strength on the surface of the rod electrode reaches the critical field strength of 2600 kV/m (Figure 11). The critical inception voltage of the streamer obtained by the simulation is close to the experimental value of -1052 kV, which proves that the calculation result of COMSOL Multiphysics is reliable.

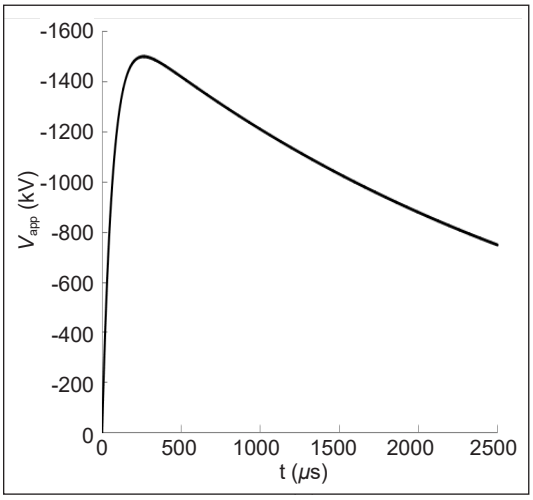

Figure 10. Switching impulse voltage waveform input by the simulation model

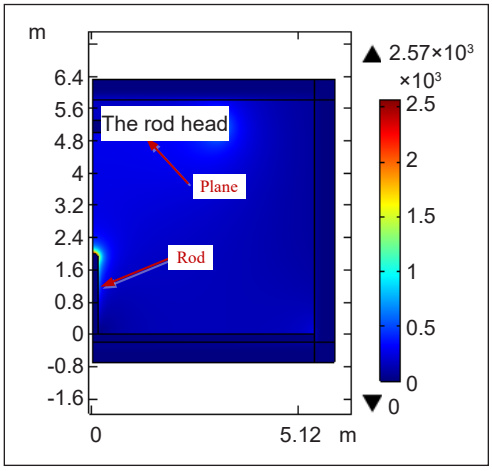

Figure 11. Electric field distribution in the 2D axisymmetric rod-plane gap under critical streamer inception voltage

The Initial Streamer Length and Streamer Space Charge

The selection of the coefficient K_Q is the key to calculating the streamer space charge. K_Q is related to the electrode structure (Becerra & Cooray, 2006a) and the streamer size (He et al., 2012). Becerra and Cooray's (2006a) model showed that the average value of K_Q is 0.035 μC/kV·m for the rod-plane electrode structure with a symmetric structure. The study by (He et al., 2012) shows that the K_Q value is in the range of (0.03-0.06) μC/kV·m. In this model, the back-calculation method is used, the space charge Q of the streamer is assumed in advance, and then the voltage distortion area A caused by the streamer space charge is calculated so that the distortion coefficient K_Q can be calculated from Equation

2. The calculation results show that K_Q is related to the gap and streamer lengths (Figure 12). With the increase of the gap distance, K_Q gradually decreases and tends to be saturated.

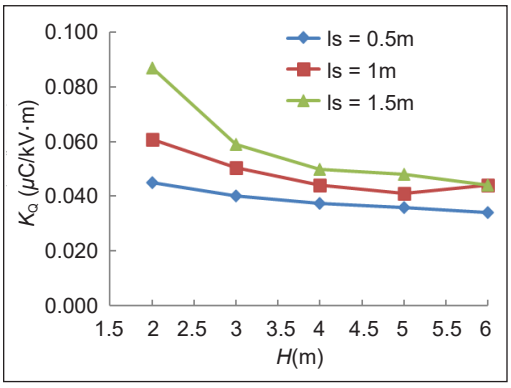

Figure 12. The relationship between K_Q and the gap distance and the length of the streamer under the negative plane-rod electrode structure

K_Q increases with the length of the streamer (Figure 12). Therefore, when using VDM to calculate the streamer space charge, different K_Q values should be selected according to the length of the streamer instead of taking a fixed average value as suggested by Becerra and Cooray (2006a) and He et al. (2012). The applied voltage and the gap length greatly affect the streamer length (Figure 13), where $V_1{}^i$ is the background potential generated by the electrode voltage, and $V_2{}^i$ is the streamer potential. The streamer length increases with the applied voltage for a certain gap length, as shown in Figure 13(a). The streamer length increases as the gap is shortened for a certain applied voltage, as shown in Figure 13(b). For this simulation model, the applied voltage to the plane electrode continues to increase until breakdown occurs. The gap length gradually decreases as the leader develops forward. Both trends will make the streamer longer. When the applied voltage exceeds -1350 kV, the streamer length can reach more than 2 m. Therefore, the value of K_Q should be between (0.04-0.08) μC/kV·m.

When the applied voltage reaches the critical corona onset voltage of 1036kV, the calculated initial streamer length is 1.04 m (Figure 13). K_Q should be taken as 0.05 μC/kV·m, from which the initial streamer space charge can be calculated to be 4.63 μC (Figure 12).

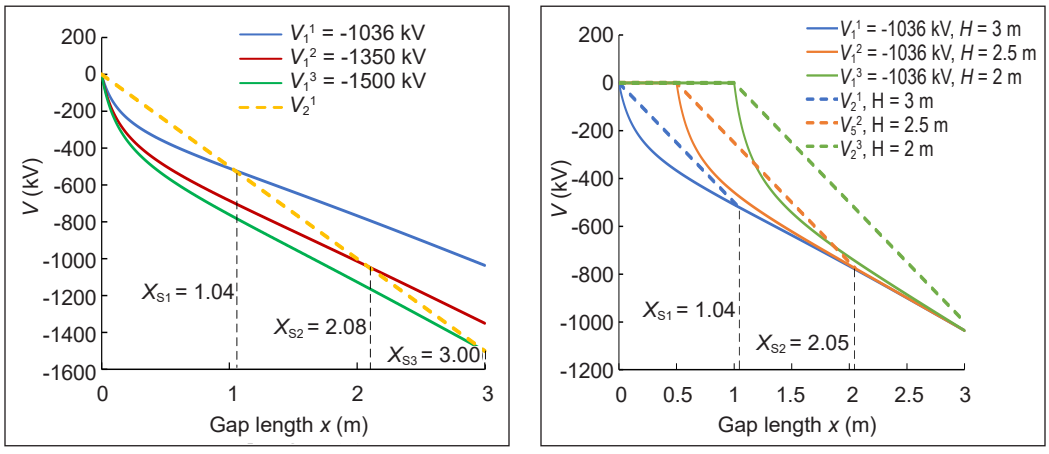

Figure 13. The effect of the: (a) applied voltage; and (b) gap length on the streamer length

Subsequent Streamer Length and Streamer Space Charge

The average speed of positive streamer propagation is assumed to be 1×10^5 m/s, from which the duration of the initial streamer can be calculated to be 10.4 μs. When the initial streamer propagation is completed, the applied voltage rises to -1117 kV. From Equation 3, the primary leader length can be calculated as 0.19 m. In the same way, as mentioned above, the secondary streamer length and streamer space charge can be calculated to be 1.41 m and 5.82 μC, respectively.

The subsequent streamer length and steamer space charge can be obtained by repeating the same calculation process (Figure 14). The final jump occurs after the streamer-leader system has developed 4 steps. In the final step, the background potential V_1^4 and the streamer potential V_2^4 do not intersect, which means that the head of the streamer has reached the plane electrode. It is generally believed that the final jump occurs when the head of the streamer reaches the opposite electrode (Cooray, 2014; Rizk, 1989). Thus, the final jump length can be obtained by subtracting the leader length from the gap length. The simulation results show that the final jump length is 2.04 m (Figure 14).

The macro parameters of each step of the leader discharge obtained by simulation are shown in Table 4. Before the final jump, the leader's velocity increases slightly with the leader's length. The average speed is about 2×10^4 m/s, close to the experiment result of 2.2×10^4 m/s (He et al., 2012). Once the final jump occurs, the leader velocity increases rapidly (Figure 15), where the abscissa l_L is the leader length, and the ordinate v_L is the leader speed. The variation trend of the leader speed is consistent with the experimental observation (He et al., 2012). The leader velocity of the final jump stage obtained by simulation is about 9.9×10^4 m/s, which is lower than the experiment results of 13.9×10^4 m/s but is highly close to the experiment result of 10×10^4 m/s observed by Les Renardières Group (1972, 1974).

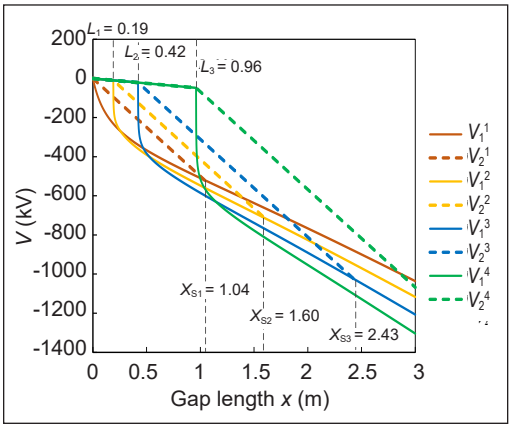

Figure 14. Gap potential distribution during the leader progression

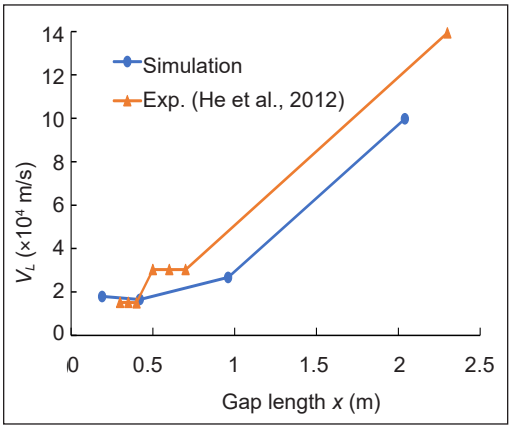

Figure 15. Comparison of the leader velocity simulation value and experimental value

Table 4
Simulation results of streamer-leader propagation system under the assumption of E_S=500 kV/m, τ=25 μC/m

Step	V_{app} (kV)	K_Q (μC/kV·m)	l_S (m)	Q (μC)	t (μs)	l_L (m)	v_L ($\times 10^4$ m/s)	l_R (m)	Final jump
1	-1036	0.05	1.04	4.63	68.7	0.00	0.00	3.00	N
2	-1117	0.054	1.41	5.82	79.1	0.19	1.79	2.81	N
3	-1207	0.072	2.01	13.43	93.2	0.42	1.65	2.58	N
4	-1304	0.072	2.04	37.16	113.3	0.96	2.67	2.04	Y
5	-1374					2.04	9.98	0	Breakdown

V_{app} is the applied voltage on the plane electrode. K_Q is the voltage distortion coefficient. l_S is the streamer length. Q is the streamer space charge. t is the moment when the new streamer is generated. l_L is the leader length. v_L is the velocity of the leader propagation. l_R is the residual length of the gap.

The streamer length and streamer space charge increase in steps. Especially the streamer space charge increases sharply in the final stage.

The comparison between the simulation and the experimental results shows that the inception voltage of the initial streamer and the 50% breakdown voltage are in good agreement with the experiment results (Table 5). The maximum streamer length, the final jump length, and the leader velocity are slightly lower than the experimental results.

However, the duration of the streamer discharge process obtained by the simulation is quite different from the experimental results. The reasons may come from initial assumptions' influence, such as the charge density of leader channel τ, streamer voltage gradient E_S, and streamer velocity v_S. The effect of these parameters on the streamer discharge duration is shown in Figures 16 to 18, where the ordinate x_s is the height of the streamer head, and the abscissa T_d is the duration of streamer discharge. Reducing the charge density of the leader channel, reducing the streamer voltage gradient, or increasing the streamer velocity can reduce the discharge duration.

Table 5
The comparison between the simulation results and the experimental results under the assumption of E_S=500 kV/m, τ=25 μC/m

Parameters	Simulation results	Experimental results (He et al., 2012)	Unit	Error (%)
V_{ini}	-1036	-1052.00	kV	-1.5
l_{SM}	2.04	2.30	m	-11.3
l_F	2.04	2.30	m	-11.3
v_L	2.04	2.20	$\times 10^4$ m/s	-7.3
T_d	44.6	29.7	μs	50.2
$V_{50\%}$	-1374	-1365.00	kV	0.7

V_{ini} is the critical inception voltage of the streamer. l_{SM} is the maximum streamer length. v_L is the average velocity of the leader propagation. T_d is the duration of the streamer discharge process. l_F is the length of the final jump. $V_{50\%}$ is the 50% breakdown voltage.

Based on the above analysis, two other simulations were carried out assuming that E_S=450 kV/m, τ=25 μC/m. The simulation results are shown in Table 6. The comparison between the simulations and experiment is shown in Table 7. Among the three simulations, the assumption of E_S=450 kV/m, τ=25 μC/m, and v_S=1×10^5 m/s yields the simulation results closest to the experimental values.

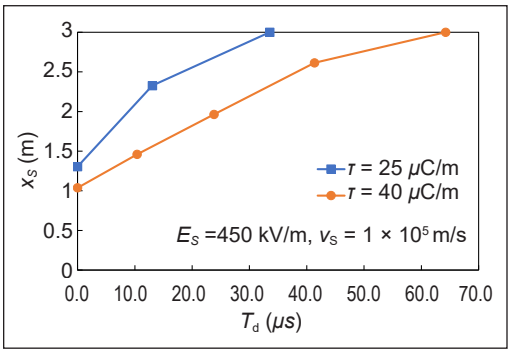

Figure 16. The effect of charge density τ on discharge duration under the assumption that E_S=450 kV/m, v_S=1×10^5 m/s

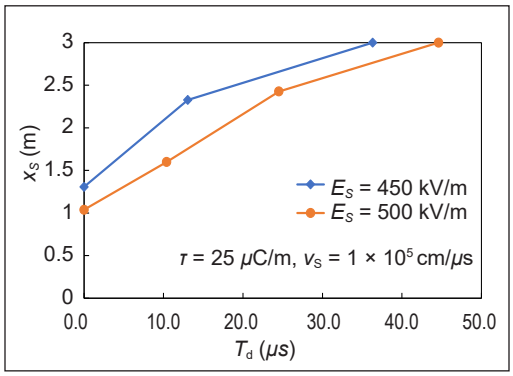

Figure 17. The effect of the voltage gradient of the streamer on discharge duration under the assumption that τ=25 μC/m, v_S=1×10^5 m/s

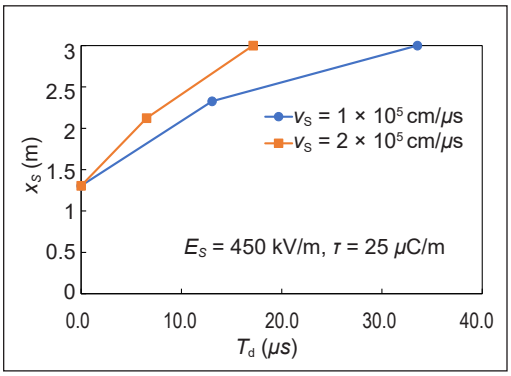

Figure 18. The effect of streamer velocity on discharge duration under the assumption that E_S=450 kV/m, τ=25 μC/m

Table 6
Simulation results of streamer-leader propagation system under the assumption that E_S=450 kV/m, τ=25 μC/m

Step	V_{app} (kV)	K_Q (μC/kV·m)	l_S (m)	Q (μC)	t (μs)	l_L (m)	v_L (×10^4 m/s)	l_R (m)	Final jump
v_S=1×10^5 m/s									
1	-1036	0.055	1.31	6.96	68.7	0.00	0.00	3.00	N
2	-1136	0.08	2.33	15.90	81.8	0.28	2.13	2.72	N
3	-1268	0.10	2.72	56.70	105.0	0.91	2.73	2.09	Y
4	-1369					3.00	7.68		Breakdown
v_S=1.5×10^5 m/s									
1	-1036	0.055	1.31	6.96	68.7	0.00	0.00	3.00	N
2	-1105	0.08	2.20	14.59	77.4	0.28	1.90	2.72	N
3	-1201	0.10	2.72	55.32	92.1	0.86	3.22	2.14	Y
4	-1291					3.00	12.35	0.00	Breakdown

Table 7
The comparison between the simulation results and the experimental results under the assumption that E_S=450 kV/m, τ=25 μC/m

Parameters	Simulation results	Experimental results (He et al., 2012)	Unit	Error (%)
		v_S=1×10^5 m/s		
V_{ini}	-1036	-1052.00	kV	-1.5
l_{SM}	2.72	2.30	m	18.3
l_F	2.09	2.30	m	-9.1
v_L	2.43	2.20	×10^4 m/s	10.5
T_d	36.3	29.7	μs	22.2
$V_{50\%}$	-1369	-1365.00	kV	0.3
		v_S=1.5×10^5 m/s		
V_{ini}	-1036	-1052.00	kV	-1.5
l_{SM}	2.72	2.30	m	18.3
l_F	2.14	2.30	m	-7.0
v_L	2.56	2.20	×10^4 m/s	16.4
T_d	23.4	29.7	μs	21.2
$V_{50\%}$	-1291	-1365.00	kV	-5.4

DISCUSSION

The leader discharge develops in a stepwise fashion. The electric field after the streamer discharge is a quasi-static electric field at each stage. Therefore, FEM is a suitable and effective method to investigate the electric field distribution in the air gap at each stage of the leader development. The electric field in the streamer zone is constant so that the discharge parameters for each stage of leader propagation can be easily calculated using FEM-VDM. The above simulation process shows that FEM-VDM can simulate the dynamic process of positive leader discharge without complex physical calculations. However, the validity of the simulation model depends on a reasonable assumption of initial parameters, such as charge density τ of the leader channel, streamer voltage gradient E_S, and streamer velocity v_S. This model successfully predicted the leader onset and breakdown voltage with small errors (Table 6). The leader velocity, the largest streamer length, and the discharge duration are close to the experiment results. It shows that the value of 450 kV/m for the voltage gradient of the streamer is suitable, which is consistent with the recent studies by Tao et al. (2022), Zixin et al. (2020), and Ping et al. (2022).

However, it should be pointed out that this model cannot accurately predict the macro parameters of leader discharge under any gap length or any electrode structure, such as breakdown voltage, leader velocity, and leader length, because the development speed of the streamer and the charge density of the leader channel are not the same for different electrode structures and different gaps (Gu et al., 2010, 2012; He et al., 2012). Different initial parameters should be matched according to different model structures when doing

simulation research. It is also a research direction in the leader discharge simulation research. The main contribution of this study is that it demonstrated that FEM-VDM could simulate the dynamic process of the leader discharge, which provides a new method for research in this field. Compared with the traditional CSM model, such as those proposed by Bondiou & Gallimberti (1994), Goelian et al. (1997), and Becerra and Cooray (2006a), FEM does not require the configuration of complex charge simulation systems and the writing of complex computer programs, thereby making the calculation process simple and efficient.

CONCLUSION

A simplified self-consistent numerical model used to simulate the dynamic process of positive leader discharge in an inverted rod-plane gap was modeled based on FEM and VDM. The voltage distortion coefficient K_Q used to calculate the streamer length and space charge was analyzed. The physical dynamic process of the positive leader discharge was simulated with the help of COMSOL Multiphysics and MATLAB co-simulation technology. The simulation results are in good agreement with the experimental results. This model is based on FEM, which can deal with arbitrary electrode configurations and complex boundary conditions. In addition, the calculation process of the model is simple without complex multiphysics computing. The above advantages make the model capable of conducting leader discharge simulation under any complex electrode configuration and arbitrary boundary conditions without simplifying the model structure, which makes the model more flexible in engineering applications than traditional CSM models, such as those proposed by Bondiou and Gallimberti (1994), Goelian et al. (1997) and Becerra and Cooray (2006a).

ACKNOWLEDGMENT

The authors thank Universiti Putra Malaysia, Malaysia, for the research funding provided for this study under the GP-IPB scheme (GP-IPB/2022/9717001) for the financial support of this research.

REFERENCES

Arevalo, L., Cooray, V., Wu, D., & Jacobson, B. (2012). A new static calculation of the streamer region for long spark gaps. *Journal of Electrostatics*, *70*(1), 15-19. https://doi.org/10.1016/j.elstat.2011.07.013

Becerra, M. (2013). Glow corona generation and streamer inception at the tip of grounded objects during thunderstorms: Revisited. *Journal of Physics D: Applied Physics*, *46*(13), Article 135205. https://doi.org/10.1088/0022-3727/46/13/135205

Becerra, M., & Cooray, V. (2006a). A simplified physical model to determine the lightning upward connecting leader inception. *IEEE Transactions on Power Delivery*, *21*(2), 897-908. https://doi.org/10.1109/TPWRD.2005.859290

Becerra, M., & Cooray, V. (2006b). A self-consistent upward leader propagation model. *Journal of Physics D: Applied Physics*, *39*(16), 3708-3715. https://doi.org/10.1088/0022-3727/39/16/028

Bondiou, A., & Gallimberti, I. (1994). Theoretical modelling of the development of the positive spark in long gaps. *Journal of Physics D: Applied Physics*, *27*(6), 1252-1266. https://doi.org/10.1088/0022-3727/27/6/024

Brezmes, A. O., & Breitkopf, C. (2014). Simulation of inductively coupled plasma with applied bias voltage using COMSOL. *Vacuum*, *109*, 52-60. https://doi.org/10.1016/j.vacuum.2014.06.012

Chen, S., He, H., Zou, Y., He, J., & Chen, W. (2016, September 19-22). *Simulation of corona space charge generated from the ±800kV UHVDC overhead transmission line in a thunderstorm*. [Paper presentation]. 2016 IEEE International Conference on High Voltage Engineering and Application (ICHVE), Chengdu, China. https://doi.org/10.1109/ICHVE.2016.7800706

Cigre, W. G. (2021). *Procedures for Estimating the Lightning Performance of Transmission Lines – New Aspects*. CIGRE.

Cooray, V. (2014). *The Lightning Flash* (2nd ed.). Institution of Engineering and Technology.

Diaz, O., Cooray, V., & Arevalo, L. (2018). Numerical modeling of electrical discharges in long air gaps tested with positive switching impulses. *IEEE Transactions on Plasma Science*, *46*(3), 611-621. https://doi.org/10.1109/TPS.2018.2802039

Ding, Y., Lv, F., Zhang, Z., Liu, C., Geng, J., & Xie, Q. (2016). Discharge Simulation of typical air gap considering dynamic boundary and charge accumulation. *IEEE Transactions on Plasma Science*, *44*(11), 2615-2621. https://doi.org/10.1109/TPS.2016.2600179

El-Zein, A., Talaat, M., & Samir, A. (2018). Positive streamer in gases: Physical approach from low to high energies. *Vacuum*, *156*, 469-474. https://doi.org/10.1016/j.vacuum.2018.07.051

Gallimberti, I., Bacchiega, G., Bondiou-Clergerie, A., & Lalande, P. (2002). Fundamental processes in long air gap discharges. *Comptes Rendus Physique*, *3*(10), 1335-1359. https://doi.org/10.1016/S1631-0705(02)01414-7

Gao, J., Wang, L., Li, G., Fang, Y., Song, B., Xiao, B., & Liu, K. (2020). Discharge of air gaps during ground potential live-line work on transmission lines. *Electric Power Systems Research*, *187*, Article 106519. https://doi.org/10.1016/j.epsr.2020.106519

Goelian, N., Lalande, P., Bondiou-Clergerie, A., Bacchiega, G. L., Gazzani, A., & Gallimberti, I. (1997). A simplified model for the simulation of positive-spark development in long air gaps. *Journal of Physics D: Applied Physics*, *30*(17), 2441-2452. https://doi.org/10.1088/0022-3727/30/17/010

Gu, J., He, K., Yu, H., Chen, W., Bian, K., & Shi, W. (2020, September 6-10). *Effect of space charge on lightning shielding performance of UHVDC transmission line under lightning downward leader.* [Paper presentation]. 2020 IEEE International Conference on High Voltage Engineering and Application (ICHVE), Beijing, China. https://doi.org/10.1109/ICHVE49031.2020.9279506

Gu, S., Chen, W., Chen, J., He, H., & Qian, G. (2010). Observation of the streamer–leader propagation processes of long air-gap positive discharges. *IEEE Transactions on Plasma Science*, *38*(2), 214-217. https://doi.org/10.1109/TPS.2009.2037004

Gu, S., Xiang, N., Chen, J., He, H., Xie, S., & Chen, W. (2012, September 2-7). *Observation of 3m rod-rod discharges under switching impulse voltage*. [Paper presentation]. 2012 International Conference on Lightning Protection (ICLP), Vienna, Australia. https://doi.org/ 0.1109/ICLP.2012.6344360

He, H., He, J., Chen, W., Xie, S., Xiang, N., Chen, J., & Gu, S. (2012). Comparison of positive leader propagation in rod–plane and inverted rod-plane gaps. *IEEE Transactions on Plasma Science*, *40*(1), 22-28. https://doi.org/ 10.1109/TPS.2011.2172002

Hnatiuc, B., Sabau, A., & Astanei, D. (2019). Classic spark simulation using COMSOL software. *IOP Conference Series: Materials Science and Engineering*, *591*, Article 012050. https://doi.org/10.1088/1757-899X/591/1/012050

Lalande, P., Bondiou-Clergerie, A., Bacchiega, G., & Gallimberti, I. (2002). Observations and modeling of lightning leaders. *Comptes Rendus Physique*, *3*(10), 1375-1392. https://doi.org/10.1016/S1631-0705(02)01413-5

Les Renardières Group. (1973). *Research on Long Air Gap Discharges at Les Renardières*. https://e-cigre.org/publication/ELT_023_3-research-on-long-air-gap-discharges-at-les-renardieres

Les Renardières Group. (1974). *Research on Long Air Gap Discharges at Les Renardières:1973 Results*. https://e-cigre.org/publication/ELT_023_3-research-on-long-air-gap-discharges-at-les-renardieres

Li, Z., Zeng, R., Yu, Z., Chen, S., Liao, Y., & Li, R. (2013). Research on the upward leader emerging from transmission line by laboratory experiments. *Electric Power Systems Research*, *94*, 64-70. https://doi.org/10.1016/j.epsr.2012.05.016

Mohammadi, R., Vahidi, B., & Rahiminejad, A. (2019). Estimation of HVDC transmission lines shielding failure using LPM method and an adapted SLIM model. *IET Science, Measurement & Technology*, *13*(9), 1345-1351. https://doi.org/10.1049/iet-smt.2018.5180

Naidu, M. S., & Kamaraju, V. (2013). *High voltage engineering*. McGraw-Hill Education (India) Pte Ltd.

Nijdam, S., Teunissen, J., & Ebert, U. (2020). The physics of streamer discharge phenomena. *Plasma Sources Science and Technology*, *29*(10), Article 103001. https://doi.org/10.1088/1361-6595/abaa05

Petrov, N. I., & Waters, R. T. (2021). Lightning to earthed structures: Striking distance variation with stroke polarity, structure geometry and altitude based on a theoretical approach. *Journal of Electrostatics*, *112*, Article 103599. https://doi.org/10.1016/j.elstat.2021.103599

Ping, W., Yaxi, C., Xiuyuan, Y., Yujian, D., Jianghai, G., Fangcheng, L., Ling, J., & Weidong, S. (2022). Transformation characteristics of large-size ball-plate gap discharge under positive polarity operating impact at an altitude of 2200m. *Chinese Journal of Electrical Engineering,* 1-11. Advance online publication. https://kns.cnki.net/kcms/detail/11.2107.TM.20220708.1730.031.html

Rizk, F. A. M. (1989). A model for switching impulse leader inception and breakdown of long air-gaps. *IEEE Transactions on Power Delivery*, *4*(1), 596-606. https://doi.org/10.1109/61.19251

Rizk, F. A. M. (2009). Modeling of proximity effect on positive leader inception and breakdown of long air gaps. *IEEE Transactions on Power Delivery*, *24*(4), 2311-2318. https://doi.org/10.1109/TPWRD.2009.2027494

Rizk, F. A. M. (2020). New approach for assessment of positive streamer penetration of long air gaps under impulse voltages. *IEEE Transactions on Dielectrics and Electrical Insulation*, *27*(3), 791-798. https://doi.org/10.1109/TDEI.2020.008588

Rodrigues, E., Pontes, R., Bandeira, J., & Aguiar, V. (2019). Analysis of the incidence of direct lightning over a HVDC transmission line through EFD model. *Energies*, *12*(3), Article 555. https://doi.org/10.3390/en12030555

Talaat, M., El-Zein, A., & Samir, A. (2019). Numerical and simulation model of the streamer inception at atmospheric pressure under the effect of a non-uniform electric field. *Vacuum*, *160*, 197-204. https://doi.org/10.1016/j.vacuum.2018.11.037

Tao, Y., Xiaotian, W., Wenxia, S., & Ming, Y. (2022). Space charge criterion of the initial streamer for the stable inception of positive upleader under lightning strikes. *Chinese Journal of Electrical Engineering*, 1-13. Advance online publication. https://kns.cnki.net/kcms/detail/11.2107.tm.20220419.1016.004.html

Wang, X., He, J., Yu, Z., Zeng, R., & Rachidi, F. (2016). Influence of ground wire on the initiation of upward leader from 110 to 1000 kV AC phase line. *Electric Power Systems Research*, *130*, 103-112. https://doi.org/10.1016/j.epsr.2015.08.022

Xu, Y., & Chen, M. (2013). A 3-D self-organized leader propagation model and its engineering approximation for lightning protection analysis. *IEEE Transactions on Power Delivery*, *28*(4), 2342-2355. https://doi.org/10.1109/TPWRD.2013.2263846

Yang, N., Zhang, Q., Hou, W., & Wen, Y. (2017). Analysis of the lightning-attractive radius for wind turbines considering the developing process of positive attachment leader: Attractive radius for wind turbines. *Journal of Geophysical Research: Atmospheres*, *122*(6), 3481-3491. https://doi.org/10.1002/2016JD026073

Zeng, R., Li, Z., Yu, Z., Zhuang, C., & He, J. (2013). Study on the influence of the dc voltage on the upward leader emerging from a transmission line. *IEEE Transactions on Power Delivery*, *28*(3), 1674-1681. https://doi.org/10.1109/TPWRD.2013.2252371

Zhou, Q., Liu, C., Bian, X., Lo, K. L., & Li, D. (2018). Numerical analysis of lightning attachment to wind turbine blade. *Renewable Energy*, *116*, 584-593. https://doi.org/10.1016/j.renene.2017.09.086

Zixin, G., Qingmin, L., Wanshui, Y., Hongbo, L., Li, Z., & Wah Hoon, S. (2020). The dynamic critical length criterion of initial streamer for the stable upward leader inception under negative lightning strikes. *Proceedings of the CSEE*, *40*(5), 1713-1721. https://doi.org/10.13334/j.0258-8013.pcsee.190881

REFEREES FOR THE PERTANIKA
JOURNAL OF SCIENCE & TECHNOLOGY

Vol. 31 (4) Jul. 2023

The Editorial Board of the Pertanika Journal of Science and Technology wishes to thank the following:

Adam Glowacz
(AGH University of Science, Poland)

Adnan Ashraf
(MUET, Pakistan)

Afaq Ahmad
(UET, Pakistan)

Ahmad Farid Abu Bakar
(UM, Malaysia)

Ahmad Sofiman Othman
(USM, Malaysia)

Amirah Amalina Ahmad Tarmizi
(UiTM, Malaysia)

Amnorzahira Amir
(UiTM, Malaysia)

Angel de Jesus Mc Namara Valdes
(CIIEMAD, Maxico)

Arjulizan Rusli
(USM, Malaysia)

Asiah Mohd Nor
(UiTM, Malaysia)

Aweng Eh Rak
(UMK, Malaysia)

Azura Ishak
(UKM, Malaysia)

Bambang Karsono
(UNIMAS, Malaysia)

Behnam Talaee
(BNUT, Iran)

Dhariwal Sandeep
(Alliance University, India)

Dian Darina Indah Daruis
(UPNM, Malaysia)

Elysha Nur Ismail
(UPM, Malaysia)

Fadhilah Mat Yamin
(UUM, Malaysia)

Fairuz Izzuddin Romli
(UPM, Malaysia)

Farzaneh Mohamadpour
(USB, Iran)

Gabriele Ruth Anisah Froemming
(UNIMAS, Malaysia)

Ghasan Fahim Huseien
(NUS, Singapore)

Hasnuri Mat Hassan
(USM, Malaysia)

Hazrul Abdul Hamid
(USM, Malaysia)

Jamarosliza Jamaluddin
(UTM, Malaysia)

Jeevan Kanesan
(UM, Malaysia)

Khuzaimah Zailani
(UPM, Malaysia)

Kiki Adi Kurnia
(ITB, Indonesia)

Leticia Sarmento dos Muchangos
(Osaka University, Japan)

Lim Wei Jer
(Southern University College, Malaysia)

Loh Kar Hoe
(UM, Malaysia)

Mark Lee Wun Fui
(UTM, Malaysia)

Mohamad Hasnul Bolhassan
(UNIMAS, Malaysia)

Mohammad Khoveyni
(Islamic Azad University, Iran)

Mohan Reddy Moola
(Curtin University, Malaysia)

Mohd Azlis Sani Md Jalil
(UTHM, Malaysia)

Mohd Bijarimi Mat Piah
(UMP, Malaysia)

Mohd Shahrul Nizam Mohd Danuri
(KUIS, Malaysia)

Muhammad Imran Tariq
(Superior University, Pakistan)

Muhammad Nadzir Marsono
(UTM, Malaysia)

Noazzizi Nordin
(USM, Malaysia)

Noor Hidayah Zakaria
(UTM, Malaysia)

AYBU	*– Ankara Yıldırım Beyazıt Üniversitesi*
BNUT	*– Babol Noshirvani University of Technology*
CIIEMAD	*– Centro Interdisciplinario de Investigaciones y Estudios sobre Medio Ambiente y Desarrollo*
MUET	*– Mehran University of Engineering and Technology*
NGBTC	*– Nandalal Ghosh B.T. College*
NUS	*– National University of Singapore*
STU	*– Slovak University of Technology*
TAMU	*– Texas A&M University*
UET	*– University of engineering and technology Taxila*
UFPE	*– Universidade Federal de Pernambuco*
UiTM	*– Universiti Teknologi MARA*
UKM	*– Universiti Kebangsaan Malaysia*
UM	*– Universiti Malaya*
UMK	*– Universiti Malaysia Kelantan*
UMP	*– Universiti Malaysia Pahang*
UNIB	*– Universidade Internacional Iberoamericana*
UNIMAP	*– Universiti Malaysia Perlis*
UNIMAS	*– Universiti Malaysia Sarawak*
UNITEN	*– Universiti Tenaga Nasional*
UPM	*– Universiti Putra Malaysia*
UPNM	*– Universiti Pertahanan Nasional Malaysia*
USB	*– University of Sistan & Baluchestan*
USM	*– Universiti Sains Malaysia*
UTeM	*– Universiti Teknikal Malaysia Melaka*
UTHM	*– Universiti Tun Hussein Onn Malaysia*
UTM	*– Universiti Teknologi Malaysia*
UUM	*– Universiti Utara Malaysia*

While every effort has been made to include a complete list of referees for the period stated above, however if any name(s) have been omitted unintentionally or spelt incorrectly, please notify the Chief Executive Editor, *Pertanika* Journals at executive_editor.pertanika@upm.edu.my

Any inclusion or exclusion of name(s) on this page does not commit the *Pertanika* Editorial Office, nor the UPM Press or the university to provide any liability for whatsoever reason.

Pertanika Journal of Science & Technology
Vol. 31 (4) Jul. 2023

Content

Pertanika Editorial Office, Journal Division,
Putra Science Park,
1st Floor, IDEA Tower II,
UPM-MTDC Center,
Universiti Putra Malaysia,
43400 UPM Serdang,
Selangor Darul Ehsan
Malaysia

http://www.pertanika.upm.edu.my
Email: executive_editor.pertanika@upm.edu.my
Tel. No.: +603- 9769 1622

PENERBIT UPM PRESS

http://www.penerbit.upm.edu.my
Email: penerbit@upm.edu.my
Tel. No.: +603- 9769 8851

ISSN 0128-7680
07 >
9 770128 768083